PROCEEDINGS

FIRST INTERNATIONAL CONFERENCE ON ADVANCED MATERIALS AND PROCESS ENGINEERING (AMPE)

14TH-15TH DECEMBER 2015

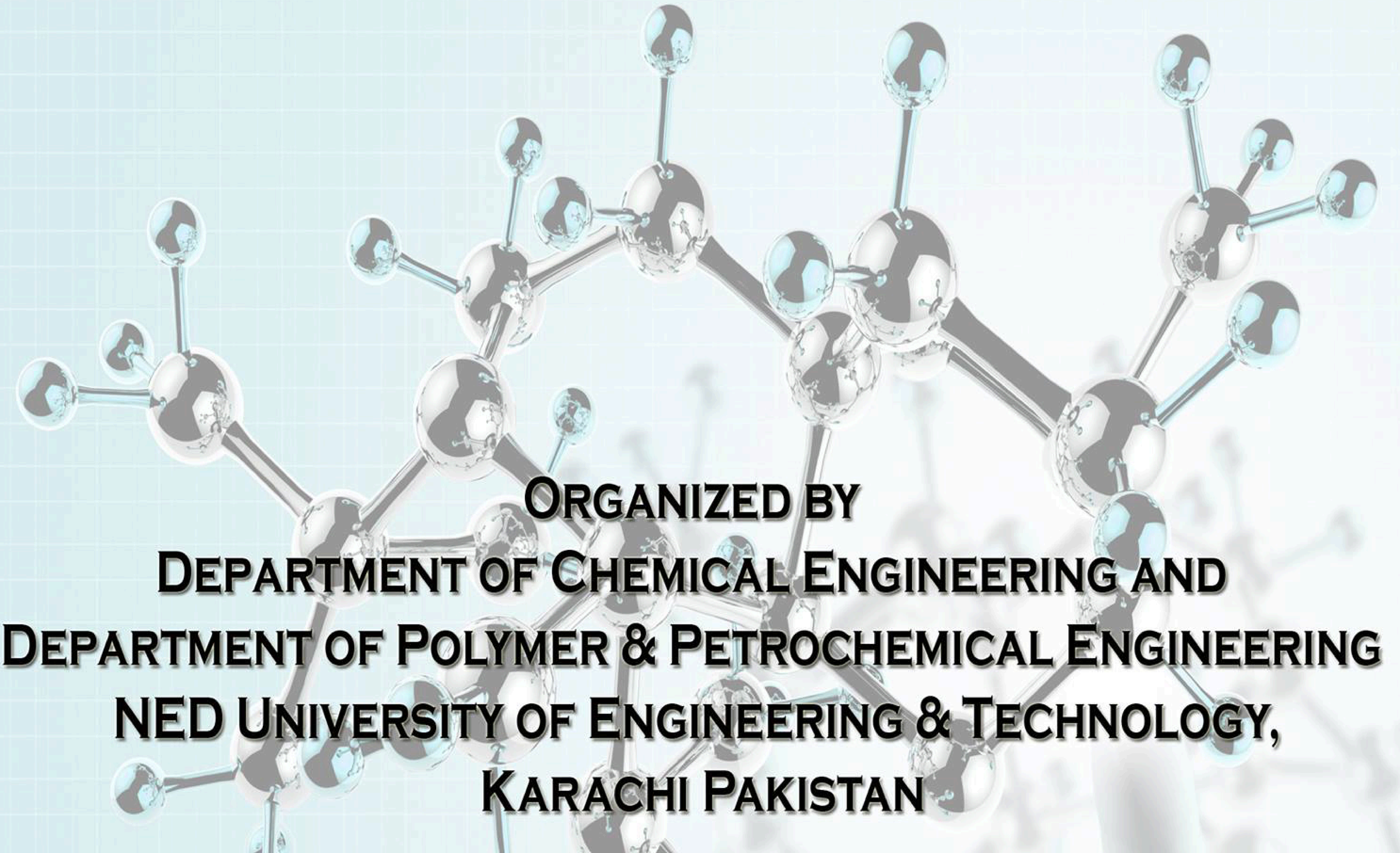

ORGANIZED BY
DEPARTMENT OF CHEMICAL ENGINEERING AND
DEPARTMENT OF POLYMER & PETROCHEMICAL ENGINEERING
NED UNIVERSITY OF ENGINEERING & TECHNOLOGY,
KARACHI PAKISTAN

SPONSERS

GENERAL TYRE

ICI PAKISTAN

BASF
The Chemical Company

REMEMBER
A1
A MARK OF QUALITY

PPL
Pakistan Petroleum Limited

SAFETY TRENDS

Saima
Group

engro corp

PAKISTAN PLASTIC MANUFACTURERS ASSOCIATION
PAKPLAS

HEC

TECHNOLOGY LINKS

ChemTech

CONFERENCE PROGRAM – 2015

Day – 1: 14th December, 2015

INAUGURAL SESSION

08:30 – 09:45 hours	Registrations
10:00 – 10:05 hours	Recitation of Holy Quran
10:05 – 10:10 hours	National Anthem
10:10 – 10:20 hours	Inaugural address by The Vice Chancellor (Prof. Dr. Muhammad Afzal Haque)
10:20 – 10:40 hours	Keynote Speech (Prof. Dr. Ikram Ul Haq, Australia)
10:40 – 11:00 hours	Welcome address by Dean (CPE) (Prof. Dr. Muhammad Tufail)
10:40 – 11:00 hours	Vote of Thanks by Conference Secretary (Dr. Zahoor ul Hussain Awan)

11:00 – 11:30 hours Refreshment

Technical Session –I

11:30 – 13:10 hours **Advanced Materials**

05 presentations (20 minutes each)

Chair : Dr. Ikram ul Haq **Co-Chair : Dr. Rafiq Ahmed**

Study on morphology, thermal, and mechanical properties of electrospun PVA/Wood flour nanofibrous composites (KEYNOTE SPEECH) Ghaus Rizvi, Sheikh Rasel
Department of Automotive, Mechanical and Manufacturing Engineering,
University of Ontario Institute of Technology,Simcoe Street North Oshawa, Ontario, Canada

Coating of transparent and conducting graphene film when wrapped with DMF doped PEDOT:PSS
Adila Rani, Min Park , Jung Hoon
Polymer Hybrid Center, Korea Institute of Science and Technology, Republic of Korea University of Science and Technology, Dejeon, Republic of Korea
NOROO Holding, Republic of Korea
Ewha Womans University, Republic of Korea.

Sensitivity Analysis of Thar Coal Gasification Using Steam
Fahim Uddin, Inayatullah Memon and Syed Ali Ammar Taqvi
Chemical Engineering Department, Universiti Teknologi PETRONAS,Bandar Seri Iskandar, Perak Darul Ridzuan, Malaysia.
Chemical Engineering Department, NED University of Engineering & Technology, Karachi, Pakistan

Carbon Nanotubes laced Superabsorbent Hybrid Polymer for Enhanced Oil Recovery Technology
Saud Hashmi, **Muhammad Mohsin**.
Chemical Engineering Department, NED University of Engineering & Technology, Karachi, Pakistan.

Synthesis and characterization Bentonite composite with emphasis on its Swelling behavior and adsorption efficiency for selected Heavy Metals
Mahmood Khattak, Ghazala Abid, Mahmood Iqbal, Kausar Ali Syed , Manzoor Iqbal, Muhammad Aijaz, Inayat-Ur-Rehman, Tanveer ul Hassan Shah.
Institute of Chemical Science, University of Peshawar

Department of Polymer & Petrochemical Engineering, NED University of Engineering & Technology, Karachi, Pakistan.
PCSIR labs Complex, University Road Karachi Pakistan.

13:10 – 14:00 hours Lunch and Prayers break

Technical Session –II

14:00 – 16:00 hours Polymers and Nanocomposites
05 presentations (20 minutes each)

Chair : Prof. Dr. Kausar Ali Syed Co-Chair : Prof. Dr. Syed Amir Iqbal

Enhanced Mechanical Properties of Organo-clay based UHMWPE nanocomposite Films
Rafiq Ahmed, Kausar Ali Syed, Asra Shabbir, Maria Idrees, Maryam Ansari, Iqra Majeed,
Polymer & Petrochemical Engineering Department, NED University of Engineering & Technology, Karachi, Pakistan

Study on the Effects of Epoxy Resin based PDLC Films using Triethanolamine (TEA) as catalyst
Mujtaba Ellahi, Muhammad Yasir Rafique, Abdul Qadir and Muhammad Furqan Ali
Department of Physics, Comsats Institute of Information Technology, Punjab .Pakistan
Department of Electrical Engineering, Sukkur Institute of Business Administration
State Key Laboratory of Chemical Resource Engineering, Beijing University of Chemical Technology, Beijing P.R.China.

Soft Drink Tins as Fiber Reinforcement in Concrete.
Uroosa Iqbal, Muhammmad Akram, Abdullah Saand
Structural Engineering Department, Mehran University of Engineering & Technology, Jamshoro, Pakistan
Civil Engineering Department, Quaid-e-Awam University of Engineering Science and Technology, Nawabshah, Pakistan.

Synthesis of Super-Absorbent Polymer (SAP) via Industrially Preferred Route
Rafiq Ahmed , M. Qaiser, S.M. Shujaat, **Waqar Ahmed**, M. Tahir, S. Imran Ali
Polymer & Petrochemical Engineering Department, NED University of Engineering & Technology, Karachi, Pakistan
Department of Applied Chemistry & Chemical Technology, University of Karachi – 75270

Synthesis and Characterization of Copper Nanoparticles
Ayesha Ikram, Humair Ahmed Siddiqui, Saqib Anjum, Ashraf Ali
Physics Department, NED University of Engineering & Technology, Karachi.
Material Engineering Department, NED University of Engineering & Technology, Karachi.
Ghulam Ishaq Khan Institute of Engineering Sciences and Technology, Topi, KPK

16:00 – 16:20 hours Refreshment

Technical Session –III

16:20 – 18:00 hours Process Modeling & Simulation – I
05 presentations (20 minutes each)

Chair : Prof. Dr. Inayat Ullah Memon Co-Chair : Dr. Sohail Hanif

Simulation of Coal Slurry Burner Using Fluent
Nadia Khan, Alia Ahrar and Sumera Rehman

Polymer and Petrochemical Engineering Department, NED University of Engineering & Technology, Karachi, Pakistan
Chemical Engineering Department, NED University of Engineering & Technology, Karachi, Pakistan
ENGRO polymer and chemicals limited, Karachi, Pakistan.

Analysis of Electromagnetic Wave Propagation through Photonic Crystal Fibers
Muhammad Imran Aslam, Irfan Ahmed, **Shafaq Mustafa**
Department of Electronic Engineering, NED University of Engineering and Technology, Karachi, Pakistan.
Emerging Technologies Research Group, NED University of Engineering and Technology, University Road, Karachi, Pakistan

Numerical Investigation of the Effect of Thermal Conductivity and Porosity of Gas Diffusion Layer on Performance of PEMFC
Obaid ur Rehman, Syed Mushahid Hussain Hashmi and Inayat Ullah Memon
Chemical Engineering Department, University of Karachi, Karachi, Pakistan
Automotive and Marine Engineering Department, NED University of Engineering & Technology, Karachi, Pakistan
Chemical Engineering Department, NED University of Engineering & Technology, Karachi, Pakistan

MHD Maxwell Fluid Over an Oscillating Plane
Kashif Ali Abro
Department of Basic Sciences and Related Studies, Mehran University of Engineering and Technology, Jamshoro Pakistan.

Technical Session –III (Seminar Hall)

16:20 – 18:00 hours Process Industry (Problems and Solutions)
05 presentations (20 minutes each)

Chair : Muhammad Ali Ansari Co-Chair : Dr. Mahmood Khattak

Hydrometallurgical extraction of Zinc from Indigenous Electric Arc Furnace Dust
Junaid Saleem, Zeeshan A. Hameed, Hira Lal, Syed Sajid Hussain, **Ahsan Abdul Ghani**
Department of Quality Assurance, Peoples Steel Mills Ltd., Karachi, Pakistan
Department of Chemical Engineering, University of Karachi, Karachi, Pakistan.

Boiler Feed Water Failure And High Temperature Shift Convertor's Bottom Flooding-Engro's Unique Experience And Innovative Solution
Muhammad Zaghum Riaz, Ali Javed Akhter, **Sara Ahsan**
Engro Fertilizers Limited Sindh, Pakistan

Implementation of Risk Based Inspection (RBI) Methodology in Process Industry
Mobin Ahmed, Muzaffar Hussain
National Refinery Limited Karachi, Pakistan

Improvisations to Decrease Startup Failure Frequency and Environmental Pollution in Urea Plant
Naveed Raza, and Ali Ayub
Engro Fertilizers Limited, Daharki, Pakistan

Trends and Future Perspectives in Additive Manufacturing
Shaheen Perween, Muhammad Fahad, Maqsood Ahmed Khan
Department of Industrial and Manufacturing Engineering, NED University of Engineering and Technology, Karachi, Pakistan.

CONFERENCE PROGRAM – 2015

Day – 2: 15th December, 2015

Technical Session –IV

09:00 – 10:40 hours **Energy and Environment**

05 presentations (20 minutes each)

Chair : Prof. Dr. Muhammad Tufail Co-Chair : Dr. Umair Alam

Production of Methane from Municipal Solid Waste (MSW)
Saud Hashmi, **Muhammad Danish**, Raheel Alavi, Aly Ismail, Ayesha Munir
Chemical Engineering Department, NED University of Engineering & Technology, Karachi, Pakistan.

Liquid Fuel Production By Co-Pyrolysis Of Waste Cooking Oil And Waste Engine Oil
Sajid Muhbat, Tufail M., Aniqa Saleem, Kainat Amin Ismail Bora, Sheheryar Arshad, Hafiz Amin-Ur Rehman, Saud Hashmi, Awan Zahoor.
Chemical Engineering Department, NED University of Engineering & Technology, Karachi, Pakistan

Synthesis of Iron Oxide Magnetic Nanoparticle by Sol-Gel Method and their Characterization.
Maria Arshad, Humair Ahmed Siddiqui, Saqib Anjum, Ashraf Ali
Physics Department, NED University of Engineering & Technology, Karachi.
Material Engineering Department, NED University of Engineering & Technology, Karachi.
Ghulam Ishaq Khan Institute of Engineering Sciences and Technology, Topi, KPK.

Synthesis and Rheology of Coal-Water Slurry for used as liquid Fuel
Aliya Ahrar, **Nadia Khan**, Awan Zahoor and Saud Hashmi.
Chemical Engineering Department, NED University of Engineering & Technology, Karachi, Pakistan

10:40 – 11:30 hours Tea Break & Poster Presentation

Technical Session –V

11:30 – 13:10 hours **Process Modeling & Simulation – II**

05 presentations (20 minutes each)

Chair : Prof. Dr. Mubashir Ali Siddiqui Co-Chair : Dr. Syed Imran Ali

Numerical simulation and mathematical modelling in coordination with experimental investigation of process parameters associated with the Fischer Tropsch fixed bed reactor performance
Shahid Hussain Ansari, D. Hildebrandt and X Liu
Materials and Process Synthesis (MaPS), University of South Africa (UNISA), South Africa

Near-Perfect Metamaterial Absorber for the Visible Spectrum
Syed Asad Ali Shah, Muhammad Imran Aslam, Irfan Ahmed, Syed M. Usman Ali
Department of Electronic Engineering, NED University of Engineering and Technology, Karachi, Pakistan.
Emerging Technologies Research Group, NED University of Engineering and Technology, Karachi, Pakistan.

Modeling of Bainitic phase transformation in Fe-Mn-Si-C Alloy
Asjad Mazahir, **Talha Mahfooz**, Muhammad Samiuddin
Pakistan Institute of Engineering & Applied Sciences (PIEAS), Pakistan.

Modelling for improving efficiency of Nano solar cell energy conversion
Allahrakhio Junejo, Shahzad.Memon
Sindh University Jamshoro Pakistan

Design of Solar Concentrated Linear Parabolic Trough Collector with Simulations Using Different Thermal Fluids
Naveed ur Rehman, Bilal Baloch, Jasir. Jawad, Zeeshan Uddin. Sheikh, Zohair. Aijaz
Mechanical Engineering Department, NED University of Engineering & Technology, Karachi, Pakistan
Chemical Engineering Department, NED University of Engineering & Technology, Karachi, Pakistan.

13:10 – 14:00 hours Lunch & Prayers

Technical Session –V (Parallel Session) at CIS Auditorium

11:30 – 13:00 **05** presentations (20 minutes each)

Chemical Processes – I

Chair : Prof. Dr. Khursheed Mahmood Co-Chair : Dr. Humaira Athar

Simultaneous Determination Of Alprazolam With Antihistamine In Bulk Drug And Pharmaceutical Formulations By Liquid Chromatography
Syed Akram , Saeeda Nadir Ali, Amtul. Qayoom , Inayat Ullah Memon and **Nida Naz**
Department of Chemistry, NED University of Engineering & Technology, Karachi, Pakistan
Department of Chemical Engineering, NED University of Engineering & Technology, Karachi, Pakistan.

Development & Characterization of Novel Antimicrobial Alginate Fibers for Woundcare Applications
Muhammad Umar, Tahir Hussain, Rashid Masood
National Textile Research Centre, National Textile University, Faisalabad, Pakistan
Faculty of Engineering and Technology, National Textile University, Faisalabad, Pakistan.

Improving Different Parameters Of Transformer Oil From Pakistan National Refinery Limited
Amtul Qayoom, Tariq Ali, Ghazanfar Hussain, Syed **Wajid Hussain**.
Department of Industrial Chemistry, NED University of Engineering and Technology, Karachi, Pakistan

Exact Solution of Fractionalized MHD Maxwell Fluid
Muhammad Jamil, Muhammad Nasir Ansari, Muhammad Jawed Iqbal
Department of Mathematics, NED University of Engineering and Technology, Karachi, Pakistan
Institute of Space and Planetary Astrophysics, University of Karachi.

Synthesis and Characterization of Anatase Titanium Dioxide Nanoparticles By Sol-Gel Method
Sidra Jamil Ahmed, Humair Ahmed Siddiqui, Saqib Anjum, Ashraf Ali
Physics Department, NED University of Engineering & Technology, Karachi.
Material Engineering Department, NED University of Engineering & Technology, Karachi.
Ghulam Ishaq Khan Institute of Engineering Sciences and Technology, Topi, KPK

13:10 – 14:00 hours Lunch & Prayers

Technical Session –VI

14:00 – 15:20

Chemical Processes – II

04 presentations (20 minutes each)

Chair : Dr. Ghaus Rizvi Co-Chair : Dr. Saud Hashmi

Validation of Temperature Sensitivity of Superhydrophobic Surfaces as Applied on 316 LSS
Hamza Shams, Sajid Saleem and Bilal A. Siddiqui
National University of Sciences and Technology (NUST), Islamabad, Pakistan DHA Suffa University (DSU), Karachi, Pakistan.

Characterization of Fluorspar for metallurgical slag making application
Junaid Saleem, **Zeeshan A. Hameed**, Hira Lal, Syed Sajid Hussain, Ahsan Abdul Ghani.
Department of Quality Assurance, Peoples Steel Mills Ltd., Karachi, Pakistan
Department of Chemical Engineering, University of Karachi, Karachi, Pakistan.

Boiler Feed Water Treatment Through Ion-Exchange Technology-Design And Testing
Mariam Sohail, **Syed A. Taqvi**
Chemical Engineering Department, NED University of Engineering & Technology, Karachi, Pakistan
Chemical Engineering Department, Universiti Teknologi PETRONAS, 32610 Bandar Seri Iskandar, Perak Darul Ridzuan, Malaysia

15:20 – 15:35 hours	Concluding Session
15:35 – 16:00 hours	Refreshments

Poster presentations

P-01: Helical flows of a fractionalized second grad fluid through a circular cylinder.
Iftikhar Ahmed, Muhammad Jamil
Department of Mathematics, NED University of Engineering and Technology, Karachi- Pakistan.

P-02: Effect of MHD on fractionalized Maxwell fluid between coaxial cylinders
Vijay Kumar, Muhammad Jamil.
Department of Mathematics, NED University of Engineering and Technology, Karachi- Pakistan.

P-03: Production of Biogas from Small-Scale Bio-Digester by Utilizing Blend of Cow Dung and Sludge Water.
Waqar Ahmed, Danish Lakhani, AhmedUllah Mazullah, Raheel Perwaiz, Muhammad Saqib Soherwerdy.
Chemical Engineering Department, NED University of Engineering & Technology, Karachi, Pakistan.

P-04: New exact solutions of MHD second grade fluid through the moving porous cylindrical domain.
Muhammad Zafarullah, Muhammad Jamil
DJ Sindh Govt Science College Karachi, Pakistan
Department of Mathematics, NED University of Engineering and Technology, Karachi- Pakistan.

P-05: To Develop a Laboratory Scale Equipment For The Extraction of Magnesium Particles (Pak-Tech Process)
Muhammad Samiuddin, Farhan Iqbal, Hafiz Muhammad Arqum Saleem, Alina Aziz, Lubna Kamran
Metallurgical Engineering Department, NED University of Engineering & Technology, Karachi, Pakistan.

P-06: Design and Development of Laboratory Scale Cupola Furnace.
Mr. Muhammad Samiuddin, Syed Muhammad Taha, Haris Haider Ali, Maaz Khan
Metallurgical Engineering Department, NED University of Engineering & Technology, Karachi, Pakistan.

P-07: Evaluation of the Effect of Infill Pattern on Mechanical Strength of Additively Manufactured Specimen
Shaheryar Atta Khan, Muhammad Fahad, and Maqsood Ahmed Khan Mechanical Engineering Department, DHA Suffa University, Karachi, Pakistan
Industrial and Manufacturing Engineering Department, NED University of Engineering & Technology, Karachi, Pakistan.

P-08: Comparative analysis of absorption and membrane technology for post-combustion carbon capture.
Rizwan Ahmed Qamar, M. Zubair Aslam, Abdul Haseeb, Ahsan Khurram, Amjad Mahmood
Chemical Engineering Department, NED University of Engineering & Technology, Karachi, Pakistan

P-9: Analysis of Wind Farm Located Near Gharo – Pakistan

Muzaffar Hussain, Mobin Ahmed, Saeed Ahmed
National Refinery Limited.

P-10: Effect Of Ball Milling Of Mechanical Alloying On Structural Characteristics Of Shape Memory Cu–Al–Mn Alloy.

Umer Hussain, M. Anas Khalid Khan1, Humair Ahmed and Ashraf Ali
Materials Engineering Department, NED University of Engineering & Technology, Karachi, Pakistan

P-11: Synthesis and Characterization of Zinc Oxide and Titania Nanoparticles.

Ailia Touqir, Ariba Khan, and Syed M. Mohsin
Materials Engineering Department, NED University of Engineering & Technology, Karachi, Pakistan.

P-12: Manufacture and Characterization of Honeycomb Sandwiched Carbon Fiber Reinforced Polymer Composite

Taha Zafar, M. Afnan Shakeez, Farrukh Fahim and Danish Majeed
Materials Engineering Department, NED University of Engineering & Technology, Karachi, Pakistan.

P-13: Green Synthesis and characterisation OF Zinc Oxide Nanoparticles using Aloe Vera

Huba Kamal, Yusra Mohi Khan, Mehwish Naeem and Danish Majeed
Materials Engineering Department, NED University of Engineering & Technology,
Karachi, Pakistan.

P-14: Simulation, Optimization And Economic Analysis Of Platformer Plant.

Muhammad Humayun, Syed Aijaz Rasool, Areeb Akmaal, Rizwan Ahmed Qamar.
Chemical Engineering Department, NED University of Engineering & Technology, Karachi, Pakistan.

P-15: Synthesis and Characterization Of Magnetorheological Fluids

Syed Shan Ahmed, Sarah Humayun1, Arsalan Shahid and Faaz Ahmed
Materials Engineering Department, NED University Of Engineering & Technology, Karachi, Pakistan.

P-16: Synthesis and characterization of Barium Titanate Powder by Solid-State and Hydrothermal Routes.

Engr. Muhammad Ali Siddiqui, Alishah Jamaluddin Virani, Waqar Ahmed.
Metallurgical Engineering Department, NED University of Engineering & Technology, Karachi, Pakistan

P-17: Synthesis And Characterization Of Bamboo Fiber Reinforced Polymer Composite

Sana Shaikh, Rimsha Javed, Muhammad Faizan.
Materials Engineering Department, NED University of Engineering & Technology, Karachi, Pakistan.

P-18: Effect of light curing units on micro-hardness of dental restorative material. The resin modified Glass Ionomer Cement

Afreen Bilgrami, Fazal-ur-Rehman, Wasif Iqbal,Kausar Ali Syed, Madiha Pirvani

P-19: Polymer Matrix Nanocomposites: A New life to Conventional Polymer Composites

R. R.Ahmed, A. Shabbir , M. Idrees, M. Ansari, I. Majeed, K.A. Syed.
Polymer & Petrochemical Engineering Department, NED University of Engineering & Technology, Karachi, Pakistan..

P-20: Exploring Indigenous Route for Super Absorbent Polymer Synthesis.

R. Ahmed, M. Qaiser, S.M. Shujaat, W. Ahmed, M. T. Raza, S. I. Ali
Polymer & Petrochemical Engineering Department, NED University of Engineering & Technology, Karachi, Pakistan
Department of Applied Chemistry & Chemical Technology, University of Karachi - 75270

P-21: Manufacturing of High Fuel Efficient Green Tyres Using Low PAHs Oils

A.A. Baig,R. Ahmed, A. Saleem, S.O. Ali, S. Nadeem, R.A. Ali, M. Sarwar

Polymer & Petrochemical Engineering Department, NED University of Engineering & Technology, Karachi, Pakistan
The General Tyre & Rubber Company of Pakistan Ltd., L.I.E. Landhi - Karachi

P-22: Simulation and Validation of Resin Infusion Process for Thick Composite Laminates

K.A. Syed, R. Ahmed, T. Zia, B.A. Khan, S. Siddiqui
Polymer & Petrochemical Engineering Department, NED University of Engineering & Technology, Karachi, Pakistan.

P-23: High Abrasive Resistant Coatings for Wind Turbine Blades Applications

M. Mashhood,R. Ahmed, A. Ali, S.A. Haq, S. I. Ali
Polymer & Petrochemical Engineering Department, NED University of Engineering & Technology, Karachi, Pakistan
Department of Applied Chemistry & Chemical Technology, University of Karachi.

P-24: Design and Fabrication of Small Scale Portable Floating Dome Biodigester

Waqar Ahmed, Danish Lakhani, Zahoor UlHussain Awan, Saud Hashmi, AhmedUllah
Department of Chemical Engineering, NED University of Engineering & Technology, Karachi, Pakistan.

P-25: Synthesis of Hydrogel Membrane and Its Characterization

Asif Jan, Raza Wasim, Ahmer Saeed and Muhammad Faizan
Materials Engineering Department, NED University of Engineering & Technology, Karachi, Pakistan.

Table of Contents

Poster presentations

LOW TEMPERATURE CARBOTHERMIC REDUCTION OF ALUMINA: AN OVERVIEW (Keynote)

M. Ikram-ul-Haq
Centre for Sustainable Materials Research and Technology, School of Materials Science and Engineering,
UNSW Australia, Sydney, NSW 2052, Australia

Corresponding Author. *Email address*: ikram@unsw.edu.au

ABSTRACT

This paper presents an overview of research carried out in our group over the past several years. We report results on the low temperature decomposition of alumina at 1550 °C, which is 650-850 °C lower than typical temperatures required for carbothermic reduction of alumina (2200-2400 °C). High temperature interactions of Al_2O_3-C/Fe system were investigated at 1550 °C in argon atmosphere with specific focus on the decomposition of alumina in the simultaneous presence of carbon and iron. SEM/EDS and micro x-ray diffraction results showed the presence of additional diffraction peaks belonging to Fe_3Al system. These experimental results showed enhanced decomposition of alumina in the presence of molten iron. Molten iron was found to act as a reducing agent and a metallic solvent in both cases. From these results, it has been concluded that alumina can be reduced into aluminium based products at much lower temperatures which could lead to economical and energy efficient processes.

Keywords: carbothermic reduction, alumina, molten Iron, Fe-Al intermetallics

1 INTRODUCTION

The carbothermic reduction of alumina has been investigated extensively as an alternative to electrolytic reduction (Hall-Heroult Process) [1-5]. This approach has the potential to reduce energy consumption by up to 38%, capital costs by more than 60% and decrease CO_2 emissions by up to 30% [6]. Pechiney reacted alumina with carbon at 2400-2500°C, producing a gaseous mixture of aluminium suboxides, aluminium vapour and CO gas [7]. These gases were further reduced with excess carbon to form aluminium carbides which were subsequently decomposed in vacuum to produce aluminium. ALCAN and ALCOA developed a two stage reactor that formed aluminium carbide-alumina slag at temperatures lower than 2000°C; this slag was then transformed to Al-20 wt% C at temperatures higher than 2000°C. Precisely controlled reactor temperatures were required to achieve phase separation and to minimise aluminium losses due to evaporation and by limiting the volume of CO gas percolating through the liquid Al-C alloy [8]. Cox and Pidgeon[9] investigated the Al-O-C system in the temperature range 1427 °C to 1927 °C at reduced pressures and reported the formation of small quantities of aluminium-bearing compounds, such as oxy-carbides and carbides (Al_4O_4C, Al_2OC, and Al_4C_3). Yeh and Zhang have investigated the carbothermic reduction of bauxite ore at 1600 °C in the form of ferroalloys of silicon and aluminium, carbides of titanium, silicon and aluminium and unreacted alumina [6]. Yaghoub has reported that the production of aluminium based on above approaches would not be practical due to low reaction rates, low yield, high energy requirements (above 24 kWh/kg Al) and high level of inert gas usage [10]. Frank et al. used a different approach for the carbothermic reduction of alumina in the presence of a metallic solvent (Cu and Sn) in the temperature range 1700°C to 1850° C and pressures between 0.08 to 0.20 atm. [11]. The overall driving force for the reduction reaction was determined by the activity of aluminium in the metallic solvent, the temperature and the pressure of CO gas. The reduction was approximately 80% complete in 60 minutes at 1800°C and 0.1 atm.; the formation of Al_4C_3 was reduced significantly due to poor solubility of carbon in molten copper. Iron is known to have a high affinity for Al [12]. In this study, we have investigated the possibility of using molten iron as a metallic solvent at 1550 °C and 1atm pressure.

An in-depth investigation of the behaviour of pure Fe/Al_2O_3–C system at low temperature (1550 °C) is therefore quite important for developing a fundamental understanding of decomposition of alumina into aluminium or aluminium based products. Results are reported for Al_2O_3-(10-30) pct C/Fe (0.06 pct C) system. Two key issues that need to be investigated are the influence of carbon and the role, if any, played by the simultaneous presence of molten iron that can act both as a reducing agent as well as a metallic solvent.

2 EXPERIMENTAL

High-purity (99.8 pct), fused alumina was mixed thoroughly with 10, 20 and 30 % graphite and 5 wt pct phenolic resin as a binder in the form of substrates labelled as AS1, AS2 and AS3 respectively. These substrates were baked at 150°C for 48 hrs to cure the resin and to remove volatiles and moisture [13]. The effective carbon content of these substrates has been shown in Table 1; these values were determined taking into account carbon contributions from the binder which on pyrolysis yields ~ 50-60% carbon [14].

Table 1. Composition of alumina-synthetic graphite substrates

Sample label	Al_2O_3-Graphite ratio (%)	Binder (wt %)	Calculated Value	
			Wt. % Al_2O_3	Wt. % C
AS1	90:10	5	87.09	12.91
AS2	80:20	5	77.18	22.82
AS3	70:30	5	67.27	32.73

Iron for these experiments was supplied by LECO Australia in the form of rings weighing 1 g each. Chemical composition of Iron used for these experiments is shown in Table 2.

Table 2. Chemical composition of Iron

Elements	Mn	Si	Al	Ca	Cr	Cu	Fe
Wt %	0.738	0.085	0.0008	0.0016	0.0059	0.0391	Balance

Substrates were prepared by compacting the mixture in a steel die using a hydraulic press and pressing to a pressure up to 10 MPa. Sessile drop investigations were carried out for these experiments. This setup has been used successfully previously to study dynamic wetting behaviour including contact angle variations in the metal refractory systems.[15] High temperature investigations on these three sets of substrates were carried out at 1550 °C in a laboratory scale, horizontal tube resistance furnace (**Figure 1**).

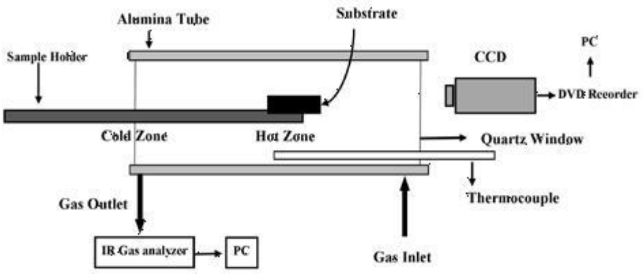

Figure 1. A schematic representation of the experimental arrangement

The furnace tube was purged with 99.99% pure argon throughout the duration of the experiment with a flow rate of 1.0 L/min. The furnace was initially purged with argon for 20 minutes with a slight positive pressure (~1.3 atm.) to ensure that no gas could leak into the furnace; oxygen levels in the outgoing gases were measured continuously and were below 2 ppm. The assembly was held in the cold zone of the furnace until the desired temperature was attained and was then inserted into the hot zone. The assembly was quenched after fixed periods of reaction time (up to 30 minutes) by withdrawing the tray into the cold zone of the furnace. Using an IR gas analyser, CO and CO_2 concentrations in the outlet gas mixture were measured continuously. A high resolution charge-coupled device (CCD) camera fitted with an IRIS lens was used to capture the live phenomena in-situ. The output from the CCD camera was channelled to a digital video recorder (DVD) and a television monitor to record the entire experimental process as a function of time.

To examine the chemical transformations and interfacial region between the metal and substrate; two sets of samples were prepared. In Set I, the reacted assembly was cross sectioned with metal and substrate, which was then set in epoxy resin and polished to a 1µm finish. In Set II, the interfacial region between the metal and substrate was analysed by removing the metal droplet from the top surface of the substrate. These samples were not cross-sectioned for microscopic examination unlike the samples in Set I. The polished samples were examined by SEM (Model S-3400X, Hitachi, Tokyo, Japan). Energy dispersive spectroscopy (EDS) was used to identify the elemental distribution in the selected region. Phase changes for these samples were investigated using x-ray micro-diffraction (selected area diffraction) based on epitaxial technique. Detailed procedure of conducting x-ray micro diffraction analysis has been given elsewhere [15].

3 RESULTS

EDS analysis of Cross-sectional samples (Set I)

A microstructural image of the cross-sectional region of sample AS1 just below the metal droplet after 30 minutes of interaction (**Figure 2**) indicated some of the iron penetrated regions of the substrate. Bright region showed the metal penetration into alumina carbon substrate. While grey region showed dominant alumina region and black region were rich in carbon. These regions were analysed using EDS for elemental spectrum. Position A in the substrate (where the contents of both aluminium and oxygen are high) indicated the presence of alumina. The area analysed at Position 'B' showed partial penetration of iron into AS1 substrate and EDS analysis of this position showed that at this point, the oxygen content was very low clearly indicating that alumina was partially reduced with carbon or iron could also be playing a role in reacting with alumina.

The combined effect of iron and carbon would be crucial in dictating the chemical interaction for the reduction of alumina. This effect could be observed, when iron had penetrated deeply into the alumina carbon matrix, (position 'C')

where the levels of oxygen had decreased to a minimum level such that hardly any oxygen peak could be observed. The absence of oxygen was reconfirmed by elemental analysis at position 'D', where only iron, aluminium and carbon were observed. The area represented by position D in **Figure 2** has been magnified in **Figure 3**.

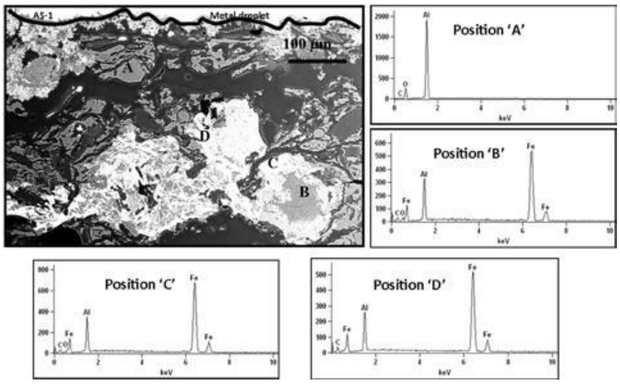

Figure 2. SEM image showing AS1/iron interaction after reaction at 1550 °C along with EDS analysis.

EDS analysis shown in **Figure 3** at positions 'A' and 'B' did not show any presence of oxygen indicating that alumina has reduced to Al in the iron penetrated regions such that only Al and Fe were observed in the matrix. The cross-sectional image of AS1 showed phase changes indicating that partial decomposition of alumina had occurred under these experimental conditions.

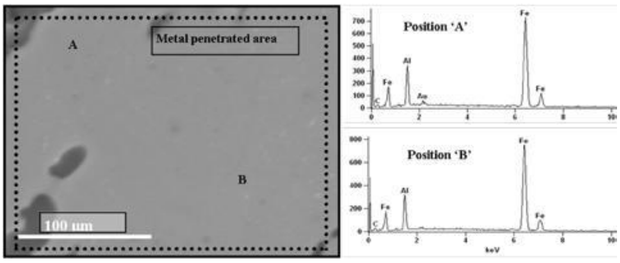

Figure 3. SEM image of AS1/iron interaction showing magnified view of position 'D' along with EDS analysis.

AS2 and AS3 samples showed relatively lower extents of iron penetration into the substrates than AS1 substrate as shown in **Figures 4 and 5**. The microscopic and EDS analysis of AS2 and AS3 substrates showed the presence of Al, oxygen and carbon at position 'A'. The position 'B' in both AS2 and AS3 substrates showed the reduction of alumina into Al along with the combined presence of both iron and carbon in the system. A small peak of Si was also detected in the matrix that could be due to infiltration of iron as iron contains 0.085 wt% Si.

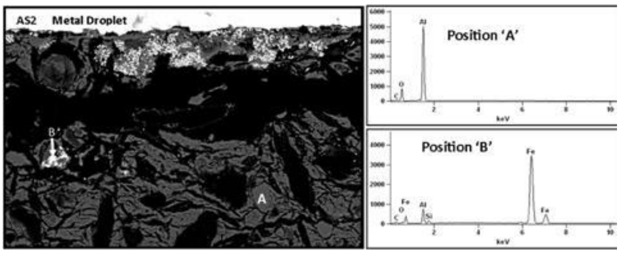

Figure 4. EDS analysis of AS2/iron sample reacted at 1550 °C for t=30 minutes

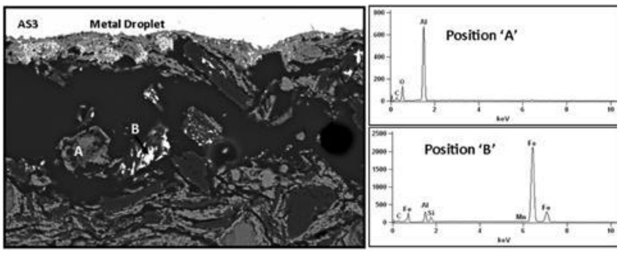

Figure 5. EDS analysis of AS3/iron sample reacted at 1550 °C for t=30 minutes

EDS analysis of topographic samples (Set II)

In this set, the entire surface of the interfacial region was under investigation to compare the results of chemical interaction between molten iron and Al_2O_3-C substrate with the cross-sectional study of the Set I substrates. **Figure 6** clearly showed the amount of metal penetrated into the AS1 substrates; the metal/substarte interface had significant concentration of molten iron. The EDS analysis at position 'A' showed the presence of alumina, where Al and oxygen are the key elements observed. In these samples, the presence of carbon in the proximity of alumina was also analysed to observe any interaction between alumina and carbon. Experimental results revealed the presence of only Al and C at position 'B' which clearly indictates the decomposition of alumina either with carbon or with the combined presence of iron and carbon in the substrate. In the metal penetrated area, the EDS analysis at position 'C' showed Al and Fe as the main phases with small amounts of C and Si. The presence of C and Si could be due to the small levels of impurities present in iron. Since Al in the iron is very low (0.008 wt%), it is assumed that Al observed from the EDS analysis of position 'C' is from alumina reduction, where peak height of Al was almost equal to the peak height of Fe.

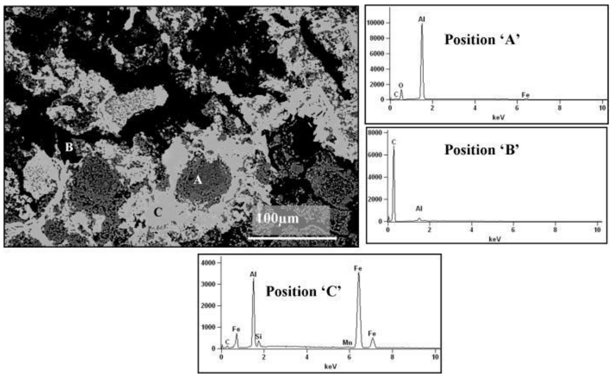

Figure 6. EDS analysis of topographic sample of AS1/iron interaction at 1550 °C

Figure 7 shows the image of Al_2O_3-C/Fe interface of AS2 substrate, where the amount of metal observed was much higher than the cross - sectional sample of AS2 substrate. The EDS analysis of AS2 sample shows the presence of alumina at position 'A', while position 'B' shows the presence of Al and C indicating the reduced aluminium resulting from the decomposition of alumina. The presence of reduced Al was much higher at this position which interacted with carbon. Position 'C' shows that reduced Al had interacted with iron indicating the presence of Al and Fe composite in the sample matrix. A small peak of Mn could be seen probably from small levels of Mn present in iron.

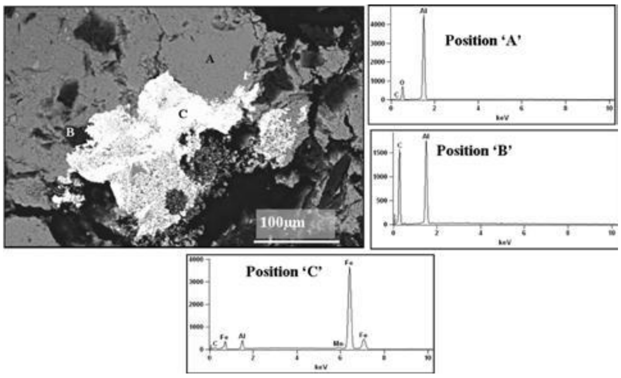

Figure 7. EDS analysis of topographic sample of AS2/iron interaction at 1550 °C

Figure 8 shows SEM image of AS3 substrate. This substrate showed a similar trend of metal penetration as observed for cross-section metal/substrate interface. Due to much larger amounts of carbon present in the mixture, the composition of position 'B' appears to be aluminium carbide. The EDS analysis of the sample at positions ‘A’, ‘B’ and ‘C’ show almost similar elemental analysis as that observed for AS1 and AS2 substrates.

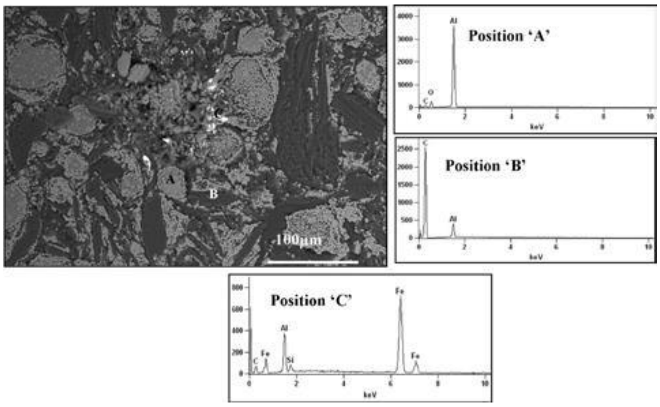

Figure 8. EDS analysis of topographic sample of AS3/iron interaction at 1550 °C

From the SEM image for AS3 substrates, it could also be observed that morphology of the substrate was different in the region where metal had interacted with alumina and carbon. This was observed clearly in the magnified area where metal was present (**Figure 9**).

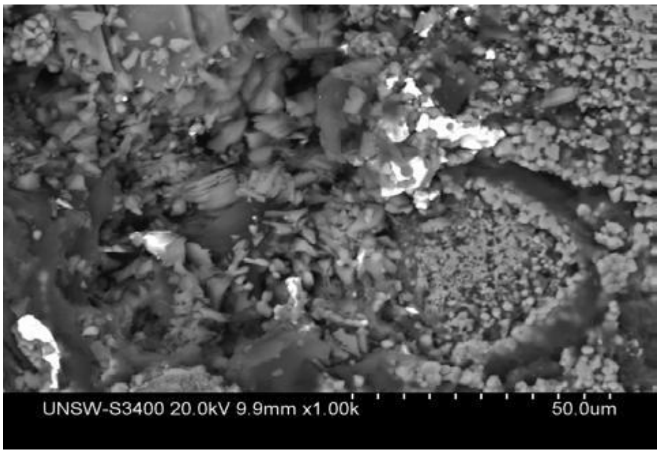

Figure 9. SEM image of topographic sample of AS3/iron interaction showing morphological change

From the SEM image of **Figure 9**, it was observed that metal penetration had an impact on the morphology and chemical nature of the reaction where alumina undergoes reduction reactions. The area in AS3 substrate, where no metal penetration was observed was further magnified to observe the decomposition of alumina and its interaction with carbon (**Figure 10**).

The SEM image and EDS analysis clearly indicated the presence of only Al and C at position ‘A’ and ‘B’. It is clearly observed from EDS analysis at positions ‘A’ and ‘B’ that alumina interaction with carbon has led to the decomposition of alumina which has led to the formation of aluminium carbide since no oxygen peaks were visible. This shows partial reduction of alumina occurring into the Al_2O_3-C/Fe samples.

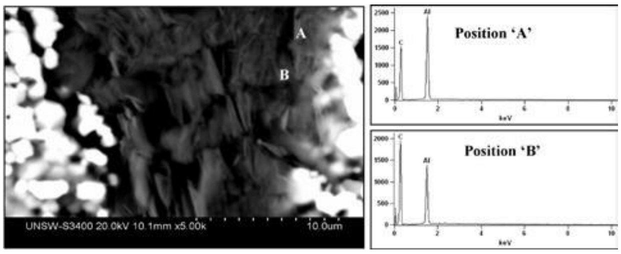

Figure 10: EDS analysis of topographic sample of AS3/iron interaction highlighting morphological change and alumina carbon interaction.

X-ray Diffraction results

The surface x-ray diffraction scan of the reacted assembly was carried out using conventional materials research Diffractometer (MRD) using Cu Kα radiation. Surface scan of the sample showed one additional peak other than alumina and carbon [15]. Using novel experimental procedure for identification of trace quantities [15], a 3-dimensional epitaxial map of the surface showed the location of phases belonging to 44.19° peak on the substrate surface is shown in **Figure 11**. The high intensity green and red coloured regions represent locations where molten iron had reacted with Al_2O_3 and C to locally produce significant amounts of the reaction product.

Figure 12 shows the XRD scan of the reacted AS1 substrate on MRD after epitaxial mapping. The analysis of the diffraction spectrum in **Figure 12** confirmed the presence of a new phase (cubic aluminium-iron alloy) in addition to alumina and carbon, as determined by stand-alone peaks at 30.840° (200), 44.187° (220), 64.258° (400) and 81.289° (422) [16]. Fe_3Al system also shares two peaks at 26.628° (111) and 54.851° (222) with graphite [16]. The numbers in parenthesis represent (hkl) indices of various peaks.

Figures 13 and 14 shows diffraction pattern of samples AS2 and AS3 after epitaxial mapping and also confirm the presence of Fe_3Al reaction product.

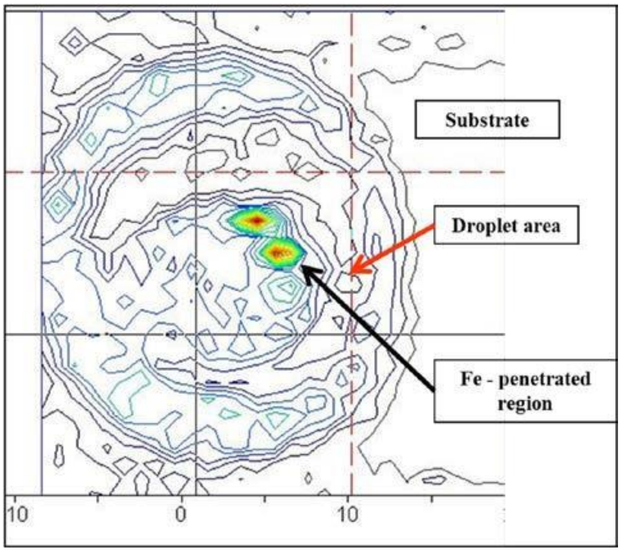

Figure 11: Epitaxial mapping at 44.19° peak position showing the peak location for the secondary product formed in the AS1 substrate.

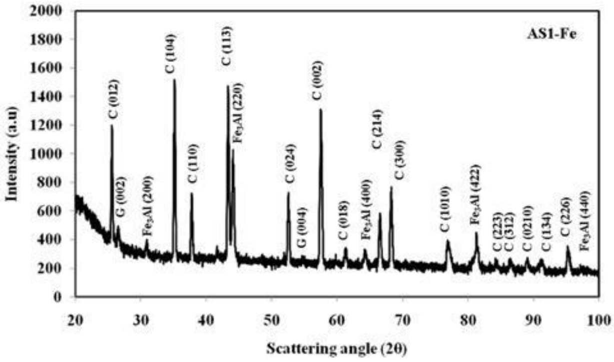

Figure 12. XRD pattern of AS1/iron substrate after heating at 1550 °C for 30 minutes showing Fe_3Al as reaction product other than alumina (C) and carbon (G)

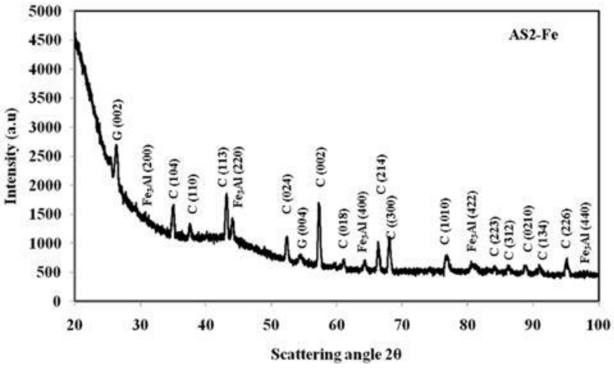

Figure 13: XRD pattern of AS2/iron substrate after heating at 1550 °C for 30 minutes showing Fe_3Al as reaction product other than alumina (C) and carbon (G)

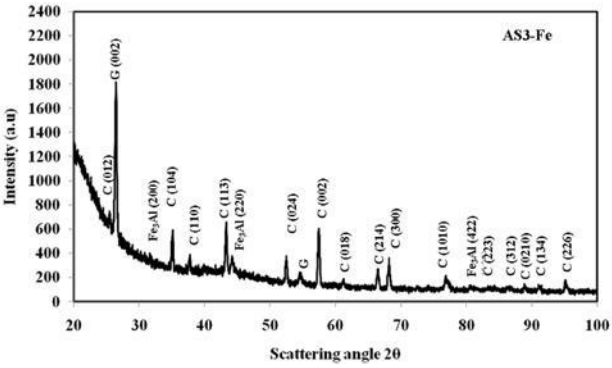

Figure 14: XRD pattern of AS3/iron substrate after heating at 1550 °C for 30 minutes showing Fe_3Al as reaction product other than alumina (C) and carbon (G)

The probability of Fe_3Al diffraction peaks being actually iron was also considered, iron peaks are quite close to Fe_3Al peaks in diffraction pattern. Diffraction peaks of iron from database of JCPDS No 085-1410 shows iron to be observed at peak position of 44.354°, 64.528° and 81.657° and JCPDS No 006-0696 shows diffraction peaks to be at peak positions 44.674°, 65.023°, 82.335° and 98.949°. These Fe peak positions are slightly different from the peak positions observed in the pattern of AS1, AS2 and AS3 systems. Peak positions observed in these samples matched the diffraction pattern of JCPDS No 45-1203 for Fe_3Al.

Epitaxial mapping and scans were also conducted at several other peak positions for possible secondary products such as Al, Al_4C_3, Al_4O_4C and Al_2OC. None of these scans showed peak heights significant enough to indicate their presence in the Al_2O_3-C/Fe system.

4 DISCUSSION

Our results have clearly shown that the reduction of alumina could be achieved at 1550 °C in the presence of molten iron. These temperatures are much lower than those conventionally reported for the carbothermic reduction of alumina; these are also significantly lower than those reported by Frank et al. [11] in the presence of metallic solvent Cu and Sn.

In the alumina-carbon system alone, alumina has been reported to decompose into suboxides such as AlO and Al_2 O, which can lead to secondary aluminium bearing compounds Al_4O_4C and Al_2

OC in the temperature ranges between 1300 to 1927 °C [1-5, 9]**.** In this study, due to inert Ar environment and the absence of an oxygen source, the chemical interactions in the Al_2O_3-C/Fe system, iron could be playing a greater role in carbothermic reduction of alumina at 1550 °C due to high affinity of iron for Al [12]. No chemical reaction is known to occur between Fe and Al_2O_3 at 1 bar; pressures above 60 GPa and temperatures of 1927 °C were required for iron and alumina to react to form iron oxide and an iron–aluminum alloy [17].

Khanna et al. reported that C and Fe are among some of most important elements involved in redox reactions. So, dissolution of the carbon from Al_2O_3-C system into iron will also be critical as carbon in iron could be playing the role of solute carbon. It is well known that the presence of even small amount of solute carbon can affect the kinetics of chemical reactions. [18]

In the combined presence of C and Fe with Al_2O_3, the role of iron was analysed through off-gas analysis, where interaction with alumina, carbon and iron generated more CO/CO_2 gases than blank run of AS1 substrate as shown in **Figure 15**.

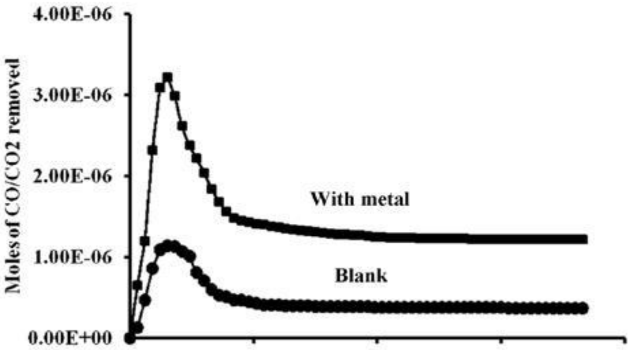

Figure 15: Moles of CO/CO_2 removed from in-situ reaction of alumina-carbon substrate (Blank run) and AS1/iron interaction

Thermodynamic predictions using FactSage software also revealed the evolution of higher CO gas in combination with CO_2, Al_2O, AlO and Al (**Figure 16a**). The formation of reaction gas could also be playing the part and gas like CO, AlO and Al_2O may be enhancing the reaction rate to increase the reduction. Reduction may occur via gas transport mechanism between alumina and carbon source. A similar observation has also been reported by Heyrman and Chattilon [3]. If AlO and Al_2O gases are formed due to carbothermic reaction of alumina then carbon pickup by iron could lead to a further reduction of those suboxide gases of alumina into aluminium which is then absorbed by Fe as observed from thermodynamic predictions and microscopic and XRD results. Theoretical and experimental results indicate partial conversion of alumina into aluminium and its interaction with iron and carbon to form carbides. Thermodynamic calculations also showed that Al formed partially reacted with Fe. The Fe reacted and picked up both Al and carbon as shown in **Figure 16b**. With increase in temperature, the pick-up of both Al and C by Fe increased steadily and simultaneously that solid carbon available for the reaction is depleted.

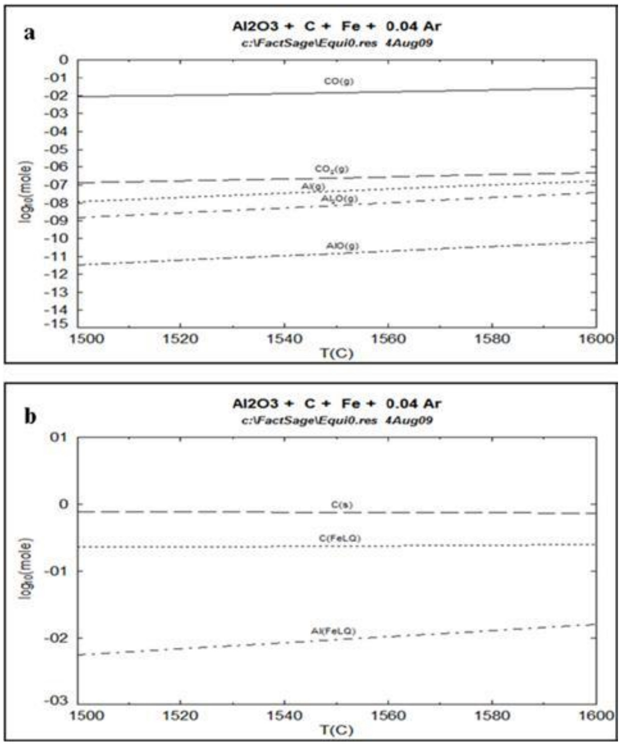

Figure 16. (a) Generation of gases in Al_2O_3-C-Fe system (b) Product species formed in Al_2O_3-C-Fe system

Ramachandran et al. [19] has reported similar finding for Al_2O_3-C/Fe interaction in presence of Ar. They concluded that Al (g) formed will be deposited in the iron as inclusions. The chemical reaction as Fe -Al species could not be predicted from the currently available thermodynamic software packages such as FactSage; the input data for the theoretical software need to be upgraded to take into account these ternary reactions.

These results clearly show that the carbothermic reduction of alumina can indeed take place under these operating conditions and reduction temperatures are 650-850 °C are lower from typical temperatures of carbothermic reduction of alumina. The key characteristics of molten iron, e.g. the phenomena of carbon pickup by iron which acts as a strong reducing agent and its role as a metal solvent, played a significant role in enhancing the reduction kinetics at such low temperatures and pressures.

5 CONCLUDING REMARKS

These experiments have laid the foundations for the development of a new approach for reduction of alumina in the simultaneous presence of C and Fe at 1550 °C to produce aluminium based alloys. Further studies on this system are in progress to determine optimal compositions, temperatures, gas flow rates towards enhanced product yields.

REFERENCES

[1] H. Chen and C. Lin, Mechanism of the reduction of carbon/alumina powder mixture in a flowing nitrogen stream**,** *Journal of Materials Science,* 29, 1352-1357, 1994

[2] P. Lefort, D. Tetard and P. Tristant, Formation of aluminium carbide by carbothermal reduction of alumina: Role of the gaseous aluminium phase, *Journal of Euro Ceramic Society*, 12, 123-129, 1993

[3] M. Heyrman and C. Chatillon, Thermodynamics of the Al–C–O Ternary System I. Second and Third Law Critical Analysis of Oxycarbide Enthalpies from Vapor Pressure Determinations, *Journal of Electrochemical Society*, 153, 119-130, 2006

[4] M. Halmann, A. Frei, and A. Steinfeld, Carbothermal reduction of Alumina: Thermochemical Equilibrium Calculations and Experimental investigation, *Energy*, 32, 2420-2427, 2007

[5] C. Chen, C. Lin, and S. Chen, Kinetics of synthesis of silicon carbide by carbothermal reduction of silicon dioxide, British *Ceramic Transactions,* 99, 57-64, 2000

[6] C. H. Yeh and G. Zhang, Stepwise Carbothermic reduction of Bauxite Ore, *International Journal of Mineral processing*, 124, 1-7, 2013

[7] W.B. Frank, W.E. Haupin, H. Vigt, J. Thonstad, H. Kvande and O.A. Taiwo, *Aluminium*, Wiley-VCH Verlag GmbH, 2005

[8]C. Cochran, *Carbothermic reduction of Alumina*, US Patent: 3,971,653, 1976.

[9] J.H. Cox and L.M. Pidgeon: An investigation of the Aluminum-Oxygen-Carbon System, *Canadian Journal of Chemistry*, 27, 671–83, 1963

[10] S.Y. Yaghoub, Carbothermic Processes to Replace the Hall-Heroult Process, *IBAAS-CHALIECO Conference Aluminium industry conference*, November 27–29, 2014 Visakapahtnam, India

[11] R.A. Frank, C.W. Finn and J.F. Elliot, Physical Chemistry of the Carbothermic Reduction of Alumina in the Presence of a Metallic Solvent: Part I1 Measurements of Kinetics of Reaction, *Metallurgical and Materials Transactions. B*, 20, 161-173, 1989

[12] O. Akinlade, R.N. Singh, F. Sommer, Thermodynamics of liquid Al–Fe alloys, *Journal of Alloys and Compounds*, 299, 163-168, 2000

[13] M. Ikram-ul-haq, R. Khanna, P. Koshy, and V Sahajwalla, High-temperature Interactions of Alumina - Carbon Refractories with Molten Iron, ISIJ International, 50, 804-812, 2010

[14] P.L. Smith, J. Liddle and J. White, "Equilibrium relationships of carbon -metal oxide refractories, *Transactions and journal of the British Ceramic Society*, 84(2): 62-69, 1985

[15] L. Zhao and V. Sahajwalla, Interfacial Phenomena during Wetting of Graphite/Alumina Mixtures by Liquid Iron, ISIJ International, 43 (1), 1-6, 2003

[15] M. Ikram-ul-Haq, R. Khanna, Y. Wang and V. Sahajwalla V, A Novel X-ray Micro-diffraction Approach for Structural Characterization of Trace Quantities of Secondary Phases in Al_2O_3-C/Fe System, *Metallurgical and Materials Transactions. B*, 45(6), 1970-1973, 2014

[16]C. Hubbard, 1993, *Private Communications*, Oak Ridge, TN, USA

[17]L. Dubrovinsky, H. Annersten, N. Dubrovinskaia, F. Westman, H. Harryson, O. Fabrichnaya, and S. Carlson, Chemical interaction of Fe and Al_2O3 as a source of heterogeneity at the Earth's core-mantle boundary, *Nature*, 412, 527-529, 2001

[18] R. Khanna, M. Ikram-ul-Haq, Y. Wang, S. Seetharaman and V. Sahajwalla, Chemical Interactions of Alumina–Carbon Refractories with Molten Steel at 1823 K (1550 °C): Implications for Refractory Degradation and Steel Quality, *Metallurgical and Materials Transactions. B*, Vol. 42B, 2011, No. 4, pp. 677-684

[19] S. Ramachandran, K.D. Peaslee and J.D. Smith, Thermochemistry of Steel-Refractory Interactions in Continuous Casting Nozzles, *Iron and Steelmaker*, 30, 55-63, 2003

STUDY ON MORPHOLOGY, THERMAL, AND MECHANICAL PROPERTIES OF ELECTROSPUN PVA/WOOD FLOUR NANOFIBROUS COMPOSITES

Sheikh Rasel[1,*] and Ghaus Rizvi[2,*]
[1] Department of Automotive, Mechanical and Manufacturing Engineering, University of Ontario Institute of Technology, 2000 Simcoe Street North Oshawa, Ontario, Canada L1H 7K4

[*]Corresponding author. Tel.: +1905-7218668 ext 5745; fax: +1905-7213370
E-mail address: Ghaus.rizvi@uoit.ca (Ghaus Rizvi)

ABSTRACT

Nanofibrous polyvinyl alcohol (PVA) reinforced with wood flour were fabricated via electrospinning. Electrospinning is a simple, versatile, and economical technique that is capable of fabricating ultrafine fibers with high specific surface area and desired functional properties from a rich variety of materials. We adopted the rotating drum electrospinning technique to prepare nanofibrous composite with a rotation of 1000 rpm. Morphological, thermal, and mechanical properties were characterized for the PVA/WF nanocomposites containing 0, 5, 10, and 20 wt % of WF. Morphological results indicated that the reinforced WF were well embedded in the PVA matrix and the average diameter of electrospun PVA/WF nanofibers were slightly higher compared with pure PVA fibers. The addition of WF improved both the thermal stability and mechanical properties of PVA/WF composites. The tensile strength increased significantly (45 % compared to pure PVA) after adding small amount (5 wt %) of WF in PVA_5 WF composite. Likewise, 67 % and 228 % increment of tensile strengths were observed in PVA_10 WF (6.55 MPa), and PVA_20 WF (12.87 MPa) sample. In summary, the nanofibrous PVA/WF composites were successfully prepared using electrospinning with good dispersion of reinforcement into the matrix as reflected by the characterization of morphological, thermal and mechanical properties.

Keywords: Electrospinning; nanocomposite; nanofibers; wood flour

1 INTRODUCTION

One dimensional nanofibrous structures are found to be of great potential because of their inherent properties such as high surface-to-volume ratio, tunable porosity, and desired functional properties [1-3].The functionality and applicability of these structures can be further enhanced by incorporating a secondary phase. Advanced reinforced composites with fillers and with the reduction of their size, from microscale to nanoscale, can exhibit enhanced structural properties including high strength to weight ratios and high modulus. Electrospinning [4, 5] in situ polymerization [6], Solvent casting [7], and melt mixing [8], are important methods for the fabrication of nanocomposites. Electrospinning has been adopted as a simple, versatile, and economical technique that is capable of fabricating ultrafine fibers from a rich variety of materials. With the aid of electrospinning nanocomposite can be developed when nanoadditives such as nanoclays, carbon nanotubes, titanium dioxide, etc, are added to the polymer solution. Polymeric nanocomposites are of significant interest because of their outstanding end use applications. Zhou et al. [9] have studied with electrospun cellulose nanocrystals (CNC) reinforcing maleic anhydride grafted PLA bio-nanocomposite scaffolds and showed that adding 5 wt % CNC improved the tensile strength up to 10 MPa. Similarly, it is reported that inclusion of cellulose nanofibers in PVA improved the mechanical properties as well as thermal properties [10-12]. Zhang and co-workers [13] found that the introduction of TiO_2 into PLA has improved the thermal stability, toughness, and UV resistance of nanocomposites. A number of research groups developed carbon nanotubes polymer nanocomposites and claimed that composites with carbon nanotubes carried higher mechanical strength and stiffness and higher electrical and thermal conductive properties [14-16].

Wood flour (WF) have also been used as effective reinforcement material as it carries various advantages including low cost, availability in abundance, low abrasiveness, high specific strength & stiffness, biodegradability and relatively low density [17, 18]. Mechanical properties of PLA composites filled with a mixture of softwood or hardwood floor have been focused in many literatures [19, 20]. Thermal and mechanical characteristics of poly(vinyl alcohol) modified by phthalic anhydride (PA) compounded with the WF in hot press have been studied by Ozaki et al [21].

In many applications, for example filtration, it is required to have high mechanical strength on the electrospun nanofiber membranes [22]. The agglomeration of nano-additives which prevents good filler dispersion in the matrix, is the biggest barrier in order to develop the high potential applicable advanced nanocomposite. Although a number of research groups have investigated the improvement in the functional properties of nanoadditive based composite [10, 23]. The performance of electrospun fibrous nanocomposite needs to be investigated further. Therefore, in this study, we focus on introducing WF as additives in electrospun PVA nanofibers. Fibrous PVA nanocomposites consisting of WF were fabricated using electrospinning method. Morphological, mechanical, and thermal properties of nanocomposite scaffolds were investigated.

2 EXPERIMENTAL PROCEDURE

2.1 Materials

PVA is white, odorless, tasteless, and translucent granular powder. It is water soluble, partial soluble in ethanol, and insoluble in all other organic solvents. The melting point of polyvinyl alcohol is around 180 to 190°C. The molecular weight ranges from 26,300 to 300,000 and a degree of hydrolysis is 86.5 to 89 %. The chemical formula for PVA structure is $[CH_2CH(OH)]_n$. PVA has huge applications in the food industries, various pharmaceutical, biomedical and textile industries [24, 25]. PVA based commercial products exhibit low environmental impact due to its biodegradability, aqueous solubility, and high chemical resistance. In food packaging systems, PVA films show outstanding protective properties. In medical devices, PVA can be engaged as a biomaterial because of their excellent properties of biocompatible, nontoxic, swelling, and bio-adhesive.

Wood flour also referred as wood fiber is a finely ground wood cellulose produced from dry wood waste by various types of grinders. All high grade (high durability and high strength) WF is produced from hardwoods and low grade wood flour comes from softwoods. Wood pulverization method can be divided into two types, such as wet and dry pulverization. Dry pulverization is suitable for industrial applications where the size of wood floors are more than 100 µm. In wet pulverization, the wood floors are less than 100 µm in size. Moreover, wood can be pulverized along the direction of fiber in higher water content media, leading to a fibrous wood floor [26]. The size and shape of the WF greatly affects the performance of the composite materials [27].

The WF that was used in this study was purchased from the American wood fibers company (USA).

2.2 Fabrication of Nanofibrous Composite Mats

PVA was dissolved in distilled water by continuous magnetic stirring for four hours using a hot plate at 70^oC. After that, WF were added to the aqueous PVA solution in order to produce composites with 5, 10, and 20 wt % WF. Prior to that, WF were filtered with 106 µm standard test sieve (Gilson company, Inc., USA) to remove agglomeration. The total concentration of PVA/WF was fixed at 12 wt %. Stirring was continued for three hours at room temperature. Then, aqueous composite solution was immediately loaded into the plastic syringe which was pumped through the needle tip (0.51 mm inner diameter) with the flow rate of 500 µL/h. A 20 KV high voltage was applied to the needle tip and the collector electrodes which were kept a 10 cm apart. The electrospun fibers were collected on a rotating drum with 1000 rpm. The electrospun fibrous scaffolds were dried at 40^0C for 12 h.

2.3 Characterization

Scanning Electron Microscopy (SEM)

The surface morphologies of electrospun fibers were examined using an SEM (JSM 6060) operated at 5 kV. Prior to examination, all the samples were sputter-coated with a thin layer of platinum.

Digital Optical Microscope (DOM)

Digital optical microscopy (DOM) (VHX – 1000E, Keyence) was employed to determine surface morphologies, fiber diameter, and thickness of electrospun mats. Custom MATLAB image processing algorithm was developed to calculate the fiber diameter from DOM image.

Dynamic Mechanical Analysis (DMA)

Tensile strength tests of nanofibrous mats were performed using dynamic mechanical analysis (DMA) Q800 (TA instruments) at 25ºC with a force ramp of 0.5 N min^{-1}. Samples were cut using razor blade with a width of 6.5 mm; thickness were measured under optical microscope and gauge lengths of the sample were evaluated by the instrument directly. The average thickness measured for all the electrospun scaffolds was in the range of 40 to 60 µm. As the samples were soft and flexible, therefore, both ends of tested sample were covered with the scotch tape to distribute the load uniformly along the sample. The sample was then loaded to the film tension clamp where the maximum force was set at 18 N with an initial preload force of 0.05 N. The data reported are the average of five observations. From the test results, Young's modulus (E), tensile strength (σ_t), and elongation at break (ε_b) were evaluated.

Thermogravimetric Analyzer (TGA)

The thermal stability of electrospun nanofibrous mats was evaluated by thermogravimetric analyzer Q50 (TA instruments) from room temperature to 600ºC at a heating rate of 10ºC min^{-1} under nitrogen atmosphere. Approximately 3.5 mg of nanofibrous scaffolds were used for each test.

3 RESULTS AND DISCUSSION

3.1 Surface Morphology

Raw WF and aqueous composite solution reinforced with WF are shown in Figure 1. The optical image (Fig. 1B) demonstrates that the WF dispersed homogeneously throughout the aqueous PVA solution without agglomeration.

Surface morphology of pure PVA and PVA/WF nanocomposite is presented in Figure 2. Although it is not visible the WF distribution in SEM image (Fig. 2B), but the surface morphology of nanocomposite fibers is quite different in comparison to pure PVA fibers (Fig. 2A). The DOM image shows the filler distribution in the PVA matrix. Majority of the WF are fully embedded by the PVA materials whereas, the large wood fillers compared to fiber diameter are also adhered to the polymers making beads on the fiber surface. These results indicate that nanofibrous composites are possible to be developed by electrospinning method even with larger particle filler materials compared to fiber diameter.

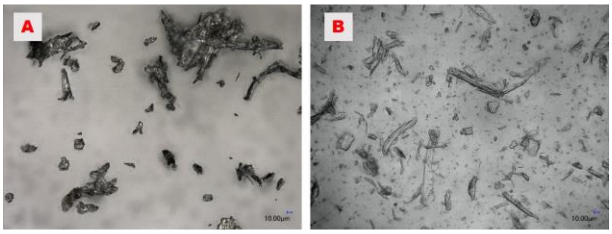

Figure 1. Optical micrographs of raw wood (A), and dispersion of WF in PVA aqueous solution (B).

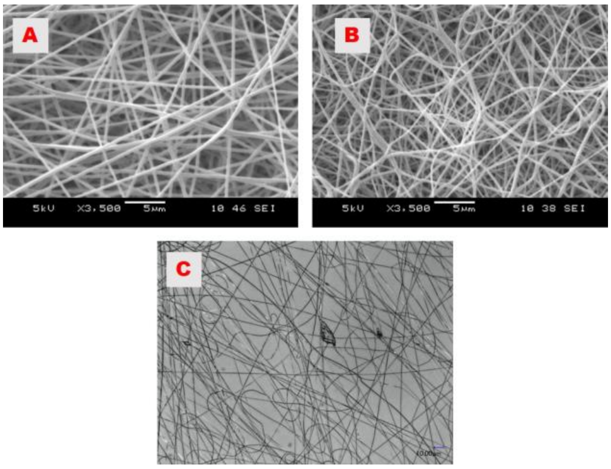

Figure 2. SEM image of pure PVA nanofiber (A), and PVA/Wood flour (20 wt %) nanocomposite (B), OM image of PVA/Wood flour (20 wt %) nanocomposite (C).

Fiber Diameter

Fiber diameters of PVA and PVA/WF nanocomposites were calculated using custom made MATLAB algorithm from optical micrograph images. The optical image of electrospun pure PVA nanofibers and its frequency chart of diameter are presented in Figure 3A & E, respectively. Figure 3B-D depict optical images of 5, 10 and 20 wt % of WF reinforced PVA nanocomposites and their corresponding fiber diameter distribution charts are displayed in Figure 3F-H, respectively. The addition of the WF slightly increased the average fiber diameter as compared to the pure PVA nanofiber although they lie in the error ranges of PVA nanofibers.

3.2 Mechanical Properties

Tensile Tests

Figure 4 shows the stress-strain curves of pure PVA and PVA/WF fibrous nanocomposites. The tensile strength, Young's modulus and elongation at break are listed in the Table 1. As compared to the tensile strength of pure PVA (3.92 MPa), 5 wt % addition of WF increased the tensile strength by 45 % to

5.69 MPa. The tensile strength improved by 67 % in 10 wt % WF nanocomposite. A significant improvement is observed in the tensile strength of PVA + 20 wt % WF nanocomposite (228 %) as compared to pure PVA. The improvement of tensile strength of the PVA/WF nanocomposites indicate the presence of WF in the composites and the superior ability to transfer load from matrix to filler materials.

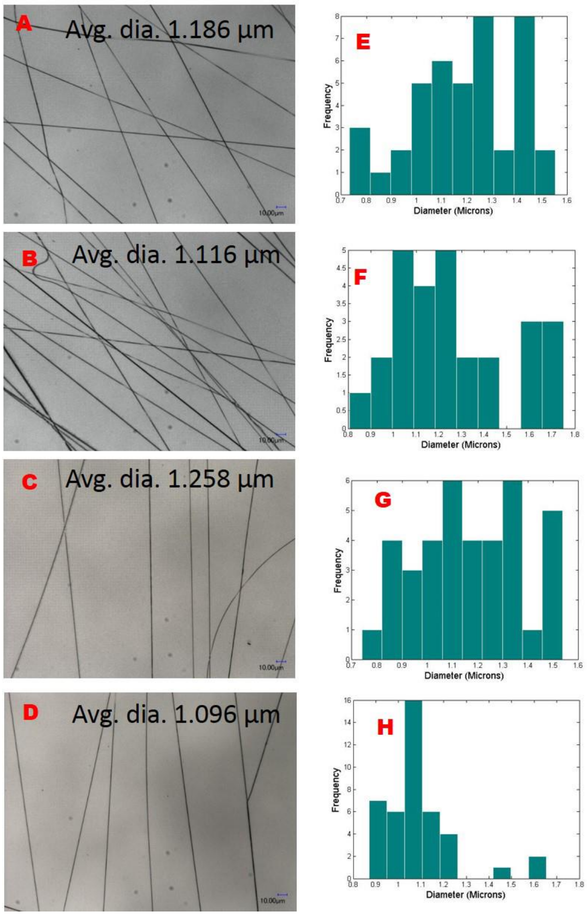

Figure 3. Optical micrograph images of pure PVA nanofiber (A), and 5 wt% (B), 10 wt% (C), 20 wt% (D), of WF reinforced PVA nanocomposites. Their corresponding fiber diameter distribution chats (from E to H) are shown, respectively.

A significant improvement in Young's modulus thus stiffer nanofibers were observed in all the PVA/WF nanocomposites as compared to pure PVA nanofibers. Similar trend is also observed in tensile modulus of composite materials. 21 %, 90 %, and 157 % improvements were achieved in Young's modulus when PVA nanofibers were reinforced with 5 %, 10 %, and 20 % WF, as compared to PVA scaffolds. These results further emphasized the uniform distribution of filler materials and exchange of load from matrix to reinforcement materials.

In contrast, a decreasing trend was observed in the elongation at break of PVA/WF nanocomposites as compared to pure PVA mat. The remarkable decrease in the elongation at break observed as 58.59 % for pure PVA to 15.41 % for PVA + 20 wt % WF nanocomposite. The large aspect ratio of WF and the interaction between the WF and PVA which restricts the polymer chain's movement thus limits mechanical deformation can be considered as the main reasons for reduced ductility.

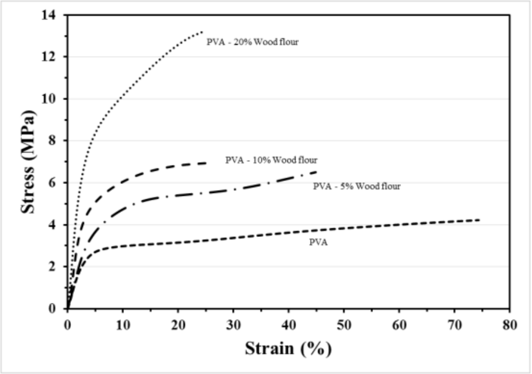

Figure 4. Typical tensile stress-strain curve of PVA scaffolds and PVA/WF composites

Table 1. Tensile properties of PVA scaffolds and its composites

Materials	Tensile Strength (MPa)	Young's Modulus (MPa)	Elongation at break (%)
PVA	3.92 ± 0.39	83.27 ± 9.60	58.59 ± 21.88
PVA + 5 % WF	5.69 ± 1.09	100.96 ± 30.60	46.89 ± 7.86
PVA + 10 % WF	6.55 ± 0.57	157.87 ± 10.92	23.10 ± 4.88
PVA + 20 % WF	12.87 ± 1.73	214.13 ± 42.12	15.41 ± 8.35

3.3 Thermal Properties

The TGA and the differential TG (DTG) curves are depicted in the Figures 5 (a) & 5 (b), respectively, in order to investigate the thermal properties of PVA/WF nanocomposites. Onset temperature, maximum thermal decomposition temperature and char yield is shown in Table 2. A single step decomposition was observed in PVA scaffold as well as its composite materials pointing there were no chemical bonds created with the addition of WF. Only strong adhesion is occurred between the PVA matrix materials and WF reinforcement materials. The onset and degradation temperatures of all the nanocomposite slightly dropped as compared to pure PVA. Therefore, the thermal stability of nanocomposites did not undergo any noticeable change with the addition of WF.

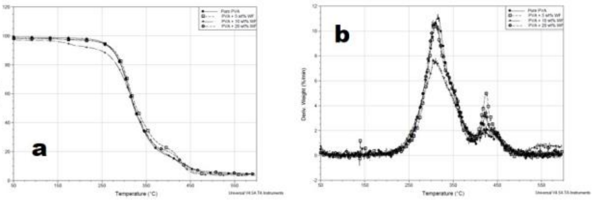

Figure 5. TGA (a), DTGA (b), profiles of PVA and PVA/WF nanocomposites.

Table 2. Summary of TGA results of PVA and PVA/WF nanocomposites

Materials	On-set temperature (ºC)	Degradation rate (°C)	Residue (%)
PVA	281.31	315.30	4.47
PVA + 5 % WF	282.85	310.28	4.30
PVA + 10 % WF	271.74	310.07	5.01
PVA + 20 % WF	278.84	304.46	4.75

4 CONCLUSIONS

Nanofibrous PVA scaffolds and PVA/WF composites were successfully prepared via electrospinning. Morphological results exhibited that the reinforced WF were well distributed into the PVA matrix. The mechanical properties such as tensile strength and tensile modulus improved significantly with the addition of reinforcements indicating good adhesion and dispersion of filler materials into the matrix. PVA + 20 wt % WF nanofibrous composite showed the maximum tensile strength, and tensile modulus but minimum elongation at break when it was reinforced by 20 wt % of WF. Thermal results show that the introduction of WF had no distinct change in the thermal stability of composites. In short, the developed nanofibrous PVA/WF composites could be of potential use for many applications where high mechanical strength and thermal stability are needed, for instant, filtration and bone tissue engineering.

ACKNOWLEDGEMENTS

This work was supported by Ontario Trillium Scholarships.

REFERENCES

[1] Z. Qi, H. Yu, Y. Chen, and M. Zhu, Highly porous fibers prepared by electrospinning a ternary system of nonsolvent/solvent/poly(l-lactic acid), *Materials Letters*, 63, 415-418, 2009.

[2] L. Natarajan, J. New, A. Dasari, S. Yu, and M. A. Manan, Surface morphology of electrospun PLA fibers: mechanisms of pore formation, *RSC Adv.*, 4, 44082-44088, 2014.

[3] H. M. Powell and S. T. Boyce, Fiber density of electrospun gelatin scaffolds regulates morphogenesis of dermal–epidermal skin substitutes, *Journal of Biomedical Materials Research Part A*, 84A, 1078-1086, 2008.

[4] D. K. Sharma, J. Shen, and F. Li, Reinforcement of Nafion into polyacrylonitrile (PAN) to fabricate them into nanofiber mats by electrospinning: characterization of enhanced mechanical and adsorption properties, *RSC Advances*, 4, 39110, 2014.

[5] I. Turku and T. Karki, Research progress in wood-plastic nanocomposites: A review, *Journal of Thermoplastic Composite Materials*, 27, 180-204, 2013.

[6] Y. Ou, F. Yang, and Z.-Z. Yu, A new conception on the toughness of nylon 6/silica nanocomposite prepared via in situ polymerization, *Journal of Polymer Science Part B: Polymer Physics*, 36, 789-795, 1998.

[7] B. K. Kuila and A. K. Nandi, Physical, Mechanical, and Conductivity Properties of Poly(3-hexylthiophene)−Montmorillonite Clay Nanocomposites Produced by the Solvent Casting Method, *Macromolecules*, 37, 8577-8584, 2004.

[8] R. K. Shah and D. R. Paul, Nylon 6 nanocomposites prepared by a melt mixing masterbatch process, *Polymer*, 45, 2991-3000, 2004.

[9] C. Zhou, Q. Shi, W. Guo, L. Terrell, A. T. Qureshi, D. J. Hayes, et al., Electrospun bio-nanocomposite scaffolds for bone tissue engineering by cellulose nanocrystals reinforcing maleic anhydride grafted PLA, *ACS Appl Mater Interfaces*, 5, 3847-54, 2013.

[10] A. Ramezani Kakroodi, S. Cheng, M. Sain, and A. Asiri, Mechanical, Thermal, and Morphological Properties of Nanocomposites Based on Polyvinyl Alcohol and Cellulose Nanofiber fromAloe veraRind, *Journal of Nanomaterials*, 2014, 1-7, 2014.

[11] Y. Srithep, L.-S. Turng, R. Sabo, and C. Clemons, Nanofibrillated cellulose (NFC) reinforced polyvinyl alcohol (PVOH) nanocomposites: properties, solubility of carbon dioxide, and foaming, *Cellulose*, 19, 1209-1223, 2012.

[12] M. S. Peresin, Y. Habibi, J. O. Zoppe, J. J. Pawlak, and O. J. Rojas, Nanofiber Composites of Polyvinyl Alcohol and Cellulose Nanocrystals: Manufacture and Characterization, *Biomacromolecules*, 11, 674–681, 2010.

[13] H. Zhang, J. Huang, L. Yang, R. Chen, W. Zou, X. Lin, et al., Preparation, characterization and properties of PLA/TiO_2 nanocomposites based on a novel vane extruder, *RSC Adv.*, 5, 4639-4647, 2015.

[14] S. Mazinani, A. Ajji, and C. Dubois, Morphology, structure and properties of conductive PS/CNT nanocomposite electrospun mat, *Polymer,* 50, 3329-3342, 2009.

[15] N. G. Sahoo, S. Rana, J. W. Cho, L. Li, and S. H. Chan, Polymer nanocomposites based on functionalized carbon nanotubes, *Progress in Polymer Science,* 35, 837-867, 2010.

[16] Q. Wang, J. Dai, W. Li, Z. Wei, and J. Jiang, The effects of CNT alignment on electrical conductivity and mechanical properties of SWNT/epoxy nanocomposites, *Composites Science and Technology,* 68, 1644-1648, 2008.

[17] M. Ichazo, C. Albano, J. Gonzalez, R. Perera, and M. Candal, Polypropylene/wood flour composites: treatments and properties, *Composite structures,* 54, 207-214, 2001.

[18] S. M. Nachtigall, G. S. Cerveira, and S. M. Rosa, New polymeric-coupling agent for polypropylene/wood-flour composites, *Polymer Testing,* 26, 619-628, 2007.

[19] Y. Wang, R. Qi, C. Xiong, and M. Huang, Effects of coupling agent and interfacial modifiers on mechanical properties of poly (lactic acid) and wood flour biocomposites, *Iran Polym J,* 20, 281-294, 2011.

[20] B. L. Shah, S. E. Selke, M. B. Walters, and P. A. Heiden, Effects of wood flour and chitosan on mechanical, chemical, and thermal properties of polylactide, *Polymer Composites,* 29, 655-663, 2008.

[21] S. K. Ozaki, M. B. B. Monteiro, H. Yano, Y. Imamura, and M. F. Souza, Biodegradable composites from waste wood and poly(vinyl alcohol), *Polymer Degradation and Stability,* 87, 293-299, 2005.

[22] L. Huang, J. T. Arena, S. S. Manickam, X. Jiang, B. G. Willis, and J. R. McCutcheon, Improved mechanical properties and hydrophilicity of electrospun nanofiber membranes for filtration applications by dopamine modification, *Journal of Membrane Science,* 460, 241-249, 2014.

[23] J. Yao, C. Bastiaansen, and T. Peijs, High Strength and High Modulus Electrospun Nanofibers, *Fibers*, 2, 158-186, 2014.

[24] D. Yang, Y. Li, and J. Nie, Preparation of gelatin/PVA nanofibers and their potential application in controlled release of drugs, *Carbohydrate Polymers*, 69, 538-543, 2007.

[25] S. Wu, F. Li, H. Wang, L. Fu, B. Zhang, and G. Li, Effects of poly (vinyl alcohol)(PVA) content on preparation of novel thiol-functionalized mesoporous PVA/SiO_2 composite nanofiber membranes and their application for adsorption of heavy metal ions from aqueous solution, *Polymer*, 51, 6203-6211, 2010.

[26] H. Ito, Wood plastic composites using cellulose nanofiber technique, *Nippon Gomu Kyokaishi,* 2, 41-45, 2013.

[27] N. M. Stark and R. E. Rowlands, Effects of wood fiber characteristics on mechanical properties of wood/polypropylene composites, *Wood and fiber science,* 35, 167-174, 2003.

COATING OF TRANSPARENT AND CONDUCTING GRAPHENE FILM WHEN WRAPPED WITH DMF DOPED PEDOT: PSS

Adila Rani*[a,b,c,d], Min Park[a], Jung Hoon[c]
[a]Polymer Hybrid Center, Korea Institute of Science and Technology, Republic of Korea
[b]University of Science and Technology, Dejeon, Republic of Korea
[c]NOROO Holding, Republic of Korea
[d]Ewha WOmans University, Republic of Korea

**Corresponding Author*: Adila Rani
Email: adila78@gmail.com

ABSTRACT

We report the deposition of graphene / Poly (3, 4-ethylenedioxythiophene): Poly styrene sulfonate (Graphene/PEDOT: PSS) films onto flexible, transparent, and non conducting polyethylene terepthalate (PET) substrates. This room-temperature solution process is completely compatible with polymeric substrates and does not require a sophisticated transfer process, allowing uniform and controllable deposition of Graphene/PEDOT: PSS thin films with tailored optical and electrical properties over large areas. In particular, 94 % transmittance persist sheet resistance of 500 Q / □. Further conducting, transparent, and flexible film on PET substrate is checked for electronic ink paper using white, black, and colored ink. To form an electronic ink electronic display, the ink is filled onto a sheet of Graphene/PEDOT: PSS on PET substrate, which is laminated to a layer of circuits or thin film transistors. The circuitry forms a pattern of pixels that can be controlled by a display driver. The imaging film is compared with nonflexible ITO substrates and finds same performance as compared to ITO substrate and to be the most visually attractive active matrix electronic paper display.

Keywords: graphene, PEDOT: PSS, transparent, flexible, electrode, electrophoretic devices

INTRODUCTION

Flexible displays have fascinated people for at least 50 years, and have been discussed seriously for at least 20 years. The difference now is that display and backplane technology have evolved to the point where reasonably attractive-looking demonstrations of flexible screens are possible. This has had two effects. It has spurred an intense drive to finally realize the long-time dream of flexible displays. And it also has allowed industry participants to experience directly the real-world challenges of building these displays, rather than granting them the luxury of imagining that products were just around the corner. [1]

Flexible displays are rather new for the display industry. Now days many display technologies are introduced like Liquid Crystal Display, Organic Light-Emitting Diode Display, and Electrophoretic Display. [1, 2]

Electrophoretic display (EPD) has the advantages of thin, flexible, lightweight, wide viewing angle, and is easy to read in all lighting conditions.[3] With the properties of invariably reflective and bistable, an EPD is considered to be the best candidate for electronic paper (E-Paper). The images on the display can be electrically written and erased repeatedly; moreover, the power supply of an EPD can be turned off after updating images. An EPD film contains electrophoretic material which is composed of charged white particles suspended in a colored fluid.[4-7] The charged particles can be moved to the top (white state) or the bottom (black state) of the display according to the applied electric field on the EPD film. Electrophoretic displays are almost invariably reflective and bistable. The main limitation is slow switching speed (hundreds of milliseconds), making electrophoretics a poor choice for video or even rapid scrolling. This largely eliminates the cell phone, game, and parts of the auto market. [2] In this paper, flexible and transparent display is fabricated [8, 9] and used as display controller for supporting various types of EPD panel. [5] In this regard, Graphene/PEDOT: PSS thin film on flexible PET substrate with tailored optical and electrical properties (94 % and 500 Ω / □) were developed. Further conducting, transparent, and flexible film on PET substrate is checked for electronic ink paper using white, black, and colored ink.

EXPERIMENTAL PROCEDURES

Synthesis of GO and reduced graphene oxide

GO was prepared using the modified Hummer's method. [8-10] Graphite powders (12 g) were charged in a reaction flask containing H_2SO_4 (150 mL). After $KMnO_4$ was gradually added to the flask keeping the temperature below 20 C. The mixture was then heated, and the reaction continued at 35 C. After 2 h, distilled water was added. The GO was then washed repeatedly with deionized water until the pH of the filtrate was neutral. The GO slurry was then freeze-dried and stored in a vacuum oven.

Reduction of graphite oxide was done according to the procedure reported by stankovich et al.[11] In a typical procedure for chemical conversion of graphite oxide to reduced graphene, the resulting homogeneous dispersion (0.3 % in acetic acid) was mixed with HI (5.3 ml) was then added and the mixture was stored at 40 °C for 40 h with constant stirring. The product was isolated by filtration, washed with saturated sodium bicarbonate (10x100 ml; 200g in 1400mL distill water).

Synthesis of reduced graphene oxide and PEDOT: PSS solution and fabrication of flexible display

Disperse the reduced graphene oxide in DMF by using branson sonicatior for ~ 2hours. Add PEDOT: PSS and sonicate the mixture for 1 hr. PET substrates were cleaned with Methanol and MEK and dry under blowing nitrogen or air. Deposit the reduced graphene and PEDOT: PSS by using coating technique. [12] (See Figure. 1) (Coating speed 100mm, coater number # 8). Dry the sheet first room temperature (5 minutes) then dried the substrate at 120 C for 1 minute and cooled for 5 minutes at room temperature after every coating. Coating is repeated many times (4-5 times) to get desired sheet resistance.

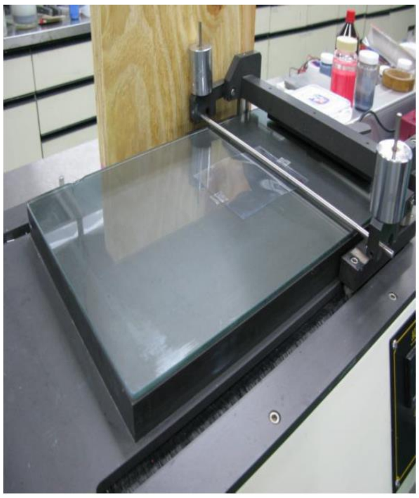

Figure 1. Coating technique of graphene with PEDOT: PSS in DMF on PET substrate

CHARACTERIZATION

Thermal analyzer instruments TGA Q50 was used for the thermo gravimetric analysis (TGA) in nitrogen at a heating rate of 1 C/min from room temperature to 800 C. The XPS spectra were recorded on a PHI 5800 ESCA system with A1Kα excitation at an acceleration voltage of 10 kV and 250 W for a probe size of 400 μm. The chamber pressure was maintained at 10^{-10} Torr. Electrical conductivity measurements of thin films on the glass substrate were performed using a four-point probe method. The probe head was a four-point cylindrical probe (JANDEL Engineering Ltd.). A DC precision power source (Keithley, Model 6220) and voltmeter (Keithley, Model 2182A) were used for all measurements. Thickness and roughness measurements of deposited films on glass substrates were measured by AFM (Asylum Research MFP3D) in the non- contact mode with 10-nm standard cantilevers (AC160TS, Olympus).

Results and Discussion

Photoelectron spectroscopy (XPS) was used to analyze the structure of the graphite oxide (GO) before reduction and after reduction in acidic medium. It is observed that the after reduction graphene exhibited a significantly higher carbon signal compared to that observed for the GO. The photoelectron peak of GO was curve-fitted with three peaks at ~284.8 eV (C-C), ~286.8 eV (C-O), and ~288.2 eV (C=O). In the case of reduced graphene oxide, only one dominant peak was observed (Fig. 2) at ~284.6 eV, which was attributed to graphitic carbon.

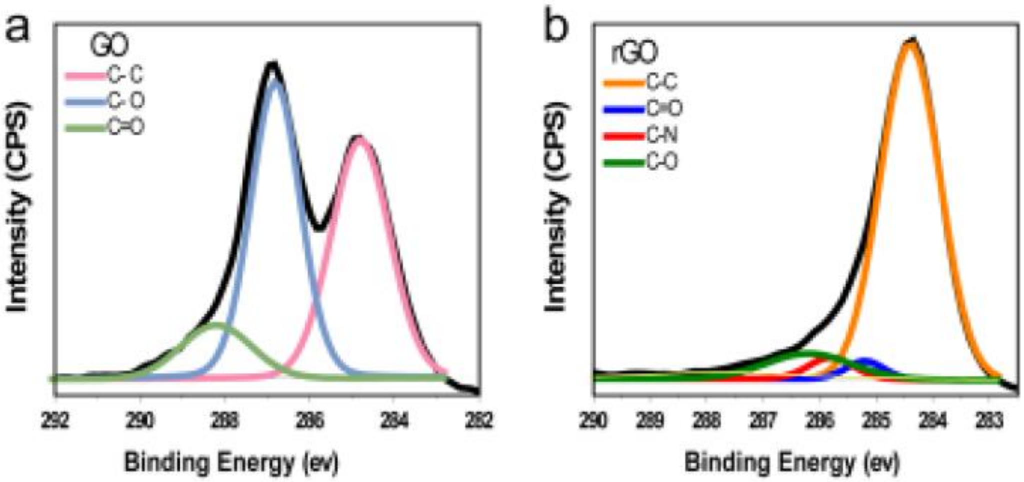

Figure 2. High resolution N 1s XPS spectra of (a) GO and (b) rGO

Low peak intensity was resolved after the peak deconvolution process, which indicated that less oxygen existed in reduced graphene oxide compared to the starting graphite oxide. The results are consistent with previous reports. [8, 9, 11]

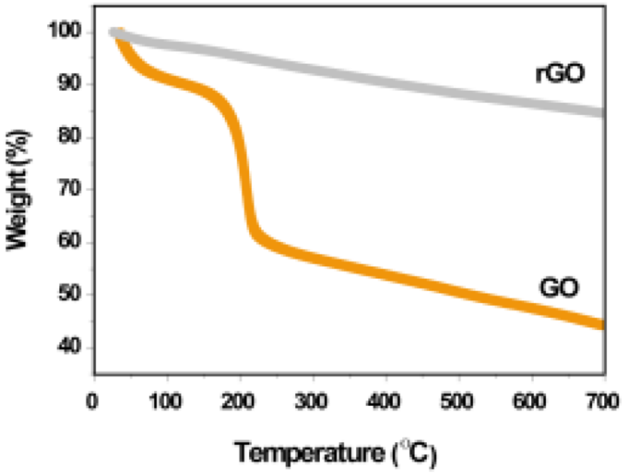

Figure 3. Thermogravimetric Analysis (TGA) of (a) GO and (b) rGO

Figure 3 shows the TGA curves of GO, and reduced graphene. The TGA of GO showed a significant loss of mass (~60%) at ~180 C due to the decomposition of oxygen-containing functional groups in GO. On the other hand, chemically reduced graphene showed smaller loss of mass (~16%) than GO at 700 C in the nitrogen atmosphere.

The powder X-ray diffraction (XRD) pattern of the prepared G-O was compared with those of the reduced graphene depicted in Figure 4. The peak position for graphite powder was 20 = 26.7° (J-spacing ~3.34 A). [11] A typical broad peak near 10.27° (J-spacing ~8.60 A) was observed for the G-O powder. Compared with the parent G-O the peak of acid reduced graphene showed a dramatic shift to higher 20 angles (24.57°; J-spacing ~3.62 A) and was narrower than that of highly RG-O (~23°; J-spacing ~3.86 A), suggesting that acid reduced graphene was well ordered with two-dimensional sheets without nitrogen incorporation and there was a decrease in the average interlayer spacing of the RG-O platelets depicted in Figure.

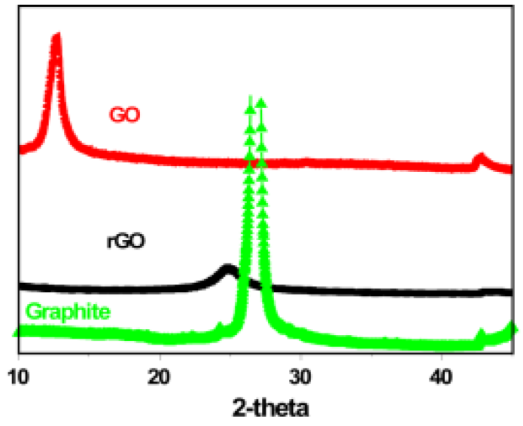

Figure 4. XRD of grapahite, GO, and rGO

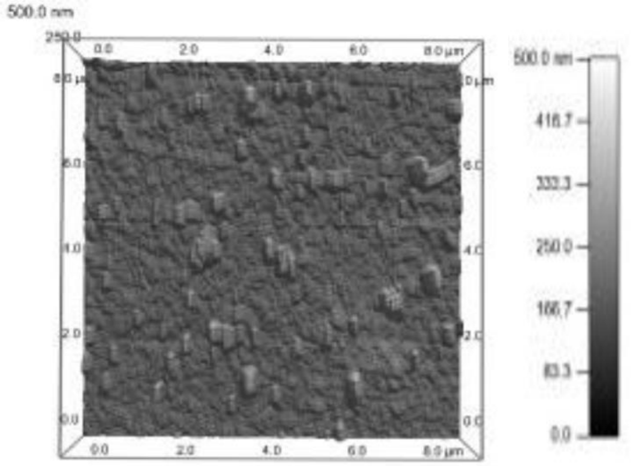

Figure 5. Atomic Force Microscopy (AFM) image of the coating of rGO with PEDOT: PSS

The morphological changes are confirmed in Fig. 5 by tapping-mode AFM images of the Graphene/PEDT: PSS films deposited by simple coating method onto PET substrate. It is revealed the presence of flakes of graphene, which led to the conclusion that the exfoliation of GSs was achieved.

To study the influence of electrical conductivity of these multilayer coatings, which were composed of graphene/PEDOT: PSS, their sheet resistances were investigated (Figure. 6). The conductive behavior improved as the number of coating is increased and after 5 coating it show 500 Q / □ sheet resistance with 94% transmittance at 550 nm. The transmittance was plotted (Figure. 6 c) against sheet resistance at 550 nm during the deposition process.

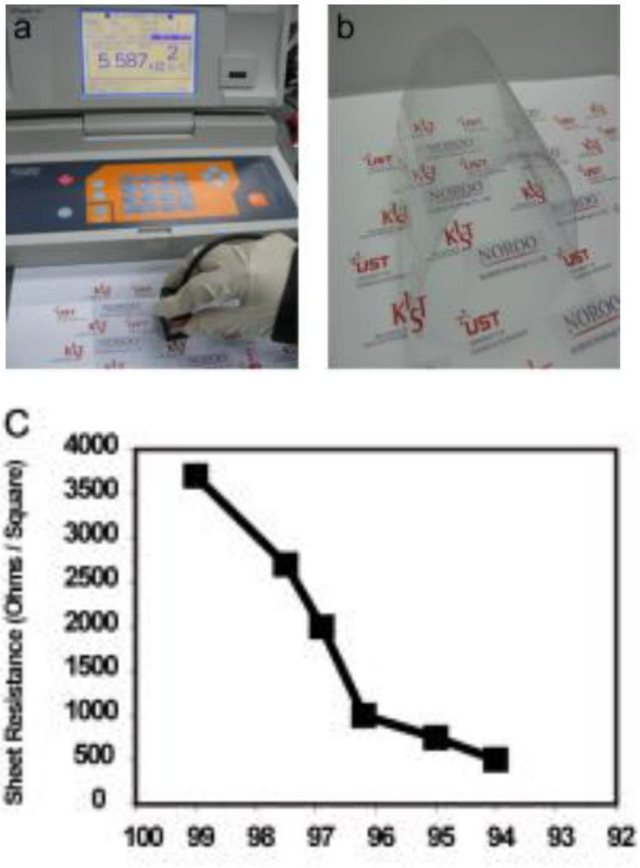

Figure 6. (a) Photograph showing the resistance value of the fabricated flexible film using rGO:PEDOT:PSS. (b) Photograph showing the flexibility and transparency of the film, and (c) Sheet resistance of the films with respect to transmittance

The electrophoretic device or device for electronic ink is fabricated by two flexible PET sheets, consisting of graphene/PEDOT: PSS coatings (5 times coating with 500 Q / □ sheet resistance at 94 % transmittance), which are parallel and -0.7 mm spaced a part and regionally covered with electrodes. [3] A direct current signal was used to produce a locally defined electric field between overlapping electrode segments on the two flexible sheets or plates. Enclosed between the plates or electrodes is a generally inert dielectric liquid phase consisting of white, and colored ink; blue and white, provided by NOROO Holding company. This ink was sandwiched between two parallel conducting electrode panels. The particles of this solid phase are electrophoretically active and migrated to the positive or negative electrode under the influence of an applied field. The electrophoretic particles move efficiently (Fig. 7a & b) with flexible graphene/PEDOT: PSS coating PET substrate.

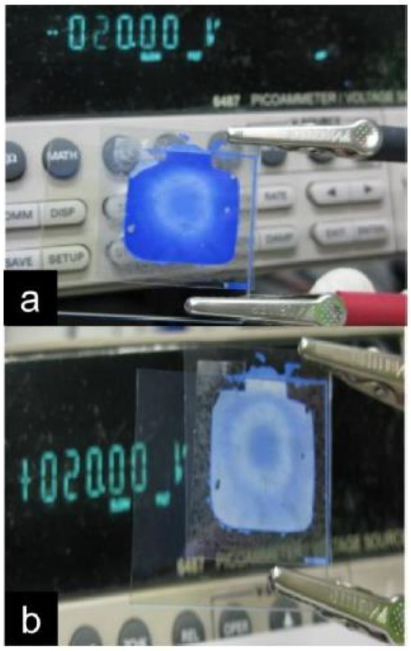

Figure 7. Electrophoretic device fabricated showing the color change with respect to derive voltage (a) at -20V the Blue color is dominant and (b) at +20 V, white color is dominant.

CONCLUSIONS

A flexible and transparent electronic paper using the blue and white ink, provided by NOROO Holding company has been developed. The flexible and transparent electrode was based on reduced graphene with PEDOT: PSS in DMF solution.

REFERENCES

1. Allen, K.J., *Reel to Real: Prospects for Flexible Displays*. Proceedings of the IEEE, 2005. **93**(8): p. 1394-1399.

2. Chung, I.-J. and I. Kang, *Flexible Display Technology - Opportunity and Challenges to New Business Application.* Molecular Crystals and Liquid Crystals, 2009. **507**(1): p. 1-17.
3. Dalisa, A.L., *Electrophoretic display technology.* Electron Devices, IEEE Transactions on, 1977. **24**(7): p. 827-834.
4. Hopper, M.A. and V. Novotny, *An electrophoretic display, its properties, model, and addressing.* Electron Devices, IEEE Transactions on, 1979. **26**(8): p. 11481152.
5. Kao, W.-C., *Electrophoretic Display Controller Integrated With Real-Time Halftoning and Partial Region Update.* Journal of Display Technology, 2010. **6**(1): p. 36-44.
6. Ota, I., J. Ohnishi, and M. Yoshiyama, *Electrophoretic image display (EPID) panel.* Proceedings of the IEEE, 1973. **61**(7): p. 832-836.
7. Fitzhenry-Ritz, B., *Optical properties of electrophoretic image displays.* Electron Devices, IEEE Transactions on, 1981. **28**(6): p. 726-735.
8. Rani, A., et al., *Multilayer films of cationic graphene-polyelectrolytes and anionic graphene-polyelectrolytes fabricated using layer-by-layer self- assembly.* Applied Surface Science, 2011. **257**(11): p. 4982-4989.
9. Rani, A., et al., *Reduced graphene oxide based flexible organic charge trap memory devices.* Applied Physics Letters, 2012. **101**(23): p. 233308.
10. Hummers, W.S. and R.E. Offeman, *Preparation of Graphitic Oxide.* Journal of the American Chemical Society, 1958. **80**(6): p. 1339-1339.
11. Moon, I.K., et al., *Reduced graphene oxide by chemical graphitization.* Nat Commun, 2010. **1:** p. 73.
12. Yang, H. and P. Jiang, *Large-Scale Colloidal Self-Assembly by Doctor Blade Coating.* Langmuir, 2010. **26**(16): p. 13173-13182.

SENSITIVITY ANALYSIS OF THAR COAL GASIFICATION USING STEAM

Fahim Uddin[1,2,*], **Inayatullah Memon**[1] **and Syed A. Taqvi**[1,2]
[1] Chemical Engineering Department, NED University of Engineering & Technology,
Karachi, Pakistan
[2] Chemical Engineering Department, Universiti Teknologi PETRONAS, 32610 Bandar Seri
Iskandar, Perak Darul Ridzuan, Malaysia

[*]Corresponding author. Tel.: +60-17-352-2492
E-mail address: fahim_nedian@yahoo.com (Fahim Uddin)

ABSTRACT

Depletion of conventional fuels and the current energy crisis have been a strong driving force in order to propose alternate fuels and assess their feasibility. Many of the research is funneling towards coal due to its abundance as energy resource. This paper provides a new model for indirect gasification with steam, in which the flue gas produced by syngas is used to provide the reaction heat. Steady-state simulation has been developed using Aspen Plus® and sensitivity analysis of flue gas temperature has been carried out. Coal from Thar reserves is selected as feedstock. Results shows that that high temperature of flue gas at the bayonet inlet aids to better temperature profiles and is causes higher quantity of Syngas produced. However, lower temperatures provide Syngas with higher hydrogen content.

Keywords: Energy; Indirect Gasification; Syngas; Thar Coal.

1 INTRODUCTION

Oil and gas have served the world as energy resource for many decades, and now their reservoirs are at the verge of being exhausted. Due to this and the fluctuations of petroleum prices in the international market, humanity is seeking for other solutions for energy supply. Oil has lost 14% of its share in the global energy mix in the last 40 years, particularly in the power sector [1]. In Pakistan, energy demand is surging as the alternate energy resources were not utilized despite being proposed by the researchers for more than 25 years.

Coal is an ample resource, providing a host of processing opportunities [2]. Half of the world-wide coal utilization is claimed by Asian continent, particularly China and India. Currently it delivers more than two-fifths of the electricity produced globally [3].

Gasification is an ecological and viable method for coal processing as the polluting compounds of sulphur as well as nitrogen are easily taken care of [4]. Being an endothermic process, it requires heat to proceed. If this heat is afforded by an external source, the process is referred to as Indirect Gasification [5]. Steam is a better indirect gasifying medium than air or pure oxygen due to its availability and ability to produce syngas with high calorific value [6].

Owing to the complications of gasification process, it is difficult to model the process and completely capture the spatially varying dynamics of the system. Consequently, not many researchers have covered the modelling of gasifiers and there is still room for better modelling so that more assumptions could be relaxed. Moving bed counter-current gasifier was developed, improved and compared with the industrial gasifiers [7] [8] [9].

A steady state Aspen Plus® simulation has been developed to present a novel indirect gasification model [10]. The gasifier assembly contains a bayonet heat exchanger through which flue gases pass to provide reaction energy. Bayonets scheme is used due to its ability to deal with abrupt temperature fluctuations and fluids as hot as 1400°C [11]. The flue gases to be fed to these bayonets are produced by the combustion of a portion of raw product.

Sensitivity of this scheme to the flue gas temperature has been studied. Aspen Plus® model has been developed for the proposed scheme. Bussman's model for heat transfer has been used for the bayonets heat exchange in the process [12].

2 MODEL DEVELOPMENT

2.1 Components

The conventional components C (solid), CH_4, CO, CO_2, H_2, H_2O, H_2S, N_2, O_2, S (solid) and Tar (as C_6H_6*) were included in the Aspen Plus® model. Proximate, Ultimate and Sulphur Analyses were used to define the non-conventional components. Thar indigenous coal has been selected as feedstock with the specifications shown in Table I as reported by Jaffri et. al. [13].

2.2 Process Description

In this process, coal is fed from the top of the fixed bed gasifier while steam enters from the bottom of gasifier. Reaction heat is provided by the flue gases passing through the vertical bayonet exchanger assembly within the gasifier. Syngas produced in the gasifier consists of CO, CH_4, CO_2, H_2 and unreacted steam. Unreacted char and ash leaves the gasifier through the bottom.

Raw Syngas is divided into two parts; one is drawn off as product syngas while the other is combusted to produce heat required for endothermic gasification process.

Adiabatic processes i.e. Drying, Pyrolysis and Partial Gasification of the char will take place in the upper section of the gasifier. The heat required for these processes is provided by the product stream passing through this section at a higher temperature until the thermal equilibrium is established.

Feed in gaseous and solid state passes through the lower section of the gasifier with a bank of bayonets in between. The heat is thus transferred to the feed for the endothermic reaction to take place until the desired conversion is achieved.

2.3 Kinetics

Pyrolysis process can be curtailed to the reaction:

$$\text{Coal} \rightarrow CO + H_2 + CO_2 + H_2O + H_2S + N_2 + CH_4 + C_6H_6 + \text{Char} \quad (1)$$

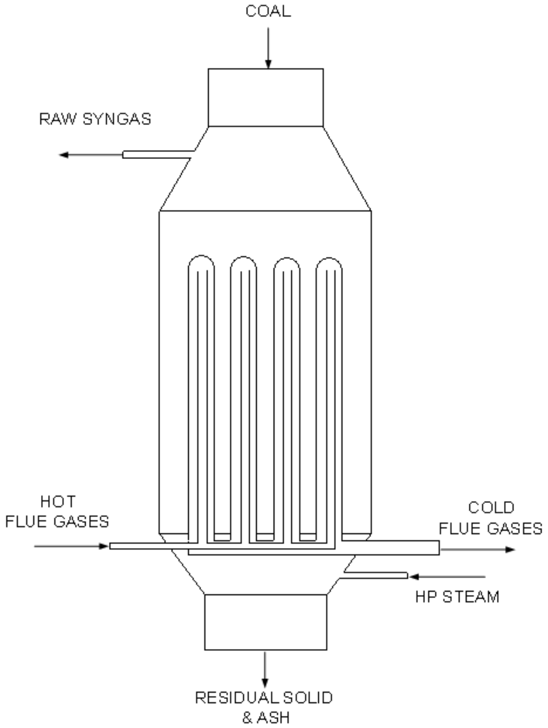

Figure 1. Proposed indirect gasifier with bayonets

Following reactions are considered in the process of char gasification [14] [15].

$$C + (z+2)(2z+2)^{-1}\ O_2 \rightarrow z(z+1)^{-1}\ CO + (z+1)^{-1}\ CO_2 \quad (2)$$

$$C+H_2O \rightarrow CO + H_2 \quad (3)$$

$$C+CO_2 \rightarrow 2CO \quad (4)$$

$$C+2H_2 \rightarrow CH_4 \quad (5)$$

$$CO+H_2O \rightarrow CO_2 + H_2 \quad (6)$$

$$H_2+0.5O_2 \rightarrow H_2O \quad (7)$$

Where [16],

$$z = [CO] / [CO_2] = 2500\text{exp.}-6249T^{-1} \quad (8)$$

Table 1. Thar Coal Analyses

Proximate Analysis		**Ultimate Analysis**		**Sulphur Analysis**	
Element	**Value (wt. %)**	**Element**	**Value (wt. %)**	**Element**	**Value (wt. %)**
Moisture (wet basis)	8.5	C	54.57	Pyritic	1.46
		H	3.21		
Fixed carbon (dry basis)	25.83	N	1.07	Sulphate	1.47
		Cl	0		
Volatile Matter (dry basis)	53	S	4.39	Organic	1.46
		O	15.59		
Ash (dry basis)	21.17	Ash	21.17		

Char gasification reactions are of mainly two types; gas-solid and gas-gas. In the solid-gas reaction (1), reaction rate is usually fast relative to oxygen diffusion rate into coal; therefore it is categorized as surface reaction. Reactions (2)-(4) are rather slow reactions occurring below 1000°C, thus they are volumetric.

2.4 Assumptions

Following assumptions were taken into account while developing this model:

1. Steady-state process of which pressure losses have being neglected.
2. Thermal equilibrium between solid and gas phases.
3. Pyrolysis gas does not enter the area of char gasification.

2.5 Heat Integration

Syngas available from the gasifier is at sufficiently higher temperature than the temperature required for further processing and purification. To utilize this heat, it is introduced in a cross flow heat exchanger to produce saturated steam from water. The stream is further sent for superheating. The Syngas which has been cooled is now split into two parts. One part is drawn as the product stream for further processing and the other part is mixed with the preheated air to be fed in the furnace for the combustion process.

Mixture of Syngas and the preheated air is fed to the Furnace. As a result, high temperature flue gases are produced. The saturated steam produced in the Complementary Steam Generation and Syngas cooling sections utilizes the heat from the hot furnace gases and produce high pressure superheated steam. This steam is introduced in the gasifier for the main process.

After leaving the bayonets, the flue gas stream is used to preheat the air which is needed for combustion in the furnace. Then it further loses their heat content in order to produce saturated steam as a process utility. This steam is mixed with the steam coming from the Syngas Cooler to be further heated to superheated steam. Cooling of ash available preheats the water circulating the cooler jacket.

3 NUMERICAL MODELING

Bayonet heat exchanger model in the gasifier is based on the one presented by Bussman [12]. It consists of a number of bayonets tubes installed vertically. Each tube consists of two parts. The inner part or the centre tube is made of ceramic in which hot flue gases are introduced from the bottom and rise to the top. Then the gases turn around and flow down the metallic annular section and leave the bayonet to join the structure at downstream.

The geometry of the bayonet tubes distribution in the gasifier is supported by a representation in Figure 2.

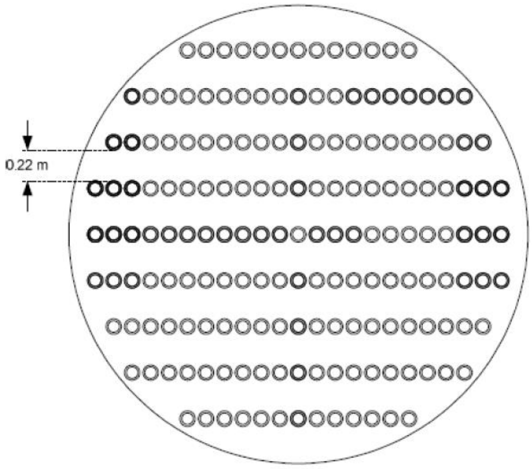

Figure 2. Bayonets distribution across the reactor cross-section

Following assumptions are taken into account while developing the calculation model for the heat transfer through the bayonet tubes to the reactor.

1. Thermal properties of the gas streams in each cell are calculated at the mean temperature of each cell.
2. Radial heat transfer is dominant, so axial heat transfer can be neglected.
3. Flow of coal is along the length of the tube heat exchanger.
4. Heat transfer by radiation is considered to take place from centre pipe wall to the annulus inner wall and from annulus outer wall to the reactor volume.

The energy balance equations are formed for each cell *'i'* of the bayonet tube by taking into account the three modes of transference of heat i.e. conduction, convection and radiation. The zones of transfer were the centre pipe, annular section and gasifier environment. Total heat transferred to gasifier and between adjacent cells was also considered.

The properties (C_p, μ, k, and ρ) of the flue gases passing through the bayonet tube heat exchangers and those of the mixture of steam and syngas flowing over the outer surface of the bayonets are retrieved from the properties of streams. The volume flow rate over the bayonet surface and heat transfer q_i for each cell is also brought into agreement with the heat transfer taking place in the gasifier reactors, in the Aspen Plus® scheme.

The model for energy balance developed is designed in Microsoft Excel®. In the topmost portion of the bayonet, an assumption is made that gases leaving the centre pipe and entering the annular section are in thermal equilibrium and heat losses in the top hemispherical section can be ignored. For each cell, the value of the residual is calculated to be minimized for each equation.

The system of six equations is then resolved to find the temperature profiles in the gasifier.

4 RESULTS AND DISCUSSIONS

Table 2 presents the feedstock of the process.

Table 2. Feedstock Conditions

COAL	Temperature	20	°C
	Pressure	3.5	MPa
	Particle Diameter	0.02	m
STEAM	Temperature	800	°C
	Pressure	3.5	MPa

Lower Heating Value of Thar Coal is found to be 8956 Btu/lb or 4979 kCal/kg using a correlation presented by Mason and Gandhi.

$$Q = 198.11\ C + 620.31\ H + 80.93\ S + 44.95\ A - 5153 \qquad (9)$$

The pyrolysis yield for Thar coal is devised on the basis of ultimate analysis and their comparison with the pyrolysis yield for Thar Coal.

There is a direct effect of heat transfer on the reaction kinetics by altering the temperature profiles and thus conversion of the reactor. So, the simulation model of gasification kinetics on Aspen Plus® is merged with the energy balances in Microsoft Excel® and the heat integration scheme again in Aspen Plus®. The height of each bayonet was divided into 12 cells, and all of these are modelled for heat balance equations. Gasifier is modelled by a CSTR battery, each corresponding to the particular bayonet heat exchanger cell. Each portion of the reaction is characterized by a single average temperature. As a result of this temperature consistency, CSTR reactors are used to model the different portions of the gasifier.

Heat integration simulation in Aspen Plus® is used to find entering and exiting properties of the flue gases across the bayonets.

The volumetric flowrate and physical properties of flue gas are temperature-dependant parameters. In recognition of this fact, specified correlations for these parameters are defined. Using the values from the simulation, temperature dependencies of density ρ, dynamic viscosity μ, specific heat C_p, and thermal conductivity k of flue gases are defined as a its linear function.

For any given cell with temperature T (K), the Dynamic Viscosity (Pa.s.) is given as:

$$\mu = C * T^{0.5} \qquad (10)$$

The models are run in an iterative sequence to find a temperature and energy distribution which satisfies all of them.

Figures 3 and 4 present the typical trends of temperature profile and heat distribution profile in the bayonets along the length. This representation shows that the flue gases entering the bayonet centre pipe cool down, giving away heat to the cooler gases in annular section which subsequently transfer this heat to the endothermic gasification reaction taking place over the surface of bayonets. Also, an increasing trend is observed in the temperature profile of the gases in annular section.

The temperature of the incoming gasifier gases drastically increase in only one-third of the bayonet height due to the heat provided by the hot flue gases and due to some combustion in char because of high oxygen content.

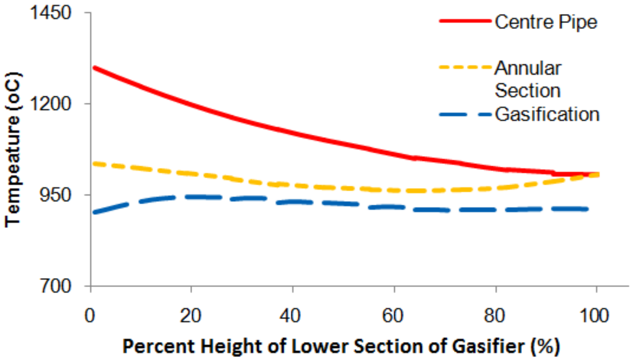

Fig. 3: Temperature Profiles along the Length of the Gasifier

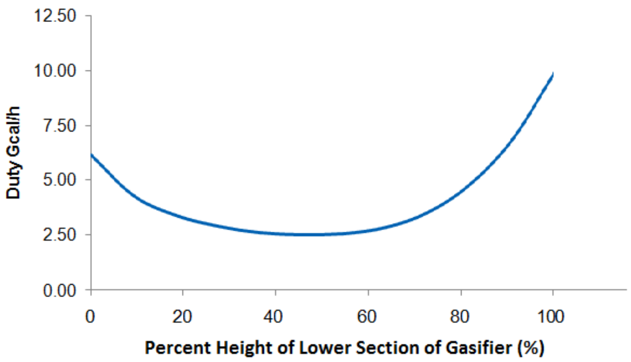

Fig. 4 : Heat Distribution Profiles along the Length of the Gasifier

4.1 Sensitivity Analysis

Simulation trials have been conducted by varying the flue gas temperature at the bayonet inlet so as to vary the heat and temperature profiles of the reactor and note the effects on the fore stated parameters.

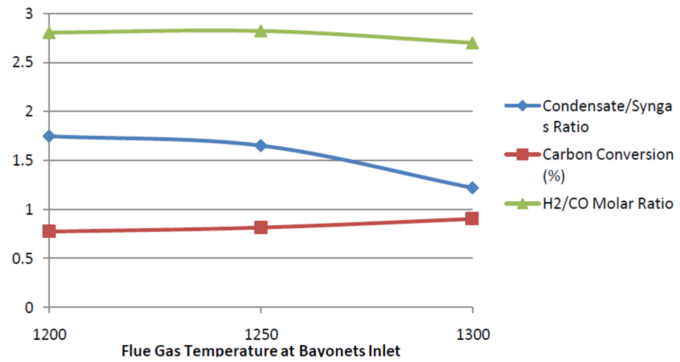

Figure 5. Flue gas inlet temperature analysis: Comparison of parameters (a)

Figure 5 shows that lowering the temperature of flue gas at bayonet inlet results in a better H_2/CO ratio as compared to the value in the base case. The reason of this behaviour can be the relatively lower conversion of carbon in the gasifier, hence giving away less amount of carbon monoxide.

As far as the conversion of carbon is concerned, it shows a decrease in its magnitude as the flue gas inlet temperature is reduced. It can be stated that heat and temperature profiles of the reactor are rearranged and result in low heat transfer thus causing a decline in the carbon conversion.

It is also shown that the inlet temperature of flue gas at 1300°C has the least Condensate/Syngas ratio. A lesser value of this ratio leads to a relatively lesser condensate production, hence lower wastewater treatment costs.

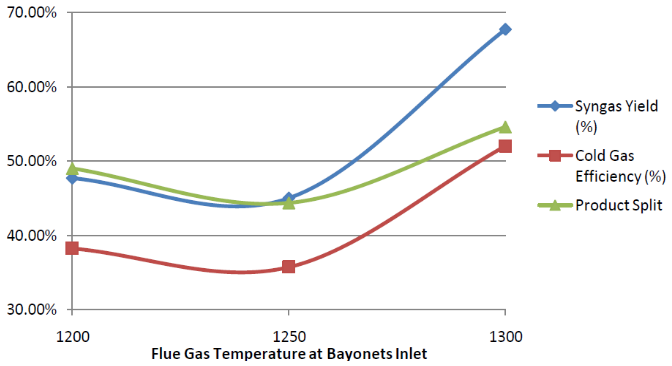

Figure 6. Flue gas inlet temperature analysis: Comparison of parameters (b)

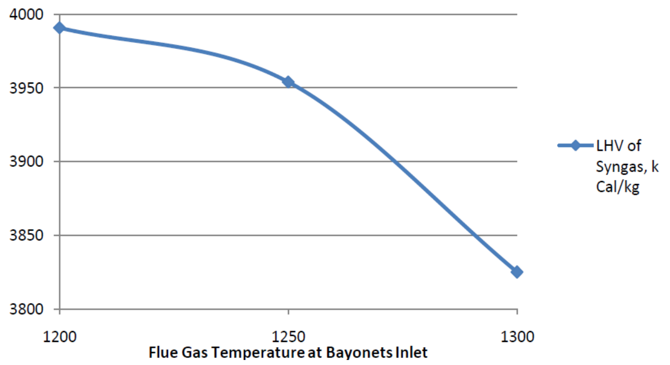

Figure 7. Flue gas inlet temperature analysis: Comparison of parameters (c)

Figure 6 shows that syngas yield, cold gas efficiency and product split attain their highest values at the inlet temperature 1300°C. Thus this temperature is most feasible as far as the quantity of production is concerned. But it is at the higher bound of the range and it can be said that this may or may not be the best temperature and better points may lie outside the higher bound.

The Lower Heating value of syngas produced i.e. LHV has a decreasing trend as depicted in Figure 7. Therefore it can be concluded that the temperature 1200°C is the most feasible point according to this measure. But, as stated earlier, it is at the lower bound of the range and it can be said that this may or may not be the best temperature for LHV and better points may lie outside the lower bound.

In short, the results of lowering the flue gas temperature at bayonets inlet were poor in quantity aspects (such as Cold Gas Efficiency, Syngas Yield and Carbon Conversion) but have a solid edge over the other two ratios (considering the quality criteria H_2/CO and LHV). It can be concluded that high temperature of flue gas at the bayonet inlet aids to better temperature profiles and thus better results but lower temperatures offer higher hydrogen content and thus high quality syngas.

5 CONCLUSION

The results of lowering the flue gas temperature at bayonets inlet were poor in quantity aspects (such as Cold Gas Efficiency, Syngas Yield and Carbon Conversion) but have a solid edge over the other two ratios (considering the quality criteria H_2/CO and LHV). It can be concluded that high temperature of flue gas at the bayonet inlet aids to better temperature profiles and thus better results but lower temperatures offer higher hydrogen content and thus high quality syngas.

ACKNOWLEDGEMENT

The authors would like to recognize and appreciate the efforts and inputs of Mr. Junaid Akhlas, (Polymer & Petrochemical Engineering Department, NED University of Engineering & Technology, Pakistan). He was always there to aid whenever required and provided insights and trends of the research. His guidance in troubleshooting of the simulation files can never be forgotten.

REFERENCES

[1] BP Energy Outlook 2030, Beyond Petroleum Ltd., 2012.

[2] "The Coal Resource: A Comprehensive Overview of Coal," World Coal Institute, 2005.

[3] BP Energy Outlook 2035, Beyond Petroleum Ltd., 2015.

[4] J. Phillips, "Different Types of Gasifiers and Their Integration with Gas Turbines".

[5] B. V. G. D. F. C. D. Rocca., "Energy from Gasification of Solid Wastes," *Waste Management*, no. 23, pp. 1-15, 2003.

[6] C. Z. A. B. L. B. M. F. Maria Sudiro, "Dual-Bed Gasification of Petcoke: Model Development and Validation," *Energy Fuels*, no. 24, p. 1213–1221, 2010.

[7] M. L. Hobbs, P. T. Radulovic and L. D. Smoot, "Modeling Fixed-Bed Coal Gasifiers," *AIChE Journal*, vol. 38, no. 5, May 1992.

[8] P. T. Radulovic, M. U. Ghani and L. D. Smoot, "An improved model for fixed bed coal combustion and gasif ication," *Fuel*, vol. 74, no. 4, p. 582–594, April 1995.

[9] E. M. Grieco and G. Baldi, "Predictive model for counter current coal gasifiers," *Chemical EngineeringScience*, vol. 66, no. 23, p. 5749–5761, December 2011.

[10] J. Akhlas, S. Baesso, A. Bertucco and F. Ruggeri, "Coal gasification by indirect heating in a single moving bed reactor: Process development & simulation," *AIMS Energy*, vol. 3, no. 4, pp. 635-665, 2015.

[11] M. H. Wesenberg., "Gas Heated Steam Reformer Modelling," 2006.

[12] W. C. B. K. F. Bussman, "Variable Test Furnace Cooling," in *2005 Summer Heat Transfer Conference* , San Francisco, July 17-22, 2005.

[13] Z. J. Jaffri G.R., "Catalytic gasification of Pakistani Lakhra and Thar lignite chars in steam gasification," *Journal of Fuel Chemistry and Technology*, vol. 37, no. 1, pp. 11-19, 2009.

[14] H. C. M. O. C.Y. Wen, "User's Manual for Computer Simulation and Design of the Moving Bed Coal Gasifier," 1982.

[15] B. B. I.H. Rinard, "Great plains ASPEN model development: gasifier model. Literature Review and Model Specification," Morgantown, WV, 1985.

[16] T. C. C.Y. Wen, "Entrainment coal gasification modelling," *Ind. Eng. Chem. Process Des. Dev.*, no. 18, pp. 684-695, 1979.

[17] J. Akhlas, F. Ruggeri and A. Bertucco, "Simulation of Steam Gasification of Coal with PreCombustion," *Chemical Engineering Transactions*, vol. 43, pp. 2017-2022, 2015.

[18] D. M. G. K. Mason, "Formulas for Calculating the Heating Value of Coal and Coal Char. Development, Tests and Uses," *Fuel Processing Technology*, vol. 7, no. 1, pp. 11-22, 1983.

CARBON NANOTUBES LACED SUPERABSORBENT POLYMER FOR ENHANCED OIL RECOVERY TECHNOLOGY

Muhammad Mohsin Yousufi[1], Saud Hashmi [*2]
[1] Department of Petroleum Engineering, NED University of Engineering and Technology, University Rd, Karachi 75270, Pakistan, moshyousufi@hotmail.com
[2]Department of Chemical Engineering, NED University of Engineering & Technology, University Road, Karachi 75270, Pakistan,

[*] Corresponding Author: Saud Hashmi
[*]Email: saudhashmi@neduet.edu.pk

ABSTRACT

Hybrid nano-composite hydrogel of super absorbent polymer (SAP) containing Carboxylated Multi-Walled Carbon Nanotubes (CMWCNTs) was synthesized to enhance the properties of the polymer in reservoir conditions having a low pH value and high temperature. The hybrid hydrogels were tested at different temperatures and pH values and comparison between super absorbent polymers with CMWCNTs and without them were made to observe the osmotic changes in the material as well as increase in the swelling efficiency by the addition of CMWCNTs. It was clearly evidence that the addition of CMWCNT significantly enhanced the swelling capability as well as the mechanical stability of the hybrid hydrogel. FTIR (Fourier Transform Infrared Spectroscopy) analysis was done for characterization of the hydrogel and FESEM (Field Emission Scanning Electron Microscope) was conducted to study the surface morphology.

1. INTRODUCTION

An oil reservoir generally produces around 10% of the reserves present via its natural drive mechanism (primary recovery). An additional 25%-30% is recovered by pressurizing (secondary recovery) the reservoir through water and gas injection. However there is still 50%-70% of crude oil left inside for production. [1] This is where Enhanced Oil Recovery (tertiary recovery) comes into action, as the oil in place is stuck and requires mobility enhancement or a change in the interfacial tension for it to move out of the pore spaces, this way an additional 20%-30% recovery is obtained.

In order to do so chemicals, surfactants, thermal injections are conducted through an injection well. Polymer flooding being one of the Enhanced Oil Recovery methods has been in use for more than 40 years. Being effective in recovery of un-swept oil by improving the mobility ratio. Up to 5%-30% has been obtained by it various cases throughout the world. It is cheaper than water flooding due to decreased water production and increased oil production.

Superabsorbent polymer composites are three-dimensionally cross-linked hydrophilic polymers, capable of swelling and retaining possibly huge volumes of water in swollen state. The experiences of using SAP as plugging agent were conducted in some oilfields in China to meet the need of enhanced oil recovery. After long year operation of water flooding, the water content in crude oil increased which actually decreased the oil output. The higher water content in the crude oil may cause many problems such as increased corrosion, sand production, emulsion formation and disposal, etc. [2, 8]

This is because in pure water or brines with little buffering capacity, like seawater, the addition of gas containing CO_2 at high pressure can depress the pH to less than 2.9, making the water very reactive. Many oil reservoirs in the world use seawater to help produce oil. It is injected into the reservoir in order to push the oil to the production wells. The pH of oilfield waters usually is controlled by the CO_2/bicarbonate system. [3]

Figure 1a SAP-CNT 1% & SAP-CNT 2%

This water will dissolve and corrode steel with great rapidity or, if in the reservoir, will dissolve minerals either wholly or partly. This can lead to formation damage and dramatically reduce injection and production because the newly dissolved species reprecipitate as the pressure drops at the producer well.

Being non-Newtonian, polymers are prone to salinity and high temperature causing a decline in the properties as well as degradation unless reinforced by a certain composite. Hence lowering the swelling capacity and eligibility for working in an environment having pH value less than 2.9. [2, 3, 4]

Figure 1b. SAP with 1% CMWCNT in swelled state

This is where the carbon nanotubes have been taken into consideration because of their surface area enhancing properties along with being highly stable. A hybrid polymer absorbent was considered to increase the efficiency as well as the swelling capacity which might be suitable for use in Enhance Oil Recovery.

2. EXPERIMENTAL SECTION

2.1. Materials

Acrylic acid (AA, Dae-Jung), MBA (Sigma Aldrich) were used as purchased, Acrylamide (AM, Mitsubishi) was recrystallized from Methanol, KPS and NaOH (Dae-Jung) were used as received. CMWCNTs were from Sigma Aldrich. All the solutions were prepared in double distilled water.

2.2. Synthesis

The sonicated 1gm solutions of CMWCNT (in the specified percentages respectively) were mixed with the solutions of methylenebisacrylamide (MBA), acrylamide, and acrylic acid (neutralized partially NaOH up to 75% in a cold bath) in a flask placed on a magnetic stirrer. With the temperature set at 131˚Fahrenheit along with Nitrogen gas being introduced to keep the atmosphere inert.

Initiator (Potassium persulphate) was added for the purpose radical formation. With the passage of time the viscosity increased and eventually after a period of 20 minutes the gel formed rapidly. The gel was allowed to cool down for a while, then was cut down into small pieces and was placed in an oven at 140˚ Fahrenheit for 24 hours.

Afterwards the tiny gel pieces assumed the form of crystals and were milled in a hammer-type-mini-grinder to obtain a powder form. [4] The ratio of MBA with the monomer was 0.23 mole% for the purpose of having maximum capacity in the polymer. Table 1. Indicates the content used for the synthesis of both the samples.

Table 1. (Contents for the synthesis)

Sample Name	Content				
SAP-CNT 1%	Acrylic acid 15gm in 7.5gm of water, neutralized via NaOH up to 75%	Acrylamide 15gm in 13.5gm of distilled water.	Potassium persulphate (initiator) 0.2gm in 4gm of distilled water	MBA (Methylenebisacrylamide) 0.015gm in 4g of distilled water. (0.023 mole % ratio with monomer)	CMWCNT (Carboxylated Multi-walled Carbon Nanotubes) sonicated 1% in 1gm of distilled water
SAP-CNT 2%	Acrylic acid 15gm in 7.5gm of water,neutralized via NaOH up to 75%	Acrylamide 15gm in 13.5gm of distilled water	Potassium persulphate (initiator) 0.2gm in 4gm of distilled water	MBA (Methylenebisacrylamide) 0.015gm in 4g of distilled water. (0.023 mole % ratio with monomer)	CMWCNT (Carboxylated Multi-walled Carbon Nanotubes) sonicated 2% in 1gm of distilled water
SAP	Acrylic acid 15gm in 7.5gm of water,neutralized via NaOH up to 75%	Acrylamide 15gm in 13.5gm of distilled water.	Potassium persulphate (initiator) 0.2gm in 4gm of distilled water	MBA (Methylenebisacrylamide) 0.015gm in 4g of distilled water. (0.023 mole % ratio with monomer)	

Structural Characterization and Morphological Observation

Variable pressure field emission scanning electron microscopy (FESEM; Zeiss Supra 40VP) was used to observe fractured morphologies of the as-prepared hydrogels. In order to evaluate the morphology and uniform dispersion of CMWCNTs in the hybrid hydrogel network, dried hydrogels were fractured into fine particles and dispersed in ethanol and sonicated for 20 min.

Fourier transform infrared spectroscopy (FTIR, Perkin-Elmer Spectrum One, USA) was employed to study the successful synthesis of CMWCNT based hybrid hydrogels. The samples were dried powder that were molded into discs using KBr.

FTIR Analysis

From the FTIR analysis it was interpreted that the absorption peaks at 3421.07cm-1 belong to O-H stretch, H-bonded being of the functional group consisting of alcohol and phenol. The frequency at 2929.67cm-1 belongs to the alkane unit (C-H stretch), 2361.7 cm-1 wave number having C ≡ N stretching. 1670.48cm-1 shows evidence of the functional group of alkenes from the -C=C- stretch bond, 1457.49cm-1 attributed C-H bend bond of alkanes, 1169.66cm-1 highlighted C-H wag (-CH2X) a bond of the alkyl halide group, C-N stretch bond from 1023.13cm-1 wave number showed the existence of aliphatic amines. Alkyl halides being represented by the C-Br stretch bond with the peak at 669.19cm-1. Figure 5b shows the FTIR analysis of SAP 2.

The 2361.7cm-1 wave number indicates that the molecule peak at 2361.7 cm-1 shows C=N group stretching [6], the polymer chains being wrapped around the CMWCNT due to the presence of amide group in both the samples. During swelling CMWCNTs aren't released into the fluid because of this interaction.

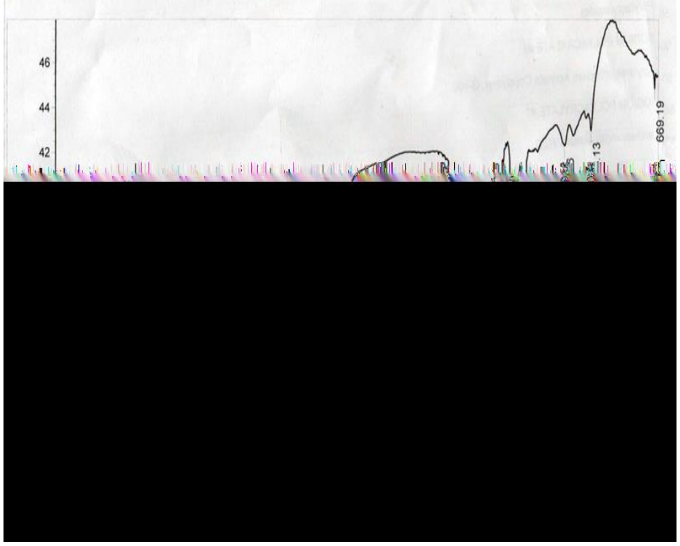

Figure 2a. FTIR Analysis of SAP 2

FESEM Analysis:

Field Emission Scanning Electron Microscope was used for a better resolution of the surface morphology. The working distances at which the beam was focused were 3.6mm and 4.0mm. The figure 2b. having 4.0mm of working distance shows a dispersed image of a fractured gel which clearly illustrates the uniform dispersion of CMWCNTs into the hydrogel network, no accumulations were formed. Whereas the figure 2c. with 3.6mm working distance shows a more focused image of the polymer being wrapped around the MWCNT's surface, which has increased its thickness.

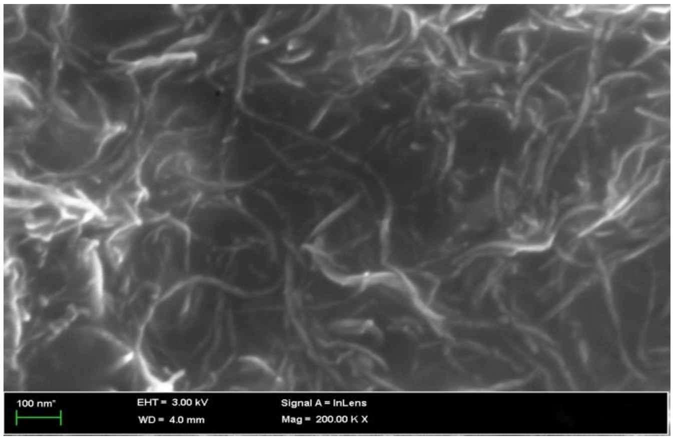

Figure 2b. FESEM image showing dispersion of CMWCNTs into the gel

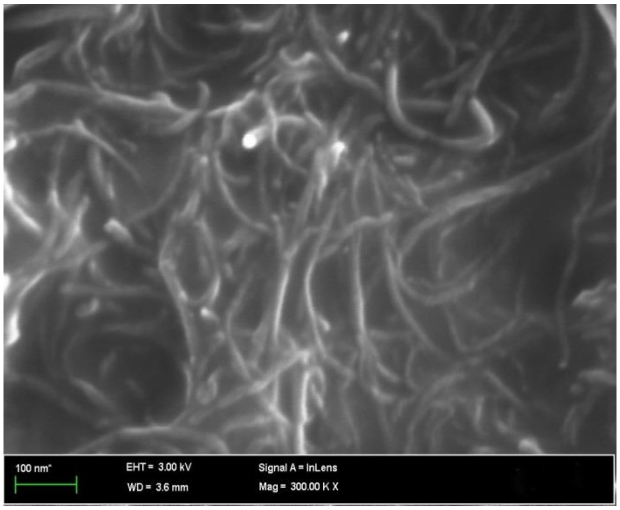

Figure 2c. Focused image of the wrapping of polymer around the CMWCNTs

3. RESULTS AND DISCUSSION

3.1 Dynamic Swelling Test

The compositional effect of CMWCNT on the swelling behavior of hybrid hydrogel at various saline conditions and at different temperature ranges is the main objective of this study. The gravimetric method was used to evaluate the swelling kinetics of the hydrogels. For this purpose hybrid hydrogel was displaced in the saline water at different temperatures. After each minute the SAPs were filtered out via a 100 mesh screen, the weight was noted and was again displaced into the solution.

The degree of swelling at different times can be calculated from the equation:

$$\mathbf{W\ (\%) = (mt - m0/mt) \times 100}$$

Where mt and m0 are the weights of the hydrogels at the predetermined time and at time 0 (xerogel), respectively.

3.1.1. Swelling Average Weight Gain:

The average weight gain difference between the SAP-CNT 1% and SAP-CNT 2% is significantly prominent ranging from 18grams to 3grams. The salinity of 0.5% at temperature 150˚F favors SAP-CNT 2%, showing a significant absorption increase in comparison to that at ambient condition. Although at 1% salinity the capacity decreases for both the SAPs SAP-CNT 1% has a 15 gram loss in comparison to the prior. The SAP-CNT 2% has loss of only 2grams.However the weight loss at 150˚Fahrenheit at this salinity was significant for the 2% CMWCNT mixed SAP (in comparison to the ambient) which was of 15grams. Figures 3a and 3b depict the observations discussed.

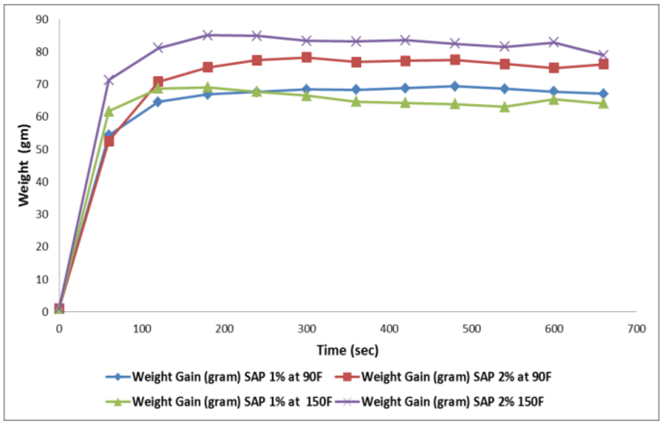

Figure 3a. Weight gain at 0.5%

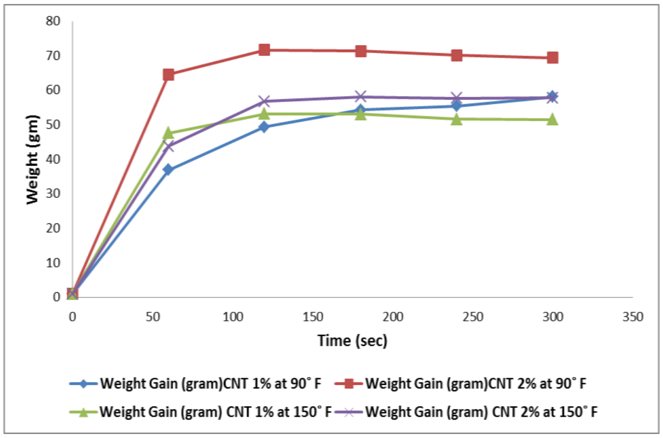

Figure 3b. Weight gain at 1%

3.1.2. Relationship between Weight Gain and Temperature

Maximum weight gain with time in which it is achieved depends upon the temperature. The higher the temperature the faster is the transmission towards the peak capacity attainment. However the storage capacity decreases with increase in the temperature it can be moderated via increase in the CMWCNT percentage. Table 3a shows the impact of temperature on the absorption rate.

Table 3a. Maximum Weight Gain in Swelling

Salinity %	Temperature ˚F	SAP-CNT 1% (gm.)	Time (sec.)	SAP-CNT 2% (gm.)	Time (sec.)
0.5	90	75.06	540	78.18	300
0.5	150	65.2	180	85	180
1	90	58.08	300	71.61	120
1	150	53.19	120	58.11	180

3.2. Comparison in weight gain at different salinities between SAP and SAP-CNT

The weight gain difference between SAP and SAP-CNT is prominent. The results when comparing the maximum weight between the two in distilled water shows a swelling increase of 17 grams in the SAP-CNT. When measuring in a 1% saline constituency a notable weight boost of 61.61grams was observed by the SAP-CNT. Confirming the enhancement in swelling capacity by addition of CMWCNTs in the polymer system. Figure 3c illustrates the difference.

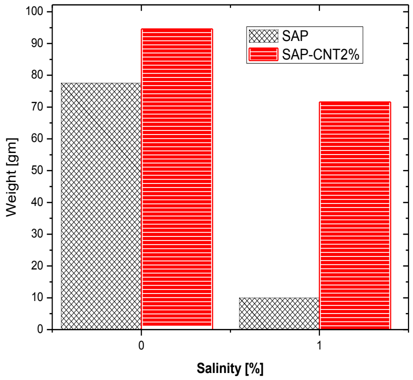

Figure 3c. Comparison between SAP & SAP-CNT

3.2. Effect of pH on Swelling:

Five solutions of different pH were taken for scrutinizing the performance of SAP at different pH conditions since the reservoir fluid is generally acidic in nature and can be below the pH level of 2.9 therefore testing was done in a at different pH values especially below 2.9 ph.

The SAP-CNT showed the highest absorption rate in acidic medium contrary to the SAP this is because in the case of SAP at lower PH swelling capacity decreases as the sodium carboxylate group on the polymer network is protonated. The polymer shrinks and become hydrophobic, as a result decreases the degree of ionization hence decreasing the swelling ratio. Whereas a reverse behavior was observed for SAP-CNT, there could be two possibilities either; we have excessive carboxylate (COO) and hydroxyl (OH) groups present in the system (due to CMWCNT), leading to electrostatic attraction in the system. The carboxylate/hydroxyl groups have electrostatic interaction with carbonyl groups

(COONa), addition of HCl could protonate the carboxylic group leading to electrostatic repulsion between Na+ ions. Hence enhancing the swelling capacity. The second possibility could be that on the addition of HCl in the system the Cl- ions bond with Na+ ions of the carbonyl group due to which excessive COO-¬ groups form an electrostatic repulsion with one another causing enhancement in the swelling capacity. [7]

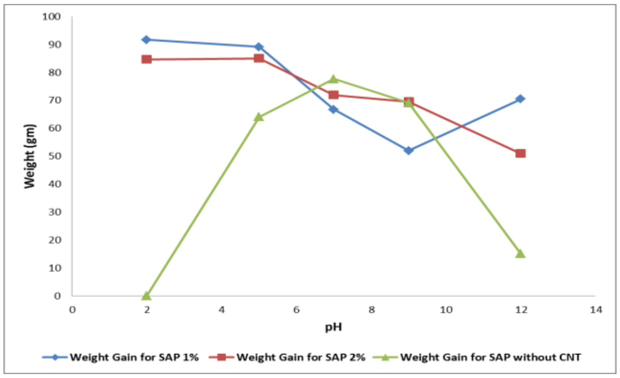

Figure 3d. Effect of pH on Swelling

In case of SAP-CNT 1% the swelling dropped at a pH value of 8.31 however its rate of absorption increased at 12 ph.

4. CONCLUSION:

It is clear from the study conducted that SAPs have a major role play in the field of Enhanced Oil Recovery and can be applicable to further usage in the oil and gas sector. The CMWCNTs increase the swelling capability as well as stabilize the performance in low pH conditions and moderate the absorption capacity at high temperatures with the increase in the percentage of the CCMWNT. The process of absorption is safe since no carbon nanotubes are released in the environment.

5. REFERENCES

[1] EOR Methods, Chandran Udumbasseri, Technical Consultant.
http://petrowiki.org/Produced_water_properties

[2] A.Z. Abidina, T. Puspasaria, W.A. Nugrohoa, “Polymers for Enhanced Oil Recovery Technology”, Procedia Chemistry 4 (2012) 11 – 16

[3] Produced Water Properties, Petrowiki, published by SPE International.

http://petrowiki.org/Produced_water_properties

[4] A. A. S. Al-Rossies, B. D. Al-Anazi and A. M. Paiaman, “Effect of pH-values on the contact angle and interfacial tension”, NAFTA 61 (4) 181-186 (2010)

[5] E. M. A. Hydrogel: Preparation, characterization

[6] Preparation and characterization of Poly-o-anisidine Sn(lV) tungstate & Poly-o-toluidine Sn(IV) tungstate A Nano Composite Cation-Exchange Materials

[7] Giuseppe Cirillo, Silke Hampel, Umile Gianfranco Spizzirri,

Ortensia Ilaria Parisi, Nevio Picci, and Francesca Iemma, “Carbon Nanotubes Hybrid Hydrogels in Drug Delivery: A Perspective Review”, BioMed Research International

[8] Mohammad J. Zohuriaan-Mehr and Kourosh Kabiri, “Superabsorbent Polymer Materials: A Review”, Iranian Polymer Journal 17 (6), 2008, 451-477

STUDY ON THE EFECTS OF EPOXY RESIN BASED PDLC FILMS USING TRIETHANOLAMINE (TEA) AS CATALYST

Mujtaba Ellahi*[1], M.Y.Rafique[2], A.Qadir[3], and M.Furqan Ali[4]
H.E.J. Research Institute of Chemistry, International Centre for Chemical and Biological Sciences (ICCBS), University of Karachi, 75270 Karachi, Pakistan[1]
Department of Physics, Comsats Institute of Information Technology, Lahore 54000.Pakistan[2]
Department of Electrical Engineering, Sukkur Institute of Business Administration[3]
State Key Laboratory of Chemical Resource Engineering, Beijing University of Chemical Technology, Beijing 100029, P.R'China[4]

Corresponding author. Mujtaba Ellahi. (mujtaba.ellahi@gmail.com.);
Tel. & Fax: 0092-111-222-292, Ext-196, 0092-3332991136

ABSTRACT

The present work has been performed to investigate the effects of the structure of epoxy resin based polymer dispersed liquid crystal (PDLC) films using Triethanolamine (TEA) as catalyst with 4- cyano-4'-penthylbiphenyl (5CB) liquid crystal. In this study we have been prepared PDLC films or smart glass by the thermal polymerization-induced phase separation (PIPS) method, with a thickness of 15.0 ± 1.0 ^m controlled by a polyethylene terephathalate (PET) spacer and optimal preparation condition was 30% 5CB LC with a curing time 6 hours at 80°c and 3 hours at same temperature. The morphology of phase separation, dispersed states of the PDLC films, and the microstructure of the polymer matrix with 5CB LC contents were characterized under scanning electron microscopy (SEM). in this study, the effects of tea as a catalyst on the curing process and the electro-optical properties of PDLC films were studied using liquid crystal device (LCD) parameters tester with a halogen tungsten lamp as an incident light source and the incident wavelength (X) through the samples was fixed with the wavelength (X) filter (632.8nm). In addition, PDLC films were prepared with different amounts of tea to investigate the best ratio of the catalyst. Results showed that when the weight ratio of LC 5CB was 30% in PDLC and 3% of tea, then dispersed state of LC were well proportioned, and the variation of transmittance reached the highest value. The optical characterization of the PDLC indicates an improvement of the angular transmission of visible light. Meanwhile, it is examined that by adjusting the mol% of catalyst and LC content we can possesses good electro-optical properties with a low energy efficient method for preparing PDLC display technology.

Keywords: polymer dispersed liquid crystal, epoxy resins, Triethanolamine, electro-optical properties.

1 INTRODUCTION

Recently, saving energy is one of the most significant issues related with global warming, and glass is often regarded as a less energy efficient constituent. A new class of glass, the so-called ‘smart glass’, is expected to be a solution for buildings and transportation vehicles to reduce heating and cooling energy. PDLC films (smart glasses) are a technologically important class of materials that find many applications as electrically switchable optical devices [1-3]. PDLC films are formed by LC micro domain size embedded in a polymer matrix. PDLC can be used not only for smart windows, but also for displays and tunable optical modulators [4]. In the turn off state, no electric filed is applied between ITO electrodes, the orientation (i.e. director) of liquid crystal molecules inside each droplet are different in different domain size. When the incident light of electromagnetic wave having a specific polarization [5] perpendicularly enters into PDLC, the refractive index [6] inside each droplet (with respect to the incident light) is determined by the director. For the reason that the directors in the droplets are arbitrarily distributed, so most of the refractive index inside the droplets is different from the refractive index of polymer surrounding the droplets. From Snell Law, we know that the incident light will be refracted at the interface between liquid crystal and polymer. There are thousands of micron domain size distributed in 10 p,m volume of PDLC, so thousands time of refraction occur when the Incident light passing through PDLC, the light is sprinkled, and an opaque milky white state is experiential in the other side. PDLC films can be prepared by five different techniques: Thermally Induced Phase Separation

(TIPS), Polymerization Induced Phase Separation (PIPS), Solvent-Induced Phase Separation (SIPS), frontal polymerization induced phase separation (FPIPS), and microencapsulation process (MP).Generally, the most suitable method to prepare PDLC devices is PIPS method via heat curing technique is more consistent to provide homogeneity, simple processing, less pollution, cheaper, strong bonding power and forms a homogeneous morphology of polymer networks [710]. The main advantages of PIPS method of heat curing process are that, it requires no evaporation, the fabrication process is relatively simple, clean, and solvent free. It also has advantages over Ultra-Violet (U.V.) curing PIPS methods because it avoids both the changes in LC properties produced by U.V. irradiation and the resulting contamination of radical initiator reagents [11]. Among the different families of cross-linking resins, epoxies are extensively used due to their excellent performance, coupled with very easy convention methods and limited cost. Previously, we have studied two groups with influence of the multi-functional epoxy monomers structure and characterization on the electro-optical properties and morphology of PDLC films [12, 13]. Having all these in view, the present work is concerned with research of epoxy resins system with Triethanolamine (TEA) catalyst to investigate briefly the influence the effect on polymer network of PDLC films. In this paper, we have been studied that the optical properties of PDLC films with 4-cyano-4'-penthylbiphenyl (5CB) LC with same LC concentrations, thicknesses, and curing times, comprehensively. Furthermore, the aim of the present contribution is devoted to report an example of fabrication method by using 4-cyano-4'-penthylbiphenyl (5CB) LC with epoxy resins structure which reinforces the stability and strength of the PDLC films. In this paper in both systems, we added the Triethanolamine (TEA) catalyst with variable mol% and different composition ratio.

2 EXPERIMENTAL DETAIL

2.1. Material

In this research, the PDLC films have fabricated by PIPS heat curing process.The 4-cyano-4'-penthylbiphenyl (5CB) LC used in this study was (Shijiazhuang Yongsheng Huatsing Liquid Crystal Co., Ltd). The curable epoxy resins used were Poly propylene glycol diglycidyl ether (PPGDE, Sigma Aldrich Company), Ethylene glycol diglycidyl ether (EGDE) resin (XY 669, Anhui Hengyuan Chemical Co., Ltd.),Triethanolamine (TEA) (Heowns Biochem Technologies Tianjin) is used as catalyst and 2, 2'-(ethylene di oxy)bis (ethylamine) (EDBEA, Alfa Aesar, A Johnson Matthey Company). EDBEA is a polyamine hardener for epoxy resins.The chemical structures of these materials shown in Figure 1. All of the above materials were used as received without additional purification.The compositions of curable epoxy monomers/hardener/LC mixtures are listed in Table 1 for 6.0 hours and Table 2 for 3.0 hours at 80°C temperature respectively.

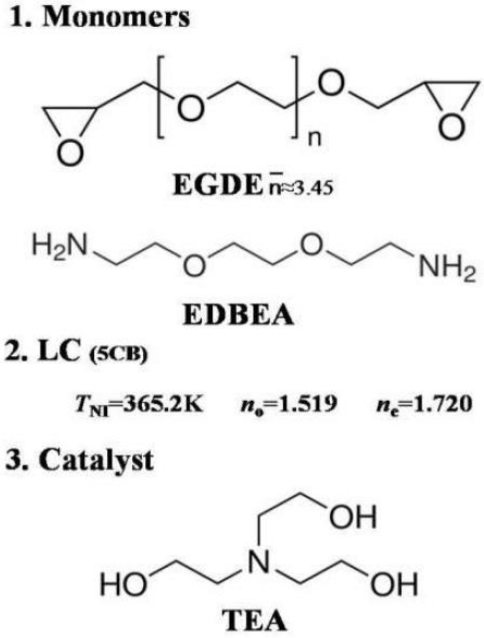

Figure.1 Chemical structures, names and abbreviations of the materials used

Functionality is referred to standard functional of numerous curable epoxy monomers. It is calculated by Fav=£Oi fi, where Fav is the average functionality of composite resin, Oi and fi stand for the relative proportion and functionality respectively [14]. In both systems the PDLC films were obtained by the PIPS via heat curing procedure.

2.2. 2.2. The sample preparation

The samples were prepared consisting of heat curable epoxy monomers, hardener and the same amount (30%) of 4-cyano-4'-penthylbiphenyl (5CB) LC. Initially, the compounds were mixed in various percentages and stirred for 2 hours until they had been homogenized. After that, based on capillary action, the mixtures were sandwiched between two pieces of indium tin oxide (ITO) coated glass substrates, with a thickness of 15.0 ± 1.0 |im controlled by a polyethylene terephathalate (PET) spacer and optimal preparation condition was 30% 4-cyano-4'-penthylbiphenyl (5CB) LC with a curing time 6.0 hours at 80°C and 3.0 hours at same temperature.

Table 1. The compositions of the samples A1-A5 studied

Sample	Epoxy Resins (70 wt%) (6.0 hours at 80°C)	LC/wt%
	TEA/EGDE/EDBEA/mol%	
A1	5.0/1.0/1.0	30
A2	4.0/2.0/1.0	30
A3	3.0/3.0/1.0	30
A4	2.0/4.0/1.0	30
A5	1.0/5.0/1.0	30

Table 2. The compositions of the samples B1-B4 studied.

Sample	Epoxy Resins (70 wt%) (3.0 hours at 80°C)	LC/wt%
	TEA/EGDE/EDBEA/mol%	
B1	1.0/1.0/1.0	30
B2	2.0/2.0/1.0	30
B3	3.0/3.0/1.0	30
B4	4.0/4.0/1.0	30

2.3. Analysis and measurement

The morphology of PDLC samples was observed by scanning electron microscopy (SEM) (ZEISS, EVO18, Germany). The electro-optical (E- O) properties of PDLC films were studied using a liquid crystal device (LCD) parameters tester (LCT- 5016C, Changchun Liancheng Instrument Co., Ltd.). A halogen tungsten lamp was used as an incident light source and the incident wavelength (X) through the samples was fixed with the wavelength (X) filter (632.8nm).

3 RESULTS AND DISCUSSION

3.1.a. Morphology of Polymer Network at 6.0 hours at 80°C

In order to suitably measure the domain size, Figure 2a shows the morphology of SEM micrographs of the polymer network of the samples A1-A5. The morphology of PDLC systems are dependent on the mol% ratio, curing conditions, time, temperature, chemical structures materials, and on the details of the film formation technique [15].

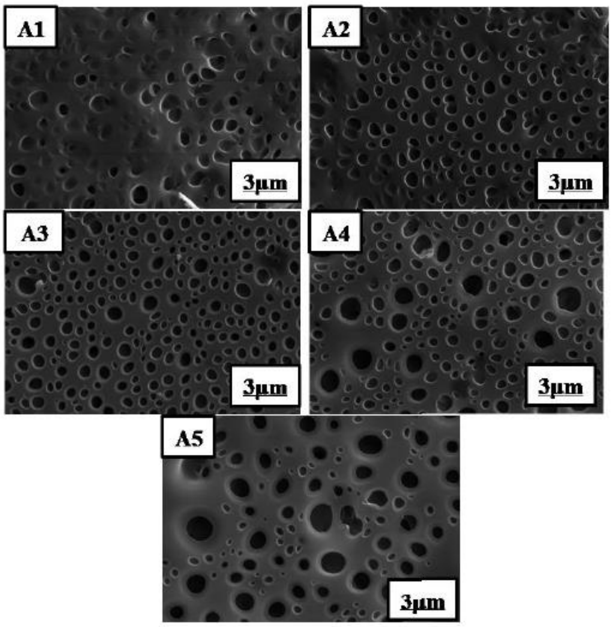

Figure 2.a SEM micrographs of the polymer networks of the samples A1- A5.

The composition ratio of samples A1-A5 with same LC content and similar heating temperatures is listed in Table 1. Figure 2a shows the domain size morphology of the polymer network of PDLC system for samples A1-A5. Triethanolamine (TEA) reacts with the epoxy monomers to form polymeric network with the ring opening addition polymerization reaction process. To begin with the hydroxyl group (-OH) opened and adds a new epoxy ring to form polymer network chain of the PDLC systems. In addition, the TEA hydroxyl group (-OH) then capable to form a link with one more epoxy group to form continue polymer network chain. It can be seen that the LC domain size of the polymer network with decreasing the mol% of catalyst TEA. The effects of the structure of alkoxy chain length and flexible curable epoxy monomer EGDE on PDLC films were showed the microstructures of the PDLC films as shown in Figure 2a.When polymerization was initiated, the molecular weight and cross linking density of the polymer network increase and hence the solubility of the LC decreases leading to the formation of domain size. This was related to the relative content of the curable epoxy monomers composition and the 30% of LC content. The average LC domains sizes have been observed of all samples approximately 2.2 ^m, 1.8 ^m, 2.1 ^m, 3.0 ^m, and 3.6 p,m for samples A1-A5 respectively. It can be clearly seen that the LC domain size have different variations with increasing the mol% of TEA catalyst as shown in Figure 2a.

The solubility of the LC decreases stiffening polymers until the LC phase separates and form domain size during the heat curing method. Domain size controlled by the relative amounts of the epoxy resins, the rate of polymerization, and some physical parameters such as the viscosity, diffusion rate, and solubility of the LC in the polymer [16].In this paper, the LC domain size and cross-linking density were mainly influenced by the relative ratio of the EGDE and TEA. Epoxy monomers mostly influences to form cross-linking density with alkoxy group chain length with decreasing catalyst which decreases the cross-linking density of PDLC films. For a perfect system, the relative content of the heat curable monomers and LC have a great effect on the microstructure of the polymer matrix. Consequently, the size of the LC domains 3% TEA catalyst is ideal and smooth than others as shown in Figure 2a.

3.1.b. Morphology of Polymer Network at 3.0 hours at 80°C

It is evident from Figure 2b that morphology is appreciably influence by adding the group Triethanolamine (TEA) hydroxyl group (-OH) as a catalyst in samples B1-B4.Formerly, we have been prepared the epoxy monomers based PDLC films without catalyst [12, 13]. The TEA accelerates the rate of polymer network reaction speedily and prepare the PDLC films with reducing the 6.0 hours to 3.0 hours heating time at 80°C same temperature as shown in Figure 2b. We have prepared sample B1 catalyst at 1% and remaining samples prepared with catalyst 2%,3%,and 4% respectively with curing time 3.0 hours.

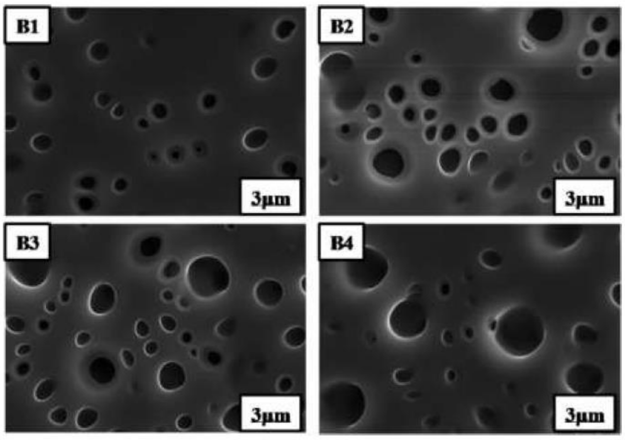

Figure 2.b SEM micrographs of the polymer networks of the samples B1-B4.

It is noticeable thing is that with a 3.0 hours curing time had a similar polymer matrix to that of sample A1-A5 with a 6.0 hours heating time. From Figure 2b it can be seen that as the mol% ratio of TEA increased from 1% to 4%, the number of LC domains increased and the epoxy domain sizes increased and the LC domain size distribution was narrow, which would make the PDLC films easier to drive in practical devices. Furthermore, to illustrate the effect of TEA, the electro-optical (E-O) properties of the PDLC system needed to be studied.

3.2.a. Electro-optical (E-O) properties of PDLC films at 6.0 hours at 80°C

The electro-optical (E-O) properties are very important to assess LC system. The E-O properties of PDLC systems mainly depend on the chemical nature of the epoxy monomers, hardener and LC content. As well as, the effect of epoxy monomers structures on PDLC systems can be obtained by the E-O properties of samples A1-A5.The transmittance applied voltage curves of samples A1-A5 are shown in Figure 3a. It can be seen from Figure 3a, that transmittance of the samples reached the saturation level, when the applied voltage increased. Comparatively studies showed that the Figure 3.a with Figure 2.a, the morphology of the polymer network in the PDLC systems had a vital effect on the E-O properties of the PDLC films. Good E-O properties of the PDLC systems can be obtained when the microstructure of the PDLC film is appropriate. It is well examined that when the TEA catalyst % reached at 3% the transmittance of the PDLC films were very best and good.

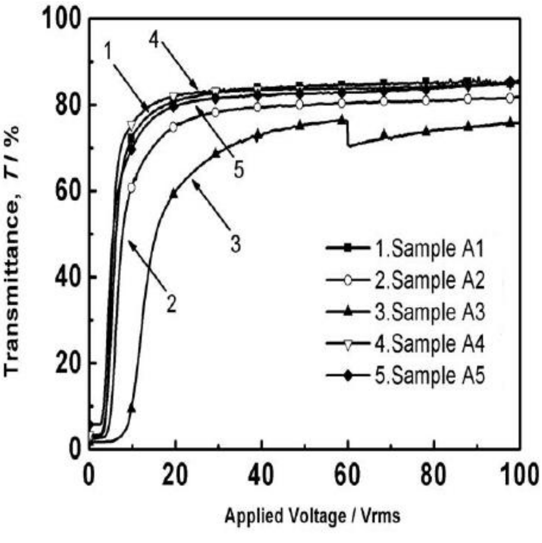

Figure 3.a Applied voltage dependence of transmittance for samples A1-A5.

3.2b. Electro-optical properties of PDLC films at 3.0 hours at 80°C

The applied voltage transmittance curves of samples B1-B4 are shown in Figure 3b.In heating process, the epoxy monomers and hardener (EDBEA) reacted to form a polymer matrix and the LC coalesced; resulting the phase separation process occurred. When the heating time was insufficient, the LC domain sizes were formed relatively big. When this occurred the films were hard to drive since the anchoring energy at the boundary between the polymer matrix and LC droplets was large when the LC domain size were small, and small LC domains suppress light scattering in the visible region [17].

Progressively, with the passage of time more epoxy monomers and EDBEA reacted to form the polymer matrix and the LC separated from the polymer matrix, forming more and larger domain size; then the film became easier to drive [18]. For the sample B1 prepared with 1% TEA catalyst, it took 3.0 hours to get a film with a good response to the electric field. In the meantime, using catalyst TEA and 3.0 hours curing time, the curves of samples B2, B3 and B4 were similar. It indicates that the samples cured for 3.0 hours have similar E-O properties as sample A1-A5, consequently; it suggesting that with TEA as the catalyst, the heating process needed only 3.0 hours. By analyzing the curves of samples A1-A5 and B1-B4, it can be observed that the E-O properties of samples B1-B4 were no worse than those of samples A1-A5, but the heating time was effectively reduced from 6.0 hours to 3.0 hours.

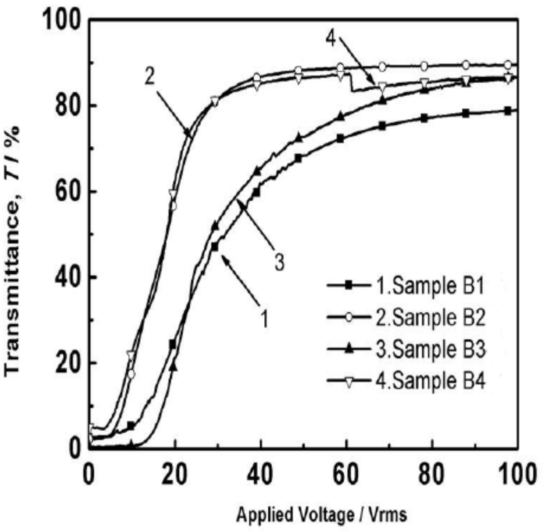

Figure 3.b Applied voltage dependence of transmittance for samples B1-B4.

CONCLUSION

The optimized conditions for fabricating PDLC films containing 4-cyano-4'- penthylbiphenyl (5CB) and epoxy monomers were found to be the weight% of LC and monomers 3 0% and 70% respectively. We have been investigated two PDLC film systems. The Systeml, at 6.0 hours at 80°C using curable epoxy monomers with heat curing processes mol%, composition ratio, various molecular structures and decreasing catalyst Triethanolamine (TEA) effects the morphology of the PDLC systems. Additionally, the effect on microstructures of the PDLC systems was strongly influenced by the hydroxyl group (-OH), which in turn influenced the E-O properties of PDLC systems. The effect of the composition of the mixture and curing temperature on the microstructure of the polymer network were examined. Moreover, using TEA catalyst variable driving voltages were optimized.

In system 2, using the catalyst TEA effects the immaculate morphology and E-O properties of PDLC systems .In addition, with different amounts of TEA reduce the heat curing time of PDLC films from 6.0 hours to 3.0 hours, and save 3.0 hours; with good E-O properties. As a result, this study presents a low energy method for preparing PDLC films as well as our experimental findings will help more to understand the extent of epoxy monomers and LCs for further developments in the PDLC smart glass field.

ACKNOWLEDGEMENTS

This work was supported by the HEC fund for distinguished Young Scholars and the research fund of the State Key Laboratory for Advanced Metals and Materials. The authors also thankful to the University of Karachi & Beijing University of Science & Technology for laboratory facilities.

REFERENCES

[1] Doane JW, Vaz NA, Wu BG, Zumer S. Field controlled light scattering from nematic microdroplets, *Journal of Applied Physics Letters*, 48,269-271,1986.

[2] Kitzerow HS, Polymer-dispersed liquid crystals from the nematic curvilinear aligned phase to ferroelectric films, *Journal of Liquid Crystals,* 16(1), 1-31. 1994.

[3] Kim YB, et al , Fabrication of flexible polymer dispersed liquid crystal films using conducting polymer thin films as the driving electrodes, *Journal of Thin Solid* Films,517(10), 3066-3069,2009.

[4] S.Park,J.W.Hong, polymer dispersed liquid crystal films for variable transparency glazing, *Journal of Thin Solid* Films,517(10), 3183-3186,2009.

[5] Mujtaba Ellahi, Yanzi Gao and M. Y. Rafique. Influence of enhanced curing temperature of epoxy monomers structure on the electro-optical properties and morphology of polymer-dispersed liquid crystal films, *Journal of American Journal of Engineering Research,* 2(3), 01-06, 2013.

[6] Lee SH, Lee SL, Kim HY, Electro-optic characteristics and switching principle of a nematic liquid crystal cell controlled by fringe-field switching, *Journal of Applied Physics Letters*, 73:2881-2883,1998.

[7] Mujtaba Ellahi, et al, Effects of di and tetra functional epoxy monomers structure on the morphology andthe electro-optical properties of polymer-dispersed liquid crystal films, *Journal of International Journal of Scientific & Technology* Research,2(3),127-131,2013.

[8] Yun HJ, Jo MH, Jang IW, Lee SH, Ahn SH, Hur HJ, Achieving high light efficiency and fast response time in fringe field switching mode using a liquid crystal with negative dielectric anisotropy, *Journal of Liquid Crystals*, 39, 11411148, 2012.

[9] Farzana A, Jamil M, Lee JW, Jeon YJ, The investigation of molecular affinity involved in poly(ethyleneglycol)-based polymer-dispersed liquid crystal display, *Journal of* Colloid *Polymer Science*, 290 (7), 599-606, 2012.

[10] Farzana A, Jamil M, Lee JW, Ri YH, Jeon YJ.Characteristics of di- and tri-block copolymers: polymer disperse liquid crystal display, *Journal of Modern Optical,61* (12),1027-1032,2014.

[11] H.Murai and T.Gotoh, Stabilization of Epoxy-Based Polymer-Dispersed Liquid Crystal Films by Addition of Excess Hardener. *Journal of Molecular Crystals and Liquid Crystal*, 226(1), 13-26, 1993.

[12] Mujtaba Ellahi, Fang Liu, Ping Song, Yanzi Gao, Hui Cao, M. Y. Rafique, Murad Ali Khaskheli, M.Zubair Iqbal,Huai Yang , Influence of the multi-functional epoxy monomers structure on the electro-optical properties and morphology of polymer-dispersed liquid crystal films, *Journal of Polymer Bulletin,70* (11),2967-2980,2013.

[13] Mujtaba Ellahi, Fang Liu, Ping Song, Yanzi Gao, , M. Y. Rafique, Dil Faraz Khan, Hui Cao, Huai Yang, Characterization and Morphology of Polymer-Dispersed Liquid Crystal Films, *Journal of Soft* Materials,12(3),339-345,2014.

[14] De Sarkar, M.; Gill, N.L.;Whitehead, J. B.; Crawford, G. P, Effect of Monomer Functionality on the Morphology and Performance of the Holographic Transmission Gratings Recorded on Polymer Disperse Liquid Crystals . *Journal of Macromolecules,* 36(3):630-638, 2003.

[15] Song P, Yu L, Cao H, Wang F, Liu F, Zhang C, Yang C,Yang H , Studies on electro-optical properties of polymer dispersed liquid crystal films based on epoxy resins prepared by UV-initiated cationic polymerization *Journal of Liquid* Crystals,39(3),313-321,2012.

[16] Song P, Cao H, Wang F, Liu F, Wang J, Ellahi M, Li F,Yang H, The UV polymerisation temperature dependence of polymer-dispersed liquid crystals based on epoxies/acrylates hybrid polymer matrix components, *Journal of Liquid Crys tals*, 39(9),1131-1140.2012.

[17] Mujtaba Ellahi, M.Y.Rafique, Shagufta Ishtiaque,M.Furqan Ali, Jameel Memon,Study on the effects of epoxy resin based PDLC films using polythiol group (-SH) as hardener and catalyst , *Journal of Materials Focus* , 4 (03), 197-201,2015.

[18] Mujtaba Ellahi, et al, Study on the effects of isotropic cross-linked pristine morphology and electro-optical properties of PDLC films, *Journal of Polymer Bulletin.* 72 (11), 2917-2930, 2015

SYNTHESIS AND CHARACTERIZATION OF COPPER NANOPARTICLES

Ayesha Ikram[1*], Humair Ahmed Siddiqui[2], Dr. Saqib Anjum[1], Dr. Ashraf Ali[3]
[1]Physics Department, NED University of Engineering & Technology, Karachi.
[2]Material Engineering Department, NED University of Engineering & Technology, Karachi.
[3]Ghulam Ishaq Khan Institute of Engineering Sciences and Technology, Topi, KPK

Corresponding Author: Ayesha Ikram, E-mail address ayesha.ikram411@yahoo.com

ABSTRACT

Metal nanoparticles have attracted scores of care due to their specific properties. Copper nanoparticles have attracted more interest among all metal nanoparticles. Copper nanoparticles can be considered as the replacements for the noble nanoparticles in metallurgical processes because of their properties and economical approach as compared to copper nanoparticles, noble metals are much more expensive; copper nanoparticle are candidates for the conductive inks and for printed electronics. Synthesis of nanoparticles has drawn tons of attention due to their size dependent physical and chemical properties, several synthetic protocols have been sprung up such as vapor deposition, green method, electrochemical reduction, laser ablation, sputter deposition and chemical reduction methods. The objective of the study was to synthesize and characterizes the copper nanoparticles using different techniques. For the synthesis purpose green chemical reduction method was employed. Extract of papaya was used as a stabilizer to prevent copper nanoparticles from oxidation, the experiment was done at room temperature. An inorganic qualitative test was taken for the confirmation of copper nanoparticles, absorption peak was followed by a spectrometer, which corroborates the presence of copper nanoparticles, crystal structure was analyzed by X-Ray diffraction, and SEM was used to define the particle morphology of nanoparticles.

Keywords: Copper, Nanoparticles, Green synthesis, Papaya Extract, Nanotechnology

1. INTRODUCTION:

Nanotechnology and nano- science become the benchmark in the recent times, in the arena of nanotechnology the matter can be manipulated at molecular and atomic scale. A nanoparticle is the most ultimate factor in the output of a nanostructure. Nano-particles are in the range of 1-100 nm and possess many special properties, for which they are passionate being studied in a large bit of research fields. Surface area to volume ratio of nanoparticles is very high as compared to the bulk material. Nanoparticles can also enrich strength and homogeneity of composite materials [1].

A quantum confinement effect occurs in the nano-structures that serve as the foundation in emerging high technology devices. Physical and chemical properties of nano-particles are purely size and shape dependent. In this advanced epoch, there are several applications of nano-particles such as medicine, food, agriculture, electronic devices, paints, cleaning waste water and wear. Metal nanoparticles drawn lots of attention due to their specific properties. Super plasticity in nano-crystalline metals accelerates the assembly process for manufacturing components with complex conditions. Copper nanoparticles have attracted more interest among all metal nanoparticles. Copper nanoparticles can be considered as the replacements for the noble metals in metallurgical processes because of their properties and economical approach; copper nanoparticles become the most desirable candidate for the conductive inks and for printed electronics due their high electrical and heat conductivity property.. Cu nano-particles are employed in a broad scope of subjects such as paints, hybrid integrated circuits, multilayer ceramic capacitors and low cost bioactive nano-complexes. The copper nanoparticles also show antibacterial, antimicrobial activity [2-5] and greater catalytic activity.

Synthesis of nanoparticles requires a method that fulfills the conditions such as control of particle size, size distribution, physical body, crystal structure, less impurities, higher volume production and lower prices. Several synthetic protocols have been built up, such as vapor deposition, electrochemical reduction, thermal decomposition, polyol processes, laser ablation, sputter deposition, chemical reduction and green chemical reduction methods. Methodical study of the synthesis and colors of colloidal gold by chemical reduction method was described by Michael Faraday in 1857, for the first time. The chemical reduction method is more frequently used due to its ease of control on reaction parameters, by enhancing the reaction parameters, for example, molar ratios of reducing agents and capping agents with the precursor salts could be modified to get different sizes of nanoparticles.

In this simple laboratory method, copper salts are reduced by different reducing agents such as hydrazine hydrate, sodium borohydride, sodium tetrahdidoborate, glucose, CTAB, L-ascorbic acid. The synthesis of nanoparticles by chemical reduction methods are normally performed in the presence of stabilizers [6-9].

Green method is one of the finest methods to synthesize the nano-particles in the current age. Green methods are usually cost effective, simple and could accelerate at the room temperature. For the synthesis of metal nanoparticles like gold, silver and copper green synthesis methods are being used by researchers due to the environmental friendly properties. Different plant extract has been covered for the synthesis of nanoparticles, as an example Capparis Zeylanica, Ocimum Sanctum, Nerium oleander, Eucalyptus plant, Trianthema decandra, M. balbisisana (banana), A. Indicia (neem) Amaranthus spinosus extracts have been utilized for the synthesis of Cu, silver and gold nanoparticles [10-13].

Along with the growth of different synthetic methods there is a large number of characterization techniques have also been developed like TEM, AFM, XRD, SEM etc. is being used study the sound structure of nanoparticles.

The primary objective of the study is to synthesis the copper nanoparticles using a green chemical reduction method using papaya extract as a stabilizer.

2. EXPERIMENTAL:

The required materials and instruments for the synthesis of copper nanoparticles and complete methodology with papaya extract as a stabilizer is described below.

2.1 Materials:

Copper (II) sulfate Penta-hydrate ($CuSO_4.5H_2O$), L-ascorbic acid ($C_6H_8O_6$), sodium hydroxide (NaOH), methanol (CH_4O), deionized water is purchased from Karachi scientific traders, Hydrazine Hydrate (H_6N_2O) 80AR-Malaysian obtained from Karachi chemical services, All chemicals are lab grade and used without further refining.

2.2 Preparation of solutions with desired molarities:

Copper (II) sulfate Penta-hydrate solution with 0.04M was prepared 100 ml of de-ionized water, then the solutions of L-Ascorbic acid, Sodium hydroxide and hydrazine hydrate with the molarities 0.001M, 0.01M and 1M respectively was prepared by using 100 ml of deionized water.

2.3 Preparation of papaya extract:

For the preparation of papaya extract unripe (green papaya) having botanical name Carica papaya, weighing 25 g is used. Papaya fruit was thoroughly rinsed with deionized water, dried, cut into fine slices and was crushed. The crushed papaya was poured into 100 ml of deionized water and mixed properly. The solution was filtered through filter paper for its function in the synthesis of copper nanoparticles

2.4 Methodology:

100 ml solution of Copper (II) sulfate Penta-hydrate was used up in 1000 ml beaker, place the beaker on the magnetic stirrer, after that 100 ml of papaya extract and 10 ml solution of anti-oxidant agent L-Ascorbic acid added to Copper (II) sulfate Penta-hydrate solution while stirring. The vividness of the solution was initially blue, and then after 15 minute sodium hydroxide was added to the solution mixture to maintain the PH, the PH of the solution becomes constant at 5.4 (getting same PH results while repeating the process several times). In the last hydrazine hydrate was added drop by drop to the solution (which is in the 1000 ml beaker) until the color of the solution mixture, turn to dark brown or brown black while stirring fast, this brown black color shows the reduction of copper salt. Stirring was continued for 1 hour at room temperature for the windup of the response.

One hour afterwards, the precipitates were washed twice with methanol after filtration and then dried to obtain copper nanoparticles.

2.5 Systematic illustration:

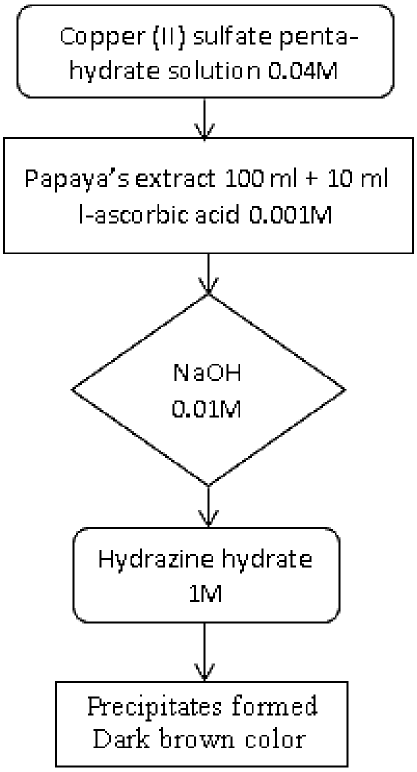

Fig.1: Process Layout

3. CHARACTERIZATI-ON TECHNIQUES:

The chemistry and crystal structure of copper nanoparticles was determined by the X-Ray Diffraction (XRD) (XPERT-PRO); coupled with copper mono-chromator using Cu Kα radiation (λ =1.54060 A) at 40kv, 30mA in range of 2 theta from 10-80. Particle size was estimated by the Scherer's formula.

Moreover, Sound structure of copper nanoparticles was investigated using scanning electron microscope (FEI Quanta 200) and absorption peak was observed by spectrometer(Spectrum Lab 22PC), spectrum was set against the background spectrum of water as reference.

4. RESULTS AND DISCUSSION:

4.1 Inorganic qualitative tests:

For confirmation of copper inorganic qualitative test was conducted. For this test 4 mg of freshly prepared nanoparticles was taken in the beaker and 10 ml of sodium hydroxide of 1 M was added to it. A brown color precipitation was observed in the beaker which confirms the presence of copper nanoparticles.

4.2 UV-Vis Spectrum Study:

The UV-Visible absorption spectrum of freshly synthesized copper nanoparticles from copper sulfate and stabilized by papaya extract is shown in Fig.2 the synthesized copper nanoparticles show an absorption peak at 576 nm. This peak can be assigned to the absorption of copper nanoparticles. This spectrum confirms the presence of copper. The absorption spectrum was required in the range of 450 nm – 650 nm.

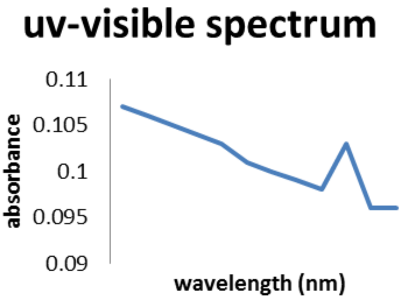

Fig.2: UV-Visible Spectrphotometer Spectrum of Copper Nanoparticles

4.3 SEM analysis:

The SEM images copper nanoparticle stabilized by papaya extract is presented in Fig.3 (a), Fig.3 (b) and Fig.3 (c) SEM results show that the morphology of prepared nanoparticles from green method is spherical.

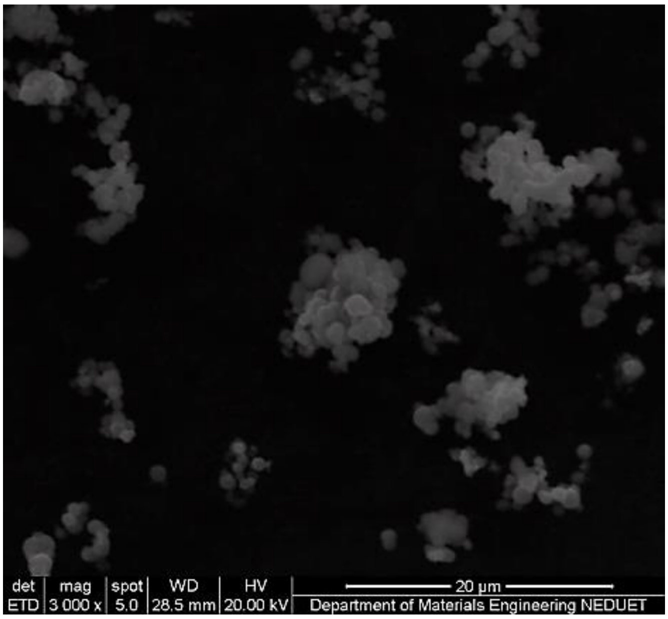

Fig.3 (a): Spherical morphology of Particles as observed in SEM

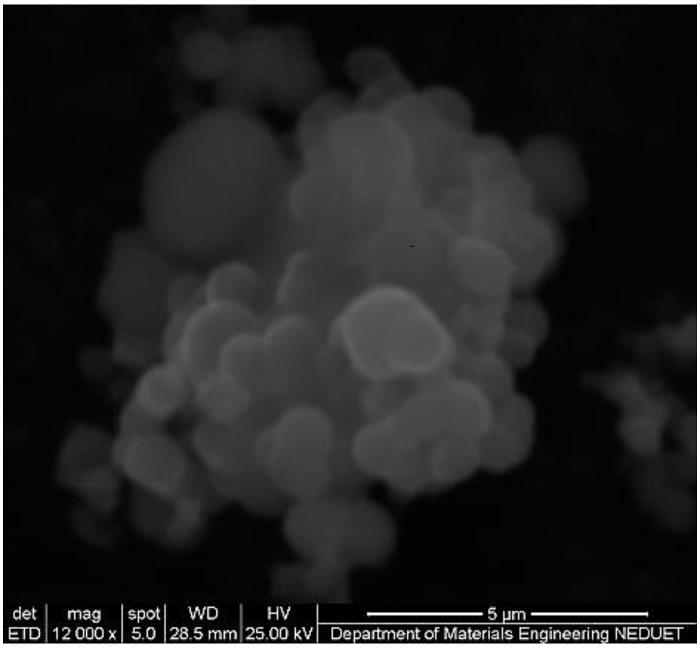

Fig.3 (b): Closer view of Spherical morphology of Particles as observed in the SEM

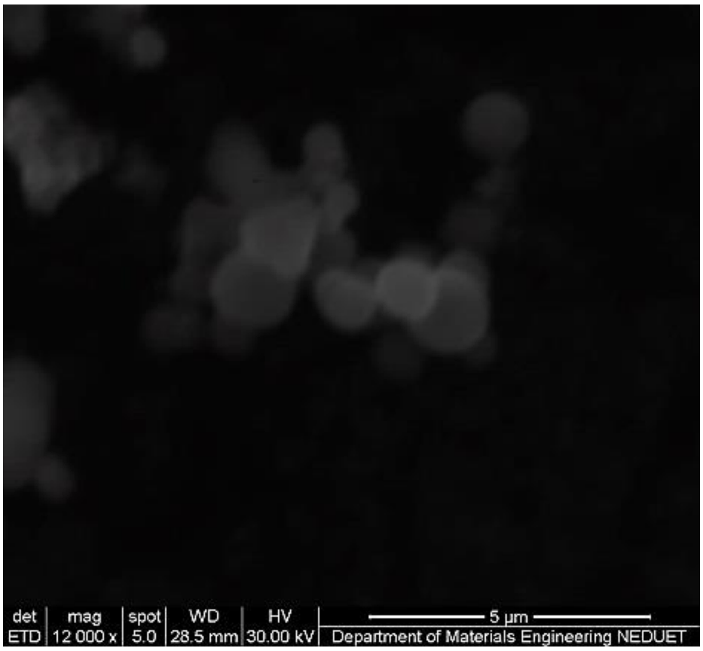

Fig.3 (c) Copper Particles as observed in SEM

4.4 XRD analysis:

Particle size of copper nanoparticles synthesized by green method is found to approximately 10 nm calculated by equation 1.

$$D = 0.9\lambda/\beta \, \mathrm{Cos}\, \theta \qquad (1)$$

Where β is the full width at half maximum of the X-ray profile, θ is the Bragg angle and λ is the wavelength of X-rays.

The X-ray diffraction pattern is shown in Fig. 4, which is a typical pattern of copper nanoparticles.

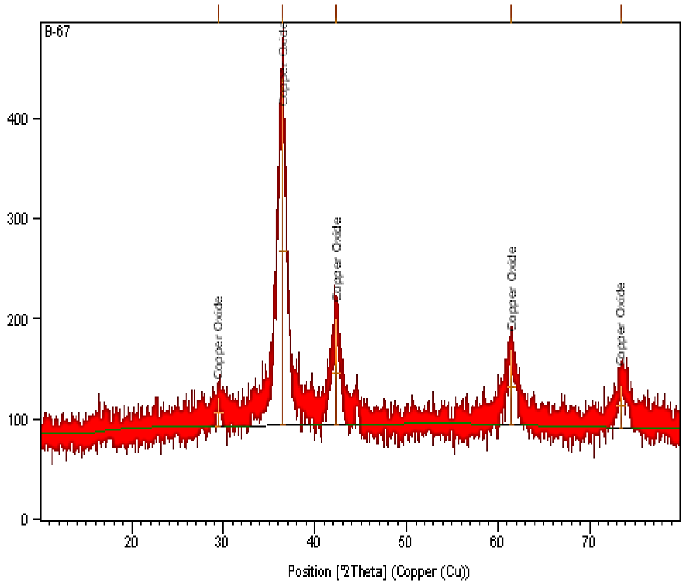

Fig.4: XRD spectrum of Copper Nanoparticles

With the passage of time due to oxidation, copper nanoparticles converted to copper oxide. The structural analysis showed that the prepared nanoparticles are of copper I oxide (face centered cubic, JCPDS 03-065-3288). Particle size and d-spacing of the diffraction pattern is presented in table 1.

Table no. 1: Dspacing of Copper Nanoparticles

Particle size	D-spacing
8.6962E-09	3.035
8.8547E-09	2.466
1.0823E-08	2.135
1.1741E-08	1.509
8.9948E-09	1.289

Miller indices calculated from the XRD pattern are shown in table 2, lattice parameter was found by the equation 2

$$1/d^2 = (h^2 + k^2 + l^2)\,/a^2 \qquad (2)$$

Table no.2: Lattice constant of Copper Nanoparticles

h+k+l	Lattice constant (A)
210	6.786913525
111	4.271947432
200	4.27144
211	3.697137343
210	2.883096607

Average of lattice parameter is found to be 4.32A

5. CONCLUSION

Synthesis of copper nanoparticles has been reported by using green reduction method; nanoparticles formed are of spherical morphology. The average size of nanoparticles was found to be 10 nm. Absorbance peak at 576 nm confirms the presence of copper nanoparticles.

ACKNOWLEDGEMENT:

Acknowledged to NED University of engineering and technology for providing needful assistance.

REFERENCES:

1. Michael F. Ashby, Paulo Ferreira and Daniel L. Schodek, “Nanomaterials, Nanotechnologies and Design: An Introduction for Engineers and Architects”, 2nd Ed. , pp. 1-4, Elsevier ltd. Butterworth-Heinemann, 2009
2. Pattanawong chokratanasombat and ekasit nisaratanaporn” preparation of ultrafine copper powders with controllable size via a polyol process with sodium hydroxide addition”, “Engineering journal” vol. 16 (4), 1st July 2012
3. Shlomo magdassi, Michael grouchko and Alexander kamyshny “copper nanoparticles for printed electronics: routes towards achieving oxidation stability”, “Journal of materials science and engineering”, 3, pp. 4626-4638; doi: 10.3390/ma3094626, 8 September 2010
4. Hassan hashemipour, Maryam ehtesham Zadeh, robe pourakbari and payment Rahimi “investigation of synthesis and size control of copper nanoparticle via electrochemical and chemical reduction method”,” International journal of the physical sciences” vol. 6 (18), pp. 4331-4336, 9 September, 2011
5. N. Cioffi. N deterrent, l, torsi. R.a. picca, e. De Giglio. L, Sabbatini. L. Novello. G. Tantillo t, bleve-zacheo, p. G. Zambonin “synthesis, analytical characterization and bioactivity of ag and Cu nanoparticles embedded in poly-vinyl-methyl-ketone films” “Journal of analytical and Bioanalytical chemistry”, 382: pp. 1912–1918 day 10.1007/s00216-005-3334-x, 20th July 2005.
6. Y. Suresh, et.al,” Green Synthesis and Characterization of Tea Decoction Stabilized Copper Nanoparticles”, International Journal of Innovative Research in Science, Engineering and Technology, Vol. 3, Issue 4, 2014.
7. Asim Umer, Shahid Naveed and Naveed Ramzan, “ Selection Of A Suitable Method For The Synthesis Of Copper Nanoparticles”, NANO: Brief Reports and Reviews Vol. 7, No. 5 , 2012.
8. Sani Usman, et.al, “Copper Nanoparticles Mediated by Chitosan: Synthesis and Characterization via Chemical Methods”, Molecules-Open Access Organic Chemistry Journal, 2012.
9. Shlomo Magdassi, et.al “Copper Nanoparticles for Printed Electronics: Routes towards Achieving Oxidation Stability”, Materials-Open Access Materials Science Journal, 2010.
10. K. Saranyaadevi, et.al, “Synthesis and Characterization of Copper Nanoparticle using Capparis Zeylanica leaf Extract”, International Journal of Chem-Tech Research, Vol. 6, No.10, pp. 4533-4541, 2014.
11. R. Geethalakshmi et.al, “Synthesis of plant-mediated silver nanoparticles using Trianthema decandra extract and evaluation of their antimicrobial activities”, International Journal of Engineering Science and Technology, vol. 2(5), 2010.
12. Vasudev D. Kulkarni, Pramod S. Kulkarni, “Green Synthesis of Copper Nanoparticles Using Ocimum Sanctum Leaf Extract”, vol. 1 Issue 3, 2013.
13. Ridzuan Ramli, et.al, “In-Situ Impregnation of Copper Nanoparticles on Palm Empty Fruit Bunch Powder”, Advances in Nanoparticles, 2014.

SIMULATION OF COAL SLURRY BURNER USING FLUENT

Nadia Khan[1,*] Alia Ahrar[2] and Sumera Rehman[3]
[1]Polymer and Petrochemical Engineering Department, NED University of Engineering & Technology, Karachi, Pakistan
[2]Chemical Engineering Department, NED University of Engineering & Technology, Karachi, Pakistan
[3]ENGRO polymer and chemicals limited, Karachi, Pakistan

E-mail address: *nadiakhan@neduet.edu.pk

ABSTRACT

Coal water slurry is an attractive alternative fuel to oil due to its lower cost and similarity to oil with respect to transportation and handling. Coal water slurry is a mixture of pulverized coal, demineralized water and additives. Coal water slurry can be used in conventional burning system with some retrofitting. The temperature, molecular viscosity, turbulent kinetic energy and turbulent dissipation rate of coal slurry burning is analysed through the combustion chamber. The combustion chamber has central tubing defining the CWS passageway and annular passage way defining the air flow inside the chamber. The characteristics of the coal slurry combustion chamber were studied by using computational fluid dynamics software Fluent (V12.0). For simulation geometry of a burner is created using a top-down geometry construction method in GAMBIT. For defining combustion chemistry non-premixed combustion model is used. And convergence behaviour is observed using second order upwind scheme. High temperature of fuel is used to initiate the combustion. The flame is very small and can no longer be seen for most of the part. Homogeneity in temperature molecular viscosity is notable characteristic of combustion chamber.

Keywords: mesh; coal water slurry; contour, CFD, combustion.

1 INTRODUCTION

Continuously increasing demand of energy have drawn the attention of scientist towards coal water slurry for power generation .Coal water slurry (CWS) is a fuel consist of fine coal particles suspended in water. Typical CWS consists of 60-75% coal and 25-40% water and 1% additive. CWS can be used as a fuel in place of oil and gas in boiler and furnace after modification in combustion chamber nozzle.CWS is attracted because of ease of transportation and storage. Due to low cost of coal when compared with other energy resources, CWS is competitive alternate to oil and gas.

Pakistan is the 6th richest nation of the world in the coal reserves. The coal reserves were discovered at the place of Lakhra which was suitable for power generation. The quality of Lakhra coal is lignite A.In the preparation of CWS Lakhra coal is used in this paper.

CFD is widely used to predict the performance of system before installation .In this paper CFD is used to analyse the flow characteristics of CWS in combustion chamber. Combustion of CWS possess number of problems, due to large amount of water, ignition time increases and high preheat temperature is required. Combustion has been modelled with the non-premixed combustion model, while the P1 model has been adopted for radiative heat transfer. The k-ε realizable model and second order upwind has been chosen for turbulence convergence.

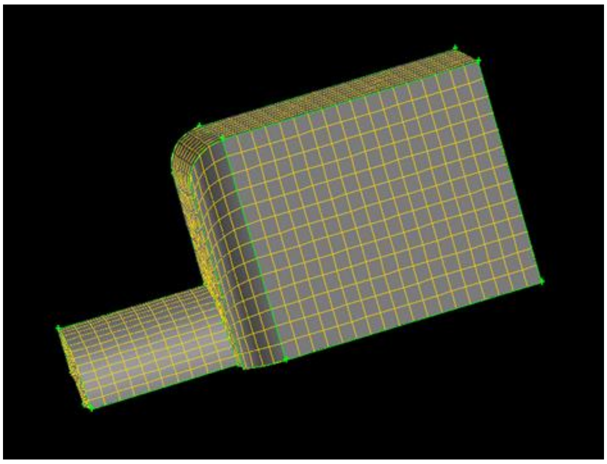

Figure 1.combustion chamber mesh

2 OBJECTIVE OF THE STUDY

The objective of present work is to simulate CWS flow through nozzle of combustion chamber to precisely understand the flow dynamics and variation of different flow properties of CWS.The simulation is done by using Gambit and Fluent.

Gambit is used for geometry and meshing while simulation is done on Fluent.

Table 1. Intensity and Hydraulic Diameter

Stream	Turbulent intensity (%)	Hydraulic diameter(mm)
Air	17	29
Slurry	5	1.8
Outlet	5	600

3 CONSTRUCTION OF CFD MODEL

3.1 Combustion chamber

Coal water slurry and is introduced into burner via concentric pipes. slurry consist of 50% coal loading(lakhra mine lignite coal used for slurry making).slurry enters at 900K through 4mm ID PIPE while air enter at 1200K thorough 10 mm ID pipe.

3.2 Geometrical model and mesh grid:

The physical model considered is a 3D, standard K-epsilon turbulence model, reacting, non-premixed combustion. Combustion chamber geometry is designed using GAMBIT .burner consist of two concentric pipes with radii of 4mm and 10mm respectively and Height of burning chamber is 40mm. Meshing scheme using here is pave scheme for z-direction faces and cooper meshing scheme for x and y direction faces. The 1/4th of the chamber is shown in figure 1 because of symmetry.

3.3 Turbulent and combustion model

The turbulence model used is the standard K-Epsilon turbulence model. This is a two-equation model in which transport equations are solved for turbulent kinetic energy and its dissipation rate [1].

$$\frac{Dk}{Dt} = +\nabla \cdot (\nu + C_2 \nu_T)\nabla k - \tau_{ij}\frac{\partial U_i}{\partial x_j} - \varepsilon \qquad (1)$$

$$\frac{D\varepsilon}{Dt} = \nabla \cdot (\nu + C_3 \nu_T)\nabla \varepsilon + C_4 \frac{\varepsilon}{k}\tau_{ij}\frac{\partial U_i}{\partial x_j} - C_5 \frac{\varepsilon^2}{k} \qquad (2)$$

Where

$$\nu_T = C\frac{k^2}{\varepsilon} \quad \text{and} \quad \tau_{ij} = < u_i u_j > = \frac{2}{3}k\delta_{ij} - \nu_T\left(\frac{\partial U_i}{\partial x_j} + \frac{\partial U_j}{\partial x_i}\right)$$

$$C_1 = 0.09; \quad C_2 = 1.0; \quad C_3 = 0.769; \quad C_4 = 1.44; \quad C_5 = 1.92$$

The value of intensity and hydraulic diameter used in numerical analysis are shown in Table 1.

For analysis a non-premixed combustion model is a used .This model uses a modelling approach that solves transport equations for energy, radiation and the mixture fractions. For simulation Use the P-1 radiation model for combustion applications. Property data for the species are accessed through a chemical database and turbulence chemistry interaction is modelled using a β-function for the PDF.

3.4 Chemical scheme and boundary conditions:

For the numerical analysis of coal slurry combustion a chemistry model involving 4 combustible components is considered. Ultimate and proximate analysis of coal sample as given in Table 2

$$C + O_2 \longrightarrow CO_2 \qquad (3)$$

$$H_2 + 1/2\ O_2 \longrightarrow H_2O \qquad (4)$$

$$S + O_2 \longrightarrow SO_2 \qquad (5)$$

$$N_2 + O_2 \longrightarrow NO_2 \qquad (6)$$

Table 2.Proximate & Ultimate Analysis of Lakhra coal

Ultimate analysis (%)	Proximate analysis (%)
Carbon=35.23	Moisture =10
Hydrogen=4.43	Volatile matter=35
Nitrogen=0.79	Ash = 42
Oxygen=7.74	Fixed carbon=13
Sulphur =1.8	

Table 3 shows the data of velocity component and temperature, both for fuel and air and they are used as boundary conditions in the simulations.

Table 3.Velocity & Temperature

	Air	Coal slurry
Velocity component(m/s)	X=0,Y=0 & Z=70	X=0,Y=0& Z=50
Temperature(K)	1200	900

Burner solid model was set 3D, Stationary and constant density model. The properties of the burner wall as shown in Table 4.

Table 4.Wall Properties

WALL PROPERTIES	
Temperature(K)	300
emissivity	0.6
Thermal conductivity(W/m.K)	202.4
Specific heat(J/kg.K)	871.5

4 RESULT AND DISCUSSION

In this paper the flow inside a combustion chamber, viscosity behaviour of particles and turbulent conditions has been examined using Fluent.

4.1 Static Temperature

The maximum static temperature observed in chamber is 1325K .At all the wall temperature is constant that is 300K and from nozzle to chamber has the temperature ranges from 800 to 1200K.

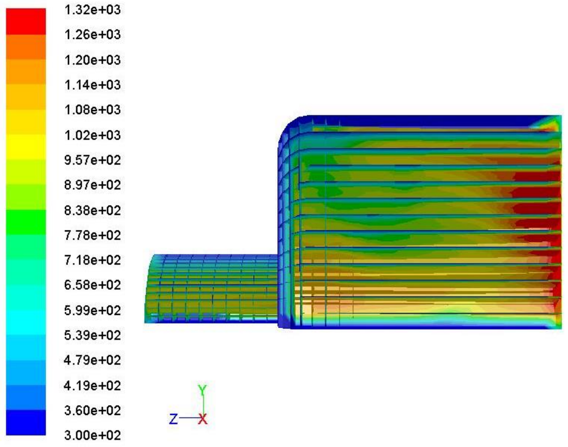

Figure2.Static Temperature

4.2 Turbulent Kinetic

As observed from turbulent kinetic energy contour, it is almost uniform throughout the chamber and having a kinetic energy of 56.1 m^2/s^2.the maximum kinetic energy observed in nozzle area that is 504 m^2/s^2.

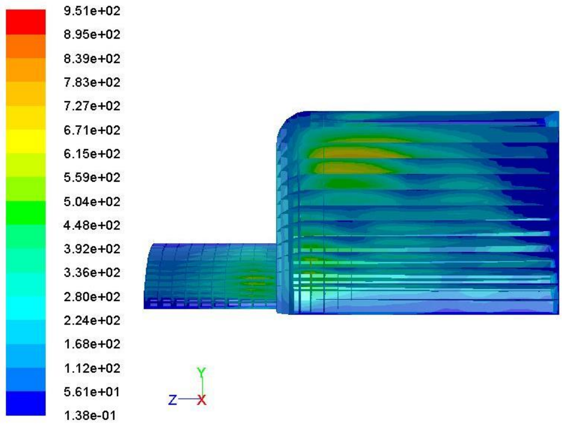

Figure 3.Turbulent Kinetic

4.3 Turbulent Dissipation

As observed from dissipation rate contour, it is almost uniform throughout the chamber having a value of 235 to 1.76e +06 m^2/s^3.

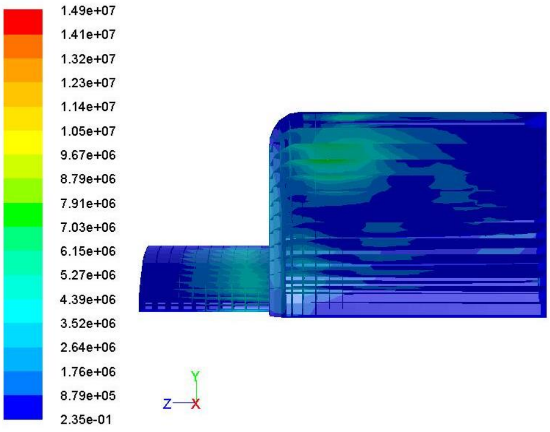

Figure 4.Turbulent Dissipation Rate

4.4 Velocity Magnitude

The velocity contour is almost uniform; velocity ranges from 21.0 to 52.6 m/s. The velocity of the flow becomes zero at the wall of the chamber.

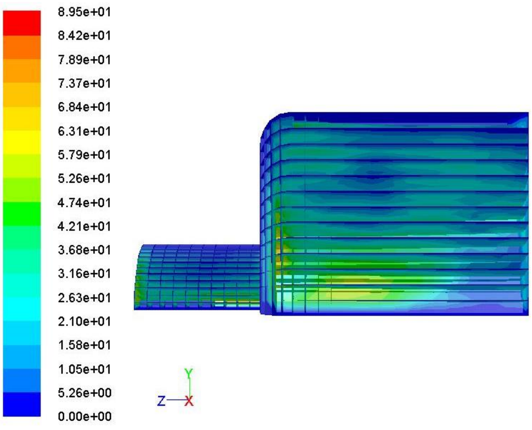

Figure 5.Velocity Magnitude

4.5 Molecular viscosity

The molecular viscosity contour is almost uniform throughout the combustion chamber.

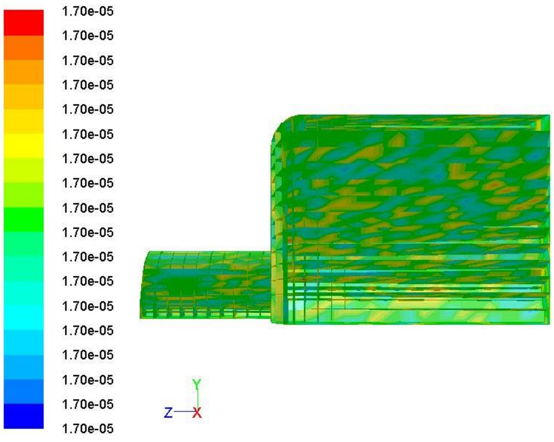

Figure 6.Molecular Viscosity

5 CONCLUSION

In this paper combustion analysis is done. It is observed that temperature is constant throughout the chamber except wall which shows the uniform distribution of fuel in chamber. In the contour of turbulent kinetic energy and turbulent dissipation rate it is observe that the region where turbulent kinetic energy is high dissipation rate is also high which shows that the kinetic energy of eddies is converted into heat energy. In the contour of velocity it is observed that highest velocity is achieved at the nozzle of chamber and the contour of molecular viscosity is homogeneous throughout which shows that the molecules are not grouped they are moving randomly in the chamber.

ACKNOWLEDGEMENT

The authors are greatly thankful the teachers Department of Chemical Engineering NED university of engineering and technology, Karachi for their valuable suggestions and encouragement given time to time during the completion of the above project.

NOMENCLATURE

CFD	Computational fluid dynamics
CWS	Coal water slurry
µ	Viscosity
ε	Emissivity
ID	Internal diameter

REFERENCES

[1]. **Malasekera, H K Versteeg & W.** *An introduction to computational fluid dynamics ,the finite volume method.* s.l. : second edition.

[2]. *CFD Analysis of Flow Field inside the Expansion Chamber of Internal Combustion Engines.* **K. M. Pandey, Upendra Kumar, Subho Deb Verma.** Issue-3, s.l. : International Journal of Engineering and Advanced Technology (IJEAT), February 2012, Vols. Volume-1. ISSN: 2249 – 8958,.

[3]. *CFD Study of Effects of Geometry Variations on.* **Y. Yu, M. Shademan, R. M. Barron & R. Balachandar.** No.3, canada : Engineering Applications of Computational Fluid, Vol. Vol. 6. ISSN: 1994-2060 (Print) 1997-003X.

[4]. *TURBULENCE KINETIC ENERGY AND DISSIPATION RATE ESTIMATED FROM A VIRTUAL.* **Chilson, D. E. Scipion E. Fedorovich R. D. Palmer P. B.**

[5]. *Clean Coal Technologies in Japan Technological Innovation in the Coal Industry.* 2004.

ANALYSIS OF ELECTROMAGNETIC WAVE PROPAGATION THROUGH PHOTONIC CRYSTAL FIBERS

Shafaq Mustafa[1,*], Muhammad Imran Aslam[1,2], Irfan Ahmed[1,2]
[1] Department of Electronic Engineering, NED University of Engineering and Technology, University Road, Karachi-76270, Pakistan.
[2]Emerging Technologies Research Group, NED University of Engineering and Technology, University Road, Karachi-76270, Pakistan.

[*]Corresponding *author*: shafaq_mustafa@hotmail.com

ABSTRACT

In this paper, an index-guiding photonic crystal fiber (PCF) has been modelled and analysed using Finite Element Method based software package COMSOL Multiphysics. The effective mode index, dispersion and confinement loss have been calculated for the fundamental mode of the fiber with the objective to achieve minimum dispersion at the wavelengths of interest. The effect of variations in the structural parameters on the electromagnetic wave propagation through the PCF has been studied. It was observed that the dispersion and confinement loss are depended on the physical geometry of the PCF; hence by tailoring the geometry, a minimum value of dispersion and/or confinement loss may be obtained at wavelength of interest.

Keywords: Dispersion; Finite Element Method; Holey Fibers; Photonic Crystal Fiber

1 INTRODUCTION

Photonic Crystal Fiber (or sometimes referred to as micro-structured optical fibers or holey fibers) is a new class of optical fibers having properties like controllable nonlinearity and dispersion over wide wavelength range [1], endless single mode operation [2], ultralow loss [3] and large effective area [4], etc. These enhanced properties make PCFs suitable for the use in wide range of applications such as optical fiber communications, nonlinear devices, amplifiers, fiber lasers, high power transmission, highly sensitive sensors and many more [5].

Two types of PCFs depending on light guiding mechanisms are index guiding (IG) fibers and photonic band gap fiber (PBF) [6]. IG-PCF consists of a solid core which is surrounded by a periodic array of air holes in the cladding region. The light is guided in the fiber through modified total internal reflection. In PBF light propagates in a low index defect in the photonic crystal. The wavelengths within the bandgap of the photonic crystal cannot leak out through the cladding and therefore will be confined to propagate in the hollow core [7, 8].

This paper summarizes preliminary findings of our research work on the optimization of dispersion characteristics of PCFs. A modal analysis of PCF is carried out by using finite element method (FEM) based software package COMSOL Multiphysics. The simulated results for the effective index and dispersion are compared to the literature values and found to be in good agreement. Moreover, the effects of variations in the structural parameters on the electromagnetic propagation properties are also studied.

Rest of the paper is organized as follows. In section 2, we provide an account of the propagation characteristics and the simulation setup. Results and discussion is presented in section 3. Section 4 concludes the paper.

2 MATERIALS AND METHODS

Unlike conventional fibers, the electromagnetic properties of a PCF can be controlled by the variation of physical geometry of the PCF. There are three parameters; the spacing between the holes (or pitch denoted by Λ), the diameter of the holes (d) and the number of rings (Nr). Dispersion is one of the most important characteristics of the fiber as it limits the network capacity. It is defined as the spreading of light into it constituents either due to variations in the propagation constant of the wave or variations in the refractive index of the material. Chromatic dispersion parameter (*D*) of a fiber can be represented in terms of the effective refractive index (n_{eff}) as [7]

$$D = -\frac{\lambda}{c}\frac{d^2 Re[n_{eff}]}{d\lambda^2} \qquad (1)$$

Where, Re[·] shows the real part, c is the speed of light in free space and λ is the wavelength of the light propagating through the fiber. Another important parameter in respect to the wave propagation through a fiber is the Confinement Loss (CL) that determines the light confinement ability within the core region of a single material fiber. If Im[·] represents the imaginary part, the confinement loss (in dB/m) can be given as [7]

$$CL = 8.686\,\frac{2\pi}{\lambda}\,Im[n_{eff}] \qquad (2)$$

These above mentioned properties and many more can be qualitatively calculated by using fully vectorial techniques. One of the most widely used and successful approach is FEM that can be used to determine the propagation constants and the electric field distributions of the guided mode by solving eigenvalue equation [9]. It performs meshing by sub-dividing the structure into finite size elements. A set of characteristic equations governed each element by describing its physical properties and boundary conditions. Then the effective mode index is evaluated by simultaneously solving these equations.

Figure 1 shows the geometry of IG-PCF used in the study. The material of the fiber is assumed to be Silica defined by Sellmeier's equation [10] as

$$\begin{aligned} n(\lambda) = 1.4508554 &- 0.0031268\lambda^2 - 0.0000381\lambda^4 \\ &+ \frac{0.0030270}{(\lambda^2 - 0.035)} - \frac{0.0000779}{(\lambda^2 - 0.035)^2} \\ &+ \frac{0.0000018}{(\lambda^2 - 0.035)^3} \qquad (3) \end{aligned}$$

Where, λ is the wavelength measured in μm. The silica core is surrounded by a periodic array of air holes arranged in a hexagonal geometry as shown in Figure 1. Flow chart of the FEM simulation used in the study [8, 11] is shown in figure 2.

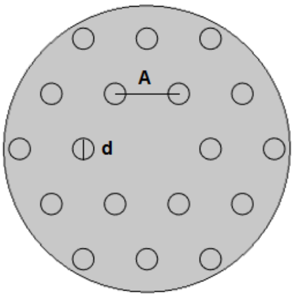

Figure 1: Cross section of the PCF under study

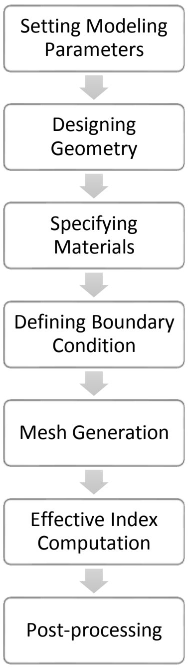

Figure 2: Flowchart for PCF modelling

3 RESULTS AND DISCUSSION

The solid-core PCF having A=3μm, d=0.6μm and Nr=2 is simulated as elaborated in Figure 2. The electric field plot (Figure 3) is obtained for λ=1.5μm showing the light is confined in the central defect (core) of the PCF.

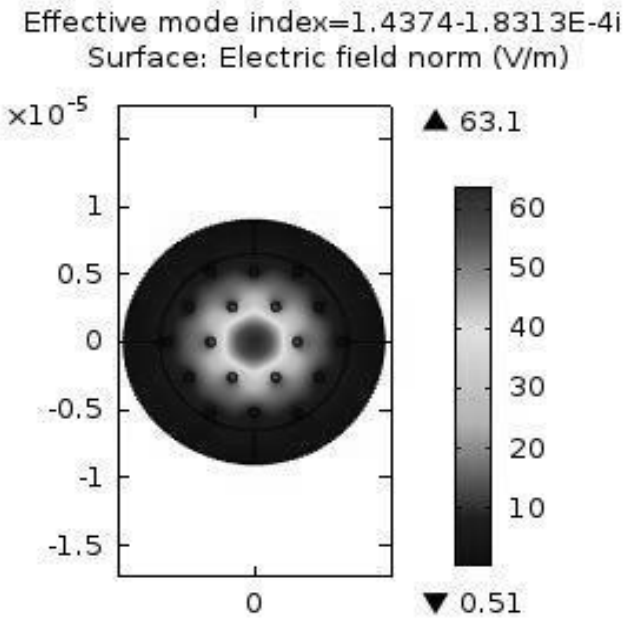

Figure 3: Electric field intensity at 1.5μm

The effective refractive index n_{eff} of the PCF is calculated and is found to be in good agreement with the literature values [12]. The effective indices and the percentage error are tabulated in Table 1.

Table 1: Effective indices and percentage error

S#	**λ (μm)**	**Refractive Index (Silica)**	**Reference n_{eff} [12]**	**n_{eff} using COMSOL**	**% Error in n_{eff}**
1	1.5	1.4450	1.437978	1.437407	3.9724×10^{-2}
2	1.2	1.4484	1.443370	1.443064	2.1205×10^{-2}
3	1.10	1.4495	1.445168	1.444887	1.9448×10^{-2}
4	1.00	1.4507	1.447012	1.446784	1.5759×10^{-2}
5	0.6	1.4584	1.456844	1.456858	0.0961×10^{-2}
6	0.50	1.4626	1.461572	1.461511	0.4174×10^{-2}

Figure 4 shows the variation of effective index as a function of wavelength. It is observed that the effective index decreases as wavelength increases.

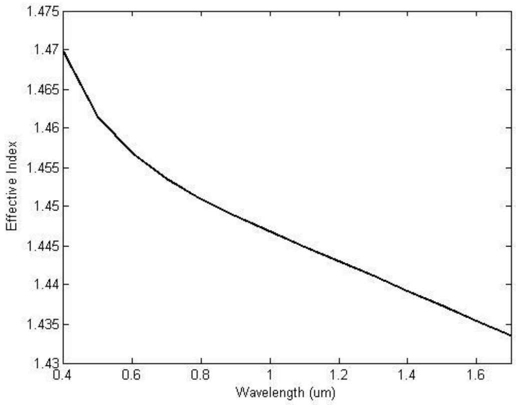

Figure 4: Effective index versus wavelength

The dispersion calculated by (1) represents the total chromatic dispersion as the material dispersion has been already included by Sellmeier's formula. Figure 5 shows the dispersion of the PCF calculated at different wavelengths. The zero dispersion is observed at four wavelengths. Negative dispersion is also obtained from 0.5μm to 0.8μm which can be expedient for the use in dispersion compensating fibers.

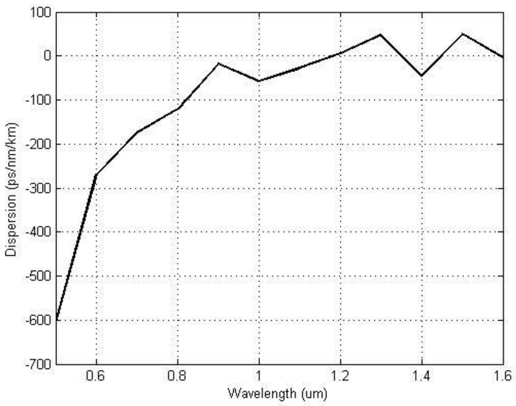

Figure 5: Dispersion profile of the PCF

The dispersion of the fiber can be modified by changing the size of the innermost ring of holes. The diameter of first ring of holes (d1) is halved i.e. decreased to 0.3μm. From figures 6 and 7, it is clear that the effective index increases while the dispersion decreases with the decrease in d1.

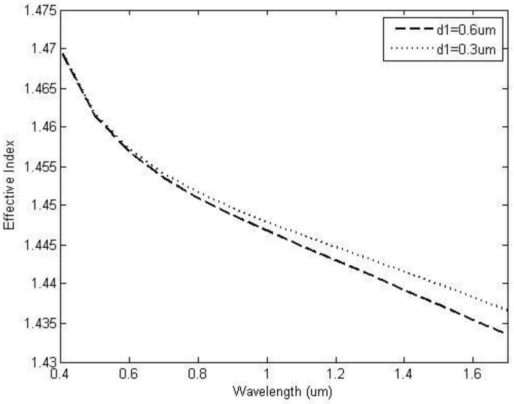

Figure 6: Effective indices versus wavelength for different hole diameters

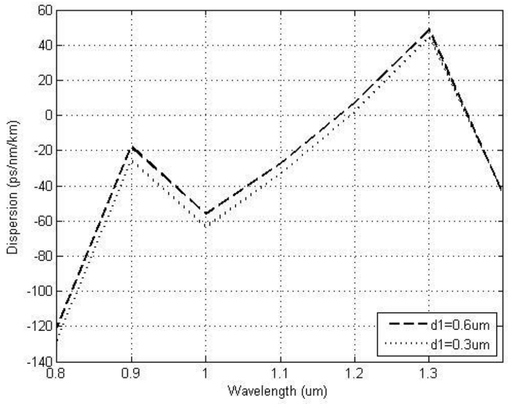

Figure 7: Dispersion versus wavelength for different hole diameters

In order to decrease the confinement loss, number of rings are increased. Figure 8 shows the confinement loss as a function of wavelength for different number of rings. It is evident that confinement loss significantly decreases as number of rings increases.

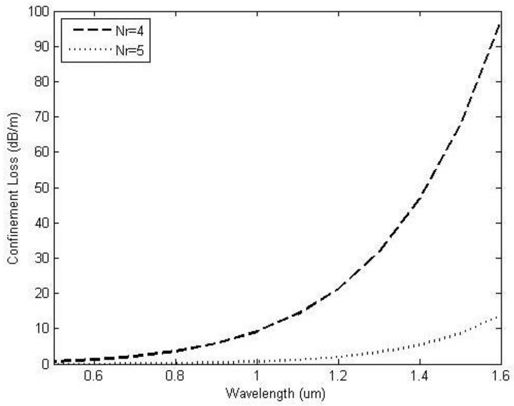

Figure 8: Confinement loss variation against wavelength for different number of rings

4 CONCLUSION

The analysis of PCF has been carried out using FEM. The effective index has been found to be increasing with the decrease of wavelength and air hole diameter. The dispersion profile is giving four zero-dispersion wavelengths and negative dispersion over a broad range of wavelengths. As the number of rings increases, the electric filed has been found to be more concentrated to the core lowering the confinement loss. Dispersion and confinement loss can be further improved by optimizing the geometry of the PCF under study. Also, analysis of numerous other fiber designs like square, octagonal and face centre cubic geometries can be carried out using this method.

REFERENCES

[1] J. Lizier, "Applications of Holey Fiber Splicing, Spot-size conversion and Coupling," School of Electrical and Information Engineering, School of Electrical and Information Engineering, University of Sydney, Sydney, 2000.

[2] J. C. K. T. A. Birks, and P. St. J. Russell, "Endlessly single-mode photonic crystal fiber," *Optics Letters*, vol. 22, pp. 961-963, 1997.

[3] J. Z. Tajima K., K. Nakajima, K. Sato, "Ultralow Loss and Long Length Photonic Crystal Fiber," *Journal of Lightwave Technology* 2004.

[4] M. D. N. J.R. Folkenberg, N.A. Mortensen, C. Jakobsen, and H.R. Simonsen, "Polarization maintaining large mode area photonic crystal fiber," *Optical Society of America,* 2004

[5] https://en.wikipedia.org/wiki/Photonic-crystal_fiber.

[6] J. M. Senior, *Optical Fiber Communications Principles and Practice*, Third ed.: Pearson Education Limited, 2009.

[7] K. P. L. Reichenbach, "Numerical analysis and experimental study of fiber bundles and multi-core photonic crystal fibers for use in endoscopes ", Cornell Univeristy, January 2007

[8] M. I. A. Immad Girach, Irfan Ahmed, Syed M. Usman Ali and Muhammad Khalid, "Photonic Band Gap Materials- Theory, Techniques and Application," *Bahria University Journal of Information & Communication Technologies,* vol. Vol. 8, pp. 126-129, 2015.

[9] M. S. a. W. Urbanczyk, "Comparison of different methods for rigorous modeling of photonic crystal fibers," *Optics Express*, vol. 14, June 2006.

[10] A. Ghatak, *Optics*, 4th ed. New Delhi: Tata McGraw Hill.

[11] *COMSOL Multiphysics User's Guide*.

[12] K. Y. V. Jandieri, A. Sharma and H. Chauhan "Modal analysis of specific microstructured optical fibers using a model of layered cylindrical arrays of circular rods," *IEICE Trans. Electron.*, vol. E93.C, pp. 17-23, January 2010

NUMERICAL INVESTIGATION OF THE EFFECT OF THERMAL CONDUCTIVITY AND POROSITY OF GAS DIFFUSION LAYER ON PERFORMANCE OF PEMFC

Obaid ur Rehman[1,*] Syed Mushahid Hussain Hashmi[2] and Inayat Ullah Memon[3]
[1]Chemical Engineering Department, University of Karachi, Karachi, Pakistan
[2]Automotive and Marine Engineering Department, NED University of Engineering & Technology, Karachi, Pakistan
[3]Chemical Engineering Department, NED University of Engineering & Technology, Karachi, Pakistan

[*]Corresponding author. Tel.: +0321-2536798
E-mail address: obaid.cheme@live.com

ABSTRACT

In this study a three dimensional steady state model of a five-channel PEMFC, with an active area of 50 cm^2 and serpentine flow pattern, is studied to identify the effects of thermal and transport properties of gas diffusion layer on performance of a PEMFC. This study has aided in making good approximation to the actual behaviour of PEMFC at different material properties. The fuel and oxidant are fed into the cell in a cross flow pattern. A finite volume based solver, ANSYS FLUENT is employed to handle a large scale computational domain with parallel computing in order to solve the coupled transport equations of the model. The results obtained provide sensible insight to the transport phenomena and kinetics of the electrochemical reactions inside the PEMFC which were illustrated through contours of different parameters. The results suggest that the thermal conductivity of the GDL (gas diffusion layer) can play a crucial role in preventing the polymer electrolyte from drying as well as for efficient protonic conduction. It is also observed that the rate of electrochemical reaction can be enhanced by optimizing the GDL porosity. The numerical results are validated using the polarisation curve developed through experiments and found to be in good agreement.

Keywords: PEMFC; CFD; gas diffusion layer; thermal conductivity & porosity

1 INTRODUCTION

The impact of immense utilization of fossil fuel in the automotive and power generation sector has drawn enormous damage on environment of today's world. The development of renewable and clean energy resource has been a key topic of researchers from few decades. PEM fuel cells (PEMFCs) has emerged as a promising substitute for internal combustion engines (ICEs) in automotive sector. Though yet the fuel cell technology has not been commercialized due to its high manufacturing cost and lack of infrastructure available for hydrogen, but still it has a great deal of potential as an alternative energy conversion technology.

Fuel cell technology has been widely recognized as a clean energy resource for its high energy density and conversion efficiency [1],[2]. PEM fuel cells have remained a most suitable choice in automobile application as it requires low operating temperatures.

The main components of the PEM fuel cell are represented in Fig. 1. Air is injected from cathode side of the cell while Hydrogen gas enters from anode. At anode, hydrogen oxidation reaction (HOR) occurred as shown in the reactions below. On the other hand the oxygen reduction reaction (ORR) occurs at cathode side. The hydrogen ions (protons) travel through the polymer electrolyte membrane, and reach the cathode side where it reacts with oxygen to from water and heat is released as this combustion of hydrogen is exothermic.

$$Anode: \; H_2 \rightarrow 2H^+ + 2e^-$$

$$Cathod: \; 1/2O_2 + 2H^+ + 2e^- \rightarrow H_2O$$

$$Overall: H_2 + 1/2O_2 \rightarrow H_2O + heat$$

The performance of PEM fuel cells is highly dependent upon the thermal and transport characteristics of the porous CL (catalyst layers) and GDL (gas diffusion layers) [3]. GDLs are employed to distribute the reactant gas to the reaction sites of the catalyst by increasing the diffusion capacity. They also provide the pathway for the removal of water and heat from catalyst layer to the gas flow channels. In order to achieve high current densities the GDL must be porous to allow flow of both water and reactant gases. It must also be thermally and electrically conductive for the flow of product heat and electric current in both in-plane and through plane directions [4]. These requirements make GDLs to play a key role in PEMFC operation. Due to low operating temperature of the cell the water condenses in the cell which may lead to the flooding of the gas diffusion and catalyst layers. The water droplets block the pores of CLs and GDLs which decreases the number of reaction sites and ultimately lower the output cell voltage [5]. On the other hand, proton conductivity of the membrane increases with its water content at low temperatures [6] while the diffusivity of gases depends on high temperatures. This conflicting situation demands for an optimum operating parameters of the PEM fuel cells as well as favorable transport characteristics of GDLs and CLs for high output c.

Numerical modelling and simulation provide relatively agile methods to design and analyze complex systems as compared to the experimental procedures and it also provide access to diversified results. Currently various numerical models are available in the published literature covering the transport phenomena as well as electrochemical kinetics inside the PEM fuel cell [7-17]. Based on the numerical models various simulations have been produced to analyze the performance of PEM fuel cell at different operating conditions and design configurations.

Most of the work has been done experimentally to analyse the structural and thermal effects of GDLs on PEM fuel cell performance [18-20]. In this paper a simulation study has been performed using FLUENT fuel cell model for single cell geometry with 50cm^2 of active area. There are five number of flow gas channels which are arrayed in a serpentine design. A multiphase mathematical model is incorporated to compare different GDLs having thermal conductivities and porosity variations.

2 MODEL DESCRIPTION

The governing transport phenomena and reaction kinetics of the PEM fuel cell has been modelled in numerous works. Some good reviews on the model of PEM fuel cell can be found in [21-23]. In this study a commercial finite volume based solver FLUENT was used to solve the PEM fuel cell model. The geometrical and mathematical model is described in subsequent paragraphs.

2.1 Geometric Model

The three dimensional geometry of a five channel single cell PEM fuel cell is developed using GAMBIT pre-processor. The model consists of seven layers as shown by the schematic in Fig. 1. The geometry was meshed by hexahedral cells as shown in Fig. 2. The actual photograph of the channels is presented in Fig. 3. The geometrical dimensions are given in the Table 1.

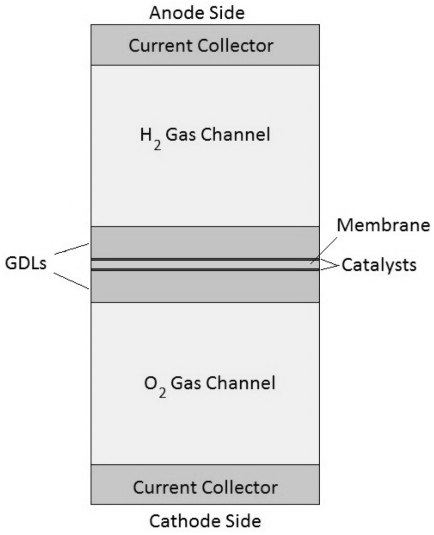

Figure 1. Schematic of PEMFC layers

The mesh was developed using hexahedral cells with approximately 1.6 million mesh nodes.

Table 1. Dimensions in cell geometry (mm)

Channel height	1
Channel length	70
Channel width	0.75
Rib width	0.82
GDLs thickness	0.19
Catalyst layers thickness	0.05
Membrane thickness	0.0508
Current collector thickness	0.25

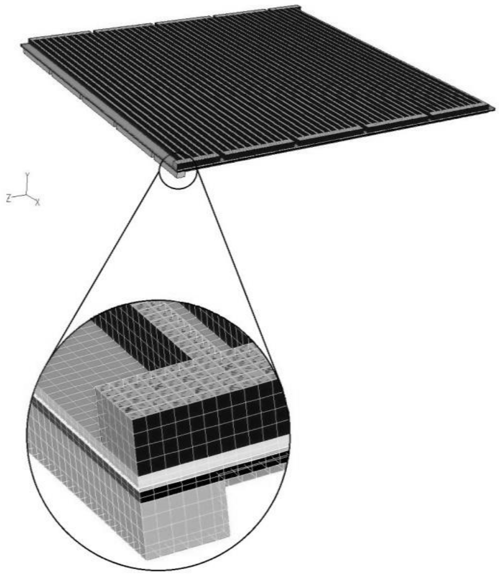

Figure 2. Mesh

Figure 3. Gas flow channels engraved in bipolar plate

2.2 Mathematical Model -Governing Equations

Conservation equation

The multiphase mathematical model is employed in this study. The reaction takes place at catalyst layer where three phases namely gas, liquid and solid are involved. Hydrogen ion formed at anode travel to cathode where they oxidized to from water. .

In a finite volume method the basic equation for a conservation of a general property φ over a control volume in a steady state problem is given as [24]

$$\int_A n.(\rho\varphi u)dA = \int_A n.(\Gamma\nabla\varphi)dA + \int_{CV} S_V dV \qquad (1)$$

where n represents the vector normal to a differential surface d*A* and Γ is a diffusion coefficient. The left hand side gives the convective flux and right hand side gives the diffusive flux plus the generation or consumption of the property.

The continuity equation for the model is given as

$$\frac{\partial(\rho\varepsilon)}{\partial t} + \nabla\cdot(\varepsilon\rho\vec{u}) = S_m \qquad (2)$$

where ρ is the density, ε is the porosity, $\vec{u}$ is the fluid velocity vector and S_m denotes the mass production term.

The momentum conservation equation is given as follows

$$\frac{\partial(\rho\varepsilon\vec{u})}{\partial t} + \nabla\cdot(\varepsilon\rho\vec{u}\vec{u}) = -\varepsilon\nabla p + \nabla\cdot(\varepsilon\mu\nabla\vec{u}) + S_u \quad (3)$$

where *p* represents the pressure, and S_u is the force per unit volume.

For the species conservation following equation is employed

$$\frac{\partial(\varepsilon C_k)}{\partial t} + \nabla\cdot(\varepsilon\rho\vec{u}C_k) = \nabla\cdot\left(D_k^{eff}\nabla C_k\right) + S_k \qquad (4)$$

where C_k is the concentration of species and D_k^{eff} represents the diffusivity which is given for porous material by Bruggman equation as follows

$$D_k^{eff} = \varepsilon_m^{1.5} D_k \qquad (5)$$

The species production term S_k is related to electrochemical reaction in the fuel cell which is given in the following form

$$S_k = -\frac{M_{w,k}}{nF} R_j \qquad (6)$$

where k shows the specie, n is the electron transfer number, and subscript j is for anode or cathode.

Energy conservation equation is given as follows

$$\frac{\partial(\rho\varepsilon h)}{\partial t} + \nabla(\varepsilon\rho\vec{u}h) = \nabla\left(k^{eff}\nabla T\right) + S_h \qquad (7)$$

The energy source is a sum of different source terms like heat of reaction, ohmic heating and electric work and latent heat of water, and is given by

$$S_h = \mathrm{h_{react}} - \mathrm{R_{an,cat}}\eta_{\mathrm{an,cat}} + I^2 R_{ohm} + h_L \qquad (8)$$

The equation for conservation of charge is given as

$$\nabla \cdot \left(\sigma_e^{eff} \nabla \Phi_e\right) + S_\Phi = 0 \qquad (9)$$

where Φ_e is the charge potential for membrane or solid phase, σ_e^{eff} is the ionic conductivity, S_Φ is the source term which depends on exchange current density (A/cm^2). The dependence of exchange current density on reactant concentration can be expressed by Butler-Volmer's [9] equation whose simplified form known as Tafel equation is given below

$$S_\Phi = \begin{cases} I_{an} = I_{an}^{ref} \left(\dfrac{[H_2]}{[H_2]_{ref}} \right)^{\gamma_{an}} \left(e^{\alpha_{an} F \eta_{an} / RT} \right) \\ I_{cat} = I_{cat}^{ref} \left(\dfrac{[O_2]}{[O_2]_{ref}} \right)^{\gamma_{cat}} \left(e^{-\alpha_{cat} F \eta_{cat} / RT} \right) \end{cases} \qquad (10, 11)$$

where I^{ref} is the reference exchange current density, γ is the concentration dependence factor, α is the transfer coefficient, F is Faraday constant, and η is the overpotential.

2.3 Model Parameters and Boundary Conditions

A steady state and non-isothermal condition is assumed and reaction is carried out at a pressure of 1atm and temperature of 353K (80°C). The relative humidity of reactant gases were taken to be 100%. The calculations were carried out by fixing the output current density at 0.6 A/cm^2 and the output voltages were calculated. The hydrogen gas flow rate at anode side was taken to be 0.4 SLPM (9.477×10^{-7}kg/s) while air flow rate at cathode was taken to be 1.26SLPM (2.82×10^{-5}kg/s). The electrochemical parameters for the model are given in Table 3.

Table 3. Electrochemical Parameters

Quantity	Value
Anode reference current density [25]	100 A/m^2
Anode reference molar concentration [25]	0.04 kmol/m^3
Anode concentration exponent [13]	0.5
Anode exchange coefficient [26]	0.5
Cathode reference current density	0.00035 A/m^2
Cathode reference molar concentration [25]	0.04 kmol/m^3
Cathode concentration exponent [13]	1
Cathode exchange coefficient	0.6
Open circuit voltage	1.1 V
Hydrogen reference diffusivity [25]	1.1028×10^{-4} m^2/s
Oxygen reference diffusivity [25]	3.2348×10^{-5} m^2/s
Water reference diffusivity [25]	7.65×10^{-5} m^2/s
Nitrogen reference diffusivity [25]	3×10^{-5} m^2/s

2.4 Solver Specification

A finite volume based FLUENT solver is implemented to solve the governing equations. The large scale computational domain was handled by parallel processing technique. An in-house 17 node Linux based cluster with Beowulf architecture was employed which is situated in high performance computing centre (HPCC) at NEDUET. Each node contains double Quad core processors with 2.4 GHz processing capacity of each.

3 RESULTS AND DISCUSSION

3.1 Grid Independence Study

In order to rely on the numerical results the grid independence study is highly recommended. Kamarajugadda et al. [25] reported the grid independence study of a two dimensional model. They observed about 4% and less than 1% variation in the result when the number of cells in the membrane was increased to 10 and 4 times.

In our study we tested a large scale three dimensional model to be independent of the meshing criteria. The parameter set for the criterion is the current density which was calculated for different mesh sizes at 0.67V. Due to large computational time for each iteration less than 10% variations in the criterion parameter were considered as an acceptable limit. It was observed that the results were converged as the mesh is finer and small variation is observed. The medium grid was selected for all the calculations in this work.

Table 4. Grid independence study [CD: current density]

Mesh	Cells	CD(A/cm^2@0.67V)
Fine	1858725	0.425
Medium	1352475	0.407
Coarse	1099350	0.375

3.2 Experimental Validation

The simulation was validated with the experimental results by comparing the polarization curves, as shown in Figure 4. The in-house experiments were carried out to generate a polarization curve by operating a PEM fuel cell of 50cm^2 active area at fuel cell lab in Automotive Department, NEDUET. A standard test fuel cell manufactured by ElectroChem Inc. is used for the experiments. The measurement of current density was carried out at varying cell voltages. Fuel cell testing system (FCTS) was employed for data acquisition.

A good approximation is achieved and the numerical results follow the experimental curve. The polarization curve represents three overpotentials regions by different slopes. Initially at low current density the voltage was maximum and suddenly dropped representing the first region called activation overpotential. The slope then decreased in the middle section corresponding to ohmic overpotential region. Finally the slope increased in the last section at high current density where concentration overpotential is dominant.

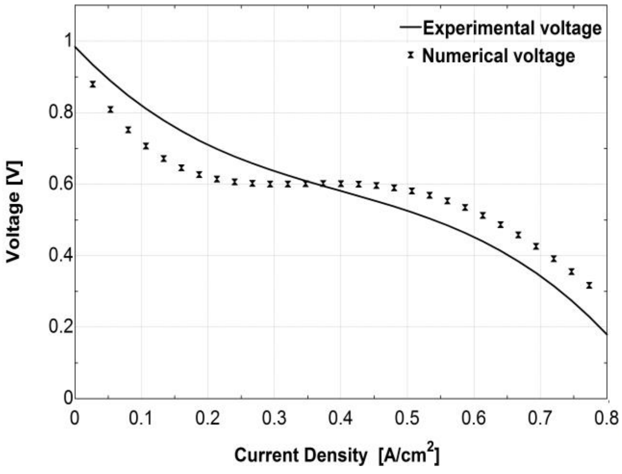

Figure 4 Polarization curve at 50°C and 1atm

3.3 Effect of GDL’s thermal conductivity

The effect of different thermal conductivities of GDLs on the water content and temperature of polymer electrolyte membrane (PEM) was illustrated by contours shown in Figure 5 and 6. Water content of membrane was estimated by using Springer et. al. equation [7] as follows

$$\lambda = 0.043 + 17.18a - 39.85a^2 + 36a^3 \ \ for\ a < 1 \qquad (12)$$

$$\lambda = 14 + 1.4(a - 1) \ \ for\ a > 1 \qquad (13)$$

where a is water activity and is defined mathematically as:

$$a = \frac{P_{WV}}{P_{sat}}$$

The vapor pressure can be related to molar fraction and total pressure as follows:

$$P_{WV} = x_{H_2O}P$$

Four different values of thermal conductivities were implemented. The contours in Figure 5 depict the overall decrease in water content of PEM as thermal conductivity of GDLs is increased. This result clearly represents the GDL function as it transfers the product heat from membrane to flow channels. The temperatures of PEM are compared at different thermal conductivities in the range of 356 K to 371 K in Figure 6. A low temperature profile is significant in the regions of rib-GDL interfaces where more heat is conducted due to contact with bipolar plates. The gradual increase of water content along the channel indicates the product water is being accumulated as reaction proceeded and simultaneously removed through GDL.

At different thermal conductivities (TC) the calculated output voltages are represented in Table 4. The current density is fixed at 0.6 A/cm^2 and the corresponding output voltages were estimated. The efficiency of PEM fuel cell is increased with the thermal conductivity corresponding to higher proton conductivity in the membrane which is the result of its increased water content.

Table 5. Calculated output voltages of different GDLs at 0.6 A/cm^2 of current density.

GDL	**TC (W/m-K)**	**Output Voltage (V)**	**Reference**
Toray carbon – TP60	1.7	0.425739	[26]
E-Tek, EC-CC1-060T	1.4	0.4231	[26]
Spectracarb, Carbon Paper	0.6	0.41067	[26]
Sigarcet 35BC	0.16	0.3897	[26]

The contours represent the iso-surfaces in the mid of membrane layer. The temperature of membrane play a significant role in the PEM fuel cell performance. High temperature will cause drying and consequently lowering the proton conductivity σ_{mem} as related in the following equation

$$\sigma_{mem} = (0.514\lambda - 0.326)\ e^{1268\left(\frac{1}{303}-\frac{1}{T}\right)} \qquad (14)$$

The osmotic drag coefficient (α_d) for protonic conductivity of membrane also depends upon its water content and is related as follows

$$\alpha_d = 2.5\frac{\lambda}{22} \qquad (15)$$

The flooding of catalyst layer is also a major problem in the PEM fuel cell operation which occur when very low temperature is maintained in the cell. This can be prevented using a GDL with optimum thermal conductivity and heat capacity.

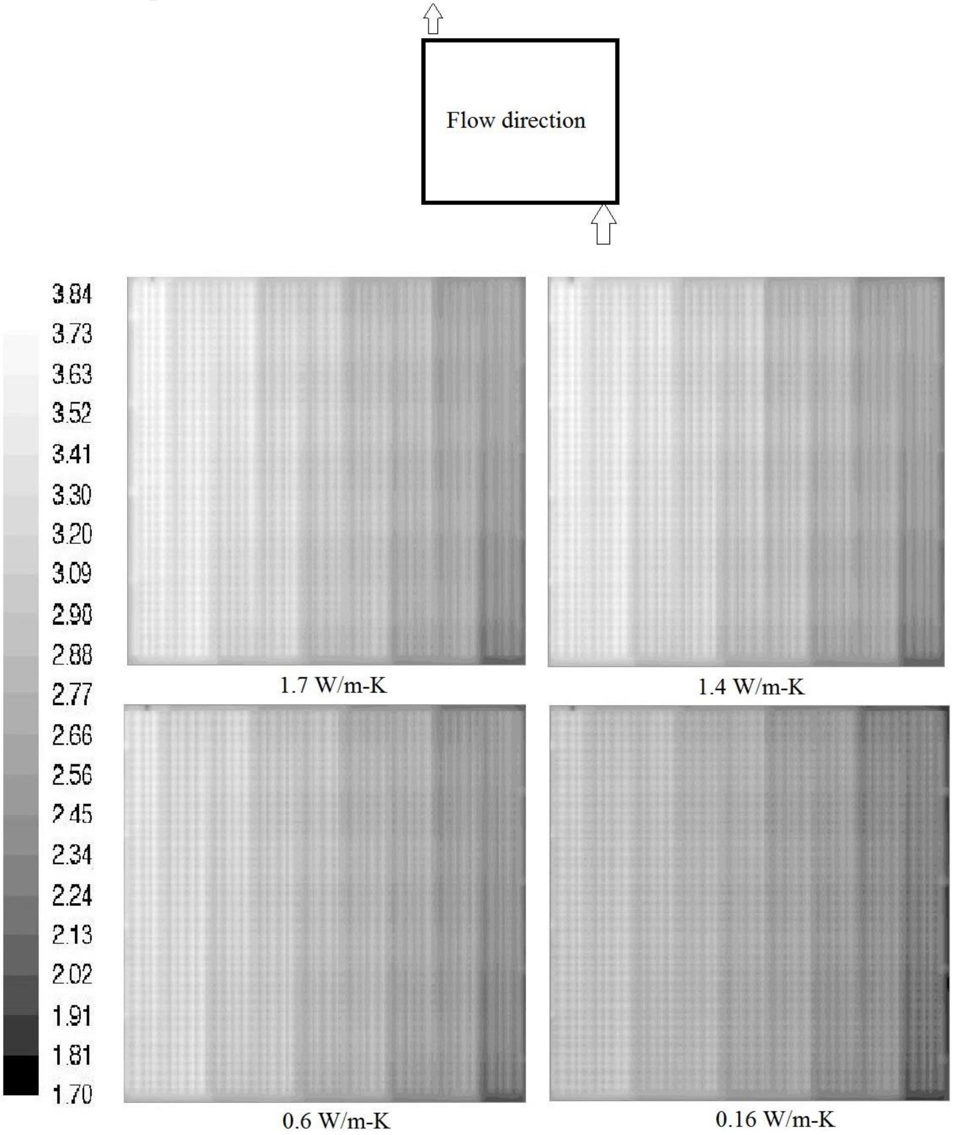

1.7 W/m-K

1.4 W/m-K

0.6 W/m-K

0.16 W/m-K

Figure 5 Contours of PEM water content (λ)

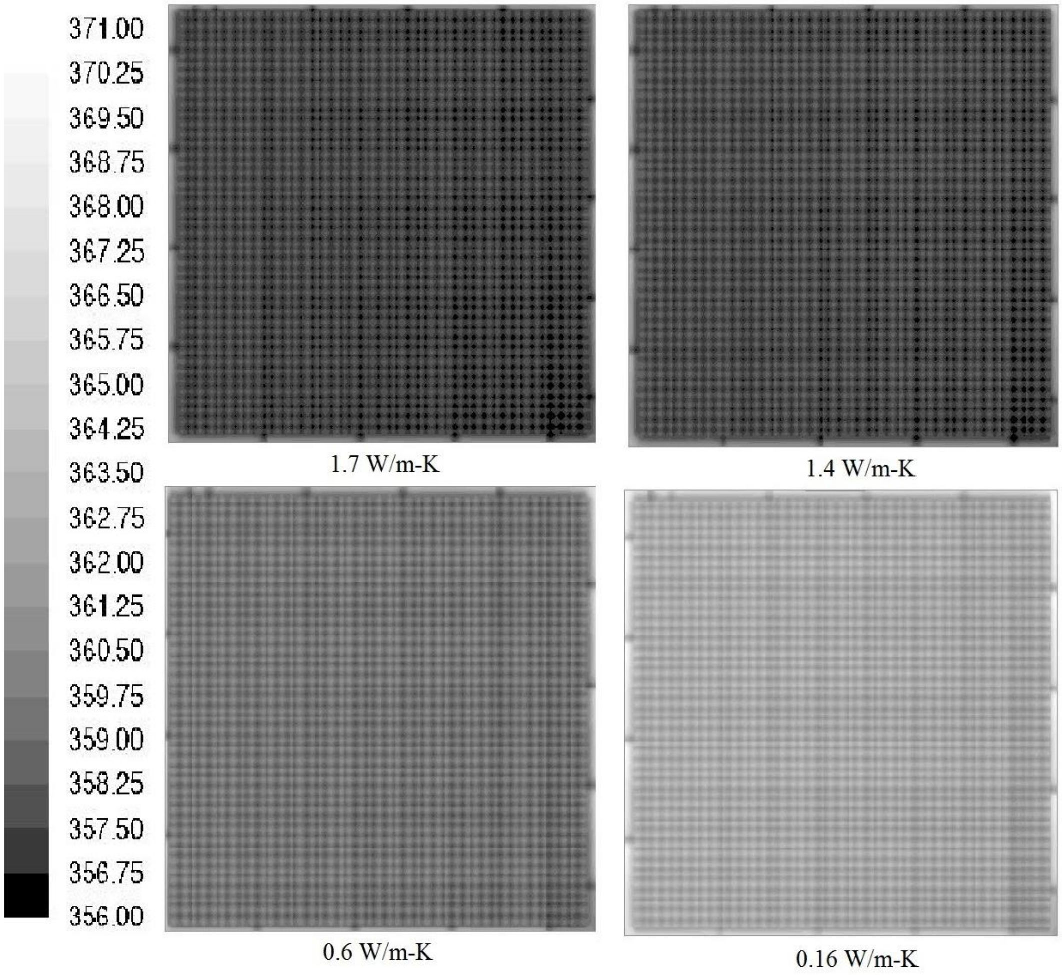

1.7 W/m-K 1.4 W/m-K

0.6 W/m-K 0.16 W/m-K

Figure 6 Temperature (K) contours of PEM

3.4 Effect of GDL porosity

Among the main functions of GDL the distribution of reactant gas to the active surface area of catalyst layer is very important. The diffusivity of gases in porous medium highly depends upon its porosity as shown in Equation 5. The high porosity will lead to increased transport of reactant gases which results in higher output voltage. On the other hand, increasing porosity may lower the electrical conductivity of the GDL [27] which decrease the performance. Consequently, an optimum porosity is desired for better performance of PEM fuel cell. The Table 5 shows the output voltages that generated in the simulation at different porosities of commercially available GDLs namely Sigracet 10 BA, Toray carbon –TP60, Sigarcet 34BC and ELAT LT 1400 W. The results depict that voltages get increased as the porosities of GDLs decreased from 0.88 to 0.63. This phenomenon represents the lowering of the electric conductivity of GDLs. The variation in output voltages due to porosity changes are negligible as compared to the variations with thermal conductivities as shown in Table 4.

Table 6. Estimated voltages of different GDL's at 0.6 A/cm^2 of current density.

GDL	Porosity	Output voltage (V)
Sigracet 10 BA	0.88	0.4174
Toray carbon –TP60	0.78	0.425739
Sigarcet 34BC	0.75	0.4273
ELAT LT 1400 W	0.63	0.432

The effect of GDL porosity on oxygen concentration and product heat at GDL-catalyst interface on cathode side of PEM fuel cell is depicted in Figure 7 and Figure 8. A subtle change can be noted in both figures with GDLs having low porosity of 0.63 and high porosity of 0.88. In Figure 7, it is significant to note that oxygen depletion is higher in GDL of 0.88 in comparison to the GDL with 0.63 porosity which denotes higher transport of reactant gases to the catalyst layer. The oxygen in the air supplied from cathode side is reduced to form water and electric current as reaction proceeds. It is also clear from Fig. 7 (a), (b) that oxygen mole fraction is decreased along the channel from 0.22 to 0.09 at the discharge section.

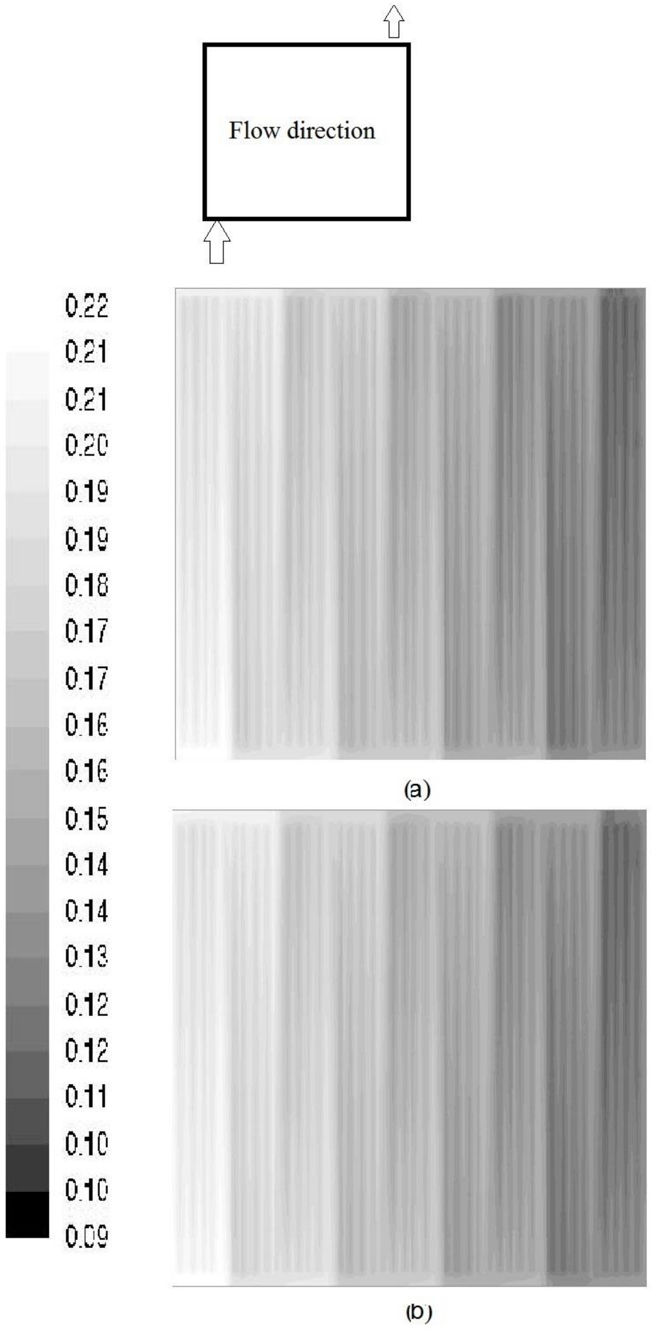

Figure 7 Oxygen mole fraction at cathode side GDL-catalyst interface. Porosity in (a) 0.63, (b) 0.88

The heat generated by the oxygen reduction reaction (ORR) is illustrated in Fig. 8. Again any appreciable change is notable in both diagrams (a) and (b) which signifying the rate of reaction at the catalyst surface. Figure. 8 also confirm the same phenomenon represented in Figure. 7 that product heat increases along the channel and higher porosity led to increased rate of reaction.

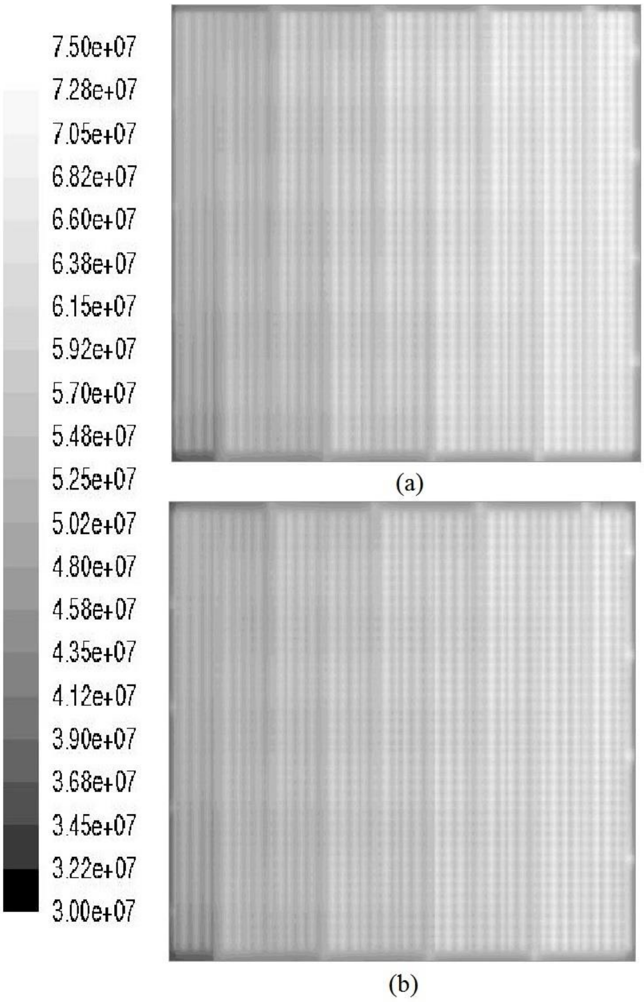

Figure 8 Reaction heat source (W/m3) at GDL-catalyst interface. Porosity in (a) 0.63, (b) 0.88

CONCLUSION

This study provided a numerical investigation of the effect of thermal and transport properties of GDL on the performance of PEM fuel cell. The mathematical model was validated with in house experimental results through a polarisation curve. Contours of different iso-surfaces presented to show the effect of thermal conductivities and porosities of GDL on the electrochemical behaviour of the PEMFC. The finding of the study provided a substantial basis in understanding the actual phenomenon occur inside the complex system of PEM fuel cell. It is reported that higher thermal conductivities of GDL led to high efficiency of PEM fuel cell by increasing the water content and maintaining low temperatures (i.e. without drying) in PEM. It was found that higher porosity of GDL increases the reactant gas transport to the catalyst layer but at the same time result in lower electrical conductivity which led to lower output voltages. These results suggest that the optimum

characteristics of GDL is required for better performance of PEMFC.
This study can be enhanced further in future by incorporating the effect of other GDL properties like gas permeability, thickness, electrical conductivity and incorporating the interface resistance between the layers adjacent to GDL.

ACKNOWLEDGEMENTS

Authors acknowledge the technical support from the Department of Automotive and Marine Engineering and High Performance Commuting Centre of NED University of Engineering and Technology, Karachi.

REFERENCES

1. B. Sundén, M.F., *Transport phenomena in fuel cells—series: develop-ments in heat transfe*. 2005: WIT Press.
2. Sammes, N., *Fuel cell technology—reaching towards commercialization*, in *Engineering Materials and Processes*. 2006, Springer.
3. D. P. Wilkinson, J.Z., *Proton Exchange Membrane Fuel Cells: Materials Properties and Performance*. 2009: CRC Press.
4. Mench, M.M., *Fuel Cell Engines*. 2008: WILEY.
5. Pasaogullari, U. and C.Y. Wang, *Liquid Water Transport in Gas Diffusion Layer of Polymer Electrolyte Fuel Cells.* Journal of The Electrochemical Society, 2004. **151**(3): p. A399-A406.
6. Rieke, P.C. and N.E. Vanderborgh, *Temperature dependence of water content and proton conductivity in polyperfluorosulfonic acid membranes.* Journal of Membrane Science, 1987. **32**(2): p. 313-328.
7. Springer, T.E., T.A. Zawodzinski, and S. Gottesfeld, *Polymer Electrolyte Fuel Cell Model.* Journal of The Electrochemical Society, 1991. **138**(8): p. 2334-2342.
8. Nguyen, T.V. and R.E. White, *A Water and Heat Management Model for Proton-Exchange-Membrane Fuel Cells.* Journal of The Electrochemical Society, 1993. **140**(8): p. 2178-2186.
9. Um, S., C.Y. Wang, and K.S. Chen, *Computational Fluid Dynamics Modeling of Proton Exchange Membrane Fuel Cells.* Journal of The Electrochemical Society, 2000. **147**(12): p. 4485-4493.
10. Ju, H., H. Meng, and C.-Y. Wang, *A single-phase, non-isothermal model for PEM fuel cells.* International Journal of Heat and Mass Transfer, 2005. **48**(7): p. 1303-1315.
11. Lum, K.W. and J.J. McGuirk, *Three-dimensional model of a complete polymer electrolyte membrane fuel cell – model formulation, validation and parametric studies.* Journal of Power Sources, 2005. **143**(1–2): p. 103-124.
12. Wang, Y. and C.-Y. Wang, *A Nonisothermal, Two-Phase Model for Polymer Electrolyte Fuel Cells.* Journal of The Electrochemical Society, 2006. **153**(6): p. A1193-A1200.
13. Ferng, Y.M. and A. Su, *A three-dimensional full-cell CFD model used to investigate the effects of different flow channel designs on PEMFC performance.* International Journal of Hydrogen Energy, 2007. **32**(17): p. 4466-4476.
14. Shah, A.A., et al., *Transient non-isothermal model of a polymer electrolyte fuel cell.* Journal of Power Sources, 2007. **163**(2): p. 793-806.
15. Le, A.D. and B. Zhou, *A general model of proton exchange membrane fuel cell.* Journal of Power Sources, 2008. **182**(1): p. 197-222.
16. Wang, Y., S. Basu, and C.-Y. Wang, *Modeling two-phase flow in PEM fuel cell channels.* Journal of Power Sources, 2008. **179**(2): p. 603-617.
17. Baschuk, J.J. and X. Li, *A comprehensive, consistent and systematic mathematical model of PEM fuel cells.* Applied Energy, 2009. **86**(2): p. 181-193.
18. Owejan, J.P., et al., *Effects of flow field and diffusion layer properties on water accumulation in a PEM fuel cell.*

International Journal of Hydrogen Energy, 2007. **32**(17): p. 4489-4502.

19. Parikh, N., J.S. Allen, and R.S. Yassar, *Microstructure of Gas Diffusion Layers for PEM Fuel Cells.* Fuel Cells, 2012. **12**(3): p. 382-390.
20. Khazaee, I., M. Ghazikhani, and M.N. Esfahani, *Effect of gas diffusion layer and membrane properties in an annular proton exchange membrane fuel cell.* Applied Surface Science, 2012. **258**(6): p. 2141-2148.
21. Djilali, N., *Computational modelling of polymer electrolyte membrane (PEM) fuel cells: Challenges and opportunities.* Energy, 2007. **32**(4): p. 269-280.
22. Siegel, C., *Review of computational heat and mass transfer modeling in polymer-electrolyte-membrane (PEM) fuel cells.* Energy, 2008. **33**(9): p. 1331-1352.
23. Wu, H., X. Li, and P. Berg, *On the modeling of water transport in polymer electrolyte membrane fuel cells.* Electrochimica Acta, 2009. **54**(27): p. 6913-6927.
24. H. Versteeg, W.M., *An Introduction to Computational Fluid Dynamics*. 2nd ed. 2007.
25. Kamarajugadda, S. and S. Mazumder, *On the implementation of membrane models in computational fluid dynamics calculations of polymer electrolyte membrane fuel cells.* Computers & Chemical Engineering, 2008. **32**(7): p. 1650-1660.
26. Andreas P., D.V., Georgios T., *Computation of Thermal Conductivity of Gas Diffusion Layers of PEM Fuel Cells*, in *Convection and Conduction Heat Transfer*, A. Ahsan, Editor. 2011, InTech. p. 215-232.
27. Song, C. T., Yanghua Z., Jian L. Z., J. Wang, *PEM fuel cell reaction kinetics in the temperature range of 23–120 °C,* Electrochimica Acta, 2007. **52**(7): p. 2552-2561.
28. Huang, Y. C., C. H. Wang, X. D. Jang, *Effects of porosity gradient in gas diffusion layers on performance of proton exchange membrane fuel cells,* Energy, 2010. **35**(12): p. 4786-4794.

HYDROMETALLURGICAL EXTRACTION OF ZINC FROM INDIGENOUS ELECTRIC ARC FURNACE DUST

Zeeshan A. Hameed[a], Junaid Saleem[b*], Ahsan Abdul Ghani[b], Hira Lal[b], Syed Sajid Hussain[a]
a: Department of Quality Assurance, Peoples Steel Mills Ltd., Karachi, Pakistan
b: Department of Chemical Engineering, University of Karachi, Karachi, Pakistan

*Corresponding Author: Dr. Junaid Saleem;
Email: Junaid@uok.edu.pk; Junaidupm@gmail.com

ABSTRACT

Steel industry using electric arc furnace (EAF) generates hazardous waste in the form of flue dust which is mainly comprised of zinc along with other valuable metals. In this paper EAF flue dust was characterized and zinc extraction was performed using acid treatment technique. Sulphuric acid was used as a leaching agent with different acid concentrations and temperatures to extract zinc from dust particles. The results of flue dust characterization were compared with global EAF dust composition. The observed results indicate that unlike global flue dust composition which is higher in iron, dust from Pakistani EAF unit was found to be rich in zinc. It also contains iron along with trace amount of lead and other metals. It is anticipated that implementation on these findings will not only lead towards sustainable environment but will also generate economic benefits.

Keywords: Flue dust, EAF, Acid leaching, Sustainable environment, Zn recovery

1. INTRODUCTION

Huge quantity of particulate matter is released from steelmaking Electric arc furnace (EAF) which has been categorized as one of the critical hazardous wastes. Volatile components are fumed off and are collected with particulate matter in the off-gas cleaning system during the processing of steel scrap [1]. The projected world generation of EAF dust is 5-7 million tons per year. Each steel industry produces around 15-20 kg of fine dust per ton of steel [2]-[3]. The EAF Dust contains larger fraction of hazardous metals lead Pb, cadmium Cd and chromium Cr(VI) whereas, zinc Zn due to the relatively large amount present, is the most valuable component. [4]–[6] Therefore, the selective recovery of zinc from EAF dust with a high percentage is an attractive option considering its low production cost [1]. As varistor and additives in ceramics, glass, pigments and paints, zinc oxide brags huge industrial applications, particularly in the form of 1D ZnO nanorods that hold a promising key to the world of nanotechnology [7].

The EAF Dust mostly contains the components in oxide form, thus zinc in found as ZnO and $ZnFe_2O_4$ while iron can be found mostly as Fe_2O_3, FeO, Fe_3O_4 and $ZnFe_2O_4$. The extraction of ZnO does not cause difficulties for any of the leaching agents, however zinc ferrite substantially acts as a strong barrier against leaching [8]. Alkaline solution seems to be an attractive agent for leaching in presence of $ZnFe_2O_4$ but at the cost of high concentration requirements [9].

There are two well-known processes for the extraction of valuable metals in the steel making industry: (1) hydrometallurgical and (2) pyrometallurgical extraction processes [2],[10]. Pyrometallurgy is the oldest known process that uses some reducing agents and relatively high thermal energy with generation of toxic gases. These challenges were fulfilled by, variety of hydrometallurgical processes which requires very low thermal energy such as atmospheric acid leaching [11], high pressure acid leaching [12], two-stage acid leaching [13], microwave caustic leaching [14] and the use of solution with various acids [11], [15]–[18] or highly concentrated alkaline solution have been studied [6]-[12]. Hydrometallury has taken over the rest of the techniques applied for EAF dust treatment due to its low energy, atmospheric pressure operation, more refined control and highest yield. [19].

In Pakistan several types of zinc-containing waste material are available which includes electric arc furnace flue dust, zinc scrap and spent dry cell batteries out of which greatest percentage of zinc is found in EAF dust. It is found that highest percentage of zinc is available in Pakistani EAF flue dust, which is due to the fact that the scrap used in steelmaking is of old automobile galvanized steel. Hence to meet economic benefit and environmental constrain by environmental protection agency (EPA) it is practical to recover zinc from flue dust.

This paper addresses the optimization of kinetic parameters of leaching process and claims for having a largest fraction of zinc in the EAF dust of Pakistan. The main factors investigated are the effect of different acid concentrations on percent recovery of different metals, the effect of leaching time on recovery of zinc, iron and lead. Also the quantitative analysis of residual solid was accomplished and the effect of residual metals composition was analyzed as well as the compositional changes of metals before and after leaching has been presented.

2. EXPERIMENT

2.1 Characterization Techniques

Chemical composition of the sample in solid state was determined by wet chemical method (WCM). Trace elements were analyzed as pressed pellet through Axios^{max}, WD-XRF spectrometer of 3KW X-ray tube. The pressed pellet were prepared at 6:1 (sample: binder) with the help of Omnian standard application of PANalytical origin.

2.2 Materials and Experimental Procedure

Leaching experiments of EAF flue dust were performed in the glass reactor of 500 ml provided with opening at top in which the axis of propeller type mechanical stirrer for adjustable revolutions was placed (300 rev/min in each experiment for optimum zinc recovery).Opening for sampling liquid specimen, alcoholic thermometer and powdered sampling were situated on periphery of reactor and baffle fitted along the wall. The reactor was made isothermal to conduct leaching at preferred temperatures using water bath controlled by a thermostat. To study kinetics, experiments were performed with solution of 400 ml of different acid concentrations 0.1, 0.5 and 1M H_2SO_4. The sample weight was taken as 8g measured on analytical weight balance. A solution with acid-to-EAF dust ratio (ml/g) of 50 was used. The residual solid was analyzed for different temperatures 30, 60 and 80 ^{0}C, under normal atmospheric pressure.

The liquor sample for chemical analysis was taken according to fixed-schedule after 0.5, 1, 2, 5, 10, 15, 30, 45, 60 and 90 min respectively. At fixed schedule three samples at same temperature and three different concentrations were taken. The samples were filtered on ash free filter paper and inserted into vial bottles revealing clear solutions. The solution was colorless, weakly yellow or light green depending on leaching conditions and proportion of valuable component transferred into the solution.

The elementary analysis of leached samples, carried out in order to determine Zn, Fe and Pb was made by means of the ICP Plasma SpectroFlame EOP machine. No other components in the rest of the solution were traced as well as no chemical analyses of solid leaching rests were made. Residue left after leaching was weighed, then dried in oven at around 120 ^oC to remove all the moisture present. The analysis of the residue was made using XRF i.e. the same instrument used for sample characterization.

3. RESULTS AND DISCUSSION

3.1 Characterization of samples

Chemical composition of the sample was determined by wet chemical method (WCM). Trace elements were analyzed as pressed pellet through Axios^{max}, WD-XRF spectrometer of 3KW X-ray tube. The pressed pellet were prepared at 6:1 (sample: binder) with the help of Omnian standard application of PANalytical origin. The chemical composition of EAF flue dust depends on types of steel, quality of scraps being processed, operating conditions, recycling of dust and efficiency of de-dusting plant to capture the dust and molten metal to slag thermodynamic reactions. Chemical composition of dust samples was provided in Table 2, which shows that it is rich in valuable metals including Zn 40.85% and Fe 15.32% and Pb 1.81%. In addition, Na, K and Ca are also present with around >1 % each, and can be easily leached out by ion exchange technique[18]. Heavy metals like Pb & Cd as well as Halides of Cl are also found. They all are beyond the range of disposable landfills as per EPA, USA [21]. (Recommended safe limits for EAF flue dust Cd: 0.19, Pb: 0.37 mg/L).

Table 1 Chemical Composition by Wet Chemical & XRF Spectrometer

Comp	Si	Al	Zn	Fe	Mn
%	1.587	0.323	40.85	15.32	0.697
Comp	K	Ca	Na	Pb	Cd
%	1.162	0.615	1.699	1.81	0.0057

3.2 Leaching Reaction

The reactions of the main species occurring in the sample and their stoichiometry can be stated as follows:

$ZnO + H_2SO_4 \rightarrow ZnSO_4\,(aq) + H_2O$ (1)

$ZnFe_2O_4 + 4H_2SO_4 \rightarrow ZnSO_4(aq) + Fe_2(SO_4)_3(aq) + 4H_2O$ (2)

$ZnFe_2O_4 + H_2SO_4 \rightarrow ZnSO_4(aq) + Fe_2O_3 + H_2O$ (3)

$ZnFe_2O_4 + H_2SO_4 + H_2O \rightarrow ZnSO_4(aq) + 2Fe(OH)_3$ (4)

$Fe_2O_3 + 4H_2SO_4 \rightarrow Fe_2(SO_4)_3 + 3H_2O$ (5)

$Fe_3O_4 + 4H_2SO_4 \rightarrow Fe(SO_4) + Fe_2(SO_4)_3 + 4H_2O$ (6)

Reaction (2) is thermodynamically preferable to Reaction (3) and (4) within the temperature that was used on the experiments.

3.3 Effect of Sulphuric Acid Concentration

The effect of sulphuric acid concentrations was investigated at 30 minutes by keeping other conditions constant as liquid-to-solid ratio of 50 ml/g and temperature 80 ^oC in the concentration range of 0.1-1.0 M. The results obtained are shown in Figure 1. From these tests it could be deduced that the rates of zinc, iron and lead dissolution are functions of the acid concentrations, the concentration of acid influences the leaching of zinc preferentially. The highest zinc recovery obtained was 69% at 1M concentration of acid while its recovery decreases at lower concentration. In case of iron, % recovery increases with increasing acid concentration and the highest recovery obtained is 46% at 1M concentration of sulfuric acid which is lesser than that of zinc. Dissolution of lead also increases with increasing concentration with highest recovery of 54 % at 1M obtained.

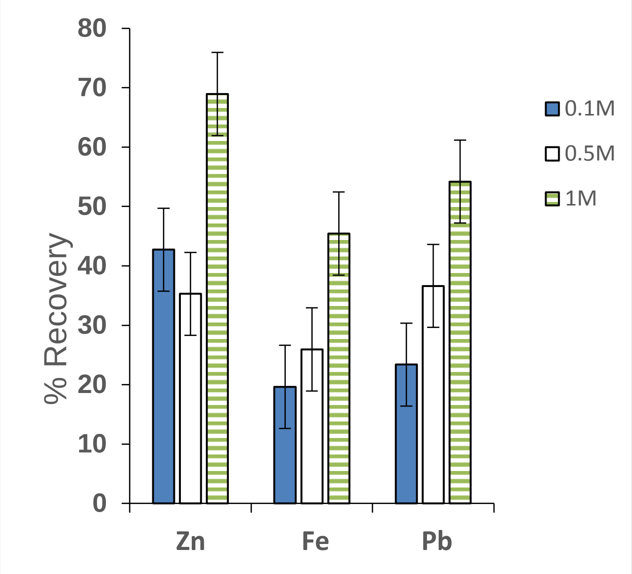

Figure 1: % Recovery of different metals at different concentrations and at 30min and 80^oC

3.4 Effect of Leaching Time

The effect of different times (30 and 90 min) at acid concentration of 1M, liquid-to-solid ratio of 50 ml/g and temperature 80 ^oC is shown in Figure 2. The comparison of metals recovery at different time shows that keeping constant temperature and concentration, increase in leaching time increases the recovery of zinc i.e from 67% to 76% while iron recovery is slightly changed from 46% to 48%. Also lead has drastic decrease in recovery with increasing time from 54% to 32%.

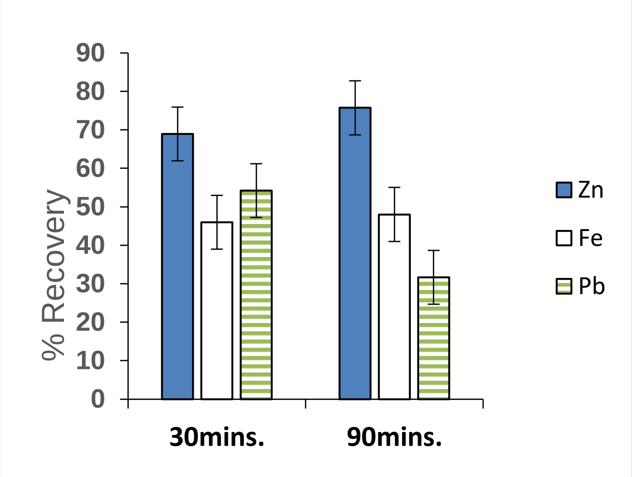

Figure 2: % Recovery of different metals at 1M and 80^oC

3.5 Effect of Concentration on Metal Composition in Residue

The effect of temperature was investigated for the metals remaining in the residue after leaching has been completed. From Figure 3 it could be deduced that at 80 ^{0}C, as the concentration of acid increases, composition of both Zn and Fe decreases while composition of Pb increases. Hence this confirms that at 1M concentration highest % of Zn is leached. The % recovery of Zn at 80 ^{0}C reaches close to its maximum value at lower concentration (0.5M). Temperature of 80 ^{0}C should be used in order to extract maximum amount of zinc at low acid concentration (0.5M).

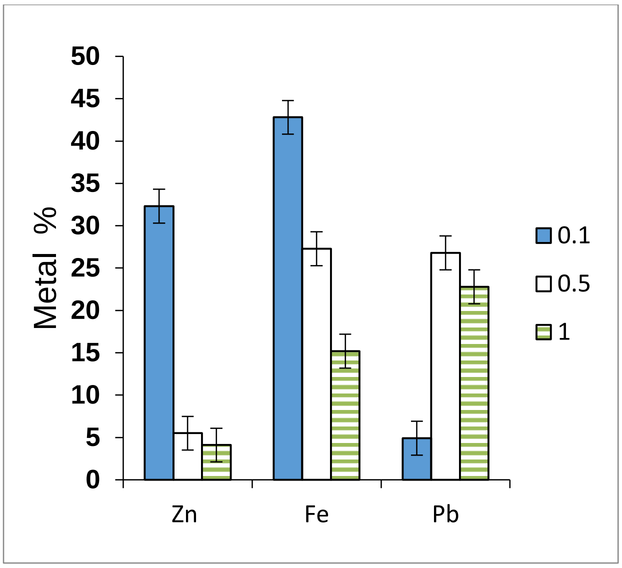

Figure 3: Metal % in residue w.r.t concentrations 0.1M, 0.5M, 1.0M at 80 ^{0}C.

4. CONCLUSION

The indigenous EAF flue dust from people's steel mill, Pakistan collected and characterized. Characterization depicts that EAF dust is rich in ZnO & Fe_3O_4 phases with trace amount of PbO phase. This zinc in EAF dust is obtained from scrap of automobiles. This dust is environmentally harmful due to presence of toxic metals. International regulations have strictly prohibited the disposal of flue dust to the environment either in the air or as landfills without treatment.

Effective leaching of EAF flue dust was done and through experiment it was found that extent of recovery will be highest for zinc in our case, intermediate recovery for iron and lowest for lead. This research is the stepping stone towards the actual goal of achieving environmentally sustainable society.

ACKNOWLEDGEMENT

The authors would like to acknowledge Higher Education Commission (HEC) Pakistan, Peoples Steel Mills Ltd., HEJ Research Institute of Chemistry, University of Karachi, NED University of Engineering & Technology, Industrial Analytical Center (IAC) to provide necessary support.

REFERENCES

[1] M. Kul, K. O. Oskay, M. ŞİMŞİR, H. Sübütay, and H. Kirgezen, "Optimization of selective leaching of Zn from electric arc furnace steelmaking dust using response surface methodology," *Trans. Nonferrous Met. Soc. China*, vol. 25, no. 8, pp. 2753–2762, 2015.

[2] T. Havlik, B. Souza, a Bernardes, I. Schneider, and a Miskufova, "Hydrometallurgical processing of carbon steel EAF dust," *J. Hazard. Mater.*, vol. 135, no. 1–3, pp. 311–318, 2006.

[3] J. MACHADO, F. BREHM, C. MORAES, C. SANTOS, A. VILELA, and J. CUNHA, "Chemical, physical, structural and morphological characterization of the electric arc furnace dust," *J. Hazard. Mater.*, vol. 136, no. 3, pp. 953–960, 2006.

[4] Š. Langová and D. Matýsek, "Zinc recovery from steel-making wastes by acid pressure leaching and hematite precipitation," *Hydrometallurgy*, vol. 101, no. 3–4, pp. 171–173, 2010.

[5] M. Cruells, a. Roca, and C. Núñẽz, "Electric arc furnace flue dusts: characterization and leaching with sulphuric acid," *Hydrometallurgy*, vol. 31, no. 3, pp. 213–231, 1992.

[6] A. J. B. Dutra, P. R. P. Paiva, and L. M. Tavares, "Alkaline leaching of zinc from electric arc furnace steel dust," *Miner. Eng.*, vol. 19, no. 5, pp. 478–485, 2006.

[7] B.-S. Yu, Y.-R. Wang, and T.-C. Chang, "Hydrothermal treatment of electric arc furnace dust.," *J. Hazard. Mater.*, vol. 190, no. 1–3, pp. 397–402, 2011.

[8] J. Vereš, Š. Jakabský, and M. Lovás, "Zinc recovery from iron and steel making wastes by conventional and microwave assisted leaching," *Acta Montan. Slovaca*, vol. 16, no. 3, pp. 185–191, 2011.

[9] P. E. Tsakiridis, P. Oustadakis, A. Katsiapi, and S. Agatzini-Leonardou, "Hydrometallurgical process for zinc

recovery from electric arc furnace dust (EAFD). Part I: Characterization and leaching by diluted sulphuric acid.," *J. Hazard. Mater.*, vol. 179, no. 1–3, pp. 8–14, 2010.

[10] A. Stefanova and J. Aromaa, "Alkaline leaching of iron and steelmaking dust," *Aalto University publication series SCIENCE + TECHNOLOGY*, pp. 1–72, 2010.

[11] T. Havlik, M. Turzakova, S. Stopic, and B. Friedrich, "Atmospheric leaching of EAF dust with diluted sulphuric acid," *Hydrometallurgy*, vol. 77, no. 1–2, pp. 41–50, 2005.

[12] T. Havlik, B. Friedrich, and S. Stopic, "Pressure leaching of EAF dust with sulphuric acid," *Erzmetall*, pp. 113–120, 2004.

[13] L. X. ZHANG Y, YU X, "Zinc Recovery from franklinite by sulphation roasting," *Hydrometallurgy*, pp. 211–214, 2011.

[14] X. D K and C. a. Pickles, "Microwave caustic leaching of electric arc furnace dust," *Miner. Eng.*, vol. 13, no. 1, pp. 79–94, 2000.

[15] D. Herrero, P. L. Arias, B. Güemez, V. L. Barrio, J. F. Cambra, and J. Requies, "Hydrometallurgical process development for the production of a zinc sulphate liquor suitable for electrowinning," *Miner. Eng.*, vol. 23, no. 6, pp. 511–517, 2010.

[16] G. Lee and Y. Song, "Recycling EAF dust by heat treatment with PVC," *Miner. Eng.*, vol. 141, no. 1, pp. 33–6, 2007.

[17] R. a. Shawabkeh, "Hydrometallurgical extraction of zinc from Jordanian electric arc furnace dust," *Hydrometallurgy*, vol. 104, no. 1, pp. 61–65, 2010.

[18] B. Asadi Zeydabadi, D. Mowla, M. H. Shariat, and J. Fathi Kalajahi, "Zinc recovery from blast furnace flue dust," *Hydrometallurgy*, vol. 47, no. 1, pp. 113–125, 1997.

[19] H. Tomas, "The possibility of treatment of the EAF dusts and sludges, Present and Future of Metallurgy, Material Science and Refractories," in *Proceedings of the 50th Anniversary of Metallurgical Faculty of Technical University of Kosice*, 2002, vol. 93, no. November, p. 2002.

[20] F. Kukurugya, T. Vindt, and T. Havlík, "Behavior of zinc, iron and calcium from electric arc furnace (EAF) dust in hydrometallurgical processing in sulfuric acid solutions: Thermodynamic and kinetic aspects," *Hydrometallurgy*, vol. 154, pp. 20–32, 2015.

[21] Environmental Protection Agency, "Land disposal Restrictions for Electric Arc Furnace Dust," vol. 56, no. 160, p. 41164, 1991.

BOILER FEED WATER EXCHANGER FAILURE & HIGH TEMPERATURE SHIFT CONVERTOR BOTTOM CATALYST FLOODING-ENGRO'S UNIQUE EXPERIENCE AND INNOVATIVE SOLUTION

Muhammad Zaghum Riaz, Ali Javed Akhter*, Sara Ahsan
Engro Fertilizers Limited
Sindh, Pakistan

*Corresponding Author. Tel.: +92723- 641001 Ext: 4243
E-mail address: ajakhter@engro.com

ABSTRACT

Engro Fertilizers Limited, one of the leading fertilizers company in Pakistan, commissioned one of the largest single train Urea manufacturing site with a capacity of 3835 MTPD of urea. At its early operational age, it faced a number of startups and shut downs due to gas curtailments but finally sustained them after two and half years. This document explicates one of the major incidents confronted by Engro fertilizers which would have otherwise resulted in plant and catalyst damage. It was in April 2015 that a leakage was spotted in LTSC downstream BFW pre heater. The paper encompasses the experiences, problems encountered, key lessons and innovative ideas implemented to preserve catalyst from poisoning and during dry out procedure to reduce delay in startup.

Keywords: LTSC, BFW Pre -Heater, Catalyst Dry out

1 INTRODUCTION

Haldor Topsoe divides Ammonia plant into four major sections i.e.

1. Desulphurization Section
2. Reforming Section
3. Shift conversion section
4. Purification Section
5. Synthesis Section

1,2,3,4 forms the front end of ammonia plant where raw materials are used to prepare the synthesis gas that is majorly composed of hydrogen and nitrogen while in synthesis (#5) synthesis gas is reacted to form NH_3 and section 5 is commonly referred to as backend of Ammonia plant. Feed of an NH_3 comprises of Natural gas, air and steam. Feed gas consists of 84.24% CH_4, 12.11% N_2, 1.97% CO_2, 1.16% C_2H_6, 0.27% C_3H_8 and 0.25% C_4H_{10} by volume on dry basis. This gas is purified in the desulphurization section, sulphur being poisonous for primary reformer and low temperature shift convertor catalysts. Organic sulphur is converted to inorganic in the hydro-treator by the action of H_2 on natural gas over NiMo catalyst. This inorganic sulphur (H_2S) is then absorbed on ZnO bed in sulphur absorbers.

Desulphurized gas is then reformed in the reforming section after pre-heating, which comprises of a direct fired primary reformer and an auto thermal secondary reformer. In the reforming section hydrocarbons are converted into carbon oxides and hydrogen by reaction with steam over Nickel based catalyst. Steam to Carbon ratio is maintained at 3:1. The gas enters primary reformer at ~40 kg/cm^2g, ~520°C and leaves at ~38.5 kg/cm^2g, ~825°C. Following reactions occur in primary reformer.

$$\mathbf{CH_4 + H_2O \leftrightarrow CO + 3H_2} \text{ ------------ } \mathbf{(1)}$$

$$\mathbf{C_2H_6 + 2H_2O \leftrightarrow 2CO + 5H_2} \text{ -------- } \mathbf{(2)}$$

$$\mathbf{C_3H_8 + 3H_2O \leftrightarrow 3CO + 7H_2} \text{ -------- } \mathbf{(3)}$$

$$\mathbf{C_4H_{10} + 4H_2O \leftrightarrow 4CO + 9H_2} \text{ ------- } \mathbf{(4)}$$

$$\mathbf{CO + H_2O \leftrightarrow CO + H_2O} \text{ ------------- } \mathbf{(5)}$$

1, 2, 3 & 4 are reforming reactions while 5th reaction represents shift conversion reaction.

The gas from primary reformer goes to secondary reformer where preheated air is added from top. Approximately 39.4 kcal/mole heat is required for endothermic reforming reaction which is generated by combustion reaction of added air and process gas. Up to 0.4% of CH_4 is reformed in this auto thermal reformer and the gas leaves at ~36 kg/cm^2g

and ~999°C. After recovering heat and generating steam from this high heat content gas, it is sent to the shift conversion section, reaction-5 occurs in this section. Shift reaction is an exothermic reaction and liberated ~9.84kcal/mole. This section is further divided into High temperature shift convertor and low temperature shift convertor. The purpose of this section is to convert CO into CO_2.

The gas enters HTSC at ~360°C and ~35.8 kg/cm^{2}g and CO is converted into CO_2 whereas iron oxide catalyzes the reaction. In LTSC shift reaction occurs over a bed of copper oxide based catalyst and the gas leaves at ~227°C comprising of 0.29% CO. The outlet gas from LTSC is introduced into BFW preheater and cooled down to ~161°C which is then exported to urea plant after purification.

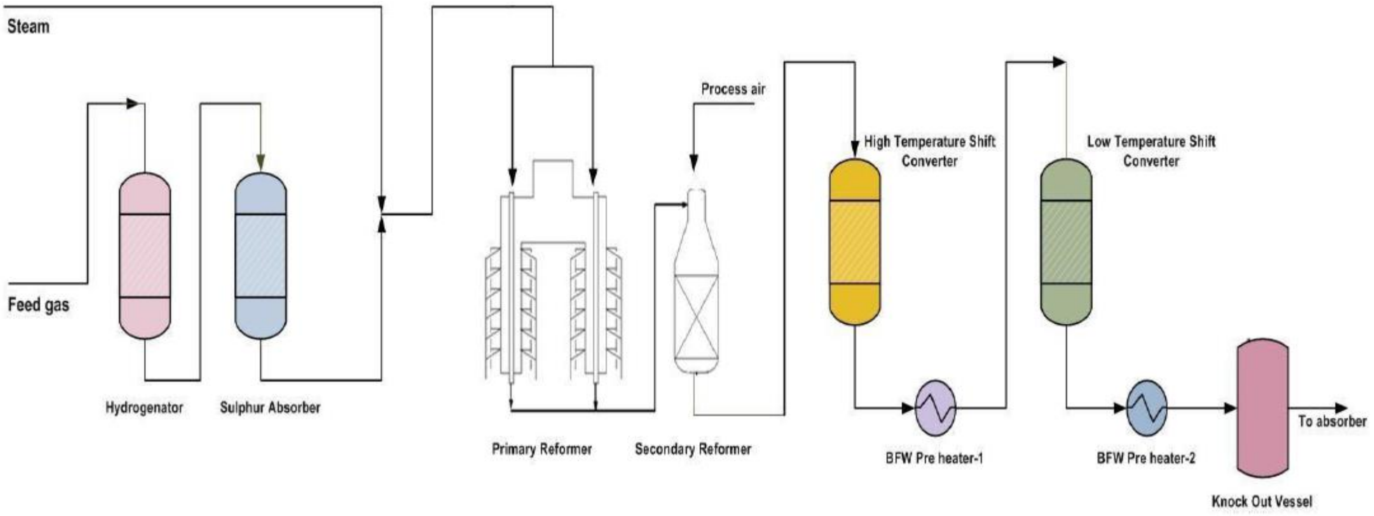

Figure-1: Basic process description

2 BOILER FEED WATER PRE-HEATERS AND THE SHIFT CONVERTERS- AN EXPERIENCE AT ENGRO:

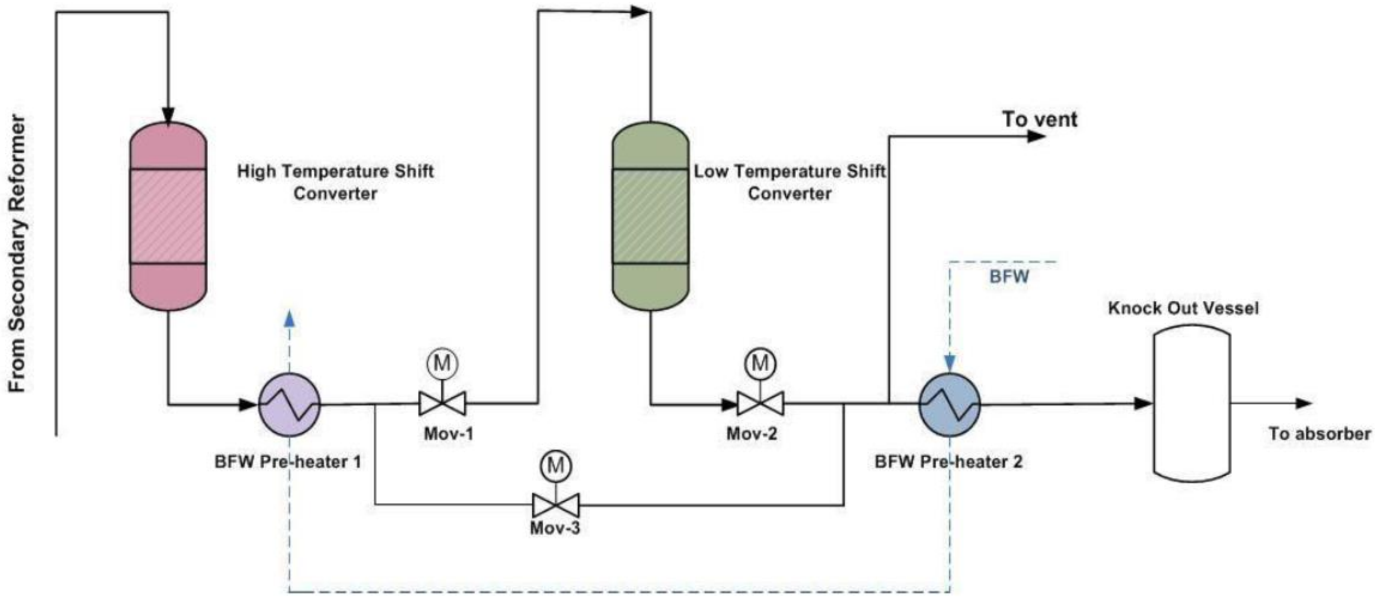

Figure-2: BFW circuit and shift converter

The boiler feed water is heated in a number of preheaters prior to going to steam drum. Some part of boiler feed water is first entered in BFW Preheater-2 at LTSC outlet. This BFW is then split into two parts. One is passed through BFW Preheater-1 at HTSC outlet while other is passed through BFW preheater in backend.

Boiler feed water Preheater-2 is a double split flow, two pass exchanger. During the normal operation it heats up BFW from ~130 to 184°C at a pressure of ~150kg/cm^{2}g and the medium being the process gas from LTSC. For startup/shutdown, LTSC is isolated by closing MOV-1 and MOV-2 while opening MOV-3. Since, water causes serious physical damage to LTSC catalyst it is always secluded from the system to avoid condensation of steam on the catalyst. The process gas bypasses LTSC and is discharged from downstream vent.

On April 7 at ~10:15 hours, during planned plant shutdown, it was observed that there was an abrupt increase in the level of downstream knock out vessel. High level alarm appeared but was disregarded considering it as a nuisance alarm since plant was shut down. Later, nitrogen circulation for the purpose of cooling got ceased as a result of nitrogen blower tripping on high amperes. However, process vent at LTSC outlet opened without any gas circulation. For troubleshooting of this incident, system was isolated and all process drains were opened to check our doubt of BFW preheater-2 tube leakage. When this activity was carried out, the drains at the outlet of HTSC trickled water. The presence of water at HTSC outlet drain signified water ingression in HTSC. Furthermore, the data history showed dip in temperatures across the bottom thermocouples which further strengthened our doubt (figure-3).

To discover how much catalyst is soaked with water, temperatures trending and comparison was done. This analysis revealed that ~35% of the bottom catalyst has been flooded by BFW backflow. This created an aggravating situation for the management as well as process engineering department because now the new challenge was to preserve the catalyst and avoid it from any kind of thermal shock and damage. Detailed analysis on equipment failure / repair and modifications on plant was conducted and a drying out procedure was established in consultation with HTAS.

As shown in figure-3, the sharp drop in temperature from ~142C to ~90C in a few minutes at the temperature indicator inserted at 65% bed depth illustrated presence of water in high temperature shift convertor. There was no temperature drop in other temperature indicators. If this leakage had not been detected at this time, it could have resulted in soaking of all HTSC catalyst with BFW. There was no HTSC catalyst charge available at that time and it could have resulted in prolonged plant shut down.

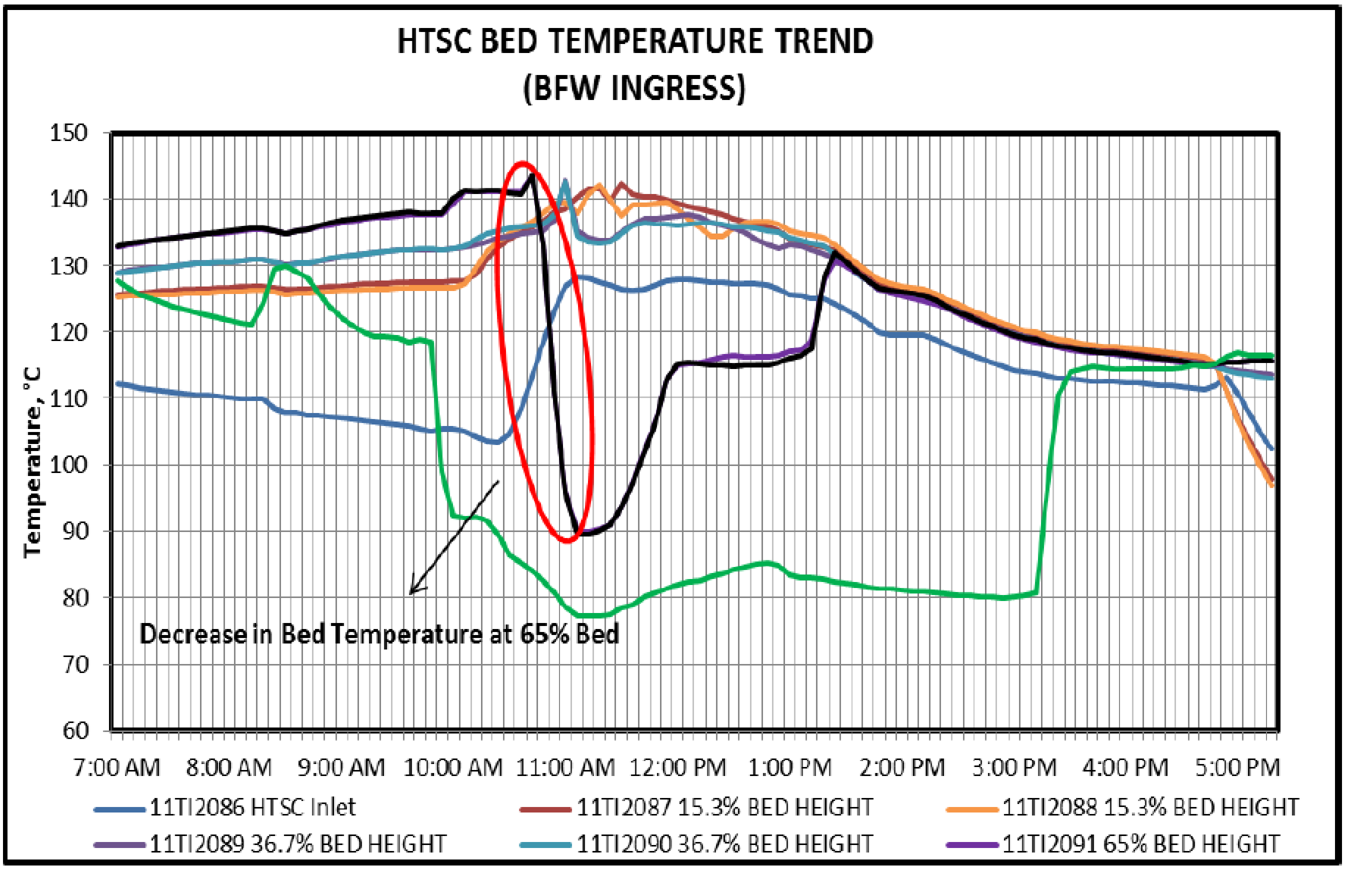

Figure-3: HTSC temperature profile

3 CATALYST DRY-OUT PROCEDURE EMPLOYED:

An in-house procedure in consultation with HTAS was developed with innovative idea for control heating with series operation of additional steam heater, coupled with primary reformer furnace firing to reduce delay in plant startup. This procedure was developed keeping in mind the following key points to be taken care of:

1. Although, reactor draining will remove water, but the catalyst itself may still contain substantial amounts of water. This is due to large catalyst and pore volume.
2. The water has to be removed through a controlled evaporation. If the catalyst is heated up too fast, the evaporating water/steam may not have time to migrate out of the pellets, and the expanding steam (flash evaporation) may cause pellets to explode/break down.
3. By heating the catalyst slowly and by keeping the temperature close to the boiling temperature, the rate of evaporation will be slow and the catalyst would be able to remain largely intact.

After keeping in mind the above parameters following steps were suggested for HTSC catalysts dry out.

1. Pressurize the HTSC with nitrogen at 4 kg/cm2g and normal temperature ~30°C.
2. Follow pressurizes / depressurizes sequence for 1 hour hold time with nitrogen at 4 kg/cm^2.g to remove water from catalyst pores.
3. Continue this sequence for 6 times and observe extend of moisture coming out form depressurization drain.
4. If moisture is still observed from drain, continue sequences till the drain began to dry.
5. Increase hold time to 4 hour and continue pressurization / depressurization sequence throughout duration of outage.
6. Start nitrogen circulation at 4 kg/cm^{2}g through U-203 for 3 hours to remove further water from catalyst pores.
7. Start increasing nitrogen temperature at 10°C/hr to 151°C (saturation temperature at 4 kg/cm^2.g). Important point is to make sure that good temperature control is established.
8. Hold bed inlet temperature at saturation temperature i.e. 151°C for 2 hours.
9. If heat loss contribute to keep the temperature low. It is suggested to increase the inlet temperature more 5°C to enable the temperature further down in the catalyst bed to be above the boiling temperature.
10. After stabilization at the saturation temperature, increase the inlet temperature by 10°C/hr and use this as driving force for the further drying.
11. Continue the drying out until the bottom and outlet temperatures increase to a level close to that in the top of the bed.
12. Further heat catalyst bed slowly to normal operating temperature, by 10°C per hour

4 HTSC PERFORMANCE COMPARISON BEFORE AND AFTER INCIDENT:

The plant was re-started after dry out and the effectiveness of this dry out procedure was analyzed. No increase in pressure drop and decrease in temperature drop across HTSC signified the perseverance of catalyst charge.

Table: 1 HTSC performance after outage

Parameter	May 28,2014	March 3,2015	April 28,2015
Age, Months	1	10	12
HTSC ΔP, kg/cm^2	0.42	0.42	0.43
CO slippage	2.58	2.62	2.94
HTSC ΔT, °C	67.2	67.1	72.6

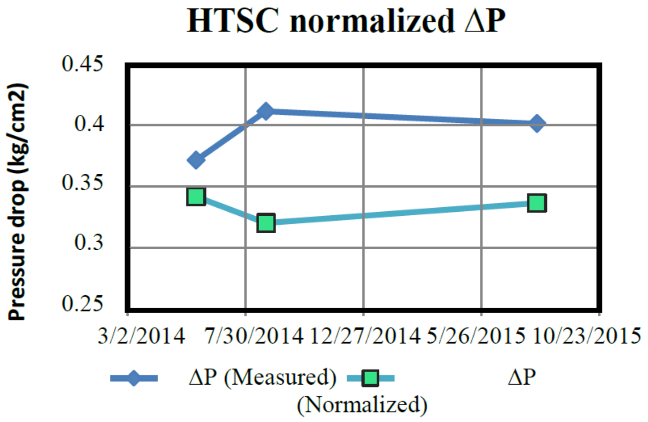

Figure-3: HTSC normalized ΔP

If the HTSC charge have not been dried out properly, delta T across the reactor should have shown a decreasing trend owing to the exothermic reaction occurring in HTSC.

Table-1 and figure3, 4 illustrate successful recovery of HTSC catalyst. The charge came back in line with the previous performance values ad continues to operate well.

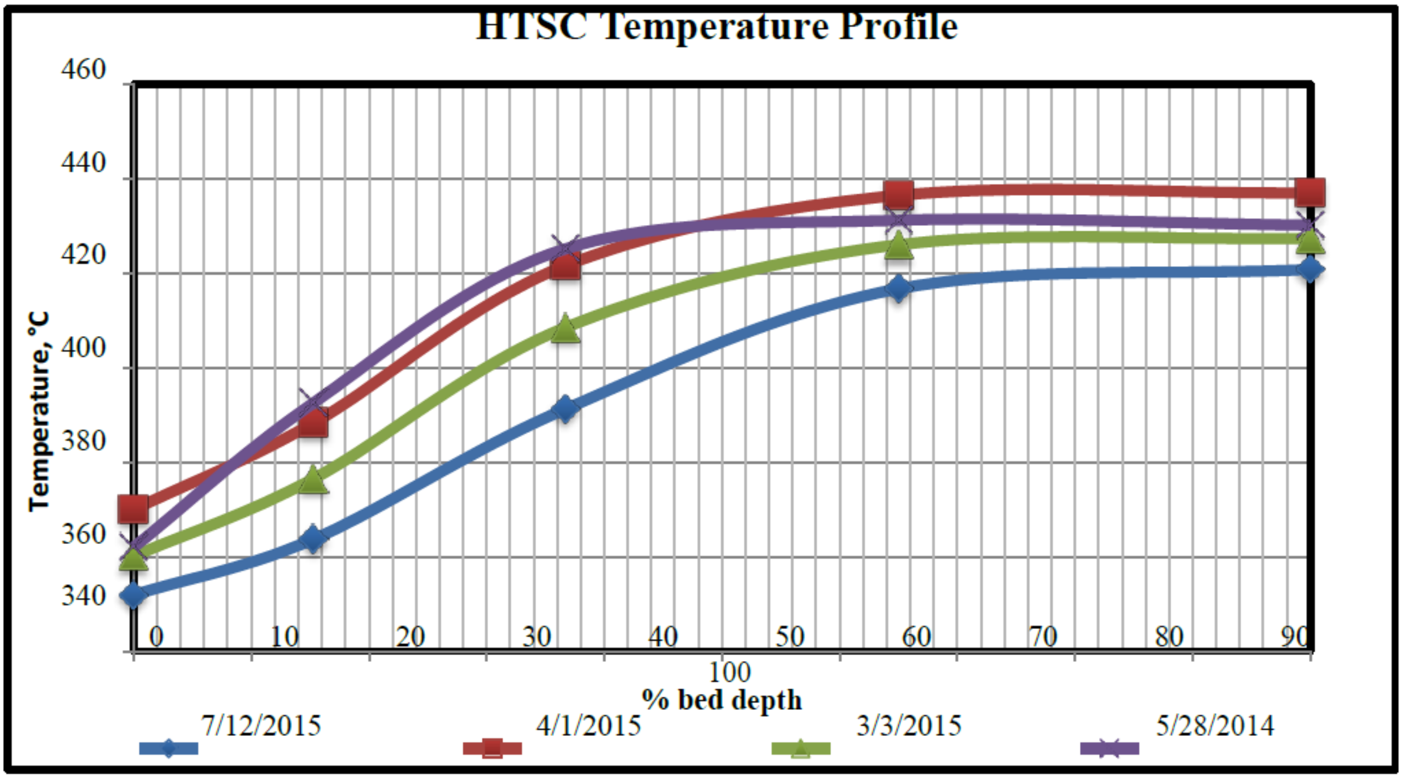

Figure-4: HTSC Temperature Profile

5 FURTHER IMPROVISATIONS IN OUR PROCESS:

Few things hampered the early detection of this incident at our site. Some modifications were done based on the recommendations of this incident investigation. As a precautionary measure and for prompt detection of BFW preheater failure in future, a process drain has been provided at the outlet of preheater. Further, thermocouples are installed on process gas outlet of BFW preheater-1&2 (each shell) for early detection of any tube leakage via energy balance and temperature comparison.

Figure-5 shows how these thermocouples have been installed at both boilers feed water pre heaters.

6 RESULTS AND SUMMARY:

The probability of detecting and surviving this kind of event can be exponentially increased by following some of the guidelines enlisted in paper. Summarizing, drain the vessel as quickly as possible by utilizing all bleed valves in the system. As this will not allow soaking of catalyst in water for a longer period of time. Carry out purging of catalyst with nitrogen at lower pressures- if available. Adhere to the heating rates and hold up times as mentioned in the procedure. This is done to guard against extreme heat up rates that could swiftly vaporize moisture and lead to catalyst break down.

This is a general procedure advice, if you experience such incident contact your catalyst manufacturer for details adjoining your particular startup conditions.

7 CONCLUSION:

HTSC catalyst dry out took approximately 17 hours. This was a tough challenge since a smooth and safe startup was required within a very short period of time. It is evident that by commitment of management, innovative and unique ideas of process engineering and with HTAS help, we carried out a successful HTSC catalyst dry out.

New modifications have been done at plant which will ensure prompt detection of such leakage in future.

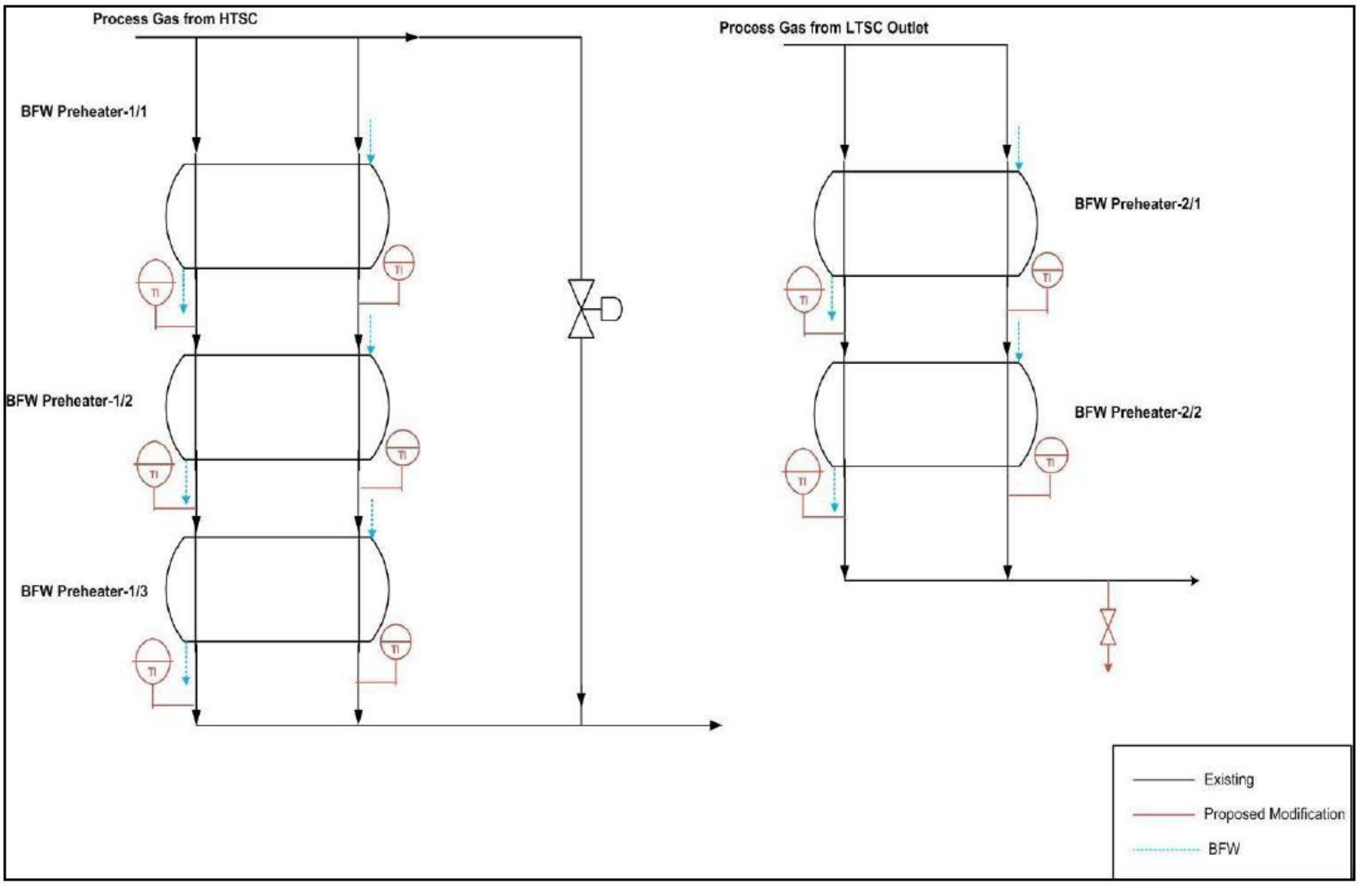

Figure-5: Modification to the process

IMPLEMENTATION OF RISK-BASED INSPECTION (RBI) METHODOLOGY IN PROCESS INDUSTRY

Mobin Ahmed[1,*] and Muzaffar Hussain[2]
[1]Oil & Gas Asset Integrity Management System
[2]Mechanical Engineering Department, NED University of Engineering & Technology, Karachi, Pakistan

[*]*Corresponding author*. Tel.: +92343-2000591
E-mail address: mobinmechsonic@gmail.com (M. Ahmed)

ABSTRACT

The objective of this research is to propose and implement RBI methodology to LPG bullet vessels and distinguish the results with normal and conventional inspection approaches.

LPG bullet vessels are very susceptible to corrosion due to storage at very low temperatures which causes moisture on the outer side of the tank. Sulphuric Acid attack and Hydrogen Embrittlement are the most important deterioration mechanisms and causes weakening of weld joints on the inner side due to which they fail before any prior notice resulting in the loss of containment as well as asset whose worth is thousands of dollars. When normal inspection approach was applied, results were not effective and the loss was uncalculated.

After applying the proposed quantitative RBI methodology, remarkable results were obtained which were more economic than the previous generation approaches. Remaining-life of each of nineteen LPG bullet vessels was drastically increased to **20** to **25** years which was **7** to **8** years previously and corrosion rates, allowances were in much control that is; before the RBI methodology was applied, corrosion rates were up to **0.5 mm/yr** which were significantly reduced to **0.2 mm/yr** resulting in healthy increased asset life and an economic benefit of 8 to 12 million dollars within 20 years.

Keywords: Chemical Process Industry; Risk Based Inspection; Mechanical Integrity; Pressurized Equipments; Economic Benefit

1 INTRODUCTION

Engineering systems are ideally designed to ensure an economical operation throughout the anticipated service life in compliance with given requirements. Process plants are an investment of trillions of dollars and maintaining their mechanical integrity is an essential task. Various deterioration mechanisms harm the process equipments excessively and they fail without prior notice or before their calculated remaining life. Inspection and maintenance activities are usually designed for an interval of 4 to 5 years but due to unplanned shutdowns and turnarounds, industries in Pakistan usually go out of inspection and maintenance budget. Thus, to avoid unnecessary shutdowns, excessive containment & asset loss RBI has come in demand. Lawrence (2012) [1] reported that refineries and other petrochemical facilities that run continuously must shutdown operations every few years to provide access to production units so that essential maintenance, modification and inspection work can be carried out. But shutdown of the whole plant is not an optimal solution in many cases. According to Tan and Kramer (1997) [2], typical refinery experiences approximately 10 days of downtime per year due to equipment failure, with an estimated economic loss of $20,000 to $30,000 per hour. Shutdown maintenance becomes much critical when it comes to oil and gas industry because it causes the plant to be offline for some hours resulting in much higher revenue losses. Khan, Sadiq and Haddara (2004) [3] proposed a risk based inspection and maintenance methodology that emphasizes risk minimization but it cannot be considered economical since it does not focuses on asset management. Asset management is the most important part when it comes to RBI hence it cannot be ignored.

To achieve a reliability goal, companies adopt preventive maintenance strategies based on original equipment manufacturer's suggested fix intervals of maintenance but they may not be optimum maintenance strategy since the operating conditions may vary significantly from company to company.

2 ADVANCEMENTS IN INSPECTION & MAINTENANCE APPROACHES

Recent years have marked tremendous advancements in inspection and maintenance approaches. Companies have now started to develop maintenance strategies which are coupled with the specific risk associated with the operating plant or specific equipment. Maintenance strategies have progressed from primitive breakdown maintenance to more refined strategies like condition-monitoring and reliability centered maintenance. Another link added to this chain is the risk-based inspection which has set news limits in the horizon of asset integrity management. For this reason researchers are focusing more on risk-based inspection maintenance strategies.

Krishnasamy, Khan and Haddara (2005) [4] proposed a risk based maintenance strategy for power plant. It meant to propose an optimized inspection and maintenance approach based on integrating a reliability approach and a risk assessment strategy. Keshavarz, Thodi and Khan (2011) [5] proposed a risk based management strategy for LNG units. A combination of preventive maintenance, active redundancy and standby redundancy was considered to achieve optimized shutdown maintenance strategy. Courtois and Delsarte (2006) [6] presented a model for risk reduction in cost effective manner based on inspection time and cost but it was limited since it cannot be applied on complex systems. Vaurio (1995) [7] has presented a general procedure for risk optimization. The main drawback of this procedure is that the failure probabilities are linearly related to maintenance intervals. According to Krishnasamy, Khan and Haddara (2005) [4], a risk-based maintenance approach helps in designing alternative strategy to minimize the risk resulting from breakdowns or failure. Khan and Haddara (2004a, 2004b) [8] [9] applied the risk-based maintenance strategies to offshore oil and gas processing facilities to develop maintenance plan and extended similar strategies to an ethylene oxide production plant. Ghosh and Roy (2009) [10] proposed optimizing the maintenance intervals by maximizing the reliability based cost/benefit ratio.

API RP 580 (2009) [11] provides necessary guidelines to owners, operators, and designers of pressure containing equipments, including pressure vessels, process piping, heat exchangers, storage tanks, and pressure-relief devices but in this study we kept our focus on the pressure vessels.

Various researchers have worked on finding out the interval between shutdowns of the equipment and it is available in the literature. Some of them were limited to only modeling and others included estimating the optimal maintenance and inspection interval considering cost, risk,, availability and reliability. Profitability is directly related to the availability of the equipment. Hence, in this study, it is made sure that the equipment is available for the maximum time to ensure maximum profitability. This study provides framework for the selection criteria of equipments exhibiting higher risk and then applying the proposed methodology to the selected equipments. It provides an efficient way to select equipment based on risk and direct impact on the plant operability and to manage asset efficiently by utilizing inspection and maintenance resources and achieve better with less operating expenses.

3 PROPOSED RISK BASED INSPECTION METHODOLOGY (RBIM)

In this study, a methodology is presented based on RBI. The methodology is further broken down in to 4 phases as shown in **Figure 1**.

1. Objective & Identification of Scope
2. Risk–based Equipment Selection
3. Calculation of Failure Probabilities and Consequences.
4. Appropriate Action

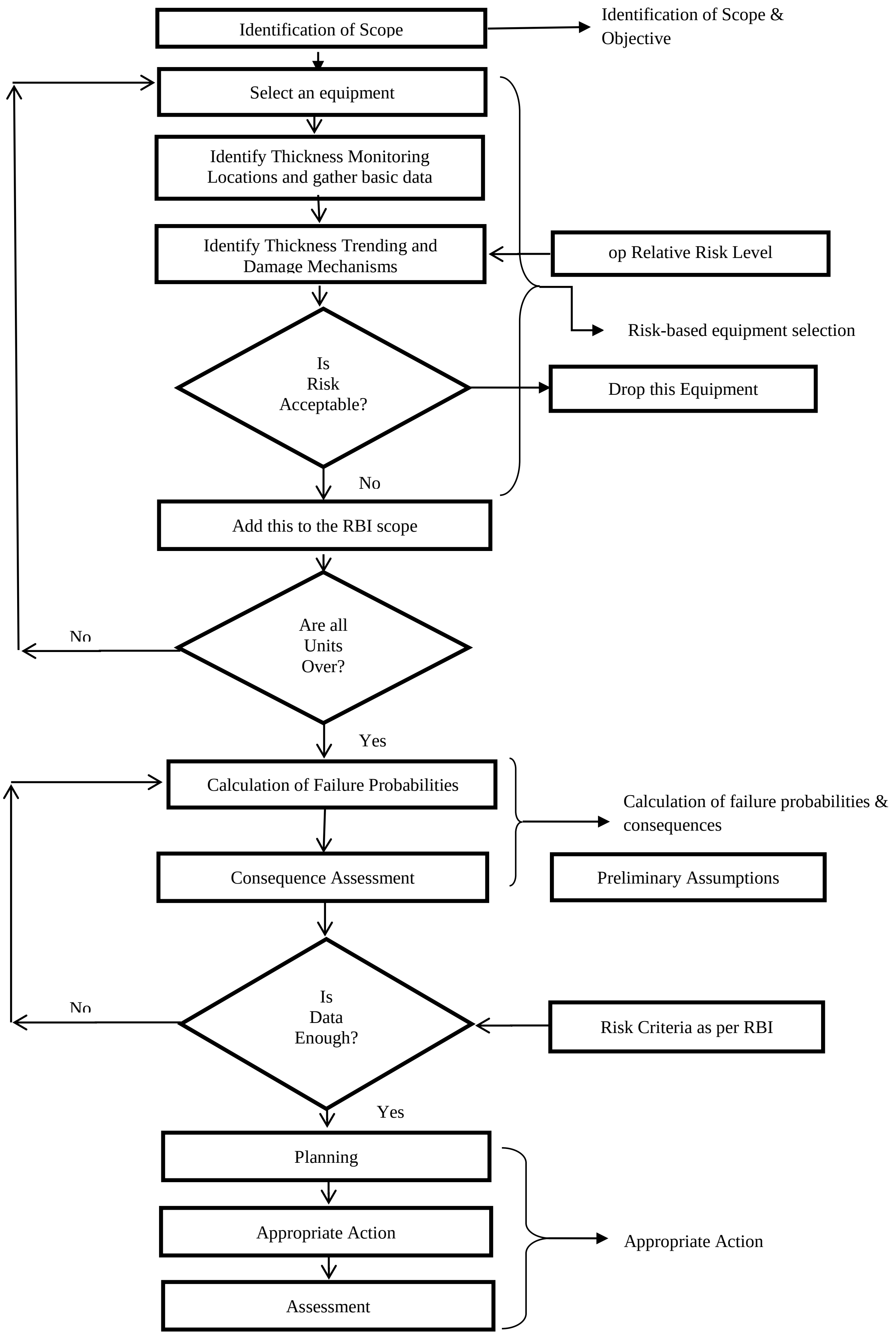

Figure 1. Proposed risk-based inspection methodology

3.1 Phase 1: Objective & Identification of Scope

The objective and scope of the analysis must be clearly mentioned and specified. At this level, work-orders are developed, RBI team is developed. For every particular area, an incharge is employed whose is either inspection engineer or senior technician who is continuously monitoring every equipment performing various conventional NDTs. If any equipment undergoes drastic reduction in observed measurements which are related to mechanical integrity, he reports Asset Integrity Engineer (AIE) or senior then further planning is done regarding RBI.

3.2 Phase 2: Risk—based equipment selection

This phase proposes a unique risk assessment strategy to filter out the critical equipments that affects the functionality of the system. To reduce the exposed risk, each equipment should be individually assessed in order identify equipment with higher impact on the process economy (asset loss, loss due to shutdown), reliability, availability. This process is repeated until every equipment is assessed.

Initially a risk matrix is developed as shown in Fig. 3, which prioritizes risk associated with every equipment. Consequences can either be quantitative or qualitative. On the initial level, qualitative assessment should be preferred. Risk associated with each equipment can be seen through it. The top-right most area represents highest risk level and any equipment falling in that area needs to be inspected immediately. Consequently, the equipments falling into higher risk category are selected.

3.3 Phase 3: Calculation of failure probabilities and consequences

Failure is defined as the inability of anything to perform specific task as per the stated requirements. Failures can be either partial (leaks, weld seam loosening etc.) or complete failure (catastrophe). Failure probabilities for various equipments can be found using the proposed model by Torres-Echeverría (2009) [12]. But this method is costly and time consuming. Failures are also usually modeled using exponential, normal, log-normal and weibull distribution. More commonly, Weibull distribution is used because of its flexibility. It can also depict behavior of other distributions too, such as normal (for $\beta = 3.4$) and exponential (for $\beta=1$) distributions. Failure is complementary to reliability and can mathematically be written as,

$$R_{eqp}(t) + F_{eqp}(t) = 1 \tag{1}$$

$$F_{eqp}(t) = 1 - R_{eqp}(t) \tag{2}$$

Reliability of the equipment in useful life region can be modeled as,

$$R(t) = e^{-\lambda t} \tag{3}$$

$$\lambda = \frac{1}{MTBF} \tag{4}$$

where MTBF is the Mean Time Between Failure and is usually calculated from the equipment's operating history and used for specific causes of failure.

$$R(t) = -\exp\left(\frac{t}{MTBF}\right) \tag{5}$$

For the ageing period, weibull distribution models the failure in excellent manner which can be written as,

$$R(t) = e^{-\left(\frac{t}{\theta}\right)^{\beta}} \tag{6}$$

where β and θ are weibull shape parameters.

The consequences associated to petrochemical, process and oil industry are not only limited to mechanical damage equipment but can also cause serious damage to nearby assets, production loss, health and safety and environmental issue which must be evaluated in monetary ($) terms and are assumed to be invariant with time. Economic loss can comprise of various consequences varying from company to company. Some of them are:

1. Economic Consequence of Asset Loss (ECAL): Loss suffered as a result of equipment failure or the damage caused to any surrounding nearby asset as a result of explosion, loss of fluid, etc.
2. Economic Consequence of Production Loss (ECPL): For any downtime, plant always suffers production loss which is a key factor that needs to be assessed seriously.

3. Economic Consequence of Maintenance Cost (ECMC): These are calculated for one or group of equipment(s). They may include technical cost, inspection cost (NDTs) , preparation cost (scaffolding, insulation removal etc)

$$Economic\ Consequence\ of\ Failure = \sum_{i=1}^{n} ECAL + \sum_{i=1}^{n} ECPL + \sum_{i=1}^{n} ECMC + \ Other \quad (7)$$

where i=1, 2, 3 … … …, n is the number of equipments included in the analysis.

After the consequence and probability of failure is determined, risk can be calculated.

Muhlbauer (2004) [13] defined risk mathematically as,

$$Risk_e = Event\ Likelihood \times Event\ Consequence \quad (8)$$

$$Risk_e = \ F_{sys} \times \sum Economic\ Consequence\ of\ Failure\ (\$) \quad (9)$$

$$Risk_e = \left(1 - R_{sys}\right) \times \sum Economic\ Consequence\ of\ Failure \quad (10)$$

Where $Risk_e$ is the operational risk which varies with time because probability of failure is a function of time.

3.4 Phase 4: Appropriate Action

Based on the calculated probabilities and consequences, appropriate action should be taken. These actions include **mitigation**, **repair** or **replacement** of equipment(s) according to the consequences and remaining life. The sole purpose of taking appropriate action is to reduce the risk associated with the equipment which ultimately reduces the losses and minimizes downtime of facility. Downtime becomes a severe issue if the equipments are in series.

4 IMPLEMENTATION OF RBIM TO THE LPG BULLET VESSELS

The above proposed methodology was implemented to LPG processing facility in a process industry. It consisted of more than hundred (100) LPG bullet vessels and each of the LPG vessels went through the same framework as proposed. LPG bullet vessels are of much importance in Process as well as Oil & Gas Industry and constitute a vital part of static equipments. Due to such low temperatures, LPG vessels are always under the threat of corrosion at their inner weld joints as well as on their outer surface. Internal and external pitting on the LPG bullets is the main driver of the failure. If consequences of failure are very low, minimum amount of maintenance activities can be performed at the time of failure. However, if the consequences are high and they are not addressed in a timely manner, the deterioration of equipment may occur and result in production loss, asset loss and various serious accidents.

5 RESULTS & DISCUSSION

The objective of this study was to:

- Identify the main damage mechanisms (such as Sulphuric Acid attack and Hydrogen Embrittlement) responsible for corrosion on the inner and outer side and weakening of weld seams of the LPG bullet vessels.
- Identify Condition/Thickness Monitoring Locations (CMLs or TMLs)
- Maximize the operational life for equipment
- Establish and maximize end-of-life strategies
- Develop relative risk level
- Increase the profitability by either methods (increasing the inspection cycle/interval or control the corrosion rate)
- Provide necessary recommendations and
- Compare the results of RBI methodology and conventional inspection approaches

5.1 Data Trending for LPG Bullet

For the conventional inspection and maintenance approaches, inspection was done on the regular basis at an interval of 2 years. **Figure 2** shows the plot of data trending at different Thickness Monitoring Locations (TMLs) of one LPG bullet vessel and the same method was repeated for remaining every LPG bullets. At each TML, 3 readings were taken rigorously but due to the complexity, the plot of one reading of every TML is shown in **Figure 2**. (All readings are in mm) and its description of locations are shown in **Table 1**.

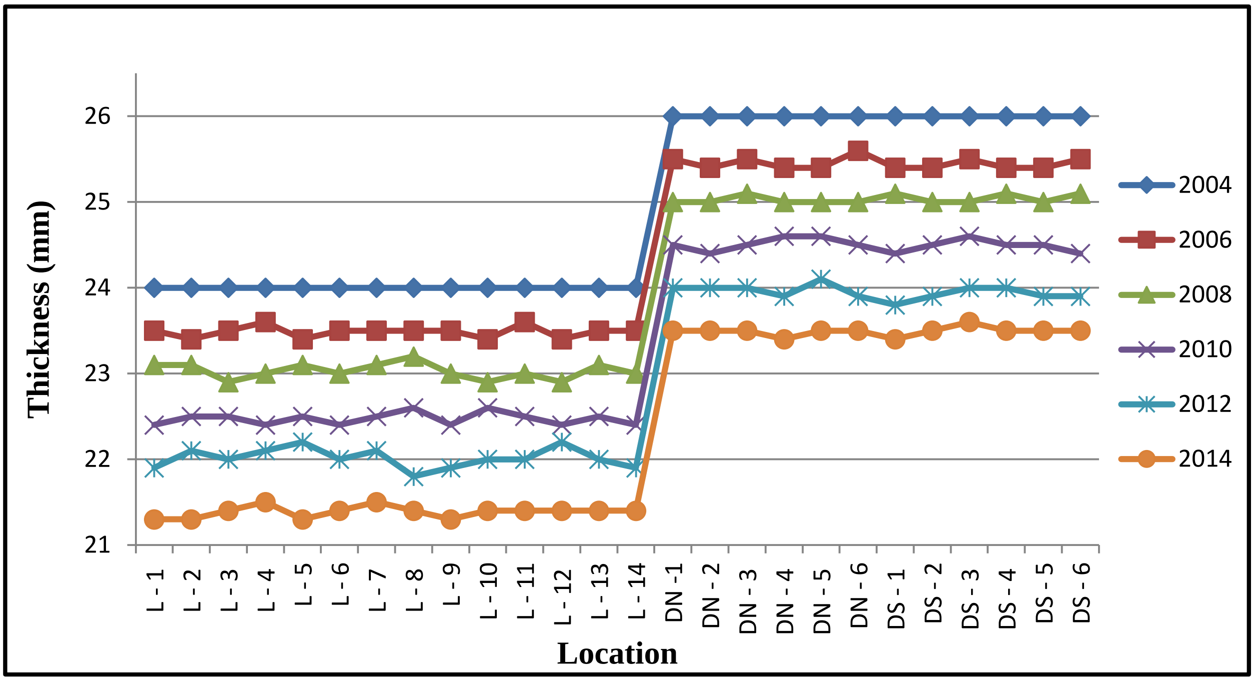

Figure 2. Data trending for conventional inspection

Table 1. Description of Locations

Location	Description
L - 1	1st point on the **Left** side of vessel where readings were taken.
L - 2	2nd point on the **Left** side of vessel where readings were taken.
. .	. .
L - 14	14th point on the **Left** side of vessel where readings were taken.
DN - 1	1st point on the **Dish North** end of vessel where readings were taken.
DN - 2	2nd point on the **Dish North** end of vessel where readings were taken.
. .	. .
DN - 5	5th point on the **Dish North** end of vessel where readings were taken.
DS - 1	1st point on the **Dish South** side of vessel where readings were taken.
DS - 2	2nd point on the **Dish South** side of vessel where readings were taken.
. .	. .
DS - 6	6th point on the **Dish South** side of vessel where readings were taken.

5.2 Previously Used Approach

Previously used approach was totally based on a preventive maintenance programs. As it can be seen from **Figure 2**, inspection was done on a scheduled time period at an interval of 2 years. There was no concept of risk involved at that time. It was much cost-consuming as well as time-consuming. Each LPG vessel had to undergo inspection no matter what was its condition. The deterioration of some vessels had reached such a level that ultimately we had to discard them or make them offline from the facility for its repair.

5.3 Initial Risk Analysis

At the initial level, risk analysis was done based on the gathered data as shown in **Figure 3** and nineteen out of more than hundred LPG bullet vessels were selected which fell in the medium high and high risk category. Risk was measured against pre-developed criteria which states that,

- Vessels whose failure can cause great damage to environment and cause fatalities.
- Vessels exhibiting greater corrosion rates i.e. up to 0.5mm/yr.
- Vessels whose failure cannot be repaired without disrupting the operation.
- Vessels showing high probability of failure e.g. vessel corroded by Hydrogen Embrittlement or Sulphuric Acid attack.

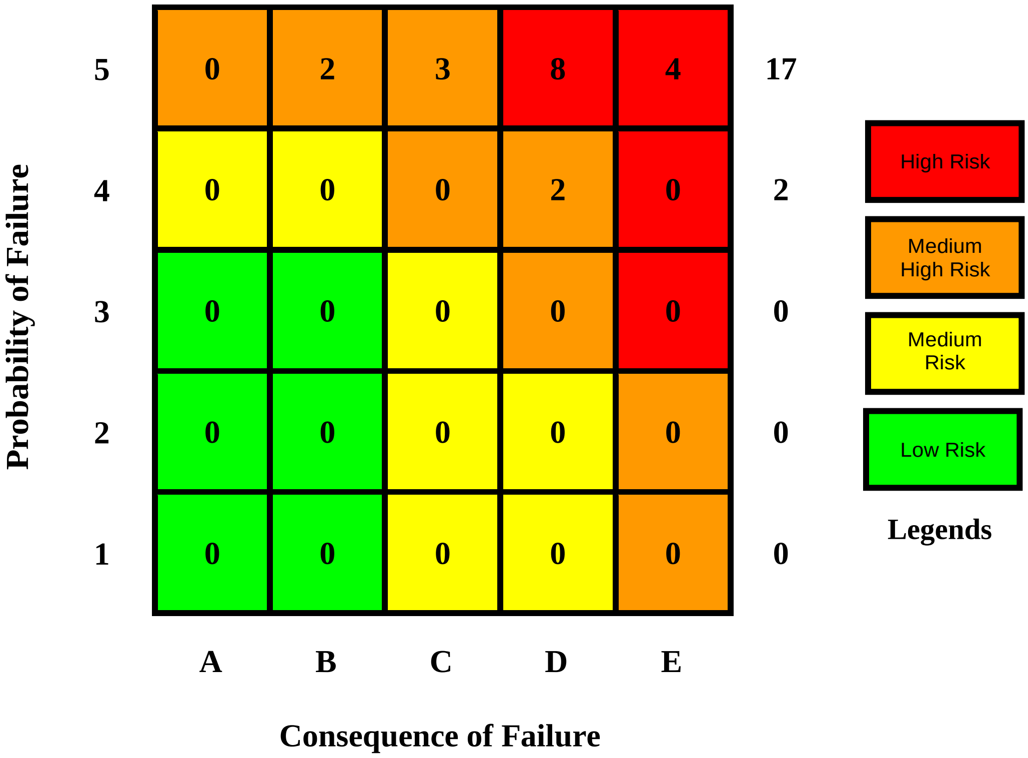

Figure 3. Universal risk matrix of vessels before RBI

Table 2. Description of POF

Category	Probability of Failure	Description
1	Failure occurs in 30 or more years.	Less severe, hence less attention should be given which is economically justified.
2	Failure occurs in 20 years.	More Severe than Category 1.
3	Failure occurs in 10 years.	--------
4	Failure occurs in 5 years.	Increased severity; attention should be given.
5	Failure occurs in < 5 years.	Most severe, take action immediately.

The results that can be concluded from the **Figure 3** are as follows:

- The criticality risk matrix shows that 73.15% of the equipments lie in the higher risk category and 31.58% lie in medium high risk zone.
- The vessels lying in the higher risk zone have both high probability of failure as well as consequence of failure. The probability analysis shows that they have got remaining lives which is below the acceptable level. The consequence analysis shows that internal pitting on shell and dishes due to sulphur is the main factor that causes rapid degradation on the internal side.
- Although the analysis of some vessels shows that they have remaining lives more than 5 years but since internal repair or maintenance is not possible hence they need to be discarded.

Only 5.26% of the vessels lye in the medium risk zone which means that some alleviation can be given to their maintenance and inspection strategy.

5.4 Calculation of Failure Probabilities and Consequences of Failure

Since ample data was present to calculate the failure probabilities and consequences based on the past experiences, we did not use any of the above mentioned formula. But it is highly recommended to use above formulae to calculated actual reliability and failure probability. For this study, the descriptions of Probability of Failure (POF) are listed in **Table 2** and COF are summarized in **Table 3**.

Table 3. Description of COF

Category	Consequence of Failure
A	Internal localized pitting on shell and dish ends due to salts of sulphur and chlorine.
B	Internal pitting on welding seams due to sulphur.
C	External metal loss and pitting due to humid environment created by cooling towers
D	External corrosion on shell and dish ends due to icing.
E	Internal pitting on shell and dishes due to sulphur.

5.5 Preliminary Information / Assumptions

For any RBI study, it is essential to gather preliminary information and make certain assumptions depending upon refinery practices and international codes and standards. General information and assumptions regarding this study are as follows:

- Internal pitting on shell and dish ends due to sulphur is the main cause of metal loss inner side which and weakening of weld joints causes thickness loss in equipment.
- The cost of each LPG bullet vessel was \$0.14 million (ECAL).
- The production loss in case of failure of equipment or any catastrophic shutdown was estimated to be \$15000/day per LPG Vessel (ECPL).
- The inspection and maintenance cost for each LPG Bullet vessel was estimated to be \$10000 (ECMC).
- The time estimated for the approval of new LPG Bullet vessel budget was approximately 8 months.
- The estimated time for inspection and maintenance activities for each LPG bullet vessel was 3 days.
- Long Term (LT) and Short Term (ST) Corrosion rates were found using API 510 (i.e. Pressure Vessel Inspection Code: In-service Inspection, Rating, Repair, and Alteration) [14] Section 6.

5.6 Actions Taken

Depending on the condition of the LPG vessels, various actions were taken on different LPG vessels which include but were no limited to: fillet-welded patches, welding and hot tapping, reinforcement of vessel, insertion of plates, repair of the coating, applying new insulation, etc.

Previously no such actions were performed on spot and since the inspection was done at an interval of 2 years, the defect had extended to an appreciable level that it was too difficult and costly for it to be repaired.

5.7 Assessment after implementing RBIM

After the successful implementation of proposed methodology, results were much different as compared to the previous conventional approach of inspection.

The risk was reduced drastically and some of the deterioration mechanisms were brought in control and consequently risk was also reduced to the acceptable value.

After the successful deployment of respective actions, thickness monitoring was done at an interval of three months to assure that the asset is operating in its improved condition. **Figure 5** shows the thickness of those same TMLs after corresponding actions.

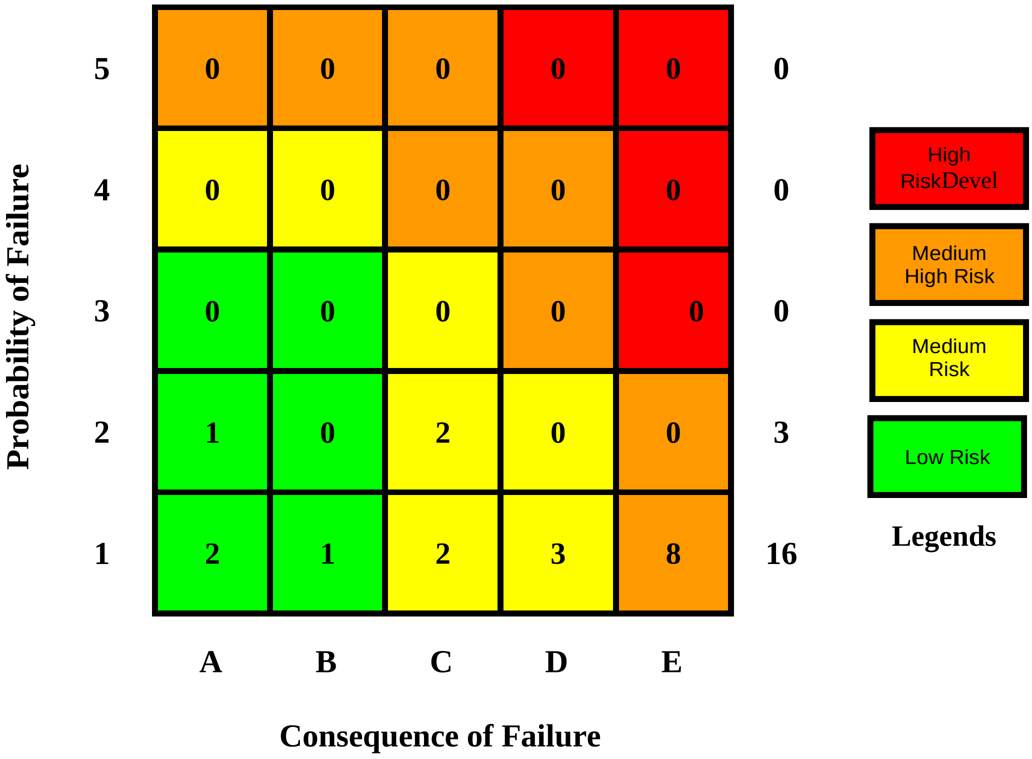

Probability of Failure	A	B	C	D	E	
5	0	0	0	0	0	0
4	0	0	0	0	0	0
3	0	0	0	0	0	0
2	1	0	2	0	0	3
1	2	1	2	3	8	16

Consequence of Failure

🟥 High RiskDevel

🟧 Medium High Risk

🟨 Medium Risk

🟩 Low Risk

Legends

Figure 4.Universal risk matrix after RBIM

- From **Figure 4**, it is clear that the risk has reduced drastically and the equipments which exhibited high risk are 0% now which implies that the facility is working as per its desired conditions.
- Sixteen (84%) LPG vessels have got remaining life of more than 20 – 25 years.
- Damage mechanisms are under control up to a large extent.
- **Figure 5** clearly shows that the thickness of vessels does not does not drop drastically and remains almost same up to an year which means that corrosion rates are in much control. The legends for **Figure 5** are same as for **Figure 2** indicated in **Table 1**.

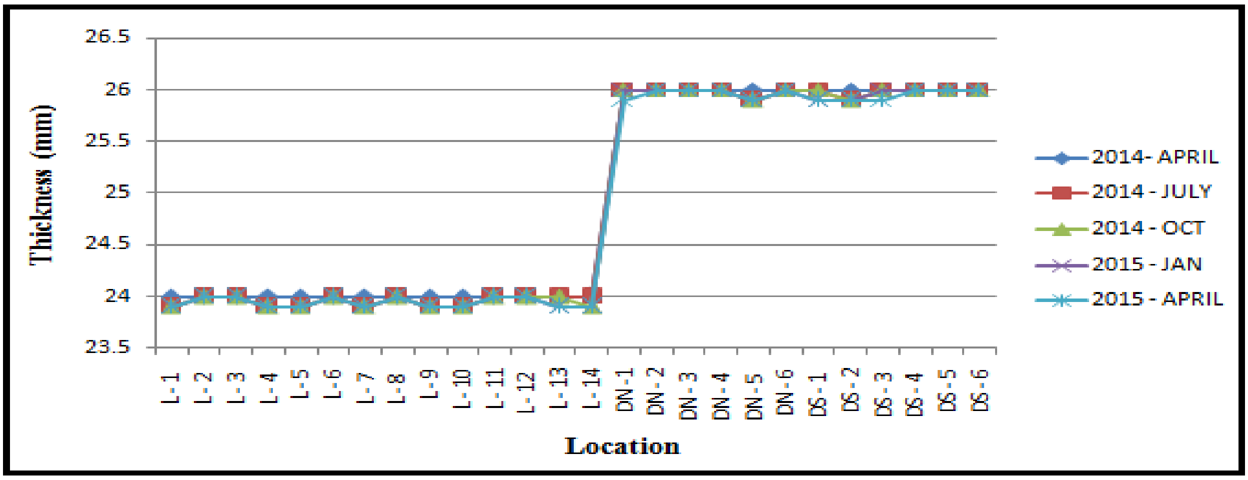

Figure 5. Data trending after RBIM

5.8 Financial Benefits

- The savings accounted for ECAL were calculated to be 19×\$0.14 million × $\frac{2}{3}$ = \$1.77 million per year and \$17.7 million in a span of 10 years because the anticipated life of each vessel was up to 15 years and now it has been extended up to 25 years.
- The ECPL which was saved were \$15000 × 3 × 19 = \$0.855 million.
- The ECMC which was saved in a period of 10 years was \$10000×19 = \$ 0.19 million
- The total financial benefits were, \$17.7m+\$0.855m+\$.19m = \$18.745million in 10 years time period.

As it can be seen from cost comparison graph (**Figure 6**) the savings by proposed RBIM are much higher than the previous inspection approach. For this analysis it came out to be surprisingly \$18 million but this methodology was applied to other equipments also and on an average, \$8 to \$12 million is approximately saved.

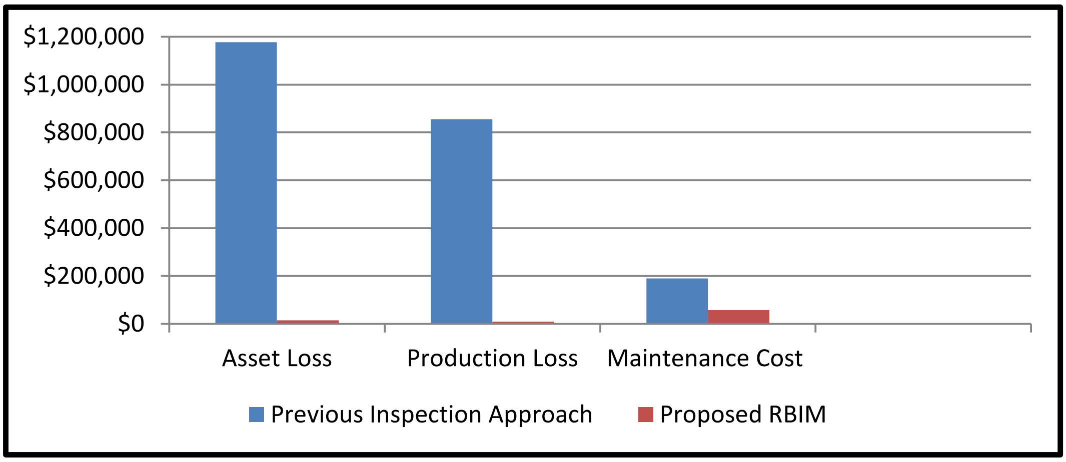

Figure 6. Cost comparison graph

6 COMPARISON

The proposed methodology is totally based on a predictive approach rather than previously used preventive maintenance approach and is better in many aspects which include but not limited to:

- Routine monitoring is being done and wherever a metal loss or any flaw is encountered, on-spot repair is done. Such metal losses and flaws restrict the equipment life to 7 to 8 years only but now the equipment life gets much extended.
- It is much cost-saving in the sense that equipment does not go offline which saves the industry from production and other losses.
- It is time-saving since every equipment is not inspected. Only the equipments exhibiting higher risk are inspected and closely monitored.

7 CONCLUSION AND DISCUSSION

In this study, a risk-based methodology for inspection and maintenance is proposed. It can broadly be broken into four phases: 1-identification of scope and objective, 2- risk-based equipment selection, 3- calculation of failure probabilities and consequences, 4- appropriate action. It differs from other methodologies since it is based on the actual risk to which is the equipment is exposed. All the financial consequences related to the process industries (production losses, asset loss, safety and environmental issues) have been kept in mind while developing this methodology. Industries in Pakistan are not much aware of risk-based inspection so they have to suffer huge amount of losses in account of preventive maintenance and/or run-to-failure maintenance. This methodology is based on actual conditions of process industries in Pakistan so it can prove itself state-of-the-art in current scenario.

When applied to LPG processing facility, this methodology proved to be cost-effective in various manners such as: downtime was minimized, inspection and maintenances costs were reduced, actions were taken corresponding to the actual condition of the equipment and most importantly actual risk of each and every equipment was exposed so that next inspection interval could be set or predicted based on the current risk. Pertaining to the results of study, the financial benefits shown were much appreciable. The most important point while applying this methodology is to keep in mind that risk criteria for each company may differ from others. So, the management must decide risk criteria first.

8 REFERENCES

[1] Lawrence, G. (2012). Cost estimating for turnarounds: Petroleum Technology quarterly Q1-2012

[2] Tan, J. S., & Kramer, M. A. (1997). A general framework for preventive maintenance optimization in chemical process operations. *Computers and Chemical Engineering*, 21(12), 1451 – 1469.

[3] Khan, K., Sadiq, R., & Haddara, M. (2004). Risk-based inspection and maintenance (RBIM): multi-attribute decision making with aggregative risk analysis. *Process Safety and Environmental Protection*, 82, 398–411.

[4] Krishnasamy, L., Khan, F., & Haddara, M. (2005). Development of risk-based maintenance (RBM) strategy for a power generating plant. *Journal of Loss Prevention in the Process Industries*, 18, 69 – 81.

[5] Keshavarz, G., Thodi, P., & Khan, F. (2011). Risk based shutdown management of LNG Units. *Journal of Loss Prevention in the Process Industries*, 25, 159 – 165.

[6] Courtois, P. J., & Delsarte, P. (2006). On the optimal scheduling of periodic tests and maintenance for reliable redundant components. *Reliability Engineering and System Safety*, 91, 66 – 72.

[7] Vaurio, J. K. (1995). Optimization of test and maintenance intervals based on risk and cost. *Reliability Engineering and System Safety*, 49, 23 – 36.

[8] Khan, F. I., & Haddara, M. (2004a). Risk-Based Maintenance (RBM): a new approach for process plant inspection and maintenance. *American Institute of Chemical Engineers Process Safety Progress*, 23(4), 252 – 265.

[9] Khan, F. I., & Haddara, M. (2004b). Risk-based maintenance of ethylene oxide production facilities. *Journal of Hazardous Materials, A108*, 147 – 159.

[10] Ghosh, D., & Roy, S. (2009). Maintenance optimization using probabilistic cost – benefit analysis. *Journal of Loss Prevention in the Process Industry*, 22, 403 – 407.

[11] API. (2009). *Risk Based Inspection; Recommended Practice 580* (2nd ed.). Washington, D.C., USA: American Petroleum Institute.

[12] Torres-Echeverría, A. C., Martorell, S., & Thompson, H. A. (2009). Modeling and optimization of proof testing policies for safety instrumented systems. *Reliability Engineering and System Safety*, 94, 838 – 854.

[13] Muhlbauer, W. K. (2004). *Pipeline risk management manual, ideas, techniques, and resources* (3rd ed.). Burlington, MA, USA: Gulf Professional Publishing.

[14] API. (2006). *Pressure Vessel Inspection Code: In-Service Inspection, Rating, Repair, and Alteration 510* (9th ed.). Washington, DC., USA: American Petroleum Institute.

IMPROVISATIONS TO DECREASE STARTUP FAILURE FREQUENCY AND ENVIRONMENTAL POLLUTION IN UREA PLANT

Naveed Raza, and Ali Ayub
Engro Fertilizers Limited, Daharki, Pakistan

Tel.: +92302-9856339, +923455516552
E-mail address: nraza@engro.com (Naveed Raza), alayub@engro.com (Ali Ayub)

ABSTRACT

This document explicates the improvisations made to overcome the startup failures and hardware limitations, decreasing startup failure frequency & environmental constraints at Engro Fertilizers Limited, Pakistan's Toyo "Total Recycle C Process" Urea plant which was relocated from Bellingham, UK in 1992. Since the commissioning of the Toyo ACES plant in 1998, the success rate of the Urea-2 plant startup has been low, because of instability of the high pressure scrubber U-seal which also results in environmental pollution & excessive venting.

This paper enlists startup failures experienced during the operating period spanning more than 20 years. Each cause & scenario was studied in detail with thorough Root Cause Analysis resulting in successful implementation of Process & Operational optimizations, careful review and update of Standard Operating procedures. In detail covering of all aspects of improving the success rate of Urea Plant Startup are shared depicting how startup time reduction and quick startup post seal failure scenario is made possible; preventing the excessive venting and resultantly eliminating the environmental concerns and helped Engro team keeping their promise to Clean & Pollution Free Environment.

Keywords: Seal, Startup Failure, Urea, Environment

1 INTRODUCTION

Engro Fertilizers Limited, a wholly owned Engro Corporation subsidiary, is a premier fertilizer manufacturing industry being the second largest urea manufacturer company in Pakistan. Engro Fertilizer was incorporated in 1965 and is a former subsidiary of Exxon Mobil Chemical Company. The manufacturing site is located at Daharki and is capable of producing annually 2.3 million tons of urea. In 1992, Engro relocated a 1,000 t/d urea plant, from ICI Billingham, UK, to its manufacturing site in Daharki, Pakistan. The ammonia for the production of prilled urea is supplied from a relocated ammonia plant from Pascagoula, USA. The Toyo Total Recycle C urea plant from ICI was commissioned in 1993. Ever since its commissioning, the urea plant has undergone various debottlenecks and capacity enhancement programs, energy index improvement schemes and various environmental control measures.

2 UREA PROCESS DESCRIPTION

The relocated urea plant now employs Toyo's ACES process to manufacture prilled urea. In this CO_2 stripping process, NH3 is recovered within the HHP loop (ACES loop), and sent back to the reactor along with CO_2 (Fig. 01). The Urea-2 plant synthesis loop is designed to operate at isobar equivalent to 174 kg/cm^2, and liquid mass flows inside the HHP loop under gravitation effect (liquid head). The plant is operated at N/C = 3.79, H/C =0.79 and 66% CO_2 conversion is attained at the reactor outlet. Raw materials (CO_2 and NH3) are imported from the ammonia plant and reacted to produce 46.6% nitrogenous fertilizer. Carbon dioxide from the ammonia plant, at a pressure of 0.50 kg/cm^2 and temperature of 43.3°C, containing 2,500 ppm oxygen, is compressed by reciprocating compressors operating in parallel. Ammonia at 25.5°C is stored in the ammonia receiver, which receives fresh ammonia from the ammonia plant and recovered ammonia from the ammonia condenser and ammonia absorbers. Ammonia is fed to the reactor after passing through the pre-heat stages, where steam and LPD off gases heat is utilized to maintain the ammonia temperature at 80°C. Carbamate from the high pressure absorber cooler (HPAC) is pumped to the HHP scrubber and Carbamate condenser-2, where reactor off- gases and gases from stripper are absorbed to recover reactive mass. The urea concentration at the stripper outlet is 42%, rising to 61% at the high pressure decomposer (HPD or MPD in modern plants) outlet. The HPD is operated at 16.8 kg/cm^2 pressure, using 12.3 kg/cm^2 steam as thermal medium in the thermo syphon reboiler to decompose unreacted mass and recover it in the HPA. The concentration is further enriched to 68% urea at the LPD which is operated at 2.1 kg/cm^2 pressure and 4.92 kg/cm^2 saturated steam is used in the reboiler for breakdown of unconverted mass. The low pressure and vacuum loop operate at slight positive atmospheric pressure and 178mm Hg (0.24 kg/cm^2 abs) pressure respectively. Concentrated urea (76%) at pre-concentrator outlet is pumped to the atmospheric falling film evaporators to produce 98.6% urea. Evaporator off gases, mainly air, is directly routed to atmospheric. Scrubbers to recover ammonia and urea and prevent the release of these gases to the atmosphere. Urea (98.6%) is sent to a wide umbrella Vibro priller through melt urea pumps to the natural draft prill tower to convert the urea melt into prilled urea, which is transported to the bulk storage and bagging facility.

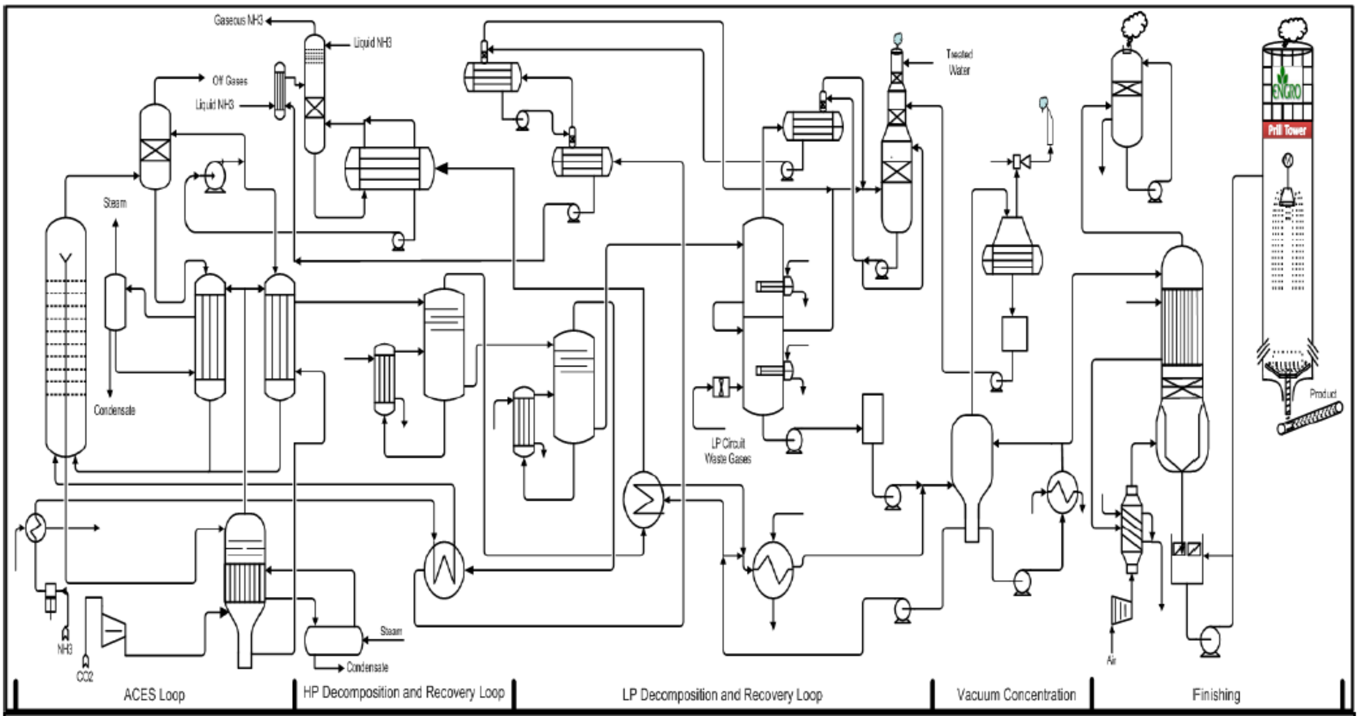

Fig 01: Urea Plant Process flow diagram

3 BACKGROUND

Since the commissioning of the Toyo ACES plant (ECES-850KT), the success rate of the Urea-2 plant startup has been low, due to instability of the high pressure scrubber U-seal. With the passage of time the issue became more agitated due to Carbamate Condensers tubes plugging and stripper inefficiency. Apart from low successful rate the startup is also associated with environmental complaints and pollution due to excessive venting.

With the failure of the HP scrubber U-seal, feed needs to be cut, followed by reactor draining, and flushing before the feeds are fed again. This produces a lag of 8-12 hours once startup fails hence inculcating in production loss. Listed in the paper are the Improvements which were made in the standard startup procedures, and operational techniques.

4 STARTUP FAILURE ROOT CAUSE ANALYSIS AND IMPROVISATIONS

High pressure scrubber U-seal instability has always remained a challenge for Urea plant technical staff. Multiple brainstorming sessions and root cause analysis were carried out to identify the root cause of startup failure. Today our efforts have led us to overcome this mystery. Improvements have been made in the standard operating procedures and operational techniques to improve the success rate of urea plant startup based upon experimental results. Below is a complete description of the research that has been carried out which have actually decreased startup failure frequency.

4.1 Bypassing stripper due to Carbamate Condenser tube Plugging

Once the reactor overflows during ACES startup the reactor solution is transferred to stripper via reactor "U" seal. Reactor solution contains urea, unconverted ammonia, carbon dioxide and water. These uncovered gases are stripped off in the stripper and shifted to carbamate condensers. Carbamate condensers control the ACES loop pressure by condensing the stripper off gasses. Due to tubes plugging of Carbamate Condensers-1 & 2, their heat duty has decreased significantly. This leads to stripper pressurization as the gasses are not condensed in carbamate startup the reactor solution is transferred to stripper via reactor "U" seal. Reactor solution contains urea, unconverted ammonia, carbon dioxide and water. These uncovered gases are stripped off in the stripper and shifted to carbamate condensers. Carbamate condensers control the ACES loop pressure by condensing the stripper off gasses. Due to tubes plugging of Carbamate Condensers-1 & 2, their heat duty has decreased significantly. This leads to stripper pressurization as the gasses are not condensed in carbamate condensers. Pressurized stripper produces a high back pressure on reactor "U" seal which doesn't allows reactor solution to flow to the stripper hence leading to reactor level hold up. A high Reactor level increases ACES loop pressure, while further rise in reactor level lets the reactor solution to overflow to scrubber, resulting in ACES startup failure due to high loop pressure.

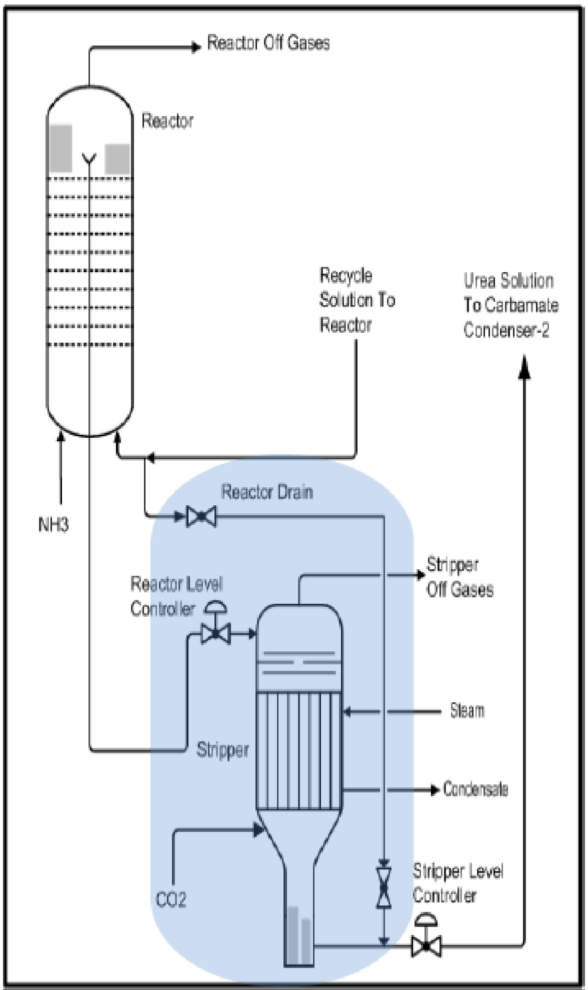

Fig 02: Stripper bypass scenario

Remedial Action

Stripper over pressurization is the key factor contributing towards reactor level hold up. An improvised way to maintain reactor level is bypassing the stripper through reactor drain valve during plant startup as shown in figure 02. Stripper generates lots of vapors due to high volatility and very low first pass conversion through the reactor as the reaction is not well established during startup. By operating the bypass valve lesser solution will flow to the stripper hence it will not be pressurized, at the same time this will help to control reactor level. After this improvisation, urea-2 plant startup failure rate has decreased significantly.

4.2 Steam generation drum pressure controller set point reduction

Carbamate Condenser No. 1 (CC-1) is used for condensing stripper off gasses in the tube side. The heat generated by the formation of carbamate solution in the tubes is utilized in generating 4.9kg/cm2g steam in the shell side. This is achieved by circulating steam condensate from steam generation drum through the shell side of carbamate condenser (CC-1). A pressure controller (PIC-1153) is installed at the steam outlet line of steam drum (FA-1102) to control the pressure of drum. Varying the set point of PIC-1153 has a direct impact on condensation of the stripper off gasses inside the Carbamate condenser-01. The gasses generated in the stripper should be condensed inside the Carbamate condenser 01 and 02 else they will produce a back pressure on the scrubber U-seal leading to ACES startup failure. We are facing similar problem these days due to reduced heat duty of Carbamate condenser-01 and 02 because of their tubes plugging. Figure 03 describes the pictorial view of the above mentioned process.

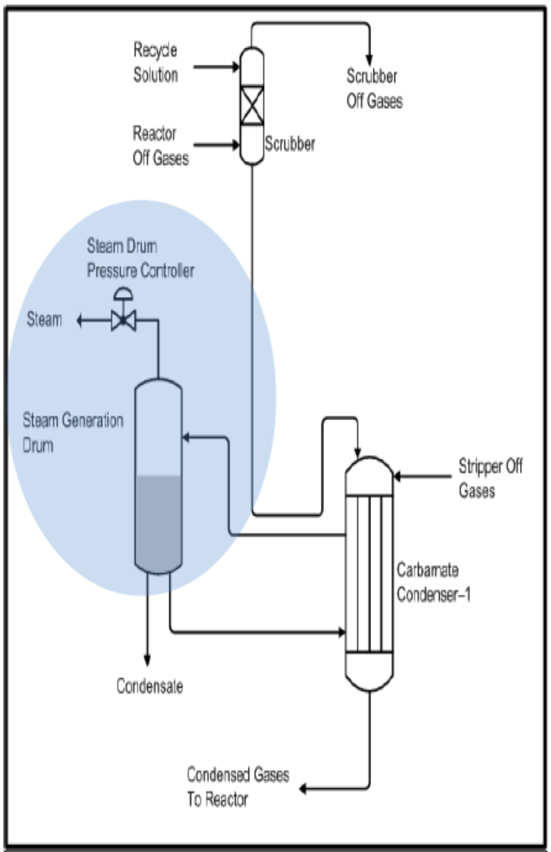

Fig 03: Steam generation drum

Remedial Action

As per normal startup procedure the set point of PIC-1153 should be 5.3 Kg/cm^{2}g.

To overcome the scrubber U-seal failure due to CC-1 tubes plugging, a decrease in set point of PIC-1153 is improvised from 5.3 Kg/cm2g to 4.6 Kg/cm2g. Decreasing the set point increases the heat transfer across Carbamate condenser-01. The impact of this improvisation has been successfully realized and this is now the part of our standard startup procedure.

4.3 Scrubber U-seal temperature profile variation and control

Scrubber U-seal is in place to provide the necessary head pressure required for the carbamate solution to restrict stripper off gasses and flow inside the Carbamate condenser-01. By the time the reactor overflows into the stripper it generates lots of vapors due to high volatility and very low first pass conversion through the reactor. Under high vapor load it becomes difficult to maintain the scrubber U-seal, as vapors overcome the head pressure of the U-seal. The success rate of the startup is highly dependent on the scrubber U-seal stability. Instability causes high pressure in the ACES loop leading to startup failure. The probability of scrubber U-seal failure is greater in startup as the reaction is not well established and quantity of unreacted gasses inside the loop is greater. For that reason during startup a continuous supply of HP Flushing water is lined up in the scrubber U-seal, as rate of absorption of unreacted gasses will be greater in a lean solution. If in any case the gasses inside the Carbamate Condenser are not condensed, they will produce back pressure upon the seal. This leads to restriction of flow inside the scrubber U- seal. If the liquid holds up, the solution required for gasses condensation inside the Carbamate condenser-01 will not be available hence an abruptly increase in loop pressure will be observed and eventually to scrubber U-seal failure. Variation in the Temperature element installed at Scrubber U-seal explains the clear picture of level holdup. The phenomenon of variation in temperature due to flow restriction in Scrubber U-seal is known as kink. We are facing similar problem these days due to reduced heat duty of Carbamate condenser-01 because of its tubes plugging.

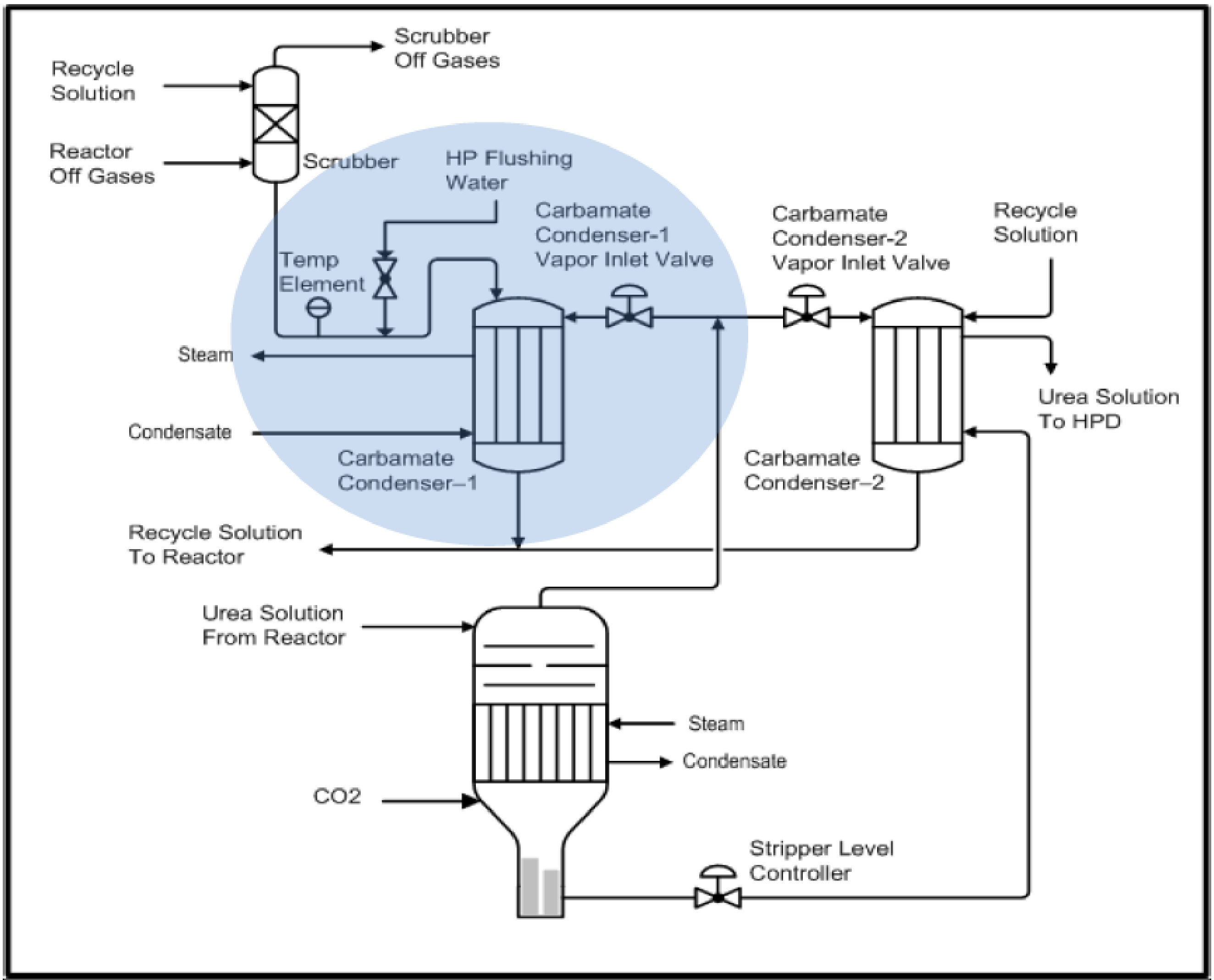

Fig 04: Scrubber U-seal temperature profile variation and control

Remedial Action

As per normal plant startup procedure stripper off gasses inlet valve opening towards carbamate condenser-01 is 90 percent and this opening remains constant.

During startup, a downward kink in U-seal temperature is observed due to restriction of recycle solution through the U-seal, which results due high vapor load and low heat duty of carbamate condenser-01. To attain the recycle flow again, stripper off gases inlet valve opening is decreased from 90 percent to 80 percent. This decreases the vapor load on scrubber U- seal. Consequently, flow is recovered through the U-seal and later its opening is normalized. The impact of this improvisation has been successfully realized and this is now the part of our standard startup procedure. Scrubber U- seal temperature profile variation (in green color) is shown in Fig 5 with respect to stripper off gasses inlet valve opening (in white color). This trend is taken from the DCS snap shot of the recent startup. Trend shows stability in Scrubber U-seal temperatures once the load on the Carbamate Condensor-01 is reduced by decreasing the stripper off-gasses flow via decreasing CC-1 gasses inlet valve.

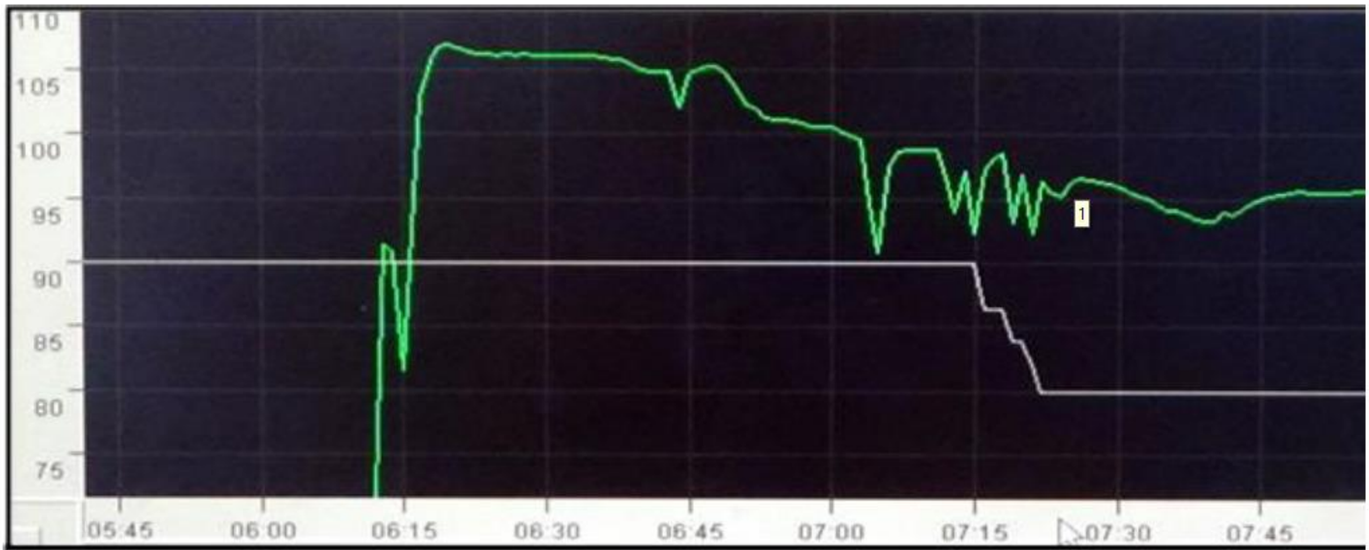

Fig 05: Scrubber U-seal temp variation v/s gasses flow to Carbamate condenser

4.4 Startup with improved urea concentration feed solution

Earlier practice was to start urea plant by feeding low concentration carbamate solution i.e. 15-25% to the urea reactor. A low concentration means greater quantity of water in the system. As the reaction conversion in already low during startup, a higher H/C ratio will aggravate the situation. As the loop pressure is controlled by reaction conversion and condensation, a low reaction conversion will lead to higher vapor load and eventually towards scrubber U-seal instability.

Remedial Action

1. A solution was suggested for level make-up of low pressure and high pressure absorbers with 25-30% concentrated by weight urea solution.
2. Increased liquid density and relatively low vapor pressure helped in maintaining the U-seal head pressure, as concentrated liquid mass would be flowing against the vapors flowing into Carbamate condenser-1.

5 UREA PLANT STARTUP TIME OPTIMIZATION

The startup time duration is significantly improved after optimization of the startup process. Since commissioning, it was normal practice to drain reactor for two hours, even for hold startup. Startup after a plant tripping usually took longer, initially for draining the reactor, and then waiting for the reactor to overflow after feed in. Similarly for an unsuccessful startup due scrubber U- seal failure; it normally took two to three hours to establish that a seal had actual given away, before stopping all the feeds to ACES and again draining for the re-attempt. After technical discussions, it was decided to reduce the reactor draining time gradually in steps from two hours to 60 minutes for hold startup. It was also difficult to detect scrubber U-seal partial failure in the startup until the load was increased to 80% load. After a lot of brainstorming and troubleshooting, few signs and indications were picked up that could indicate the failure in the very initial phase of startup as soon as reactor overflows. An earlier depiction of scrubber U-seal failure will save the time for reattempt. Mentioned below are the earlier indications of Seal failure:

1. A downward kink in U-seal temperature is observed when the back pressure on the scrubber U-seal increases.
2. The temperature profile becomes linear from the carbamate condenser top to the scrubber bottom when the vapors pass through the scrubber U-seal.
3. Carbamate comes out of the drain valve of the ACES vent instead of going inside the scrubber due to high back pressure.

It was also decided to cut the feed to ACES as soon as any similar indication of a scrubber U-seal failure was observed in order to save time. This improvement reduced the reprocessing cost of recovering the urea from the drained mass. Almost 200 tonnes of urea was saved per startup by reducing startup time.

6 ENVIRONMENTAL POLLUTION CONTROL

The urea plant has a 83.8 m high atmospheric vent to relieve pressure from the high pressure loop if required. Urea-2 plant startup was renowned for its excessive venting and failures due to scrubber U-seal failure resulting in carbamate showering from the ACES vents.

With improved environmental standards and stringent checks on venting, modern plants have developed administrative controls and engineering checks like atmospheric scrubbers or flare systems to avert the release of hazardous chemicals into the open air.

A low cost and effective solution was a big challenge for the urea plant team. Environmental complaints from the surrounding area and within plant premises were routine during and after startup due to the frequent startups and improved community awareness about environment checks.

As per standard operating procedure it was recommended to start the urea plant on a 40% load basis with a 15-25% carbamate solution concentration. Reactor feed rates, overflow timings, and vapor dynamics inside the ACES loop were calculated on this basis. This used to happen because, unlike other plants, steam to the stripper cannot be increased immediately after the reactor overflow due to the fear of U-seal failure. The load is hence shifted to the downstream circuit which resulted in increased pressure and thus venting. As the stripper liquid outlet valve is opened to release solution from 100 kg/cm2 pressure to the HPD it was a challenge for plant operators to maintain the HP circuit pressure within limits i.e. 100 kg/ cm2. Due to the high feed rate of solution equivalent to 40% load coming from ACES and low conversion of initial pass solution, vapor load on the HP circuit is very high, which triggers the opening of the atmospheric vent to release ammonia and inerts to control HP loop pressure. Almost 30 t/h of the vapors escape from the atmospheric vent, releasing ammonia with a concentration of 99% to the environment.

6.1 Remedial Action

1. Today urea plant is started with 30% load basis instead of 40% to avert the uncontrolled condition of rapid vapor generation once the stripper liquid outlet valve opens and the first pass of solution reaches the HPD.
2. Early line-up of ammonia refluxes in the high pressure absorber helps to minimize the opening of the atmospheric vent to release inert gasses that were initially used to pressurize the HP circuit as a startup permissive.

With the control on the HP circuit pressure, the reflux ammonia condensers and absorbers are lined up during startup. This helps to recover ammonia instead of venting to atmosphere. So that environmentally hazardous vapors are recovered and returned to the process. This reduces the number of environmental complaints from the local vicinity and other operating areas to zero from five recorded the previous year.

7 CONCLUSION

A remarkable increase in Urea plant successful startup rate has been achieved through various improvisations in the Standard startup procedure and operational techniques. Even though Low heat duty of Carbamate condenser and inefficiency of stripper opposed much to the cause, still we managed improving the success rate of Urea Plant Startup, reduction in startup time and quick startup post seal failure scenario was made possible; preventing the excessive venting and resultantly eliminating the environmental concerns.

TRENDS AND FUTURE PERSPECTIVES IN ADDITIVE MANUFACTURING

Shaheen Perween[1,*], Muhammad Fahad[2], Maqsood Ahmed Khan[3]
Department of Industrial and Manufacturing Engineering, NED University of Engineering and Technology, Karachi, Pakistan.
(shah30@neduet.edu.pk, mfahad@neduet.edu.pk, maqsoodahmed@neduet.edu.pk)

[*]Corresponding author. Tel.: +99261261-68
E-mail address: shah30@neduet.edu.pk

ABSTRACT

Additive manufacturing also known as freeform fabrication brings a revolutionary change in design, development and manufacturing aspects of fabricated parts. This technology contain a number of manufacturing processes based on the principle of sequential layer by layer accumulation of part slices into a 3-D object. Apart from the limiting constraints of these processes, objects of complex geometry with customizable material properties can be manufactured without any tooling requirements. The beginning of this technology was the result of invention of computers and Stereolithography technology became the first AM process in 1990s. Current advancements in additive manufacturing has been highly contributed by computer technology, process simulation & modeling techniques. Other related technologies that have developed variations and advancements in AM processes include laser technology, printing technologies (inkjet or droplet), programmable logical controllers and materials science. Recent advancements in designing and modeling technique include multi representation techniques of solid models and material design. Most of the commercial CAD/CAM systems are based on solid modeling kernel, boundary representation (B-rep) which lacks in numerical robustness in solid models. For solid modeling, a recent approach Layered Depth Natural Images (LDNI) based on ray-representation is suggested. The objective of this paper is to surround the current body of knowledge contributed by recent research findings of simulation and modeling techniques and material technology; at the end section gaps and future research areas are suggested.

Keywords: Additive manufacturing, Computer aided design, Boundary representation, Layered Depth Natural Image, Engineering materials.

1 INTRODUCTION

Rapid prototyping is the vital phase of product development meant to ascertain the form, fit & functionality of the artifact, before start of manufacturing. Rapid prototyping which encirclements variety of processes with new technologies capable to produce accurate parts directly from 3D CAD model data in few hours and with little need for human involvement and tooling [1]. For many years, rapid prototyping was used and preferred as overall name of these technologies but with the rapid and huge growth of this field, direct manufacturing of parts become possible, RP becomes one of AM technique used for the creation of models and prototypes [2].

Additive manufacturing (AM) represents a family of processes used to manufacture parts by depositing layers of material on top of the previous one. Numerous application areas are automotive, aerospace, marine, oil & gas, Machinery, Consumer, Biomedical, Architectural models, Building construction, Electronic, Food industry and Repair works of worn out parts. The versatility of these processes is ma.de possible by variety of materials used for manufacturing and their physical state of condition at the time of manufacture [3].

History of additive manufacturing starts back in 1987 with the introduction of Stereolithography by 3D Systems. The process involves layer by layer solidification of ultraviolet light sensitive material when exposed to laser. SLA-1 becomes the first commercial available stereolithography machine [4]. From 1987 to date advancements in material addition technologies may be divided by the physical state of involved material prior to the material addition and before part formation. The liquid based technologies may involve solidification of a resin when exposed to a laser beam, solidification by electro-setting fluid, or a repeated cycle of heating, melting and solidification of the material. Powder based technology do not require a change in state, the powder compound are mixed with binding agents or laser beam to join or fuse together. Solid sheets lamination processes are divided according to whether the sheets are bonded with a laser or by an adhesive [5].

This paper provides a brief review regarding the classification scheme in AM and process steps of popular commercial AM processes in Section 2. In Section 3 we discuss the general process steps followed in AM, starting from conceptualization to the application. Section 4 summarizes the recent developments of enabling technologies in AM, whereas Section 5 discusses the developments related to materials technology.

2 CLASSIFICATION OF AM PROCESS TECHNOLOGY

Classification scheme are presented by a number of researchers like Kruth et al., [6] group AM processes according to the state of bulk materials used as liquid, powder, solid and gas. Another classification scheme is presented by Pham [7] which divide the AM processes with respect to input materials as liquid, discrete particle and solid sheets in 1997. The classification scheme of Pham is further modified by Gibson to include the specific processes related to line, layer or volume processing.

The above classification schemes lacks in a clear cut division of AM processes according to processes and material (e.g. SLS and 3DP), also some of the processes do not fit and stays outside of these classification. The anomalies in above classification schemes provide a basis for the development of a standard classification scheme ASTM F2792-12a, and group processes in seven categories shown in Fig 1.

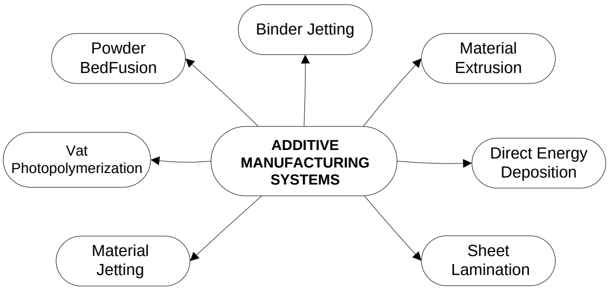

Figure 1. Additive manufacturing classification scheme

From the early stages of AM most of the processes were in the early development and pre-commercial stages and among those few did not reach the commercialization stage and are still under development stages or rejected. Among the popular commercial AM processes of today are Stereo-Lithography (SL), Fused Deposition Modeling (FDM), Three dimensional printing (3DP), and Selective Laser Sintering (SLS) [8].

2.1 Stereolithography (SL)

Among a number of most commonly commercial AM processes in 1990’s, SL with over 500 commercial SL machines installed worldwide could be considered, the most popular technology of that time era developed by 3-D Systems Inc., USA [7, 9]. The process involves solidification of photosensitive monomer on the surface of elevator, into a polymer. Elevator is dipped inside the tub, filled with monomer and raised to maintain a thin layer of monomer between the surfaces. The solidification of the thin layer takes place, when exposed to ultraviolet (UV) light. The solid layer is then lowered just below the surface to create a new slice. This procedure repeats until the part is completed. After completion the part is removed from the tub and excess resin is drained off. The drain time depends on the viscosity of the resin and may take several hours. The supports are removed and the green part is placed inside an UV oven to dry off and remove the remaining liquid and partially cured resin [7].

2.2 Fused Deposition Modelling (FDM)

In 1991 three AM commercial machines were introduced, FDM by Stratasys, Solid ground curing (SGC) by Cubital and Laminated object manufacturing (LOM) by Helisys [4]. FDM process involves extrusion of plastic or wax material through a nozzle that follow a layer by layer predefined path according to cross sectional geometry of the object. The material is supplied in filament or plastic pellets form, heated and maintained at 0.5^{o}C above the melting temperature through heating coils installed just a the nozzle. The molten material is extruded through the nozzle, deposit and solidifies immediately over the previously extruded layer [10]. Layer by layer deposition of material takes place on a heated platform to minimize the distortion in part after cooling. After completion of a single layer the platform is lowered to a height according to the nozzle diameter.

2.3 Selective Laser Sintering (SLS)

SLS technology was commercialized by DTM Corp., USA in 1992 [4]. SLS uses heat-fusible powder of polycarbonate, glass filled composite nylon, sand wax or metal to manufacture the part by heating with a computer controlled laser beam such that the powder particles fuse together [7, 9, 11]. Powder fusion takes place on a heated bed, maintained just below the melting temperature of powder to minimize thermal distortion and to ensure proper fusion. The entire bed is lowered immediately after the fusion and powder feed box is raised to supply a new layer of powder. A rotating roller spread a new layer of powder for next layer. Excess powder remains with the sintered layers to provide support to the part and after the completion of the part it can restored and reused [7].

2.4 Three Dimensional Printing (3DP)

In 1996, 3D systems sold its first commercial 3D printer that use inkjet printing mechanism for layer by layer deposition of wax. The same year Z Corp. utilizes this mechanism with binder and launched Z402 3D printer [4]. Metal or metal-ceramic composite powder is supplied to a substrate in stages to form the layers. Binder is supplied to each layer to bind the powder particles selectively through a nozzle [12]. After layer by layer deposition of powder and the binder, as soon as the part is completed it is heated to set the binder and powder. The excess powder which provides support to the part is removed by immersing the part in water bath. The part is then heated to 900^{o}C for two hours to sinter it. The porosity and density can be increased by isostatic pressing of the part before the final firing. To improve the strength, and to impart various other mechanical properties, infiltration process is applied on the part [3].

3 THE EIGHT STAGE PROCESS STEPS IN AM

Additive manufacturing processes follow some general process steps, from initial plan to the application of the product. These steps includes conceptualization and 3D CAD design, conversion of CAD design to STL/AMF format, manipulation and verification of the CAD design, machine setup and 3D part printing, removal and post processing and application of part [3] shown in figure 2.

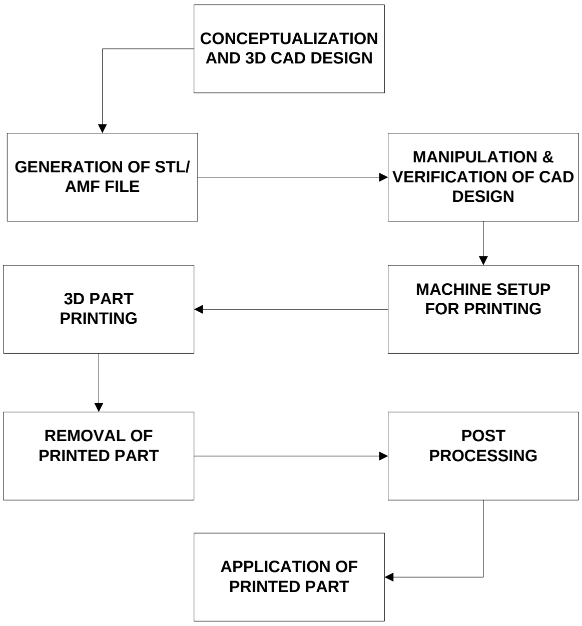

Fig 2. Process steps in AM

Although the process steps and digital input data (CAD data) are identical to all AM machines, the resulting product from each process differ in surface finish, feature tolerances and mechanical properties. Difference in end product is result of differences in manufacturing technique, material type, geometric position or orientation of geometric features [13].

This section covers the detail of each process step which enables to understand the variety of supporting technologies embedded in the process from conceptualization to application, and without these supporting technologies AM could never exist. Further advancement in AM technology is actually the further improvement into these areas.

3.1 Conceptualization and 3D CAD Design

Conceptualization is outlining the idea through defining the geometric and functional features of product. The idea can be represented or communicated by a narrative description through text, sketch or physical representative models. AM processes requires digital 3D CAD model of the product, produced by modeling software or 3D scan of a physical part.

Previously, CAD modeling software lacks to generate mathematically closed models, which result in capricious output from AM machines. Advanced CAD modeling software are now capable to create models without gaps but if the problem persists, it can be detected and fixed during conversion of CAD to STL file [3].

3.2 Generation of STL/AMF File

For the last three decades, STL is used by nearly all AM technologies to transfer information between design programme and AM machines. STL is derived from STereoLithography and abbreviated as Standard Tessellation Language. STL describes the CAD model in terms of its geometry and approximate the surfaces by series of triangular facets.

Limitation of STL is that it only describes the surface by the vertices of triangles and a unit normal vector without any unit, colour, dimension, material or any feature information. These limitations are resolved by the introduction of Additive Manufacturing File (AMF) format, an ASTM/ISO standard format developed by ASTM in 2011[3, 14, 15].

3.3 Manipulation and Verification of CAD Design

After creation of STL file it is sent directly to the AM machine, a number of operations are performed according to requirements. First correctness of the part is verified and afterwards, the functions like orientation, reposition, scaling up or down of a part, add text to STL file for identification of part, manual segmentation or combining of multiple STL files is made possible by system supplied visualization tool.

3.4 Machine Setup

After the verification and manipulation of STL file it is then send to AM machine. Before the layering of part, some process parameters and material selection is required. Process parameters and material selection options depends on the type of AM machine, not all the machines are designed to provide variety of materials and layer thickness. For processes which requires a base plate, the plate must be placed and adjust according to the machine axes.

The operator also needs to check that enough amount of material is available to complete the build.

3.5 3D Part Printing

Once the process parameters are set the part, the process shift to the computer controlled layer based manufacturing phase. All AM machines utilize the same sequence of layering and height adjustments, whereas the supply of material and layer formation differs. Some processes combines deposition and layering process whereas other process perform separately [3]. The deposition and layering process continues until the part is completed

3.6 Removal

The part is separated from the baseplate and surrounding excess build material. For some AM process different material other than the build material is used to support the part. The support material can be removed manually.

For parts with metal supports machining operations are required. A trained operator is required at this stage and after cleaning the part is ready for post processing.

3.7 Post Processing

Post processing refers to the application of (mostly manual) to improve the functionality, aesthetic, appearance or mechanical properties. It mainly depends on the process type e.g., for the parts produced by three dimensional printing (3DP), a infiltration is applied to improve the strength [3], whereas to improve appearance and surface finish of hearing aids manufactured by stereolithography (SL) a film of lacquer or some sort of polishing operation is applied[16].

3.8 Application

Before application, the user must be informed that the parts manufactured by AM will differ from those manufactured using other manufacturing techniques. The part can have voids, gaps and have different microstructure. AM produced parts are anisotropic and behave differently at different area which can result in failure also, in some cases. The user should have the latest knowledge about the processes and select the best available option of AM processes.

4 ENABLING TECHNOLOGIES IN ADDITIVE MANUFACTURING

The success of AM technology is supported by developments in number of related technologies that integrated into the process. The major advancements related to computer technology are in the area of 3D graphics, CAD modeling software, processing power & geometry design, and machine control system for AM. Similarly there is much advancement in the material design and manufacturing technology [3, 13] .

Much advancement is observed in solid model representation techniques in the past few decades. Most of the CAD/CAM systems are designed and developed based on solid modeling kernel using boundary representation (B-rep) which lacks in numeric robustness, and are prone to generate numerical errors. Alternative method to Voxel based representation which can directly be obtained from CT or MRI volumetric images is limited by huge memory consumption [17, 18]. Wang et al. introduced layer depth normal image (LDNI) to overcome the problems of memory and processing time [19, 20]. The approach of LDNI representation is also very effective in hollowing/thickening as well as support generation of a model.

With the reduction in cost of 3D printers it is now possible for a common person to afford it. To create a 3D model it needs a lot of training and practice, and for a novice person it is not an easy task. Researchers are now looking to develop natural user interface (NUI) design and modeling tool.

Optimization of process parameters and technique to address a process planning task has a vital role provide physical properties to manufactured part. Initially four task, layer slicing, orientation consideration, supports location and path planning are considered for process plan. Kulkarni et al. [21] splits process planning into model domain and layer domain. Model domain includes orientation and supports generation, whereas path planning falls in layer domain. Different approaches are present to achieve the objective through selection among orientation, number of layers, volume of support material, surface inaccuracy, strength, and volume of trapped material. With the advancements in the material technology, new process planning and optimization techniques need to be developed for complex, functionally graded as well as multi-distributed materials.

5 MATERIAL ENGINEERING TECHNOLOGIES

The role of material technology in AM is to make use of material properties of the constituent material/materials which are combined either uniformly, by geometry, on any size scale or randomly. It includes the modeling of material distribution, patterns of material distribution. Material engineering technologies include the distribution of material within a solid object as well as material modeling to define the distribution, such type of distribution is non-uniform known as heterogeneous material distribution.

5.1 Non- uniform material distribution with controlled structure

Expansion in the application areas of AM and recent developments in computation technology brings advancements in geometric modeling techniques. Most of the mechanical parts are modelled as homogenous solid structure. Inspired by natural occurring structures by nature, AM technology is designed to reduce the amount of material used and increase the strength of the printed part. The use of cellular structures efficiently achieves the objective with cost reduction [22-24].

Cellular structures, also denoted in literature as lattice structure or scaffold structure are made up of cells composed of faces and struts on nanometre or micrometre scale. Cellular structure mostly comprise of struts with least number of faces the structure is an open structure, and with most of struts are enclosed by faces, is a closed structure[23].

Cellular structures have tremendous application opportunities in the areas of bioengineering, aerospace, automobile, arts and architecture. Existing tactic to model microstructures relies on boundary representation and discrete volume representation. The problems and limitation (size, processing time, validity, precision, machinability and parameterization) of both approaches expands with the geometric complexity of the structure.

Pesko et al. [24] describes microstructures in terms of real functions of point coordinates of C^o continuity. The real functions are combined in constructive manner by Function Representation (FRep) approach. For modelling of infinite regular lattice structure, trigonometric periodic functions and R-functions are used. For modeling of infinite cellular structure, periodic function is defined which specifies a space mapping to the FRep model of unit cell. Medeiros et al. [23] proposed an automatic adaptive void algorithm for the tessellation of primal or dual adaptive cellular structure within a given volume boundary. The objective is to reduce the amount of infill material for any given triangulation. The division of the space is such that the bigger tetrahedrons are placed at the inner side of the triangulation whereas the smaller tetrahedrons are closer to the edges, shown in figure 3.

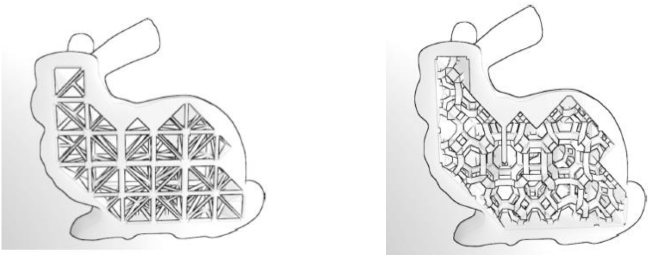
(a) (b)

Fig 3. Cellular structure (a) Primal open cell structure mesh (b) Dual open cell structure mesh [23].

5.2 Non- uniform material distribution with multi-material distribution.

Heterogeneous objects (He-Object) are different from homogenous materials, which are made with uniform material distribution of same material. Heterogeneous materials are made spatially with different material composition. Examples of He-Object are functionally graded materials (FGM) distribution, embedded sensors/actuators, Micro-Electro-Mechanical Systems (MEMS), and Composite materials. Kou and Tan [25] classified He-Objects based on data distribution and distribution method of the material as; evaluated model, unevaluated model and composite model. Evaluated model include heterogeneous objects with intense space segmentation (voxel based model and volume mesh based model). Unevaluated model are defined by rigorous mathematical expression, single or multiple feature based model or control points based model.

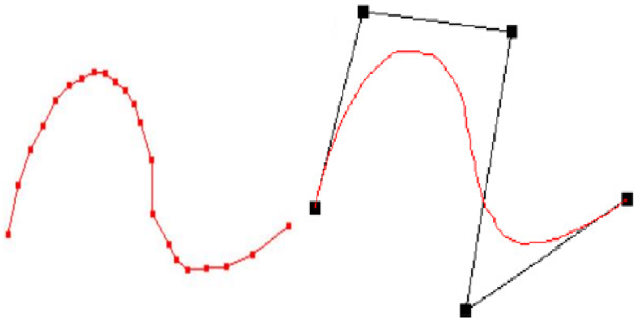
(a) (b)

Fig 3.Evaluated and unevaluated representation of a curve (a) evaluated representation (b) an unevaluated representation [25]

Composite models are models with complex material distribution; two or more material can be included in a complex model with different material distribution at different areas. Complex models include assembly model, cellular model and hybrid composite model.

In addition to the material modeling of heterogeneous materials, research is being carried out to manufacture functional parts of single material with different material distribution.

6 CHALLENGES RELATED TO MATERIAL ENGINEERING TECHNOLOGY

21st century is witnessing a paradigm shift in manufacturing technology, AM technology made it possible to manufacture parts with intricate geometry. This is also recognized by General Electric Works as “We see advanced manufacturing (3-D printing) as the next chapter in the industrial revolution”. Currently 300 above AM machines are operating across GE works and will be producing 100k + parts for GE aviation in 2020 [26]. Although the researchers are aiming high and they are likely to do so in the coming years, they must consider below mentioned limitations and challenges associated with additive manufacturing.

Connection between design, process and machine, Design for additive manufacturing (DFAM), possibly the most thought-provoking aspect of AM which allows the freedom of design and manufacturing of products. Future DFAM systems will enable parts manufacturing by simply specifying the design performance requirements. Currently the benefits of using AM for heterogeneous and functionally graded materials are under investigation. New methods like layer depth natural image and automatic adaptive void algorithm for geometric computation, modeling and tessellation are available, but for modeling for more complex geometries and structures inspired by nature will require improved design and modeling techniques [3].

Limited material deposition rate, Baumers [27] constructed a cost model comparison between Electron Beam Melting (EBM) and Direct Metal Laser Sintering (DMLS) with conventional machining processes. Material deposition rates of 37.58g/h through DMLS and 69.24g/h by working with EBM were measured. The process cost is comparable with conventional machining well above 100kg/h which shows the productivity limitations. It can easily be concluded that currently AM systems are limited to support high volume production.

Limited range of materials, especially in medical applications. A very few polymeric materials are declared safe to work within the operation room, whereas a limited number of materials can be placed inside the human body. Metals are regularly used for implants e.g., titanium, chromium cobalt and stainless steel are used to produce implants. With the rapid growth, new biocompatible materials are required [28, 29].

7 CONCLUSION

Challenges related material technology has been presented in this article. It is observed that much work has been done to address the problem areas but as the application areas of AM is expanding day by day; AM technology fails to reach at a mature level. The situation is same for other supporting technologies, few of the problems are addressed and a solution is suggested whereas many of them still needs to work out [28]. It concludes that still AM carries a large research potential.

REFERENCES

1. Waterman, N.A. and P. Dickens, *Rapid product development in the USA, Europe and Japan.* World Class Design to Manufacture, 1994. **1**(3): p. 27-36.
2. Standard, A., *F2792, Standard Terminology for Additive Manufacturing Technologies*. 2012, ASTM International, West Conshohocken, Pa, USA.
3. Gibson, I., D.W. Rosen, and B. Stucker, *Additive manufacturing technologies*. 2010: Springer.
4. Wohlers, T. and T. Gornet, *History of additive manufacturing.* Wohlers Report 2011, 2011. **24**.
5. Kruth, J.-P., et al., *Consolidation phenomena in laser and powder-bed based layered manufacturing.* CIRP Annals-Manufacturing Technology, 2007. **56**(2): p. 730-759.
6. Kruth, J.-P., M.-C. Leu, and T. Nakagawa, *Progress in additive manufacturing and rapid prototyping.* CIRP Annals-Manufacturing Technology, 1998. **47**(2): p. 525-540.
7. Pham, D. and R. Gault, *A comparison of rapid prototyping technologies.* International Journal of Machine Tools and Manufacture, 1998. **38**(10): p. 1257-1287.
8. Kruth, J.-P., M. Leu, and T. Nakagawa, *Progress in additive manufacturing and rapid prototyping.* CIRP Annals-Manufacturing Technology, 1998. **47**(2): p. 525-540.
9. Hubinger, A.Z., J. Carvalho, and J. Lirani. *Rapid prototyping–concepts, techniques, applications and future trends*. in *XV Congresso Brasileiro de Engenharia Mecânica, Águas de Lindóia–SP, Nov*. 1999.
10. Mohamed, O.A., S.H. Masood, and J.L. Bhowmik, *Optimization of fused deposition modeling process parameters: a review of current research and future prospects.* Advances in Manufacturing, 2015. **3**(1): p. 42-53.
11. Das, S., *Physical aspects of process control in selective laser sintering of metals.* Advanced Engineering Materials, 2003. **5**(10): p. 701-711.
12. Sachs, E., et al., *Three dimensional printing: rapid tooling and prototypes directly from a CAD model.* Journal of Manufacturing Science and Engineering, 1992. **114**(4): p. 481-488.
13. Gao, W., et al., *The status, challenges, and future of additive manufacturing in engineering.* Computer-Aided Design, 2015.
14. ASTM, I., *ASTM52915-13, Standard specification for additive manufacturing file format (AMF) Version 1.1.* ASTM International, West Conshohocken, PA, 2013.
15. Monzón, M., et al., *Standardization in additive manufacturing: activities carried out by international organizations and projects.* The International Journal of Advanced Manufacturing Technology, 2015. **76**(5-8): p. 1111-1121.
16. Hopkins, N., H. R.J.M, and P. Dickens, *Rapid Manufacturing: An Industrial Revolution for the Digital Age* 2006: John Wiley & Sons.

17. Chandru, V., S. Manohar, and C.E. Prakash, *Voxel-based modeling for layered manufacturing.* Computer Graphics and Applications, IEEE, 1995. **15**(6): p. 42-47.
18. Hoffmann, C.M., *Robustness in Geometric Computations*.* Journal of Computing and Information Science in Engineering, 2001. **1**(2): p. 143-155.
19. Wang, C.C., Y.-S. Leung, and Y. Chen, *Solid modeling of polyhedral objects by layered depth-normal images on the GPU.* Computer-Aided Design, 2010. **42**(6): p. 535-544.
20. Zhao, H., et al., *Parallel and efficient Boolean on polygonal solids.* The Visual Computer, 2011. **27**(6-8): p. 507-517.
21. Kulkarni, P., A. Marsan, and D. Dutta, *A review of process planning techniques in layered manufacturing.* Rapid Prototyping Journal, 2000. **6**(1): p. 18-35.
22. Hao, L. and D. Raymond. *Design and additive manufacturing of cellular lattice structures*. in *The International Conference on Advanced Research in Virtual and Rapid Prototyping (VRAP). Taylor & Francis Group, Leiria*. 2011.
23. Medeiros e Sa, A., et al., *Adaptive voids Primal and dual adaptive cellular structures for additive manufacturing.* VISUAL COMPUTER, 2015. **31**(6-8): p. 799-808.
24. Pasko, A., et al., *Procedural function-based modelling of volumetric microstructures.* Graphical Models, 2011. **73**(5): p. 165-181.
25. Kou, X. and S. Tan, *Heterogeneous object modeling: A review.* Computer-Aided Design, 2007. **39**(4): p. 284-301.
26. Ge and works. *additive manufacturing*. [cited 2015; Available from: http://www.ge.com/stories/advanced-manufacturing/.
27. Baumers, M., et al., *The cost of additive manufacturing: machine productivity, economies of scale and technology-push.* Technological Forecasting and Social Change, 2015.
28. Oropallo, W. and L.A. Piegl, *Ten challenges in 3D printing.* Engineering with Computers, 2015: p. 1-14.
29. Melchels, F.P., et al., *Additive manufacturing of tissues and organs.* Progress in Polymer Science, 2012. **37**(8): p. 1079-1104.

PRODUCTION OF METHANE FROM MUNICIPAL SOLID WASTE (MSW)

Saud Hashmi*, Muhammad Danish, Raheel Alavi, Aly Ismail, Ayesha Munir
Chemical Engineering Department, NED University of Engineering & Technology, Karachi, Pakistan

*Corresponding author. Tel.: +92-21-99261261; fax: +92-21-9261255
E-mail address: saudhashmi@neduet.edu.pk

ABSTRACT

Anaerobic digestion is a promising technique to dispose of organic waste which depends on various parameters such as concentration of slurry, pH, moisture content, volatile solids, total solids, temperature, retention time, Carbon to Nitrogen (C/N) ratio and organic loading rate (OLR) are among the main parameters affecting the biogas production. This study investigated the possibilities of improving methane yield from anaerobic digestion of municipal solid waste including cow dung, fruit waste and vegetable waste by maintaining a constant organic loading rate at different C/N ratios of 10:1, 15:1, 20:1 and 25:1 in a semi-continuous operated 19 litre digesters. Cow dung was employed as a seed for start-up. OLR were set as 1, 2, 3 and 4 g volatile Solids per litre per day for 1st, 2nd, 3rd and 4th week respectively. The cumulative methane production for each of the substrates was measured over a 4 week period and it was observed that most gas produced at C/N ratio of 20:1. The volume of biogas produced by the substrates were measured by water displacement technique. The results suggested that better performance of anaerobic co-digestion can be fulfilled by optimizing feeding composition, OLR and the C/N ratio.

Keywords: biochemical methane potential (BMP), organic loading rate (OLR), methane yield, C: N ratio, anaerobic digestion.

1 INTRODUCTION

In the past, waste generated by humans was of little importance as the amount of waste deposited was too small caused by less population. The generated waste mainly consisted of biodegradable materials and was disposed of locally on the ground which had less environmental impact. Due to the rapid industrialization and development and growing population, the generation of MSW has significantly been increased. A number of techniques were adopted for healthy disposal of MSW. At present, generation of municipal solid waste is estimated to be two billion tons per year globally, and is expected to increase to three billion tons by 2025 [1]. The energy consumption per capita is increasing due to the growing world population and usage of high technology products. Reduction of fossil energy sources, rapid rise in the energy price, pollution prevention targets, and sustainable solutions for recycling of animal manure and organic wastes raises the significance of the renewable energy all over the world and there is an utmost need of alternative fuels around the world. Waste management technologies such as pyrolysis, gasification and incineration are potential jeopardy to human health and causes air pollution. Among all such alternatives, bio fuel is considered to be the most eco-friendly, cost effective and better way of waste management. The use of biodegradable organic material not only helps in creating energy surplus but is also an effective way to cut off the over filling land sites burden and produces the fertilizer material with less pathogens [2].

Huge amount of MSW is produced daily in Pakistan. It is estimated that 54,888 tons/day solid waste is generated in Pakistan. Karachi, the metropolitan city generates around 7,000 to 8,000 tons/day of municipal solid waste out of which 60-65% waste is based on kitchen waste, fruits and vegetables and garden waste. (ESMAP, 2010). The performance of anaerobic digestion process is affected by various factors such as organic loading rate (OLR), hydraulic retention time (HRT), carbon to nitrogen ratio (C: N), feedstock characteristics [3]. C:N ratio is an important parameter since it represents the amount of organic carbon that is available for digestion. Nitrogen present in the feedstock helps in maintaining the pH by the formation of ammonia and provides an essential element for synthesis [4]. Thus, it is important that the proper amount of nitrogen is present in the feedstock, too little nitrogen can create nutrition limitation and too much nitrogen can make the process toxic [5]. The aims of this study were to optimize the C:N ratio for biogas production using BMP test and to characterize various feed for anaerobic digestion.

2 MATERIALS AND METHODOLOGY

2.1 Waste characteristics

The vegetable waste that includes tomato, potato, onion, eggplant and cabbage used in this study were collected from the vegetable market. The inoculum was fed for first 4 days taken from existing running anaerobic digester [6]. These waste were blended to feed in four different reactors having C: N ratio of 10, 15, 20 and 25 to determine the effect of C: N ratio on biogas production. The feedstock characteristics of different wastes is given below. The total solids were determined by heating the sample at 105°C for 24 hr in heating oven whereas, the volatile solids were determined by taking the residue taken from oven and heating it at 550°C for 2 hr in a muffle furnace.

Table 1. Approximate composition of waste used

Feed	% TS (Wet)	% VS (Dry)	C/N ratio[a]	% C[a]	% N[a]
Cow dung	70	80	20	48	2.4
Potato	20.3	90.9	28	42	1.5
Onion	28	88	15	39.75	2.65
Tomato	29.5	95.73	13	42.9	3.3
Eggplant	17.2	94.1	19	51.3	2.7
Cabbage	13.2	90.8	12	43.2	3.6

[a] The Carbon/Nitrogen Ratio [7]

To check the effect of C/N ratio on bio-methane production, different C/N ratio was formulated in 4 different reactors, as shown in table 2.

Table 2. Feeding formulation in different reactors

	Feeding material in wt %	**C/N**	**Cum. Biogas Volume (L)**
R1	100% Tomato or cabbage	10	196.5
R2	100% Onion	15	253.5
R3	100% eggplant	20	308.15
R4	85% potato + 15% onion	25	214.35

2.2 Experimental setup

The study was carried out in a semi-continuously pilot scale with a total volume of 19L. Fig.1 shows the experimental set-up. Reactor was fed from the pipe located at the top that ends just above the bottom of the reactor. Sampling valve was located at the side to collect the effluent from the reactor. The gas outlet pipe was connected with a water displacement tank to determine the biogas volume produced. The contents of the reactor were mixed with manual agitation 6 times a day for 2 min. The ambient temperature was 28-35°C throughout the study.

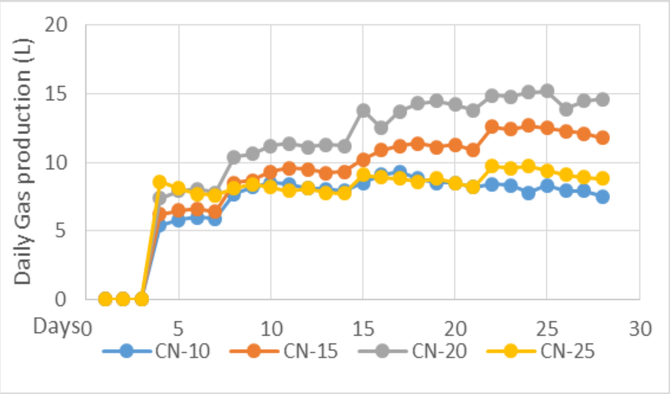

Figure 1. Bio-reactor with water displacement bottle

2.3 Anaerobic digester operation

Semi-continuous anaerobic digestion of vegetable waste was investigated under mesophilic condition with four different C: N ratios of 10, 15, 20 and 25. The OLR of 1, 2, 3 and 4 g VS/L.day was used for 1st, 2nd, 3rd and 4th week respectively for constant retention time of 20 days. Retention time was maintained by feeding 0.75L of substrate and removing 0.75L of effluent daily.

2.4 Analytical methods

The biogas produced by anaerobic digestion was measured on the daily basis by water displacement technique. The methane content of the gas was found by passing the gas through hermetically sealed water displacement aspirator bottle filled 5% NaOH solution (w/v) which scrub off CO2 and the rest was considered to be methane. Total solids (TS), volatile solids (VS), pH were determined according to the APHA Standard Methods [8].

3 RESULTS AND DISCUSSION

3.1 Biogas and methane production

The main objective of this study was to evaluate the performance of an anaerobic digestion process when operated with different C: N ratio feed. Therefore, process performance were noted in terms of biogas production daily. It was observed that most of the gas (60-70%) was produced within 6-7 hours after the point of feeding as the enzymatic activity was highest during that period. The figure below shows the biogas production daily from the four reactors. The average daily biogas production obtained from reactor 2 and 3, operating at C: N of 15 and 20 were 10.1 and 12.3 L/day respectively whereas the daily biogas production from reactor 1 and reactor 4 was found approximately 7.8 and 8.6 L/day respectively. It was observed that increasing the OLR increases the biogas production as more volatile solids will be available to the system for digestion. The overall highest cumulative biogas volume of 308 L was obtained at C: N of 20 for the study period of 28 days. The amount of biogas and its methane content is of significant parameter to evaluate the performance of digester. The higher % of carbon dioxide in biogas indicates that the acidifying micro-organisms conc. is more than the methanogenic bacteria which may lead to volatile fatty acids accumulation. The methane content in all four reactors ranged between 55-70% with highest methane content of 73% for C: N of 20.

Figure 2. Daily biogas production at different C:N ratio

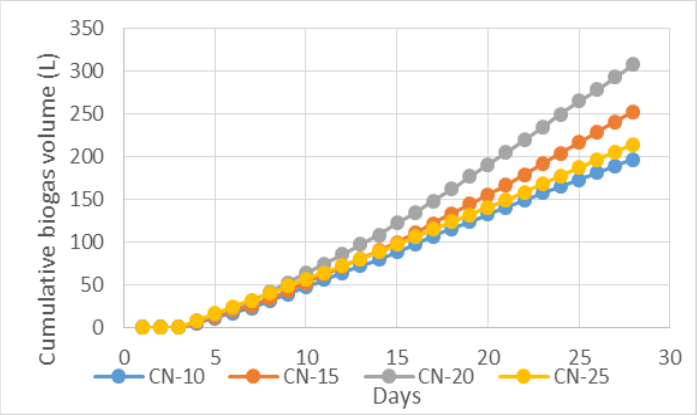

Figure 3. Cumulative biogas production at different C:N ratio

3.2 Effluent characteristics

The stability of the process was evaluated through analysis on the effluent from the digester beside biogas production and its composition. One of the most important parameter that affects biogas production is pH, which not only shows the stability of the process but also the buffering capacity of the system to neutralize the acid. The pH of effluent from the continuous digesters remained in the range of 6.8-7.1 for the OLR of 1 and 2 g VS/L.day, which indicates that the system was well buffered. When the loading rate was raised to 3 g VS/L.day, there was a reduction in pH to 6.3 which was not in the range favourable for methanogenic bacteria’s [4]. Since the methanogenic bacteria are more sensitive to pH than acidogenic and acetogenic bacteria, therefore this condition was overcome by adding 2M basic solution of NaOH.

After the completion of the retention time, COD concentration was evaluated through an experiment. It was observed that for C: N of 20 and 25, COD concentration was decreased significantly. The COD concentration for C: N 25 was less than C: N 15 but still the biogas production was higher for C: N of 15, this can be explained that there was higher hydrolysis but less methanogenesis for C: N of 25 because at higher C:N ratio, carbon load was greater which can inhibits enzymatic activity.

Table 3. COD Results

C/N ratio	COD (mg/L)
10	60800
15	52300
20	36300
25	45600

3.3 Process efficiency

For the purpose of evaluating the performance of the process, biogas yield and VS destruction were determined to assess the performance of the reactor for each C: N ratios. VS degradation value of 93% and 91% was achieved for C: N ratio of 20 and 25 respectively while operating the reactors with an OLR of 4g VS/L.day. Also biogas yield were examined for different C: N ratio. The highest biogas yield observed was 0.31 L biogas/gm VS for C: N ratio of 20 and 0.25 L biogas/gm VS for C: N ratio of 15 which was higher than early reported values of 0.26 L/gm VS [9]; 0.3 L/gmVS [10]. For this particular study, the best results were achieved with C: N ratio of 20 operating at 20 days HRT.

4 CONCLUSION

Anaerobic digestion is a promising technique for not only reducing the amount of biodegradable waste that contributes to the pollution but also it is an alternate source for producing energy from renewable resources. The study was conducted to optimize the C: N ratio for effective anaerobic digestion of MSW. The reactor showed optimum bio-methane production for C: N ratio of 20 with VS reduction of 93% and biogas yield of 0.31L/g VS. Therefore, prosperous execution of an anaerobic digestion process can lead to the effective utilization of the renewable resources.

ACKNOWLEDGEMENTS

We wish to thank to the Dr. Zuhaib Siddique, assistant professor of Environmental Engineering, NED University of Engineering and Technology for providing the laboratory facilities and sharing his expertise and knowledge about digestion process.

REFERENCES

1. *Waste Generation.* URBAN DEVELOPMENT SERIES – KNOWLEDGE PAPERS.
2. *Breif on Solid Waste Management in Pakistan.* Pak-EPA.
3. Azeem Khalid, M.A., Muzammil Anjum, Tariq Mahmood, Lorna Dawson, *The anaerobic digestion of solid organic waste.* Waste Management, 2011: p. 1737-1744.
4. H.Gerardi, M., *The microbiology of anaerobic digesters*. 2003, USA: John Wiley & sons.
5. *Biogas process for sustainable development...* FAO corporate document repository, (The effects of environaental fact ors on anaerobic digestion).
6. Zuhaib Siddiqui, N.J Horan, and Kofi Anaman, *Optimization of C:N Ratio for Co-Digested Processed Industrial Food Waste and Sewage Sludge using the BMP Test.* INTERNATIONAL JOURNAL OF CHEMICAL REACTOR ENGINEERING, 2011. **9**.
7. Jenkins, J., *The Humanure Hadbook.* **2nd**(The Carbon/Nitrogen ratio).
8. *Total, Fixed, and Volatile Solids in Water, Solids, and Biosolids*.
9. Nguyen, P.H.L., Kuruparan, Visvanathan, *Anaerobic digestion of municipal solid waste as a treatment prior to landfill.* Biosource Technlogy, 2007: p. 380-387.
10. Lidén, R.A.a.G., *Semi-continuous co-digestion of solid slaughterhouse waste, manure, and fruit and vegetable waste.* Renewable Energy, 2008. **33**: p. 726-734.

LIQUID FUEL PRODUCTION BY CO-PYROLYSIS OF WASTE COOKING OIL AND WASTE ENGINE OIL

Sajid Muhbat*, Tufail M., Aniqa Saleem, Kainat Amin Ismail Bora, Sheheryar Arshad, Hafiz Amin-Ur Rehman, Saud Hashmi, Awan Zahoor
Chemical Engineering Department, NED University of Engineering & Technology, Karachi, Pakistan

*Corresponding author. Tel.: +92-21-99261261; fax: +92-21-9261255
E-mail address: saudhashmi@neduet.edu.pk

ASBTRACT

Co-pyrolysis of waste cooking oil and waste engine oil was performed in a 1.856 liters stainless steel reactor at various temperatures ranging from 380-450 °C keeping fixed feed ratio of 1:1 by volume. It was found that the increasing pyrolysis temperature increases product yield. Pyrolytic product fuel mainly contains fraction in the boiling range of gasoline, kerosene, diesel and heavy fuel oil as indicated by ASTM D 86 distillation. Product fuel was also characterized by testing flash point, fire point, aniline point, viscosity, density, pour point and calorific value. The effect of pyrolysis temperature on product distribution i.e., liquid product yield, properties of the co-pyrolytic as well as the properties of distillate of ASTM D86 range from 165 ^{0}C to 365 ^{0}C is analyzed. Properties of co-pyrolytic oil and distillate are compared to that of petro-diesel and bio-diesel. It has been found that significant product yield is obtained at temperatures above 390 ^{0}C. Optimum yield of product and distillate is obtained at 420 ^{0}C. From Comparison with petro-diesel and bio-diesel, distillate obtained from 420 ^{0}C product has properties close enough to petro-diesel.

Keywords: Co-pyrolysis, waste cooking oil, waste engine oil, temperature, optimum yield, petro-diesel, Bio-diesel.

1 INTRODUCTION

Depleting resources of fossil fuels and their pollution behavior have driven the attention towards the recycling of waste oil sources. Waste engine oil is organic compound consists of hydrocarbon C_{15}-C_{50} alkanes and small amounts of alkenes, aromatics, solvent, heavy metal whereas waste cooking oil mainly contains saturated and unsaturated triglycerides of C_{16}-C_{22} fatty acids along with moisture, chlorophyll, and free fatty acid. Energy from wastes such as waste vegetable oil or waste cooking oil (WCO) and waste engine oil (WEO) that have a high heating value is also a solution to the environmental problems related to waste disposal.

Table 1 worldwide Statistics of canola oil

	Total	Major countries/ regions (in million tonnes/year)
Production	14.15	China 4.53, EU-15 3.68, India 1.60, Canada 1.30, Japan 0.93, Central Europe 0.62, Mexico 0.37, US 0.32, Pakistan 0.24, Bangladesh 0.15, Australia 0.15, other 0.25
Disappearance	14.28	China 4.59, EU-15 3.34, India 1.67, Japan 0.95, US 0.76, Central Europe 0.67, Canada 0.60, Mexico 0.42, Pakistan 0.26, former USSR 0.25, Others 0.77
Exports	1.65	Canada 0.79, EU-15 0.36, Hong Kong 0.17, US 0.12, Others 0.21
Imports	1.64	US 0.54, Hong Kong 0.26, China 0.13, Former USS 0.13, others 0.58

Table 2 Worldwide Production of lubricating oil

Region	Estimated Lubricant Market (2003) million metric tones
North America	8.9
Central and South America	3.2
Western Europe	5.1
Central/ Eastern Europe	4.9
Near/ Middle east	2.0
Africa	1.8
Asia Pacific	11.2
Total	41.1

Worldwide statistics of cooking oil is shown in **Table 1** [1]. Waste cooking oil is a potentially problematic stream, arises from many different sources including domestic, commercial and industrial, when disposed-off incorrectly. Whereas waste engine oil contains harmful solvents and heavy metals detrimental to environment.

From the viewpoint of waste-to- energy, WCO and WEO are considered to be as efficient and widely available feedstocks, apart from agricultural residue [2].

The volume of used cooking oil generated across the UK each year has been estimated to be 250 million liters [3] It could be converted to up to 225 million litres of WCO biodiesel per year.

In Pakistan, rapidly increasing fuel and energy prices are serious problems that needs to be resolved, as nation's growth are prosperity are directly linked to facilities it provides to citizens and provision of all such facilities requires energy at low cost. Worldwide statistics of lubricating oil (which includes engine oils as well as lubricants used for industrial purposes) are given in **Table 2** [4]. An "Unaccounted Used Oil Study" report made by British Columbia Used Oil Management Association (BCUOMA) indicates that waste oil collection is approximately 50% of oil consumed. It mainly comes from the collection of used engine oils. Out of this collectable amount of waste oil about 25 % ends up in dumping and land filling. Thus a maximum of 75% (on an average) of collectable waste oil is available for recycling.

2 EXPERIMENT

Co-pyrolysis is carried out in a semi-batch reactor provided with the residence time of 5 minutes at temperatures of 380° C, 390° C, 400° C, 410° C, 420° C, 430° C, 440° C, and 450° C using PID controller keeping the system at zero gauge pressure and using feed ratio of 1:1 for waste engine oil and waste canola oil by volume.

The cylindrical SS-316L pyrolysis reactor of capacity 1.856 L is used in this experiment. The reactor is provided with an electrical horizontal immersion heater of heating capacity of 2000 watts. Process of operating parameters are given in **Table 3.**

Table 3 Operating Parameters

Mode of reaction	Semi-batch
Capacity of Reactor	1.856 liters
Feed used	used cooking (canola) oil and engine oil of gasoline based engine
Total Volume of feed used	1400 ml
Feed Ratio	1:1 (By volume)
Heating device	electrical heater having variable power ranging from 1500-3000 watt
Temperature controller	PID controller
Voltage supplied	220 V
Control Variable	Current Supplied (in Amps)
Initial Current Supplied Till set point	11 amps
Process Variable	Reaction Temperature
Set Points	380° C, 390° C, 400° C, 410° C, 420° C, 430° C, 440° C, And 450° C
Residence time at operating Temperature	5 minutes
Nitrogen purge rate	25 lit/min.

2.1 Details of Experiment

2.1.1 Setting-Up the Apparatus

Flow diagram is shown in **Figure. 1** whereas experimental set-up is shown in Figure**. 2**

Table 4 Properties of Feed Mixture

Feed type	**Waste Canola oil and Waste engine oil**
Color	Dark Brown
Specific Gravity at 60 °F	0.891949
Kinematic Viscosity (cSt)	14
Flash Point	>100 °C
Calorific Value (kJ/g)	35.661

Available pilot setup consists of

1. Nitrogen Cylinder
2. Stainless steel Reactor
3. Condenser
4. Accumulator
5. Water tank
6. Centrifugal Pump

2.1.1.1 Preparation of Feed

Waste cooking oil contains small food and other dust particles (as well the engine oil). It is passed through suitable mesh size sieve to filter particles. 700mL of each raw material is measured using beaker and poured into the reactor ensuring that heater is completely immersed in the feed while reactor is left with suitable area for vapors to be produced during reaction. Properties of feed are listed in **Table 4.**

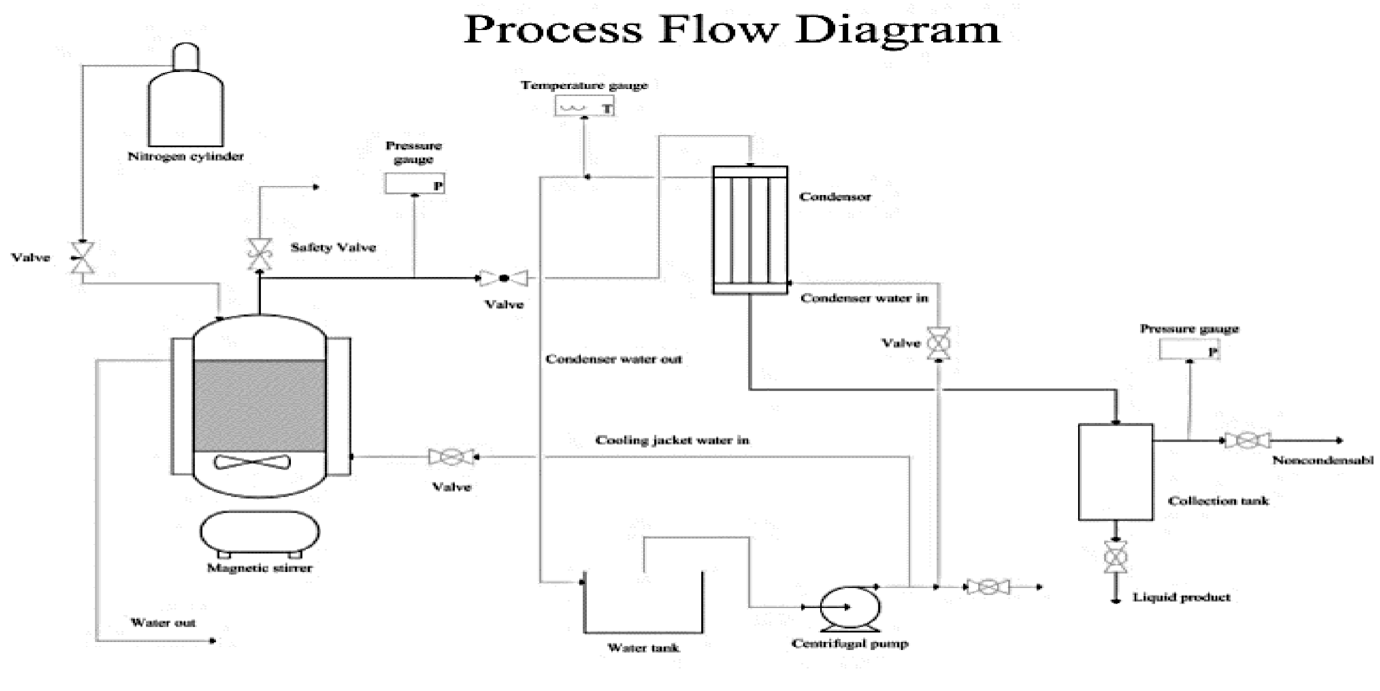

Figure 1 Process Flow Diagram

2.1.1.2 Process Control

The main operating parameter Temperature was automatically controlled using PID controller. Operating temperature was given as set value, once the desired temperature was reached PID controller automatically adjusted the heating rate to maintain the temperature. The required value of temperature was maintained for residence time of 5 minutes and then heater was manually shut off.

2.1.1.3 Experimental Observations

Feed is charged into the reactor and after tightly closing the reactor, system is set at zero gauge pressure, and purged with nitrogen at gas flow rate of 25 lit/min for about 30 min. Operating parameters for the experiment are shown in **Table 3**.

Initial heating rate is 30°C/min (variable for different experiments with +- 5 tolerance) and decreases with proceeding time and increasing temperature.

Figure 2 Complete Assembly of pilot plant

Condenser is turned on at 150 °C and condensed moisture content of oil is collected through accumulator for the sake of purity of the product.

At about 270° C some incondensable gases are observed to leave the system as gas flowmeter shows some variable reading and bubbles are produced in water container.

Amount of current is increased from 10 to 11 Amp to maintain constant heating rate during first stage of experiment. As liquid is heated to the higher temperature, heating demand is increased due to increased specific heat capacities at increasing temperatures.

Product is collected through accumulator or product collection vessel. Amount of the condensate obtained was different for different observations as shown in **Figure 3.**

After the temperature of the reactor has been dropped significantly to about 40° C, residue left in the reactor is removed and measured.

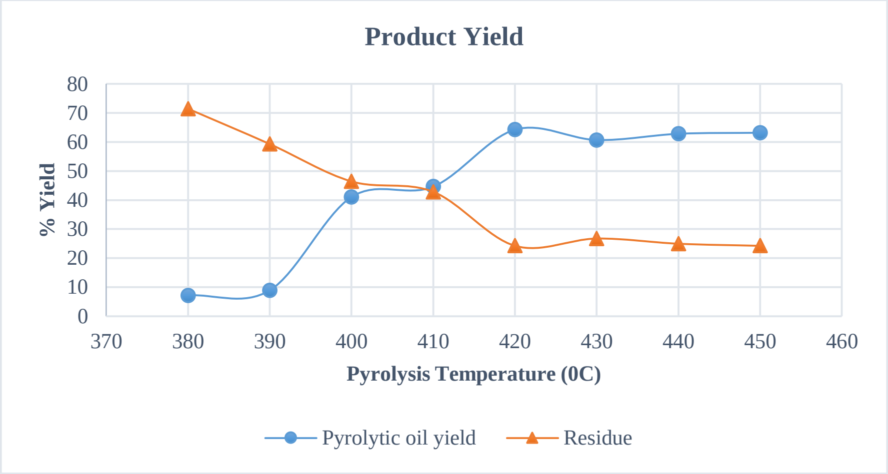

Figure 3 Variation of yield of liquid product and residue with pyrolysis temperature

Table 5 Properties of Pyrolytic oils obtained at different pyrolysis temperatures and their comparison with petroleum diesel and bio-diesel

Sample Temp (°C)	**Testing Method**	**380**	**390**	**400**	**410**	**420**	**430**	**440**	**450**	**Diesel**	**Bio diesel**
calorific value (KJ/kg)	ASTM D240			40550	41906	39409	43061	41189	41094	44800	41550
Flash point (°C)	ASTM D92	>100	>100	78	72	66	62	58	46	52 min	93.0 min
Kinematic viscosity of sample v (mm^2/sec)	ASTM D445	21.49	13.22	11.02	8.27	7.16	5.79	5.79	5.51	1.9-4.1	1.9-6.0
Specific gravity of sample at (60°F)	ASTM D1298	0.871	0.83	0.8443	0.8321	0.8382	0.8292	0.8227	0.8120	0.802-0.876	0.86-0.90

3 RESULTS AND DISCUSSIONS

3.1 Effect of pyrolysis temperature

3.1.1 Yield of liquid product

Yield of liquid product was found to increase with temperature up to 420˚ C where condensable gases up to 450˚ C where it reached the value of 800 ml. Yield of gaseous product was approximated from given liquid fuel, residue and moisture content value. Loss of liquid fuel within the system and during collection is incorporated with this value. It is found to decrease initially up to 420˚ C where it reached a minimum value of 85 ml then increased afterwards and ultimately reached the value of 175 ml at 450˚ C. Amount of residue was found to decrease up to 420˚ C where it has a minimum value of 340 ml and afterwards it slightly increased and reached a value of 350 ml at 450˚ Maximum liquid product was obtained i.e. 900 ml afterwards yield of liquid product was found to decrease at the expense of non- condensable gases.

Important fuel properties such as density, specific gravity, viscosity, flash & fire points, aniline point, pour point, calorific value and distillation characteristics etc of the products are analyzed and other properties are evaluated mathematically. Properties of distillate of ASTM D86 range from 165 ^{0}C to 365 ^{0}C are also examined and compared with that of petro- and bio-diesel.

Table 6 Properties of distillates oils obtained by ASTM D86 from products of different pyrolysis temperatures and their comparison with petroleum diesel and bio-diesel

Distillate of Temp (°C)	**Testing Method**	**400**	**410**	**420**	**430**	**440**	**450**	**Diesel**	**Bio diesel**
calorific value (KJ/kg)	ASTM D240	42621	41363	42417	41316	42605	40657	44800	41550
Aniline point (°F)	ASTM D611	129.2	136.4	136.4	136.4	123.8	129.2	160	NA
Cetane index (D.I*0.72+10)		41.8057	43.5782	41.5089	47.5335	46.1291	44	40 min (40-55)	47 min (47-65)
Flash point (°C)	ASTM D92	48	38	44	38	50	38	52 min	93.0 min
Kinematic viscosity of sample v (mm^2/sec)	ASTM D445	2.2	2.2	2.76	2.76	2.2	1.65	1.9-4.1	1.9-6.0
Pour Point (°C)	ASTM D97	-2	-1	-1	2	1	3	3 (winter)	-7 to -9 (rapeseed oil)
Specific gravity of sample at (60°F)	ASTM D1298	0.854	0.854	0.865	0.83373	0.82252	0.83	0.802-0.876	0.86-0.90

3.1.2 Distillation D86

Product of 380 ^{0}C and 390 ^{0}C were in small amount and have highest density and viscosity values that are unacceptable so the ASTM D86 was not performed for these two products. It can be seen in **Table 5** that the minimum yield of distillate is obtained from the product of 400 ^{0}C i.e., 45 % and highest yield of distillate i.e., 82.5 % is obtained from the product of 420 ^{0}C. Yields obtained in diesel range are overall sufficiently very high. Thus, we can say that a good quality product has been formed from co-pyrolysis.

3.1.3 Properties of products and their distillates

3.1.3.1 Specific Gravity

Specific gravity of pyrolytic oil ranges from 0.87 to .80 at 60 ^{0}F. Specific gravity of the product seems to be decreasing with increasing operating temperature at given pressure. Specific gravity of distillate ranges from 0.86 to .81 at 60 ^{0}F. Specific gravity seems to follow no certain trend with increasing operating temperature at given pressure

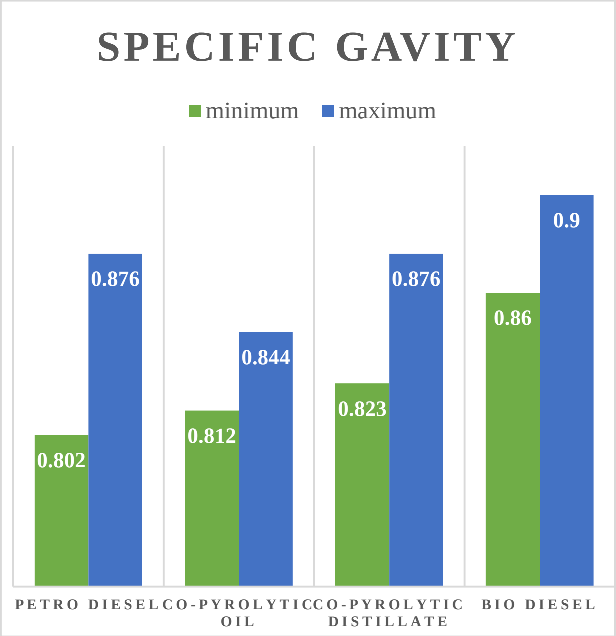

Figure 4 Comparison of specific gravities (at 60 ^{o}C) of co-pyrolytic oils and their distillates with petro diesel and bio-diesel

Specific gravity values of product and distillate are in the range of petro-diesel and bio-diesel as well. As shown in **Figure 4.**

Table 7 ASTM Distillation of Pyrolitic Oil

	ASTM D86 Temperature (^{0}C)						
Vol%	400	410	420	430	440	450	Diesel
0	100	100	98	86	90	74	183
10	318	270	240	150	230	196	224
30	330	350	278	300	334	270	256
50	360	344	320	332	340	326	281
70	475.055*	340	312	340	328	336	310
90	558.44*	436.702*	375.974*	435.181*	413*	421.002*	355
95	579.2925*	451.016*	387.282*	452.28*	426.29*	436.936*	374
100	600.14*	465.33*	398.59*	469.38*	439.56*	452.87*	404

3.1.3.2 Viscosity

Kinematic viscosity of pyrolytic oil ranges from 2.15*E-05 m^2/s (21.5 cSt) to 5.51E-06 (5.51 cSt) m^2/s at 33^{0}C and 1 atm.

Kinematic viscosity of product seems to be decreasing with increasing operating temperature at given pressure Kinematic viscosity of pyrolytic oil ranges from 2.7*E-06 m^2/s (2 cSt) to 1.65E-06 (1.65 cSt) m^2/s at 33^{0}C and 1 atm. Kinematic viscosity of the distillate retains its value around 2 cSt.

Viscosity of products is not in the range of either diesel whereas viscosity of distillates is nearly in the range of petro-diesel **Figure 5.**

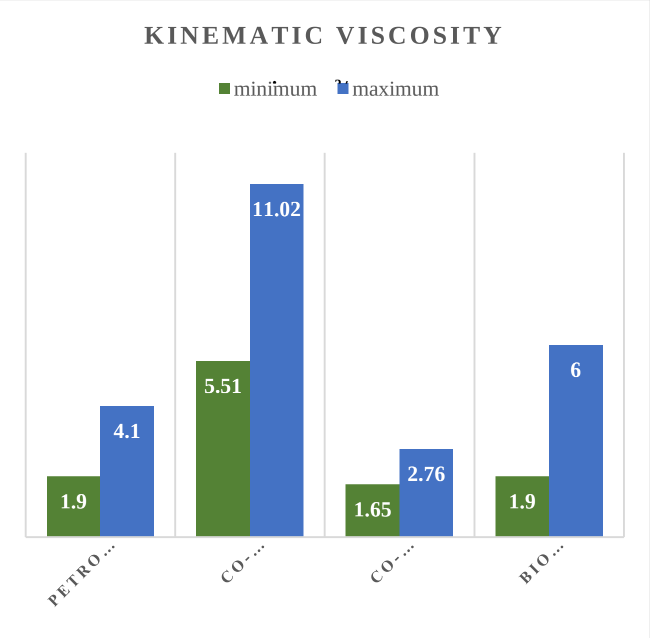

Figure 5 Comparison of kinematic viscosities of co-pyrolytic oils and their distillates with petro diesel and bio-diesel

3.1.3.3 Flash and Fire Points

Flash and fire point of product decrease with increasing co-pyrolysis temperature showing the formation of lighter (flammable) components. Flash and fire points of distillate seem to follow no specific trend but the values show that the lightest components are obtained in 450 ^{0}C product. **Figure 6**

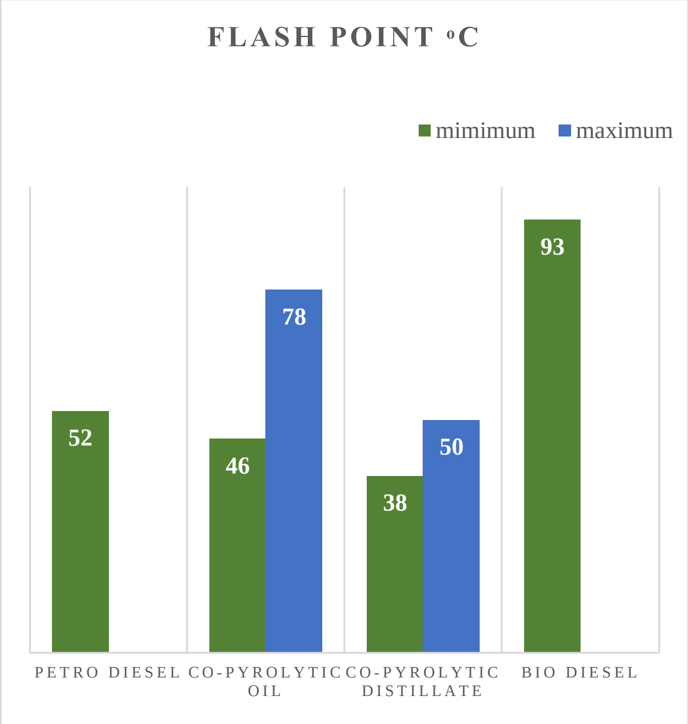

Figure 6 Comparison of flash points of co-pyrolytic oils and their distillates with petro diesel and bio-diesel

Flash and fire points of product (except products obtained at 380° C and 390° C) and distillate are close enough to petro-diesel flash and fire points **Table 7**

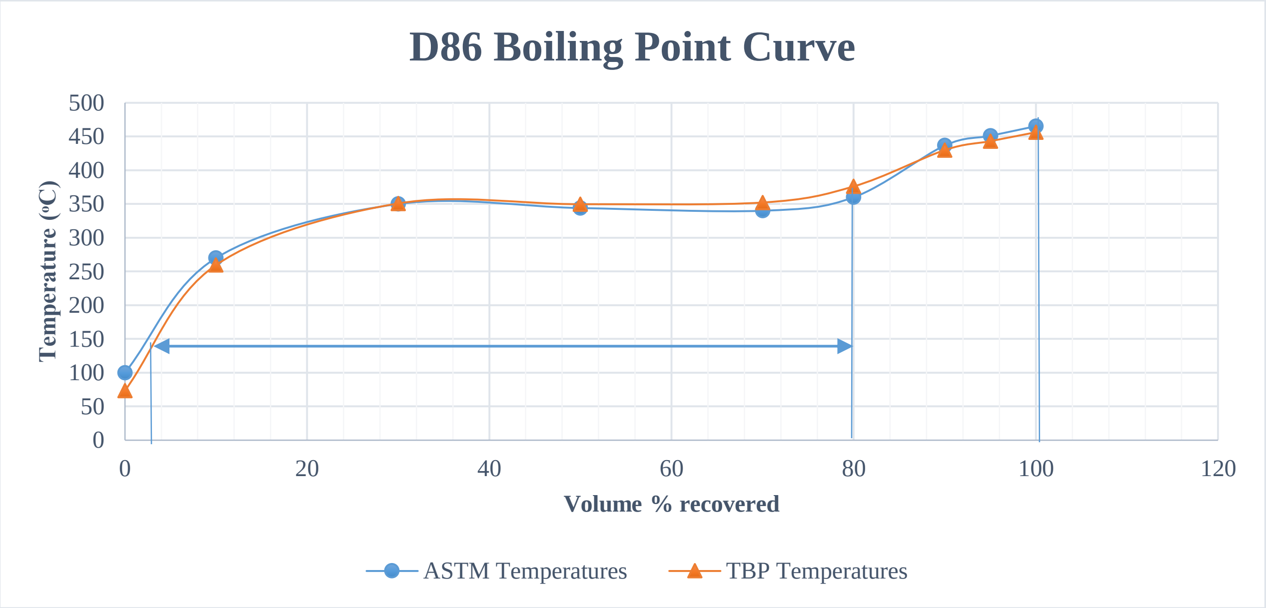

Figure 7 ASTM and TBP curve of co-pyrolytic oil obtained at 420 ºC

3.1.3.4 Cetane Index

Cetane index is dependent on aniline point as well as the oxygen content in the fuel. Higher cetane index till 56 means ignition quality of a fuel is good

Cetane and diesel index values of distillate are in the range of petro-diesel and bio-diesel as well **Figure 8.**

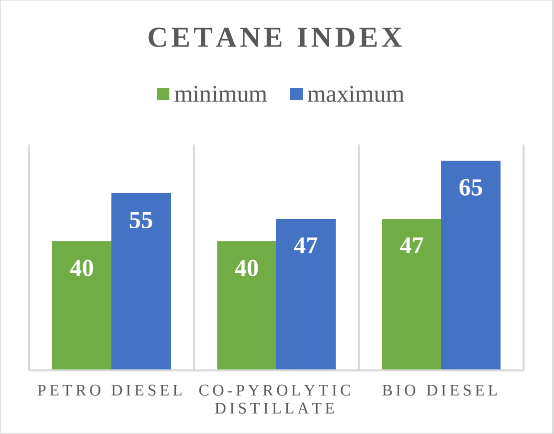

Figure 8 Comparison of Cetane index of co-pyrolytic oils and their distillates with petro diesel and bio-diesel

3.1.3.5 Pour Point

Pour point of distillate ranges from 3^0C to -2^0C with no specific trend, indicating liquid fuel is satisfactory for winter usage. Since feed contains unsaturated glycerides, the pour point is comparatively lower.

Pour point values are lower as compared to petro-diesel but higher in Comparison to bio-diesel **Figure 9.**

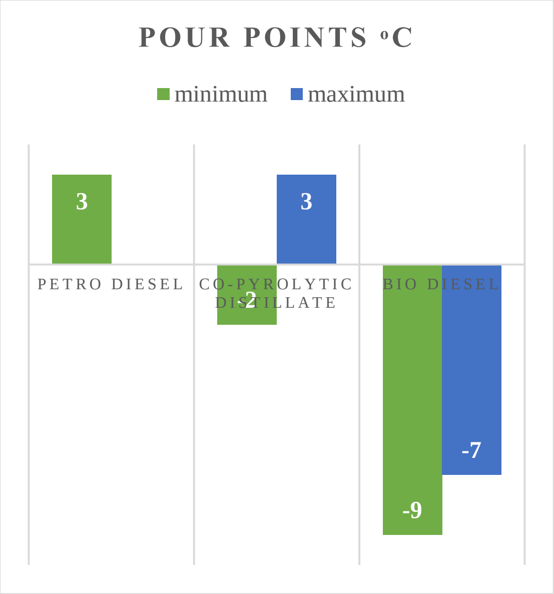

Figure 9 Comparison of Pour Points of co-pyrolytic oils and their distillates with petro diesel and bio-diesel

3.1.3.6 Calorific values

Higher calorific value means lower fuel consumption rate. Maximum calorific value is of 430 ^{0}C product that is 43.061 kJ/g

Calorific values are higher as compared to bio-diesel but are lower in comparison to petro-diesel **Figure 10.**

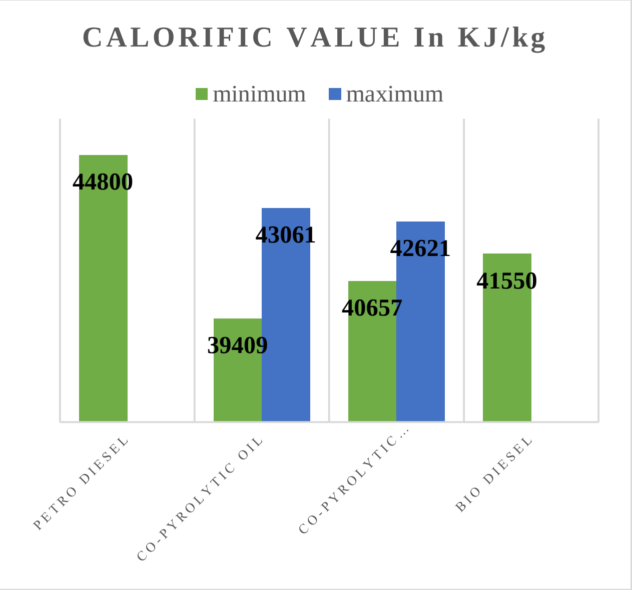

Figure 10 Comparison of calorific values of co-pyrolytic oils and their distillates with petro diesel and bio-diesel

3.1.4 Comparison with petro-diesel and bio-diesels

Fractions are formed and below 450° C predominantly diesel.

Table 5 and **Table 6** [5], [6], respectively show comparison of different properties of co-pyrolytic oil and distillate with petro-diesel and bio-diesel. **Table 7** [7], shows ASTM D 86 comparison of co-pyrolytic oil with diesel.

Product of 380° C and 390° C have highest density and viscosity values that are unacceptable Distillate obtained from 450° C product has undesirable properties as compared to any type of diesel but is much close to gasoline and other lighter compounds properties. Thus, we can conclude at very high temperatures smaller

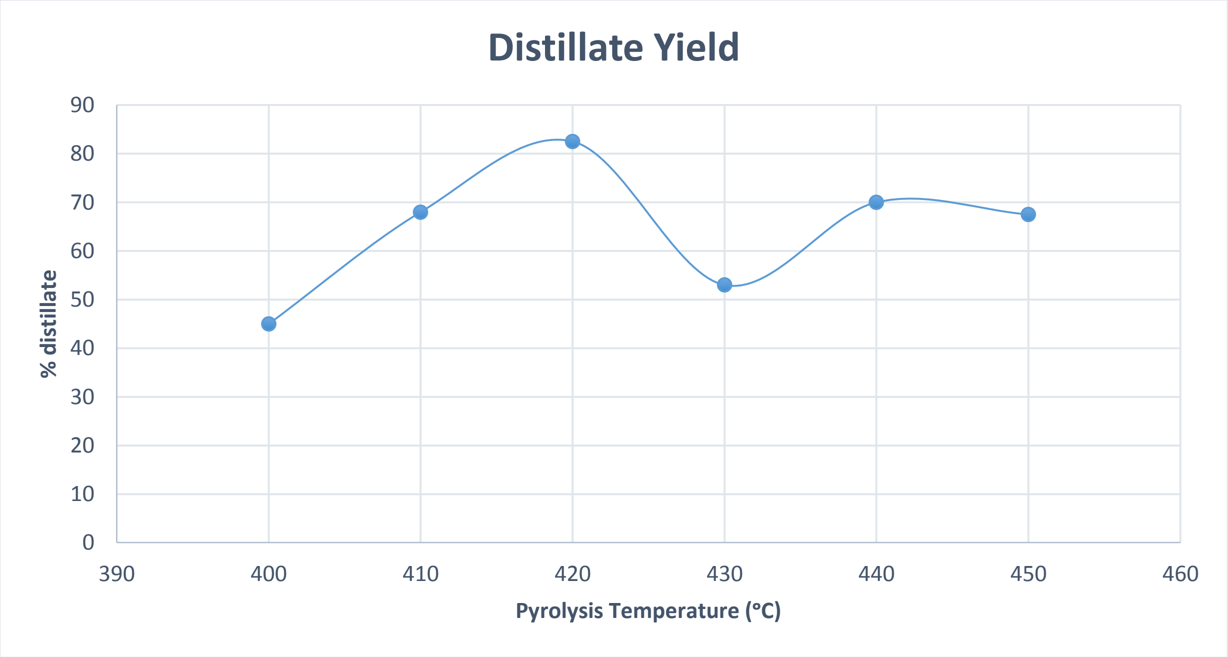

Figure 11 Variation of yield of distillate with pyrolysis temperature

ASTM D86 curves of co-pyrolytic oils are compared with co-pyrolytic oil in **Figure 12,** which show that product obtained at 420° C has very similar boiling point distribution to that of petro-diesel

4 CONCLUSIONS

Significant Product yield is obtained at temperatures above 390° C. Optimum yield of product and distillate is obtained at 420° C. Maximum calorific value of product is obtained at 430 ^{0} C From Comparison Table 5, it can be observed that mostly properties obtained for different pyrolysis temperature are in the range of petro-diesel only. Distillate obtained from 420° C product has properties close enough to petro-diesel but not to biodiesel.

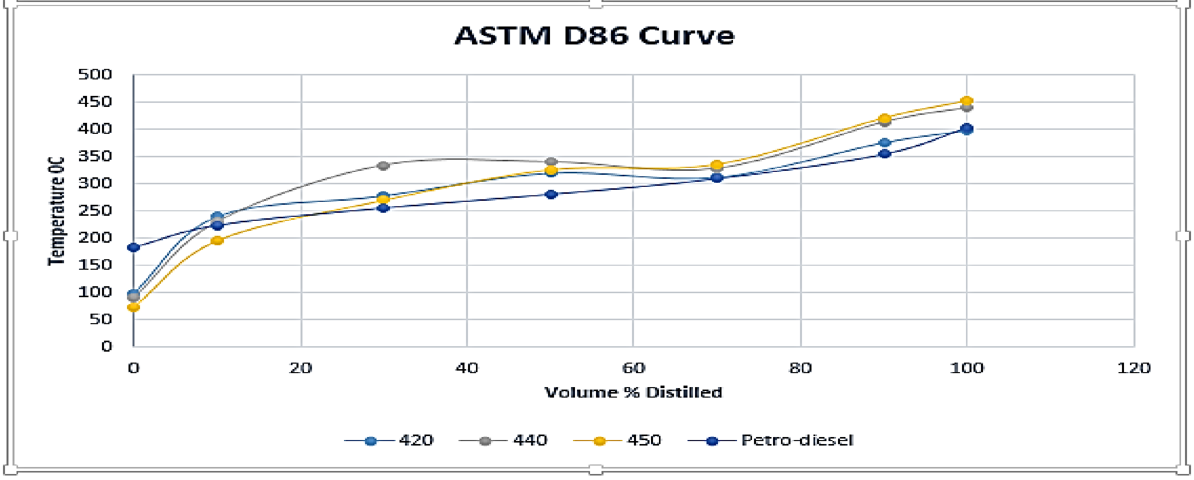

Figure 12 Comparison of ASTM d86 curve of co-pyrolytic oils obtained at different pyrolysis temperatures with petro diesel

REFERENCES

[1] Frank. D Gunstone. Vegetable oils in food technology their composition properties and uses. p. 6-9

[2] Ampaitepin Singhabhandhu, Tetsuo Tezuka. Prospective framework for collection and exploitation of waste cooking oil as feedstock for energy conversion

[3] Gemma Toop, Sacha Alberici. Trends in the UCO market (11 November 2013). Available from https://www.gov.uk/

[2] United Nations Environment Programme “Compendium of Recycling and Destruction Technologies for Waste Oils” p. 20-21

[5] ASTM D975, Standard Specification for Diesel Fuel Oils. 2007

[6] JAMES G. SPEIGHT. Handbook of Petroleum Product Analysis

[7] According to OGRA product distribution

SYNTHESIS OF IRON OXIDE MAGNETIC NANOPARTICLE BY SOL-GEL METHOD AND THEIR CHARACTERIZATION

Maria Arshad*[1], Humair Ahmed Siddiqui[2], Dr. Saqib Anjum[1], Dr. Ashraf Ali[3]
[1]Physics Department, NED University of Engineering & Technology, Karachi.
[2]Material Engineering Department, NED University of Engineering & Technology, Karachi.
[3]Ghulam Ishaq Khan Institute of Engineering Sciences and Technology, Topi, KPK

Corresponding Author: Maria Arshad, E-mail address: maria_rshad90@outlook.com

ABSTRACT

Magnetic iron oxide nanoparticles have a unique importance because of its application, specifically in the range of medical sciences. Magnetic iron oxide Fe_2O_3 nanoparticles have been synthesized by sol gel method without the use of any surfactant annealing at the temperature of 400 ℃ without vacuum furnace for 2 hr. The Fe_2O_3can easily be synthesized by using Sol-gel method because it is the most suitable method to synthesis metal oxide nanoparticle due to low reaction temperature, high purity and good homogeneity. In this method $FeCl_3.6H_2O$ used as a precursor ethanol and propylene oxide also used. The particle size, morphology and composition have been characterized by SEM scanning electron microscope (JSM 6380A) set up with an X-ray energy-dispersive spectrometer(EDS) and X-ray diffraction (XRD) patterns showed the characteristic peaks that indicate the phase of iron oxide. The average particle sizes obtained from a Scanning electron microscope in the range of 43.5nm-73.6nm and X-ray diffraction results indicate that magnetic nanoparticle was in the range of 8nm to 15nm formed.

Keywords: Sol-Gel; Surfactant;Nanotechnology; Iron Oxide; Magnetic.

1-INTRODUCTION:

Now-a-day most of the work in the whole world in the field of research is being done on nanotechnology. When we step in the world of nano then we realized that chemical physical and biological properties of nanomaterials are totally different then bulk material. Out of all magnetic nanoparticles are very important nanoparticle reason behind the importance and increasing demand in today's life is their remarkable properties and other reason its lots of application and it is prove by its application that it is an essential and useful part of science and technology. Among different magnetic nano-material iron oxide is widely used magnetic nanoparticle. Iron oxide nanoparticles are particles with diameters between 1 and 100 nanometers because of its unique application, specifically in the field of medical sciences many researchers have work on iron oxide particles like data storage, recording (1), magnetic ferrofluids [1, 2].

Due to the iron oxide outstanding magnetic properties the most important factor that affects iron oxide nanoparticles biomedical performance is the magnetic properties of the nanoparticles, which is change when the particles size, shape, oxidation state was change. There are also many application of iron oxide in the field of medical science cancer therapy and cancer detection and also used in MRI [3, 4].Now a days the demand of iron oxide nanoparticle increases due to their special properties most common types of iron oxide in nature is magnetite $Fe_3\,O_4$,hematite $(\alpha - Fe_2O_3)$ and $\gamma - Fe_2\ O_3$(meghemitite)[5,6].

There are different methods of synthesis metal oxide nanoparticle like Sol gel, hydrothermal, sonochemical, thermal decomposition [6], coprecipitation [7] and electrochemical. Among all this method sol gel method is very promising method because it is the most suitable method to synthesis metal oxide nanoparticle due to low reaction temperature, high purity and good homogeneity [8].

In this paper magnetic nanoparticle have been successfully synthesis by sol gel method using inexpensive $FeCl_3.6H_2O$ and ethanol with annealing at 400℃.Sol gel method consist of two step In the first step solution was formed, then we convert that solution in to gel.

2-EXPERIMENTAL

2.1-Materials:

Ferric chloride ($FeCl_3$.$6H_2O$), Propylene oxide and Ethanol was used in experiment and deionized water was also used in complete practical as per requirement All chemical was buy from Fanara Scientific (supplies) Co Karachi. The chemical were of Lab grade quality and were used without further purification.

2.2-Synthesis of Magnetic Iron OxideNanoparticle:

Iron oxide nanoparticles were prepared by sol gel method.Following steps was performed. Initially, the solution of ferric chloride ($FeCl_3.6H_2O$) and Ethanol was prepared, by dissolving 5.4 gm of ferric chloride ($FeCl_3.6H_2O$)in 20 ml of ethanol and then vigorously stirred for few minutes then red yellow colour solution was obtained , then 14 ml of propylene oxide was added, in that solution, after the addition of propylene oxide, solution changed its colour, within 60 second solution was transform in to gel and realised large amount of heat energy (gel changed its colour in dark red brown). The gel was aged for 3hr. Then after ageing gel was dried in oven at 60℃ for 4 hr to obtained a Xerogel. This xerogel was annealed in furnace for 2 hr at 400℃. At this temperature other impurities was removed from the precursor.

2.3- Characterization:

Initially Composition of sample was characterized by XRF (Inovex system Model No a-8000 U.S.A), which was done to initially confirm the presence of Iron. For identification of Compound and phase structure X-ray diffraction (XPERT-PRO) with Cu Kα Radiation ($\lambda =$ 1.54060)was used in the range from 2θ =10.0050 to 2θ = 79.9950. Finally the particle Size, morphology and composition have been Characterized by SEM scanning electron Microscope Jeol, Japan Model no (JSM 6380A) set up With an X-ray energy-dispersive Spectrometer(EDS) Jeol, Japan model number (Ex-54175 JMU) Coater: Joel, Japan Model number:JFC-1500 Target Gold sample were coated up to 300 ^{0} A

3- RESULTS ANDDISCUSSION:

3.1Characterization of Magnetic Nanoparticle

3.1.1-XRF Analysis of iron oxide:

XRF was the initial test of iron oxide sample which gave as the information about the composition of sample that was prepared by sol gel method annealed at 400°CXRF result shown in the table 1

Table 1: Composition of Synthesis iron oxide by XRF

Element	Ratio
Fe	94.49
C	4.79
Mn	0.76

3.1.2-XRD RESULT OF IRON OXIDE:

Fig 1, is the XRD pattern of iron oxide synthesised at 400℃.XRD result indicate that γ -Fe_2O_3Maghemite nanoparticles were prepared.

The first measure peak observed at $2\theta =$ 33.151570 , and second major peak obtained at $2\theta = 35.61279$ and others peaks at 49.496170, 54.074410, 62.481640. The full-width half-maximum (FWHM) at the first major peak is β=0.944640(FWHM) of second major peak is: $\beta =$ 0.629760 and at other peaks 0.944640, 0.944640, 0.629760.Particle size was calculated by using Debye-Scherer formula from fig-1

$$D=\frac{0.9\lambda}{\beta\cos\theta}$$

In this formula λ is the wave length of X-Ray (0.154060 nm), 'β' is FWHM (full width at half maximum),'θ' is the diffraction angle and 'D' is particle diameter size.

1) 2θ = 33.151570

β=0.944640x 3.14 / 180 = 0.016489 radians

$$D=\frac{0.9(0.154060)}{(.016489)\cos 16.57578}=\frac{0.138654}{0.015803}$$

D = 8nm

2) 2θ = 38.473850

β=0.629760 x 3.14 / 180 = 0.01098 radians

$$D=\frac{0.9(0.154060)}{(.01098)\cos 19.23692}=\frac{0.138654}{0.010366}$$

D = 13nm

3) 2θ =49.496170

β=0.944640 x 3.14 / 180 = 0.01647 radians

$$D=\frac{0.9(0.154060)}{(0.01647)\cos 24.74808}=\frac{0.138654}{0.014957}$$

D = 9nm

4) 2θ = 54.074410

β=0.944640 x 3.14 / 180 = 0.01647 radians

$$D=\frac{0.9(0.154060)}{(0.01647)\cos 27.0372}=\frac{0.138654}{0.014670}$$

D = 9nm

5) 2θ = 62.481640

β=0.629760x 3.14 / 180 = 0.01099 radians

$$D=\frac{0.9(0.154060)}{(0.01099)\cos 31.24082}=\frac{0.138654}{0.009396}$$

D = 8nm

Particle size from first major peak is 8nm. Particle size that is obtained from Debye-Scherer formula indicates that particle formed between the ranges of 8nm to 15nm.

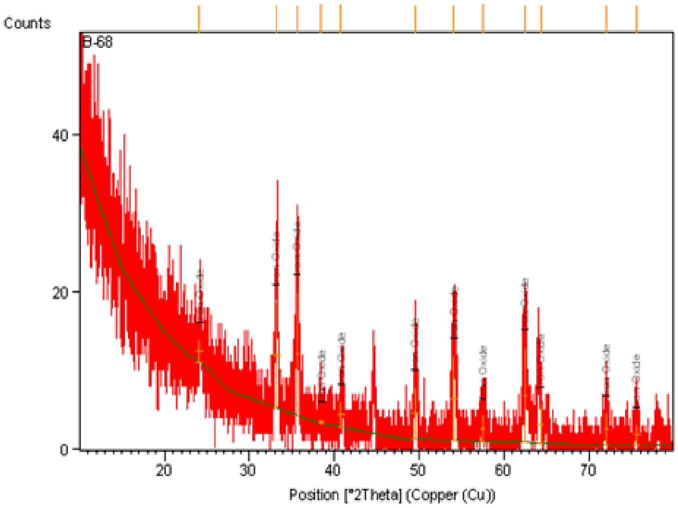

Fig 1.X-Ray diffraction pattern of Fe_2O_3 nanoparticle Xerogel annealed at 400°C without vacuum

3.1.3-SEM analysis of Iron Oxide Nanoparticle:

Scanning electron microscope (SEM) was used to analysis the morphology, size and composition of magnetic iron oxide nanoparticle synthesis by sol gel method. Fig 2 and 3 indicated that particle was formed in the range of 43.5nm to 73.6nm and selected area in the Fig 4 showed the composition of iron oxide magnetic nanoparticle. Result of EDX indicate that Fe is the 1s major element and 2nd major element is oxygen complete result of EDX show in the table 2.

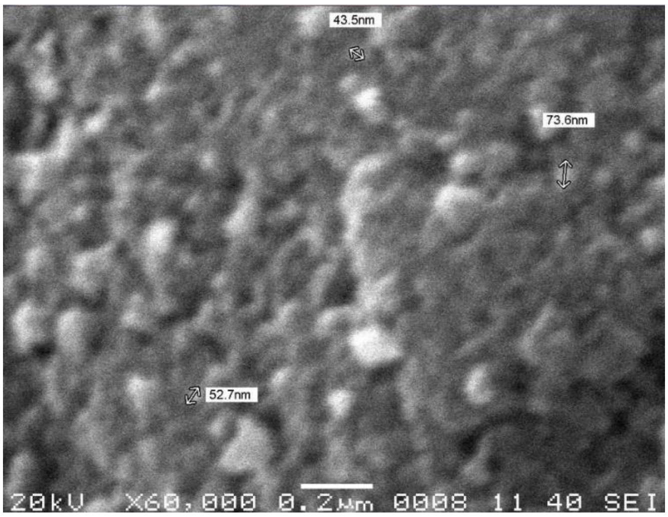

Fig 2: SEM result iron oxide nano size particles

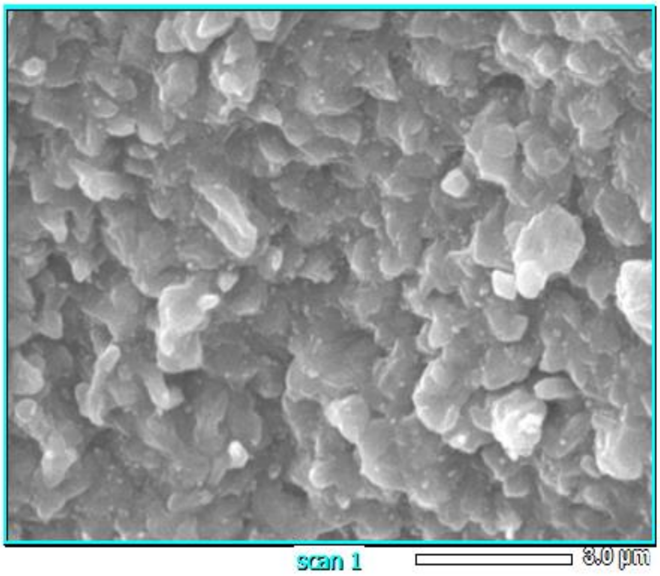

Fig 3: SEM of Iron Oxide Particles

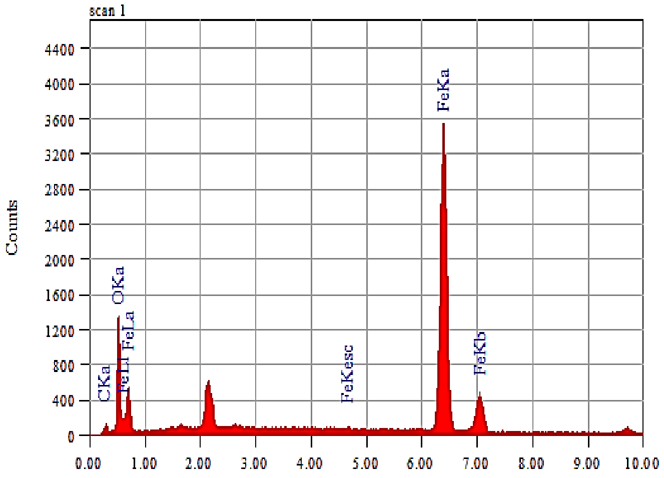

Fig 4: EDS result of Magnetite Particles

FESEM micrographs image of iron oxide nanoparticle xerogel annealed without vacuum at 400℃ and EDS results of magnetite (Table 2).

Table 2: Elemental Composition of Magentite

Element	Kev	Mass	Error	At%
C	0.277	3.43	0.15	10.74
O	0.525	14.35	0.11	33.79
Fe	6.398	82.23	0.31	55.47
Total		100.00		100.00

CONCLUSION:

In short Fe_2O_3 have been prepared by the sol gel method annealing at 400℃ at room temperature without the use of surfactant so there are the chances of agglomeration .Sol gel method offers have much advantage over other method for the preparation of iron oxide nanoparticle.The sol gel method is economical method and particle formed by this method are within the range of nano size and this method required low reaction temperature.XRD result indicate that the prepared magnetic nanoparticle were iron oxide. From XRD and SEM image particle size was calculated.The particle shape was almost a sphere. EDX result clearly indicates the element of magnetic iron oxide nanoparticles.

ACKNOWLEDGEMENT:

Author like to thanks Departmental chairpersons of Materials and Physics department of NED University.

REFERENCES:

[1] S.K. Sahoo 1,*, K. Agarwal 2, A.K. Singh3, B.G. Polke 1 and K.C. Raha “Characterization of γ- and α-Fe2O3 nano powders synthesized by emulsionprecipitation-calcination route and rheological behaviour of α-Fe2O3” International Journal of Engineering, Science and TechnologyVol. 2, No. 8, 118-126,2010

[2] C. Scherer* and A. M. Figueiredo Neto**Brazilian Journal of Physics, vol. 35, no. 3A, September, 2005

[3] R. Hiergeist, W. Andrä, N. Buske, R. Hergt, I. Hilger, U. Richter, and W. Kaiser, “Application of magnetite ferrofluids for hyperthermia,” *J.Magn. Magn. Mater,* vol. 201, 420–422, 1999.

[4] Xiang-Hang Reng,Xinei Qian,,Hui Mao, Andrew Y Wang, Zhuo Chen and Dong M Shin” International journal of Nanomedicine” 311-321, 2008

[5] H. Xu, T. Song, X. Bao, and L. Hu, “Site-directed research of magnetic nanoparticles in magnetic drug targeting,” *J. Magn. Magn. Mater.*, vol. 293, 514–519, 2005.

[6] Amyn S. Teja, Pei-Yoong Koh “Synthesis, properties, and applications of magnetic iron oxide nanoparticles”Elsevier page no 22-45

[7] Wei Wu, Quanguo He, Changzhong Jiang “Magnetic Iron Oxide Nanoparticles: Synthesis and SurfaceFunctionalization Strategies” nanoscale research letters, vol 3,2008

[8] Oznur Karaagac, Hakan Kockar, Seda Beyaz, and Taner Tanrisever “A Simple Way to Synthesize Superparamagnetic Iron Oxide Nanoparticles in Air Atmosphere” Transactions of magnetic,vol 46,2010

[9] Jing Xu, Haibin Yang, Wuyou Fu, Kai Du, Yongming Sui, Jiuju Chen,Yi Zeng, Minghui Li, Guangtian Zou “Preparation and magnetic properties of magnetite nanoparticles by sol–gel method” Journal of Magnetism and Magnetic Materials 309,307–311,2009

SYNTHESIS AND RHEOLOGY OF COAL-WATER SLURRY FOR USED AS LIQUID FUEL

Aliya Ahrar[1], Nadia Khan[2], Awan Zahoor[3], Saud Hashmi[4], Bisma Sohail, Fahad Aalam, Kanza And Abdul Mateen*

[1]Chemical Engineering Department, NED University of Engineering & Technology, Karachi, Pakistan
[2]Polymer and Petrochemical Engineering Department, NED University of Engineering & Technology, Karachi, Pakistan
[3]Chemical Engineering Department, NED University of Engineering & Technology, Karachi, Pakistan
[4,*]Chemical Engineering Department, NED University of Engineering & Technology, Karachi, Pakistan

*Corresponding author. Tel.: +92-03408588230; 99261261-2649
E-mail address: aliaahrar@neduet.edu.pk

ABSTRACT

Coal water slurry is an attractive alternative fuel to oil due to its lower cost and similarity to oil with respect to transportation and handling. Coal water slurry is a mixture of pulverized coal, demineralized water and additives. In this paper rheology of coal water slurry is studied with coal loading 40-60%.In the rheological study samples are made with different additives Triton X-100, STPP.The experimental results showed that for a constant coal loading viscosity decreases as the shear rate increases for both additives. STPP has high viscosity at low shear. This rheological behaviour is discussed with the help of power law model which shows that CWS exhibits pseudo plastic (shear thinning) behaviour. Another factor that influence the viscosity of coal water slurry is particle size distribution, In this paper it is discussed that for bimodal viscosity is lower than random model which implies that bimodal has more potential at the specified conditions.

Keywords: coal slurry, rheology, particle size distribution, Stabilizer, dispersant.

1 INTRODUCTION

In present time where resources are limited and needs are unlimited, the foremost technical challenge is to competently utilize a fuel for power generation. Since 2007, Pakistan is going through a critical energy crisis due to lack of availability of affordable fuel Pakistanis highly dependent on Furnace Oil (FO)[5]. In recent years, increased interest has been developed in utilization of other native fuels such as coal, which is cheap and widely available in Pakistan. At present; Pakistan is the 6th coal-rich nation of the world. Moreover, the coal reserves of Pakistan are appropriate for power generation and it is estimated that more than 100,000 MW of electricity can be generated for the next 30 years at a very low cost if these resources are properly exploited.

However, it is heart-breaking that, this blessing remains unutilized and unexploited. In Pakistan only 0.1% of the Power requirement is fulfilled by coal while 67.8% of the requirement is met from the Oil and Gas.

Multiple techniques that are currently used for coal combustion includes fixed bed combustion, pulverized coal firing, fluidized bed combustion, underground coal gasification, etc. A relatively new method of exploiting solid coal is to suspend it in a carrier liquid to form slurry. This slurry can then be atomized in a burner just like a usual liquid and burned efficiently.

Coal Water Slurry is also a much cleaner and environmental friendly alternative to other conventional fuels due to much lower emissions of harmful gases on combustion. [2] In boiler it is free from problems such as erosion, ash slagging and fouling hence providing higher boiler efficiency. Furthermore, its storage and transportation is also hassle free since the presence of water makes the coal explosion proof.

2 LITERATURE REVIEW

Evaluation of coal water slurry rheology has already been done in considerable research works in the past from many different perspectives.

Fei i (2014) investigated the preparation of coal water slurry using varying proportions of Powder River Basin (PRB) coal which is sub bituminous in nature. The coal loading was varied by 30% to 40% and ionic sodium polystyrene sulfonate (PSS) and non-ionic surfactant Triton X-100 were employed as additives. It was found that Triton X-100 was an effective surfactant because it reduced the sedimentation by more than 50%and viscosity was also reduced.PSS showed adverse effect on viscosity. The highest coal loading achieved was 42.5% with acceptable viscosity [6]

Sunita Panda et al (2014) analyzed different coal sample found from the reserves of India for their potential to be a viable alternative source of fuel in comparison to fuel oil. Three coal samples from different reserves were used and tested for its rheological behaviour using The HAAKE RV30 Viscometer. Different shear stress, shear rates and viscosity values were achieved for different coal varied over different coal loading concentration. Coal was also analyzed for the change of yield stress with different coal concentration and ash content in the coal samples were also determined.

Kenechukwu et al. (2013) investigated a coal water slurry prepared with a sub-bituminous (a high rank coal) by varying proportions of the coal loading and distilled water along with anionic liquid soap as a surfactant. The rheological properties of viscosity and stability was determined and investigated to study the science behind the behavioural change. The results concluded that by increasing the coal loading concentration gave rise to higher density and thus more viscous slurry. The behaviour of the slurries changed from Newtonian to non-Newtonian at higher solid concentrations and the slurries with lower solid concentrations were much faster in there settling rate compared to the higher solid concentration slurries.

Patnaree et al (2012) investigated the effects of particle size distribution and packing characteristics on the rheological behaviour and solid loading of Coal-Water Slurry. They used a sub-bituminous Indonesian coal and ball milled it to obtain six different particle size ranges: < 38μm, 38-63μm, 63-75μm, 75-90μm, 90-180μm and 180-250μm. Then they investigated the impact of three types of packing: mono-modal, bimodal and multimodal, on the rheological behaviour. Na-CMC was used as the stabilizer while Naphthalene Sulfonate formaldehyde (NSF) was the dispersant. The results showed that bimodal distribution allowed the maximum possible coal loading, whereas the mono-modal presented the lowest. Furthermore, for bimodal distribution, the optimum coarse to fine ratio obtained was at 0.6:0.4. This yielded the highest possible coal loading at 65 %wt with a good stability and acceptable rheological behaviour.

Thomas Goudoulas et al. (2010) studied the preparation and rheological characteristics of the Greek Lignite-Water Slurries (LWS) using poly-modal particle size distributions from sizes 1μm up to 300μm. Surfactants and stabilizers were also added to improve slurry properties and achieve acceptable rheological behaviour and stability. Rheology was studied using two types of rheometers: Couette geometry and parallel disks geometry. Shear rates applied were in the order of 10^{-2} s^{-1} to $10^{3}s^{-1}$. Results show that when the coal loading of 44% by volume was used, it showed non-Newtonian behaviour and these can be used as lignite compatible environmentally friendly fuels.

Mosa et al. (2008) studied the effect of chemical additives on the flow properties of CWS. Three types of dispersants were used: sulfonic acid, sodium tri polyphosphate (STPP) and sodium carbonate and two types of stabilizers were used: Na-CMC and xanthan gum. The dispersant concentration was varied from 0.5 to 1.5% by weight while stabilizer concentration was varied from 0.05 to 0.25 % by weight. Sulfonic acid recorded the best performance and the best tested dosage was found to be as 0.75 % by wt. With regard to studied stabilizers, Na-CMC recorded better performance than xanthan gum and the best dosage was found to be as 0.1 % by wt. [4]

Harmadi et al (2002) studied the effect of Particle Size Distribution on the rheology and Stability of Coal Water Slurry. They used Sub-bituminous low rank Indonesian coal. The stabilizer used was Carboxy Methyl Cellulose (CMC) while Triton X-100 was added as the dispersing agent. They achieved a coal loading of 66 wt. % when a decreasing particle size was used along with 0.03-0.05%wt.concentrations of stabilizer and dispersing agent. The rheology was studied using Bohlin Instrument and modelled with Herschel Burkley model with n<1. From curve fitting, it is found that all slurries exhibit the pseudo-plastic fluid behaviour. The stability test was performed by measuring the thickness of hard pack layer formed in the bottom of container. At the maximum concentration, the maximum stability of eleven weeks was achieved. [3]

In this paper the stability and rheological behaviour of coal water slurry is investigated by varying the chemical additives, coal loading and Particle size distribution.

3 EXPERIMENTATION

3.1Materials

CWS is prepared from Lakhra coal in Pakistan which is Lignite in nature. The Proximate and Ultimate analysis of Lakhra coal is given in Table 1 & 2.

Table 1 .Proximate analysis of coal

Moisture (%)	13.5 – 39.4
Volatile Matter (%)	26.3 – 42.5
Ash (%)	7.4 – 25
Fixed Carbon (%)	20.7 – 39.2

Table 2 .Ultimate analysis of coal

Carbon (%)	38.04
Hydrogen (%)	4.43
Nitrogen (%)	0.79
Oxygen (%)	7.74
Sulfur (%)	1.8 – 6.5
Avg. Calorific Value (kcal/kg)	2570 – 4200

Coal slurry without any additives will form dense pulp and not indicate any flow-ability. Additives decrease the relative viscosity. Samples are prepared by using Nonionic surfactant Triton X-100as dispersant with Sodium Carboxyl Methyl Cellulose (Na-CMC) as a Stabilizer and Sodium Tri Poly Phosphate (STPP) as dispersant With Xanthan Gum as stabilizer. Distilled Water is used for slurry making.

3.2 Synthesis

The coal is taken in the form of large pieces measuring about 12 – 15 cm from Sindh mines as lignite Lakhra coal.

3.3 Preparation of Pulverized coal:

The first phase of crushing is done manually by hammering down large chunks into smaller one. By estimation, the large chunks were brought down to a size of 2 – 3 cm.

For grinding, the crushed coal is then send to a hammer mill, which operates at 2800rpm to achieve fine pulverization of up to 75 microns,

The finely pulverized coal is now to be distributed into a range of different sizes, ranging between 212microns- 75microns by a vibratory sieve.

After sieving, coal is washed in distilled water and magnetite to remove impurities like sulphur contents, ash contents, unwanted rocks and minerals.

3.4 Coal water slurry preparation:

The pulverized coal over a range of 75 to 250 microns is added in distilled water for the making of CWS. Dispersing and stabilizing agents are added as 1% of solution which modifies the suspension behavior and binds coal and water molecules.

Two different dispersing and stabilizing agent are used for making slurry. Three samples of coal loading 40%,50% and 60% with balanced distilled water were prepared for each Triton X-100as dispersant with Sodium Carboxyl Methyl Cellulose (Na-CMC) as a Stabilizer and Sodium Tri Poly Phosphate (STPP) as dispersant With Xanthan Gum as stabilizer.

For particle size distribution analysis two samples of coal water slurry at 50% coal loading were prepared with 0.75% Triton X-100 and another one with 0.75% STPP. Each one was made with both the Bimodal PSD and random PSD. The coarse particle had a random range of particle size with the Biggest size as big as 1mm. The fine particle slurry was made up of sizes 75, 90, 150 and 212 microns. The samples prepared for analysis are shown in Table 3.

Figure 1 coal water without additive (left side) and coal water with additive (right side)

Table 3.CWS samples at variable coal loading

Samples	Mass kg	Coal Loading%	Triton X100 %	Na-CMC
CWS 60%-TX 0.75%	100	60	0.75	0.25
CWS 50%-TX 0.75%	100	50	0.75	0.25
CWS 40%-TX 0.75%	100	40	0.75	0.25
			STPP	X.Gum
CWS 60%-STPP 0.75%	100	60	0.75	0.25
CWS 50%-STPP0.75%	100	50	0.75	0.25
CWS 40%-STPP 0.75%	100	40	0.75	0.25

4 RHEOLOGY

The rheological testing was carries out in the BROOKFIELD DV-E viscometer.

A selected spindle is cylindrical having diameter of 5.88mm and length of 115mm [1]. Experiments were conducted at room temperature. And viscosity reading was noted after 10 minutes of rotation at different rpms.

The rheological behaviors of the CWSs were then examined according to the power-law or Ostwald de Waele model and carreau fluid model as equation 1 & 2 respectively:

$$\eta = k\dot{\gamma}^{n-1} \qquad \text{Eq (1)}$$

Where, k = consistency; n = power law index γ = shear rate consistency.

$$\eta(\dot{\gamma}) = \eta_\infty + (\eta_0 - \eta_\infty)\left[1 + (\lambda\dot{\gamma})^2\right]^{\frac{n-1}{2}} \qquad \text{Eq(2)}$$

Where η_o and η_∞ are zero shear rate and infinite shear rate viscosity,λ is time constant and n is power law index.

The rheology of the coal suspension depends on the interparticle attractive forces; these in turn depend on the chemical structure of the surface, which is specific to a particular coal and total surface area, which can be inferred from its concentration in the suspension and the particle size distribution.

5 RESULT AND DISCUSSION

5.1 Additives

Figure 2,3&4 shows that as additives dosage is low ,for our experiment that is 0.35% and 0.55% of additives; viscosity of STPP is higher as compared to Triton-X100.While at 0.75% of additives both have approx. same viscosity trend.

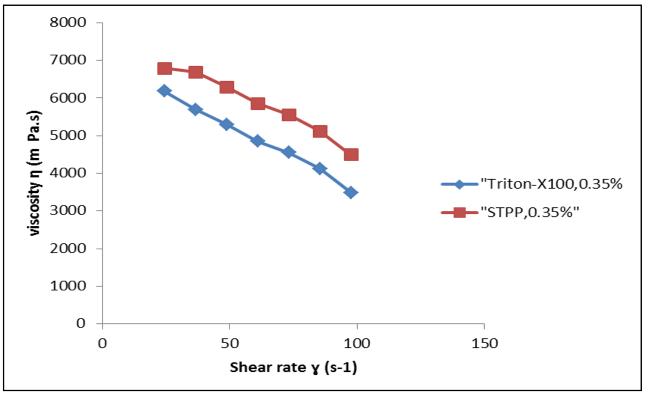

Figure 2.viscosity comparison at 0.35% Triton-X100 And STPP

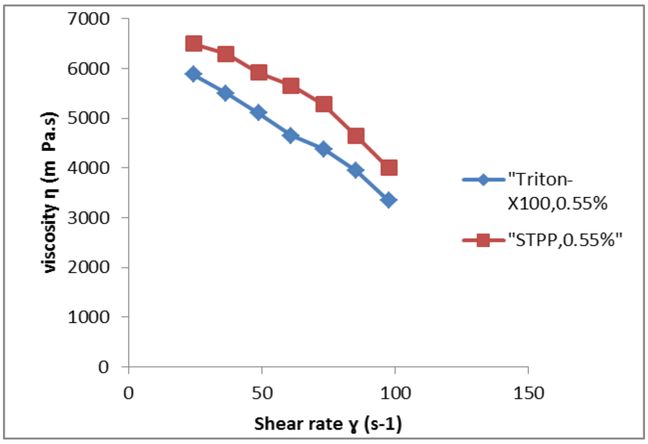

Figure 3.viscosity comparison at 0.55% Triton-X100 And STPP

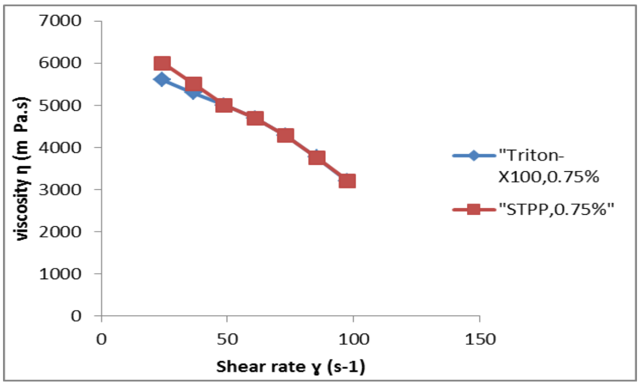

Figure 4.viscosity comparison at 0.75% Triton-X100 And STPP

5.2 Effect of coal loading

The coal water slurry was prepared at 40%, 50% and 60% coal loading respectively using 0.75% Triton X-100 and 0.25% Na-CMC and 0.75% STPP and 0.25% Xanthan gum.

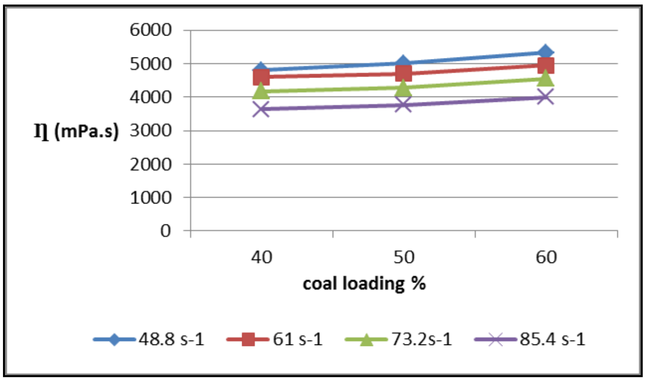

Figure 5.viscosity measurement by varying coal loading at constant shear rate of samples CWS 40%-60%-TX 0.75%

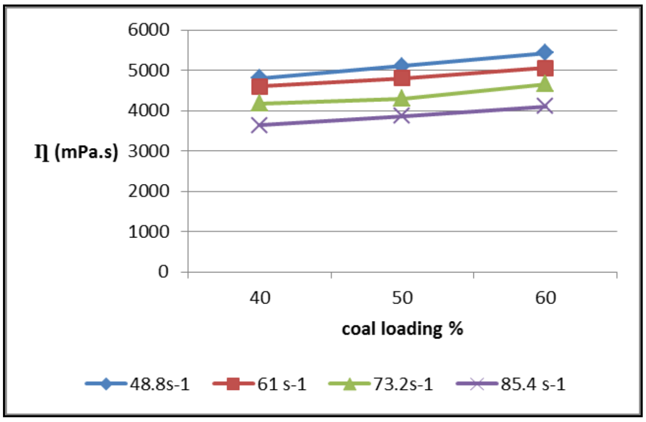

Figure 6.viscosity measurements by varying coal loading at constant shear rate of samples CWS 40%-60%-STPP0.75%

The figures 5 and 6 shows that as the coal loading is increased in the discrete amounts as 40% 50% and 60%, the viscosity increased at particular shear rate. This proves the fact that as the number of coal particles increase, it causes a rise in their inter-particle interaction resulting in a sharp increase in viscosity and shear stress.

The rheological data obtained from the experimentation was fitted into rheological models to calculate the model parameters.

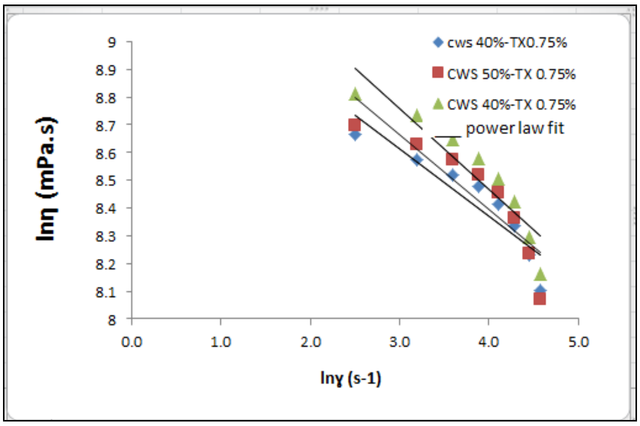

Figure 7. Rheogram with Power-Law model fit for coal samples, using Triton X-100 0.75%

In this study the descending curves indicates the viscosity decreases with increasing shear rate which shows shear thinning behaviour in all samples.

The value of power law index (n) was obtained from power law fit is 0.74,0.73 and 0.71 for CWS 40%-TX 0.75%, CWS 50%-TX 0.75% and CWS 60%-TX 0.75% respectively.

The value of power law index (n) was obtained from power law fit is 0.71,0.733 and 0.736 for CWS 40%-STPP 0.75%, CWS 50%-STPP 0.75% and CWS 60%-STPP 0.75%

Figure 15 & 16 shows carreau model can be adjusted to give a very good fit to the experimental graph for the viscosity function over the low value of shear rate but at high shear rate it doesn’t give good fit.

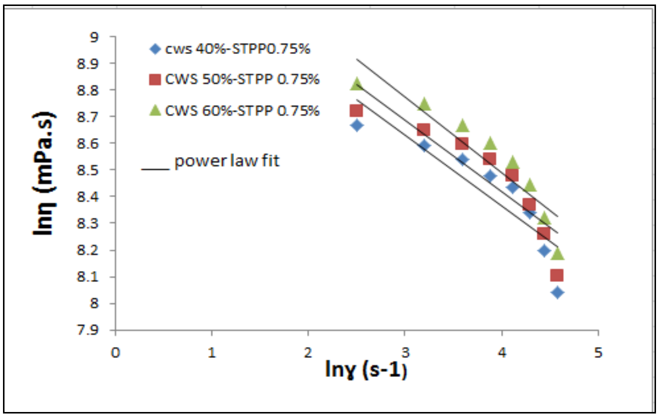

Figure 8 Rheogram with Power-Law model fit for coal samples, using STPP 0.75%.

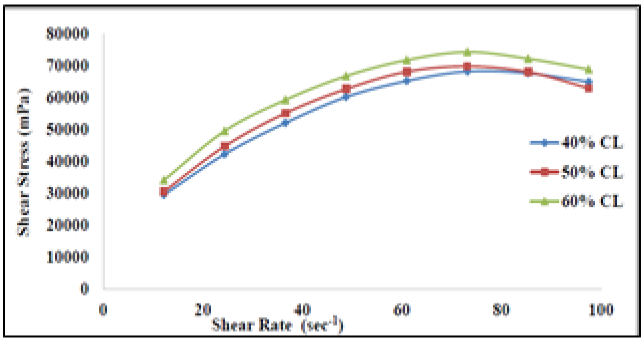

Figure 9.Shear Stress vs. Shear Rate for Coal Loading of 40%, 50% and 60% using 0.75% Triton X-100

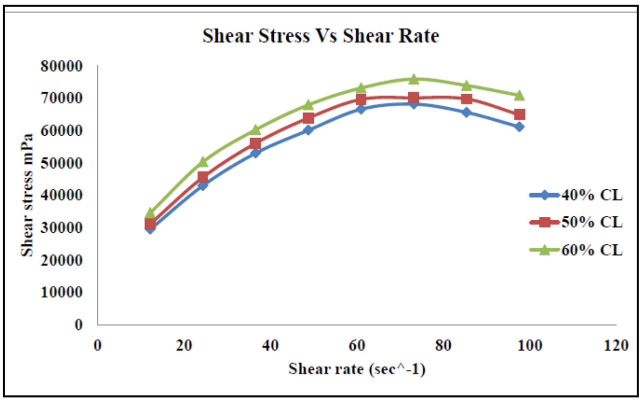

Figure 10.Shear Stress vs. Shear Rate for Coal Loading of 40%, 50% and 60% using 0.75% STPP.

The Figure 9 & 10 also confirms the pseudo plastic nature of the fluid, which is seen as shear thinning upon increased shear rates. All the three curves for different additive show the same nature fluid, however the viscosity is different.

5.3 Effect of particle size distribution

The CWS was prepared by mixing coal samples in Desired amounts with de-ionized water and chemical additives (TritonX-100 0.75%wt and STPP 0.75%wt). The coal loadings were fixed at 50 %wt. for all experiments. Figure 11 & 12 shows the variations of the apparent viscosity of CWS with the particle size in a fashion of bimodal and random model size distribution and the shear rate applied.

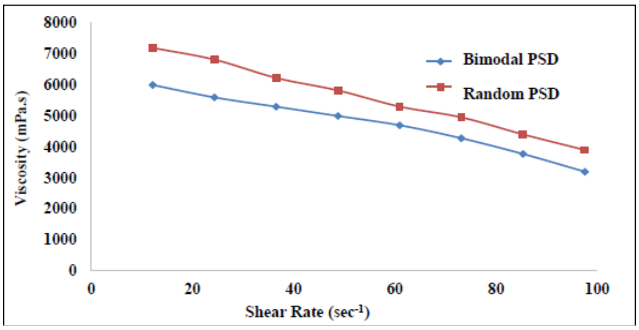

Figure 11.Effect of particle size on the apparent viscosity of CWS with 50% coal loading, Triton X-100 0.75% with Na-CMC.

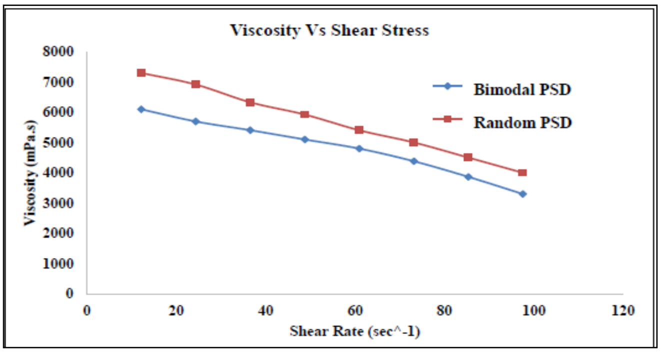

Figure 12.Effect of particle size on the apparent viscosity of CWS with 50% coal loading, STPP 0.75%with Xanthan gum

Figure 11& 12 illustrates that the vicosities of both model varies linearly with increasing shear rate.it was observed at low shear rate random model PSD showed higher viscosities as bimodal PSD and this difference becomes smaller and constant at shear rate range of 60-100 s^{-1}.At high shear rate the collision between the particles reduces due to which the viscosity reduces and both model showed same behaviour.similar effect was observed when using STPP and Xanthon gum.

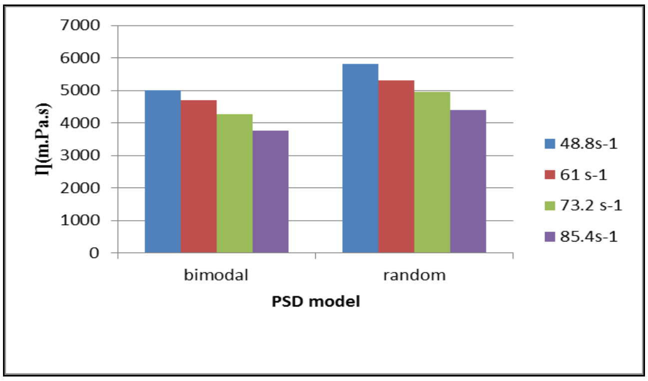

Figure 13. Effect of particle size on apparent viscosity of CWS at constant shear rate and 50% coal loading of each particle size range, Triton X-100 0.75%

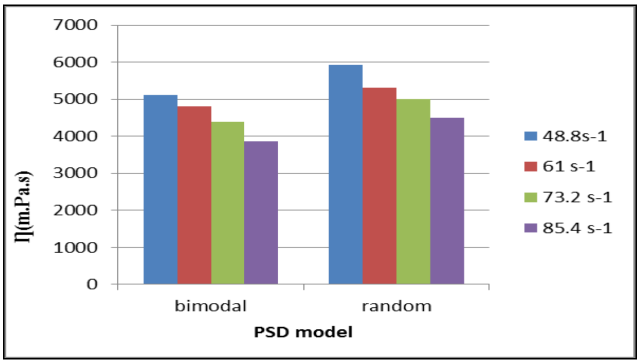

Figure 14. . Effect of particle size on apparent viscosity of CWS at constant shear rate and 50% coal loading of each particle size range, STPP 0.75%.

Figure 13 & 14 illustrates that at constant shear rate the viscosity of bimodal is lower than the random model because in bimodal (particle size range of 75-90micron),fine particles fills the voids between the coarse particles, formed packed structure with high volume fraction that's why low viscosities were observed. While in random model fine particle of multiple sizes may for agglomerates and irregular structure which decreases volume fraction and increases viscosity.

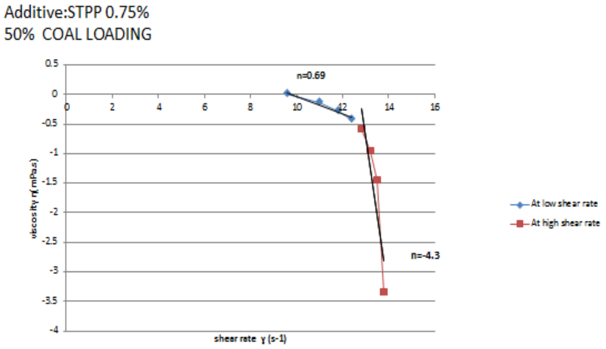

Figure 15.Rheogram with carreau model fit for coal samples, using STPP 0.75%.

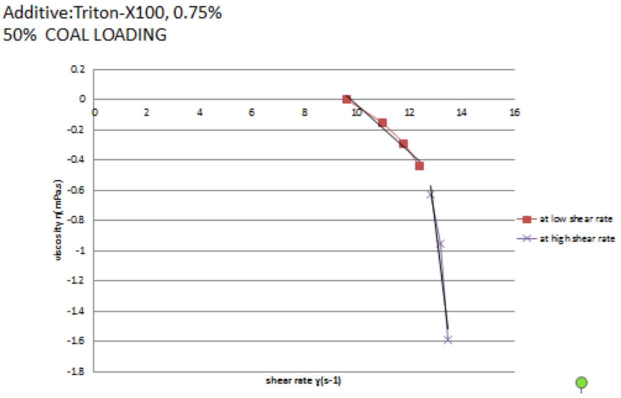

Figure 16.Rheogram with carreau-Law model fit for coal samples, using Triton X-100 0.75%

6 CONCLUSION

In this paper rheology of coal water slurry for 40-60 coal loading with different additives was studied. The results clearly indicate that the viscosity of CWS is strongly influences by the shear rate. As the shear rate increases, viscosity decreases for different coal loadings. Another parameter that effects the viscosity is coal loading, results indicates that as the coal loading increases viscosity increases at constant shear rate.

In this study slurries were prepared with two different additives and stabilizers(Triton X-100,Na-CMC, STPP,Xanthan Gum) and the experiments showed that all slurries exhibits pseudo plastic (shear thinning) behaviour.

Another important conclusion from this study is that Particle size distribution of coal has considerable influence on rheological properties of coal water slurry. The results indicates that the slurries prepared with bimodal distribution has lower viscosity at all coal loading as compared to the random modal , this implies that bimodal has greater potential to be transported.

Additive STPP shows higher viscosity at low shear rate.

ACKNOWLEDGEMENT

The authors are greatly thankful the teachers of Department of Chemical Engineering NED university of engineering and technology, Karachi for their valuable suggestions and encouragement given time to time during the completion of the above project.

NOMENCLATURE

η	Viscosity
γ	Shear rate
PSD	Particle size distribution
CWS	Coal water slurry
STPP	Sodium Tri Poly Phosphate
CL	Coal loading
TX	Triton-X100

REFRENCES

[1]BROOKFIELD DIGITAL VISCOMETER MODEL DV-E. *Operating Instructions.* No. M/98-350-F0305.

[2] Narasingha, Patnaree Buranasrisak and Monpilai H. *Effects of Particle Size Distribution and Packing Characteristics on the Preparation of Highly-Loaded Coal-Water Slurry.* No. 1, s.l.: International Journal of Chemical Engineering and Applications, February 2012, Vol. Vol. 3.

[2]Lee, Sunggyu. *Alternative Fuels.* s.l.: Taylor & Francis, 1996. p. 262. ISBN: 1-56032-361-2.

[3]Harmadi, E., Suwarmin, Machmudah, S. and Winardi, S., (2002). *Effect of particle size distribution on rheology and stability of high concentration coal-water mixture with Indonesian low rank coal.* Jurnal Teknik Mesin. v.2, pp. 93-98.

[4] E.S. Mosa, A-H.M. Saleh, T.A. Taha., A.M. El-Molla *EFFECT OF CHEMICAL ADDITIVES ON FLOW CHARACTERISTICS OF COAL SLURRIES.***.** 2008.

[5]Qaisrani, Salman. Solutions for Energy Crisis in Pakistan. *GRIDS & Infrastructures: CWS Combustion.* pp. 178-234

[6] Fei Yi, Akshay Gopan, Richard L. Axelbaum.*Characterization of coal water slurry prepared for PRB coal.* No.10, St. Louis MO 63130, USA: s.n., Oct 2014, Journal of Fuel Chemistry and Technology, Vol. 42, pp. 1167-117.

NUMERICAL SIMULATION AND MATHEMATICAL MODELLING IN COORDINATION WITH EXPERIMENTAL INVESTIGATION OF PROCESS PARAMETERS ASSOCIATED WITH THE FISCHER TROPSCH FIXED BED REACTOR PERFORMANCE

S.H. Ansari[1,*] D. Hildebrandt[2] and X Liu[3]
[1,2,3] Materials and Process Synthesis (MaPS), University of South Africa (UNISA), South Africa

[*]Corresponding author. Tel.: +270820871074;
E-mail address: 57669708@mylife.unisa.ac.za ; shahid@casen.nust.edu.pk

ABSTRACT

With rapid industrialization and increase in transportation, demand for liquid fuel increasing rapidly, this leads to a shortage of liquid fuel. In addition, commercial development and rising living standards have an influence on fuel supplies which becoming more scarce and costly. This research describes the development of a one dimensional (1-D) homogeneous model of a fixed bed reactor (FBR) for a Fischer Tropsch synthesis (FTS) system with chemical kinetics for cobalt based catalyst. A numerical simulation and mathematical modelling study has been carried out for conversion of syngas from any carbonaceous material to liquid fuel. This homogeneous model is based on the equation of continuity and the Navier Stokes equation. The mathematical model is based on the source of Langmuir-Hinshelwood-Hougen-Watson (LHHW) approach. The numerical simulation study focused on FBR with reaction kinetics. The described convective and diffusive effects of particular FTS mass and energy balances. It considered a partial differential equation (PDE) module of MATLAB. The non-linear PDE of mass and energy balance with boundary conditions are solved for hydrodynamic behaviour of syngas and product streams throughout the reactor. The numerical simulation and modelling were used to examine the effects of foremost process parameters on the reactor performance to ensure accurate prediction of carbon monoxide (CO) conversion, catalytic bed C_{5+} productivity, and temperature profile of the reactor . The resulting mathematical model will provide accurate information about operating conditions for maximum conversion of syngas to liquid fuel.

Keywords: fixed bed reactor, numerical modelling and simulation, syngas, Fischer Tropsch synthesis, chemical reaction kinetics.

1 INTRODUCTION

FTS technology has gaining interest through predominant research and development during first decade of 21st century. Therefore it is one of the most widespread and major option to produce clean synthetic transportation fuels like jet fuel oil, gasoline, diesel and others[1][2]. With the passage of time, severe energy demands and strict environmental rules & regulations favour this FTS process to meet the liquid fuels need. Actually, the technology involves a catalytic polymerization of hydrogen and carbon monoxide in the presence of specific catalyst to produce clean synthetic liquid fuel[3]. The environmental, health and safety concerns makes this technology relatively cost intensive[4]. In the processes of coal-to-liquids (CTL), gas-to-liquids (GTL), waste-to-liquids (WTL) and biomass-to-liquids (BTL) are collectively known as XTL (X – any carbonaceous source like biomass/natural gas/coal/municipal solid waste; T - to; L - liquids) technology processes[5][6]. In a first step, any carbonaceous material is converted into syngas (carbon monoxide + hydrogen) via reforming, gasification or partial oxidation. Various popular technologies are commonly used for production of syngas[7][8]. In a second step, the syngas is converted into liquid hydrocarbons (mainly paraffins and olefins) over a heterogeneous catalyst. For commercial applications, iron and cobalt used as an active metal mostly supported on ceramic supports. Cobalt is expensive than iron but is almost 250 times more active and it produces more higher molecular weight hydrocarbons than iron at a relatively low temperature[9]. Amongst the current XTL processes, FTS is assumed to become the prominent one in the nearby future. Thus having more knowledge of FTS is necessary in order to exploit unevenly dispersed unconventional feedstocks efficiently[6].

The overall FTS process is associated with a very complex reaction because of large number of surface intermediates and specific products. Additionally, mass and heat transport difficulties, catalyst deactivation, three phase operation, selectivity of final products and other factors have made more difficult to understand the exact mechanism of FTS process[10]. The pores of catalyst are filled with the liquid products that decrease the mass transport of syngas ($CO + H_2$) to active sites of the catalyst. Anfray et al. [11]proposed a scientific approach Langmuir–Hinshelwood–Hougen–Watson (LHHW) model to investigate the carbide mechanism and readsorption. For modelling and optimization of FT reactor (like multi-tubular fixed bed (MFB), slurry bubble column (SBC), circulating fluidized bed (CFB), fixed fluidized bed (FFB) and compact reactors) requires its own approach. The high temperature Fischer Tropsch (HTFT) occurs at 350 °C and 50 bar in the presence of iron catalyst is highly exothermic. This mathematical work is related to a multi tubular fixed-bed reactor with cobalt-based catalysts. But critical restrictions of fixed bed reactor (FBR) are; to control the temperature of reactor, pressure drop through the catalytic bed and deactivation of catalyst. The parameter of heat production potential (S) of a reaction is applied for selection of a suitable type of FBR. The S is function of dimensionless adiabatic temperature rise and dimensionless activation energy[12]. The Ergun equation is applied to consider the effects of flow on pressure drop across the catalytic bed[13]. For modelling and simulation of the tubular fixed bed reactor (TFBR), Irani et al. [14]used computational fluid dynamics as a technique to check the prediction of the reactor model using a novel iron catalyst. A 1-D dimensional heterogeneous model was applied by Wang et al. [15]to study the performance of the fixed bed reactor. Atwood and Bennett[16] discussed parameter effects on commercial reactors using a 1D heterogeneous model. Mazidi and Sadeghi[17] researched on the maximum gasoline yield using non uniform catalysts in a one dimensional heterogeneous model. Guttel and Turek[18] compared SBC and FBR on a 1-D approach with cobalt based catalysts. Momonov and Kustov[19] investigated the effects of linear gas velocity and tube diameter using a 1-D heterogeneous model. The complexity of chemical kinetics, mass transport and heat transport limitations in HTFT is considered in mathematical modelling and simulation to study the temperature and pressure profiles in the FT reactor.

The fundamental approach is to develop an advanced mathematical model which will describe possible mechanisms involved during HTFT. Therefore, to understand its trends, it has to be studied at a micro level before the domestic industrial level and software modelling and simulation of such a process can be extremely useful for the better future of the community. In this work, a one dimensional pseudo homogeneous plug flow model was first used to predict the general effects of operating parameters on conversion, production and thermal stability of the reactor.

2 EXPERIMENTAL INVESTIGATION

A single tube fixed bed bench-scale reactor was used with ID of 9mm and tube length of 0.3m. Co/TiO_2 catalyst with the properties shown in Table 1 was inserted in the middle of the reactor. The rest of the reactor was packed with ceramic balls and special type of cloth material. CO, H_2 flow was controlled through separate mass flow controllers (Sevenstar D07 MFC). Prior to the synthesis the catalyst went under reduction in H_2 for 16 hr at 350 °C at 0.4bar. Then the reactor was cooled down to 180 °C and pressurized to 1bar. The synthesis was started at 200 °C with the H_2/CO ratio of 2. A run time of 12 hrs for three runs with different GHSV was conducted under constant pressure and temperature. After leaving the reactor the products pass through two traps, one hot and one cold. The hot and cold traps separate the heavy and light hydrocarbons from the product stream respectively. The samples from each run were collected from the manual valves situated beneath the traps. Sample analysis was done on an offline GCMS. Temperature of the reactor was controlled by placing one thermocouple near the wall and the other in the catalyst bed. Pressure was controlled using a back-flow regulator.

Table 1: Catalyst Properties

Property	Unit	Content
TiO_2	wt%	89
Cobalt	wt%	11
Surface area	m^2/g	255
Diameter	mm	2
Bulk density	kg/m^3	800

3 MATHEMATICAL MODELLING

In 1974, Froment[20] had presented a better way for modelling and simulation of each reactor separately in order of growing complexity. Generally, mathematical models for the fixed bed reactors are broadly divided into two main divisions like pseudo-homogeneous and heterogeneous models. Although heterogeneous model clearly consider the presence of catalyst in the reactor as compared to pseudo homogeneous model. For homogeneous model, we must have to consider the form and skin friction effects of fluid on the catalyst (i.e Cg = Cs & Tg = Ts). The simplest and most basic one dimensional (1-D) is pseudo homogeneous model with plug flow in fixed bed reactor.

This model is used in most of the research study until now and it considered transport by plug flow environment in axial direction. For 1-D pseudo homogeneous model, both interfacial temperature gradients and concentration gradients are small. Following important aspects/characteristics are given in figure 1.

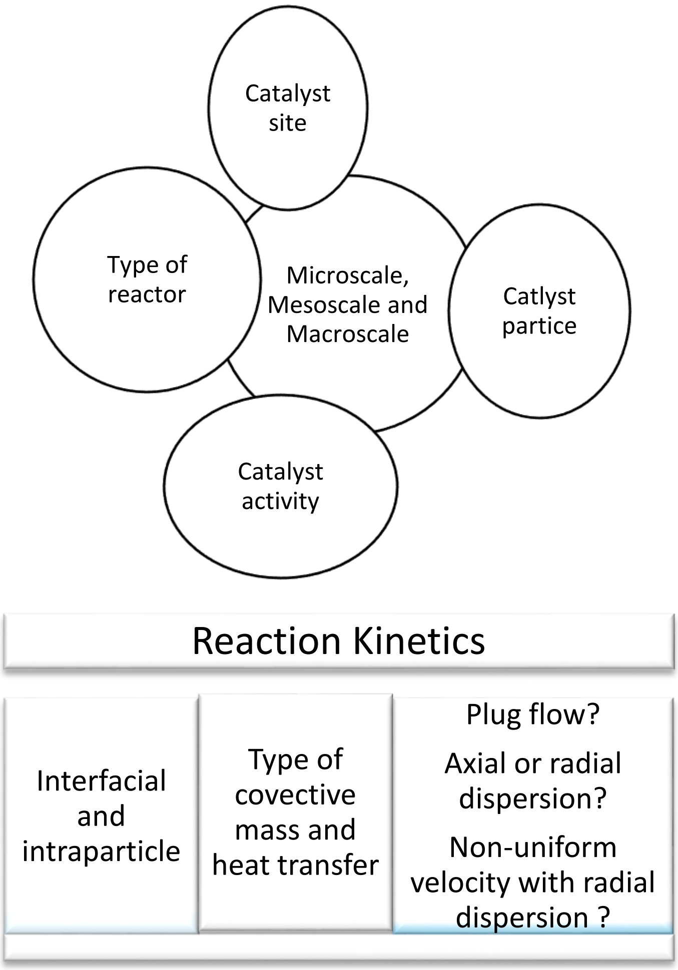

Figure 1: Important aspects for modelling

The selection criteria for pseudo homogeneous model described here are taken from Mears (1971) [21].

Interfacial temperature gradients for pseudo homogeneous model are insignificant if:

$$\left|\frac{-\Delta H_r r_{eff} dp}{2T_0 hs}\right| Ar < 0.15 \cdots\cdots (1)$$

Interfacial concentration gradients for pseudo homogeneous model are insignificant if:

$$\left|\frac{r_{eff} dp}{2C_{A0} ks}\right| < \frac{0.15}{n} \cdots\cdots (2)$$

Intra-particle mass and heat transfer gradients for pseudo homogeneous model are insignificant if:

$$\langle Da_{II}|n - Ar - P_t| < 1\rangle \cdots\cdots (3)$$

For non-ideal flow conditions, mixing in all the radial and axial direction may be superimposed on the real plug flow. This situation is valid for both homogeneous and heterogeneous models. Axial dispersions for pseudo homogeneous model are insignificant if:

$$\left|\frac{n.D_{aI}}{Pe_{a,m}} - \frac{Ar.D_{aIII}}{Pe_{a,h}}\right| < 0.05 \cdots\cdots (4)$$

$$\left|\frac{-\Delta H_r r_{eff}^* d_t^2}{\lambda_r T_w}\right| . Ar < \frac{1.6}{1 + \frac{8}{B_{iw}}} \cdots\cdots (5)$$

The correlations used for pseudo homogeneous (1-D) dispersion model is taken from Froment and Bischoff is:

$$\frac{1}{U} = \frac{1}{\alpha_w} + \frac{d_t}{8\lambda_t} \cdots\cdots (6)$$

$$\epsilon Sh = 0.357 Re_p^{0.641} S_c^{0.33} \cdots\cdots (7)$$

$$\epsilon Nu = 1.0 \left(\frac{Re_p}{\epsilon}\right)^{0.563} P_r^{0.22} \cdots\cdots (8)$$

$$\frac{1}{Pe_{a,m}} = \frac{0.3}{Re_P S_c} + \frac{0.5}{1 + \frac{3.8}{Re_p Sc}} \cdots\cdots (9)$$

$$\frac{\lambda_a}{\lambda_{fl}} = 9 + 0.75 Re_p P_r \cdots\cdots (10)$$

For an exothermic reaction, it is very difficult to control temperature and hot spot in the reactor. The main problem is to limit hot spot and to avoid extreme sensitivity to variation in the process variables. The mass and energy balance equations can be written as follows.

Mass balance:

$$u_s\rho_g \frac{\delta\, C_a}{\delta Z} = \rho_g C_a \frac{\partial u_s}{\delta Z} + C_a u_s \frac{\delta u_s}{\delta Z} - r_a \rho_{\boldsymbol{B}} \cdots\cdots (11)$$

Energy balance:

$$u_s \rho_g C_p \frac{\delta T}{\delta Z} = (-\Delta H)\rho_B r_a + \lambda_{er}.\left(\frac{1}{r}.\frac{\delta T}{\delta r} + \frac{\delta^2 T}{\delta r^2}\right) \cdots (12)$$

The Ergun's equation for flow through catalytic bed for momentum balance and overall pressure drop was used to calculate pressure drop:

$$-\frac{\delta P}{\delta Z} = f.\frac{\rho.u_s^2}{d_p} \cdots\cdots (13)$$

In above equation, the rate of accumulation is neglected for stationary model. Change in density & superficial velocity was calculated by:

$$\frac{\delta \rho_g}{\delta Z} = \frac{M}{R}\cdot\left(\frac{1}{T}\cdot\frac{\delta P}{\delta Z} - \frac{P}{T^2}\cdot\frac{\delta T}{\delta Z}\right) \cdots\cdots (14)$$

$$\frac{\delta u_s}{\delta Z} = \frac{u_s}{\rho}\cdot\frac{\delta \rho_g}{\delta Z} \cdots\cdots (15)$$

Boundary conditions:

$$\frac{\delta C}{\delta r} = 0 \qquad \textit{for all } Z \textit{ and } r$$

$$\frac{\delta T}{\delta r} = 0 \qquad \textit{for all } Z \textit{ at } r = 0$$

$$\frac{\delta T}{\delta r} = -\frac{U}{\lambda_{er}}\big((T \textit{ at } r = R) - T_W\big) \textit{ for all } Z$$

The defined component and mixture heat capacities were calculated using equations derived by Poling[22]. The overall heat transfer coefficient equation was taken from the co-relations used for 1-D model[23][24]. The effective radial thermal conductivity was calculated from equations derived by Forment[20]. The superficial gas velocity was obtained based on overall mass flux and gas mixture density. Mostly a continuum model composed of various nonlinear ordinary differential equations (ODEs) or partial differential equations (PDEs) which were solved analytically or graphically by MATLAB. Finite difference method was applied. MATLAB's ODE solver was used to conduct the numerical simulation.

Overall Heat transfer coefficient:

$$\frac{1}{U} = \frac{1}{a_w} + \frac{d_i}{2\lambda_s} ln \frac{d_o}{d_i} \cdots\cdots (16)$$

Effective radial thermal conductivity:

$$\lambda_{er} = \lambda_{er}^0 + 0.111\lambda_g \cdot \frac{Re_p + Pr^{\frac{1}{3}}}{1 + 46\left(\frac{d_p}{2\cdot r_o}\right)^2} \cdots\cdots (17)$$

$$\lambda_{er}^0 = \varepsilon\cdot\left(\lambda_g + 0.95 + \alpha_{ru} + d_p\right) + \frac{0.95\cdot(1-\varepsilon)}{\frac{2}{(3\cdot\lambda_s)} + \frac{1}{\left(10\cdot\lambda_g\cdot\alpha_{rs}\cdot d_p\right)}} \cdots (18)$$

The thermal conductivity of the catalyst bed without the presence of fluid and α_{ru} and α_{rs} are taken from literature.

Main equation of the kinetic model is:

$$r = \frac{a(\frac{E_a}{RT})C_{H_2}^{0.74}C_{CO}}{\left(1 + b(\frac{E_b}{RT})C_{CO}\right)^2} \cdots\cdots (19)$$

The conversion equation can be shown as:

$$Conversion = \left(\frac{amount\ entered - amount\ left}{amount\ entered}\right)100$$

The theoretical predicted values from the mathematical model and actual experimental values are shown in the table 2 which very closely related and reduction in conversion with increase in GHSV.

Table 2: Experimental and predicted results at 473K, 1bar

GHSV	30Nml/gcat.h		60Nml/gcat.h		90Nml/gcat.h	
	EXP	PRE	EXP	PRE	EXP	PRE
XCO%	10.2	10.9	6.9	7.5	4.5	4.9
XH_2%	13.4	14.1	9.7	10.5	6.8	7.2
SCH_4%	6.11	5.90	4.54	5.10	5.20	5.70
SC2%	1.45	2.11	1.95	2.32	1.34	1.97
SC3%	3.53	3.30	3.84	3.47	2.70	3.15
SC4%	3.70	3.95	2.95	3.75	2.53	3.67
SC5+%	85.2	84.7	86.7	85.4	87.2	85.5

To examine many other parameters and the runaway or hot spot of the reactor, the FT-single tube was scaled-up to the size of that found in a conventional multi tubular reactor with Co/TiO_2 catalysts fitted throughout the tube (Table 3).

TABLE 3: Dimensions of FT single tube

Property	Value
Length	12 m
Tube ID	0.03 m
H_2/CO ratio	2
Pressure	25 bar
Temperature	493 K (220 °C)
Volumetric flow-rate	5 (m^3/hr) ($600h^{-1}$)

4 RESULTS AND DISCUSSION

4.1 Effects of parameters

The effects of main parameters are shown in figures 2 and tables 4 and 5. The various promoters show good effects to increase the catalytic activity of cobalt supported catalysts. Morales et al [22] worked on MnO as promoter on Co/TiO_2 catalyst exposed that activity almost doubled as compared to Co/TiO_2. Bao et al [23] mentioned that selectivity after introducing CaO as promoter with Co/Al_2O_3 increases more than 2.5. Therefore, we had considered an aspect of value 3 to the main rate equation to show comparison with our already said theoretical findings. The rate had increased with of 32% carbon monoxide and 27% hydrogen from their normal values. Mainly the C5+ production and also production of CH_4 improved meaningfully.

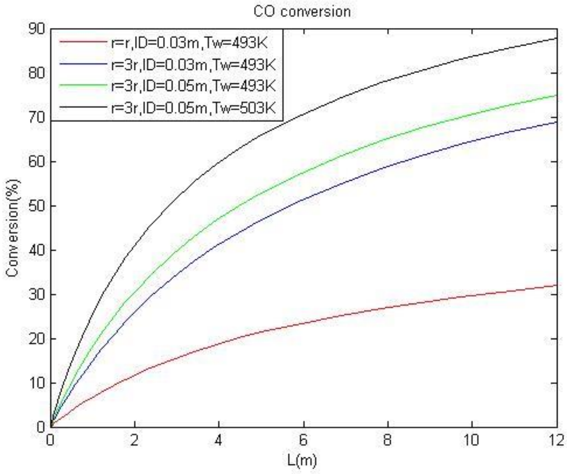

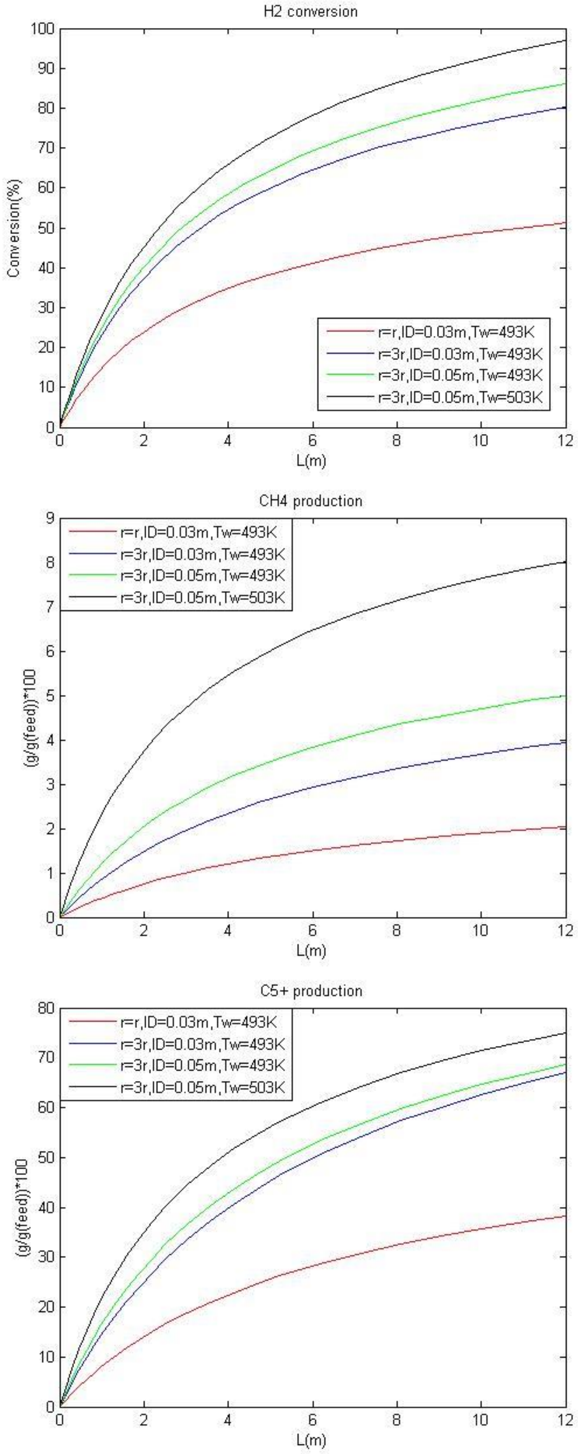

Figure 2: Conversion and production at different operating conditions $600h^{-1}$, 12m, 25bar

In order to minimize the temperature variation in the reactor, inside diameter of the tube is very important parameter. We have to optimize the diameter of tube for nearly isothermal conditions for FT reaction. The resulted mathematical forecast shows an additional improved in the conversion rate. The conversion continues to increase with an increase in this parameter for all the temperature. However, high temperatures favour the formation of lighter HCs and as such the production of methane, an undesirable product and it increases with increase in temperature and there are some rational reasons for its unusual growth at high temperatures. A conclusion made by Wang et al.[15]on increasing the wall temperature was that higher temperatures would cause the species on the surface to desorb rather than propagate to higher molecular weight compounds resulting in an increase in methane selectivity. Consequently, high temperature favours the formation of branched alkanes and aromatics which is an advantage if high octane gasoline production is being considered. Favourable results occur both in terms of syngas conversion and C5+ production although the production change is of a lesser extent whereas production of methane increased significantly, thus, indicating a change in product selectivity towards lower molecular weight HCs. The partial pressure and temperature profile along the length of the reactor is shown in the figure 3.

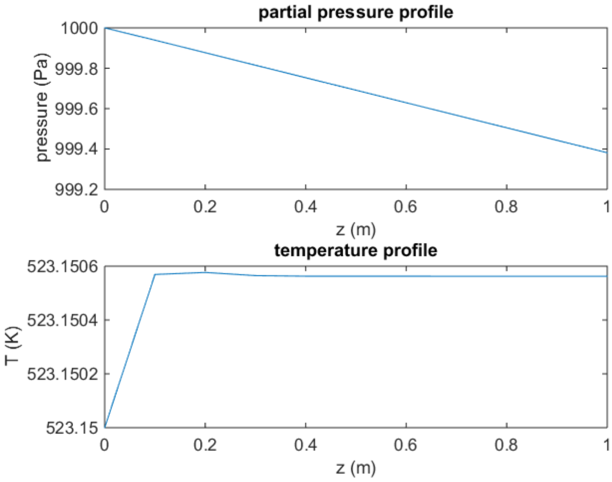

Figure 3: Partial pressure and temperature profile along the length of the reactor

4.2 Runaway or hot spot

All three parameters have one major side effect; the famous hotspot. As shown in figure 3, increasing the reaction rate by a factor of three caused a steep temperature rise due to reactions occurring thrice faster than normal. The actual experimental data for CO and H_2 conversion towards HCs depends upon the accurate hot spot evaluation inside the reactor. The hot spot evaluation shows a deviation of catalytic bed temperature from wall temperature of the reactor as a function of GHSV. Both experimental and mathematical estimation shows that there is no temperature deviation for keeping lower GHSV but it deviate for higher values. Actually with higher value of GHSV, there is possibility of boiling water boundary layer on the outer surface of the FT reactor. Because of the formation of such boiling water boundary layer will cause a problem to remove heat from the reactor which leads to rise up temperature inside the reactor and it will cause formation of hot spot in the reactor. Because we have neglected the effects of boundary layer that’s why our mathematical model does not predicted the accurate determination of hot spot formation inside the reactor. A slight shift of the hotspot near the reactor inlet was also noted. Increase in tube diameter not only increased hotspot but also moved it towards the reactor exit as well as it broadened its range over the reactors length, thus increasing the average bed reaction temperature of the reactor and increasing its exit temperature table 4, reduction in selectivity table 5.

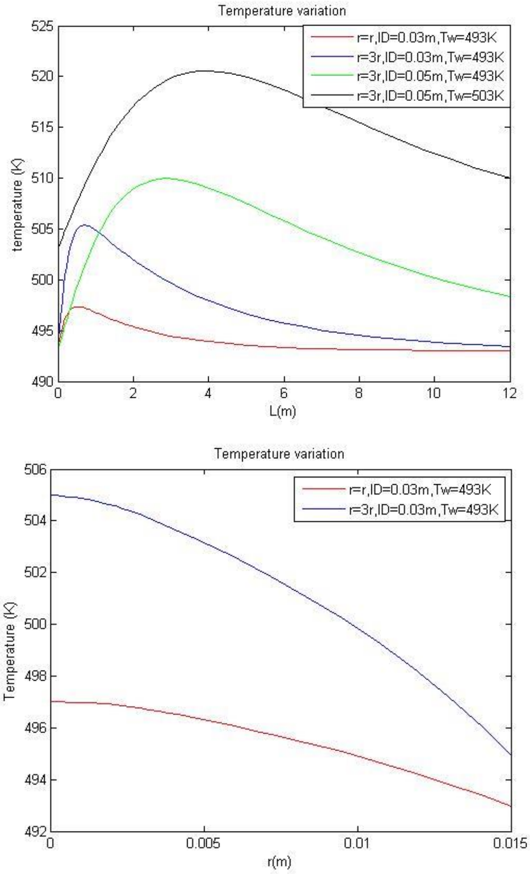

Figure 4: Axial and radial temperature profile at different conditions, 600h^{-1}, 12m, 25 bar

Ultimately it can be seen that the tube wall temperature further complicates the situation. However, these temperature profiles were noted at the centre of the reactor in previous publications and the same prediction is seen here [1].Radial temperature profiles show that the where the axial temperatures were maximum at the centre, the temperatures were close to the set reaction temperature near the tube wall (figure 2). Anyway, there are two general solutions to this problem. One is to increase overall gas space velocity [3]. It will surely diminish the hotspot but will reduce the residence time and, hence, the conversion and production. The other is to introduce nitrogen gas in the main syngas stream. Nitrogen plays an important role as an inert material that absorbs the reaction heat so as to help in reducing the average bed temperature. A downside to this is the suppression of partial pressures of H_2 and CO.

TABLE 4: FT- Fixed bed reactor temperature under various operating conditions

T_{avg} of reactor (K)	α-value	$S_{light\ HCs}$ (%)	$S_{gasoline}$ (%)	S_{diesel} (%)	S_{wax} (%)
496.07	0.806	22.05	39.93	34.20	3.42
502.21	0.795	25.29	41.94	30.83	2.65
505.12	0.787	26.54	42.51	27.14	2.19
511.27	0.770	30.50	43.32	22.64	1.45

TABLE 5: FT- Fixed bed reactor temperature under various operating conditions

Rate	Dt (m)	Tw (K)	P (bar)	Tavg of reactor (K)
r	0.03	493	25	496.07
3r	0.03	493	25	502.21
3r	0.05	493	25	505.12
3r	0.05	493	25	512.27

5 CONCLUSION

In the present work a one-dimensional pseudo homogeneous plug-flow model was successfully developed for predicting general trends and optimization in a fixed bed reactor for Fischer Tropsch synthesis. Predicted results were validated with the experimental values. The Syngas conversion, methane and C5+ productivity, CO & H_2 conversion, hot spot temperature over GHSV, partial pressure profiles and temperature profiles were measured for a scaled-up FT-FBR with cobalt supported catalyst. The theoretical estimated results were compared with actual experimental data for validation of mathematical model. The main parameters showed the excellent correlations between experimental data and theoretical estimated data. An increase in these significantly increased the gas conversion and heavy HCs but also added a noticeable increase in methane production. Furthermore, the reactor's bulk temperature was increased by increasing the parameters' values. Moreover, investigation on the use of high thermal conductivity and high heat coefficient material for tubes needs to be implemented. The most promising results of such 1-D pseudo homogeneous model for FBR confirm that it is applicable for scaling up of FTS reactor and will be most valuable for industrial FTS design.

6 ACKNOWLEDGEMENTS

The authors would like to acknowledge helpful discussions with Prof. David Glasser and Dr. Bilal Patel of UNISA. The authors would also like to acknowledge for performing laboratory work at FT synthesis laboratory Centre for advanced studies in energy (CASEN), National University of sciences & technology (NUST), Islamabad, Pakistan.

7 NOMENCLATURE

1-D	one dimensional
FBR	fixed bed reactor
FTS	Fischer Tropsch synthesis
LHHW	Langmuir-Hinshelwood-Hougen-Watson
PDE	partial differential equation
CTL	coal to liquids
GTL	gas to liquids
WTL	waste to liquids
BTL	biomass to liquids
XTL	any carbonaceous material to liquids
MFB	multi-tubular fixed bed
SBC	slurry bubble column
CFB	circulating fluidized bed
FFB	fixed fluidized bed
HTFT	high temperature Fischer Tropsch
S	heat production potential
GCMS	gas chromatograph mass spectrometer
Cs	concentration at the surface of catalyst [mole/m^3]
Cg	concentration from the gas [mole/m^3]
Ts	temperature at the surface of catalyst [K]
Tg	temperature from the gas [K]
Ta	ambient temperature [K]
r_{eff}	effective reaction rate per mass of catalyst [mole/m^3]
n	reaction order
k_s	interfacial mass transfer coefficient between fluid and catalyst [m/s]
h_s	interfacial heat transfer coefficient between fluid and catalyst [W/m^{2}s]
D_{aI}	Damkohler group II gives the ratio between chemical rate and bulk mass flow rate
D_{aII}	Damkohler group II gives the ratio between chemical rate and molecular diffusion rate
D_{aIII}	Damkohler group II gives the ratio between heat liberated and bulk transport of heat

P_t	Prater number, express maximum temperature rise
D_{eff}	effective diffusivity coefficient inside catalyst [m^2/s]
λ_s	thermal conductivity of catalyst [J/msK]
λ_a	axial thermal dispersion coefficient [J/msK]
λ_r	radial thermal dispersion coefficient for fluid[J/msK]
Da	axial dispersion coefficient [m^2/s]
T_c	inner temperature of the catalyst [K]
T_w	temperature at the wall [K]
$Pe_{a,m}$	The Peclet number for mass, ratio between bulk and conductive mass transfer
$Pe_{a,h}$	The Peclet number for heat, ratio between bulk and conductive heat transfer
r^*_{eff}	rate of reaction at the hot spot [$mole/m^3s$]
Bi_w	thermal Biot number at the wall, ratio between film and bulk thermal resistance
α_w	heat transfer coefficient at the wall [J/m^2sK]
U	overall heat transfer coefficient [W/m^2K]
d_t	tube diameter [m]
d_p	dimeter of particle [m]
Sh	Sherwood number, ratio of the total rate of mass transfer to the rate of diffusive mass transport
Re_p	Reynolds number, the ratio of momentum forces to viscous forces
Sc	Schmidt number, the ratio of momentum diffusivity to mass diffusivity
Nu	Nusselt number, ratio of convective to conductive heat transfer across (normal to) the boundary
Pr	Prandtl number, the ratio of momentum diffusivity to thermal diffusivity
ρ_B	bulk density of catalyst [kg/m^3]
ρ_g	bulk density of gas [kg/m^3]
u_s	superficial velocity [m/s]
$-\Delta H_r$	heat of reaction [KJ/kmole]
C_p	specific heat [KJ/kgK]
p_t	total pressure [bar]
Z	length of reactor [m]
R	ideal gas constant [KJ/mole.K]
GHSV	gas hourly space velocity [hr^{-1}]
E	activation energy [KJ/kmole]

8 REFERENCES

[1] B. Todić and V. Ordomsky, "Opportunities for intensification of Fischer–Tropsch synthesis through reduced formation of methane over cobalt catalysts in microreactors," *... Sci. Technol.*, 2015.

[2] J. Xu, Y. Yang, and Y.-W. Li, "Recent development in converting coal to clean fuels in China," *Fuel*, vol. 152, pp. 122–130, Jul. 2015.

[3] K. Keyvanloo, M. J. Fisher, W. C. Hecker, R. J. Lancee, G. Jacobs, and C. H. Bartholomew, "Kinetics of deactivation by carbon of a cobalt Fischer–Tropsch catalyst: Effects of CO and H2 partial pressures," *J. Catal.*, vol. 327, pp. 33–47, Jul. 2015.

[4] A. P. Vogel, B. van Dyk, and A. M. Saib, "GTL using efficient cobalt Fischer-Tropsch catalysts," *Catal. Today*, Aug. 2015.

[5] I. Ridjan, B. V. Mathiesen, and D. Connolly, "Terminology used for renewable liquid and gaseous fuels based on the conversion of electricity: a review," *J. Clean. Prod.*, Jun. 2015.

[6] David L. King and Arno de Klerk, *Synthetic Liquids Production and Refining*, vol. 1084. Washington, DC: American Chemical Society, 2011.

[7] P. Watkins and P. McKendry, "Sustainable Energy Technologies and Assessments," 2015.

[8] H. Gossler and O. Deutschmann, "Numerical optimization and reaction flow analysis of syngas production via partial oxidation of natural gas in internal combustion engines," *Int. J. Hydrogen Energy*, vol. 40, no. 34, pp. 11046–11058, Jul. 2015.

[9] S. Mousavi and A. Zamaniyan, "Generalized kinetic model for iron and cobalt based Fischer–Tropsch synthesis catalysts: Review and model evaluation," *Appl. Catal. A ...*, 2015.

[10] K. W. J. Kyoung Su Ha, Joo Young CHEON, Yun Jo Lee, Seung-Chan Baek, Geun Jae Kwak, Seon Ju Park, "Catalyst for Fischer-Tropsch synthesis having excellent heat transfer capability." US-9012352B2, 21-Apr-2015.

[11] J. Anfray, M. Bremaud, P. Fongarland, A. Khodakov, S. Jallais, and D. Schweich, "Kinetic study and modeling of Fischer–Tropsch reaction over a catalyst in a slurry reactor," *Chem. Eng. Sci.*, vol. 62, no. 18–20, pp. 5353–5356, Sep. 2007.

[12] N. Kockmann and D. M. Roberge, "Scale-up concept for modular microstructured reactors based on mixing, heat transfer, and reactor safety," *Chem. Eng. Process. Process Intensif.*, vol. 50, no. 10, pp. 1017–1026, Oct. 2011.

[13] M. Kaviany, *Principles of heat transfer in porous media*. 2012.

[14] M. Irani, "modeling of fischer–tropsch synthesis packed bed reactor for producing liquid fuels from natural gas," *Pet. Coal*, 2013.

[15] Y. Wang, Y. Xu, Y. Li, Y. Zhao, and B. Zhang, "Heterogeneous modeling for fixed-bed Fischer–Tropsch synthesis: Reactor model and its applications," *Chem. Eng. ...*, 2003.

[16] H. Atwood and C. Bennett, "Kinetics of the Fischer-Tropsch reaction over iron," *... Eng. Chem. Process ...*, 1979.

[17] "Optimization of Fischer- Tropsch Process in a Fixed- Bed Reactor Using Non- uniform Catalysts," *... Eng. Technol.*, 2013.

[18] R. Guettel and T. Turek, "Comparison of different reactor types for low temperature Fischer–Tropsch synthesis: a simulation study," *Chem. Eng. Sci.*, 2009.

[19] A. Alkhimov, "One-dimensional heterogeneous model of a Fischer-Tropsch synthesis reactor with a fixed catalyst bed in the isothermal granules approximation," *Catal. Pet. Refin. Ind. Catal. Ind.*, vol. July 2013, 2013.

[20] Prof. Dr. Ir. G. F. Froment, "Fixed Bed Catalytic Reactors. Technological and Fundamental Design Aspects," *Chemie Ing. Tech.*, vol. Volume 46, no. Issue 9, p. pages 374–386, 1974.

[21] D. E. Mears, "Tests for Transport Limitations in Experimental Catalytic Reactors," *Ind. Eng. Chem. Process*, vol. DOI: 10.10, no. Des. Dev., 1971, 10 (4), p. pp 541–547.

[22] F. Morales, E. Desmit, F. Degroot, T. Visser, and B. Weckhuysen, "Effects of manganese oxide promoter on the CO and H2 adsorption properties of titania-supported cobalt Fischer–Tropsch catalysts," *J. Catal.*, vol. 246, no. 1, pp. 91–99, Feb. 2007.

[23] A. Bao, K. Liew, and J. Li, "Fischer–Tropsch synthesis on CaO-promoted Co/Al2O3 catalysts," *J. Mol. Catal. A Chem.*, vol. 304, no. 1–2, pp. 47–51, May 2009.

[24] Y.-N. Wang, Y.-Y. Xu, Y.-W. Li, Y.-L. Zhao, and B.-J. Zhang, "Heterogeneous modeling for fixed-bed Fischer–Tropsch synthesis: Reactor model and its applications," *Chem. Eng. Sci.*, vol. 58, no. 3–6, pp. 867–875, Feb. 2003.

NEAR-PERFECT METAMATERIAL ABSORBER FOR THE VISIBLE SPECTRUM

Syed Asad Ali Shah[1,*], Muhammad Imran Aslam[1, 2,*], Irfan Ahmed[1, 2,] Syed M. Usman Ali[1, 2]

[1]Department of Electronic Engineering, NED University of Engineering and Technology, University Road, Karachi-76270, Pakistan.

[2] Emerging Technologies Research Group (ETRG), NED University of Engineering and Technology, University Road, Karachi-76270, Pakistan.

[*] *Corresponding Authors*: aashah52@gmail.com, iaslam@neduet.edu.pk

ABSTRACT

We propose a two dimensional metamaterial absorber comprising of rectangular array of dielectric (Magnesium Fluoride) and metal (silver) placed on a continuous metal film. We investigate the absorption properties of the metamaterial absorber for the visible spectrum. The electromagnetic properties of the proposed metamaterial absorber are simulated using software package “COMSOL Multiphysics”. The effect of changes in the geometry of the nanostructured metamaterial on the absorption has been studied. Our proposed metamaterial absorber exhibit near perfect absorption at about 552 THz. It is shown that the absorption characteristics of the proposed absorber can be devised by varying the geometry of the structure thereby optimizing the response for a desired frequency.

Keywords: Light absorber; Metamaterial; Near-perfect absorption; Visible spectrum.

1 INTRODUCTION

The traditional resources of energy are decreasing day by day, which ultimately increase the need of alternate energy means. The demand has been grown upto 50% during last decades, and it is expected to rise more than 40% by 2035 [1]. Most of the energy demand is fulfilled by the conventional energy sources i.e. fossil fuels [2]. Dependability on these resources is not long lasting. Energy from fossil fuels seems insufficient to meet future demands of flourishing industries and domestic purposes. The gases emitting out during the combustion of these fossil fuels have several hazardous effects on atmosphere, which blatantly disturbing the ecosystem [3, 6]. The other energy resources are nuclear energy, hydro power, wind energy and solar energy. Nuclear energy was proposed to fulfil the requirements, but it need sophisticated and secure environment for operation, furthermore the incident of Fukushima Diachhii, Japan has proved the risk and harmfulness for environment [4]. Obtaining energy from wind power also needs favourable circumstances such as big size turbines, windy location and installations on heights which bounds its. The hydro power energy requires huge amount of water reservoir as well as its turbines must be located in between this water reservoir. [5]

Solar energy may be the answer to this crisis to fulfil the future energy demands. Excessive amount of solar power is available with enormous advantages by reducing the environmental hazards caused by the hydrocarbon and fossil fuels. Solar energy has found applications from domestic utilization to industrial zones. [7, 8]. Extensive research work is going on in order to increase the efficiency of existing solar cells. An important aspect is to increase the absorbance of light by the solar cell material. One possibility of improving efficiency of solar cells is by using nanostructured metamaterials [4, 5]. In this work, we propose a metamaterial absorber for the visible spectrum with a near-perfect absorption band. We also study the effect of geometric variations on the absorption efficiency of the proposed structure.

Rest of the paper is organized as follows. A brief discussion on metamaterial absorbers is included in section II, geometry and simulation of our proposed metamaterial is in section III, followed by the effect of change in geometry in section IV. Section V concludes the paper.

2 METAMATERIAL ABSORBER

Lately, the Metamaterial absorbers has replaced the solar cells for better efficiency and capability of absorbing radiation of frequency ranges from 100THz to 1000 THz [9,10]. The interplay of Surface Plasmon Polaritons (SPPs) and metamaterials has endowed with new opportunities of research. Initially proposed structures were capable of absorbing radiations in infrared and microwave bands [11-13], the ideas were promoted to encompass the higher frequency bands of visible spectrum [14]. For the recent technology, the outcomes can be enhanced by different ways i.e. by increasing the capability of light absorption or by decreasing the threat of losing the energy after it. Lately, recent enhancements in the field of nanostructured metal-o-dielectric metamaterials have brought significant findings in the domain of plasmonic solar absorber. The proper geometry of metallic nanostructures increases the performance and capability of manipulating light, trapping it in active layer and thus improving the capabilities of energy harvesting devices.

Upon incidence of solar radiations, an absorber reflects some of the incident frequencies and absorbs some of them; these absorbed frequencies are converted into heat and can be used in any other form of energy. The efficient solar absorber have lowest reflectance and transmittance in the absorption band, thereby it exhibits maximum absorbance. In this research work, we explore the absorption properties of a metallic nanostructured absorber in the visible spectrum. We propose a two dimensional metamaterial absorber comprising of a silver metal layer and rectangular array of nanoparticles made of dielectric Magnesium Fluoride (MgF_2) and silver metal. The electromagnetic properties of the proposed metamaterial absorber are simulated using software package “COMSOL Multiphysics”. The effect of changes in the geometry of the nanostructured metamaterial on the absorption has been studied. It is shown that the absorption characteristics of the proposed metamaterial structure can be devised by varying the geometry of the structure thereby optimizing the response for desired frequency. Our simulation results represent that the proposed structure can easily be optimized to exhibit near-perfect absorption in the visible part of the electromagnetic spectrum. As an example, we present the absorption characteristics of the proposed structure optimized for the green light.

3 THE PROPOSED STRUCTURE

The Fig (1) illustrates the geometry single unit and 3×3 array of our proposed structure. A single unit cell of our proposed structure comprises of silver metal plate with period p=600nm and height of tm2=250nm. A rectangular array of width w1=300nm of MgF_2 of height ti1=290nm and silver metal of height tm1=250nm is placed on top of the continuous metal layer as shown in Fig. (1).

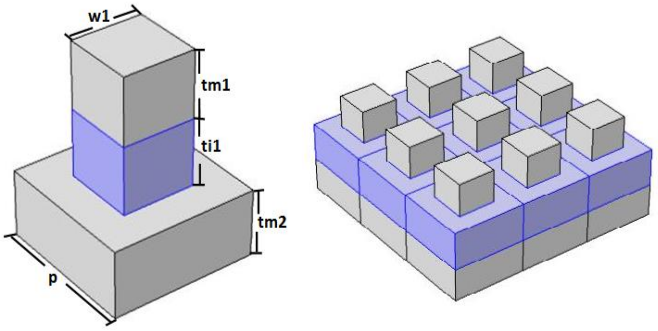

Fig (1) Unit cell and 3×3 array of proposed absorber. The grey layers represents the silver metal layer and blue represents MgF_2 of electric permittivity ε=1.9 dielectric layer.

The metallic grating plate aids in generation of Surface Plasmon Polaritons (SPPs) [5]. The SPPs electron excitation occurs at the boundaries of the metal and dielectric layers, this increases the absorption. For simulation purpose, silver metal was modelled using Drude model with plasma frequency fp=2180THz and collision frequency fc = 13.5THz. The **s** parameters calculated using COMSOL simulation were used to calculate the transmittance and reflectance by $T=|\mathbf{s}_{21}|^2$ and $R=|\mathbf{s}_{11}|^2$. Transmittance of the proposed structure is almost zero due to the presence of the bottom metallic layer. The absorbance is calculated by $A=1-R-T$.

The transmission spectra in the fig (2) represent the absorbance, reflectance and transmittance of the proposed structure. The maximum absorbance of 98.24% occurs at about 552THz which lie in the visible region of electromagnetic spectrum. Another significant peak of absorbance 85.75% occurred at the 385THz lying in the infrared region. A lower absorption peak of 39.34% is also apparent in the Fig. (2) Showing the occurrence of SPPs at that frequency.

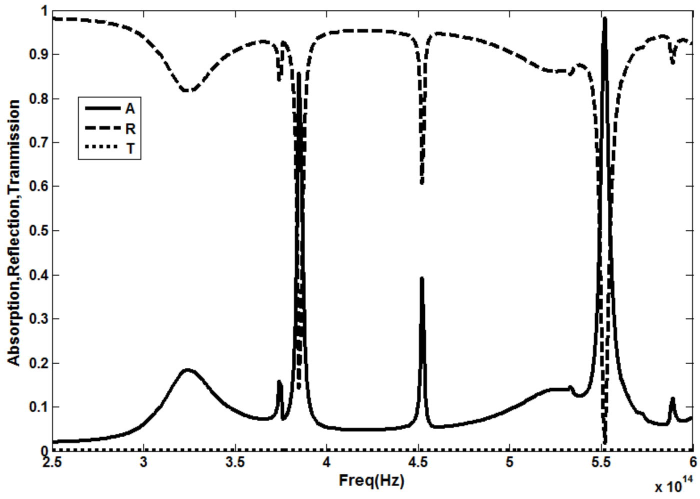

Fig (2) Transmission spectra of the proposed metamaterial absorber. Two significant absorption peaks of 98.24% and 85.75% occurred at 552THz and 385THz respectively.

4 EFFECT OF GEOMETERY

Trend of absorption band has been observed by varying the geometrical values. We have changed one geometrical parameter while keeping all others same as defined in the section 3. Fig (3) illustrates the variation in absorption efficiency with variation in the value of parameter p. The absorption peak decreases with the decrease in the value of p in the visible band region. The maximum peak 98.89% occurred at 541THz when value of p=626nm. It further decreases with decreasing value of p. In addition, similar trend has been observed in the minor peak between 440THz-460THz. In the infrared region the absorption peaks increases with the decreasing value of p between 350THz-400THz.

Fig (4) illustrates the variations in absorption of metallic absorber with the variation in the height of bottom silver layer. The highest peak of 99.32% at 552THz occurred at tm1=225nm. The absorption slightly decreases with increasing the value of tm1 although the frequency of the absorption peak remains same. The variation in the absorption spectrum by varying the value of tm2 is shown in fig (5). In the visible band region the highest absorption peak of 98.24% occurred at tm2=250nm, the absorption peak lowers to 96.77% at 555THz when value of tm2=225nm. Similar trend has been observed in the infrared region at 385THz. However, a minor peak of 71.65% is observed at 593THz when tm2=225nm.

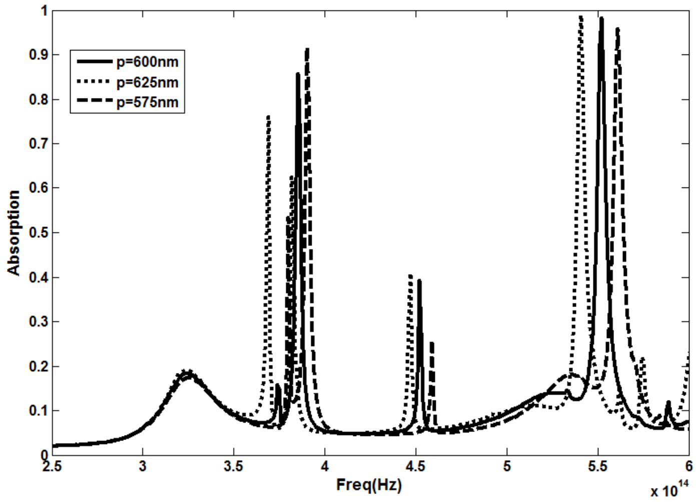

Fig(3) Absorption curves by varying geometric value of "p". The absorption decreases as the value of p decrease in the visible spectrum. However, in the Infrared region the trend increases with decrease in th value of p.

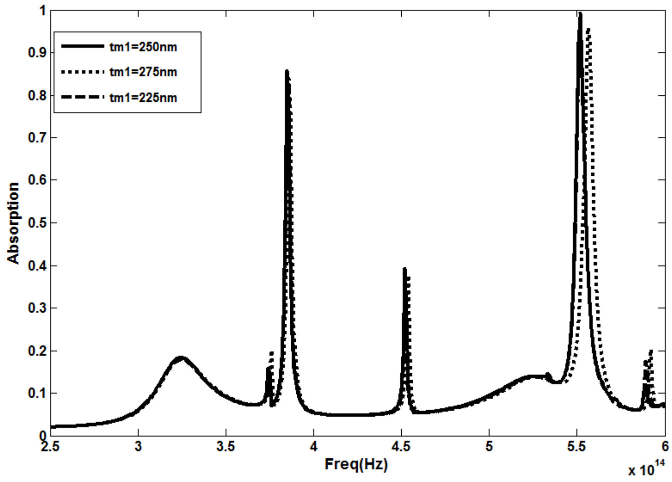

Fig(4) Absorption graph by varying geometric value of "tm1". The highest absorption peak 99.32% occurred at 552THz at tm1=225nm.

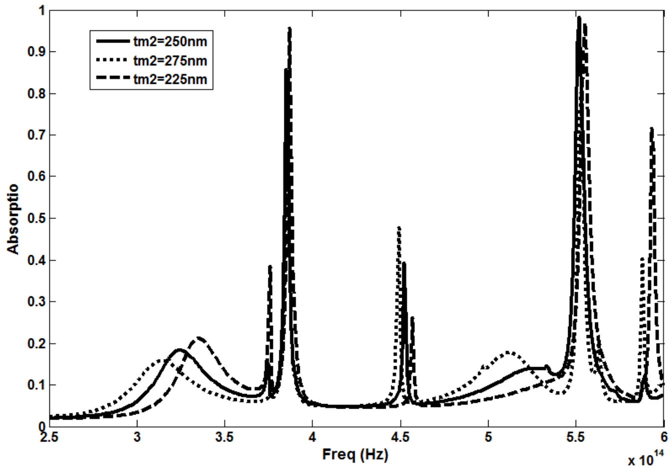

Fig(5) Absorption graph by varying geometric value of "tm2". The major absorption peaks at 387THz and 555THz at tm2=225nm. The highest peak is at 552THz. Although, the minor peaks increased with lowest value of tm2.

As in Fig (6) the absorption efficiency shows significant variation with changes in the geometrical value of w1. The absorption peaks increases with decreasing value of w1 in the infrared band. In visible region the maximum peak occurred at w1=300nm and decreases as the value of w1 is changed.

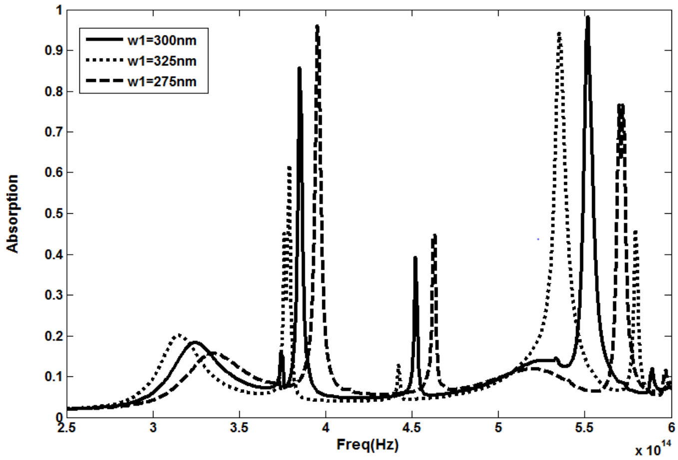

Fig(6) Absorption increases with the decrease in the value of w1 in infrared region. While in visible band the highest peak is absorbed at w1=300nm at 552THz.

The impact of variation in the value of ti1 on absorption is illustrated in fig (7). The high-frequency peak in the visible spectrum is not affected by the variations in ti1. However the absorption tend to reduce with reduction in ti1 in the infrared band. However, several peaks has been observed between the frequency range of 350THz-430THz with highest peak 97.89% at ti1=320nm. Absorbance decreases with the decrease in the value of ti1.

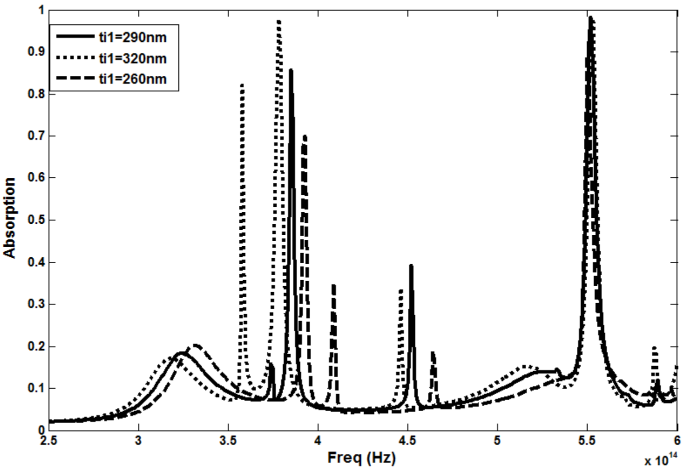

Fig (7) Absorption peaks with varying values of ti1. The peak absorption remains same at 552THz. In infrared region the absorption decreases with decrease in the value of ti1.

5 CONCLUSION

We have investigated our proposed metamaterial structure by simulating a basic structure and analysed its absorption, reflection and transmission properties in the higher frequency band of visible and infrared region. Near-perfect absorption band occurred in the visible spectrum. Furthermore, the geometry of the proposed structure was changed by varying different geometrical parameters to observe the variations in the absorption characteristics. The variations in the geometrical parameters such as w1, ti1 and p have significant impact on the absorption efficiency of our proposed metamaterial structure. Future extension of this work includes the exploration materials and structures suitable to realize wideband metamaterial absorbers for the visible spectrum.

REFERENCES

[1] David Eyton, “Strategic role of technological advances in unlocking available and affordable oil and gas supplies”, International Petroleum Week 2014, London, 17 February 2014.

[2] J. Baxter, Z. Bian, G. Chen, D. Danielson, M. S. Dresselhaus, A. G. Fedorov, T. S. Fisher, C. W. Jones, E. Maginn, U. Kortshagen, A. Manthiram, A. Nozik, D. R. Rolison, T. Sands, L. Shi, D. Shollh, and Y. Wuo, “Nanoscale design to enable the revolution in renewable energy,” Energy Environ. Sci. 2(6), 559–588 (2009).

[3] Euan Mearns, “Global Energy Trends - BP Statistical Review 2014”, Available: http://euanmearns.com/global-energy-trends-bp-statistical-review-2014

[4] Mulla B, Sabah C. Perfect metamaterial absorber design for solar cell applications. Waves in Random and Complex Media, 25:3, 382-392,DOI:10.1080/174550300.2015.1042091

[5] Aslam MI, Ali SM. “A wideband metamaterial absorber for solar cell applications.” Proceeding of International Conference on Energy And Sustainability. 2013; NED University of Engineering & Technology, Karachi Pakistan.

[6] Manabe Syukuro, Wetherald Richard T. The effects of doubling the CO2 concentration on the

climate of a general circulation model. J. Atmos. Sci. 1975; 32:3–15.

[7] Dincer, F., “The analysis on photovoltaic electricity generation status, potential and policies of the leading countries in solar energy,” Renew. Sust. Energy. Rev., Vol. 15, 713–720, 2011.

[8] Dincer, F., “Overview of the photovoltaic technology status and perspective in Turkey,” Renew. Sust. Energy. Rev., Vol. 15, 3768–3779, 2011

[9] Liu, Y., Y. Chen, J. Li, T. Hung, and J. Li, “Study of energy absorption on solar cell using metamaterials,” Sol. Energy, Vol. 86, 1586–1599, 2012.

[10] Meral, M. E. and F. Dincer, “A review of the factors affecting operation and efficiency of photovoltaic based electricity generation systems,” Renew. Sust. Energy. Rev., Vol. 15, 2176–2184, 2013.

[11] N. I. Landy, S. Sajuyigbe, J. J. Mock, D. R. Smith, and W. J.Padilla, “Perfect Metamaterial Absorber,” Physical Review Letters, vol. 100, p. 207402, 2008.

[12] H. Tao, N. I. Landy, C. M. Bingham, X. Zhang, R. D. Averitt, and W. J. Padilla, “A metamaterial absorber for the terahertz regime: design, fabrication and characterization,” Optics Express, vol. 16, pp. 7181-7188, 2008.

[13] Gu, S. Qu, Z. Pei, H. Zhou, J. Wang, B.-Q. Lin, Z. Xu, P. Bai, and W.-D. Peng, “A Wide-Band, Polarization-Insensitive And Wide Angle Terahertz Metamaterial Absorber,” Progress In Electromagnetics Research Letters, vol. 17, pp. 171-179, 2010.

[14] K. Aydin, V. E. Ferry, R. M. Briggs, and H. A. Atwater, “Broadband polarization-independent resonant light absorption using ultrathin plasmonic super absorbers,” Nature Communications, vol. 2, p. 517, 2011.

MODELING OF BAINITIC PHASE TRANSFORMATION IN Fe-Mn-Si-C ALLOY

Muhammad Samiuddin[1,*], Muhammad Asjad Mazahir[2] and Talha Mahfooz[3]
[1]Metallurgical Engineering Department, NED University of Engineering & Technology, Karachi, Pakistan
[2]Materials Engineering Department, PIEAS, Islamabad, Pakistan
[3]Metallurgical Engineering Department, NED University of Engineering & Technology, Karachi, Pakistan

[*]Corresponding author. Tel.: +92334-9551711; fax: (92-21) 99261255
E-mail address: **engr.sami@neduet.edu.pk**

ABSTRACT

Bainitic transformation can be used to design steels with high strength and toughness provided cementite precipitation is suppressed and formation of large blocky regions of austenite is minimized. Cementite formation can be suppressed by adding high silicon content (up to 1.5wt %) while large blocky regions of austenite can be minimized by adjusting certain process parameters. These process parameters mainly include transformation temperature and carbon content of the steels. There are several models present in the literatures that uses these process parameters for the prediction of yield strength, transformation time and phase fractions of bainite, martensite and retained austenite on the basis of certain assumptions. However these assumptions limits the values of process parameters up to which the model remains valid. The aim of the present work is to develop a unifying model that incorporates all the process parameters. By using this model transformation time, yield strength and phase fraction of different phases can be calculated by the knowledge of only chemical composition and transformation temperature. This model would serve as a useful tool for designing of strong and tough bainitic steels. A Fe-Mn-Si-C bainitic alloy has also been designed using these process parameters, which is expected to achieve a good combination of strength and toughness.

Keywords: Bainitic transformation, Martensite, retained austenite, Cementite formation, bainitic alloy, transformation temperature

1. INTRODUCTION

Properties in most commercial steels are optimized by either annealing or normalizing from austenising temperature or by quenching to martensite, and subsequently tempering. However it has been difficult to optimize properties in bainite due to difficulty in controlling the microstructures. Precipitation of coarse carbides between bainitic subunits is detrimental to toughness. It has been established through some research that silicon and aluminum can be used to retard the formation of carbides. These elements do not dissolve in the carbides and hence prevent its precipitation from austenite **[1]**. It has been found that 1.5 wt. % silicon can completely eliminate carbides from the microstructure and carbon diffused from bainitic ferrite enriches the residual austenite.

The enrichment of austenite leads to large fractions of blocky austenite that is unstable and transforms to brittle martensite on quenching from isothermal transformation temperature or under the influence of small stresses. The presence of hard and brittle martensite is also undesirable in the microstructure because it leads to poor toughness. Bainitic transformation occurs by diffusionless growth which requires that transformation occurs at a temperature below T° when free energy of bainite is less than the free energy of austenite of the same compositon**[2]**. Growth without diffusion can only occur if the carbon concentration of the austenite is to the left of T° curve. The growth continues till the carbon concentration of the austenite reaches T° composition and then the growth stops. This is called incomplete reaction phenomenon. It is illustrated in fig 1.

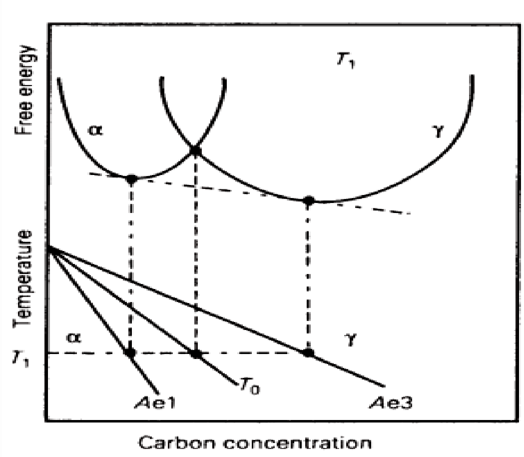

Figure 1: Schematic Illustration of Incomplete Reaction Phenomenon

It is better to have film morphology of austenite instead of block morphology. The films of austenite dispersed between bainitic plates are stable, partly because of their higher carbon concentration and partly because of constraint to transformation exerted by the surrounding plates of ferrite **[3]**. The ductile films of austenite trapped between the plates of bainitic ferrite have a crack blunting effect. They add to toughness by transforming to martensite under the influence of stress what is commonly known as TRIP (Transformation Induced Plasticity) phenomenon.

2. DESIGN/MODELING PARAMETERS

The aim of the alloy design should be to minimize blocky regions of austenite and promotes the formation of thin films of austenite. This can be achieved by increasing the volume fraction of bainite which depends on several design parameters that are discussed below;

2.1 T°' Curve:

The T° curve is the locus of all the points, on the temperature versus carbon plot at which free energy of austenite and ferrite of same chemical composition is equal. The $T^{\circ\prime}$ curve is the same but it takes into account stored energy of bainite that is typically 400J. The maximum fraction of bainite that can be obtained at any given composition and isothermal transformation temperature can be given by the lever rule.

$$Vb = \frac{x_\gamma - \bar{x}}{x_\gamma - 0.03} \qquad (1)$$

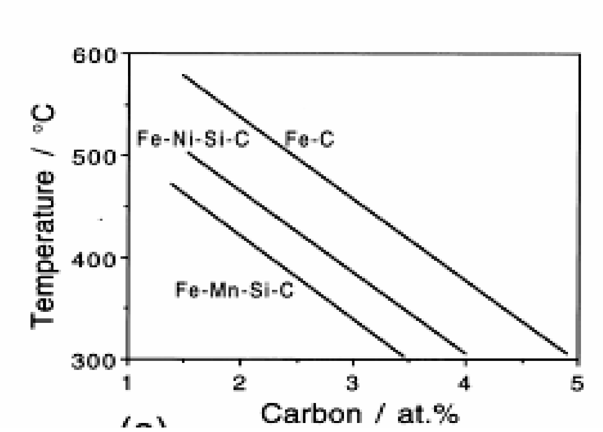

Figure 2: Illustration of role of T°'curve on the volume fraction of bainite

This equation gives the maximum volume fraction that can be obtained at a given composition and temperature. Here $\bar{x}$ gives the average carbon content of the alloy and x_γ gives the carbon concentration of the residual austenite that is defined by $T^{\circ\prime}$ line. The $T^{\circ\prime}$ curve can be calculated by considering the fact that free energy of ferrite and austenite is zero at $T^{\circ\prime}$ temperature. Here 0.03 wt% is the maximum amount carbon that can be accommodated in ferrite. However for bainitic ferrite platelets this amount may vary depending on the average carbon concentration and transformation temperature. One way to increase the volume fraction of bainite is by shifting the $T^{\circ\prime}$ line upward by varying alloying elements and their respective concentrations **[4]**.

$$\Delta G^{\gamma\alpha} = 0 \qquad (2)$$

Zener suggested that the free energy difference can be considered to be composed of two components, the magnetic and non magnetic components.

$$\Delta G^{\gamma\alpha} = \Delta G_M^{\gamma\alpha} + \Delta G_{NM}^{\gamma\alpha} \qquad (3)$$

It helps to account for the effects of alloying alements, via a modification of temperature at which the free energy is evaluated.

$$\Delta G^{\gamma\alpha}\{T\} = \Delta G_M^{\gamma\alpha}\{T - x\Delta T_M\} + \Delta G_{NM}^{\gamma\alpha}\{T - x\Delta T_{NM}\} \qquad (4)$$

ΔT_M and ΔT_{NM} are temperature changes due to a unit concentration of x of substitutional solute. The T° temperature is therefore calculated by setting $\Delta G^{\gamma\alpha}$ to zero:

$$\Delta G_M^{\gamma\alpha}\{T - x\Delta T_M\} + \Delta G_{NM}^{\gamma\alpha}\{T - x\Delta T_{NM}\} = 0 \qquad (5)$$

ΔG can be expressed as a function of temperature by $\Delta G = a + bT$. Therefore, for pure iron, the above expression can be written as

$$a_{NM} + b_{NM}T_0^{Fe} + a_M + b_M T_0^{Fe} = 0 \qquad (6)$$

And for an iron alloy

$$a_{NM} + b_{NM}(T_0^{FeX} - x\Delta T_{NM}) + a_M + b_M (T_0^{FeX} - x\Delta T_{NM}) = 0 \qquad (7)$$

The shift in T° temperature by the addition of substitutional alloying elements can be given by the difference between these two equations:

$$\Delta T_0 = \frac{\sum_i x_i(b_{NM}+\Delta T_{NMi}+b_M+\Delta T_{Mi})}{b_{NM}+b_M} \qquad (8)$$

In order to calculate the shift in $T^{\circ\prime}$ temperature, $\Delta G^{\gamma\alpha}$ is set to the value of stored energy of bainite (i.e 400J/mol). For Fe-C alloy:

$$T_0^{'}(K) \cong 970 - 80x_c \qquad (9)$$

Where x_c is the at % of carbon.

And with the addition of other alloying elements the equation becomes.

$$T_0^{'}(K) \cong 970 - 80x_c + \Delta T_0 \qquad (10)$$

This equation the $T_0^{'}$ curve for a given alloy and has a vital significance for alloy designing.

2.2 Carbon Content

The other important aspect for designing of bainitic alloy is the average carbon content. By looking at the $T^{\circ\prime}$ curve, it is clear that volume fraction of bainite can be increased by lowering the average carbon content of the alloy. However it has to be kept in mind that lowering the carbon content will decrease the strength of the alloy so this has to be considered before setting the carbon content of the alloy.

2.3 Transformation Temperature:

Volume fraction of bainite can also be increased by lowering the isothermal transformation temperature. The lower limit of transformation temperature is defined by Ms temperature. Several equations have been reported in the literature for calculating Ms temperature **[5]**. Bhadehia**[6]** expressed the Ms temperature in terms of driving force for transformation. Using Artifical Neural Network model, an equation has been derived **[7]**. This equation is given below:

$$M_s(K) = 764.2 - 302.6w_C - 30.6w_{Mn} - 16.6w_{Ni} - 8.9w_{Cr} + 2.4w_{Mo} - 11.3w_{Cu} + 8.58w_{Co} + 7.4w_W - 14.5w_{Si} \qquad (11)$$

Here concentrations are given in wt%.

The Ms temperature is also useful in predicting the fraction of austenite that is retained upon quenching after isothermal transformation. The carbon content of retained austenite can be estimated by $T^{\circ\prime}$ line and thus the corresponding Mstemperature can be calculated. Using that, volume fraction of retained austenite can be calculated by the equation:

$$1 - V_{\alpha'} = \exp\{\beta(M_s - T_q)\} \qquad (12)$$

Here,

$M_s = Martensite\ start\ temperature$
$T_q = Temperature\ below\ which\ the\ sample\ is\ undercooled$
$V_{\alpha'} = Volume\ fraction\ of\ martensite$
$\beta = -0.011$

It should be emphasized here that volume fraction of martensite obtained by the above equation may differ significantly from the experimental observation due to the fact that after going through bainitic transformation, the plastic deformation of austenite leads to its mechanical stabilization**[8,9].**

2.4 Prediction of Transformation Time

Using classical nucleation theory, neglecting strain energy, Russell obtained several expressions for different grain boundary nucleation phenomenon for calculating the time τ_s needed to reach a steady–state nucleation rate. The general form of these equations is given below **[10]**:

$$\tau s \propto \frac{T}{(\Delta G_m)^p D} \qquad (13)$$

Where p is an exponent which depends on the nature of the interface between the nucleus and matrix, and D is a diffusion coefficient. If τ_s is empirically identified with the incubation time τ observed for the beginning of transformation in time–temperature transformation diagrams, then it is possible to establish a reasonable method for calculating the initiation of transformation by generalizing equation as follows:

$$\ln\left\{\frac{\tau(\Delta G_m)^p}{T^z}\right\} = \frac{Q^{'}}{RT} + C \qquad (14)$$

Where Q’, C4, p and z are obtained by fitting to well–behaved experimental TTT diagrams. The method has proved extremely successful in a variety of computer programs, ranging from the design of steel weld metals to steel processing.

Numerical values of ΔG_m can be obtained by following equations**.**

$$\Delta G_{Fe}^{\gamma\alpha} + RT\ln\frac{a_{Fe}^{\alpha}\{1-x\}}{a_{Fe}^{\gamma}\{1-\bar{x}\}} - RT\ln\frac{a_{c}^{\alpha}\{x\}}{a_{c}^{\alpha}\{\bar{x}\}} = 0 \qquad (15)$$

$$\Delta G_m = \mathrm{RTln}\frac{a_c^{\alpha}\{x_m\}}{a_c^{\gamma}\{\overline{x}\}} \qquad (16)$$

where $a_{Fe}^{\alpha}\{1-x\}$ refers to the activity of iron in ferrite evaluated at the concentration (1- x), and a similar rationale applies to the other activity terms. The term $\Delta G_{Fe}^{\gamma\alpha}$ a refers to the free energy change accompanying the austenite-ferrite transformation in pure iron and R is the gas constant. The term x is the average carbon concentration of the steel concerned and x_m represents the composition of ferrite which satisfies equation. After iteratively solving first equation the ideal nucleus composition obtained is substituted into second equation to determine ΔG_m.

The activity of carbon and iron can be determined by Moon equation **[11]** as follows:

$$\ln a_c = ln\frac{x_c}{n-(n+1)x_c} + \frac{\Delta G^{xs}}{RT} + zln2\frac{[n-(n+1)x_c]}{[\delta+n-(n+2)x_c]} \qquad (17)$$

$$\ln a_{Fe} = \frac{n(z-2)}{2}\ln\frac{n(1-x_c)}{n-(n+1)x_c} + \frac{nz}{2}\ln\frac{\delta+n-(n+2)x_c}{\delta+n(1-x_c)} \qquad (18)$$

$$\delta = \left\{[n-(n+2)x_c]^2 + 4x_c[n-(n+1)\,x_c]e^{-\frac{\omega}{RT}}\right\}^{\frac{1}{2}} \qquad (19)$$

The values of certain parameters for above equations are given below (Table 1).

Table 1. Equation Parameters

Parameters	Ferrite	Austenite
N	3	1
Z	4	12
Ω	132400	8250
ΔH_{xs}	111918	38550
ΔS_{xs}	51.44	13.46

Where,

a_c = activity of carbon in iron relative to graphite.
x_c = mole fraction of carbon in solution.
n = ratio of (active) interstitial carbon sites to lattice iron sites.
z = number of first nearest-neighbor (active) interstitial sites.
ΔG_{xs}= relative partial molar excess Gibbs free energy of solution of carbon in iron (J/mol).
ΔH_{xs}= relative partial molar enthalpy of solution of carbon in iron (J/mol).
ΔS_{xs} = relative partial molar excess non-configurational entropy of solution of carbon in iron (J/mol-K).
ω = molar sum of the interaction energies between first nearest-neighbour carbon- carbon pairs (J/mol),
R = Universal Gas Constant (8.3144 J/mol-K).

ΔH_{xs},ΔS_{xs}, and ω values are determined from **[12,13].**

2.5 Prediction of Strength

The strength of bainite and martensite can be approximated by the equation

$$\sigma = \sigma_{Fe} + \sigma_c + x_i\sigma_{ssi} + K_L(\bar{L}_3)^{-1} + K_D\rho_D^{1/2} \qquad (20)$$

where x_i is the concentration of a substitutional solute which is represented here by a subscript i. The other terms in this equation can be listed as follows:

K_L = coefficient for strengthening due to lath size,
K_D =coefficient for strengthening due to dislocations,
σ_{Fe}=strength of pure, annealed iron, 219MNm^{-2} at 300K
σ_{SSi} = Substitutional solute
σ_c = Solid solution strengthening
ρ_D = Dislocation density
L=measure of the ferrite plate size, typically 0.2 µm.

According to Solid-Solution Theory indicates that the strength increment due to dissolved carbon in ferrite should vary with the square root of the carbon concentration:

$$\sigma_c = 1722.5\sqrt{x} \qquad (21)$$

Where x is the carbon concentration given in wt %.

For constrained bainite

$$\sigma_B \approx \sigma_B^{'}[0.65exp^{-3.3V_b} + 0.988] \qquad (22)$$

An attempt has been made **[14]** to calculate the stress strain curve of three phase alloy consisting of bainite, martensite and retained austenite by considering a hard phase consisting of bainite and martensite and a soft phase consisting of austenite. It is assumed that true stress-strain relationship of the individual phases can be given by

$$\sigma = K\epsilon^n \qquad (23)$$

where K is strength coefficient and n is strain hardening coefficient.

The applied stress before the onset of plastic deformation in the hard phase is given by

$$\sigma_m = \sigma_s\left(\frac{\epsilon_m}{1-f}\right) + \frac{f}{1-f}A\epsilon_m \qquad (24)$$

$$\epsilon_m = (1-f)\epsilon_s \qquad (25)$$

$$A = \frac{E(7-5v)}{10(1-v^2)} \qquad (26)$$

where σ_m and ϵ_m are respectively the true stress and true strain of the material as a whole, f is the volume fraction of the hard phase, σ_s and ϵ_s are the true stress and true strain of the soft phase, E is Young's Modulus (210Gpa) and v is Poisson's ratio (0.33).

The onset of plastic flow in the hard phase which can be typically regarded as yield stress of the material (0.2% proof stress) can be approximated by following equations

$$\sigma_m^c = \sigma_s\left(\frac{\epsilon_m^c}{1-f}\right) + \left(\frac{f}{1-f}\right)A\sigma_m^c \qquad (27)$$

$$\sigma_m^c = \sigma_{ho} - A\epsilon_m^c \qquad (28)$$

where σ_m^c and ϵ_m^c are respectively the critical true stress and true strain to start yielding in the hard phase and σ_{ho} is the true yield stress of the hard phase.

3. SETTING UP THE PARAMETERS

Our aim of alloy designing is to optimize the properties (strength and toughness) of steel without using expensive alloying elements. Previous research **[1, 11]** shows that 0.2C3Mn2Si and 0.4C4Ni2Si gives good combination of strength and toughness. The experimental values of tensile and charpy test results are given in table 5 and Fig 3 respectively.

Table 5 tensile test results

Alloy	Fe-0.22C-3Mn-2.03Si	Fe-0.39C-4.08Ni-2.05Si
Ultimate tensile strength (Mpa)	1420	1610
0.2%proof stress (Mpa)	1060	1350
Reduction of area (%)	52	56
Elongation	22	12

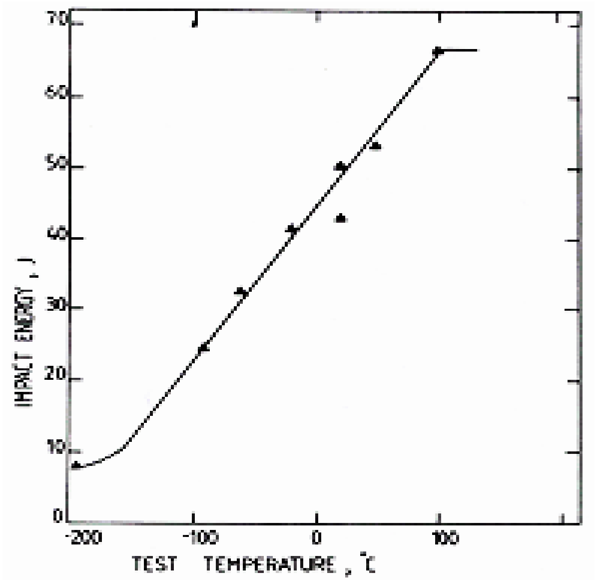

Figure 3(a) Impact test result for 0.22 C 3 Mn 2.03 Si alloy after isothermal transformation at 340°C for 30[1, 11].

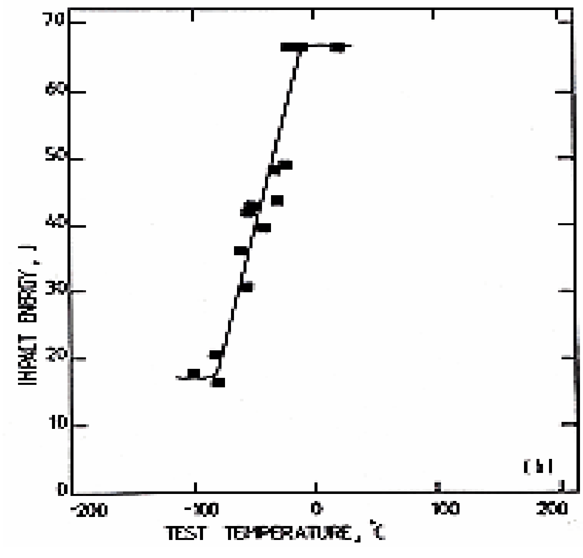

Figure 3(b) Impact test result for 0.39 C 4.08 Ni 2.05 Si alloy after isothermal transformation at 340°C for 60 min[1, 11]

In order to enhance the properties, following modifications are proposed:

1. Carbon concentration is increased to 0.25% to increase the strength of steel.
2. Silicon concentration is limited to 1.5% as it would be sufficient to suppress cementite precipitation.
3. Magnese concentration is set to 2.5% to increase the toughness because the decrease in magnese concentration would shift $T^{\circ\prime}$ curve to higher carbon concentration.
4. Isothermal transformation temperature is chosen to be 20°C above the Ms temperature. This is done to maximize volume fraction of bainite while avoiding any possible formation of martensite plates.

4. CONCLUSION

The strength model gives the yield strength of about 1172 Mpa.

The transformation start time is calculated using the model discussed previously and is found to be about 60sec. The detailed calculations are given in appendix A

ACKNOWLEDGEMENT

Authors are thankful to the support provided by the faculty members of Metallurgical Engineering Department (NEDUET). We are also thankful to the Organizing Committee of the 1st International Conference on **Advance Materials & Process Engineering** (AMPE-2015)

REFERENCES

[1] H.K.D.H. Bhadeshia and D.V Edmonds, Bainite in silicon steels: a new composition and property approach: Part 1, Metal Science, 17: 411-419, 1983.

[2] H.K.D.H. Bhadeshia, Bainite in Steels, 2nd edition, 123.

[3] F.C Caballero, H.K.D.H. Bhadeshia, K.J.A. Mawella, D.D. Jones and P. Brown, Design of novel high strength bainitic steels: Part 1, Materials Science and Technology, 17: 512-516, 2001.

[4] H.K.D.H. Bhadeshia, Steel Microstructure and Properties, 3nd edition, 311.

[5] W.G. Vermeulen, P.F. Morris, A.P. de Weijer, and S. Vad der Zwag, Prediction of martensite start temperature using artificial neural networks, Iron and Steel making, 23: 433-437, 1996.

[6] H.K.D.H. Bhadeshia, Driving force for martensitic transformation in steels, Metal Science, 175-177, 1981.

[7] C. Capdevila, F. G. Caballero, And C. García De Andrés, Determination of Ms temperature in steels. A Bayesian Neural Network Model, Centro Nacional de Investigaciones Metalúrgicas (CENIM).

[8] H.K.D.H. Bhadeshia, Steel Microstructure and Properties, 3nd edition, 118-120

[9] Hong Seok Yang. Dong Woo Suh, H.K.D.H. Bhadeshia, More Complete Theory for the Calculation of the Martensite–Start Temperature in Steels, ISIJ International, 52: 164-166, 2012.

[10] H.K.D.H. Bhadeshia, Thermodynamic analysis of isothermal transformation diagrams, Metal Science, 16: 159-165, 1982.

[11] H. K. D. H. Bhadeshia and D. V. Edmonds. Bainite in silicon steels: a new composition property approach ii. Metal Science, 17:420–425, 1983.

[12] C.R. Ure, Computer Prediction Of Iron-Carbon Phase Diagram, University of Canterbury, 17-18

[13] C.R. Ure, Computer Prediction of Iron-Carbon Phase Diagram, University of Canterbury, 21.

[14] http://www.msm.cam.ac.uk/map/map.html

Appendix A

Elements	At%	Column	Wt%
Si	2.93	8.78	1.5
Mn	2.48	-593.74	2.5
Ni	0.00	0.00	0
Cr	0.00	0.00	0
V	0.00	0.00	0
Co	0.00	0.00	0
Al	0.00	0.00	0
Cu	0.00	0.00	0
Mo	0.00	0.00	0
C	1.14		0.25
		-584.96	4.25
			4
	ΔT°	-97.49	

Column1	Ms(T°C)	Column2	x^γ(wt%)	Vb	Vἀ	Vγ
Andrews	357					
Bhadeshia			0.81	0.71	0.00	0.29
Caballero	317					
IT	337					

Ms after trans(T°C)
3.68
25.00

Xc(wt%)	Column1	Column2	T°'(Fe-C)	Column4	T°'(Fe-alloy)
0		1.81331	697		600
0.02		1.81462	690		593
0.04		1.81593	683		586
0.06		1.81724	676		579
0.08		1.81855	670		572
0.1		1.81986	663		565
0.12		1.82117	656		558
0.14		1.82248	649		551
0.16		1.82379	642		545
0.18		1.82510	635		538
0.2		1.82641	629		531
0.22		1.82772	622		524
0.24		1.82903	615		517
0.26		1.83034	608		511
0.28		1.83165	601		504
0.3		1.83295	595		497
0.32		1.83426	588		490
0.34		1.83557	581		484
0.36		1.83688	575		477
0.38		1.83819	568		470
0.4		1.83950	561		464
0.42		1.84081	554		457
0.44		1.84212	548		450
0.46		1.84343	541		444
0.48		1.84474	534		437
0.5		1.84605	528		430
0.55		1.84932	511		414
0.6		1.85260	495		397
0.65		1.85587	478		381
0.7		1.85915	462		364
0.75		1.86242	445		348
0.8		1.86569	429		332
0.85		1.86897	413		315
0.9		1.87224	397		299
0.95		1.87551	380		283
1		1.87879	364		267
1.05		1.88206	348		251
1.1		1.88534	332		235
1.15		1.88861	316		219
1.2		1.89188	301		203
1.25		1.89516	285		187
1.3		1.89843	269		172
1.35		1.90170	253		156
1.4		1.90498	238		140
1.45		1.90825	222		125
1.5		1.91153	207		109
1.55		1.91480	191		94
1.6		1.91807	176		78
1.65		1.92135	160		63

Xc vs T°'

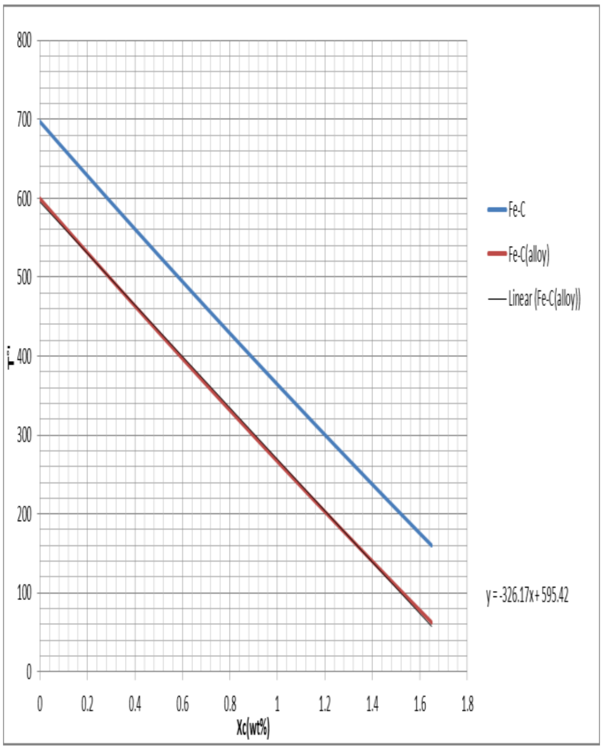

Column1	austenite	ferrite
n	1	3
z	12	4
x	0.0113	0.0014
ω	8250	132500
δ	0.9661	2.993
ln ac	1.657999358	8.203695
ln afe	-0.012296998	-0.0014

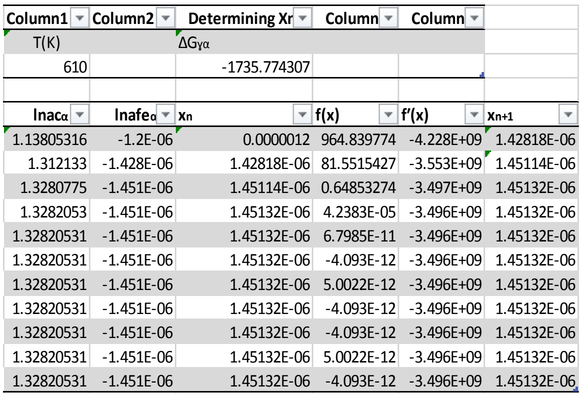

Column1	Column2	Determining Xr	Column	Column	
T(K)		$\Delta G_{\gamma\alpha}$			
610		-1735.774307			
Ina$_{c\alpha}$	**Ina$_{fe\alpha}$**	**x_n**	**f(x)**	**f′(x)**	**x_{n+1}**
1.13805316	-1.2E-06	0.0000012	964.839774	-4.228E+09	1.42818E-06
1.312133	-1.428E-06	1.42818E-06	81.5515427	-3.553E+09	1.45114E-06
1.3280775	-1.451E-06	1.45114E-06	0.64853274	-3.497E+09	1.45132E-06
1.3282053	-1.451E-06	1.45132E-06	4.2383E-05	-3.496E+09	1.45132E-06
1.32820531	-1.451E-06	1.45132E-06	6.7985E-11	-3.496E+09	1.45132E-06
1.32820531	-1.451E-06	1.45132E-06	-4.093E-12	-3.496E+09	1.45132E-06
1.32820531	-1.451E-06	1.45132E-06	5.0022E-12	-3.496E+09	1.45132E-06
1.32820531	-1.451E-06	1.45132E-06	-4.093E-12	-3.496E+09	1.45132E-06
1.32820531	-1.451E-06	1.45132E-06	-4.093E-12	-3.496E+09	1.45132E-06
1.32820531	-1.451E-06	1.45132E-06	5.0022E-12	-3.496E+09	1.45132E-06
1.32820531	-1.451E-06	1.45132E-06	-4.093E-12	-3.496E+09	1.45132E-06

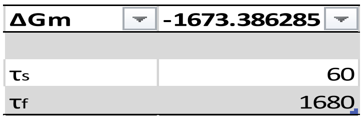

ΔGm	-1673.386285
τ_s	60
τ_f	1680

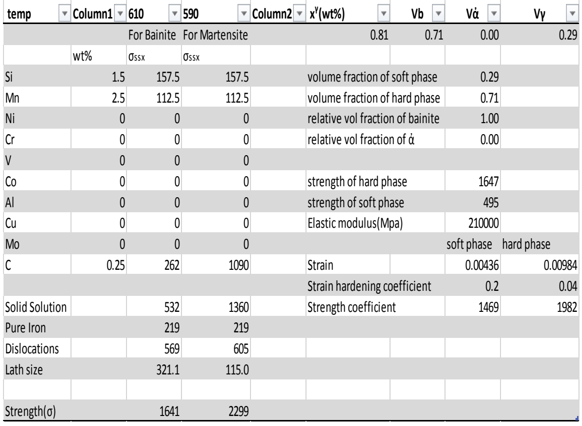

temp	Column1	610	590	Column2	x^{γ}(wt%)	Vb	Vά	Vγ
		For Bainite	For Martensite		0.81	0.71	0.00	0.29
	wt%	σ_{ssx}	σ_{ssx}					
Si	1.5	157.5	157.5		volume fraction of soft phase		0.29	
Mn	2.5	112.5	112.5		volume fraction of hard phase		0.71	
Ni	0	0	0		relative vol fraction of bainite		1.00	
Cr	0	0	0		relative vol fraction of ά		0.00	
V	0	0	0					
Co	0	0	0		strength of hard phase		1647	
Al	0	0	0		strength of soft phase		495	
Cu	0	0	0		Elastic modulus(Mpa)		210000	
Mo	0	0	0				soft phase	hard phase
C	0.25	262	1090		Strain		0.00436	0.00984
					Strain hardening coefficient		0.2	0.04
Solid Solution		532	1360		Strength coefficient		1469	1982
Pure Iron		219	219					
Dislocations		569	605					
Lath size		321.1	115.0					
Strength(σ)		1641	2299					

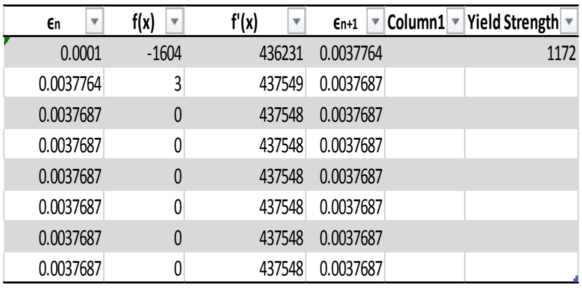

ϵ_n	f(x)	f'(x)	ϵ_{n+1}	Column1	Yield Strength
0.0001	-1604	436231	0.0037764		1172
0.0037764	3	437549	0.0037687		
0.0037687	0	437548	0.0037687		
0.0037687	0	437548	0.0037687		
0.0037687	0	437548	0.0037687		
0.0037687	0	437548	0.0037687		
0.0037687	0	437548	0.0037687		
0.0037687	0	437548	0.0037687		

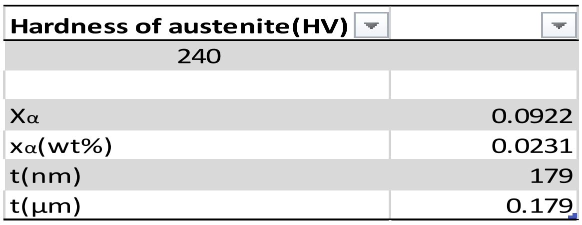

Hardness of austenite(HV)	
240	
X_α	0.0922
x_α(wt%)	0.0231
t(nm)	179
t(μm)	0.179

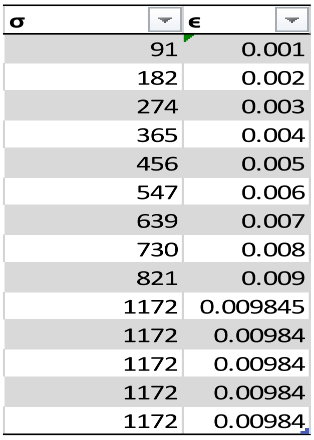

σ	ϵ
91	0.001
182	0.002
274	0.003
365	0.004
456	0.005
547	0.006
639	0.007
730	0.008
821	0.009
1172	0.009845
1172	0.00984
1172	0.00984
1172	0.00984
1172	0.00984

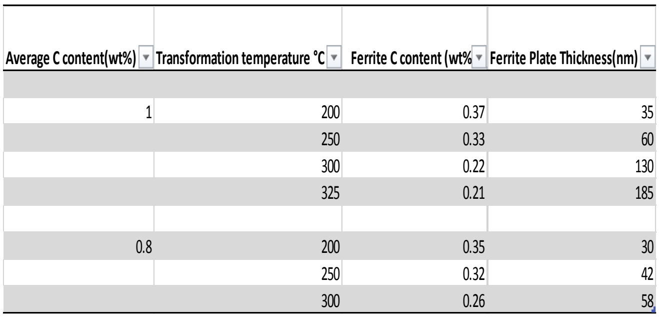

Average C content(wt%)	Transformation temperature °C	Ferrite C content (wt%	Ferrite Plate Thickness(nm)
1	200	0.37	35
	250	0.33	60
	300	0.22	130
	325	0.21	185
0.8	200	0.35	30
	250	0.32	42
	300	0.26	58

Transformation temp vs Ferrite C content

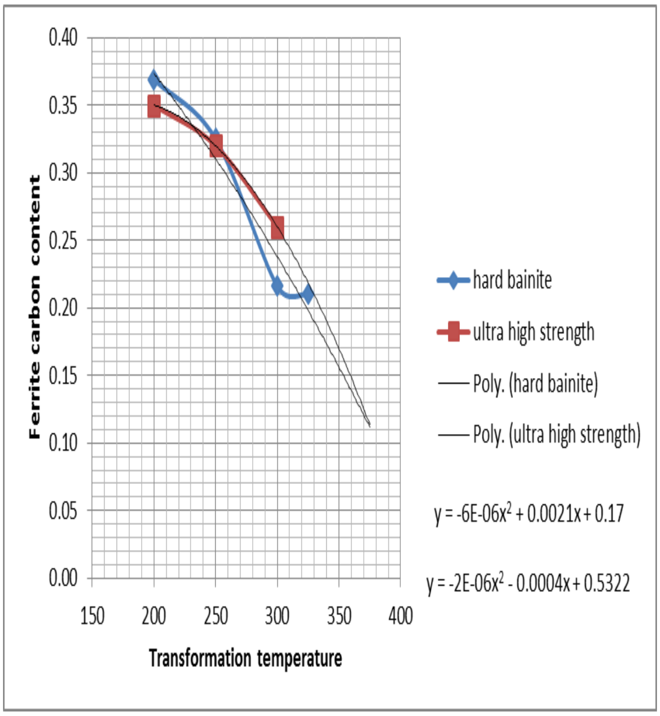

Temperature vs Ferrite plate thickness

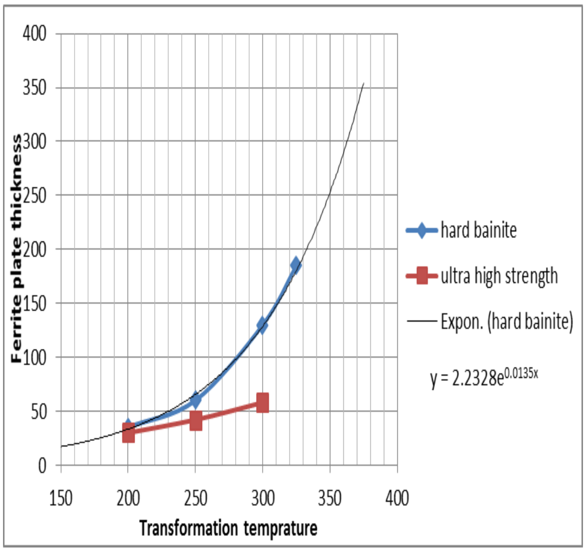

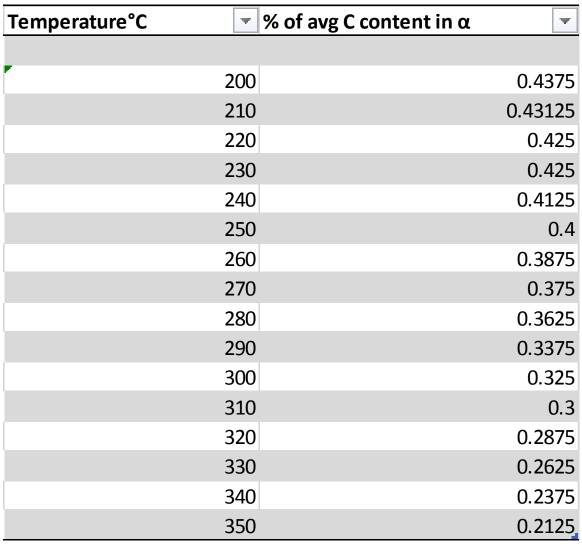

Temperature°C	% of avg C content in α
200	0.4375
210	0.43125
220	0.425
230	0.425
240	0.4125
250	0.4
260	0.3875
270	0.375
280	0.3625
290	0.3375
300	0.325
310	0.3
320	0.2875
330	0.2625
340	0.2375
350	0.2125

Temperature vs % of C in avg Ferrite

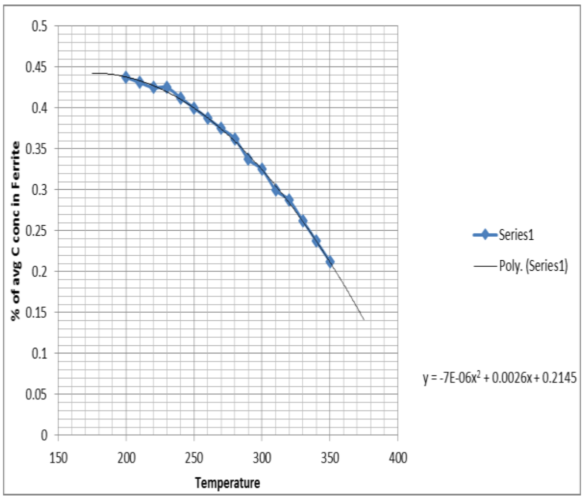

MODELING SOLAR CONCENTRATED LINEAR PARABOLIC TROUGH COLLECTOR WITH SIMULATIONS USING DIFFERENT THERMAL FLUIDS

N. Rehman[1*], B.A. Baloch[2], J. Jawad[2], Z.U. Sheikh[2], Z. Aijaz[2]
[1]Mechanical Engineering Department, NED University of Engineering & Technology,
Karachi, Pakistan
[2] Chemical Engineering Department, NED University of Engineering & Technology, Karachi,
Pakistan

[*]Corresponding author. Tel.: +92 99261261 (ext. 2532);
E-mail address: naveedurrehman@neduet.edu.pk (N.Rehman)

ABSTRACT

In this paper, an analytical heat transfer model for a solar concentrated linear parabolic trough collector has been presented and simulated for nineteen different thermal fluids which are recommended for heat transfer applications. These fluids are namely, dowtherm mx, dowtherm rp, marlotherm ch, paratherm glt, paratherm he, paratherm hr, paratherm nf, syltherm 800, therminol 59, therminol 66, therminol vp1, therminol xp, xceltherm 600, xceltherm ht, Xceltherm lv, dowtherm a, dowtherm g, dowtherm j and dowtherm q. For the purpose, twenty-six essential design parameters are highlighted and discussed in details, including but not limited to, the geometric dimensions and material properties of concentrator and receiver pipe (e.g. concentration ratio, width and length of trough, internal and external diameter of receiver pipe, pipe roughness factor, internal and external diameter of glass envelop and vacuum conditions etc.), thermal fluid properties (e.g. temperature dependent density, specific heat and thermal conductivity etc.) and operating conditions (e.g. ambient temperature, wind velocity and above all, the solar radiations etc.) The model takes into account these design and operational parameters and results in mainly, the temperature profile along the receiver pipe, maximum temperature that could be attained over a given length of a trough and overall thermal efficiency of such systems. An iterative solution scheme for solving the heat transfer model has also been presented. The results depict significant variation in temperature gain along the length of parabolic trough by utilizing different thermal fluids. More interestingly, the knowledge of maximum temperature and the distance at which it could be attained in a trough is something that can assist solar system designers to select suitable thermal fluid for their specific application. The obtained results will be helpful in designing of domestic and industrial scale collectors and selecting the optimum heat transfer fluid for the general to specific applications like water heating, steam generation, thermal and chemical processing, cooling using absorption chillers and so on.

Keywords: Parabolic trough, heat transfer fluids, advanced materials, solar energy, solar applications

1 INTRODUCTION

The increasing demand of energy with less carbon footprint and improved green culture has put forward the need of renewable source of clean energy. Solar Energy is being looked upon as a more viable means of energy due to its replenishing quality and reliability. Solar Energy is being harnessed either directly using photovoltaics (PV), or indirectly using concentrated solar power (CSP). A popular device for producing substantial power through solar energy is parabolic trough collector (PTC) that can heat a suitable fluid to high temperatures, which can be used subsequently to generate high-pressure steam for powering a turbine. PTC also has applications in heating and air-conditioning on domestic and commercial scales.

PTC uses a parabolic trough to concentrate the sunlight towards the absorber pipe through which a Heat Transfer Fluid (HTF) is flowing. The thermal oil is constantly circulated and usually reaches temperatures up to 400°C. Consequently this heated HTF is used to generate steam by heating water to run steam turbines. The trough is parabolic in the x-y plane but linear in the z direction hence also known as linear parabolic trough. PTC system is the most commercialized CSP system because it has been in wide use since the 1980s.

The heat gained by the HTF flowing through the receiver pipe depends on factors such as natural conditions, design parameters and fluid properties. Study on the factors requires accurate prediction of the HTF outlet temperature. This has prompted several studies assuming one-dimensional heat transfer perpendicular to the flow and two-dimensional energy balance on the receiver pipe. A report published by NREL [1] discusses a detailed analytical model and considers most of the variables related to PTC. They have studied the thermal performance of PTC for different operating conditions and solved their model using Engineering Equation Solver (EES). Padilla et al. [2] have carried out a one-dimensional numerical heat transfer analysis of a PTC by solving discretized versions of partial differential equations simultaneously and validating their results with experimental data for one particular design of PTC. Analytical modelling accounts for the effect that design parameters have on the outlet temperature of a particular HTF for which the model is simulated.

Selection of a Heat Transfer Fluid (HTF) for linear PTC solar plant is the most recurring issue being faced today by researchers. Some of the fluids that are being used today include molten salts, thermal oils, glycerol based and synthetic oils which can transfer heat effectively. Simulating the model for various HTFs will be critical in optimizing linear PTC systems which would help identify the factors on which the selection of a Heat Transfer Fluid must be based upon.

A heat transfer model has been developed for the receiver pipe which is validated through various published papers. The validated model is then simulated for nineteen different thermal oils. The thermal oils have been selected for the study based on their wide heat transfer applications.

2 ANALYTICAL MODEL

PTC consists of a parabolic trough reflector, a glass envelope and an absorber pipe, as shown in Fig. 1. Solar radiations are incident on the absorber pipe radially after reflecting back from the parabolic trough reflector. The temperature of the heat transfer fluid (HTF) rises as it travels through the absorber pipe. A low-pressure space is incorporated between the glass envelope and absorber pipe. The various dimensions of PTC are illustrated in Fig 2.

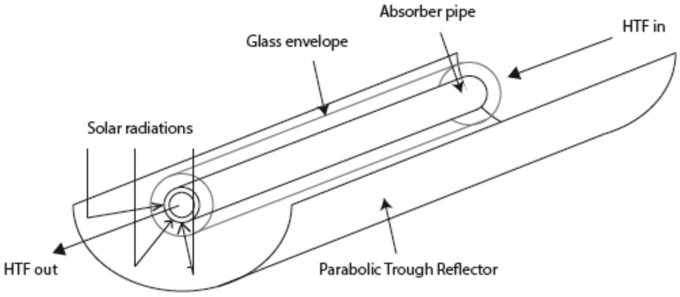

Fig. 1: Schematic of solar parabolic trough collector

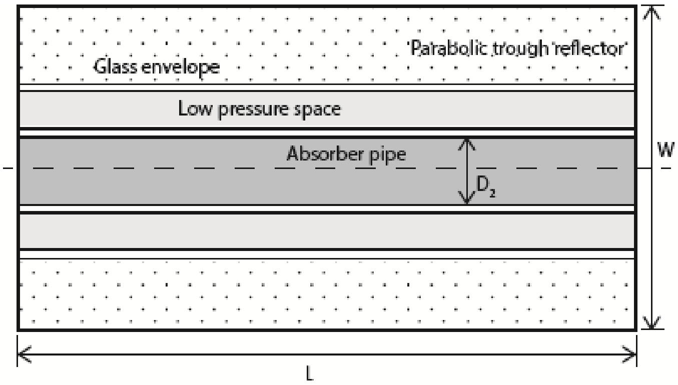

Fig. 2(a): Different dimensions of PTC and absorber pipe

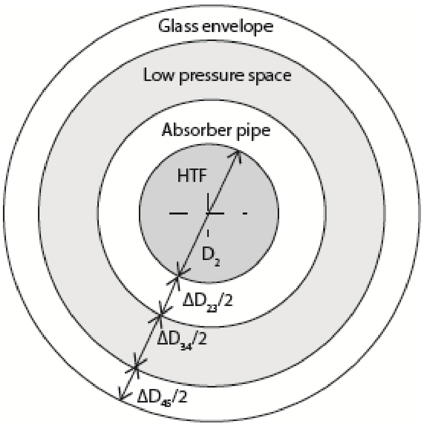

Fig. 2(b): Different dimensions of PTC and absorber pipe

Fig. 3 depicts the one-dimensional model for heat transfer between HTF and the ambient air. It incorporates the various thermal resistances and heat transfer notations.

Using the thermal resistance network, the energy balances are:

$$q_{5solenv} + q_{45cnd} = q_{57rad} + q_{56cnv} \quad (1.a)$$

$$q_{34rad} + q_{34cnv} = q_{45cnd} \quad (1.b)$$

$$q_{3solabs} = q_{32cnd} + q_{34rad} + q_{34cnv} \quad (1.c)$$

$$q_{32cnd} = q_{21cnv} \quad (1.d)$$

$$q_{21cnv} = q_f \quad (1.e)$$

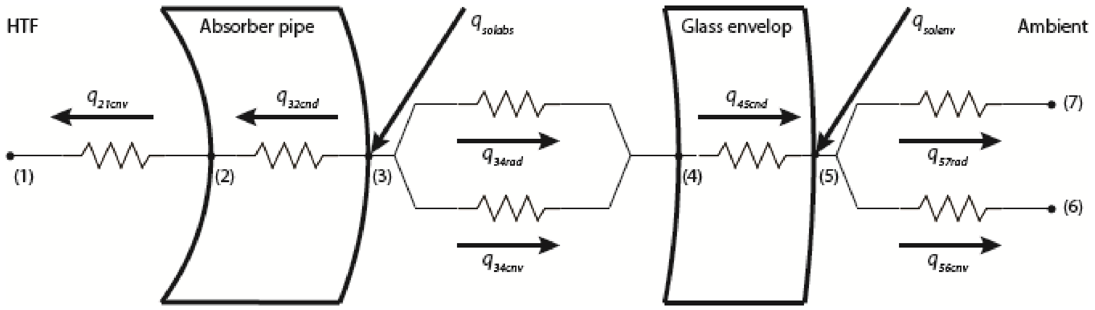

Fig. 3: One-dimensional heat transfer network

where:

$q_{5solenv}$[W]: Absorption of solar irradiation at outer surface of glass envelope.

q_{45cnd}[W]: Heat transfer through conduction from inner glass envelope surface to outer glass envelope surface.

q_{57rad} [W]: Heat transfer through radiations from outer glass envelope surface to the sky.

q_{56cnv} [W]: Heat transfer through convection from outer glass envelope surface to ambient.

q_{34rad}[W]: Heat transfer through radiation from outer absorber pipe surface to inner glass envelope surface.

q_{34cnv}[W]: Heat transfer through convection from outer absorber pipe surface to inner glass envelope surface.

$q_{3solabs}$[W]: Absorption of solar irradiation at outer surface absorber pipe.

q_{32cnd}[W]: Heat transfer through conduction from outer absorber pipe surface to inner absorber pipe surface.

q_{21cnv}[W]: Heat transfer through convection from inner absorber pipe surface to HTF.

q_f[W]: Heat absorbed by HTF.

Heat transfer through conduction from inner glass envelope surface to outer glass envelope surface can be calculated by:

$$q_{45cnd} = 2\pi L k_{env}(T_4 - T_5)/ln\left(\frac{D_5}{D_4}\right) \quad (2)$$

where:

L [m]: Length of PTC

k_{env} [W/mK]: Thermal conductivity of envelope material

T_4 [K]: Temperature of glass envelope inner surface

T_5 [K]: Temperature of glass envelope outer surface

D_4 [m]: Diameter of glass envelope inner surface

D_5 [m]: Diameter of glass envelope outer surface, such that

$$D_5 = D_4 + \Delta D_{45}$$

Heat transfer through radiations from outer glass envelope surface to the sky can be calculated by:

$$q_{57rad} = \sigma\pi D_5 L\varepsilon_{env}\left(T_5{}^4 - T_7{}^4\right) \quad (3)$$

where:

ε_{env}: Emissivity of outer surface of glass envelope

T_7 [K]: Estimated effective sky temperature, such that [1]

$$T_7 = T_6 - 8$$

T_6 [K]: Ambient temperature

Heat transfer through convection from outer glass envelope surface to ambient can be calculated as:

$$q_{56cnv} = \pi D_5 L h_{56cnv}(T_5 - T_6) \quad (4)$$

where:

h_{56cnv}: Convection heat transfer coefficient of air

Heat transfer through radiation from outer absorber pipe surface to inner glass envelope surface can be calculated as:

$$q_{34rad} = \frac{\sigma\pi D_3 L(T_3{}^4 - T_4{}^4)}{\frac{1}{\varepsilon_{abs}} + \frac{(1 - \varepsilon_{env})D_3}{\varepsilon_{env}D_4}} \quad (5)$$

where:

ε_{abs}: Emissivity of outer surface of absorber pipe

T_3 [K]: Temperature of outer surface of absorber pipe

D_3 [m]: Diameter of absorber pipe outer surface

$D_3 = D_2 + \Delta D_{23}$

Heat transfer through convection from outer absorber pipe surface to inner glass envelope surface can be calculated as:

$$q_{34cnv} = \pi D_3 L h_{34cnv}(T_3 - T_4) \tag{6}$$

where:

h_{34cnv}: Convection heat transfer coefficient of annulus gas

Heat transfer through conduction from outer absorber pipe surface to inner absorber pipe surface can be calculated as:

$$q_{32cnd} = \frac{2\pi L k_{abs}(T_3 - T_2)}{ln\left(\frac{D_3}{D_2}\right)} \tag{7}$$

where:

k_{abs} [W/mK]: Thermal conductivity of absorber material

T_2 [K]: Temperature of inner surface of absorber pipe

D_2 [m]: Diameter of absorber pipe inner surface

Heat transfer through convection from inner absorber pipe surface to HTF can be calculated as:

$$q_{21cnv} = \pi D_2 L h_{21cnv}(T_2 - T_1) \tag{8}$$

where:

h_{21cnv}: Convection heat transfer coefficient of HTF

T_1 [K]: Bulk temperature of the HTF, such that:

$T_1 = (T_{fi} + T_{fo})/2$

with:

T_{fi} [K]: HTF temperature at inlet of absorber pipe

T_{fo} [K]: HTF temperature at outlet of absorber pipe

Heat absorbed by HTF can be calculated as:

$$q_f = \dot{m} C_{p,f}(T_{fo} - T_{fi}) \tag{9}$$

where:

$\dot{m}$ [kg/s]: HTF mass flow rate

$C_{p,f}$ [J/kg.K]: HTF specific heat

Absorption of solar irradiation at outer surface of glass envelope can be calculated as:

$$q_{5solenv} = q'' W L \eta_{env} \alpha_{env} \tag{10}$$

where:

q'' [W/m^2]: Incident solar flux per unit area of collector aperture

W [m]: Aperture width of concentrator

η_{env}: Effective optical efficiency at the glass envelope

α_{env}: Absorptance of the glass envelope

Absorption of solar irradiation at outer surface absorber pipe can be calculated as:

$$q_{3solabs} = q'' W L \eta_{abs} \alpha_{abs} \tag{11}$$

where:

η_{abs}: Effective optical efficiency at absorber

α_{abs}: Absorptance of absorber

Convection heat transfer coefficient, h_{21cnv}, for q_{21cnv} can be determined using:

$h_{21cnv} = Nu k_f / D_2$

where:

Nu: Nusselt number for HTF based on internal diameter of absorber pipe

k_f [W/mK]: Thermal conductance of HTF at bulk temperature

The nature of flow can be determined using:

$Re_f = (\rho_f V_f D_2)/\mu_f$

where:

ρ_f [kg/m^3]: Density of HTF at bulk temperature

V_f [m/s]: Flow velocity of HTF

μ_f [kg/m.s]:Dynamic viscosity of HTF

For laminar flows($Re_f < 2300$), $Nu = 4.36$. Otherwise, for turbulent flows (2300≤Ref<5×106, 0.5 ≤ Pr ≤ 2000), Nusselt number correlation with friction factor given by Gnielinski [3, 4].

$$Nu = \frac{\frac{f}{8}(Re_f - 1000)Pr}{1 + 12.7\sqrt{\frac{f}{8}}(Pr^{\frac{2}{3}} - 1)}$$

where:

f: friction factor for the inner surface of the absorber pipe, such that:

$f = (0.79 \log Re_f - 1.64)^{-2}$

The effective optical efficiency at the glass envelope, η_{env} for $q_{5solenv}$ is determined using [1, 6]:

$$\eta_{env} = \varepsilon_1 \varepsilon_2 \varepsilon_3 \varepsilon_4 \varepsilon_5 \varepsilon_6 \rho_{cl} K_{inc}$$

where:

ε_1: Error due to collector shadowing due to bellows, shielding and supports, etc.

ε_2: Tracking error

ε_3: Geometry error due to reflector misalignment etc.

ε_4: Error due to dirt on reflector surface, suggested by Duffie and Beckman [8]:

$$\varepsilon_4 = \eta_o / \rho_{cl}$$

ε_5: Error due to dirt on collector, suggested by Duffie and Beckman [8]:

$$\varepsilon_5 = (1 + \varepsilon_4)/2$$

ε_6: Some unaccounted errors

ρ_{cl}: Clean mirror reflectance

η_o: Reflectivity

K_{inc}: Incident angle modifier

Similarly, the effective optical efficiency at the absorber, η_{abs} for $q_{3solabs}$ is determined using:

$$\eta_{abs} = \eta_{env} \tau_{env}$$

where:

τ_{env}: Transmittance of glass envelope

As the concentration ratio and outer diameter of absorber pipe are known, width of collector aperture can be calculated using:

$$C = W / \pi D_3$$

where:

C: Concentration ratio

In order to validate the analytical model, the above equations were utilized to evaluate the HTF outlet temperature for a particular PTC. Dimensions and input parameter values for the selected PTC are as follows:

L = 7.8 m; C = 24.11; D_2 = 66 mm; ΔD_{23} = 4 mm; ΔD_{34} = 43 mm; ΔD_{45} = 6 mm; ϵ_1 = 0.974; ϵ_2 = 0.994; ϵ_3 = 0.98; ϵ_6 = 0.96; ρ_{cl} = 0.935; η_o = 0.93; $\theta = 0^0$; ϵ_{abs} = 0.1378; ϵ_{env} = 0.85; k_{abs} = 54 W/mK; k_{env} = 1.04 W/K; α_{abs} = 0.905; α_{env} = 0.02; τ_{env} = 0.95; h_{56cnv} = 40 W/m^{2}K; h_{34cnv} = 0.0001115 W/m^{2}K

These values were selected as per the experimental setup described in Dudley et al. [9]. Three different cases for mass flow rates and heat transfer characteristics were used to evaluate three values of HTF outlet temperatures, which were compared against those listed in Dudley et al. [9], as shown in Tab. 1. The outputs of the present analytical model are found to be in agreement with the experimental data. Therefore, this model can be utilized to conduct probabilistic modeling.

Tab. 1: Comparison of results from proposed model and experimental results published in literature

Case	**q" (W/m^2)**	**$\dot{m}$ (kg/s)**	**T_a (K)**	**T_{fi} (K)**	**T_{fo} (K)**	**$T_{fo,model}$ (K)**
1	933.7	0.6782	294.2	375.2	397	396.2
2	937.9	0.6206	301.8	570.8	589.9	591.3
3	920.9	0.5457	302.5	652.5	671	673.5

3 SIMULATING THE MODEL FOR THERMAL FLUIDS

The verified model is subsequently simulated for nineteen fluids to obtain the outlet temperature and efficiency. Some critical properties of the selected thermal fluids are shown in Tab. 2.

Tab. 2: Properties of the selected thermal Fluids

Thermal Fluid	**Max Temp °C**	**Min Temp °C**	**Boiling point °C**
Therminol Vp1 [10]	400	12	257
Dowtherm A [11]	400	15	257.1
Syltherm 800 [12]	400	-40	203
Xceltherm LV [13]	371	7.2	258
Dowtherm G [14]	360	-6	289
Dowtherm RP [15]	350	-20	353
Xceltherm HT [16]	350	-25	280
Therminol 66 [17]	345	-3	359
Paratherm HR [18]	343	20	337
Marlotherm [19]	340	-5	330
Dowtherm MX1 [20]	330	-23	328
Dowtherm Q [21]	330	-35	267
Paratherm NF [22]	325	30	371
Xceltherm 600 [23]	316	-29	367
Therminol XP [24]	315	-20	358
Therminol 59 [25]	315	-49	289
Dowtherm J [26]	315	-80	181
Paratherm HE [27]	300	40	343
Paratherm GLT [28]	288	30	371

4 RESULTS AND DISCUSSION

Outlet Temperature and Efficiencies of each fluid is obtained and plotted on the graph as shown in Fig. 4 and Fig. 5 for comparison.

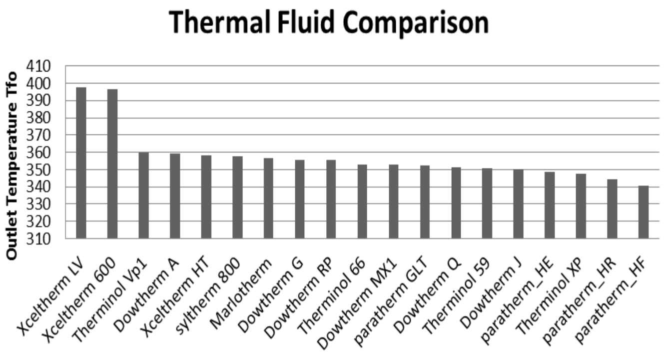

Fig. 4: Outlet Temperature of the Thermal Fluids

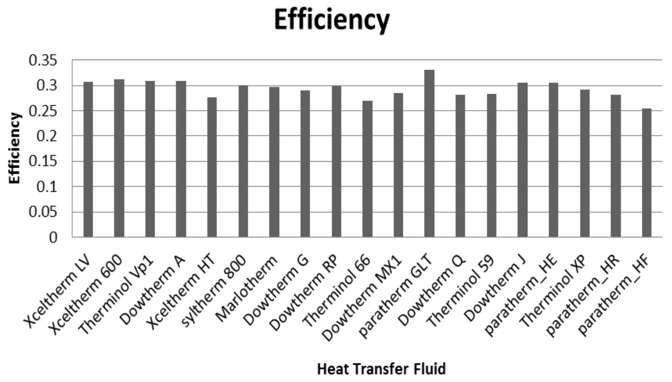

Fig. 5: Efficiency of the Thermal Fluids

It has been observed that the fluid gaining the maximum temperature in the PTC model are Xceltherm LV and Xceltherm 600 going up to 397.6 and 396.6 respectively. Rest of the fluids have outlet temperature lying within the range of 359.7 and 340.8 in our developed model. Paratherm GLT has the highest efficiency of 0.3309.

The gain in temperature with the increasing length of PTC can be observed by the Temperature Profile in Fig. 6(a) and Fig. 6(b).

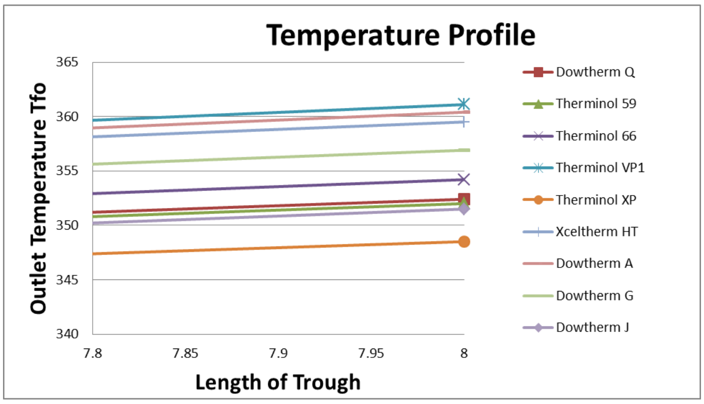

Fig. 6(a): Temperature Profile Curve of the Thermal Fluids

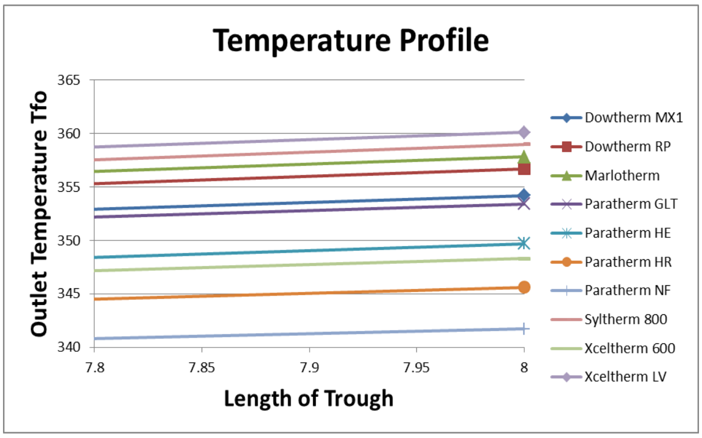

Fig. 6(b): Temperature Profile Curve of the Thermal Fluids

It has been observed that no drastic variation in the slope exist for all fluids. The slopes lie between 6.266 and 7.8411 as shown in Tab. 3.

Tab. 3: Slopes of the Temperature Profile Curves

Fluid	Slope
Therminol VP1	7.8411
Dowtherm A	7.7507
Xceltherm LV	7.7226
Xceltherm HT	7.6429
Syltherm 800	7.5851
Marlotherm	7.4317
Dowtherm G	7.3248
Dowtherm RP	7.2951
Dowtherm MX1	6.9911
Paratherm GLT	6.9744
Dowtherm Q	6.7682
Therminol 59	6.724
Dowtherm J	6.6602
Paratherm HE	6.362
Therminol XP	6.2822
Xceltherm 600	6.266
Paratherm HR	5.9447
Paratherm NF	5.5087

Pressure Drop across the length of PTC has also been studies and a profile curve has been generated as shown in Fig 7(a) and Fig 7(b). Fluids with low pressure drop are generally more preferred.

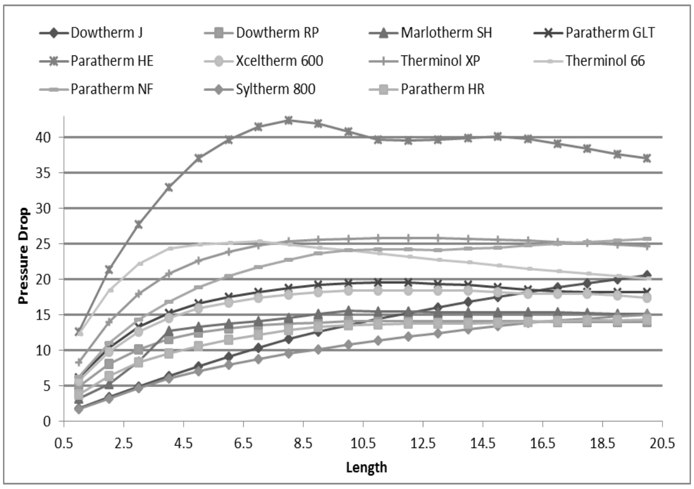

Fig. 7(a): Pressure Drop Profile Curve of the Thermal Fluids

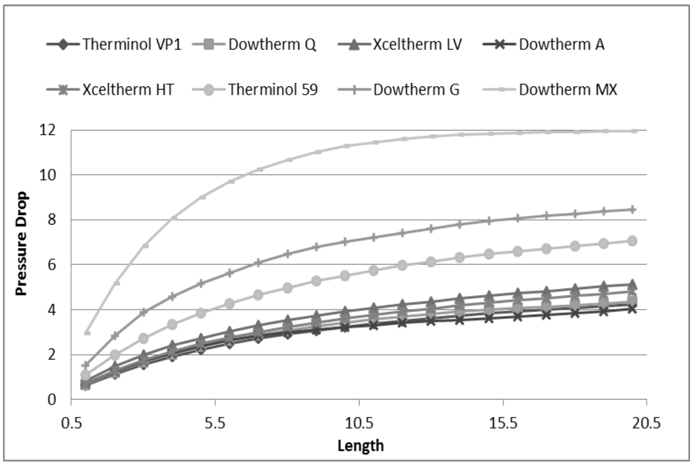

Fig. 7(b): Pressure Drop Profile Curve of the Thermal Fluids

ACKNOWLEDGEMENTS

We would like to thank Conference Convener Dr. Muhammad Tufail, Co-Convener Dr.Inayat Ullah Memon and Secretary Dr. Zahoor Ul Hussain for organizing the esteemed conference.

REFERENCES

[1] **Forristall, R.** *Heat Transfer Analysis and Modeling of a Parabolic Trough Solar Receiver Implemented in Engineering Equation Solver.* NRE. 2003. Technical Report. NREL/TP-550-34169.

[2] *Heat transfer analysis of parabolic trough solar receiver.* **Padilla, Ricardo Vasquez, et al., et al.** 2011, Applied Energy, Vol. 88, pp. 5097–5110.

[3] *New Equations for Heat and Mass Transfer in Turbulent Pipe and Channel Flow. .* **Gnielinski, V.** 2, 1976, International Chemical Engineering, Vol. 16, pp. 359–363.

[4] **Incropera, F and DeWitt, D.** *Fundamentals of Heat and Mass Transfer.* Sixth Edition. 1990.

[5] **Siegel, R and Howell, J.** *Thermal Radiation Heat Transfer.* Fourth Edition. New York, NY : Taylor & Francis, 2002.

[6] **Price, H.** *Concentrated Solar Power Use in Africa.* National Renewable Energy Laboratory. 2001.

[7] *Advances in Parabolic Trough Solar Power Technology.* **Price, H, et al., et al.** 2002, Journal of Solar Energy Engineering, Vol. 124, pp. 109–125.

[8] **Duffie, J A and Beckman, W A.** *Solar Engineering of Thermal Processes.* Second Edition. New York, NY : John Wiley and Sons, 1991.

[9] **Dudley, V, et al., et al.** *SEGS LS2 solar collector — test results.* Sandia National Laboratories. USA : s.n., 1994. SANDIA94-1884.

[10] Therminol.com, 2015, Therminol® VP-1. [online]. 2015. [Accessed 25 October 2015]. Available from: https://www.therminol.com/products/Therminol-VP1

[11] Msdssearch.dow.com, 2015, DOWTHERM A Heat Transfer Fluid Product Technical Data. [online]. 2015. [Accessed 25 October 2015]. Available from: http://msdssearch.dow.com/PublishedLiteratureDOWCOM/dh_0030/0901b803800303cd.pdf?filepath=/heattrans/pdfs/noreg/176-01337.pdf&fromPage=GetDoc

[12] Docs.google.com, 2015, Syltherm 800 Product Data Sheet.pdf. [online]. 2015. [Accessed 25 October 2015]. Available

from: https://docs.google.com/viewer?a=v&pid=sites&srcid=ZGVmYXVsdGRvbWFpbnx0aGVybWljZmx1aWRzfGd4OjNhNjc1NDdiMjliOGMxZmU

[13] RADCO, 2015, XCELTHERM LV1 Engineering - Solar Fluids. [online]. 2015. [Accessed 25 October 2015]. Available from: http://www.radcoind.com/products/solar/xceltherm-lv1-engineering/

[14] Msdssearch.dow.com, 2015, Dowtherm G Safety and Technical data Sheet. [online]. 2015. [Accessed 25 October 2015]. Available from: http://msdssearch.dow.com/PublishedLiteratureDOWCOM/dh_07ec/0901b803807ecd2a.pdf?filepath=productsafety/pdfs/noreg/233-00677.pdf&fromPage=GetDoc

[15] Msdssearch.dow.com, 2015, DOWTHERM RP Heat Transfer Fluid Product Technical Data. [online]. 2015. [Accessed 25 October 2015]. Available from: http://msdssearch.dow.com/PublishedLiteratureDOWCOM/dh_0030/0901b803800303d2.pdf?filepath=heattrans/pdfs/noreg/176-01474.pdf&fromPage=GetDoc

[16] http://www.radcoind.com/, 2015, MATERIAL SAFETY DATA SHEET XCELTHERM® HT. [online]. 2015. [Accessed 25 October 2015]. Available from: http://www.radcoind.com/wp-content/uploads/2012/10/MSDS_HT.pdf

[17] Therminol.com, 2015, Therminol® 66. [online]. 2015. [Accessed 25 October 2015]. Available from: https://www.therminol.com/products/Therminol-66

[18] Andy Andrews All Rights Reserved, Paratherm, 2015, Paratherm™ HR Synthetic Aromatic Heat Transfer Fluid |. Paratherm Heat Transfer Fluids [online]. 2015. [Accessed 25 October 2015]. Available from: http://www.paratherm.com/heat-transfer-fluids/high-temperature-heat-transfer-fluids/paratherm-hr/

[19] Globalheattransfer.co.uk, 2015, Global Heat Transfer - Marlotherm SH. [online]. 2015. [Accessed 25 October 2015]. Available from: http://www.globalheattransfer.co.uk/heat-transfer-fluids/high-temperature-thermal-fluid/marlotherm-sh

[20] Msdssearch.dow.com, 2015, DOWTHERM MX Heat Transfer Fluid. [online]. 2015. [Accessed 25 October 2015]. Available from: http://msdssearch.dow.com/PublishedLiteratureDOWCOM/dh_0030/0901b80380030696.pdf?filepath=/heattrans/pdfs/noreg/176-01544.pdf&fromPage=GetDoc

[21] Msdssearch.dow.com, 2015, DOWTHERM Q Synthetic Organic Heat Transfer Fluid. [online]. 2015. [Accessed 25 October 2015]. Available from: http://msdssearch.dow.com/PublishedLiteratureDOWCOM/dh_0918/0901b8038091807e.pdf?filepath=heattrans/pdfs/noreg/176-01467.pdf&fromPage=GetDoc

[22] Andy Andrews All Rights Reserved, Paratherm, 2015, Paratherm™ NF Heat Transfer Fluid |.Paratherm Heat Transfer Fluids [online]. 2015. [Accessed 25 October 2015]. Available from: http://www.paratherm.com/heat-transfer-fluids/high-temperature-heat-transfer-fluids/paratherm-nf/

[23] RADCO, 2015, XCELTHERM 600 Engineering - Industrial Energy Fluids. [online]. 2015. [Accessed 25 October 2015]. Available from: http://www.radcoind.com/products/industrial-energy/xceltherm-600-engineering/

[24] Therminol.com, 2015, Therminol® XP. [online]. 2015. [Accessed 25 October 2015]. Available from: https://www.therminol.com/products/Therminol-XP

[25] Therminol.com, 2015, Therminol® 59. [online]. 2015. [Accessed 25 October 2015]. Available from: https://www.therminol.com/products/therminol-59

[26] Rohsenow, Warren M and Hartnett, J. P, 1973, Handbook of heat transfer. New York : McGraw-Hill.

[27] Andy Andrews All Rights Reserved, Paratherm, 2015, Paratherm™ HE Heat Transfer Fluid |.Paratherm Heat Transfer Fluids [online]. 2015. [Accessed 25 October 2015]. Available from: http://www.paratherm.com/heat-transfer-fluids/high-temperature-heat-transfer-fluids/paratherm-he/

[28] Andy Andrews All Rights Reserved, Paratherm, 2015, Paratherm™ GLT Heat Transfer Fluid |.Paratherm Heat Transfer Fluids [online]. 2015. [Accessed 25 October 2015]. Available from: http://www.paratherm.com/heat-transfer-fluids/high-temperature-heat-transfer-fluids/paratherm-glt/

SIMULTANEOUS DETERMINATION OF ALPRAZOLAM WITH ANTIHISTAMINE IN BULK DRUG AND PHARMACEUTICAL FORMULATIONS BY LIQUID CHROMATOGRAPHY

S. Akram[1,] , S.N. Ali[1,*], A. Qayoom[1] , I.U. Memon[2] and N. Naz[1]
[1] Department of Chemistry, NED University of Engineering & Technology, Karachi, Pakistan
[2] Department of Chemical Engineering, NED University of Engineering & Technology,
Karachi, Pakistan

[*]Corresponding author. Tel.: +92333-7208120
E-mail address: saeeda_khowaja@hotmail.com (S.N. Ali)

ABSTRACT

A high performance liquid chromatographic method with UV detection for simultaneous quantification of alprazolam with antihistamine was developed and validated following the ICH guidelines. Separation was achieved on Shimadzu shim-pack CLC-ODS (M) 25 M column employing mobile phase 80:20 methanol-water adjusting pH 3.5 at 230 nm adjusting flow rate 1.0 mL min^{-1}. The linear concentration ranges were 0.2-12.5 µg mL^{-1} for alprazolam and 0.4-25 µg mL^{-1} for antihistamines with correlation coefficient greater than 0.998 and detection limits 6.92, 1.63, 0.18, 4.9 ng mL^{-1} for promethazine, levocitrizine, alprazolam, loratidine respectively. Validation which showed RSD < 2% and 98.05-101.62% recovery. Proposed method was successfully applied for quantification of studied drugs in pharmaceutical formulations without interference of excipients.

Keywords: alprazolam, antihistamine, method validation, hplc, pharmaceutical formulations

1 INTRODUCTION

Alprazolam, a short-acting anxiolytic benzodiazepine, chemically (8-chloro-6-phenyl-l-methyl-4Hs-triazolo[4,3-a] [1,4] benzodiazepine) is highly potent psychoactive drug with remarkably low toxicity [1]. It is used to treat anxiety disorders associated to symptoms of depression. Moreover, it is employed to cure agoraphobia, a medical condition in which patient frightens and avoid places that make him feel trapped [2, 3]. Literature survey revealed a number of methods for the analysis of alprazolam including spectrofluorimetry [4], second-derivative spectrophotometry [5], liquid chromatography [6], HPTLC [7], GC-MS [8], negative ion chemical ionization mass spectrometry [9], voltametry [10] and so on.

After antibiotics, the most commonly prescribed medication is antihistamines [11]. Antihistamine is the important drug class which targets the histamine receptors in the body to treat allergic conditions associated with respiratory or gastrointestinal tract. Antihistamines have been determined by spectrophotometry [11], HPLC [12], SPE/HPLC [13], LC-MS/MS [14], adsorptive stripping voltametry [15] and capillary electrophoresis [16].

Present study is aimed to report an efficient liquid chromatographic method for simultaneous determination of alprazolam with antihistamines (promethazine, levocetrizine and loratidine) at isobestic point employing UV/vis detector. Validation study has been fulfilled following the ICH guidelines [17]. Applicability of method was established by analyzing the alprazolam and studied antihistamines in commercial formulations with high recovery values and without interference of excipients.

2 EXPERIMENT

2.1 Reagents and chemicals

Standard alprazolam form Pfizer, and levocitrizine, loratidine and promethazine were obtained from Eros Pharmaceuticals Pvt. Ltd. Pharmaceutical formulations Xanax 0.5 mg (Pfizer), Jardin 10 mg (High-Q), T-Day 5 mg (Novartis) and Theoclate Avomine 25 mg (Sanofi) were obtained from pharmacy.

Analytical grade methanol, o-phosphoric acid were purchased from Merck (Darmstadt, Germany). Freshly prepared double distilled deionized water was used throughout the analysis.

2.2 Instrumentation

Analyses was performed using Shimadzu Corporation, Japan liquid chromatograph facilitated with LC-20AT binary gradient solvent delivery pump, AOC-20 auto-sampler SIL-20AHT/20ACHT UFLC fitted with auto injector AOC-20i with volume of sample injection 1 µL, UV-visible detector SPD-20A/20AV coupled with a Shimadzu CBM-20A Communication Bus Module was used for separation. Chromatographic data acquirement was performed on LC solution GPC software (version 1.25, Shimadzu Corporation, Japan). Isosbestic point was determined on Shimadzu 1800 UV/Vis spectrophotometer.

2.3 Chromatographic parameters

Chromatographic separation was carried out using Shimadzu Shim-pack CLC-ODS (M) 25M column (4.6mm i.d. × 0.25mm) using mobile phase 80:20 methanol:water having pH 3.5 maintained by o-phosphoric acid. Flow rate was set at 1.0 ml min-1 and detector wavelength was set at 230 nm.

The mobile phase was prepared fresh daily, filtered through Millipore vacuum filter system using 0.45 µm pore size filter and degassed with an ultrasonic bath (LC 30H).

2.4. Standard solution preparation

Accurately weighed 10 mg alprazolam, promethazine, levocitrizine and loratidine were separately dissolved in a small quantity of diluent in 100 mL volumetric flasks and then volume each flask was completed with diluent to bring the final concentration of each solution 100 µg mL-1. All solutions were sonicated before analysis.

2.5. Calibration standards preparation

Calibration standards at seven different concentration levels were prepared by transferring appropriate volumes of standard solutions of alprazolam and all the studied antihistamines in 10 mL volumetric flask and bring final concentration 0.2-12.5 µg mL-1 for alprazolam and 0.4-25 µg mL-1 for antihistamines. Each solution was filtered in 1.5 mL vial using 0.45 µm pore size membrane filter and placed in autosampler for injection.

2.6. Pharmaceutical formulations

Ten tablets of 0.5 mg Xanax, 10 mg Jardin, 5 mg T-Day and 25 mg Theoclate Avomine were finely grinded to homogenous powder. Weight corresponding to 10 mg of each analyte was separately introduced into 100 mL volumetric flask, dissolved in small volume of diluent and sonicated for complete dissolution, then filtered through a 0.45 µm pore size filter to remove undissolved excipients and then final concentration of 100 µg mL-1 was obtained.

2.7. Method validation

Following the ICH Q2 (R1) guidelines, the developed method was validated for system suitability test, linearity, precision, accuracy, limit of detection and quantification, robustness, selectivity and specificity [17].

2.7.1. System Suitability

System suitability of method was assessed on every day of method validation from six replicate injections of same standard.

2.7.2. Linearity and Range

Aliquots of stock standard solutions of alprazolam and antihistamines were transferred in a series of 25 mL volumetric flasks to get the concentration of 0.2-12.5 µg mL-1 for alprazolam and 0.4-25 µg mL-1for antihistamines respectively and the volumes were made up to the mark with 80:20 methanol-water (diluent). Calibration curves were constructed to evaluate linearity.

2.7.3. Precision and accuracy

Precision was assessed within the concentration range of 0.2-12.5 µg mL-1 for alprazolam and 0.4-25 µg mL-1 for antihistamines by injecting six replicates of analytes within the day and on two consecutive days of method validation. Accuracy of the method was evaluated by injecting six replicates of tablet solutions at 80%, 100% and 120% concentrations level prepared by transferring appropriate volume of tablet solutions into 25 mL volumetric flasks and final volumes were completed with mobile phase.

2.7.4. LOD and LOQ

Detection and quantitation limits were determined by employing equation LOD = 3.3 SD/α and LOQ = 10 SD/α respectively, where SD is the standard deviation and α is the slope of curve.

2.7.5. Robustness

Minor changes in chromatographic parameters were intentionally made during analysis in flow rate (1.1 and 0.9 mL min-1), mobile phase composition (82:18 and 78:22 MeOH: H_2O) and wavelength (232 and 228 nm) and effect on performance was observed.

2.7.6. Specificity

To evaluate the specificity of the method standard solutions, excipients solution, spiked excipients sample and solution of commercial formulations were analyzed to determine the possible interference of excipients.

3 RESULTS AND DISCUSSION

Please send your manuscript data files via e-mail attachment. If you don’t have the possibility to send the paper via e-mail or if the files are too big, please send the data files on a CD.No hardcopy is needed.

3.1 Method development and optimization

Anxiety, panic and sleeping disorder rate is increasing day by day. Alprazolam is a sleep-inducing drug and causes lower incidence of drowsiness comparatively [18]. Prescription of alprazolam with antihistamine [19-21] [2-4] or intake of alprazolam followed by injection of antihistamine to the patient having disturbance in mental abilities is reported in literature [22]. Simultaneous prescription of these drugs demands the need of method capable of their simultaneous identification and quantitation in bulk drug and pharmaceutical formulations. Accordingly, the aim of present study was to develop an effective and economic LC-UV method for the simultaneous determination of alprazolam with antihistamine in raw material and pharmaceutical formulations.

The method was optimized at isosbestic point of 230 nm evaluating different chromatographic parameters. Different ratios of mobile phase methanol: water (80:20, 70:30, 60:40, and 50:50) with pH range 2.6-3.6 and flow rate 0.8-1.3 ml min-1 were examined for appropriate separation. It was investigated that separation of peaks was influenced by different proportions of methanol:water; that is high ratio of methanol show elution of analyte earlier, however suitable separation with high resolution, symmetrical peaks and shorter retention time was obtained using methanol:water (80:20) with pH 3.5 maintained with o-phosphoric acid adjusting the flow rate 1.0 ml min-1. UV-visible spectra representing the isosbestic point at 230 nm is represented in figure 2 and the chromatogram showing the separation of alprazolam with antihistamine is represented in figure 3.

3.2. Method validation

3.2.1 System suitability test

System suitability test is the most essential part of method validation. It is performed to endorse the compatibility of method. It was evaluated on each day of method validation by injecting six replicate of same standard and the data is reported in terms of theoretical plates, tailing factor and resolution. Theoretical plates, greater than 2000 where as tailing factor and resolution below 2 for alprazolam and studied antihistamine confirm the suitability of the method (Table 1).

3.2.2 Linearity and range

Calibration curves for alprazolam and studied antihistamines at seven different concentration levels were plotted which showed linearity in the concentration ranges of 0.2-12.5 µg mL-1 for alprazolam and 0.4-25 µg mL-1for antihistamines respectively with correlation coefficient greater than 0.998. Regression characteristics including intercept and slope, standard error and standard error estimate are specified in table 2.

3.2.3 Precision and accuracy

Inter-day and intra-day precision was evaluated five times within the day and two consecutive days of method validation within the linearity range of 0.2-12.5 µg mL-1 for alprazolam and 0.4-25 µg mL-1 for antihistamines. The RSD was found in less than 2 percent i.e 0.01-1.17% for all the studied analytes. The data is represented in table 3.

The accuracy of developed analytical method was evaluated by six times analysis of studied analytes at 80%, 100% and 120% concentration levels in pharmaceutical formulation which showed recovery of alprazolam 98.05-101.83% and that of antihistamines 98.06-101.62% declaring the accuracy of method. The data representing the % recovery and % error are given in table 4.

3.2.4 Detection and quantification limits

The overall sensitivity of method was evaluated by standard deviation of instrumental response at lowest concentration and the slope of calibration curve. It is reported as detection and quantification limits (table 2) which are infect signal to noise ratio three times and ten times of baseline noise. The LOD was > 0.18 ng mL-1 and < 6.92 ng mL-1 and LOQ was > 0.00056 µg mL-1 and < 0.020 µg mL-1 for all the studied analytes.

3.2.5 Robustness

Robustness of method was assessed by deliberate change in methanol: water ratio up to ± 2 mL, pH (± 0.1) and flow rate (± 0.1 mL min-1). It was observed that the method is compatible and was not affected by minor changes in chromatographic parameters. Table 5 represents the data including capacity factor, theoretical plates, resolution and separation factor.

3.2.6 Specificity

Specificity of method was established by analyzing the instrumental response of blank, excipients solution, spiked excipients solution and pharmaceutical formulation (figure 4) to check the possible interference of excipients at the retention time where alprazolam and antihistamine elute. It was observed that a minor noise of excipients appeared apart from peak positions of analytes there was no significant interference of excipients confirming the specificity method.

3.3 Application

The proposed analytical method was employed for the simultaneous determination of alprazolam with antihistamine in bulk drug and pharmaceutical formulation, Xanax 0.5 mg, Jardin 10 mg, T-Day 5 mg and Avomine 25 mg. Chromatogram represented in figure 3 shows well separated symmetrical peaks for all the analytes with high quality resolution at the isosbestic point. The validated data was in good agreement with reference standards, showed high accuracy with percent error not greater than 1.98. The precision of method was high with comparable sensitivity. Thus, it is concluded that the developed liquid chromatographic method is appropriate for simultaneous determination of alprazolam with antihistamine in bulk drug and pharmaceutical formulation without interference of unwanted excipients.

4 CONCLUTION

Here, we reported a rapid and economic, RP-HPLC method for simultaneous determination of alprazolam with antihistamine at isosbestic point. Validity of method was established following ICH guidelines for suitability test, linearity, precision, accuracy, limit of detection and quantification, robustness, selectivity and specificity. Method showed high precision with good percent recovery. Sensitivity of method was high with lowest detection limits and thus method was fruitfully employed for determination of alprazolam with studied antihistamine in pharmaceutical formulation without interference of excipients.

ACKNOWLEDGEMENTS

The unconditional support of Prof. Dr. Saqib Anjum (Chairman Department of Chemistry, NED UET), Dr. Zahoor-ul-Hassan Awan (Assistant Professor, Chemical Engineering Department, NED UET) and Dr. Sajid Iqbal, (Chemistry Department, Karachi University) is highly acknowledged.

REFERENCES

[1] Hester Jr JB, Rudzik AD, Kamdar BV. 6-Phenyl-4H-s-triazolo [4, 3-a][1, 4] benzodiazepines which have central nervous system depressant activity. *Journal of medicinal chemistry*, 14(11), 1078-1081 (1971).

[2] AHFS 2003 Drugs Information®: American Hospital Formulary Service, American Society of Health System Pharmacists, Inc. (Eds.), Bethesda, 2003, 2360-2361.).

[3] Catalogo de Especialidades Farmacéuticas, Consejo General de Colegios Oficiales de Farmaceuticos (Eds.), Madrid, 2001, 1898-1903.).

[4] Nudelman NS, Cabrera CG. Spectrofluorimetric assay for the photodegradation products of alprazolam. *Journal of Pharmaceutical and Biomedical Analysis*, 30(3), 887-893 (2002).

[5] Patel RB, Patel MR, Shankar MB, Bhatt KK. Development and validation of second-derivative spectrophotometry method for simultaneous estimation of Alprazolam and Fluoxetine hydrochloride in pure powder and tablet formulation and its comparison with HPLC method.

Eurasian Journal of Analytical Chemistry, 4(1), 76-86 (2009).

[6] Perez-Lozano P, Garcia Montoya E, Orriols A, Minarro M, Tico JR, Sune-Negre JM. Development and validation of a new HPLC analytical method for the determination of alprazolam in tablets. *Journal of Pharmaceutical and Biomedical Analysis*, 34(5), 979-987 (2004).

[7] Patel RB, Patel AB, Patel MR, Shankar MB, Bhatt KK. Estimation of alprazolam and sertraline in pure powder and tablet formulations by high-performance liquid chromatography and high-performance thin-layer chromatography. *Analytical Letters*, 42(11), 1588-1602 (2009).

[8] Yilmaz B, Akba V. Determination of alprazolam in rabbit plasma by GC-MS method. *International Journal of Pharma Sciences and Research*, 1(1), 11-17 (2010).

[9] Hold KM, Crouch DJ, Wilkins DG, Rollins DE, Maes RA. Detection of alprazolam in hair by negative ion chemical ionization mass spectrometry. *Forensic science international*, 84(1-3), 201-209 (1997).

[10] Monzon LMA, Yudi LM. Voltammetric analysis of lipophilicity of benzodiazepine derivatives at the waterâˆ£ 1, 2-dichloroethane interface. *Journal of Electroanalytical Chemistry*, 495(2), 146-151 (2001).

[11] El-Kommos ME, El-Gizawy SM, Atia NN, Hosny NM. Spectrophotometric determination of some non-sedating antihistamines using erythrosine B. *ISRN Analytical Chemistry*, 2013, 1-9 (2013).

[12] Sher N, Siddiqui FA, Hasan N, Shafi N, Zubair A, Mirza AZ. Simultaneous determination of antihistamine anti-allergic drugs, cetirizine, domperidone, chlorphenamine maleate, loratadine, meclizine and buclizine in pharmaceutical formulations, human serum and pharmacokinetics application. *Analytical Methods*, 6(8), 2704-2714 (2014).

[13] Che W-j, Zhang Z, Xu C-x *et al.* Determination of Five Antihistamine Residues in Cosmetics by SPE/HPLC [J]. *Journal of Instrumental Analysis*, 8, 028 (2012).

[14] Do J-A, Kim JY, Choi JY *et al.* Development of a LC-MS/MS method for simultaneous analysis of 20 antihistamines in dietary supplements. *Analytical Science and Toxicology*, 28(2), 86-97 (2015).

[15] Alghamdi AH. Square-wave adsorptive stripping voltammetric determination of an antihistamine drug astemizole. *Chemical Papers*, 62(4), 339-344 (2008).

[16] Peris-Vicente J, Carda-Broch S, Esteve-Romero J. Validation of a Serum Analysis Method to Analyze Antihistamines by Capillary Electrophoresis. *Journal of Applied Chemistry*, 2014 (2014).

[17] International Conference on Hormonisation of Technical Requirements for Registration of Pharmaceuticals for Human Use (ICH) (2005) Validation of Analytical Procedures: Text and Methodology Q2(R1). Complementary Guideline on Methodology incorporated in November 2005, London.).

[18] G. W. Dawson, S. G. Jue, Brogden RN. Alprazolam: A Review of its Pharmacodynamic Properties and Efficacy in the Treatment of Anxiety and Depression. *Drug Evaluation*, 27(2), 132-147. (1984).

[19] Viktorsdottir O, Indridason OS, Palsson R. Successful treatment of extreme hyponatremia in an anuric patient using continuous venovenous hemodialysis. *Blood purification*, 36(3-4), 274-279 (2013).

[20] Huskey AM, Thomas CC, Waddell JA. Occurrence of Milnacipran-Associated Morbilliform Rash and Serotonin Toxicity. *Annals of Pharmacotherapy*, 47(7-8), e32-e32 (2013).

[21] Waldrep TW. Anaemia and thrombocytopenia in an elderly patient: case report. *Reactions*, 898, 20 (2002).

[22] Teimoory M, Arefi M, Behnoush B, Bastani B. Promethazine and Treatment Refractory Agitation in Clonidine Toxicity. *International Journal of Medical Toxicology and Forensic Medicine*, 3(3 (Summer)), 96-98 (2013).

DEVELOPMENT & CHARACTERIZATION OF NOVEL ANTIMICROBIAL ALGINATE FIBERS FOR WOUNDCARE APPLICATIONS

M. Umar[1,*], T. Hussain[2], R. Masood[1], Q. Zia[1], T. Areeb[1] and Azeemullah[2]
[1] National Textile Research Centre, National Textile University, Faisalabad, Pakistan
[2] Faculty of Engineering and Technology, National Textile University, Faisalabad, Pakistan

[*]Corresponding author. Tel.: +92-334-6258308
E-mail address: m.umar.ntu@gmail.com (M. Umar)

ABSTRACT

Natural plants and their extracts have immense potential for efficient treatment and management of wounds. The wound dressings made by using plants and their extracts for wound healing are biocompatible, non-allergenic, and have excellent microbial resistance. Wound dressings made by incorporation of metallic particles or any other synthetic material may have potential side effects on the body, it may react with the skin and cause allergic diseases or other kind of infections. In this research, neem alginate fibers were developed by using different concentrations of neem extract to enhance antimicrobial properties of alginate fibers. Antimicrobial properties, absorbency, tensile strength and surface morphology were studied. This work suggests that developed antimicrobial neem-alginate fibers have excellent microbial resistance as compared to alginate fibers.

Keywords: Alginate; Neem; Natural; Antimicrobial; Wound care

1 INTRODUCTION

Natural plants are more efficient healers because they promote the healing mechanism in a natural way. Therapy of wounds using natural plants not only accelerate the healing process but also maintains the aesthetics. Currently, the developed countries have increased the traditional medicinal system that includes the use of herbal drugs. According to the World Health Organization (WHO), 65% of the world’s population is using the natural plants for making medicines for health care [1]. Greater than 70% wound healing products are made from natural plants, 20% are made from minerals and the remaining contains animal products as their base materials [2], [3].

Leaf extracts of neem and oil keep away any infections by microorganisms on wound or lesion. Studies revealed that neem also inhibits the inflammation effectively due to which it further accelerates the wound healing. Margosic acid, glycerides of fatty acids, butyric acid and traces of valeric acid are present in neem oil. Alcoholic extracts of neem is useful in the cure of eczema, ringworm and scabies[4]. The aqueous ethanolic extract of four plants: neem, clove, datiwan and tulsi was developed and they found that all the four plants are effective against S.typhi but all are ineffective against E.coli and K.pneumonia [4]. In vitro study proved that methanolic extract of neem possess the excellent antimicrobial activity and effective in wound healing [5]. The fabric treated with finish of nanocomposite of neem chitosan have increased antimicrobial activity than other treated fabrics like neem chitosan composite and only neem and chitosan [6].

Alginates are typically derived from sodium and calcium salts of alginic acid, which are extracted from some types of brown algae.[7] Due to its good biocompatibility, low toxic nature and relatively low cost is used in many biomedical applications.[8] Alginates have high absorbency and are gel-forming materials with hemostatic properties which causes bleeding to stop, which makes them effective materials for rapid wound healing[9], [10]. Exudate coming out of wound converts calcium salt into sodium salt which facilitates the easy removal of dressing by dissolution. The residue of alginate wound dressing is bioresorbable thus eliminates the need of complete removal of wound dressing.[11]

Alginate also have great healing and antimicrobial properties and is mostly used in the bandages. Many treatments are done on alginate fibers to enhance its microbial resistance and healing properties but those treatments would have potential side effects on human body, it may react with the skin and cause allergic diseases or other kind of infections. There are limited number of studies to enhance the properties of alginate fibers by using natural plants which have no side effects on human body. This study proposes the method of making novel alginate fibers which have enhanced microbial resistance and healing properties using extracts of natural plant like neem.

2 EXPERIMENTAL

2.1 Materials

Fresh neem leaves were collected from the neem trees of National Textile University, Faisalabad. Fiber grade Sodium Alginate, having high guluronic acid content was purchased from F.M.C Biopolymer, Norway. Calcium chloride ($CaCl_2$) of analytical grade was purchased from RdH laboratories GmbH & Co, Germany and Acetone (99%) from Merck. Laboratory grade sodium chloride was purchased from UNI-Chem chemical reagents.

2.2 Method

Preparation of neem extract

Fresh neem leaves washed with distilled water and then excessive water was dried in sheltered area. Neem extract was prepared in distilled water. Neem leaves (100 and 200 grams) were added to distilled water (1000 ml) at room temperature and was shake in Molinex shaker for 30 minutes. The mixture was filtered through polyester mesh (pore size 150 microns); the filtrates were collected in beaker.

Development of fibers

Table 1 shows the formulation of the dope solutions. The dope was prepared by adding (4% w/v) alginate in neem extract (10% and 20% w/v) for making neem loaded fibers, dope solution was stirred at 1500 rpm for 4 hours at room temperature. The solution was then degassed by leaving it in dope tank overnight. The dope solution was extruded in a coagulation bath containing calcium chloride (1% w/v). The degassed dope solution was extruded under pressure (8 psi) through holes (250µm) of a spinneret into coagulation bath to produce the fibers. The resultant fibers were then collected by pick up rollers and passed through a wash bath containing distilled water. The fibers were then dried by immersion in a series of acetone baths 75/25, 50/50, 0/100 water to acetone solutions.

Table 1. Formulation of the dope solutions and their codes.

Sample	Alginate (% w/v)	Neem (% w/v)
C	4	-
N1	4	10
N2	4	20

2.3 Assessment of fibers

Linear density

Linear density of the fibers was calculated by using equation 1 according to test method ASTM D 1059-12. The 40 samples were prepared of 2 inch length and weighed collectively by using digital weighing balance.

$$\text{Linear density (tex)} = \frac{\text{weight in grams (g)}}{1000\ \text{m}} \qquad (1)$$

2.4 Tensile properties

The tensile properties of the fiber were measured using single fiber strength testing system M250-2.5CT (Testometric, Rochdale, England). Test method employed was EN ISO 5079 [12]. The machine works on the principle of constant rate of extension (CRE). A single fiber was clamped between moveable and fixed jaw 10 mm apart, force was applied at constant rate of extension 12 mm/min. The applied force and displacement of the moveable jaws were measured automatically. Mean breaking force, strain % and tenacity of the fibers were taken from automated report.

2.5 Total fluid absorption

Absorption of fluids in all fibers was tested in saline (0.9% w/v NaCl), distilled water and solution A (0.8298 % w/v NaCl and 0.0368 % w/v $CaCl_2$). All samples were soaked in fluids for 1 hour and then placed on blotting paper until no droplet falls from fiber on hanging in air, after that wet weights of samples were taken. The dry weights of fibers were measured after drying overnight at 105^{o}C [13], [14]. Absorption was calculated by using the equation 2:

$$\text{Absorption (g/g)} = \frac{W_w - W_d}{W_d} \qquad (2)$$

Where W_w is the wet weight of fiber and W_d refers to the dry weight of fiber.

2.6 Antimicrobial testing

Antimicrobial activity was calculated according to AATCC test method 147-2011 [15]. 0.05 ml of the 10^{-7} diluted test inoculum (*Staphylococcus aureus* and *Escherichia coli*) was loaded on the sterilized agar plates. Test specimen gently placed on agar surface to ensure intimate contact. After an incubation at 37°C for 24 hours, agar plates were examined growth of microbes and inhibition zone along the edges of the specimen. The width of zone of inhibition can be calculated using the equation 3.

$$W = \frac{(T-D)}{2} \qquad (3)$$

Where:
W= width of clear zone of inhibition, T = total diameter of test specimen and clear zone in mm and D = diameter of the test specimen in mm.

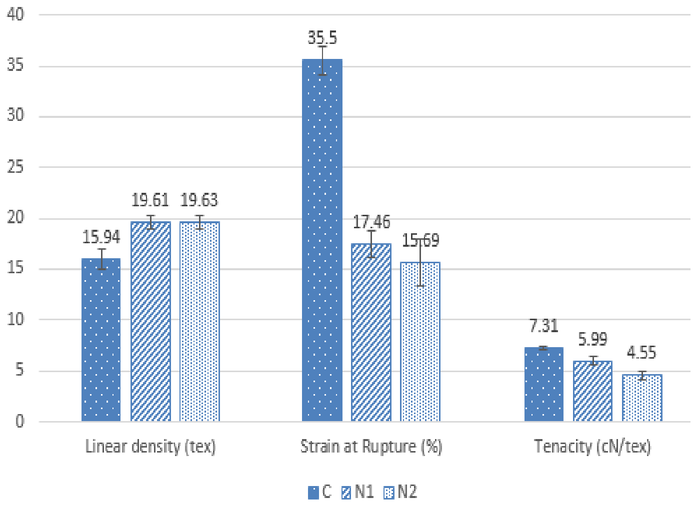

Figure 1. Graphical illustration of fibre linear density and tensile properties.

3 RESULT AND DISCUSSION

3.1 Linear Density and Tensile Properties

The results of linear density and tensile properties of all fibres are illustrated in Figure 1. The results show that inclusion of neem in dope increase the linear density. This may be due to the fact that when a spun neem loaded fibres neem also become the part of fiber and increase the weight of fiber. Strain % decreases in the neem fibres (N1 and N2) as compared to the control fibre (C). There is no significant difference in the tenacity of the produced and control fibres.

3.2 Total fluid absorption

High fluid absorption is one of the important aspect for wound dressing made especially for moist wound care applications. Table 2 illustrates that inclusion of neem in dope solution which decreases the fluid absorption. It can be due to inclusion of neem extract which have no attraction for the fluids. Overall absorption in saline solution was the highest; it is due to the fact that Ca-alginate fibre swells drastically when come in contact with solution containing Na^+ ions and are insoluble in distilled water. Solution A the absorptions are almost half of the saline absorptions, it may be due to fact that Ca^{2+} ions present in the solution A create a hindrance for the ions to exchange between the fibres and the liquid medium.

Table 2. Total fluid absorption of control and neem fibers

Sample	Saline solution (g/g)	Solution A (g/g)	Distilled water (g/g)
C	33.53 ±1.25	9.83 ±1.01	9.31 ±0.86
N1	29.81 ±1.98	7.24 ±1.03	9.15 ±1.77
N2	27.69 ±0.76	6.53 ±0.92	9.03 ±1.23

3.3 Antimicrobial activity

The prime intention of including Neem is to introduce antimicrobial activity in alginate fibre. Gram negative bacterium Escherichia coli (ATCC 4157) and gram positive bacterium, Staphylococcus Aureus (ATCC 6538) were used in this study, as they are reported to be the major cause of Hospital Acquired Infections. Staphylococcus Aureus is the most frequently evaluated bacteria in wound care practices.

The results of antimicrobial activity in Figure 2 show that all the samples developed with neem have inhibition against *S.aureus* but colonies of *E.coli* present on the neem fibers which exhibit that neem fibers have no antimicrobial activity against *E.coli*. The inhibition occurred as a result of neem release from the fibres. This founded that neem is effective against *S.aureus* but all are ineffective against *E.coli* [4].

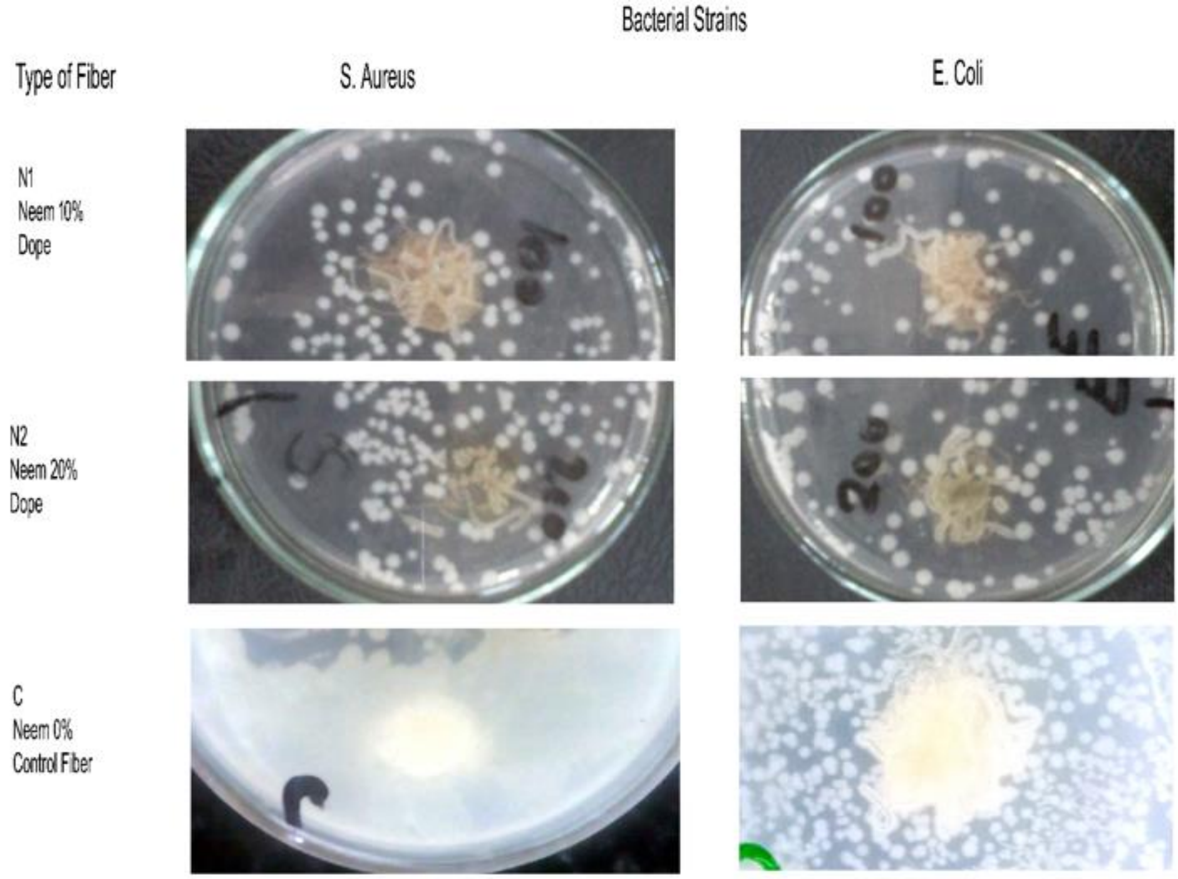

Figure 2. Antimicrobial Activity of neem Fibres on agar plates against *S.aureus* and *E.coli*.

3.4 Scanning electron microscopy (SEM) analysis

SEM images of the control and neem fibres are illustrated in Figure 3. It can be seen that surface of the control fibre is relatively smooth and have less striations (Figure 3a). On the other hand neem fibres (N1 and N2) shown in Figure 3b and 3c have characteristic irregular striations along the length of the fibres. These characteristic marking may be due to the diffusion of the neem from the spun fibre during drying in acetone baths.

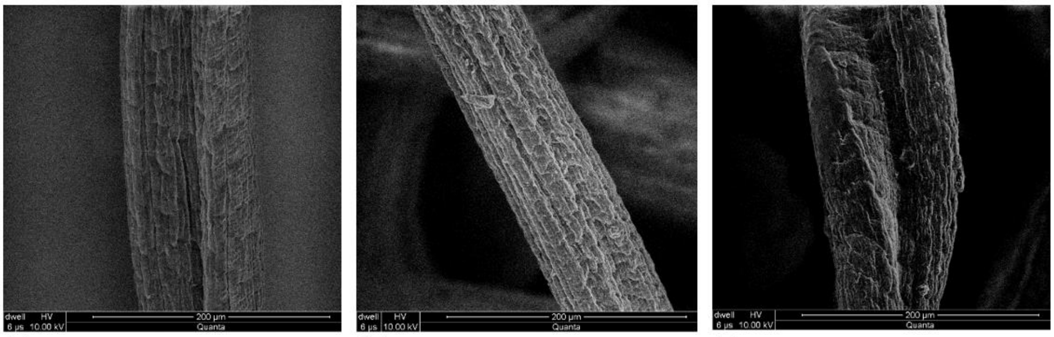

(a) (b) (c)

Figure 3. *SEM* Images of Control and neem fibres.

4 CONCLUSION

The research work deals with the synthesis of the neem loaded alginate fibre by co-extrusion in a coagulation bath containing $CaCl_2$. The technique used to produce these fibres was wet spinning. The developed fibers were tested for antimicrobial activity, total liquid absorption (gram/gram), linear density and tensile properties. It is concluded from the research that neem fibers can be produced by co-extruding neem and alginate into a calcium chloride coagulation bath. The key findings are; inclusion of neem resulted in decrease of strain at rupture, breaking force and tenacity of the neem fibers. Similarly, inclusion of neem has negative effect on the absorption of the alginate fibers. Addition of neem has resulted in adequate antimicrobial activity necessary for moist wound healing. Therefore, it is concluded that produced fibers have adequate antimicrobial activity, absorption and tensile properties necessary for an exuding wound dressing.

5 REFERENCES

[1] V. Vihar, Plants that heal wounds . A review," *Herba Pol.*, 58(1), 2012.

[2] D. Kumarasamyraja, N. S. Jeganathan, and R. Manavalan, "A review on medicinal plants with potential wound healing activity," *Int. J.*, 2(4) 105–111, 2012.

[3] Y. Sharma, G. Jeyabalan, R. Singh, and A. Semwal, "Current Aspects of Wound Healing Agents From Medicinal Plants : A Review," *J. Med. Plants Stud.*, 1–11, 2013.

[4] B. Joshi, G. P. Sah, B. B. Basnet, and M. R. Bhatt, "Phytochemical extraction and antimicrobial properties of different medicinal plants : Ocimum sanctum (Tulsi), Eugenia caryophyllata (Clove), Achyranthes bidentata (Datiwan) and Azadirachta indica (Neem)," 3(January) 3–4, 2011.

[5] S. Masyitah, H. Dzulkarnain, and A. Rahim, "Antimicrobial Activity of Methanolic Neem Extract on Wound Infection Bacteria," *Int. Conf. Biol. Chem. Environ. Sci.*, (BCES-2014), 2014.

[6] R. Rajendran, R. Radhai, C. Balakumar, M. Ahamed, C. Vigneswaran, and K. Vaideki, "Synthesis and Characterization of Neem Chitosan Nanocomposites for Development of Antimicrobial Cotton Textiles," *J. Eng. Fiber. Fabr.*, 7(1) 136–141, 2012.

[7] B. H. a Rehm, *Alginates: Biology and Applications*, Springer, 2009.

[8] K. Y. Lee and D. J. Mooney, "Alginate: Properties and biomedical applications," *Prog. Polym. Sci.*, 37(1) 106–126, 2012.

[9] W. Stęplewski, D. Wawro, and A. Niekraszewicz, "Research into the Process of Manufacturing Alginate-Chitosan Fibres," *Fibres Text. Easten Eur.*, 14(4) 25–31, 2006.

[10] O. L. Shanmugasundaram, "Development and characterization of cotton and organic cotton gauze fabric coated with biopolymers and antibiotic drugs for wound healing," *Indian J. Fibre Text. Res.*, 37(June) 146–150, 2012.

[11] S. E. Barnett and S. J. Varley, "The effects of calcium alginate on wound healing," *Annals of the Royal College of Surgeons of England*, 69 5–7, 1987.

[12] "Textiles - Fibres - Determination of breaking force and elongation at break of individual fibres," *Br. Stand.*, BS EN ISO , 1996.

[13] R. Masood and M. Miraftab, "Novel materials for moist wound management: Alginate-psyllium hybrid fibres," *J. Wound Care*, 23(3) 153–159, 2014.

[14] I. R. Sweeney, M. Miraftab, and G. Collyer, "Absorbent alginate fibres modified with hydrolysed chitosan for wound care dressings--II. Pilot scale development.," *Carbohydr. Polym.*, 102 920–7, 2014.

[15] AATCC TM 147-2011, "Antibacterial Activity Assessment of Textile Materials : Parallel Streak Method," , 2011.

IMPROVING DIFFERENT PARAMETERS OF TRANSFORMER OIL FROM PAKISTAN NATIONAL REFINERY LIMITED

[1]Syed Wajid Hussain, [2] Syed Tariq Ali, [1]Amtul Qayoom and [1]Ghazanfar Hussain
[1]Chemistry Department, NED University of Engineering and Technology, Karachi, Pakistan
[2]Department of Chemistry, University of Karachi, Karachi, Pakistan

ABSTRACT

The aim of this study is to improve the quality of selected Group I base oil by chemical treatment and study the impact of treatment on their different parameters. Hence, the different base oils were treated with sulphuric acid to remove moisture and easily oxidizable compounds followed by bleaching with earth clay. Selected properties such as; electrical and physical, were measured before and after acid/clay treatment. Initial tests indicated that the use of acid and earth clay treatment of the Group I Base oil improved dielectric dissipation factor, water content, total acidity and colour. These properties are the basic requirement of a good transformer base oil, which normally belongs to Group II Base oil. Therefore, we select Group II base oil, LP-70 (imported) as a reference and Group I base oil 65 NHVI for optimization of the method. Thus acid/clay gives an ideal treatment of transformer oil with its economic advantages.

Keywords: Transformer oil; Acid treatment and Characterization; Bleaching earth clay

1 INTRODUCTION

Insulating oil, commonly known as transformer oil use in an electrical power transformer for insulation. Normally, Its obtained by fractional distillation and subsequent treatment of crude petroleum [1]. Therefore, it also called mineral insulating oil. In the electrical transformer, the basic purpose of using the transformer oil is including, to provide liquid insulation [2]; dissipates the heat (acts as coolant); prevents direct contact of atmospheric oxygen, with cellulose made paper insulation of windings, which is susceptible to oxidation and helps to preserve the core and winding as these are fully immersed inside oil [3]. Transformer oil is a highly-refined mineral oil that is stable at high temperatures and has excellent electrical insulating properties. Besides the transformers oils, base oil is also use in capacitors, fluorescent lamp ballasts and switches, lubricating, greases, motor oil and metal processing fluids.

Group I base oils are the least refined of all the groups and easily available in Pakistan. These are darker in color, have less than 90 percent saturated hydrocarbons, greater than 0.03 percent sulfur with a viscosity-index range of 80 to 120 [4] .

Group II Base oils have clearer color as compare to Group I base oils, have more than 90 percent saturated hydrocarbon, less than 0.03 percent sulfur with a viscosity index of 80 to 120 [4]. They are often manufactured by a more complex process known as hydro-cracking. Since the percentage of saturated hydrocarbon molecules in oil are quite high, therefore, Group II base oils possess better antioxidation properties. Group II Base oils are imported and cost more in comparison to Group I Base oils.

In the present study, the main focus on transformer base oil. Therefore, the selected chemical, electrical and physical chemical properties, related to transformer base oil, of Group I base oils were comparable Group II oils after chemical treatment.

2 MATERIALS AND METHODOLOGY

Standard test methods IEC-60296 of testing and characterization of transformer oil were used as recommended by IEC **(International *Electrotechnical Commission)***.

A. *Reagents and Raw Materials Used*

Imported Group II Base Oil (LP-70), Locally Group I Base Oil (65NHVI also known as Spindle oil, Pakistan national refinery limited), Sulphuric acid, Bleaching earth clay (Bleaching earth clay also known as Bentonite clay, Tahir Asad Industries (Pvt.) Ltd).

B. *Instrument Used*

Color Comparator (Fisher Color Comparator, AF 650), Karl fisher (Karl Fischer KF-875), DDF tester (Baur oil tester DTL C) and Potentiometer titration (Metrohm SM Titrino-702).

C. *General characteristics of transformer oils*

For transformer base oils the most important properties are color [7], water content [8], dielectric dissipation factor (DDF) [9] and total acid number (TAN) [10]. The limits of these parameters for transformer base oil are shown in **Table 1.**

D. *Experimental Procedure*

In this study different combinations of earth clay were made for the method optimization, while the concentration of sulphuric acid kept constant (**Table 2**). The 500 ml of Group I base oil is used for each combination. The Group I base oil was treated with 0.5 % (v/v) of sulphuric acid with constant stirring for 3 minutes at ambient temperature then allowed to settle for four hours. The clear supernatant oil was separated by separating funnel and acidic residues were discarded. The supernatant oil was then treated with different percentages (v/wt.) of bleaching earth with continuous stirring of the mixture for eight minutes at ambient temperature. Bleaching earth treated oil was then allowed to settle for four hours. Supernatant was decanted and residues were discarded. The treated oil was finally filtered using a filter paper by buchner funnel. The above mentioned parameters were recorded for all combinations.

3 RESULT AND DISCUSSION

Sulphuric acid is well known for its oxidizing ability, while the bleaching earth clay is famous for its adsorption abilities. Hence, concentrated sulphuric acid is used to remove easily oxidizable hydrocarbons, which can easily be adsorb on the earth clay.

All observed data for the electrical, physical and chemical properties is summarize in **Table 3** which include the dielectric dissipation factor (tan δ), color, water content and total acidity were collected and all data is presented in trend plots for comparing the dielectric dissipation factor (tan δ), color, water content and acidity characteristics between Group I base oil (locally) and Group II base oil (Imported).

Physical Properties

Color

Figure 1. Color of Group I base oil (Spindle Oil) before and after Acid/Clay Treatment and Group II base oil (Imported Oil)

For a good quality transformer base oil, color should not more than 0.5 on a colorimeter scale according to ASTM D-1500. It has been observed that after acid/clay treatment process on each combination, color improved from 0.5 to L 0.5. While the color of Group II base oil (Imported) is 0.0 (Colorless).

Moisture Content

According to IEC 60814, for a good quality transformer base oil, the moisture content is not more than 30 ppm. It has been observed that, the moisture content decreases with the increase of clay percentage treatment from 108.15 ppm to 26.5 ppm. While the moisture content of Group II base oil (Imported) was found to be 27.6 ppm. (Figure 2). The results show that from combination G, there were no significant changes occurred in moisture value. Therefore, in the view of result it can be concluded that the optimum value of clay for moisture control is laying between 2.0 to 2.25% (v/wt.).

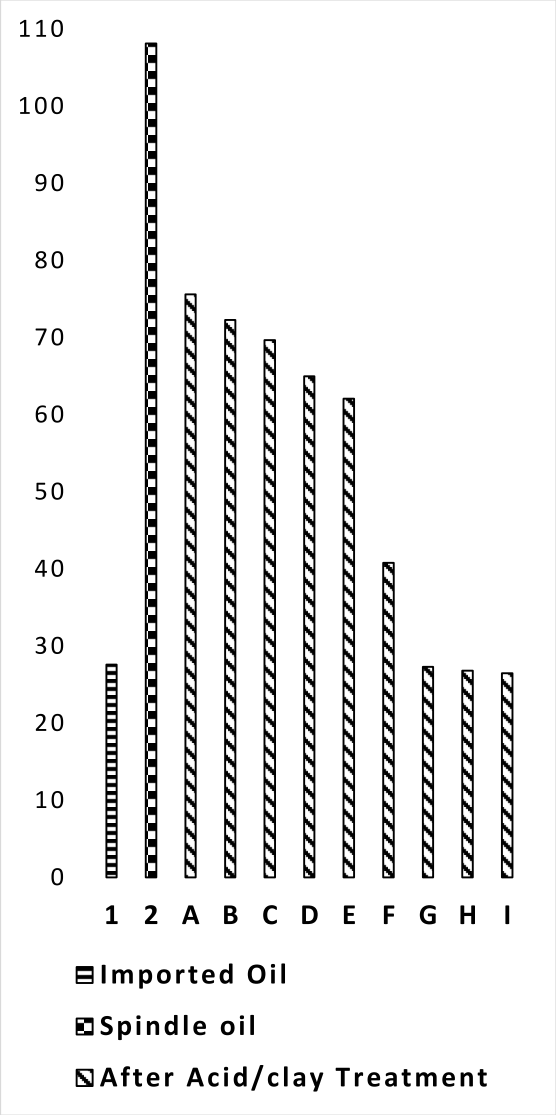

Figure 2. Water content of Group I base oil (Spindle Oil) before and after Acid/Clay Treatment and Group II base oil (Imported Oil).

Electrical Properties

Dielectric Dissipation factor (DDF)

According to IEC 60247 DDF @ 90^0 ranged not more than 0.005. It has been noticed that, the DDF @ 90^0 improved after acid /clay treatment process of Group I base oil from 0.0142 to 0.002. While the DDF @ 90^0 of Group II base oil (Imported) is 0.0025. (Figure 3) It is observed that from combination G, there were no significant changes occurred in dielectric dissipation factor. Therefore, in the view of result it can be concluded that the optimum value of clay for DDF control is laying between 2.0 to 2.25% (v/wt.).

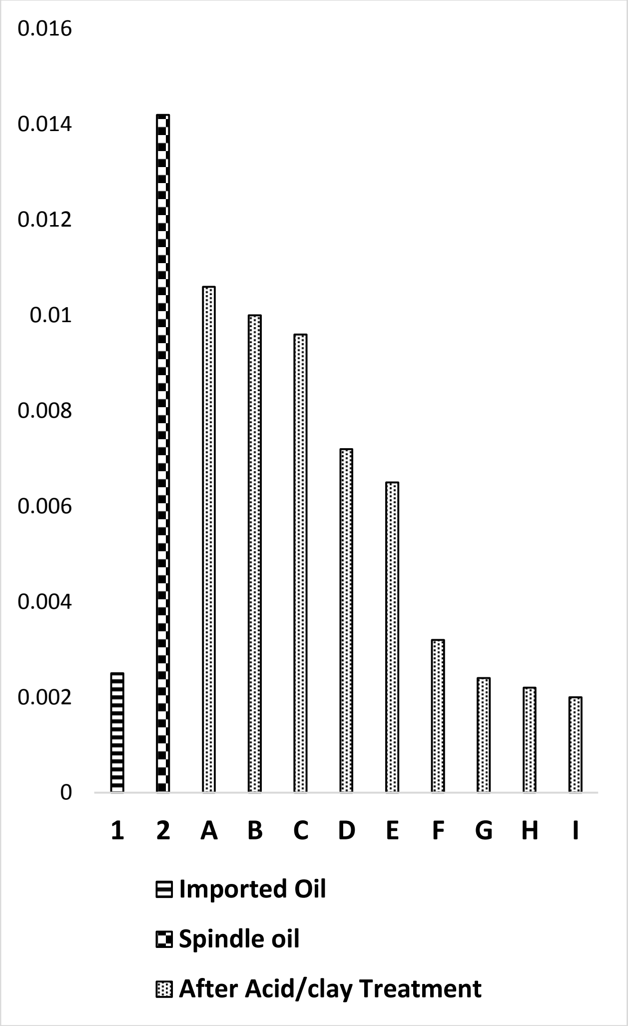

Figure 3. Dielectric Dissipation Factor of Group I base oil (Spindle Oil) before and after Acid/Clay Treatment and Group II base oil (Imported Oil)

Chemical Properties

Total Acid Number

Total acid number (TAN) is defined as mg KOH required per g of sample. According to IEC 62021-1 total acid number not more than 0.01 mg KOH/g. It has been observed that, the total acid number improved after acid /clay treatment process of Group I base oil from 0.075 to 0.0075. While the total acidity of Group II base oil (Imported) is 0.0089. (Figure 4) The results show that from combination G, there were no significant changes occurred in total acid number. Therefore, in the view of result it can be concluded that the optimum value of clay for TAN is laying between 2.0 to 2.25% (v/wt.).

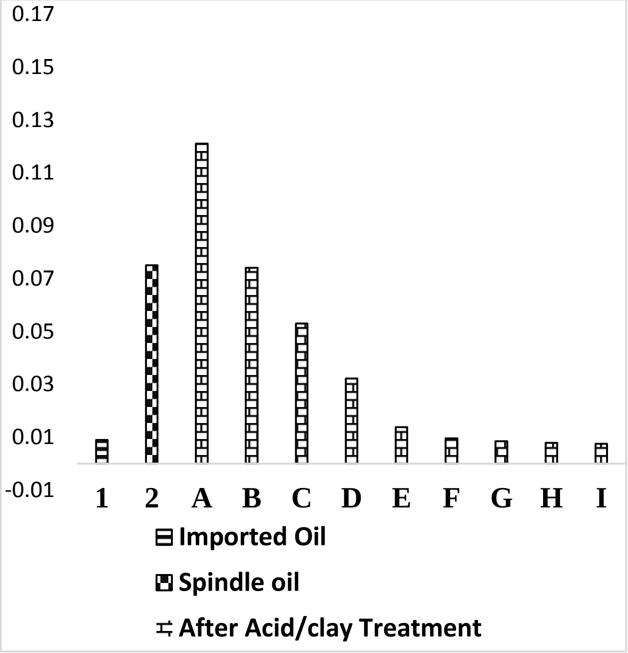

Figure 4. Total Acid Number of Group I base oil (Spindle Oil) before and after Acid/Clay Treatment and Group II base oil (Imported Oil)

Economic Importance:

On the economic aspect of this research work, it has been calculated that the cost of base oil after the process is quite lesser than its available in the market. Nowadays, the transformer base oil (LP-70) used in Pakistan is purely an imported item. While the Group I base oil, sulphuric acid and bleaching earth clay are produced in Pakistan.

4 CONCLUSION

In the light of results observed, it can be concluded that the Group I base oil can be converted into the transformer grade, base oil (Group II base oil) by the acid/clay treatment. The results show that in acid /clay treatment, with the increased percentages (v/wt.) of bleaching earth, the important properties related to transformer base oil is improves. Furthermore, no significant change was observed when the concentration of bleaching earth clay, reaching at 2.0 % (v/wt.). Hence, the optimal value of bleaching earth is found to be 2.0% (v/wt.).

On the other hand, the economic impact of this research work can be entertainment as the utilization of Pakistan made raw material and job opportunities in Pakistan as well as low cost high quality starting material for finish goods.

Further research is required in order to take this process to the commercial stage. However, while many variables have been studied in this research, there are many others that need investigation, such as Breakdown Voltage, Viscosity, Density, Flash Point, Pour Point, Polycyclic Aromatic Compounds (PCA), polychlorinated Biphynels (PCB) and Furfural.

REFERENCES:

[1] G. A. Gauger, G. L. Goedde, J. Lapp, and A. P. Yerges, "Dielectric fluid having defined chemical composition for use in electrical apparatus." Google Patents, 1997.

[2] A. Y. El-naggar, "Characterization of mineral insulating oil in view of its Power factor and dielectric strength," vol. 4, no. 4, pp. 241–246, 2014.

[3] T. O. Rouse, "Mineral insulating oil in transformers," *Electrical Insulation Magazine*, *IEEE*, vol. 14, no. 3. pp. 6–16, 1998.

[4] J. Petran and I. Polenus, "Possibility of Biodegradable Base Oils Application in Neat Metalworking Oils," pp. 211–228.

[5] IEC 60296, "Insulating liquids – Unused mineral insulating oils for transformers and switchgear," *Int. Electrotech. Comm.*, 2012.

[6] L. Nasrat, "Improvement of Used Transformer Oils with Activated Bentonite," *Engineering*, vol. 03, no. June, pp. 588–593, 2011.

[7] ISO 2049, " Determination of Color (ASTM Scale) – Test method," *Int. Standard method.*, 1996-07.

[8] 60184 IEC, "Insulating liquids–Determination of water by Coulometric Karl Fisher titration – Test method," *Int. Electrotech. Comm.*, 2008.

[9] 60247 IEC, "Insulating liquids – Determination of the dielectric dissipation factor – Test method," *Int. Electrotech. Comm.*, 2004

[10] IEC 62021-1, "Determination of Acidity-Part-1 Automatic potentiometric titration – Test method," *Int. Electrotech. Comm.*, 2003.

TABLE 1: Characteristics of transformer oil

CHARACTERISTICS	***REQUIRMENT***	***METHOD OF TEST***
Color	Max. 0.5 (as per Pakistan Requirement)	*ASTM D-1500*
Water Content	Max. 30 mg/kg (ppm)	*IEC 60184*
Dielectric Dissipation Factor *at 90 C*	Max. 0.005	*IEC 60247*
Acidity	Max. 0.01 mg KOH/g	*IEC 62021-1*

TABLE 2: Symbols codes of Group I base oil (Spindle Oil) after and before Acid/Clay treatment and Group II base oil (Imported Oil)

Oil Specimen	Symbol Code
LP-70 Imported Group II Oil	1
65 NHVI Spindle Oil	2
Spindle Oil acid treatment method with 0.5 % sulfuric acid	3
Spindle Oil acid/clay treatment method with 0.5 % sulfuric acid and 0.5% clay	A
Spindle Oil acid/clay treatment method with 0.5 % sulfuric acid and 0.75% clay	B
Spindle Oil acid/clay treatment method with 0.5 % sulfuric acid and 1.0% clay	C
Spindle Oil acid/clay treatment method with 0.5 % sulfuric acid and 1.25% clay	D
Spindle Oil acid/clay treatment method with 0.5 % sulfuric acid and 1.5% clay	E
Spindle Oil acid/clay treatment method with 0.5 % sulfuric acid and 1.75% clay	F
Spindle Oil acid/clay treatment method with 0.5 % sulfuric acid and 2.0% clay	G
Spindle Oil acid/clay treatment method with 0.5 % sulfuric acid and 2.25% clay	H
Spindle Oil acid/clay treatment method with 0.5 % sulfuric acid and 2.25% clay	I

TABLE 3: Electrical, chemical and physical properties Group I base oil (Spindle Oil) after and before Acid/Clay treatment and comparison with Group II base oil (Imported Oil)

Methods No.	ASTM D-1500	IEC-60184	IEC-60247	IEC-62021-1
Parameter / Specimen	Color	water content	Dielectric Dissipation Factor	Acidity
1	0.0	27.6	0.0025	0.0089
2	0.5	108.15	0.0142	0.075
3	Brown shade	96.5	0.0118	0.165
A	L 0.5	75.6	0.0106	0.121
B		72.3	0.010	0.0741
C	L 0.5	69.7	0.0096	0.0530
D	L 0.5	65.0	0.0072	0.0322
E	L 0.5	62.1	0.0065	0.0138
F	L 0.5	40.8	0.0032	0.0096
G	L 0.5	27.3	0.0024	0.0085
H	L 0.5	26.8	0.0022	0.0079
I	L 0.5	26.5	0.0020	0.0075

SYNTHESIS AND CHARACTERIZATION OF ANATASE TITANIUM DIOXIDE NANOPARTICLES BY SOL-GEL METHOD

Sidra Jamil Ahmed[1,*] Humair Ahmed Siddiqui[2], Dr. Saqib Anjum[1], Dr. Ashraf Ali[3]
[1]Physics Department, NED University of Engineering & Technology, Karachi.
[2]Material Engineering Department, NED University of Engineering & Technology, Karachi.
[3]Ghulam Ishaq Khan Institute of Engineering Sciences and Technology, Topi, KPK

[*]Corresponding author: Sidra Jamil Ahmed, *E-mail address*: sidraandy@hotmail.com

ABSTRACT

Nanocrystalline semiconductors have achieved significant importance as they are the cornerstones of nanoscience and nanotechnology. Titanium dioxide (TiO_2) is a transition metal oxide considered to be the most capable n-type semiconducting material due to its strength, low cost, high oxidizing capacity, non-toxicity and is potential for large scale production in industry. It has many attractive optical properties such as a high refractive index, high dielectric constant, chemical stability and a wide band gap. Titanium dioxide exists in anatase (tetragonal), rutile (tetragonal) and brookite (orthorhombic) phase. Due to the wide band gap, the anatase phase has particularly focused a great deal of attention from industry. It has a wide range of applications including its usage in photovoltaic solar cells, gas sensing devices and photocatalysts under ultraviolet (UV) light. Photocatalytic applications of Titanium dioxide eliminate environmental pollutants and are useful for the purification of air, water and soil. The Titanium dioxide nanoparticles can easily be synthesized using the sol-gel method. This method is the most suitable route to synthesize metal oxide nanoparticles due to the low reaction temperature, homogeneity, high purity and submicron particle size (typically 20Å to 50Å). In this research, Nanoparticles of Anatase Titanium Dioxide was successfully synthesised using controlled Sol-gel method and the morphology, particle size, crystalline structure and band gap of these synthesized nanoparticles have been characterized. The characterization was achieved using several instrumental techniques - specifically X-Ray Diffraction (XRD), Scanning Electron Microscopy (SEM), Ultraviolet-visible (UV-Vis) spectrophotometer and XRF Analyzer spectrometer which give evidence of the presence of Anatase Titanium dioxide nanoparticles.

Keywords: Nanotechnology, Titanium Dioxide, Anatase, Sol-gel, Nanoparticles.

1. INTRODUCTION

Nanoparticles are particles having at least one dimension in nano-scale (i.e. less than 100 Nanometre). Nanotechnology has attracted technological interest since nanoparticles are efficiently a bridge between atomic, molecular structure and bulk materials.

The properties of nanoparticles vary with particle size, but the bulk material generally has constant physical properties regardless of its size. The recent growth of nanotechnology has provided a platform for environmental decontamination through several nanomaterials, processes, and tools. [1]

1.1 Titanium Dioxide

TiO2 is a ceramic, transition metal oxide having many commercial uses. It has some excellent qualities with its usefulness in solar energy and the photocatalysis of toxic compounds in the environment. Furthermore, the strong oxidizing power of the photogenerated holes, chemically inertness and stability, non-toxicity and low production cost of TiO2 has also made it an advanced photocatalyst. It is also used widely in sunscreens as an efficient absorber of UV.

Titanium dioxide (TiO2) is found naturally as anatase (tetragonal), brookite (orthorhombic) rutile (tetragonal) phases. The most common form of TiO2 is rutile, whilst the anatase and brookite forms of TiO2 tend to convert into rutile form upon heating them at high temperature. [2]

TiO2 is used as a pigment in paints and the global oil crisis has encouraged a variety of scientists and converted interest in this material. TiO2 has also been extremely useful in overcoming the problem of splitting water molecules, based on the principles of photo-electrochemistry. It is also applicable in electronic industry as a MOSFET (Metal Oxide Semiconductor Field-Effect Transistor).

It is also useful as a gas sensor at high temperatures for the determination of oxygen, carbon monoxide and methane. [3] TiO2 is excellent for photocatalytically breaking down organic compounds. The polluted water of a shallow pool can be purified when illuminated with sunlight in the presence of catalytically active TiO2 powder. [4] TiO2 has a high refractive index (rutile - 3.87 and anatase - 2.5 - 3); the photoactivity of rutile makes it a poor pigment in spite of its high refractive index. [2]

The anatase phase is the most active photocatalyst among all the phases due to its chemical properties, charge carrier dynamics and the photocatalytic degradation of organic compounds such as dyes. TiO2 is said to be as a 'large band gap semiconductor'. This is because the band gap energies of the anatase, rutile and brookite phases of TiO2 are 3.2, 3.02 and 2.96 respectively.

The conduction band is only the 3d orbitals of titanium whereas the valence band of TiO2 is composed of oxygen hybridized 2p orbitals with 3d orbitals of titanium. Near UV light, the electrons are excited from the valence band to the conducting band, which results in the formation of electron/hole pairs. The excited electrons in the conduction band are now at the 3d state and because of different parity; there is a decrease in probability of electron transition from the valence band which decreases the electron/hole recombination probability.

In the anatase phase of TiO2, the surface-hole trapping dominates. This is affected by the precursor used, impurities added, oxygen vacancies and the particle size. [5]

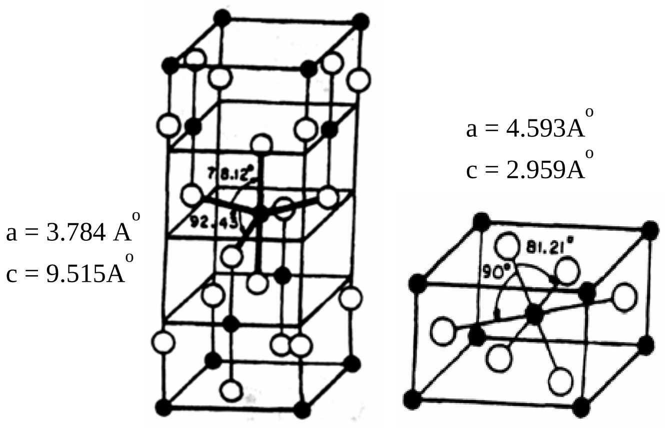

(a) (b)

Fig.1 structure of (a) anatase and (b) rutile TiO_2 [6]

TiO_2 is easy to synthesize in the laboratory. The photocatalytic activity of TiO_2 can be enhanced by increasing its surface area which depends on the crystal size, as the size decreases its surface area increase largely. A number of methods have been adopted for the synthesis of TiO_2 nanoparticles, among them chemical vapor deposition, microemulsion, hydrothermal and sol–gel. Sol-gel is the most successful technique for the synthesis of metal oxide nanoparticles due to the low reaction temperature, homogeneity, high purity and submicron particle size for high photocatalytic activities. [7]

1.2 Sol- Gel Synthesis

A sol-gel synthesis is also well known as a polymerization process by its intrinsic nature. It is a colloidal route, including a sol and gel state used to synthesize ceramics with a high purity and homogeneity. [8]

Metal alkoxides ($M(OR)_n$, M^{n+} = metal cation of valence n and OR= alkoxy group) or colloidal metal oxide or hydroxides can be used as precursor which is advantageous as these are synthetic precursors.

Their polymerization of these species occurs by hydrolysis which is initiated by water. [9]

The reaction steps can be written as:

1. Hydrolysis:

$$M(OR)_n + H_2O \longrightarrow M(OR)_{n-1}(OH) + ROH \quad (1)$$

2. Condensation:

$$M(OR)_n + M(OR)_{n-1}(OH) \rightarrow M_2O(OR)_{2n-2} + ROH \quad (2)$$

3. Gelation:
Arrangement of cluster, giving a network with high viscosity which entangles the remaining solution.

4. Ageing:
Formation of further cross-links which involves a series of processes associates with contraction of gel.

5. Drying:
Evaporation of liquid which results in the loss of water, alcohol or other volatile components.

6. Densification:
Thermal treatment which results in the formation of dense ceramic. [7, 10]

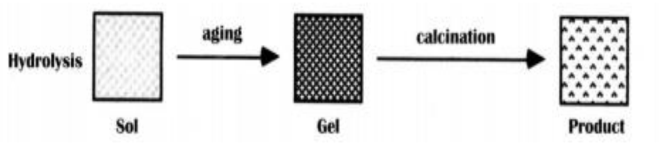

Fig.2 Schematic for Sol-Gel synthesis to show different phases of product [10]

Titanium alkoxide is used for hydrolysis as a precursor in order to obtain homogeneity in titanium oxide. Condensation involves gelation and calcinations which brings constitute particles in the form of a compact mass, which results in formation of metal oxide crystal.

Calcination is heat treatment for the removal of organic constituents. Very high calcination results in phase transformation from the anatase phase to the rutile phase due to aggregation and hence this changes the crystalline structure of TiO_2. The anatase phase is more active as a photo catalyst than the rutile phase. [7]

The aim of this research is to synthesize anatase titanium dioxide nanoparticles in which titanium tetra isopropoxide is used as a precursor. The sol-gel route is adopted for the synthesis which gives nanocrystalline TiO_2 powder. The properties including crystal structure, morphology, particle size and band gap give clear evidence of the presence of nano titania. These properties can also be helpful to predict its photocatalytic capability.

2. EXPERIMENT

2.1 Chemicals

All the chemicals used, were of Lab-grade quality and were purchased from Karachi Scientific Traders, Karachi. Titanium Tetra Isopropoxide ($C_{12}H_{28}O_4Ti$) (Company: Dae-Jung Korea), 2-Propanol or Iso-propyl alcohol (CH_3CH (OH) CH3) (Company: vRDH Germany) and deionized water was used for all experiments.

2.2 Synthesis of Anatase TiO_2

Titanium dioxide nanoparticles were synthesized using the sol-gel technique by adding 5 ml Titanium Tetra Isopropoxide, which is used as a precursor, in 5 ml Isopropanol, which is used as a solvent. The solution was prepared at room temperature under a fume hood, and 200 ml of Deionized water was added with a rate of 2 ml/min, that gave white colloidal solution. The mixture was then kept under vigorous stirring for 2 hours on magnetic stirrer for completion of hydrolysis. The solution was then covered and aged for 24 hours, after that the solution was filtered, dried in an oven for 2 hours at 90°C and then finally calcinated in a furnace at 400°C for 4 hours.

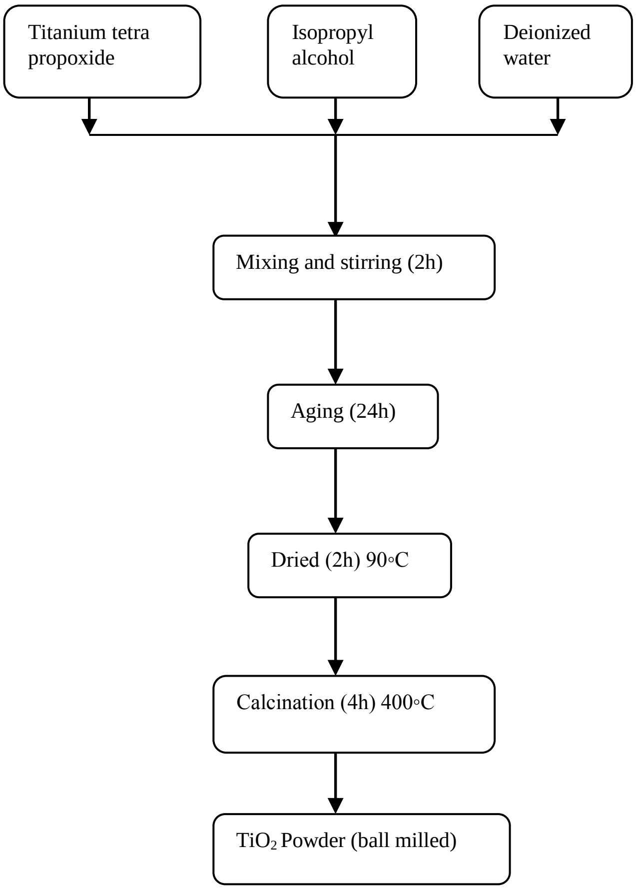

Fig.3 Flow chart for the synthesis of TiO_2 nanoparticles by Sol-Gel method

This process resulted in the formation of a white crystalline powder. In order to avoid agglomeration, the crystals were grinded/crushed using ball milling to successfully obtain a fine powder of Nano Anatase TiO_2 sample.

2.3 Characterization

The prepared Nano particles were initially characterized using portable X-ray Fluorescence (XRF) Analyzer spectrometer (INNOVX system A-8000 USA), which was used to initially confirm the presence of elemental constituents so as to get a clear picture about the level of impurity and other trace elements. For the identification of compound i.e TiO_2, crystalline structure and particle size; X-ray Diffractometer system (XPERT-PRO) was used, at 25°C, operating at 40 kV and 30 mA, using Cu$K\alpha$ radiation ($\lambda = 0.15406$ nm). The particle size was calculated by Debye Scherrer's formula. Surface morphology was studied by using Scanning electron microscope (SEM) (FEI Quanta 200), while the UV-Vis Spectrophotometer (Spectrum Lab 22PC) was used to find the band gap of anatase titanium dioxide as it is important to find the band gap of a semiconductor.

3. RESULTS AND DISCUSSION

3.1 XRF Analysis

The results obtained from XRF analysis give a clear account of the presence of Titanium. The elemental constituents in weight percent is given in the table below.

Sample	Ti	Zn
Nano-TiO_2	99.8 ± 0.03	0.16 ± 0.01

Table 1. Elemental composition in wt% of Anatase TiO_2 nanoparticles.

3.2 XRD Analysis

Xrd spectrum obtained was typically of crystalline material with sharp peaks. The sharp peaks of the sample appeared at 2θ = 25.248520°, 38.323820° and 47.978120° which confirmed the presence of anatase phase of TiO_2 and there were no peak representing any other phase of titania like rutile. The appearance of sharp peaks identifies small size, purity and crystalline structure. The peak recorded in the XRD graph resembles the peak of anatase from the literature values. The average crystallite size is calculated by using the Debye Scherrer's formula,

$$D = \frac{k\lambda}{\beta cos\theta} \qquad (3)$$

The value of *d* inter planner spacing between the atoms is calculated by using Bragg's equation

$$dsin\theta = n\lambda \qquad (4)$$

Where *k* is Scherrer's constant and its value is 0.9, whereas λ is the wavelength of X-Ray radiation, 0.15406 nm and **β** is the full width half maxima and θ is the Bragg's diffraction angle. From the strongest peak of XRD at 2θ=25.248520°, **β** = 0.7872, the particle size is found to be 10 nm which shows that particle size is inversely proportional to full width half maxima and the d-spacing is 3.5274Å as calculated by Bragg's equation.

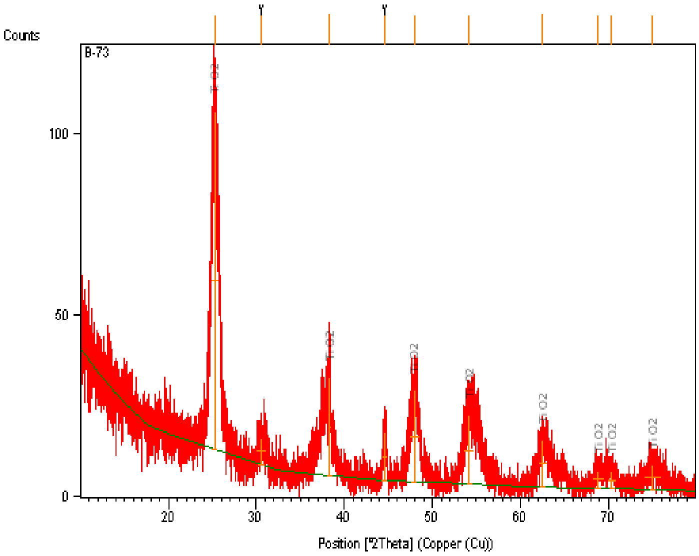

Fig.4 XRD pattern of sol-gel synthesized anatase TiO_2 nanoparticles

The lattice parameters were calculated with the equation

$$\frac{1}{d^2} = \frac{(h^2 + k^2)}{a^2} + \frac{l^2}{c^2} \qquad (5)$$

Where (*h k l*) correspond to miller indices (crystal plane indices). The experimental XRD pattern agrees with JCPDS card # 03-065-5714 and the strong peak at 25.248520° corresponds to (101) plane where as rutile phase is observed at (110) at 2θ= 27.5° [2]. This shows that the 400°C might be the appropriate calcination temperature for anatase titanium dioxide nanoparticles. For tetragonal anatase phase of TiO_2, a = b ≠ c, so the lattice constant is found to be a=3.794 Å (=b) and c= 9.514Å.

3.3 SEM Analysis

Scanning Electron Microscopy (SEM) of the sample gives surface morphology of synthesized anatase nanoparticles calcinated at 400°C. The spherical shaped non uniform particles were clearly observed with some particles being agglomerated as shown in fig.5 and 6. The image shows the uniform distribution of particles on surface without any aggregation as recorded with different magnification.

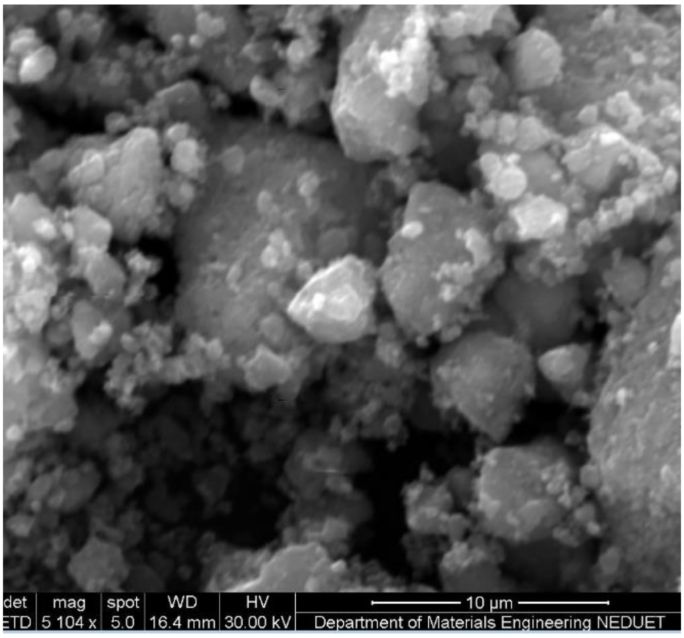

Fig .5 SEM Image showing different particle sizes of Titania

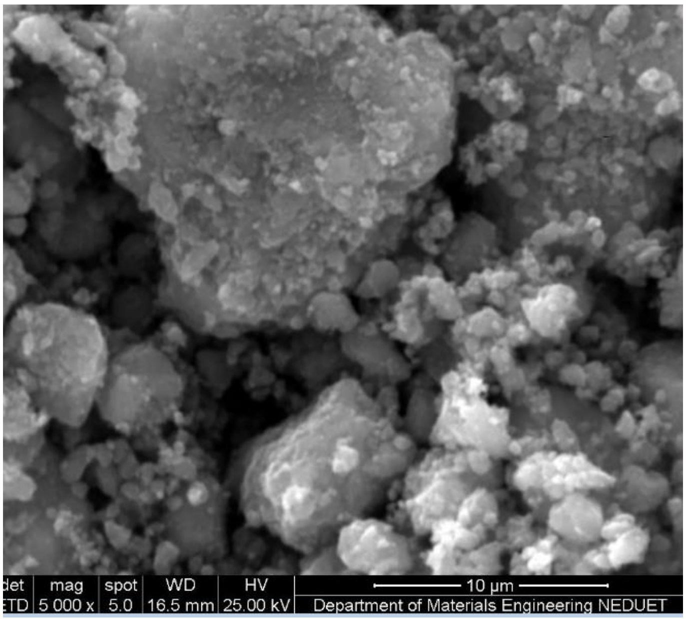

Fig .6 SEM image showing different agglomerated Titania particles

The calcinated particles can be grinded using ball milling to reduce agglomeration.

3.4 UV-VIS Spectrophotometer Analysis

Absorption edges of the semiconducting material yields the band gap of the material. In order to determine the band gap of anatase TiO_2, the equation can be used

$$E = h\nu \tag{6}$$

$$E = \frac{hc}{\lambda} \tag{7}$$

Where *h* is the Planck's constant, λ is the wavelength, ν is the frequency of the photon, *E* is the energy and *c* is the speed of light. From graph in fig.7, the cut off wavelength is found to be 413nm. So the band gap of anatase nanoparticles is found to be 3.02eV, which shows an agreement of anatase nanoparticles as an active photocatalyst in UV range. So, these anatase particles can be use to degrade organic compounds in the presence of UV light.

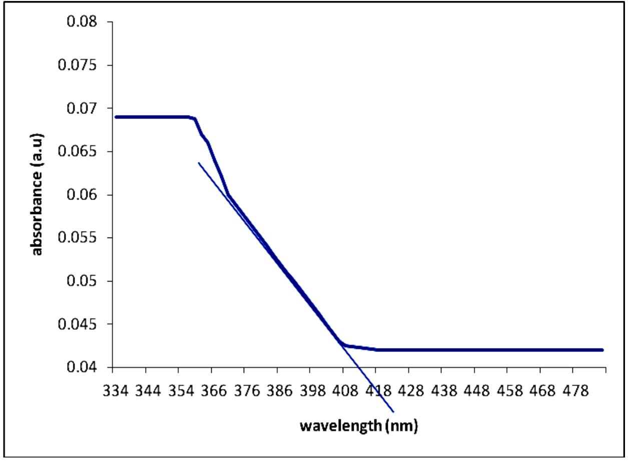

Fig. 7 a graph of absorbance versus wavelength

4. CONCLUSION

The anatase titanium dioxide nanoparticles are successfully synthesized using the sol-gel route using titanium tetra isopropoxide as a precursor, calcinated at 400°C which gives high degree of crystalline structure.

The characterization of the synthesized sample was achieved by using an X-ray diffractrometer, scanning electron microscope and UV-Vis spectrophotometer. The XRD pattern reveals that the synthesized nanoparticle is anatase TiO_2. The particle size as calculated from the XRD pattern is found to be 10 nm and the d-spacing is 3.5274Å .

The lattice constant is a=3.794Å and c=9.514Å so structure of crystallite is tetragonal as given by (101) plane. The XRF results yields the presence of TiO_2 up to 99.9%. The surface morphology as shown by SEM images gives a clear account of the presence of uniform distributed spherically shaped anatase TiO_2 nanoparticles. The band gap as determined by 413nm as the cut off wavelength is found to be 3.02eV which is very strong evidence to show that anatase TiO_2 is a semiconducting metal oxide nanoparticle. This can be seen to behave as an effective photocatalyst within UV range, in order to successfully degrade an organic compound and this can subsequently be applied conveniently to purify water also can be suited for solar cell applications.

5. ACKNOWLEDGMENTS

This research work was successfully achieved with the support of NED University of Engineering & Technology so I wish to express my gratitude to NEDUET.

6. REFERENCES

[1] Manoj Ram, E. S. Andreescu and Ding Hanming, *Nanotechnology for environmental decontamination*, Mc Graw Hill, 2011

[2] Ahmed A. Hussain and Hilal S. Wahab, synthesis and spectroscopic characterization of anatase titanium dioxide nanoparticles, *International journal of Nanotechnology and Nanoscience*, vol. 2, 1-6, 2014

[3] John McCormick, Chemistry of TiO2 nanoparticles (doctorial dissertation), *Available from ProQuest Dissertations & Thesis database*, 2006 (UMI No. 3220706)

[4] A. Fujishima, Tata N. Rao, Donald A. Tryk., Titanium dioxide photocatalysis, *Journal of Photochemistry and Photobiology C: Photochemistry Reviews I*, pp. 1-21, 2000

[5] Gupta & Tripathi, A review of TiO2 nanoparticles., *Article in Chinese Science Bulletin*, 56(16), 1639-1657, 2010, doi: 10.1007/s11434-011-4476-1

[6] Dr. A. Ahmad, Gul Hameed Awan, Salman Aziz, S*ynthesis and Application of* TiO_2 *Nanoparticles,* Pakistan Engineering Congress, 70th Annual Session Proceedings, paper no.676

[7] C. Su*, B.-Y. Hong, C.-M. Tseng, sol-gel preparation and photocatalysis of titanium dioxide, *Elsevier catalysis today,* 96, 119-126, 2004

[8] Alain C. Pierre, *Introduction to Sol-Gel Processing,* Springer Science+ Business Media, LLC, 1998

[9] A. Mortensen, Concise Encyclopedia of Composite Materials, *Elsevier,* 2007

[10] John D. Wright, Nico A.J.M. Sommerdijk, *Sol-Gel Materials: Chemistry and Applications*, CRC Press, 2000

[11] Daniel E. Sabo, *Novel synthesis of Metal Oxide Nanoparticles via the Aminolytic Method and the investigation of their magnetic properties,* Georgia Institute of Technology, 2012

VALIDATION OF TEMPERATURE SENSITIVITY OF SUPERHYDROPHOBIC SURFACES AS APPLIED ON 316L SS

Hamza Shams[1,2], Sajid Saleem[1] and Bilal A. Siddiqui[2]
[1]National University of Sciences and Technology (NUST), Islamabad, Pakistan
[2]DHA Suffa University (DSU), Karachi, Pakistan

[*]Corresponding author. Tel.: +92-345-2184377
E-mail address: hamza.shams@dsu.edu.pk (Hamza Shams)

ABSTRACT

This paper investigates the viability of commercially available superhydrophobic coatings applied over 316L Stainless Steel in extreme temperature environments. 316L SS or Marine Steel has immense importance in structural applications. Commercial superhydrophobic coatings are gaining importance in industry due to self-cleaning characteristics and effective lubrication. The coatings after application were investigated in a range of temperatures through dynamic-mode imaging of the surface by Lateral Force Microscopy (LFM). LFM revealed changes in the surface roughness and lateral force behaviour under the extremes of temperature. The analysis has been used to evaluate a value of friction coefficient which demonstrates wear behaviour due to isothermal temperature changes in the environment. This is directly associative of the optimal temperature for the coating to remain intact and indirectly predicts the ideal temperature till which the base substrate would remain protected. The analysis aims to validate the temperature sensitivity of these commercial coatings for use in structural applications in demanding environmental conditions.

Keywords: 316L Stainless Steel; Lateral Force Microscopy;Superhydrophobic Surfaces, Oleophobic Surfaces, Temperature Sensitivity of Coatings

1 INTRODUCTION

AFM was introduced as a combination of the principles of STM (Scanning Tunneling Microscope) and Stylus Profilometer [1]. Since its introduction, this technology has been widely adapted for the study of frictional effects, surface properties and changes in material properties for different conditions ranging from micro scale to nano scale. At these scales, the performance and operating lives of the micro/nano tribological devices is reduced due to high surface forces, such as adhesion and friction [2].

The need to modify AFM was to cater for the high surface forces that occur at nano level. Therefore, LFM was developed and is now considered as one of the most effective and informative technologies to measure adhesive and frictional effects. Friction and wear rate are fundamental characteristics of a machine with relative motion. LFM has played an important role in investigating co efficient of friction and other tribological properties for various materials under different conditions at nano scale [2 - 6]. AFM can also be used to study surface roughness of a material [7 - 9] because irrespective of the material, the co-efficient of friction can be altered by modifying its surface roughness [7].

Coating is a form of surface modification where one material is deposited on the other to improve properties such as hardness, roughness and wear resistance [10]. Right after the introduction of AFM technique, O. Marti, D. Brake and P.K. Hansma in 1987, carried out experiments using conducting and non conducting surfaces covered with oil and used AFM to analyze them. This research demonstrates the potential of AFM technique. [11]

Metal coatings can be hydrophobic ‘water repellent’, hydrophilic ‘water loving’ and similarly oleophobic and oleophilic. Some of the coating methods of a metal are Dip coating, Spraying, Oxidation and electrochemical deposition. There has been extensive research on different types of coatings on a metal. A small thickness chromium nitride coating on a steel substrate when oxidized at a temperature higher than 450 °C, forms a separate Cr2O3 layer on top of the nitride coating and as the temperature is increased, the thickness of the formed layer increases [12]. The word oleophobic literally corresponds to the ‘fear of oil’. Water is considered as the most oleophobic substance.

Applications of oleophobic surfaces include anti-fouling, self-cleaning, low drag and oil-water separation. Oleophobic coatings have been studied for aerospace applications under harsh environment [13]. There is a wide variety of such coatings available for composites and metals and the research for the same still continues with the development of superoleophobic and superhydrohobic coatings [14].

316L SS has been widely used in industrial applications for its corrosion resistance property and high strength. However, because of its low hardness and wear resistance their applications are limited [15]. Therefore the surface of SS 316L is hardened to improve wear and hardness resistance of the material without changing its other desirable properties. The tribological and corrosion behavior of Amorphous Carbon coatings over widely used 316L SS was investigated recently [9]. In the same year, wear test was conducted on 316L SS deposited with a layer of TiN against Titanium Alloy (Ti-6Al-4V) under different modified conditions [10].

The adhesive forces in a dry sliding contact generate high surface temperature therefore the effect of these forces under elevated temperature condition was observed by A. Gaard using Ti, Stainless Steel and low alloyed steel samples. It was found that the adhesive forces and the surrounding temperature are linearly related [16]. The effect of heat treatment over 316L SS dip coated by thin film of ZrO2 was investigated using SEM and AFM and it was observed that there was a major decrease in thickness of the film up to 700 °C and almost constant behaviour between 700 °C to 900 °C [17].

Despite its widespread usage little work has been done to confirm the effective properties and consequently the co efficient of friction at nano-level of commercially available oleophobic coating when applied over 316L Stainless Steel. In this work, 316L SS, when coated with oleophobic coating, are observed to determine the co efficient of friction and the changes in its value when the samples are kept at elevated temperature of up to 250˚C for 08 hours. LFM technique is used to record the frictional and lateral forces and consequently the coefficient of friction which will help in enhancement of surface properties and material life prediction. The analysis aims to validate the co efficient of friction value as marketed by the coating manufacturers.

2 EQUIPMENT

The equipment used in this study is the ezAFM by Nanomagnetics Instruments as shown in Figure 1. The equipment is capable of LFM scanning in contact-static mode and provides meaningful data through its output channels comprising of FN, FL and FT which in turn is used to evaluate the friction coefficient usingAmantons' Law. PPP-LFMR probes are used in this investigation.The low force constant of the PPP-LFMR probes enables more rigid tip-sample behaviour which provides accuracy of the scanning results. A low force constant also means that even minute tip deflections are carefully recorded by the detector in theezAFM.

Figure 1. ezAFM at DHA Suffa University

Isothermal heating of samples was accomplished by ESCO Isotherm OFA-32-8 in Figure 2 that allows temperature rise up to 300°C and is capable of isothermal heating.

Figure 2. ESCO Isotherm OFA-32-8 at DHA Suffa University

3 EXPERIMENTAL METHODOLOGY

Twenty-Four (24) samples each measuring 25 mm in diameter and 8 mm in height were cut from peeled round bar of 316L SS. The samples' surface was grinded using emery papers of grit size 120, 240, 320, 600 and 800 on Metkon Forcipol 2V Wet Grinding Disc maintained at 400 RPM.

Grinded samples were then labelled 1 to 24 as given in Table 1. Labelled samples were scanned by ezAFM in LFM mode to evaluate initial value of coefficient of friction, results of which are presented in Table 2. For each scanning, sample surface was divided into 10 parts and both front and back scanning was accomplished for accuracy of the results.

Scanning was accomplished on a 5µm x 5µm area at 64 pixels resolution. The scanning frequency was maintained at 5µm/s for the first run which was reduced to 1µm/s later on for recording results.

The final value of the coefficient friction of each sample surface is therefore a mean of 640 points. Anomalous values were removed from the average to maintain precision. This procedure was kept constant for all samples.

After the scanning was accomplished, labelled samples were then coated with their respective set of coatings as discussed in Table 1. Only one surface was coated on each sample as shown in Figure 3.

Aerosol based coating was positioned 8 inches from the sample surface and coating was performed in a lateral motion from left to right in 02 continuous cycles. For EnduroShield Stainless Steel Coating and Rust-Oleum NeverWet Multi-Surface Liquid Repelling Treatment, base coat was first applied followed by top coat as stated in the manufacturer's manual. For DuPont Teflon Non-Stick Dry-Film Lubricant Coating, a single coat was recommended. Each coat was applied twice in former case while four coats were applied for the latter one to make the number of coats equal.

LFM scanning was repeated on the coated samples and the results are presented in Table 3.

Oven preparation was made at the temperatures as mentioned in Table 4. The oven was preheated for two(02) hours before the final temperature was reached in the heating cycle. Coated samples were then put inside the hot oven and incubated for next 08 hours in the oven. The samples were then cooled and observed with LFM since in-situ scanning was not possible with our equipment. Scanning results are presented in Table 5.

Water repellency test was also performed on the treated samples.

This approach is in continuation to our systematic approach to generate useful data on oleophobic/ superhydrophobic surfaces for aerospace and commercial marine applications in Pakistan and would be viably applied for varied applications other than those recommended by the manufacturer once sufficient data has been obtained.

Due to lack of sufficient practical applications data available for these coatings, investigations are being carried out with the said purpose of improving surface finish and corrosion resistance of metallic parts in high-performance applications.

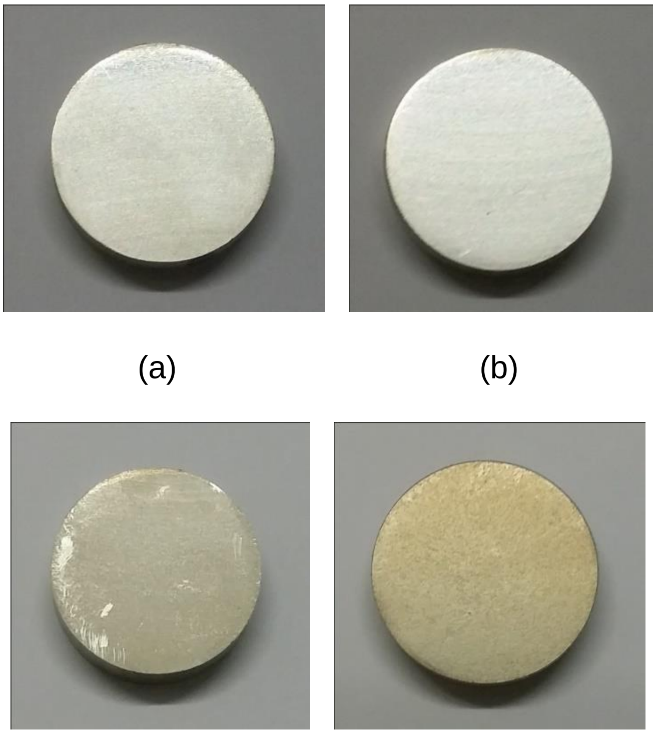

(a) (b)

(c) (d)

Figure 3. a) Original sample surface appearance without coating,

b) Sample 2 surface appearance with Enduroshield Stainless Steel Coating,

c) Sample 6 surface appearance with DuPont Non-Stick Dry Film Lubricant Coating and

d) Sample 10 surface appearance with Rust-Oleum NeverWet Multi-Surface Liquid Repelling Treatment

Table 1. Labelling of Grinded Samples based on Coating

Sample Number	Coating Applied
1,2,3,4,5,6,7,8	Enduroshield Stainless Steel Coating
9,10,11,12,13,14, 15,16	DuPont Teflon Non-Stick Dry Film Lubricant Coating
17,18,19,20,21,22,23,24	Rust-OleumNeverWet Multi-Surface Liquid Repelling Treatment

Table 2. Mean values of Coefficient of Friction as obtained from LFM on Uncoated samples

Sample Number	Coefficient of Friction
1	0.154
2	0.182
3	0.167
4	0.140
5	0.158
6	0.162
7	0.155
8	0.173
9	0.180
10	0.151
11	0.164
12	0.167
13	0.176
14	0.149
15	0.157
16	0.179
17	0.144
18	0.175
19	0.160
20	0.171
21	0.158
22	0.179
23	0.161
24	0.147

4 RESULTS AND DISCUSSION

4.1 Physical Appearance

The samples were left to cool after eight 08 hours of temperature incubation. No significant difference in texture was visible in the samples.

4.2 Water Test

Samples were tested for water repellency. EnduroShield Stainless Steel Coating and Rust-Oleum NeverWet Multi-Surface Treatment showed water repellency even after treatment at 250°C.Dupont Non-Stick Dry Film Lubricant Coating showed decreased water repellency after treatment.

4.3 Lateral Force Microscopy

Lateral Force Microscopy revealed that coefficient of friction values for the coated sample is significantly lesser as compared to the coefficient of friction values for uncoated samples. This is shown in Table 3. A comparison of Table 2 and Table 3 results is shown in Figure 4.

Table 5 shows how these values change further when treated in a convection oven.

Table 3. Mean values of Coefficient of Friction as obtained from LFM on Coated samples

Sample Number	Coefficient of Friction
1	0.148
2	0.145
3	0.151
4	0.144
5	0.152
6	0.150
7	0.151
8	0.140
9	0.124
10	0.131
11	0.128
12	0.134
13	0.136
14	0.133
15	0.129
16	0.121
17	0.144
18	0.158
19	0.142
20	0.155
21	0.148
22	0.152
23	0.141
24	0.148

Table 4. Oven temperature for coated samples

Temp. (°C)	Sample Number
75	1, 9, 17
100	2, 10, 18
125	3, 11, 19
150	4, 12, 20
175	5, 13, 21
200	6, 14, 22
225	7, 15, 23
250	8, 16, 24

The coefficient of friction value for samples treated between 75 to 150 remain fairly in range of their previous values. However, samples treated at 200°C and above show a significant change in the coefficient of friction value.

Dupont Non-Stick Dry Film Lubricant Coating shows the maximum change in coefficient of friction value at 200°C. While for EnduroShield Stainless Steel Coating and Rust-Oleum NeverWet Multi-Surface Treatment it is at 250°C.

Our previous investigation results from coating and testing value of COF on Inconel 718 samples in sand-storm conditions are given in Table 6.The conditions of this investigation are fairly different from our previous study. However, for comparison we can relate the difference in values of COF based on different surface interaction between the coating and base surface. Their closeness to our previous results suggest that our values are well in range.

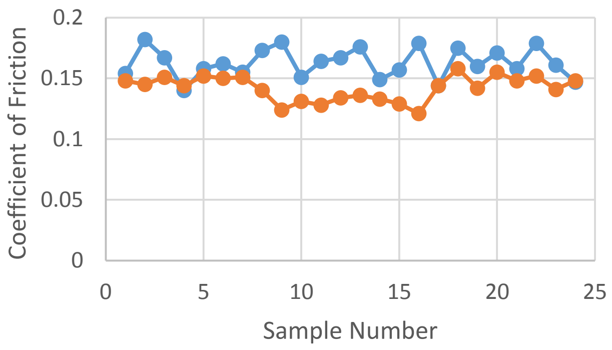

Figure 4. Coefficient of friction values against Sample Number. Blue line shows the coefficient of friction value before coating while orange line shows the values as a result of coating application

Table 5. Change in coefficient of friction values before and after isothermal heat treatment in convection oven

Coating	Sample Number	Temp. (°C)	Coefficient of Friction	
			Before	After
EnduroShield Stainless Steel Coating	1	75	0.148	0.146
	2	100	0.145	0.144
	3	125	0.151	0.155
	4	150	0.144	0.150
	5	175	0.152	0.157
	6	200	0.150	0.149
	7	225	0.151	0.157
	8	250	0.140	0.201
Dupont Non-Stick Dry Film Lubricant Coating	9	75	0.124	0.133
	10	100	0.131	0.136
	11	125	0.128	0.139
	12	150	0.134	0.141
	13	175	0.136	0.139
	14	200	0.133	0.241
	15	225	0.129	0.244
	16	250	0.121	0.250
Rust-Oleum NeverWet Multi-Surface Treatment	17	75	0.144	0.145
	18	100	0.158	0.152
	19	125	0.142	0.150
	20	150	0.155	0.156
	21	175	0.148	0.151
	22	200	0.152	0.157
	23	225	0.141	0.161
	24	250	0.148	0.247

On a general trend it is evident that the coefficient of friction changes drastically between the temperatureranges of 200°C - 250°C whereas in the lower ranges of temperture 75°C - 150°C, no significant changes are observed.

The lateral and normal forces from each of the 64 points in a scan were obtained using 'Contact mode' analysis capable of generating friction force. The ratio of the forces data obtained is related by the Amonton's Friction Law,

$$\mu = \frac{F_L}{F_N} \quad (1)$$

where μ is the coefficient of friction, $F_L$is the lateral friction and $F_N$is the normal loading force.

5 CONCLUSIONS

This research aims to investigate the co efficient of friction of 316L SS samples when coated by three different superhydrophobic coatings, kept at elevated temperature for 08 hours and observed using FFM. The results obtained were:

- The surrounding temperature and adhesive forces are linearly related to each other as confirmed from the literature.
- The coefficient of friction value for samples treated between 75 to 150 remain fairly in range of their previous values.
- Samples treated at 200°C and above show a significant change in the coefficient of friction value.
- Dupont Non-Stick Dry Film Lubricant Coating shows the maximum change in coefficient of friction value at 200°C.
- EnduroShield Stainless Steel Coating and Rust-Oleum NeverWet Multi-Surface Treatment maximum change in co efficient of friction is observed at 250°C.

6 FUTURE WORK

Building upon our earlier work, we have provided a baseline on service temperature of these coatings. This essential step would help us analyse more coatings that we have identified during this research work.

ACKNOWLEDGEMENTS

A special thank you to my wife and my supervisors for credible insight in this work. I'd also like to thank the administration of DHA Suffa University and National University of Sciences and Technology (NUST) for their support during this work.

Table 6. Mean values of coefficient of friction from investigating coated samples of Inconel 718 in sand-storm conditions [13]

Type of Coating	Coefficient of Friction	
	Before Sanding	After Sanding
No Coating	0.156	0.227
Enduroshield Stainless Steel Coating	0.161	0.209
DupontTeflon Non-Stick Dry Film Lubricant Coating	0.145	0.250
Rust-OleumNeverWet Multi-Surface Liquid Repelling Treatment	0.151	0.222

REFERENCES

[1] G. Binning, C.F. Quate and Ch. Gerber, Atomic Force Microscope, Physical Review Letters, Vol. 56 No. 9, 930-933, 1986.

[2] E. Meyer, H.Heinzelmann, P. Grütter, Th. Jung and H. R. HidberAtomic Force Microscopy for the Study of Tribology and Adhesion, Thin Solid Films, 181, pp. 527-544, 1989.

[3] E. S. Yoon, R. A. Singh, H. J. Oh, and H. Kong, The effect of contact area on nano/micro-scale friction, Wear 259, pp. 1424-1431, 2005.

[4] D. K. Hong, S. A. Han, J.H. Park, S. H. Tan, N. Lee and Y. Seo, Frictional force detection from lateral force microscopic image using Si grating, Colloids and Surfaces A: Physiochem. Eng. Aspects, pp. 313-314, 2008.

[5] M. A. S. Quintatanilla and D. T. Goddard, Lateral Force Microscopy with micrometer-sized particles: Effects of wear on adhesion and friction, Wear 268, pp. 277-286, 2008.

[6] S. Achanta and J.-P Celis, on the scale dependence of coefficient of friction in unlubricated sliding contacts, Wear 269, pp. 435-442, 2010.

[7] O. Öztürk, Microstructural and mechanical characterization of nitrogen ionimplanted layer on 316L stainless steel, Nuclear Instruments and Methods in Physics Research B 267, pp. 1526-1530, 2009.

[8] S. Achanta and J.-P. Celis, Nanotribology on individual phases of duplex steel:combining roughness, material effects, and friction, Int. J. Surface Science and Engineering, Vol. 5, pp. 331-347, 2011.

[9] S. Dhandapani, E. Thangavel, M. Arumugam, K. S. Shin, and V. Veeraraghavan, Effect of Ag content on the microstructure, tribological and corrosionproperties of amorphous carbon coatings on 316L SS, Surface & Coatings Technology 240, pp. 128-136, 2014.

[10] Saravanan, A. E. Perumal, S. C. Vettivel, N. Selvakumar and A. Baradeswaran, Optimizing wear behavior of TiN coated SS 316L against Tialloyusing Response Surface Methodology, Materials and Design 67, pp. 469-482, 2015.

[11] O. Marti, D. Brake and P.K. Hansma, Atomic Force Microscopy of liquid covered surfaces: Atomic resolution images, Applied Physics Letters, Vol. 51 Issue 7, 484, 1987.

[12] I. Milosev, J.M. Abels, H.H. Strehblow, B. Navinsek and M. Metikos-Hukovic, High temperature oxidation of tin CrN coatings deposited on steel, Journal of Vacuum Science and Technology A, Vol 14 No. 4, 2527, 1996.

[13] H. Shams, B. A. Siddiqui and S. Saleem, Evaluation of Commercial Oleophobic Coatings for Aerospace Applications in Harsh Environments (*ICASE 2015*), Pakistan, 2015

[14] J. Yang, Z. Zhang, X. Xu, X. Zhu, X. Men and X. Zhou, Superhydrophilic – Superoleophobic Coatings, Journal of Materials Chemistry, Issue 7, pp. 2834-2837, 2012.

[15] Stainless Steel,Lucifen S.p.A. I-25040 Esine (Brescia).

[16] A. Gaard, P. Krakhmalev, J. Bergstrom, J. HirvonenGrytzelius and H.M. Zhang, Experimental study of the relationship between temperature and adhesive forces for low-alloyed steel, stainless steel, and titanium using atomic force microscopy in ultrahigh vacuum, Journal of Applied Physics, Vol. 103 No. 12, 124301, 2008.

[17] Esmaiel Nouri, Mohammad Shahmiri, Hamid Reza Rezaie and FatemaTalayian, A comparative study of heat treatment temperature influence on the thickness of zirconia sol–gel thin films by three different techniques: SWE, SEM and AFM, Surface and Coatings Technology, Volume 206, Issue 19-20, pp. 3809-3815, 2012.

CHARACTERIZATION OF PAKISTANI FLUORSPAR FOR METALLURGICAL SLAG MAKING APPLICATION

Zeeshan A. Hameed[a], Junaid Saleem[b*], Hira Lal[b], Ahsan Abdul Ghani[b], Syed Sajid Hussain[a]
a: Department of Quality Assurance, Peoples Steel Mills Ltd., Karachi, Pakistan
b: Department of Chemical Engineering, University of Karachi, Karachi, Pakistan

[*]*Corresponding Author*: Dr. Junaid Saleem;
Email: Junaid@uok.edu.pk ; Junaidupm@gmail.com

ABSTRACT

Fluorite is one of the industrial minerals with commercial name as Fluorspar. It is the mineral form of CaF_2 and is widely used as a metallurgical flux (an important slag fluidizer in steelmaking). However, it needs to undergo pre-treatment process to get it concentrated using froth flotation technique before being added into the furnace. In this study, it is revealed that the indigenous Fluorspar is rich in CaF_2 (85 wt. %) and pre-treatment step may be avoided. Furthermore, unlike global composition of Fluorspar, the indigenous one does not contain apatite, a group of phosphate mineral with high concentration of OH^-, Cl^- and F^-, which makes it even more useful in steelmaking. Its composition was compared with standard specifications and a detailed characterization was carried out using chemical and mineralogical analysis.

Keywords: Fluorspar, metallurgical flux, slag, Fluorite

1. INTRODUCTION

Fluorite or Fluorspar is an inorganic mineral made up of calcium fluoride (CaF_2), the key fluorine-bearing mineral. It occurs as cubic, isometric crystals and cleavable masses. When pure, it is colourless and translucent, with a shiny surface. One-third of the Fluorite's production is in metallurgical grade which contains approximately 80% CaF_2. However, most of the Fluorite mines contain apatite which makes the Fluorite inappropriate to be directly used in steel sector [1]. Fluorite obtained from these mines is subjected to the beneficiation process to get it concentrated and then utilized in steel industry, since not all natural Fluorspar ores retain the degree of purity and physical characteristics requisite for the purpose. After beneficiation the concentrates are generally produced in powder forms which are not suitable for metallurgical operations [2]. Fluorspar fluxes are used in steel manufacture operations mainly to insure the desired fluidity in the slag without changing the basicity or acidity of the slag. For attainment of the best results in commercial practice, a Fluorspar flux usually should not contain less than 85% calcium fluoride (CaF_2) and not more than 5% silica (SiO_2) and also, a physical form such that the major fragments do not exceed in size, one-inch cube; it is commonly desirable that the particles be in more uniform size [2].

Pakistan, has Fluorite mines in two of its provinces namely Baluchistan and Khyber Pakhtunkhwa (KPK). In Baluchistan, Kalat district; Maran and pad Maran have reservoirs of low to medium grade Fluorite [3], while in KPK, Kohat basin, Sulaiman basin, and Khyber Hazara zone have Fluorite deposits. Recently, huge deposits of Fluorspar were discovered in KPK province [4].

Although considerable research has so far been conducted on Pakistani Fluorite [5–11], the focus was mainly placed to its geological studies. In this study, characterisation of indigenous Fluorspar has been performed by means of chemical, & mineralogical investigations. Furthermore, its industrial application has also been validated.

2. MATERIAL AND METHODS

Three different materials have been investigated in this study; Fluorspar, Slag formed by CaO which fluidized by indigenous Fluorspar during the ladle refining process. The Fluorspar, mined from Lora Lai collected from local supplier, Slag samples collected before & after addition of Fluorspar and lime (CaO) in ladle.

2.1 Chemical Composition

The chemical composition of Fluorspar & slag has been determined by Wet chemical method & XRF spectrometer (Axios max, PANalytical, Netherlands). Moisture has been determined at 105°C in lab oven. The C & S both were analyzed by combustion rapid analyzer (Leco CS444, USA) in Fluorspar and Slag samples. The composition of steel grade under process has been analyzed by optical emission spark spectrometer (OES, ARL, and Switzerland).

2.2 Mineralogical Study

The mineralogical characterisation of indigenous Fluorspar has been carried out by X-Rays Diffractometer (XPERT-PRO, PANalytical, Netherlands) with Cu tube; 2 Theta angle with start Position 10.00°, End position 79.995° and step size 0.01°

3. RESULT & DISCUSSION

3.1 Characterization

The chemical composition of Fluorite sample based on Wet chemical method is mentioned in Table 1. CaF_2 has been analyzed by wet chemical method, S by Leco-CS444 and remaining compounds by XRF spectrometer. The chemical composition of indigenous Fluorspar is found as per required specification of metallurgical grade (Grade 3) Fluorspar. The XRF and Leco- CS444 calibrated by certified reference material BCS 392 (Fluorspar). The accuracy of XRF and Leco CS-444 is tabulated in Table 2. This standard was developed by Ore & raw material sectional committee, SMSC 16 under the Bureau of Indian standards [10]. It is important to mention that phosphorous content is very low (less than 0.1%) in the indigenous Fluorspar which makes this type useful to be directly used in steel plant without any beneficiation process to remove phosphorous.

Table 1: Chemical composition of indigenous Fluorspar

	CaF_2	SiO_2	CaO	Al_2O_3	Fe_2O_3	R_2O_3	P_2O_5	S
Samples (%)	84.31	5.46	2.8	0.9	0.13	1.03	0.012	0.15

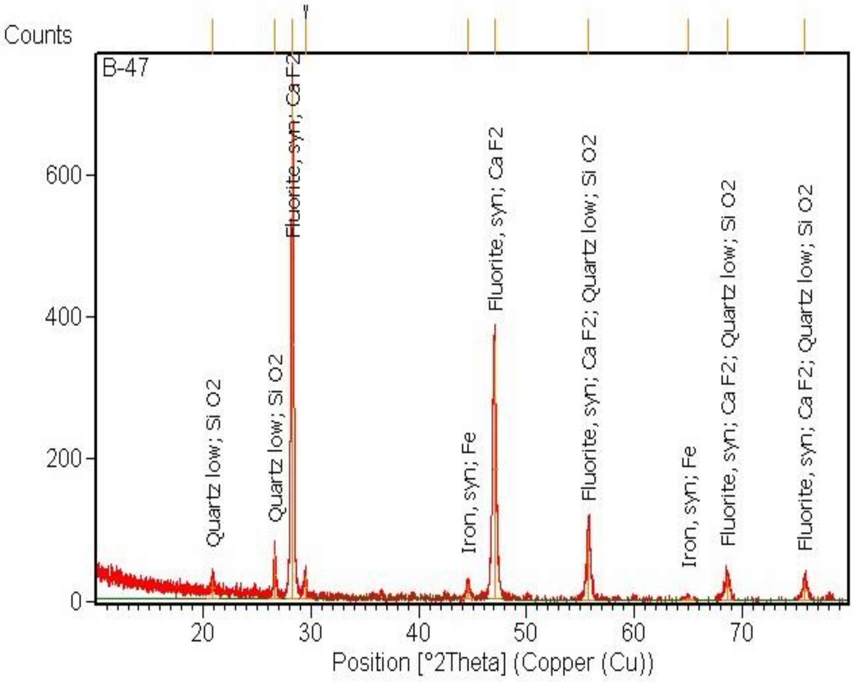

Figure 1: XRD plot of indigenous Fluorspar

Table 2: The accuracy and precision of the analytical equipments

Element	**Accuracy**	**Precision**	**Equipment**
Si	98.35%	0.001	XRF
Al	98.11%	0.001	XRF
Fe	99.1%	0.002	XRF
P	99.35%	0.0008	XRF
S	99.995%	0.00003	Leco
C	99.993%	0.000003	Leco

The XRD pattern of indigenous Fluorspar is mentioned in Figure 1 and the peak list is mentioned in Table 3. The peak list was obtained by XRD and searched and matched by power diffraction file (PDF) pattern by software and revealed the presence of CaF_2, SiO_2 and Fe content of indigenous Fluorspar. It is evident that all of Fluorine available in the sample is in the form of single phase of CaF_2.

Table 3: XRD characterization peak of indigenous Fluorspar

Pos. [°2Th.]	Height [cts]	FWHMLeft[°2Th.]	d-spacing	Rel. Int.[%]
20.84984	27.77963	0.47232	4.26057	3.83
26.65899	63.13157	0.27552	3.34389	8.7
28.23372	726.032	0.0984	3.16087	100
29.44394	32.96217	0.31488	3.03365	4.54
29.44394	32.96217	0.31488	3.03365	4.54
44.52279	23.70047	0.31488	2.03503	3.26
47.03336	370.7361	0.3936	1.9321	51.06
55.68906	100.4607	0.35424	1.65057	13.84
64.95895	5.109705	0.47232	1.43564	0.7
68.604	35.12172	0.3936	1.36799	4.84
75.8407	30.27708	0.47232	1.25444	4.17

No other fluorine compounds are present in the sample. Furthermore posphorus peak is not visible which confirms the absence of apatite (Phosphorous content, Cl^- and OH^-) in the indigenous mineral Fluorspar.

3.2 Characterization of slag formed for De-sulphurization

The sulphur (S) removal from molten steel during steel making is very important step because S limits are almost defined in every steel grade. S content in steels plays a vital role for machining capabilities of steels in the end products. Lime is the better desulphurizer and make following reaction with dissolved sulphur of molten metal and transfer it into the slag:

$$FeS + CaO = CaS + FeO$$

Once the lime saturation in the slag achieved, no more de-sulphurization is possible. At this point, Fluorspar is added into the slag to increase fluidity of the slag and hence lime solubility increases which results in more de-sulphurization. The experiment has been conducted to verify indigenous Fluorspar as a metallurgical flux without beneficiation. Low carbon steel grade has been chosen to demonstrate the slag forming with lime and fluidity effect of Fluorspar in the thick slag. Molten steel was transferred from Electric Arc Furnace to the Ladle furnace along with some slag. This molten steel & slag was collected, marked (Sample 1) and analyzed by spark spectrometer (ARL, Switzerland) and CS rapid analyzer (Leco, USA) respectively. After 15 min, lime was added to form slag and continuously purging of Nitrogen gas (N_2) for homogenization. Another sample of molten metal and slag, each was drawn and marked as Sample 2. When the slag became thick and the melter seemed that no more sulphur is removing then some indigenous Fluorspar has been added into the ladle and after 15 minutes of purging another sample of metal and slag was drawn separately and marked as sample 3. The 'S' content of metal and slag as well as degree of desulphurization (η_s) is mentioned in Table 4.

Table 4: 'S' content in steel and slag & degree of desulphurization

		S% in Slag	S% in Steel	η_s
LAS	Phase 1		0.026	
	Phase 2	0.29	0.02	23.08%
	Phase 3	0.45	0.0087	66.54%
MCS	Phase 1		0.0319	
	Phase 2	0.1192	0.0291	8.78%
	Phase 3	0.1868	0.023	27.90%
HCS	Phase 1		0.0387	
	Phase 2	0.1334	0.0293	24.29%
	Phase 3	0.173	0.0254	34.37%
LCS	Phase 1		0.0146	
	Phase 2	0.177	0.0138	5.48%
	Phase 3	0.224	0.0052	64.38%

Where: $\eta_{S\ (From\ Metal)} = \{[S]_i-[S]_t\}/[S]_t$ and
$[S]_I$ = Initial sulphur content in steel
$[S]_t$ = After addition sulphur content in steel
η_S= Degree of Desulphurization [12]
LAS= low alloy steel; MCS= medium carbon steel; HCS= high carbon steel; LCS= low carbon steel.

3.3 Investigation of slag parameters

The slag parameters in terms of basicity and Mannesmann's index was calculated by chemical composition of slags and listed up in Table 5. The slag basicity B1 shows basic nature of slags and after addition of CaF_2 the basicity increased and also doubled, it means more CaO/CaS is transferred into slag. The slag basicity B5 is decreasing and near minimum basicity ratio of 1.5 [13]. Furthermore the MM index is varying with steel grade types but it is obvious that, after adding Fluorspar the MM index is improving as shown in Figure 2.

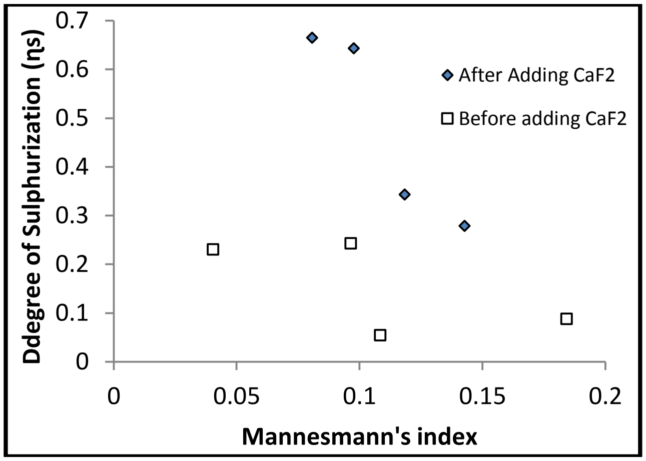

Figure 2: The relationship of η_s and MM index before and after addition of CaF_2

Table 5: Slag factors where B1 (basicity) = (CaO/SiO_2), B5 (basicity) = (CaO + MgO) /(SiO_2 + Al_2O_3)

		Slag Parameters			
		B1	**B5**	**η_s**	**MM**
LAS	**Before (CaO)**	0.410	1.610	23.08%	0.040
	After (CaF2)	0.862	1.334	66.54%	0.081
MCS	**Before (CaO)**	1.445	1.700	8.78%	0.184
	After (CaF2)	1.520	1.725	27.90%	0.143
HCS	**Before (CaO)**	2.662	1.204	24.29%	0.096
	After (CaF2)	2.134	1.441	34.37%	0.118
LCS	**Before (CaO)**	3.531	1.146	5.48%	0.109
	After (CaF2)	2.966	1.251	64.38%	0.098

4. CONCLUSIONS

The chemical composition of indigenous Fluorspar found as per metallurgical grade (Type 3) Fluorspar (70-85 % CaF_2). It may be directly used as metallurgical flux in steel industry which removes impurities such as sulfur and phosphorus from molten metal which results in increase the fluidity of slag without any beneficiation process which is essentially required by most of the world Fluorite reservoirs.

Mineralogical studies are evident that organic species are not present in indigenous Fluorspar. Also, apatite content is found to be very low which otherwise may cause alteration in the composition of molten metal in ladle furnace refining operation.

The slag basicity analysis reveals that the basicity B1 of slag is improved from 0.41 to 0.86 which indicates the increase in saturation of lime (CaO) in the slag.

5. ACKNOWLEDGEMENT

The authors would like to acknowledge the financial support of Higher Education Commission Pakistan with grant number 21-470. Authors are also grateful to Peoples Steel Mills Ltd., HEJ Research Institute of Chemistry, University of Karachi, and NED University of Engineering & Technology to provide necessary support.

5. REFERENCES

[1] R. . Hagni, “Mineralalogy of benefication problems involving Fluorspar concentrates from carbonatite-related Fluorspar deposits,” *Mineral. Petrol.*, vol. 67, pp. 33–44, 1999.

[2] John Norman Wynne, “Process for the treatment of Fluorspar,” *US Pat. 2,465,955*, 1949.

[3] M. S. Malkani, “Natural resources of Khyber Pakhtunkhwa, Gilgit-Baltistan and Azad Kashmir, Pakistan,” *J. Himal. Earth Sci.*, vol. 45, no. 2, 2012.

[4] Guilhaumou, N. et. al., “Genesis and evolution of hydrocarbons entrapped in the Fluorite deposit of Koh-i-Maran,(North Kirthar Range, Pakistan),” *Mar. Pet. Geol.*, pp. 1151–1164, 2000.

[5] R. Appiani, “Pink Fluorite from an exceptional new find at chumar bakhoor Pakistan, Milan Italy,” *Mineral. Rec.*, vol. 38, no. 2, pp. 95–100, 2007.

[6] J. A. and S. A. Abdul Khaliq, “Potential of Chakdara granite gneiss for Fluorite mineralization, an assessment study,” *J. Himal. Earth Sci.*, vol. 40, pp. 45–49, 2007.

[7] A. H. Rankin, “Unusual, oil-bearing inclusions in Fluorite from Baluchistan,” *Pakistan Mineral. Mag.*, vol. 54, pp. 335–342, 1990.

[8] M. S. Malkani, “Discovery of Fluorite deposits from Loralai District, Balochistan, Pakistan,” *J. Himal. Earth Sci.*, vol. 45, no. 2, 2012.

[9] Mohsin S.I, and Sarwar, G., “Geology of Dilband Fluorite deposits,” *Geol. Surv. Pakistan Geonews*, pp. 24–30, 1974.

[10] I. Bureaue, “Fluorspar for use in metallurgical industries,” *Bur. Indian Stand.*, 2003.

[11] M. M. Khunur, A. Risdianto, S. Mutrofin, and Y. P. Prananto, “Synthesis of Fluorite (CaF2) Crystal from Gypsum Waste of Phosphoric Acid Factory in Silica Gel,” *Bull. Chem. React. Eng. Catal.*, vol. 7, no. 1, pp. 71–77, 2012.

[12] L. Socha, J. Bažan, K. Gryc, and P. Styrnal, “Assessment of Influence of Briquetted Fluxing Agents on Refining Slags at Steel Treatment by Secondary Metallurgy”, Metal 2011 Conference, Brno, Czech Republic, EU, 2011.

[13] F. N. de Aguiar et. al., “Hot metal desulfurization by marble waste and Fluorspar,” *Rem Rev. Esc. Minas*, vol. 65, no. 2, pp. 233–240, 2012.

BOILER FEED WATER TREATMENT THROUGH ION-EXCHANGE TECHNOLOGY-DESIGN AND TESTING

Mariam Sohail[1], Syed A. Taqvi *[1 2]
[1]Chemical Engineering Department, NED University of Engineering & Technology, Karachi, Pakistan
[2]Chemical Engineering Department, Universiti Teknologi PETRONAS, 32610 Bandar Seri Iskandar, Perak Darul Ridzuan, Malaysia

ABSTRACT

Boilers are one of the most important utilities in any industry. Where, on one hand, efficient boiler operation bodes well for the general process, poor performance and frequent breakdowns can significantly reduce equipment efficiency translating to overall detrimental performance and profit reduction. This paper focuses on achieving superior feed water treatment to maximize boiler efficiency. The aim is to concentrate on ion-exchange enabled water treatment that can be adopted by small and large setups, especially those working with limited throughputs, for which membrane technologies are not much useful both in terms of capital costs and non-requirement or unavailability of high pressures as needed with such systems. A mini water treating facility comprising of filtration and ion exchange units was designed and run with water to determine extent of purification. Comparative analysis of three major properties: pH, hardness and TDS levels of raw and product water streams revealed significant lower values in the product demonstrating the practicality and effectiveness of the method.

1 INTRODUCTION

Since water is the raw material being converted into steam in the boiler, its good quality ensures reliable boiler operation [1]. Poor quality feed water can limit the process operation and cause unscheduled shutdowns. Therefore, to protect the equipment water chemistry must be controlled. Impurities in water are broadly of three types: suspended solids, dissolved solids and dissolved gases in increasing order of the difficulty of removing them from the feed water.

Water treatment encompasses all related processes to make raw water suitable for use in the boiler environment [2]. D. W. Choi [3] has explained the importance of water treatment and the methods to achieve the desired chemistry. The degree of treatment depends on the boiler's operating temperature and pressures with the accepted levels becoming more stringent at higher pressures. Calcium and Magnesium levels typically expressed as hardness levels require special attention due to their inverse solubility levels which result in their being precipitated within the extreme temperatures in the boiler, forming hard impermeable scale that eventually leads to overheating and in extreme cases thermal failure of tubes, especially in the firebox where the highest temperatures are encountered. Similarly, acidic salts like chlorides and sulphates are harmful due to their hydrolysis to their respective acids at high temperatures, rendering an acidic environment in the boiler contributing to corrosion.

The first treatment step starts with the removal of suspended solid impurities. This phase varies according to the quality of the water being used, as good initial quality precludes the need for many steps, however majority systems prefer to always first filter the feed before subsequent treatment.

The second step typically includes removal of dissolved solid impurities, which includes controlling hardness and TDS (Total Dissolved Solids) levels. Here a clear choice exists between selecting a traditional resin enabled purification or more recent membrane technologies, or even other varied methods like thermal desalination and multi flash evaporation [4]· Many authors have demonstrated the feasibility of selecting a membrane enabled technology for this purpose. Gede Wenten [5] has shed light on the efficiency on RO/EDI systems, towards this end. Experimenting with filtered water, different aspects were evaluated using an electrodeionization type model with mixed bed ion exchange filler. The obtained results were satisfactory except the pH value which was affected by dissolved CO_2. It was also found to be economically feasible. Another variation on membrane technologies include membrane contactors, suggested by Jiahui Shao [6]. Membrane contactors basically allow intimate contact in between liquid/liquid or liquid/gas phases without intermixing, for the separation of dissolved gases. Shao investigated the effect of flow rate, vacuum and temperature on the Oxygen removal efficiency.

The final treatment stage is the removal of dissolved gases like Oxygen, Carbon dioxide which due to their acidic nature have to be removed from the feed. In some setups the dissolved gas separation phase takes place outside the boiler through degassifier systems whereas others prefer to do it just before the feed enters the boiler through deaerators.

Realizing the importance of an effective boiler feed water treatment facility different equipment targeting specific impurities were designed and arranged in a working assembly. The design procedure was adopted from the ion exchange design manual published by Brian Windsor [7]. The effectiveness of the system was verified by testing the raw and effluent water streams. Neutral pH (7.5)and minimum hardness (3 ppm) can be taken as sufficient proof for the success of the overall experiment.

2 MATERIALS AND METHODS

The purpose was to a develop a working model that would treat feed water removing suspended and dissolved impurities rendering it fit for use in boilers producing low to moderate pressure steam. For this end, water was first treated via a cartridge filter, and then purified by ion-exchange processes. Here preference was given to ion-exchange process as the operation scale was not large as is typically the case for membrane systems. Capital cost was also much less than for RO systems. The ion exchange vessels were designed utilizing the vendor supplied resin design specifications.

The model specifications of the cartridge medium used for filtration are shown

Table 1. Filter medium specifications

Type	Depth filters
Filter element	Wound (polypropylene)
Filter housing	Single
Cartridge filter media	Disposable
Operating temperature	Max 125˚C
Impurities Removal	Upto 50 microns

The next step was the softening of water. This a very crucial step as hardness levels cannot be tolerated even for low pressure operations. Thus, the softener is counted as a very important equipment. The softener design first involved the resin selection as it is the basis of the whole process.

Table 2. Softener resin specifications [8]

Lewatit Monoplus S 108 resin	
Ionic form	Na+
Velocity (Operation) (max)	60 m/h
Velocity (Backwash)	15 m/h
Bed expansion (volume %)	4
Free board (volume %)	60-80
Total exchange capacity	2.2 min eq/l

The design has been based on 15m/hr velocity through the bed and 40 % regeneration efficiency [9]. The calculations were carried out at flow rates from 0.5l/min to 2.5 l/min. The design calculations have been summarized in the following graphs.

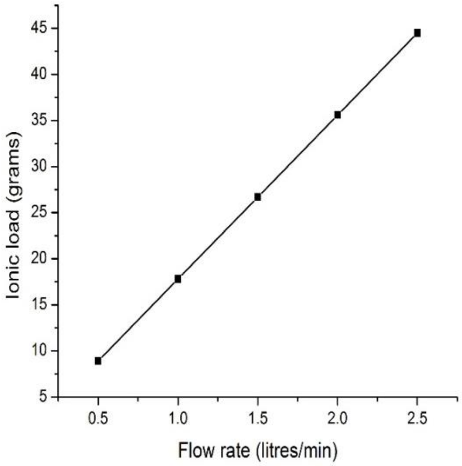

Figure 1. Softener design calculations

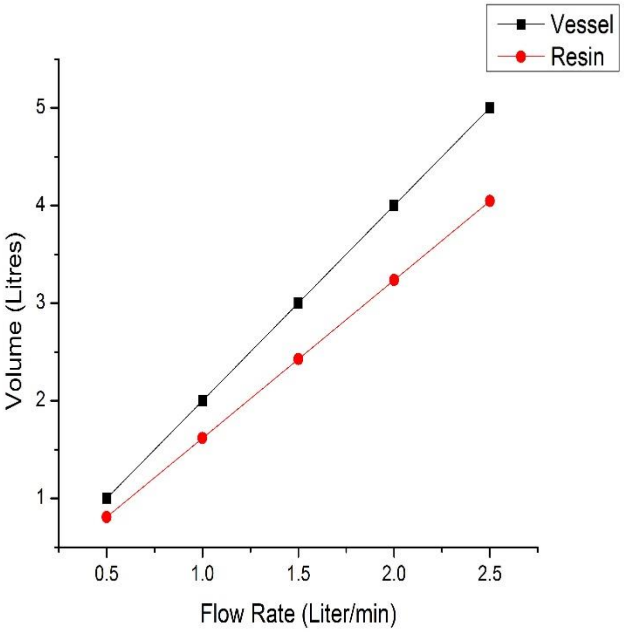

Figure 2. Softener design calculations

A final resin volume of around 2.2l was selected. The dimensions of the final vessel constructed are:

Table 3. Softner vessel dimensions

Material	Acrylic
Free Volume	2.23 litres
Diameter	0.11 m
Height	0.51 m
Volume (total)	4.83 litres

The final equipment is the pair of demineralizer units consisting of cation and anion exchange units, these units remove the cations and anions respectively in the feed, thus reducing overall TDS, of the feed. These two units were designed on the basis of again 15m/h water velocity through bed and 40% regeneration efficiency [9].The resin specifications are as follows:

Table 4 Cation exchange resin specifications [10]

Lewatit Monoplus S 100 resin	
Ionic form	H^+
Velocity (Operation) (max)	60 m/h
Bed expansion (volume %)	4.5
Free board (volume %)	60-80
Total exchange capacity	1.8 eq/l

Table 5. Anion exchange resin specifications [11]

Lewatit MonoPlus M 500 OH resin	
Ionic form	OH^-
Velocity (Operation) (max)	60 m/h
Bed expansion (volume %)	11
Free board (volume %)	80-100
Total exchange capacity	1.1 eq/l

Since the two units treat equal amounts of water their final dimensions were also identical. The design calculations are summarized in the following graphs:

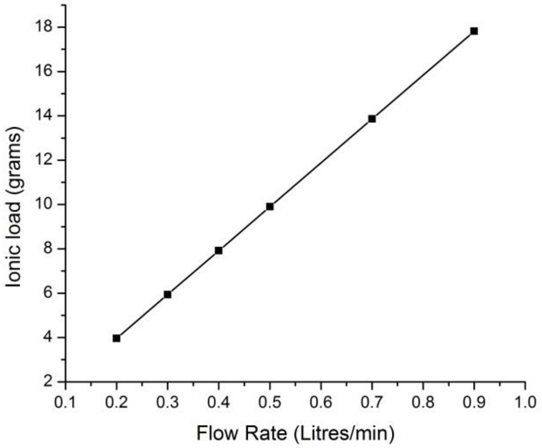

Figure 3. Cation exchange unit design calculations

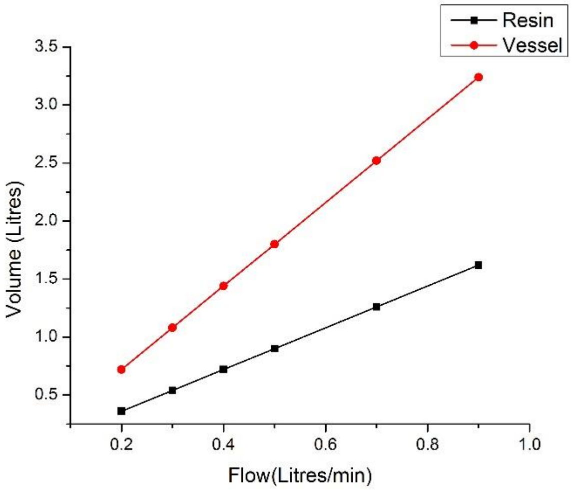

Figure 4. Cation exchange unit design calculations

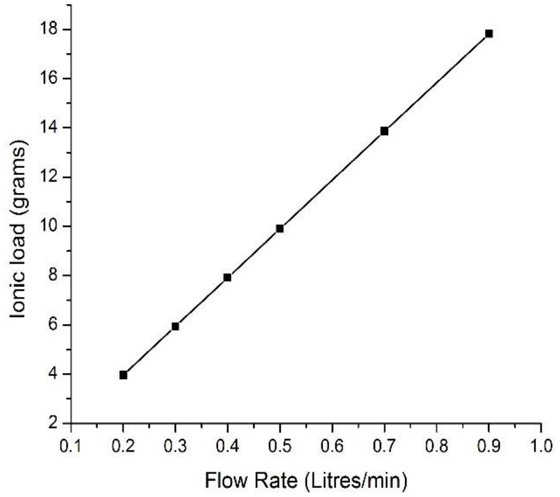

Figure 5. Anion exchange unit design calculations

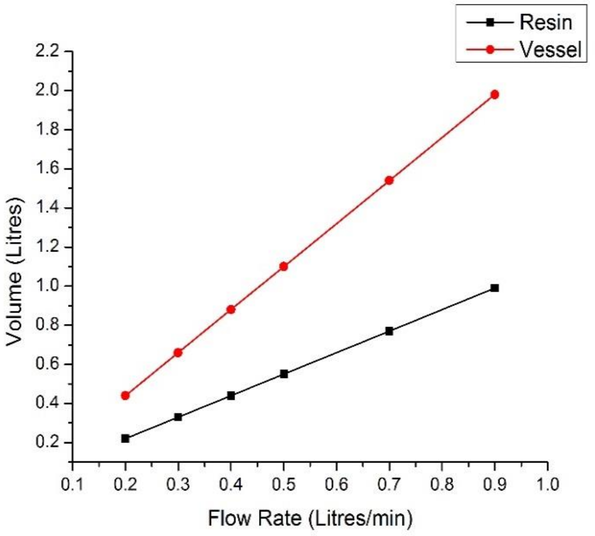

Figure 6. Anion exchange unit design calculations

Table 6. Final dimensions of demineralizer units

Glass	Glass
Free Volume	0.92 litres
Diameter	0.055 m
Height	0.508 m
Volume (total)	1.207 litres

3 EXPERIMENTAL SETUP

All the units were connected via PVC tubing and were fixed to a wooden board in decreasing order of height. A submersible pump supplied the necessary startup flow pressure. Flow rate was maintained through a rotameter. The water first passed through the cartridge filter, then the softener and finally the demineralizer units for final polishing. To control flow valves were also fitted before and after the units.

4 RESULTS AND DISCUSSION

The first experimentally obtained water samples were tested for pH, hardness, and TDS levels. The results obtained for the raw water and final product are as follows:

Table 7. First result analysis

	pH	TDS	Hardness
		(ppm)	
Raw water	7.5-8.5	380-500	200-250
Product	5	950	25

It was observed that a deterioration of properties occurred, TDS levels increased and pH also decreased. The system was analyzed for flows and it was concluded that resins might have exhausted and thus cannot give the required results.

The resins were regenerated using the following agents.

Table 8. Regeneration agents

	Reagent	**Concentration**
Softener	NaCl	10 wt% conc.
Demineralizer	NaOH	5 wt% conc.
	H2SO4	3 wt% conc.

After regeneration of the three resins, the system was run and the outlet water sample was collected and sent for testing. The inlet water was the same as tested before. The following result was obtained:

Table 9. Second result analysis

pH	7.3
TDS	75 ppm
Total hardness	10 ppm

After getting satisfactory results, the outlet of each unit was collected and tested, generating the following results:

Table 10. Vessel wise result

Unit	pH	TDS (ppm)	Hardness (ppm)
Filter	8.05	317	170
Softener	7.68	495	3
Cation exchange	3.2	560	3
Anion exchange	7.5	244	3

The filter water effluent was initially slightly basic with high hardness and TDS levels. The softener successfully brought down the hardness to 3 ppm, the TDS however increased. The cation exchange unit converted these dissolved solids into their respective cations, proved by the acidic pH of the effluent from the unit. These cations were then captured by the anion exchange unit reducing the TDS levels to 244 ppm from the 495 ppm level. Overall the quality of the zeolite resin was found to be much superior to the cation and anion exchange resins.

5 CONCLUSION

The basic purpose of checking the feasibility of traditional ion exchange process for boiler feed water treatment in limited space and budget and space considerations was realized. Through combining a submersible pump, cartridge filter, softener and demineralizer units in appropriate assembly suitable results, as verified by the water analysis, were obtained. The resultant hardness and pH levels of 73 ppm and 7.5 respectively represent the industrial accepted standards. It can be concluded that although for larger throughputs membrane technologies are gaining precedence, for existing industries operating at low scale, resin-enabled separation continues to offer an attractive option. Although there is room for improvement in the TDS levels, with better resin quality and counter-current regeneration, this can also be realized. Continuous product monitoring and control will also enhance performance.

ACKNOWLEDGEMENTS

We are indebted to all the faculty workers and staff of Chemical Engineering Department at NED University of Engineering and Technology who have guided and helped in the performance and execution of the experimental setup. The purpose could not have been realized without their support and cooperation.

REFERENCES

[1] O. N. C. Martin R.Godfrey, "For cleaner steam, focus on boiler feedwater," 1999.

[2] New Logic Research Inc, "Feed Water Treatment for Industrial Boilers & Power Plants".

[3] D. W. Choi, "Improve Plant water treatment".

[4] S. P. M. P. S. R. P. K. Tewari, "Evaluation of thermal desalination and reverse osmosis for the production of BFW from seawater for coastal thermal power stations in India".

[5] K. F. A. Z. Gede Wenton, Bench scale elecrtodeionization for high pressure boiler feed water.

[6] H. L. Y. H. Jiahui Shao, "Boiler feed water deoxygenation using hollow fiber membrane contactors".

[7] Brian Windsor (Purolite International Ltd.), "Ion Exchange Design-Hand Calculation".

[8] Lewatit, "PRODUCT INFORMATION, LEWATIT MonoPlus S108," 2010.

[9] *PROCESS STANDARD 1001*, 1996.

[10] Lanxess, "PRODUCT INFORMATION LEWATIT MonoPlus S 100 H," 2010.

[11] Lanxess, "PRODUCT INFORMATION LEWATIT MonoPlus M 500 OH," 2012.

TO DEVELOP A LABORATORY SCALE VACUUM FURNACE FOR THE PRODUCTION OF MAGNESIUM PARTICLES (PAK-TECH PROCESS)

Farhan Iqbal[1*]; Alina Aziz[1]; Arqum Saleem[1]; Lubna Kamran[1]
[1]Metallurgical Engineering Department, NED University of Engineering & Technology, Karachi, Pakistan

[*]Corresponding author. Tel.: +923312249428
E-mail address: farhan_927@hotmail.com

ABSTRACT

In this study, a vacuum furnace has been developed in order to produce magnesium particles. Magnesium has a number of peculiarities as compared to other lightweight metals and finds multiple applications due to its unique chemical and physical properties. Production of this metal can be carried out through various processes, but the most suitable process for its production is Pidgeon process because of higher availability of natural resources and low labor cost in Asian countries. The purpose of our venture is to intend and fabricate equipment for magnesium production that runs the Pidgeon process in an uncontaminated, fuel proficient, cost-effective and environmental affable setup. Such equipment has been fabricated completely, but due to various problems in its setup; the equipment did not function properly. Root cause analysis had been carried out revealing problems that contributed in the malfunctioning of the equipment. The problems that we have perceived comprises of welding defects, improper seals' usage, improper gating system, usage of casted parts and thin sheets in the vacuum chamber and usage of incompatible refractory material. All the problems were resolved by application of proper welding and polymeric seals (also called boiler's seal). The gating system was also redesigned accordingly and improper refractory material had been replaced with monolithic alumina refractory bricks.

Keywords: Magnesium Metal, Pidgeon Process, Vacuum Furnace, Vacuum Leakage.

1 INTRODUCTION

Magnesium production plays a significant role in industries, like that of mining & metallurgical as it comprises about 2.5% of the earth's surface. This metal due to its unique chemical and physical properties is applicable in Military & weapon making industries, Power generation components, aerospace industries, automotive parts manufacturing and in Integrated circuit technologies.

The existing Magnesium producing technologies are ineffective due to high level of energy consumption including the Pidgeon process, but it has dominated the production of magnesium in the world the last ten years with the proportion of almost 70% of the total magnesium produced [1] The Pidgeon process is the however simplest, oldest, least energy efficient, and most labor intensive production process. However, it requires the lowest capital investment. [2]

This fact is considered as a main reason for the development of this new and effective design that is vital for the above mentioned industries as it carries out the pidgeon process i.e a silicothermic process proposed by Dr. Lloyd Montgomery Pidgeon of the Canadian National Research Council (NRC) which mainly uses dolomite ore with other raw materials such as ferrosilicon (one of the most cheapest form of silicon) as a reducing agent and coke as an energy source, particularly in vacuum environment for an efficient production of magnesium.

This special purpose customized vacuum equipment has been fabricated as small size production unit to demonstrate the application of the Pidgeon process that will be carried out in it. It is also indicated that this vacuum technology of producing magnesium is financially sound both for the purpose of direct and indirect investments.

The customized PAK-Tech Vacuum furnace is designed to have two main chambers:

- The vacuum chamber
- The burning chamber

The vacuum chamber is a stainless steel (AISI 304) structure hung with a pulley to lift to any position away from the burning chamber, and is composed of a melting zone that melts the raw material present in the crucible and produces magnesium vapors under created vacuum, and the condensation zone in which the magnesium vapors are condensed and maintains the vacuum environment necessary to prevent oxidization of magnesium vapors. There is also a charging system attached within the melting zone.

Furthermore, the burning chamber is a galvanized steel structure mainly used to burn the coke, and is positioned at the bottom of the melting zone to provide it with heat. It can be used for simple & complex as well as Single & multiple applications.

The factors considered while designing this Vacuum system were:

- Size of the chamber
- Chamber material
- Ultimate vacuum required
- Designing techniques
- Dimensions of parts
- Conductance of the system
- Gauges choice

There were many additional accessories attached such as gauges & monitoring equipments along with a vacuum pump etc.

These parts after being assembled were then tested by experiments performed on the assembled setup to check if the fabricated equipment works as desired.

2 MATERIAL & METHOD OF REDUCTION

The PAK-Tech process, as mentioned above involves the Silicothermic method of magnesium extraction. It comprises the reduction of dolomite (magnesium ore) with ferrosilicon; under reduced pressure 13 Pa or 0.13mbar in order to reduce the softening temperatures of the raw material as dolomite has high melting temperatures of around 2560°C which is difficult to achieve and requires an enormous amount of fuel.

The process involves; mixing of dolomite with ferrosilicon and Calcium fluoride in 2:1:1 stoichiometric ratio and gives an endothermic reaction that is demonstrated by following equation:

$$2(CaO.MgO) + FeSi \rightarrow 2Mg + 2CaO.SiO2 + Fe \qquad \text{eqn. (1)}$$

This process of reduction of magnesium takes 8 to 12 hours to be completed. The mixture is then formed into briquettes (blocks of compressed molecules) and then heated uniformly to a temperature ranging from 1000ºC to 1200ºC under low pressures to vaporize the magnesium completely. These magnesium vapors evaporate towards the condensation zone and are condensed on the cooling baffles there, and can be removed after a batch of magnesium is achieved by simply detaching the condensation zone from the vacuum chamber.

While the slag produced during the reduction process is then removed through slag removal system. In this way magnesium deposit of high purity is collected as a dense “crown”.[6]

The process predicts that purities above 99.8wt% for pidgeon process. Without multi-stage condensation, at equilibrium it should be possible to condense solid impurities before the majority of the magnesium vapour is condensed below 750°C. These results are broadly consistent with existing industrial data. [6]

3 EXPERIMENTAL PROCEDURE

The designing of the furnace was integrated according to the process of magnesium extraction as depicted by the three dimensional model of PAK-Tech vacuum furnace shown in the figure. It was contrived on the machine designing graphical software, Solid Edge® of Siemens International.

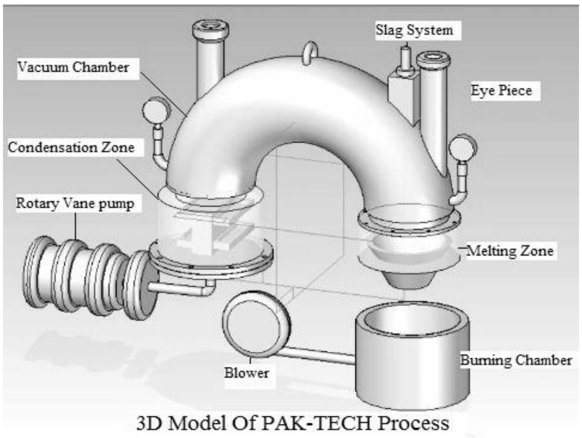

Figure 1 shows the 3D model of PAK-Tech Vacuum Furnace

The burning chamber of the Vacuum furnace is fabricated with a galvanized steel drum having a wall thickness of 1.5”inches which is equipped with water cooling jackets. It is constructed using the head of the drum plus some small carbon steel strips are welded inside the drum to reinforce the glass wool and high alumina refractory with the wall of the drum. It is then covered with 3 inches thick refractory lining. At the bottom of the burning chamber a hole is made 4 inches above the ground level, through which hot air and exhaust gases enter the burning chamber to burn the coke.

Then comes another essential part of burning chamber, which is a blower. We can achieve a much higher pressure by using positive displacement blower consisting of blades. This blade pushes the air into the burner and mixes it with liquefied petroleum gas (LPG) which is then consumed in burning the coke by its insertion into the vacuum chamber.

The next portion of the vacuum furnace is the melting zone, which is 7 inches tall, 304 stainless steel cylindrical chambers, with shell thickness of 1.5 inches. At a height of 2 inches from the ground level there is a charging door from which the raw materials are charged into the 4.5 inches diameter crucible. A k-type thermocouple with display unit is also adhered at the top of the charging door.

Also, there is an elbow duct is located at the top of the melting chamber to transmit the magnesium vapours from melting to the condensation zone. Furthermore, Viewports of diameter of 2.8 inches are present in the elbow duct to keep a check when the melting and condensation is being carried out. Borosilicate glasses with same diameter as that of the viewports, but with a thickness of 0.4 inches are fitted in these ports. Additionally, a Bourdon gauge is fitted on the side wall of the melting zone to quantify the vacuum created.

The melting zone was fabricated using a 304 stainless steel sheet which was initially bent and the welded using electric arc welding to produce a hollow cylindrical melting chamber. At the bottom mid of the melting chamber a hole was made to clamp the crucible tightly and this crucible was lined with an alumina refractory.

The next is the Condensation chamber (water cooled stainless steel cylindrical chamber) having a height and diameter of 12 inches. K-type thermocouples are attached at the upper end while a metallic pipe is attached to the bottom end for the gases to escape. It is fabricated using the same approach as in the manufacturing of melting chamber. There is another cylindrical shell with semicircular baffles attached to its walls, and a circular water cooling jacket fitted at the outer part of the condensation chamber for cooling, having an inlet & an outlet port through which the water flows.

The last portion is the charging and slag removal system which is made from stainless steel rod 5 feet long having 0.5 inches diameter. This rod is channeled with 1.8 inch flange systems, installed on the top portion of vacuum chamber along with the viewport assembly for slag removal.

Besides, a charging hole was made in the melting chamber at a height of 3 inches from the ground level, whereas for slag removal a hole at the top of the melting chamber was made in the elbow portion at the right next to the viewport. These holes were fitted with the flanges into which the rods were directed into the chamber; these rods were sealed and welded with spoons to make a complete assembly of slag removal and charging system.

After the completion of fabrication process, the setup was then ready for production

The process of extraction initially started by preparing pallets through charging the mixture of raw material into the furnace in a ratio of 2:1:1 (ratio of the raw materials – dolomite, ferrosilicon and calcium fluoride). Afterwards, these were mixed and compressed (compacted) using a hydraulic press. These pallets were then charged into the crucible of melting zone. Subsequently, the burning chamber was also filled with a mixture of coal and coke and was initially burnt by the combination of air and natural gas. Eventually, when the coal/coke mixture became red hot, the supply of natural gas was then stopped to permit the air and to keep the mixture red hot.

The next step was to evacuate the vacuum chamber by a vacuum pump. It was then lowered to insert the crucible of the melting chamber into the burning chamber. At that time the temperature was about 1100°C to 1300°C, magnesium did vaporize but did not directly condense into the condensation chamber, and got stuck to the passage wall of the elbow. Hence, the furnace for magnesium production was unable to produce this metal as desired, because of numerous flaws and drawbacks in the vacuum chamber. Later, Root cause analysis was conducted to depict the major causes that led this furnace to become non-fuctional. This was the only reason for disassembling the whole setup which became the foremost work done soon after the first test run was performed on the vacuum furnace.

Following Gantt chart provides a complete plan of the activities performed when flaws were depicted.

After disassembly of the vacuum furnace, a root cause analysis technique, Soap bubble test as well as smoke test was carried out to locate leaks if present in the vacuum chamber. In Accordance with literature survey, The most suspected areas to be analyzed for leaks were flanges, welded joints, bolted joints, valves & gauge connections, and under thermocouple bushes. These critical points were carefully assessed.

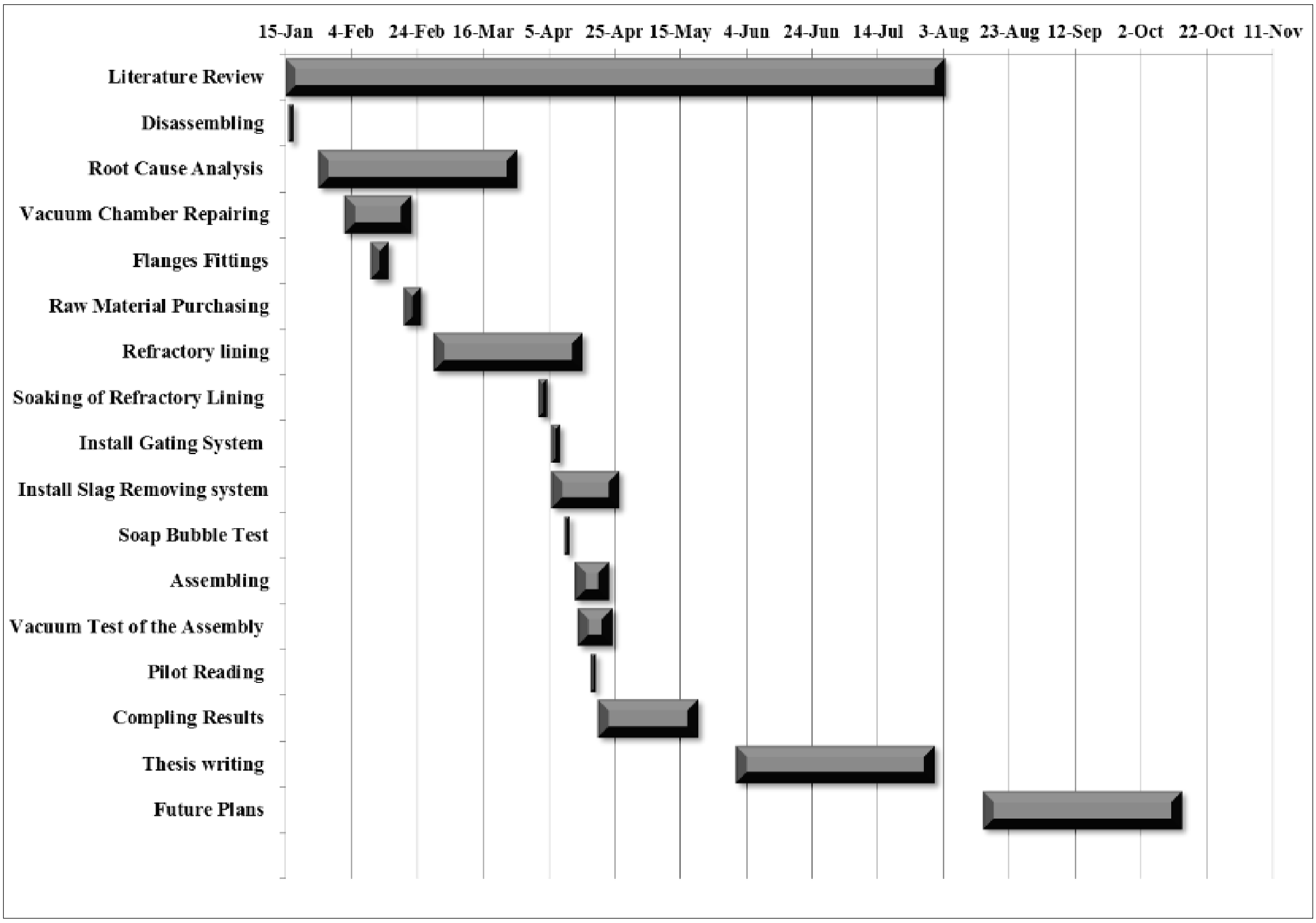

Figure 2 shows Gantt chart

This test was conducted by cleaning the areas of interest at first to remove dirt, slag, rust, or any other foreign debris. Then creating a pressure differential in the furnace. The soap or detergent solution was then poured over the area to be tested, gentle pouring will allow complete coverage; this must be done with care without creating bubbles at start. The solution was then allowed to dwell into the test area for 5min -10min (Usual Dwell time). After the time had passed, the area was inspect for bubbles, if formed, so was considered to have leaks or opening while the areas free from such behavior was considered to pass the leak test.

All such inspections were done in an adequate environment to get the best results of the test.

Figure 2 shows smoke evolving from areas of vacuum leaks

The major issue found and the causes and effects of this vacuum leakage is foreseen in the following given ISHIKAWA diagram also called cause and effect diagram.

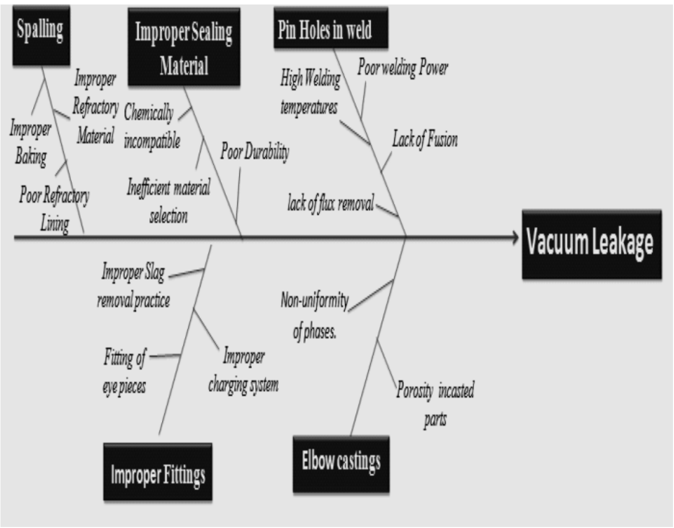

Figure 3 ISHIKAWA Diagram (cause & effect diagram)

4 RESULTS & DISCUSSIONS

Since, the components were welded for joining, hence welding defects such as pinholes, leaks, cracks were observed due to incorrect welding parameters, wrong combination of filler metal & parent metal and lack of fusion. Use of high porosity refractory material lowered the material's crack resistance and hence refractory material cracked under operating conditions. Areas where sealants and adhesives with poor impact and thermal resistance were used caused it to become rigid due to curing and allowed atmospheric air to enter the furnace.

Due to lack of temperature distribution the magnesium vapours sticked to the walls of the furnace and condensation took place on furnace walls instead of condensation baffles. Eye pieces also became the sources of vacuum leakage as clearance between the glass and the rings were packed with silicon rubber to prevent leakage instead, it lost strength at working temperatures and caused it to leak.

The wall thickness of the vacuum chamber sheet was so little that the sheet deformed on reaching 1000°C. In slag removal system the major flaw found was that no seal was employed between the nozzle and Stainless steel rods causing massive leakage and also prevented smooth rotation of steel rods to remove slag efficiently. On the other hand charging system also caused the vacuum to leak due to being opened and closed again and again to charge in, the raw material.

These problems were recognized through numerous inspections and extensive literature assessment. After getting such negative results from the first test run performed, measures taken to overcome all of them, did succeed to a great extent in eliminating this vacuum leakage issue. The furnace passed the smoke test as well as soap bubble test and was now ready to undergo the final operation of magnesium extraction whose results are yet to be obtained.

5 CONCLUSION & FUTURE RECOMMENDATIONS

In the present article, a detailed review of silicothermic Mg production using Pidgeon process, with an emphasis on achieving high purity magnesium by its vapor condensation from initial ore (dolomite) under vacuum have been presented. The pidgeon process description, 3D modeling along with a detailed construction of a Vacuum furnace fabricated for the respective purpose has also been mentioned.

After performing a whole lot of fabrication operations and test run procedures as well as after the additional work to overcome the vacuum leakage issue that had become a hurdle in the production of magnesium, the final Run of the vacuum furnace is yet to be carried out to achieve the final amount of magnesium extracted. The results obtained from this PAK-Tech Vacuum furnace operation are predicted to provide the final amount of about 99.8% pure magnesium and the present research is still ongoing with the future work consideration of finding impurity distribution in Pidgeon process. One of the future considerations is to modify the design to make it even more environment efficient or could design a recuperative system for the conservation of heat and to work on controlling the morphology of magnesium with respect to change in operating parameters.

ACKNOWLEDGEMENT

Firstly, we are very thankful to Allah S.w.t, it is His grace that we are able to participate in such venture. Secondly, we want to appreciate Lecturer

Muhammad Sami Ud din from NED University of Engineering & Technology, Karachi, Pakistan, who provided invaluable assistance in the field during study of Magnesium metal, Vacuum furnace related detail, fabrication related issues and design modification techniques along with Dr Umair Alam, Chairman, Metallurgical Engineering department, NED University, helped by allowing to carry out all the fabrication operations such as welding, machining, milling & drilling etc in NED university workshops and allowed usage of Heat treatment laboratory whenever required. In the end, we are very thankful to our parents who have always supported us and motivate and financed us to perform well in every venture.

REFERENCES

[1]http://ro.uow.edu.au/cgi/viewcontent.cgi?article=2283&context=engpapers

[2]http://www.empr.gov.bc.ca/Mining/Geoscience/IndustrialMinerals/Documents/Magnesium.pdf

[3]Distribution of impurities in magnesium via silicothermic reduction, Winny Wulandari, M. Akbar Rhamdhani, Geoffrey A. Brooks, Brian J. Monaghan, European Metallurgical Conference 2009, Innsbruck, Austria

DESIGN AND FABRICATION OF LABORTARY SCALE CUPOLA FURNACE

[1]Syed Muhammad Taha, [1]Haris Haider Ali, [1]Maaz Khan, *Mr. Muhammad Samiuddin
[1]Metallurgical Engineering Department, NED University of Engineering & Technology,
Karachi, Pakistan

*Corresponding author. Tel.: 99261621 Ext.2528
E-mail address: Engr.sami@neduet.edu.pk (Mr. Muhammad Samiuddin)

ABSTRACT

At NED University of Engineering & Technology, if any student wanted to observe the cupola furnace wanted to perform some melting work, they would have to visit industrial sites to learn about its functionality. Now we have designed 0.254 meter (working diameter) cupola furnace right here on NED main campus. To maintain the inside temperature of the furnace, a blower of 1hp is used which supplies air flow of 0.092 cubic meter/s into the furnace through tuyeres with the addition of methane petrol supply. The refractory which we used for lining the furnace is of high alumina bricks, fireclay powder and alumina powder. The tuyeres designed has an angled entry into the cupola shaft and burns the maximum amount of coke.

Keywords: Tuyeres; Pig iron; Cast iron; Fireclay powder

1. INTRODUCTION

The cupola furnace is usually used for melting pig iron and to produce cast iron which utlizes energy provided by metallurgical coke. René-Antoine Ferchault de Réaumur built the first cupola furnace on record, in France, around 1720 [1]. In all cases where the strength of the metal is not of primary importance, the cupola ideal for the foundry work. In this process, the furnace is filled with coke to a certain height to create enough amount of heat and then alternative layers of raw materials such as pig iron, coke and limestone respectively. There are certain chemical and heat processes occur during operation of the furnace for example, the important chemical reaction takes place in the reduction zone which is given as under,

$$CO_2 + C\ (\text{coke}) \rightarrow 2CO + \text{Heat}$$

$$C + O_2 \rightarrow CO_2 + \text{Heat}$$

$$Si + O_2 \rightarrow SiO_2 + \text{Heat}$$

$$2Mn + O_2 \rightarrow 2MnO + \text{Heat}$$

The whole melting process is controlled by the composition and the amount of materials added in the furnace.

The main purpose to build a 0.254 m (diameter) cupola is to practice the theoretical knowledge (which is a parting of our study) and to study different operations regarding the furnace. To maintain the inside temperature of the furnace, a blower of 1 hp is used which supplies air flow of 0.092 cubic meter/s into the chamber through tuyeres in additional to methane gas supply. The purpose behind methane gas supply is to burn metallurgical coke with more efficiency. The construction of a cupola consists of a vertical steel shell which is lined with a refractory brick [2]. The refractory used for lining the furnace is made of high alumina bricks with fireclay powder lining to prevent fireclay powder from accumulating slag, the working diameter of the furnace is lined with alumina powder. The melting temperature of alumina brick is near 2473.15 k and furnace temperature reached to 1873.15 k maximum. The tuyeres were designed to be more user friendly and their entry was angled in order to facilitate checking of the tuyeres and blast penetration. In addition, the iron to coke ratios were calculated to minimize fuel consumption.

Most cupolas are of the drop bottom type with hinged doors under the hearth, which allows the bottom to drop away at the end of melting to aid cleaning. We have also used drop door system in our design to clean the furnace after process is completed.

2. EXPERIMENTAL WORK:

2.1 Construction of cupola furnace shell:

The cupola furnace was designed to run without cooling system and heat exchanger, the shell design was mainly dependent upon the selection of the refractory system. Based on data from books, temperature requirements for the shell were purposeful to be at least 700 k, providing a sufficiently insulating refractory system. The thermal conductivity, oxidation resistance, stability at high temperature and price of the shell material were all considered and optimized during the selection process. We have seen these properties in some common alloys, 304 and 316 stainless steel and 1025 and 1080 plain carbon steel in which stainless steel has the maximum service temperature and appropriate resistance to oxidation at 775 k, but it's very costly and has a lower thermal conductivity than that of steel. [3] Whilst on the other side when we see the carbon steel properties it has a maximum service temperature lower than stainless steel. Additionally it is much economical and has better thermal conductivity whilst maintaining satisfactory resistance to oxidation. All these properties are shown in table 1.

Table 1: Possible shell and material properties [3]

Material	**Thermal conductivity**	**Oxidation resistance at 775 K**	**Max. Service Temp. (K)**	**Price (Pk.R)**
304 stainless steel	97.08	Excellent	1199	600/kg
316 stainless steel	90.12	Excellent	1199	600/kg
AISI 1025	360	Acceptable	755	80/kg
AISI 1080	332.4	Acceptable	613	80/kg

The thickness of a sheet of which we have made cupola furnace was 11 gauge or 3mm sheet and the material we used was AISI 1025 (shown in fig.1 & fig.2).

Figure 1: Lower cylinder of Cupola Furnace

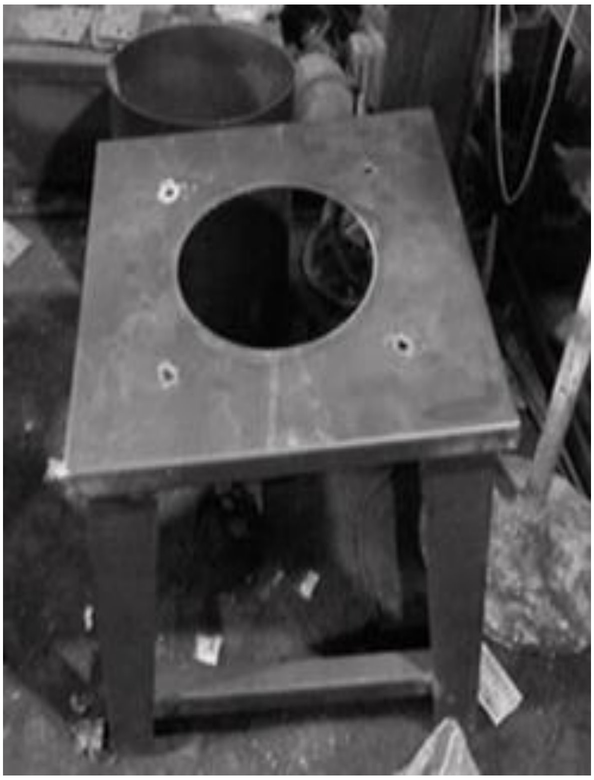

Figure 2: Table stand of Cupola Furnace.

2.2 Calculations:

Tuyere area:

The tuyere area is based on the inside diameter of the cupola at the tuyere level. According to standards, the tuyeres diameter for small cupula furnace is 1/4 or 1/6 of the cross sectional area of the furnace. However modern practice favors smaller tuyeres and high blast pressure pressures (fig. 3).

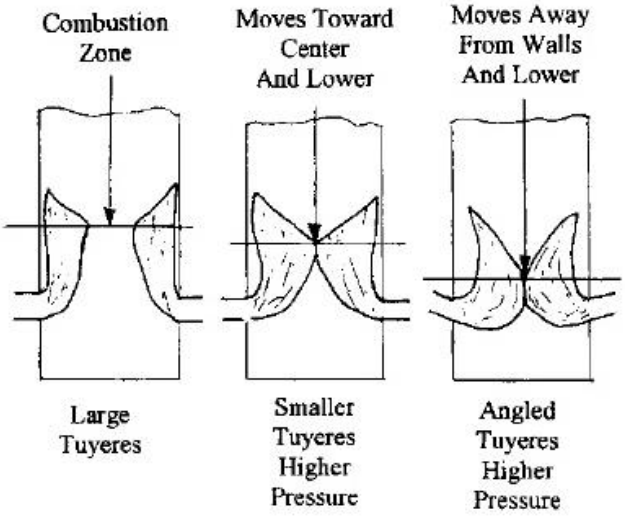

Figure 3: Different angles of tuyere [4]

Large tuyeres lose heat through the walls (fig.3).By using small tuyeres, when the blast increases the combustion zone will move closer to the center of the cupola, reducing the heat loss through the walls. Also, further lowering the combustion zone by angling the tuyeres downward will decrease heat loss.Therefore we used angled tuyeres (fig.4) in our design, through which air roatate inside the furnace shaft and burn maximum amount of coke.

Figure 4: Angle tuyeres design used in structure

Calculate the tuyere area for the 0.254 m cupola using the ratio 1/6 the sectional area at tuyere level,

$$A= \pi \left(\frac{D}{2}\right)^2 \tag{1}$$

A= area

π = 3.14

D =Diameter = 0.254 m

$$A = \pi \left(\frac{0.254}{2}\right)^2 = 1.993 \text{ m}^2$$

$$\text{Tuyere area} = \frac{1}{6} \times \text{Area} \tag{2}$$

$$\text{Tuyere area} = \frac{1 \times 1.993}{6} = 0.332 \text{ m}$$

0.332m is the area which we have calculate.Now find suitable diameter pipe for tuyeres,

$$\text{Area of pipe} = \pi \times \left(\frac{D}{2}\right)^2 \tag{3}$$

$$\text{Area for 0.063m pipe} = \pi \times \left(\frac{0.063}{2}\right)^2 = 0.124\text{m}$$

$$\text{Number of tuyeres} = \frac{\text{Tuyere area}}{\text{Area of pipe}} \tag{4}$$

$$\text{Number of tuyeres} = \frac{0.332}{0.124} = 2.6 \approx 2$$

Cupola height:

Cupola height (before legs) is determined in two steps. The stack height above tuyeres and the well depth + constant make up the two calculations. For small cupolas a constant of 0.127m will be used [4]. Figure.5 show complete information about 0.254m Cupola Furnace structure.

For a 0.254m (Working diameter) cupola this tap would be approximately 35 Kg. A tap of 15 Kg should certainly be attainable, therefore we will calculate for a 15 Kg tap.

The density of iron is approximately 7850 Kg/m^3

$$\text{Cubic inches of iron} = \frac{\text{15 Kg of iron}}{\text{Density of material}} \tag{5}$$

$$\text{Cubic inches of iron} = \frac{\text{15 Kg of iron}}{\text{7850 Kg/m3}} = 0.0019\text{m}^3$$

Well volume available for iron = 0.46 total well area,

(6)

$$\text{Total well volume} = \frac{0.0019 \text{ m}^3}{0.46} = 0.0041\text{m}^3$$

Height to slag hole (from bottom of well)

$$= \frac{\text{total well volume}}{\text{area of well}} \qquad (7)$$

Area of well = 1.99 m^2,

Putting these values in equation (7) we get,

Height to slag hole (From bottom of well) $= \frac{0.0041 m3}{1.99\ m2}$

Height to slag hole (From bottom of well) = 0.0020 m,

Height to tuyeres includes the (height of sand bottom) + (height of the slag hole} + (0.127 m (constant)). (8)

By putting all the values in equation (8) we get,

Height to tuyeres = 0.05m + 0.0020m + 0.127m

Height to tuyeres = 0.26m

Now calculate height above tuyeres, Height above tuyeres is a simple calculation. The minimum stack height is

4.5×Working diameter (9)

at tuyere level. Calculate the height above tuyeres using equation (9) by putting the value of working diameter,

4.5 X 0.254 m = 1.143 m

The total height of the cupola less legs = height to tuyeres + height above tuyeres + tuyere diameter,

(10)

$\sum$ = 0.267m + 1.143m + 0.050m = 1.465 m

Height of cupola without legs = 1.465 m.

Leg height may be accommodate to increase operator comfort.

Material size:

The size of the metal making up the charge is critical to maintaining efficient preheating and melting. If the pieces are too large, they will not melt in the melt zone but will work their way down to the tuyere level. The iron will not superheat and this could lead to a frozen tap hole. If small pieces are charged without some type of grouping, they often burn up or will clog up the voids in the stack. This could lead to bridging in the cupola. Small and thin pieces should be gathered and pressed into a briquette.

Coke must be screened to proper size, being 1/ 10 to 1/12 the inside diameter of the cupola. The space between larger pieces allows the gases to rise faster is the stack. This raises the combustion zone there by reducing the preheat of the charge. Smaller pieces could pack too tightly increasing resistance to the gas flow. If limestone is used as a desulfurizing flux, it should be in pebble form. Larger pieces will not decompose properly. However, if it is too fine, it will clog the furnace or be blown out of the stack. [4]

A good size for the 0.254 m cupola is 0.076 m and this we melted this size pig iron ingots in our cupola furnace

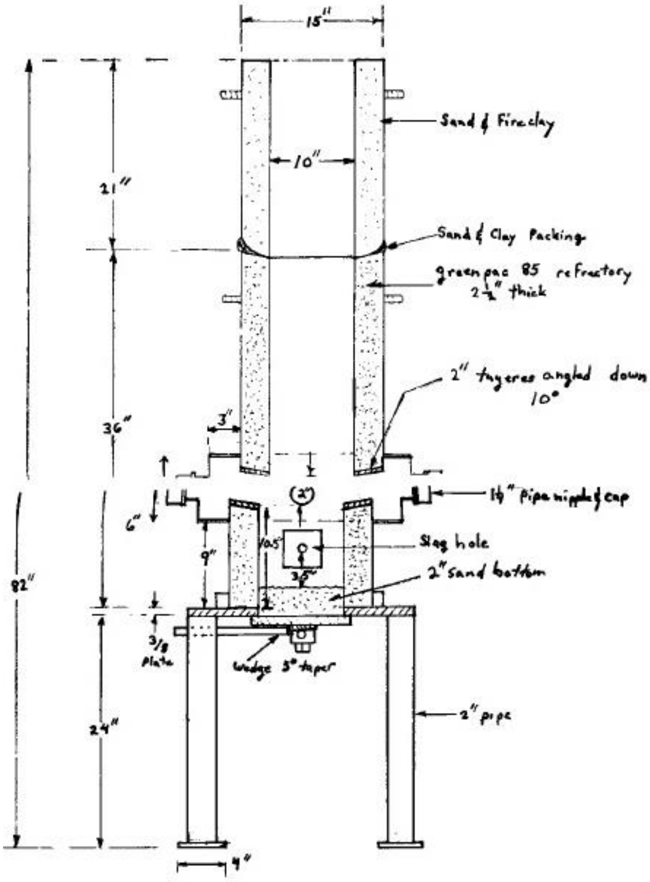

Figure 5: Drawing of 0.254 m cupola furnace

Calculation of charge weights

The weight of coke used per charge is estimated by:

0.0356 Kg/m^2 x Sectional Area m^2 (11)

The weight of iron charges is proportional to the weight of the coke charges.

Common ratios are from 6:1 to 10: 1.

Calculate the charge weights for the 0.254m (Working diameter) cupola using equation 11:

Weight of coke: 0.0356 $\frac{Kg}{m2}$ x 1.993 m^2 = 0.070 Kg

Weight of iron at a 6:1 ratio:

6 x 0.070 Kg = 0.425 Kg

Weight of lime stone: 5% x Weight of iron (12)

Weight of lime stone = 5% x 0.425 = 0.021 Kg

Conventional cupolas melt 4030.7 Kg/m^2 of area between the tuyeres per hour. The 0.254 m (Working diameter) cupola furnace could theoretically melt 356.07 Kg of iron per hour. [1]

Melt rate in Kg = $10\,\pi\,(\frac{D}{2})^2$ Kg/hour (13)

D= diameter, $\pi = 3.14$, D = 0.254 m

Melt rate = $10\,\pi\,(\frac{0.254}{2})^2$= 356.07 Kg/hour

2.3 Selection of cupola blower:

Cupolas will normally melt 1814.369 Kg of iron for every 0.471 cubic meter/s of air supplied. The 0.254 m (Working diameter) cupola is melting 150 Kg / hour at 0.042 cubic meter/s. It is operating at approximately 92% of the above as a general rule. Usually cupola blowers are sized at 0.001 cubic meter/s per square inch of sectional area between the tuyeres. [1]

The calculation of blower for 0.254 m cupola furnace is:

Area of the cupola = 1.993 m^2

0.001 cubic meter/s × Area of the cupola = recommended cubic meter/s (14)

0.001 cubic meter/s × 1.993 = 0.092 cubic meter/s,

Blowers are normally sized up 10% to make up for leaks in the system and variations in temperature. However they are run at 80% to 90% of the calculated value.

This blower shown in fig.6, we used in our cupola furnce and its specifications are:

Horse power = 1hp

cubic meter/s ≅ 0.092

rpm = 3000

3 RESULT & DISCUSSION:

We have tested our design of cupola furnace by performing melting practice on it (Shown in fig.7) We have Charge pig iron ingots, metallurgical coke and lime stone in a layers. The first layer is metal, second is flux, third coke and the quantities of these substances used is shown in Table no.2.

Figure 6: Blower

The tempertaure required to melt pig iron ingot is 1873.15 K and and the temperature we reached was 2073.15 K. We used temperature controller system to maintain the inside temperature of the furnace as well as K-type thermocuple. (shown in figure. 8).To minimize energy losses we used high alumina bricks with fireclay & alumina powder filling.The ratio of mixing these powders was 60% fireclay and 40% alumina powder.

Pig iron ingots were successfully melted by using our furnace in (fig.9).Therefore, we have prove that the design which we have fabricated is optimal for melting purposes.

XRF test of the final product also conducted by Materials Engineering Department,NEDUET yielded the following results,

99% Fe & 0.05%

Accuracy of the XRF testing machine is 0.01 Wt. percentage and the model number of machine is Oxford XRF analyser X-MET7000.

Table 2: Cupola furnace operation data.

Charging start	3.15 P.M
Pig iron	16 Kg
Output metal with slag	10 Kg
Coke input	30 Kg
Limestone	1.5 Kg
Tap out	4:30 P.M
Melting time	1:15 min.
Melting efficiency	62.5%
Melting efficiency spected	≥80%

4 CONCLUSION:

Melting of pig iron was conducted in cupola furnace. After receiving result, we send samples to lab for further testing. This achievement will help future students of the metallurgical department in their studies and encourage them to do some research work by doing melting. This furnace also melts the steel scrap, iron ore, copper ore, so if someone wants to do research in making new alloy of steel then this furnace will make his work easier.

5 ACKNOWLEDGEMENTS:

The authors thank to Mr.Irfan Danish for sample metallography and Engr. Syed Muhammad Mohsin Jafri for XRF test.

Figure 7: Cupola furnace during operation.

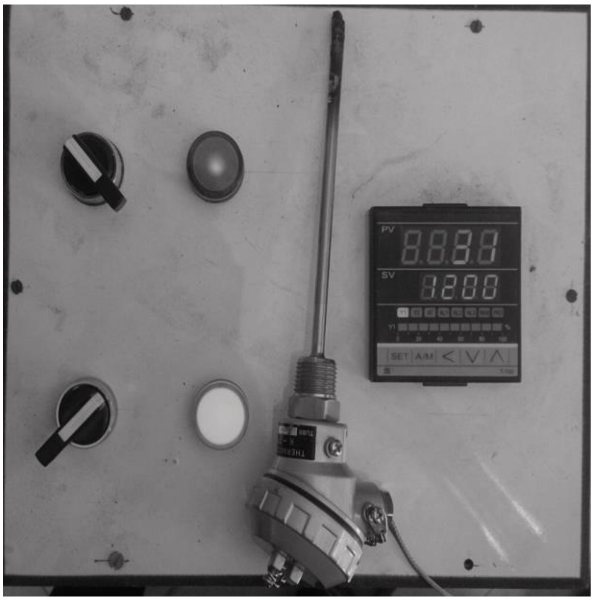

Figure 8: Temperature controller system

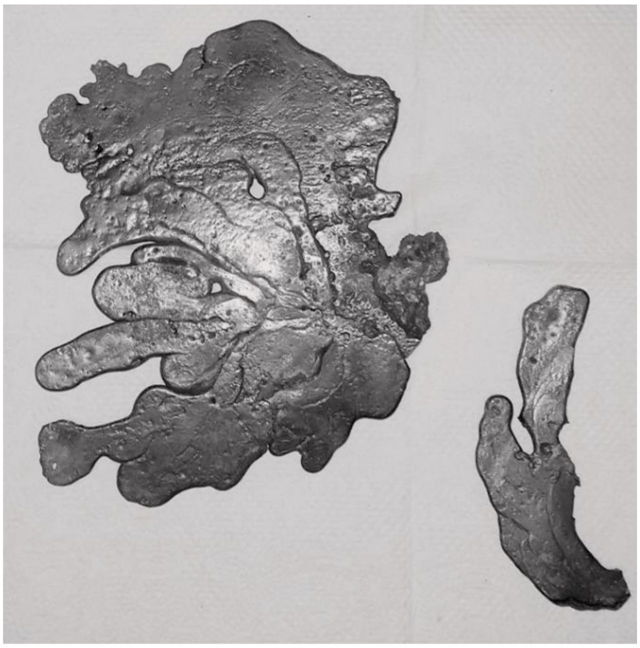

Figure 9: Melted sample

6 REFERENCES:

[1] http://www.atlasfdry.com/cupolafurnace.htm

[2] http://www.britannica.com/technology/cupola-furnace.

[3] J. E Hurst, Melting iron in the cupola, Penton library, 1929.

[4] Steve, Iron Melting Cupola Furnaces, First Edition, Jacksonville, USA, 2000.

COMPARATIVE ANALYSIS OF CHEMICAL ABSORPTION AND MEMBRANE SEPARATION FOR POST-COMBUSTION CARBON CAPTURE

Rizwan Ahmed Qamar*, M. Zubair Aslam, Abdul Haseeb, Ahsan Khurram, Amjad Mahmood
Chemical Engineering Department, NED University of Engineering & Technology,
Karachi, Pakistan

* *Corresponding Author:* Rizwan Ahmed Qamar
E-mail address: rizwanaq@neduet.edu.pk

ABSTRACT

Carbon dioxide being a major contributor in global warming poses a serious danger to environment. The risk of environmental pollution may be reduced by downstream treatment of post-combustion flue gases which mainly come from Power plants, Cement industry, Oil and Gas fields etc with the primary focus on carbon dioxide capture. Post combustion is widely used technique because of its compatibility with existing power plant infrastructure. The process was carried by absorption using 30 wt% MEA solvent and Hollow-fiber Cellulose Acetate membrane system. The purpose of our project is to carry comparative analysis of above stated techniques for flow rate of flue gas ranges between 1 to 200 MMSCFD. Our objective is to achieve 90% recovery of CO_2 with carbon reduction from 10.66 mol% to 2 mol%. Absorption technology is simulated using ASPEN HYSYS V8.4 and program for membrane system is developed by linking values from ASPEN HYSYS to Microsoft EXCEL. The operating cost for membrane separation is found to be lower than that of Absorption process but from results we conclude that absorption technique is better than membrane technology until the issues like membrane degradation, high capital cost and membrane life-cycle would be resolved.

Keywords: CO_2 recovery; CO_2 purity; permeate fraction; permeability; selectivity

1 INTRODUCTION

In Post-combustion technology carbon dioxide is captured after the combustion of the fuel. The gas is captured from flue gases coming from power plants, cement industry, oil and gas fields etc. The technology is well understood and is currently used in other industrial applications.

As compared to other two techniques of capturing carbon dioxide, post capture technique has an advantage. It is compatible with existing plant infrastructure without requiring substantial change in basic combustion technology. Furthermore, it can be applied to other industrial equipments like downstream treatment of flare flue gases.

All capture processes use either absorbent (solvent), adsorbent (solid sorbent) or membranes [1].

Absorption is widely used in the chemical, petrochemical and other industries. In solvent based post combustion capture process, flue gas is contacted with the solvent which typically contains a reagent that selectively reacts with CO_2. This contact occurs in traditional gas-liquid contractors and CO_2 transfers from the gas phase to the liquid phase. The CO_2 loaded rich solution is pumped to a regenerator vessel where it is heated to liberate gaseous CO_2 and the lean solution is circulated back to the absorber. The liberated CO_2 gas is collected in dried form, compressed and transported to a storage reservoir.

Commonly used solvent is 30 wt% aqueous Monoethanolamine (MEA) which has been used commercially capturing up to 1000 tons/day [2].

Adsorption refers to the uptake of CO_2 molecules on to the surface of another material. A claimed advantage of adsorption is that the regeneration energy should be lower relative to solvents since the heat capacity, working capacity and heats of reaction. Potential disadvantages for adsorbents include particle attrition, handling of large volumes of sorbent and thermal management of large scale adsorber vessels.

Membranes can separate CO_2 from the flue gas by selectively permeating it through the membrane material. If CO_2 has a higher permeability in some cases, chemical agents that selectively react with CO_2 are also added to increase membranes selectivity for CO_2. CO_2 transports a membrane only if its partial pressure is higher on one side of the membrane relative to the other side. This partial pressure gradient can be obtained by pressurizing the flue gas on one side of the membrane, applying a vacuum on the other side of the membrane, or both[3].

Like adsorbents, membranes are claimed to potentially offer low energy capture processes. The major challenge for membranes comes from the potential fouling of the membrane surfaces from any particulate matter, uncertainty about the performance and cost of large scale efficient vacuum pumps and compressors required for post combustion capture and the ability to integrate the process into a power plant.

2 ABSORPTION

Simulation of Absorption and stripping unit for Carbon capture is done using ASPEN HYSYS V8.4. Simulation was run for flue gas flow ranges from 1 to 200 MMSCFD; the composition of flue gas was taken from a coal-fired power plant which is as under.

Table 1. Flue Gas Compositions

Components	Mole fractions
Nitrogen	0.7872
Carbon dioxide	0.0922
Water vapors	0.0545
Oxygen	0.0622

For simulation of CO_2 absorption unit, anime package is used. HYSYS offers two amine packages; Kent-Edinburg and Li-Mather.

Simulation was performed on Kent-Edinburg model. Simulation sheet is shown in Figure 1.

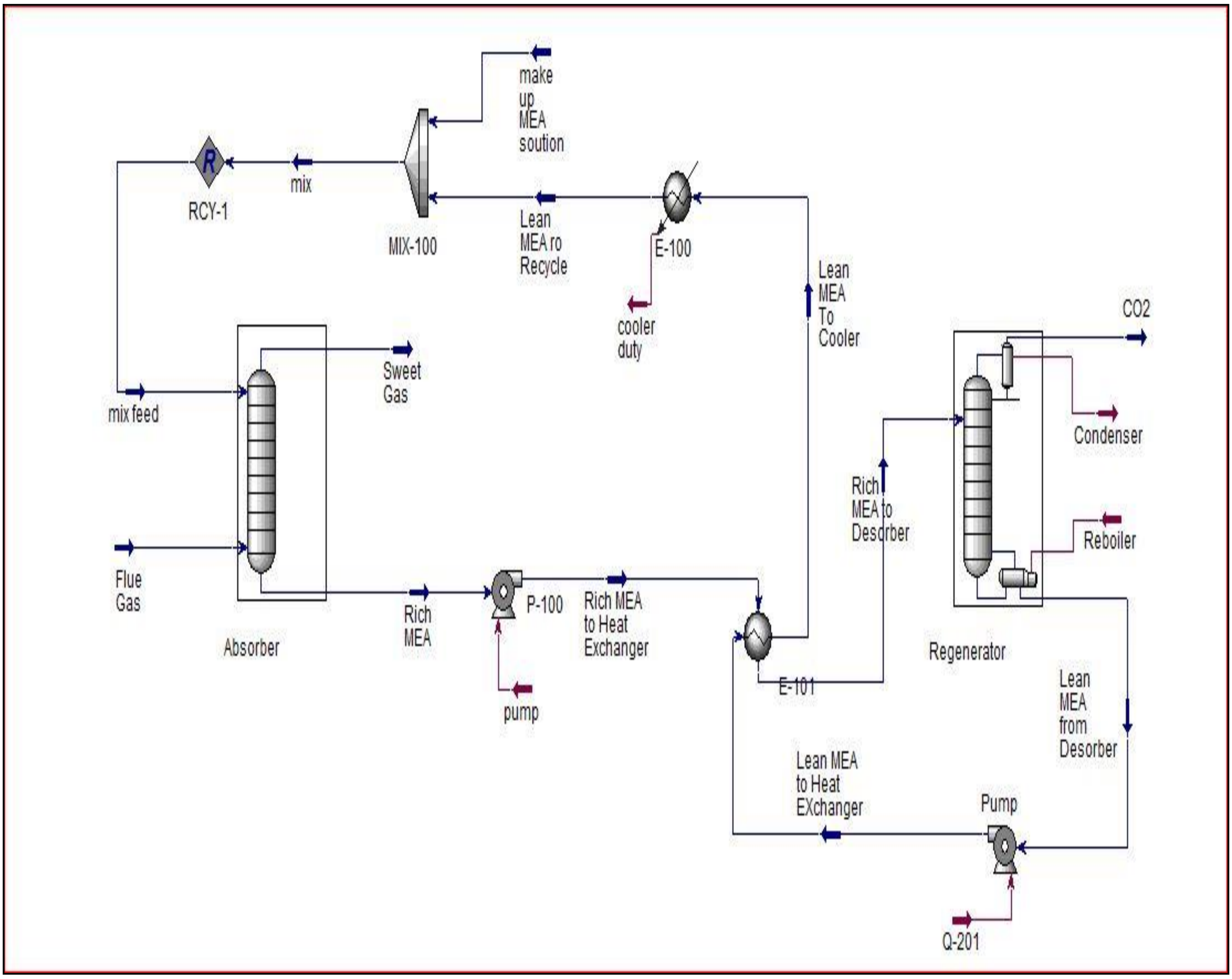

Figure 1. Aspen HYSYS Simulation Sheet

By increasing Flow of MEA solution beyond 13.5 MMSCFD in absorption column, CO_2 recovery becomes constant. Therefore 13.5 MMSCFD flow is selected for base case at flue gas flow of 10 MMSCFD as shown in Figure 2.

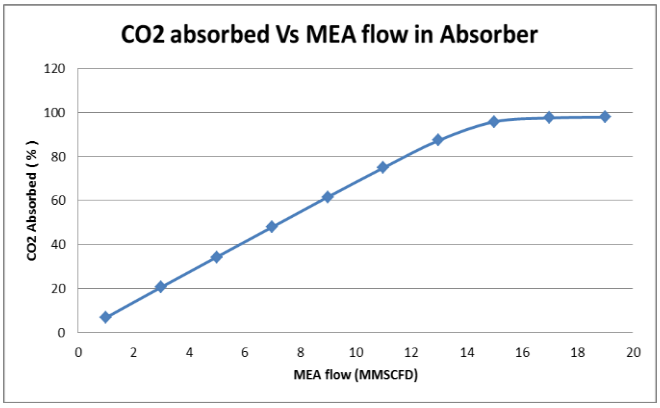

Figure 2. Effect of MEA Flow on CO_2 Absorbed

A base case of 10 MMSCFD of flue gas is selected for comparative analysis. Simulation is performed for different CO_2 recoveries in stripper in order to measure reboiler and condenser duties as shown in Figure 3. By increasing recovery beyond 80%, reboiler and condenser duties increase drastically. Therefore recovery of 80% is selected for base case.

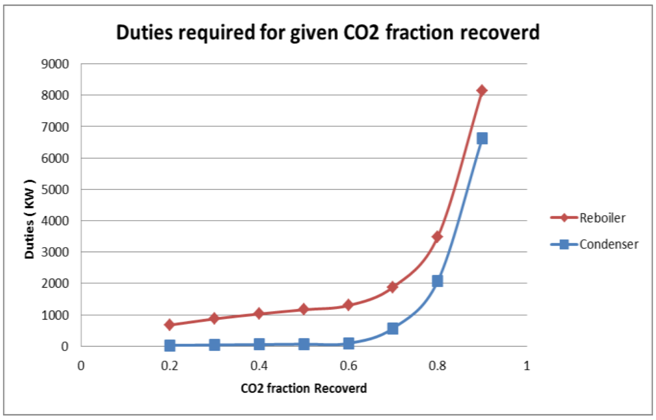

Figure 3. Reboiler and Condenser Duties

3 MEMBRANE

The simulation of membrane separation was performed using Microsoft Excel linked with Aspen HYSYS. The membrane separation process requires the gas to be treated to be free from any moisture. The flue gases from the flare contain water. The removal of moisture was performed on Aspen HYSYS. The simulation sheet of 1st stage water removal and compressor system is shown below in Figure 4.

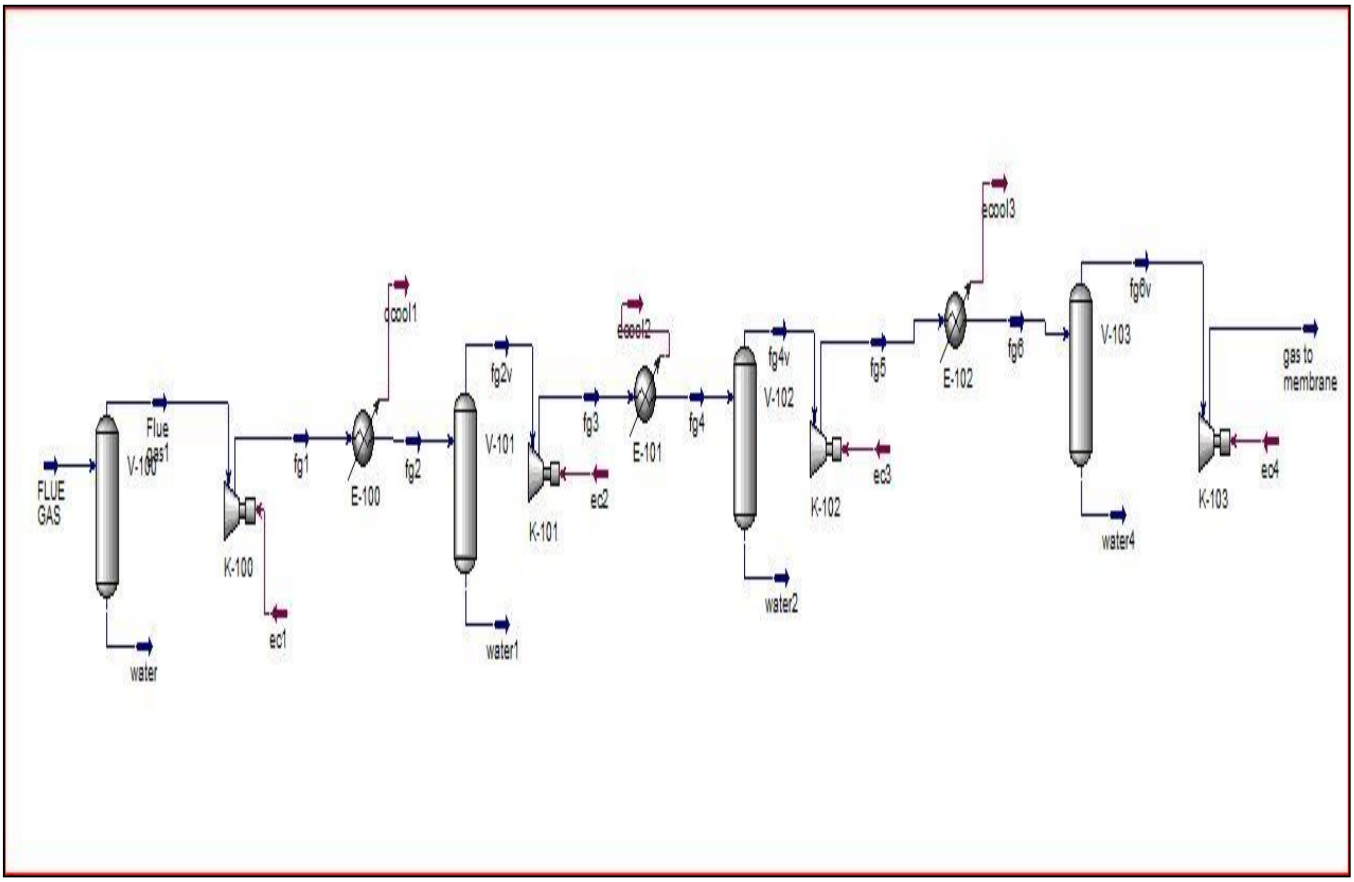

Figure 4. 1st Stage Water Removal System

The flue gas was first sent to a separator in which some quantity of water was removed, the resulting treated gas was sent to cooler. A second separator was employed to further achieve moisture removal. The resulting gas was compressed using two compressors to 20bar and feed to the first stage of membrane separation unit.

Permeate of 1st stage is again compressed to 20 bar before entering the 2nd stage and similarly permeate of 2nd stage is compressed to 20 bar before entering the 3rd stage.

The membrane separation calculations were performed using Excel. The equation [4] used is as follows.

$$(\Theta\,(1-\alpha) + R\,(1-\Theta)\,(1-\alpha))\,Y_p^2 + (1-(1-\alpha)\,(\Theta+Y_f) - R(1-\Theta)(1-\alpha))Y_p - \alpha(Y_f) = 0 \qquad (1)$$

$$A = \frac{\Theta(1-\Theta)FfYp}{Q(P1(Yf-\Theta Yp)-(P2Yp(1-\Theta))} \qquad (2)$$

The mole fraction of CO_2 in permeates, effective membrane area and CO_2 recovery were plotted against permeate fraction and trends are shown in Figure 5.

Table 2. Membrane Separation Parameters

Parameter	Value
Permeability of CO_2	10 barrer
Selectivity of CO_2/N_2 mixture	25
Permeability of N_2	0.4 barrer
Θ (1st stage)	0.45
Θ (2nd stage)	0.3
Θ (3rd stage)	0.6
Permeate side pressure of each stage	1 bar
Inlet pressure of each stage	20 bar

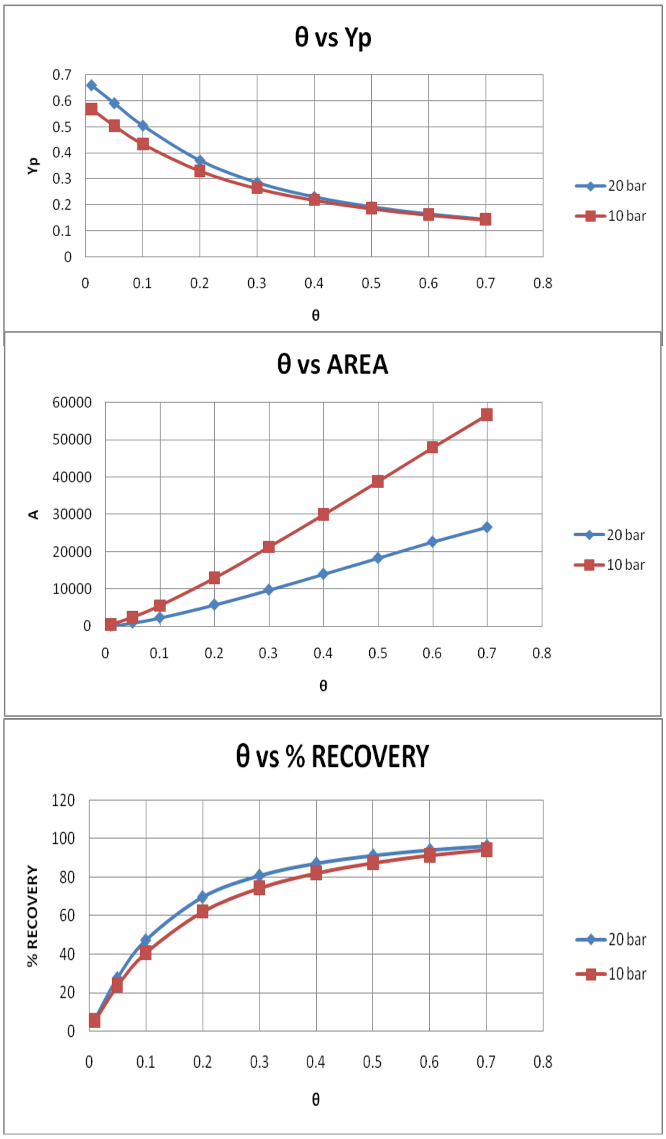

Figure 5. Membrane Separation Trends

4 ECONOMIC COMPARISON

The economic analysis of Absorption and Membrane process is carried using ASPEN Economic Analyzer V8.4. **Aspen Process Economic Analyzer** is cost estimating software that provides CAPEX estimates and OPEX estimates for comparing and screening multiple process schemes. Aspen Process Economic Analyzer relies on model-based estimation to generate project capital cost estimates and operating cost estimates. Key features include interactive equipment to determine operating costs and investment analysis, and automatic generation of block and process flow diagrams. Aspen Process Economic Analyzer is integrated with process simulators Aspen HYSYS and Aspen Plus, saving time and eliminating errors caused by manually transferring data between process design and estimation departments. With Activated Economics, process simulation users can generate CAPEX estimates and OPEX estimates using the same cost estimating software as estimators [5].

The simulated Absorption and Membrane processes are analyzed through ASPEN Economic analyzer. The equipments utilized in absorption process include absorption column, stripping column, pumps, heat exchangers, re-boiler, condenser and mixer. And the equipment utilized in membrane process are Hollow-fiber Cellulose Acetate Membrane Skids, Compressors, coolers and two-phase separators. The economic analysis for capital cost of equipment is carried for flue gas flow rate of 10 MMSCFD.

For the flue gas flow of 10 MMSCFD the equipment cost of membrane process is greatly higher than that of absorption process. For membrane process the equipment cost is 8.87 million USD and for absorption process it is 4.69 million USD as shown in Figure 6.

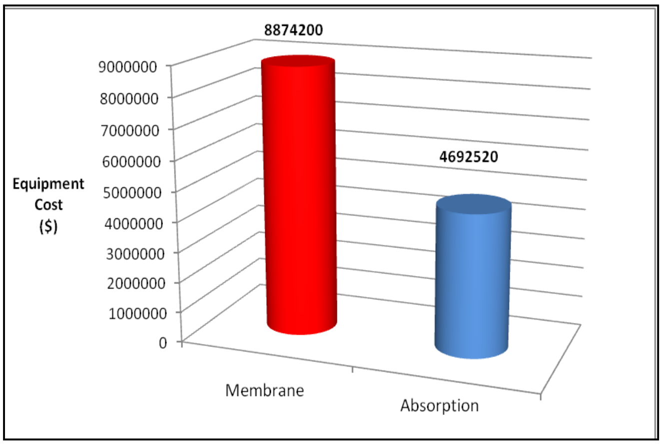

Figure 6. Equipment Cost Comparison

Operating cost is compared on the basis of utilities consumption by each process. The major utility in absorption process is steam that is used in re-boiler for regeneration of MEA solvent other utilities are cooling water and electricity. In membrane process the major utility consumption is electricity and cooling water is also used. Operating comparison is made for flue gas flow rate ranging between 1 and 200 MMSCFD.

The operating cost is higher for absorption process as compared to membrane process. For 10 MMSCFD flow of flue gas the operating or utility cost of membrane process is 162.4 USD/hr and for absorption process it is 179 USD/hr. this gap in operating cost increases as flow rate of flue gas increases.

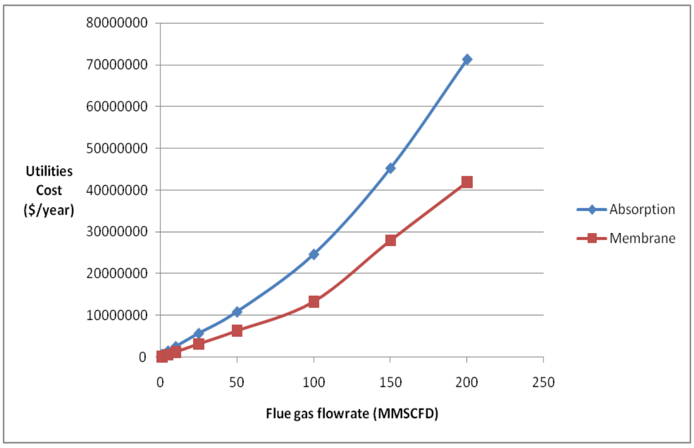

Figure 7. Operating Cost Comparison

5 CONCLUSION

Absorption process is still a better process because it is widely implicated and produces reliable results whereas membrane process is still under study for commercialization. Factors like membrane degradation, membrane life-cycle and membrane permeability and selectivity need to be properly addressed and improved in order to replace absorption technology with membrane separation. Although according to our study membrane separation has lower operating cost than absorption technique but the result are for new membrane and the degradation factor of membrane is not considered.

Another factor of choice is utilities available, since membrane separation mainly required electricity and little quantity of water, therefore membrane separation is prior choice in the remote areas where utilities like cooling water and steam are not easily available.

Absorption process has the ability to produce high purity of CO_2 capture up to 98 mole% whereas in membrane separation it is not feasible to get that much purity of CO_2 leaving the system. In order to get high purity of CO_2 leaving the system the membrane scheme is followed by a small scale absorption process.

Other factors to consider include maintenance cost which is higher for absorption process, performance decline with time which is a major concern in membrane separation caused by degradation or plugging of membrane, normally the life of a membrane skid is 5 to 10 years.

Conclusively, membrane separation is economical for small to medium flow of flue gases and for higher flow rates Absorption is preferred process. In future if the issues like membrane degradation and high membrane replacement cost have improved only then the membrane separation can replace absorption process.

ACKNOWLEDGEMENTS

All thanks to ALMIGHTY ALLAH. We would like say thanks to our teaching faculty specially our project advisor for making this work done.

REFERENCES

[1] *Carbon Capture Overview* . Rameshni Mahin.

[2] Amine Gas Treating, Wikipedia

[3] Membrane-based CO2 Capture Systems for Coal-fired Power Plants, Carnegie Mellon University Pittsburgh, September 2012

[4] Chemical Process Design, Robin Smith

[5] Tech, ASPEN**.** [Online] http://www.aspentech.com/products/activated-economics/.

ANALYSIS OF WIND FARM LOCATED NEAR GHARO – PAKISTAN.

Mobin Ahmed[1,*], Muzaffar Hussain[2] & Saeed Ahmed[3]
[1]Oil & Gas Asset Integrity Management System
[2,3]Mechanical Engineering Department, NED University of Engineering & Technology, Karachi, Pakistan

[*]*Corresponding author*: Tel.: +92343-2000591
E-mail address: mobinmechsonic@gmail.com (M. Ahmed)

ABSTRACT

Pakistan is in the grip of a serious energy crisis that is affecting all sectors of the economy and the various segments of the society. Karachi, the largest city by population and area experiences up to 12 hours load-shedding. Shortage ranges from 200 MW to 2500 MW resulting in various criticalities during heat waves and economic loss. Electric Power Generation Potential and Sensitivity Analysis of a 44 MW wind farm located near the city Gharo – Pakistan is carried out to assess the impact of each input parameter on the input feasibility of the farm. **RETScreen** software analysis demonstrates that with a **capacity factor of 30%,** the farm generates **128169 MWh** of electrical power. The electricity generation cost from the farm was calculated to be **$0.07/kWh**. Calculated value of payback period is **9.5 years** and the wind farm is capable of avoiding **812565 tons of carbon dioxide per year**. Sensitivity analysis show that the electricity production cost is strongly dependent on initial project cost, electricity export price and electricity price escalation rate. The study shows that electricity produced at the proposed site is both economically and environmentally better than the electricity by fossil fuel based power plants and can contribute significantly to the development of the city.

Keywords: Renewable and Alternate Energy; Wind Farm Analysis; Energy Crisis; RETScreen

1 METHODOLOGY

The present study consists of two major parts; the electricity production potential evaluation of a 44MW wind farm located at Gharo for this analysis RETScreen validated (6) energy system simulation software was used. RETScreen free software was created by Can met Energy Research Centre, Natural Resource for performing preliminary evaluation of renewable energy projects.

The city of Gharo is located in the Sindh province of Pakistan. It has good wind speed regime that sets it among the better wind energy sites of Pakistan. The wind data of site was obtained from Pakistan Meteorological Department. The data revealed that Gharo site has an annual average wind speed of 6.9 m/s with the potential to generate significant electric power using modern wind turbines. There is considerable potential for industrial growth in this area. Availability of cheap electric power will spur industrialized and job creation in region. Gharo is small town located around 30 kilometres East of Karachi, Pakistan. The wind speed data was being recorded by Pakistan Meteorological Department at monitoring stations spread all over the country for around 50 years. The original data was recorded at different heights above ground and was simulated to standard height of 30 meters for each month that indicated high wind speed zone near Gharo. This initiative was followed by the series of positive steps to collect wind data.

2 BASIS OF SITE SELECTION

Selection of site for wind power projects is a complex job. Various factors are involved that need to be addressed before finalizing the location where the project is proposed. Gharo site was selected on the basis of studies that revealed that the site has outstanding wind characteristics.

RET Screen software (7) required a number of input related to proposed 44MV wind electric power project. The inputs included; wind speed data for a year, rotor area, hub height etc. During modeling phase of the wind farm different kind of losses such as airfoil losses, etc were supplied as inputs to the software.RET Screen was provided cost of different project components. Suzion I MV wind turbine model S.64/1000-65m was chosen for the wind farm; shows important wind farm parameters. RETScreen calculates different project indicators using formulas; few of the important relations are described here.

Capacity Factor (CF) is defined as the ratio of actual electric energy (kWh) generated by the turbine in a year to the electric energy (kWh) generated by the turbine had it operated at full capacity for one year.

$$CF = \frac{P_{average}}{P_{rated}} \tag{1}$$

With the provided climatic and product data RETScreen calculated a capacity factor of 30% for the farm. An important financial indicator is the net present value of the project (NPV) NPV of a project is defined as the value of all future cash flow, discounted at discount rate in today money is given by.

$$NPV = \frac{\sum C_n}{(1+r)^n} \tag{2}$$

Positive value of NPV suggests feasibility of the proposed project. Payback period of a project is the time required for a project to recoup its own initial cost, out of the income or saving it generates.

$$Payback = \frac{C-IG}{(C_n + C_{copa} + C_{RE} + C_{GHG}) - (C_{O\&M} + C_{fuel})} \tag{3}$$

Payback period is a useful financial indicator and short payback period indicates that the project is financially viable.

Another important marker is the benefit-cost ratio of the project, which is the ratio of the net benefit to costs of project. Net benefits represent the value of annual income and savings less annual cost, while the cost is defined as the project equity. RETScreen calculates benefit cost ratio using following relation.

$$B = \frac{NPV + (1+f_d)C}{(1+f_d)} \tag{4}$$

A benefit-cost ratio value of greater than unity indicates that project financially feasible. Annual life cycle savings (ALCS) is the levelized nominal yearly savings which is calculated using this relation.

$$ALCS = \frac{NPV}{\frac{1}{r}\left(1-\frac{1}{r+1}\right)^N} \tag{5}$$

Table 1. Financial Analysis

Summary of economic input			**Summary of financial feasible indicator**		
Item	**Units**	**Value**	**Item**	**Units**	**Value**
Project cost	$m	100	Energy production cost	$/KWh	0.094
Project life	Year	28	Electricity export rate	$/kWh	0.1
Inflation rate	%	10	Net present value	MS	45.75
Dept ratio	%	70	Benefit cost ratio	-	3.01
Dept interest rate	%	12	Annual life cycle saving	M$/yr	5.0
Dept term	year	14	Simple payback time	year	9.5

3 FINANCIAL ANANLYSIS OF WIND ENERGY FARM

Financial analysis of the wind farm was carried out using the site inputs data such as; initial cost of the project life, interest rate, and equity to debt ratio, inflation rate and term. The electricity export rates of $0.1/kWh were chosen for wind farms, this is the current electricity rate for domestic users in Pakistan.

RETScreen calculated a simple payback period of 9.5. The money payback period was found to be inversely proportional to the electricity export rate. The economic viability of a wind energy farm increases as the dept rate decreased and dept term increased.

Table 2. Calculation Inputs

Item	Unit	Value	Item	Unit	Value
Rated power	KW	1750	Capacity factor	%	36.8
Rotor diameter	m	66	Array losses	%	1.2
Hub Height	m	78	Air foil Losses	%	3
Swept area of Blades		3384	Miscellaneous losses	%	95
Rotor speed	Rpm	18	Availability	%	2
Cut-in Speed	m/s	3.4	Shape factor	…..	
Cut-out Speed	m/s	26.6			

4 EMISSION ANALYSIS

A renewable energy electric power project such as wind farm does not produce any pollutant during its operation therefore beneficial effects on environment of any renewable energy project are positive. For Pakistani oil (Furnace oil) based thermal power plants RETScreen suggested GHG emission factor of 0.773too2MWh. If 44MW thermal power plants are replaced with the proposed wind farm of same capacity then it will help avoid 812565 ton of CO_2 in year.

5 SENSITIVITY ANALYSIS

In performing sensitivity analysis on RETScreen software input variables are changed one at time to study the effects on other parameters. This is done while keeping the other variable constant. The following table in the upcoming paragraph will demonstrate these effects.

A decrease in value of capacity factor from 30%to 24% results in reduced electricity production rate and increased production cost. However a positive value of NPV suggests that even with such large decrease in CF electricity can produced economically.

Table 3. Emission Analysis

Input variable	**Increment in input**		**Increment in out (%deviation from original)**		
	Original value	**New value**	**New energy production (GWh)**	**Generation cost (cents/KWh)**	**NPV(US$ million)**
Capacity factor	30%	24%	84.6(-23.2)	10.8(37)	42(-89.2)
Electricity price hike	5%	7.5%	NC*	5.3(-24.1%)	83.4(+105.5%)
Capital cost	$120million	$144million	NC	10.0(+23.96)	22.9(-49.8%)
Electricity export rate	10cents/KWh	15cents/KWh	NC	NC	67.4(+166%)
Debt interest rate	10%	15%	NC	8.0(+15.2)	26.1(-35.6)
GHG emission reduction income	0	24.6/ton CO_2	NC	6.9(-11.4)	52.1(+23.8%)

NC*=NO Change

Electricity price increase has positive impact on the energy production. If electricity price escalation rate is increased from 5% to 7.5% per annum then electricity generation cost experiences drops of 24.1% to 5.3 cents/KWh. At the same time NPV more than doubled to a value of $ 83.4 million. This clearly demonstrates the importance of favorable price for wind project success.

A 20% escalation in capital cost of the wind farm results in almost same rise in production cost 23.69% while there is no change in electricity generated.

6 CONCLUSION

This work determined the wind energy yield potential of a hypothetical wind farm located in Gharo city, Pakistan. The study showed that the farm is capable of generating 128169MWh electricity at a cost of $0.07/kWh. RETScreen estimated value of payback period to be 9.5 years and the wind farm is capable of avoiding 812565 tons of Carbon dioxide per year. The sensitivity analysis showed that the sites with low value of capacity factors or low wind speeds are also feasible. If Gharo wind site is developed for harnessing wind energy resources, it will be economically viable and availability of electricity will result in improved environmentally impact and social uplift.

7 REFERENCES

[1] Alternate Energy Development Board (AEDB), Ministry of Water and Power, Government of Pakistan.

[2] Clean Energy Project Analysis: RETScreen Engineering and Cases Textbook, Clean Energy Decision Support Centre, RETScreen International. www.retscreen.net/ang/centre

EFFECT OF BALL MILLING OF MECHANICAL ALLOYING ON STRUCTURAL CHARACTERISTICS OF SHAPE MEMORY CU–AL–MN ALLOY

Umer Hussain[1*], M. Anas Khalid Khan[1], Humair Ahmed[1] and Prof. Dr. Ashraf Ali[1]
[1] Materials Engineering Department, NED University of Engineering & Technology, Karachi, Pakistan

[*]Corresponding author. Tel.: +92 345 626 3952
E-mail address: umer_hussain25@hotmail.com

ABSTRACT

Cu- based shape memory alloy (SMAs) along with its associate's Copper-Aluminum, Copper Zinc and Copper-Tin demonstrated excellent shape recovery and dynamism to heat and electric, and comfort of fabrication. This research is concerned with the mechanically alloyed powder (MAed powder) of Cu-based (Cu-Al-Mn) Alloy, which is a potential material for fabrication of shape memory devices. A powder metallurgy technique convoluted with fracturing, cold welding and rewelding of powder particles with appropriate energy of milling balls is stated as Mechanical Allowing and hence, make known as adequate process for developing compositions for different shape memory alloys. Mechanical Alloying is also capable of synthesising a variety of metastable phases, and in this respect, the capabilities of mechanical alloying are somewhat superior to those conventional alloys processing methods. Controlling of grain size and compositional variation is a major concerned for conventional manufacturing methods of Shape memory alloy as they can shift the transformation temperature. In this study Cu-Al-Mn alloy was prepared under different ball milling conditions i.e. with variation of time (5, 10, 15, 20, and 25 hrs). The MAed powder was characterised by Optical microscope, X-Ray Fluorescence, Scanning Electron Microscope (SEM) and R-Ray Diffraction. XRD results revealed that the increase in milling time, decrease the crystallite size and an increase in lattice parameters. Afterwards, it is being observed that the crystallite size as well as powdered morphology becomes uniform as the milling time increased upto 20 hr. EDX analysis result showed a homogeneous dispersion of Mn and Al in Cu matrix. SEM concluded that shape of particle size converted from lamellar to globular and the distribution of particle size and particle morphology became narrower with change in milling time.

Keywords: Shape Memory, Cu based alloys, Mechanical Alloying, Ball milling, Lattice Parameters.

1. INTRODUCTION

Shape Memory Alloys (SMA's), a member of smart materials' family well known for their magnificent memory characteristic along with their practical usage. Shape Memory Effect (SME) and Superelastic Effect (SE) are the significant features of these alloys. Usually, they have two different kinds of Shape Memory Effect; known as 'One-way Shape Memory Effect (OWSME)' and 'Two-way Shape Memory Effect (TWSME)'. With temperature variation Shape Memory Effect (SME) changes are generally correlated to martensitic phase transformation.

Ordinarily these alloys have two transformation phases: Austenitic (parent phase B2 cubic) at high temperature and Martensitic (B19' monoclinic phase) at low temperature. Turnout effect of thermoelastic martensite can also be characterised in Shape Memory Alloy, as the alloy endure a martensitic transformation of a type that grant the allow to mutilate by twinning mechanism under transformation temperature, then its mutilation is conversed when the twinning structures regress to the parent phase when heated. [1].

Phase transformation is correlated with four distinctive temperatures involved in the process. Initiated with forward transformation, when austenite, under zero load, commence to mutate into twinned martensite at the start of martensitic temperature (Ms) and finishes its conversion to martensite at the martensitic finish temperature (Mf). At this point, the revolution is complete and twinned martensitic phase is thoroughly achieved by material. Moreover, reverse transformation commence at austenitic start temperature (As) all along with heating and this transformation concluded at austenitic finish temperature (Af). [7]

A broad study have been conducted on Cu–Al–Ni and Cu–Zn–Al by long [8, 9]. It is been observed that while discussing Cu-based SMAs, Cu–Al–Ni alloys have shown exceptional thermal characteristics and betters usage at higher temperatures [10] at the same time Cu-Zn-Al alloys within convinced compositional boundaries display shape memory [9]. In a nut shell, constructive utilisation of Cu-Al-Zn and Cu-Al-Ni alloys are finite to those equipment's and instruments requiring bit changes in shape, for their susceptibility to brittle intergranular cracking and indigent workability [11], it is observed that Cu-Al-Mn SMAs with small amount of Al show superlative ductility due to its low degree of order of L21 parent phase. Shape memory effect with better ductility found through MT from β1(L21) to β'1(6M) monoclinic. This study subjected to Cu-Al-Mn SMAs due to these impressive properties.

Dispersion-strengthened alloys can be produce through one of the technique called mechanical alloying (MA). [2-5] the inventor of this technique for the stated purpose is BENJAMIN [6].

2. EXPERIMENTAL WORK:

For the synthesis of Cu-Al-Mn Shape Memory Alloy, Powder Metallurgy technique is used. Chemical composition and size of the grain found in Cu-based SMAs cannot be improved through conventional methods of manufacturing. Slight changes in any concerned alloy content i.e. Al and Mn may alter the transformation temperatures along with the coarse grain which do not support lofty mechanical properties. To overcome these deficiencies an innovative technique required that grant complete control over transformation conditions along with PE and SME characteristics.

2.1 Raw Materials

The 99.99% pure raw materials (Copper, Aluminium and manganese) for the synthesis of shape Memory alloys have been purchased from the FS Corporation, Karachi. Copper and Aluminium purchased in powder form whereas manganese in flake form which convert into powder by mortar pestle and then for getting further fine powder did, ball milling.

Table 1: Mesh size and sample percentage of raw material

Specifications	Cu. powder	Al. powder
Size (mesh)	200	200
Purity (%)	99.9	99.9
Composition (%)	82.5	12.5

2.2 Mechanical Ball Milling

Mechanical ball milling is done in a high energy ball mill available in material engineering department. Hardened steel balls were utilised. The speed of ball milling is set up to 350 rpm. 75 gm. of Cu-Al-Mn sample was use for the ball milling. The specification of elemental powders and the initial mixture are given in Table 1. The mixture was then milled for 5, 10, 15, 20 and 25 hours. The pre alloyed mechanical ball milled Cu-Al-Mn powder can be seen in figures 1(a, b, c, d, e), respectively.

2.3 Characterisation

The samples have been characterised using x-ray diffraction (PCSIR Karachi), scanning electron microscopy having (Beam voltage 0.4 kV-40kV; Resolution 10 nm; Magnification ×10 to ×300 000, Make: Jeol, Japan Model no (JSM 6380A)), Energy Dispersive Spectroscopy: EDS (Energy resolution: 120ev, Jeol, Japan model number (Ex-54175 JMU)) and XRF (Energy resolution:120 ev, Inovex system Model No a-8000 U.S.A). All these techniques were available in material engineering department.

3. RESULTS AND DISCUSSION

XRF of Cu-Al-Mn SMA is given in table 2. The percentage of Al was not achieved, mainly due to its oxidation, as vacuum milling was not used for mechanical alloying. Mn also decreasing as the time of mechanical alloying increases. Presence of Fe is mainly due to the erosion of steel balls used for ball milling.

Table 2: Compositional changes during Ball milling

Hours	**Weight %**		
	Cu	Mn	Fe
5	95.76	3.99	0.28
10	95.8	3.96	0.24
15	95.81	3.94	0.25
20	95.89	3.86	0.25
25	96.17	3.67	0.16

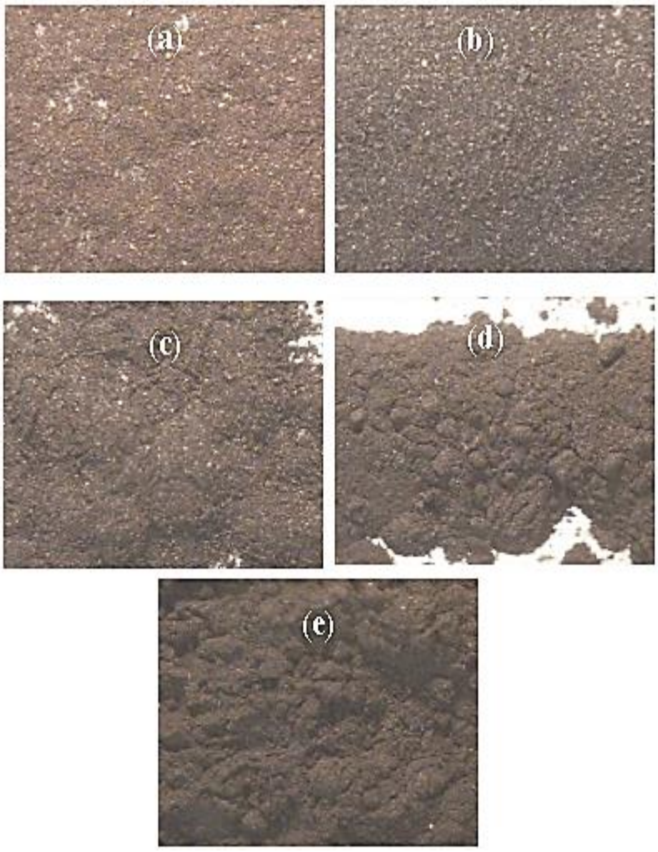

Figure 1: showing stereomicroscope images of (a) 5hr (b) 10 hr (c) 15 hr (d) 20 hr (e) 25 hr ball milled sample, all images were taken at 5x magnification

Figure 2-1, 2-2, 2-3, 2-4, 2-5 shows SEM images of 5, 10, 15, 20 and 25 hours respectively at 100x.

The figures show that particle size as well as powder morphology becomes uniform as the milling time increases.

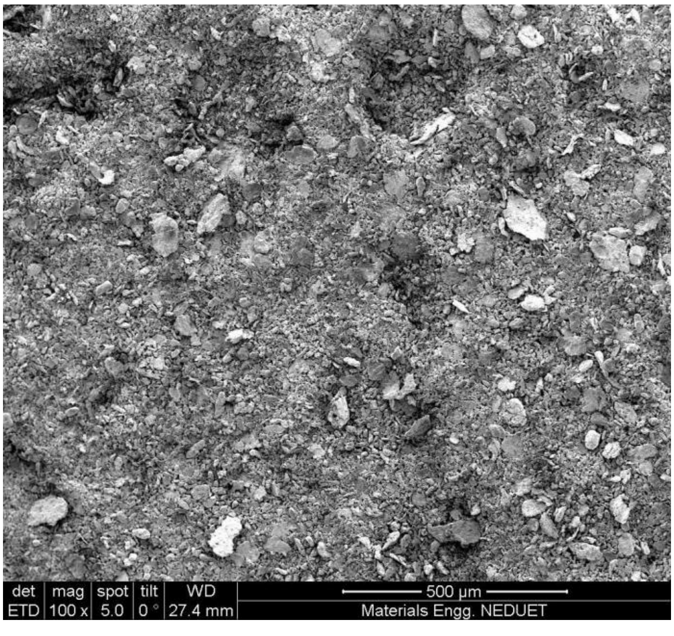

Figure 2-1: SEM image at 100X of 5 hour sample.

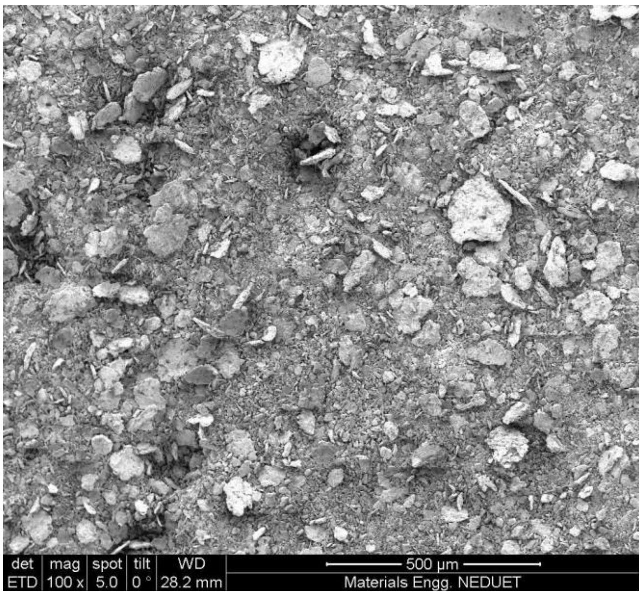

Figure 2-2: SEM image of 10 hour sample at 100X.

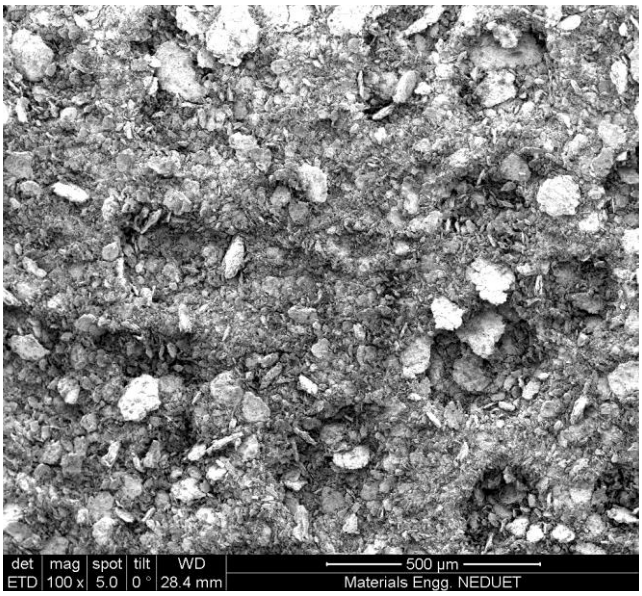

Figure 2-3: SEM image of 15 hour sample at 100X.

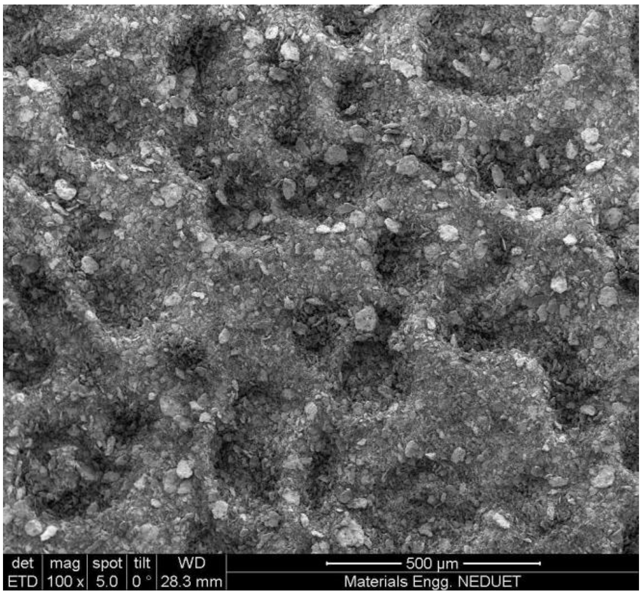

Figure 2-4: SEM image of 20 hour sample at 100X.

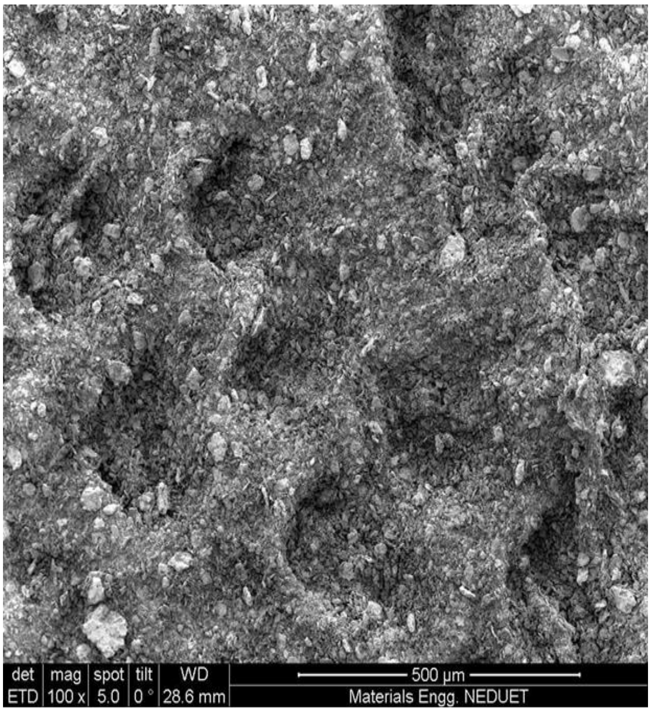

Figure 2-5: SEM image of 25 hour at 100X.

Figure3-1, 3-2, 3-3, 3-4 shows SEM images of 5, 10, 20 and 25 hours at respectively at high magnification (800X).

Figures show that structure becomes globular from laminated as the milling time increases. Also these figures show that welding is going to be held in some part of the powder.

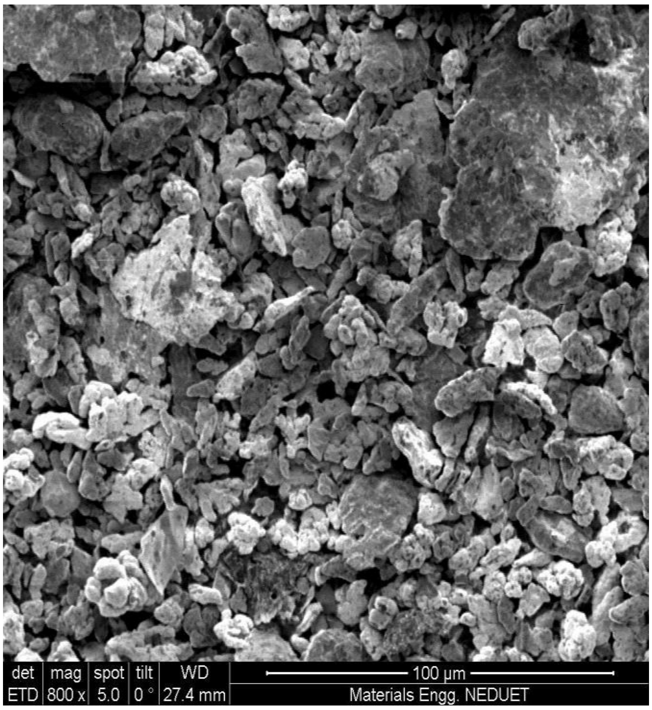

Figure 3-1: SEM image of 5 hour ball milled sample at 800X.

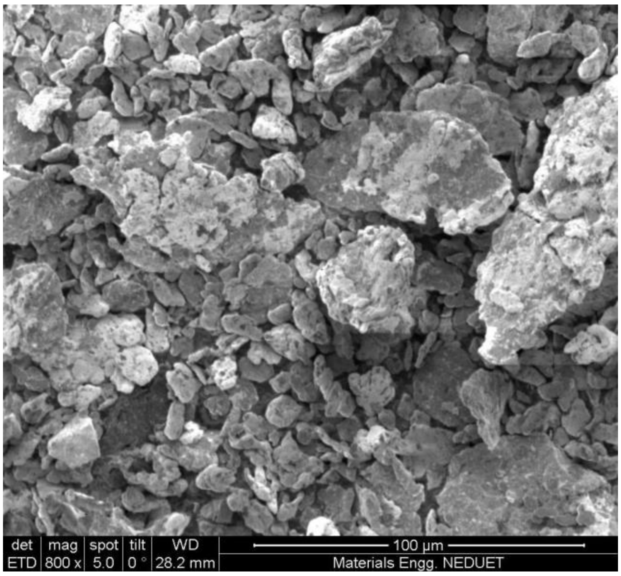

Figure 3-2: SEM image of 10 hours ball milled sample at 800X.

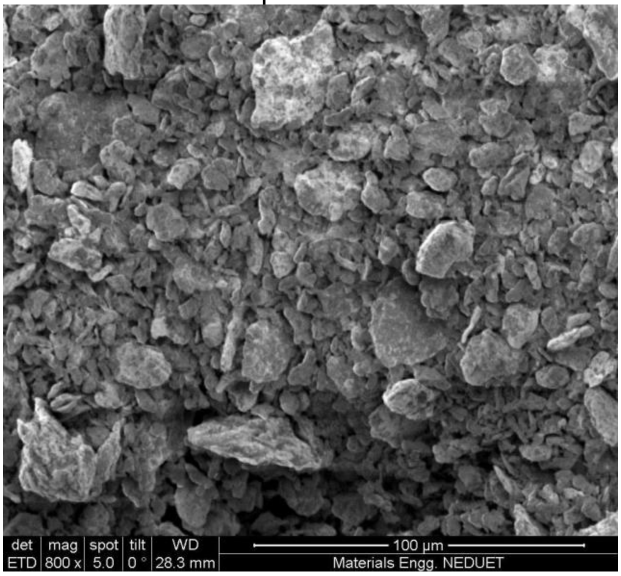

Figure 3-3: SEM image of 20 hours ball milled sample at 800X.

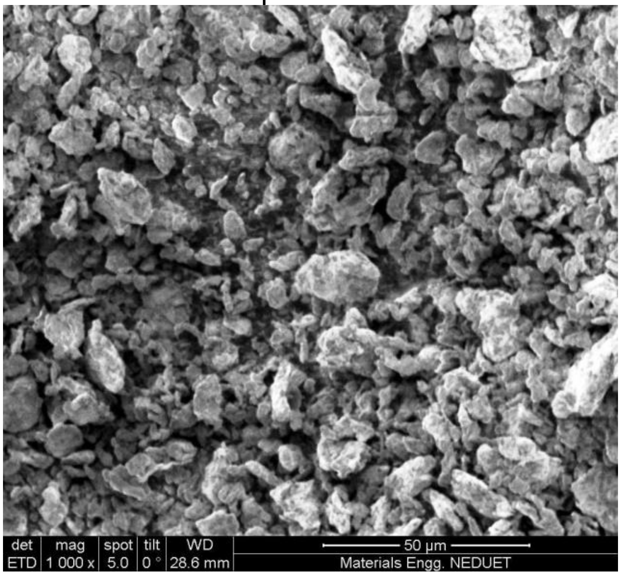

Figure 3-4: SEM image of 25 hours ball milled sample at 1000X.

The EDX of Cu-Al-Mn SMA is shown in figure 4 and table 3. EDX shows that all the elements were properly alloyed at the molecular level. Result also shows that oxygen also reacts with Cu and Al and oxidises the powder. Also Fe is also present in shape memory alloy but in trace quantity as balls used in ball milling was of steel.

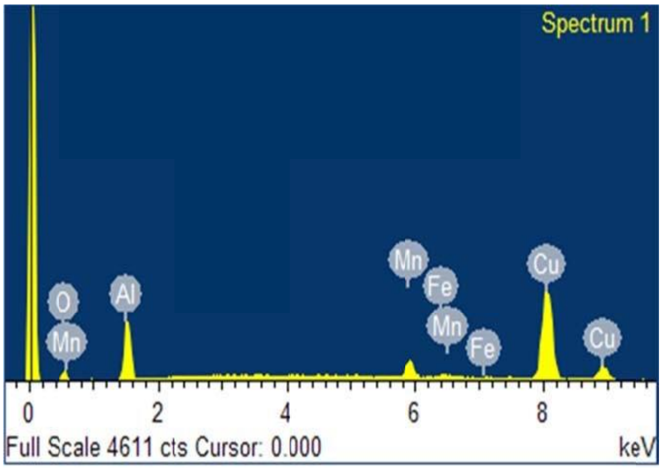

Figure 4: EDX result of Elemental composition of Sample

Table 3: EDX result of 5 hours ball milled CuAl-Mn Shape Memory Alloy.

Element	Weight%	Atomic%
O K	10.80	23.24
Al K	32.86	41.96
Mn K	43.21	27.09
Fe K	7.91	4.88
Cu L	5.22	2.83
totals	100	

XRD result of 10 and 20 hours are shown in figure 5 and 6 respectively. XRD result of the sample matches with standard XRD pattern of CU–AL–MN alloy .

By comparison with M. Reza Rezvani, A. Shokuhfar [2] work it was found that Cu peak is increasing, along with the reduction in Al and Mn peak, which signifies the diffusion of Al and Mn in copper matrix, due to increase in Milling time.

Similarly the result showed that oxygen makes oxide of copper and aluminum. There was also a peak of impurity in 10 hours which starts decreasing as milling time increases.

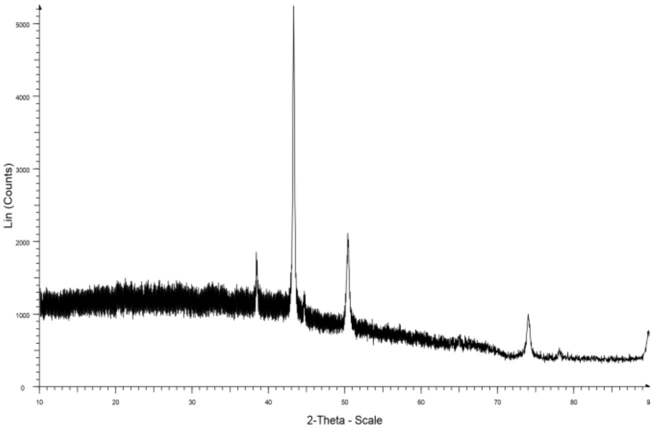

Figure 5: XRD of Cu-Al-Mn 10hr milled shape memory alloy.

Figure 5 shows four different peaks. The 1st peak is of copper oxide and aluminium oxide. 2nd and 4th peak is of $AlCu_2Mn$ in which Cu and Mn diffuse in Aluminium matrix. The 3rd one is an impurity peak.

Table 4: Shows different position, d-spacing and intensities of 10 hours ball milled XRD result.

Pos. [°2Th.]	Height [cts]	FWHM Left [°2Th.]	d-spacing [Å]	Rel. Int. [%]
38.447910	538.397800	0.295200	2.34145	12.83
43.296420	4194.857000	0.196800	2.08982	100.00
50.491610	1181.302000	0.246000	1.80761	28.16
74.138010	535.019100	0.492000	1.27900	12.75

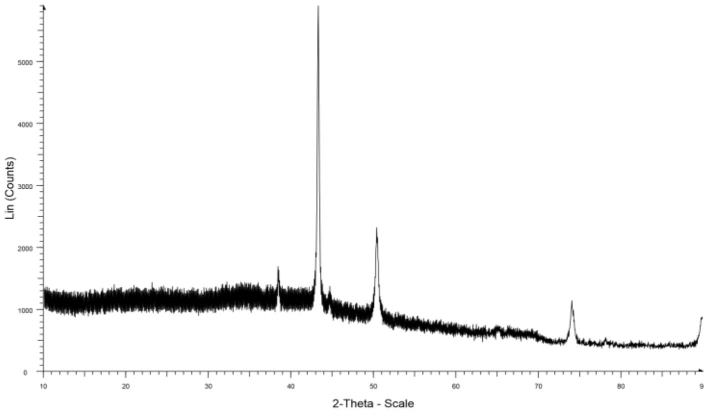

Figure 6: XRD of 20 hours ball milled Cu-Al-Mn shape memory alloy.

Figure 6 shows that the intensity of 1st peak which is Copper and aluminum oxide peak decreases which means these oxides diffuses in copper matrix. 2nd and 4th peak also decreasing which tells that they are also diffusing in copper matrix. The impure peak remains unchanged.

4. CONCLUSION:

XRD result shows the diffusion of Aluminum and Manganese in Copper alloy. Also XRD results also matching with standard spectrum of this alloy.

SEM images show the homogeneity of pre alloyed powder. Also the transfer of lamellar to globular can also be seen in SEM images as the milling time increases.

EDX result showed the presence of elements in the Copper system.

ACKNOWLEDGEMENT

Author like to appreciate all the support provided by NED University, in general and Materials Engineering Department, in Particular.

REFERENCES:

[1] Darel E. Hodgson, Shape Memory Applications, Inc., Ming H. Wu, Memry Corporation, and Robert J. Biermann, Harrison Alloys, Inc.

[2] MENG Jie, JIA Cheng-chang, HE Qing. Fabrication of oxide-reinforced NilAl composites by mechanical alloying and spark plasma sintering [J]. Materials Science and Engineering A, 2006, 434(112): 246-249.

[3] LOPEZ M, CORREDOR D, CAMURRI c, VERGARA v, JIMENEZ J. Performance and characterisation of dispersion strengthened Cu-TiB2 composite for electrical use [J]. Materials characterisation, 2005, 55(4/5): 252-262.

[4] HU Chia-jung, WU Hsin-ming. Formation of Cu-Zr-Ti amorphous powders with B and Si additions by mechanical alloying technique [J]. Journal ofAlloys and Compounds, 2007,4341435: 390-393.

[5] CHENG Xiao-yin, OUYANG Yi-fang, SHI Hong-wei, ZHONG Xia-ping, DU Yong, TAO Xiao-ming. Nano-amorphous (FeAI)I-,Zr,

[6] Mel Schwartz “Smart Materials”, CRC Press.

[7] Texas A&M Smart Lab, “Detailed Introduction to Shape Memory Alloys”,

[8] Ch.mo prof. Ferdinando Auricchio, Ch.mo Prof. Vincenzo Massarotti Eleonora Zanaboni,”One-way and two-way shape memory effect,journal, 2007/2008.

[9] Marc Mantel,Albertville,shape memory alloy, usoo5173131A,dec 22,1992.

[10] Dimitris C. Lagaoudas, “Shape Memory Alloys- Modelling and Engineering.

[11] Srinivasan A. V., McFarland Michel D., Smart structures – analysis and design, Cambridge University Press (2011), pp.26-2

SYNTHESIS AND CHARACTERIZATION OF ZINC OXIDE AND TITANIA NANOPARTICLES

Ailia Touqir[1*], Ariba Khan[1], and Syed M. Mohsin[1]
[1] Materials Engineering Department, NED University of Engineering & Technology, Karachi, Pakistan

*Corresponding author. Tel.: +92 3152217762
E-mail address: ailiatouqir@outlook.com

ABSTRACT

Zinc oxide and titania nanoparticles exhibit unique physical and chemical properties such as high chemical stability, antibacterial, high photo stability, photocatalyst, anti-corrosive, antifungal and UV filtering properties due to which these nanoparticles find extensive use in sunscreens, solar cells, paints, gas sensors, UV protection coatings, etc.

The objective of the research was to synthesize and characterise zinc oxide and titanium dioxide nanoparticles for the application in UV protection coating. Bottom up approach was opted in the synthesis of zinc oxide nanoparticle using precipitation method while Titanium Oxide nanoparticles were synthesize using a top down approach using ball milling.

The nanoparticles are characterized using techniques like X-Ray diffraction (XRD), Scanning electron microscope (SEM), UV-Vis spectroscopy. The morphology was determined using SEM. UV absorbance was checked using UV-Vis spectroscopy. Phase identification and Particle size distribution was determined using X-Ray diffraction and the particle size was found to be 21 nm.

Zinc oxide and titanium dioxide nanoparticles were applied on Wood, along with isopropanol using spray coating technique. Isopropanol was used as a coating carrier on wood for protection against UV radiation.

Keywords: Titania, Zinc oxide, Nanotechnology, wood, protection.

1. INTRODUCTION

Nanoparticles of titanium dioxide (TiO_2) and Zinc oxide (ZnO) are receiving increasing attention due to their widespread applications. Titanium dioxide finds extensive use in a wide range of applications such as photo catalysis, water purification systems, sensors and solar cells. [1]

The reactivity of TiO_2 nanoparticles is greatly enhanced compared with large molecules. The enhanced reactivity of TiO_2 nanoparticles is due to the large surface area, creating a large number of unsatisfied surface atoms leading to substantially more reactive surface sites. Synthesizing TiO_2 nanoparticles of controlled size, shape and of specific crystalline phase using sol–gel and gel–sol or hydrothermal methods has taken geat efforts. However, these synthesis methods are primarily based on reactions containing organic compounds, which are difficult to remove from the particle surfaces. [3]

The morphology and particle sizes are often obtained from scanning electron microscopy (SEM) or transmission electron microscopy (TEM). In such an analysis only a portion of the particles, generally few hundred, can be mapped for particle size determination. [5]

Zinc oxide (ZnO) has been used significantly for its many useful properties such as catalytic, electrical, optoelectronic, and photochemical properties. ZnO nanostructures have large surface area and high catalytic activity. Zinc oxide shows different physical and chemical properties depending upon the morphology of nanostructures, which can be varied by using different synthesis methods. [1]

2. MATERIALS AND METHODS

2.1. Materials

Zinc sulphate heptahydrate and sodium hydroxide were used in the experiments for the preparation of zinc oxide nanoparticles. For the synthesis of titania nanoparticles, titania powder was used. All the chemicals used were of lab grade with 99% purity obtained from Merck, and deionized water is used for the preparation of solutions. Lab grade Ethanol with 99% purity was obtained from Sigma Aldrich, used for the cleaning purpose of beakers and crucibles used during the experiments.

For the coating purpose, isopropanol, obtained from Sigma Aldrich was used. Specimens of partal wood were obtained from defect free wood. All the chemical used were of analytical grade.

2.2. Synthesis of ZnO Nanoparticles

Aqueous solution of zinc sulphate was made by adding 16 grams of powdered zinc sulphate in 100 ml of deionized water. Similarly aqueous solution of sodium hydroxide was obtained by adding 8 grams of sodium hydroxide in the tablet form, in 200 ml of deionized water.

To the aqueous solution of zinc sulphate, sodium hydroxide solution was added slowly in a dropwise under vigorous stirring, placed on a magnetic stirrer and the stirring was continued for 12 hours. The precipitates obtained were then filtered and washed thoroughly with deionized water. The precipitates were dried in an oven at 100°C for 2 hours. The powder obtained from this method was calcined at different temperatures such as 250°C, 350°C for 2 h. [1]

2.3. Synthesis of TiO_2 Nanoparticles

Titania nanoparticles were synthesized by using high-purity (99.9%) elemental powder of Titania of ~ 0.47 µm size.   . The powder was mechanically reduced to nanoparticles in a desk-top planetary ball miller, using top-down approach [3]. Wet ball milling was carried out using ethanol (lab grade) in an alumina jar.

The grinding balls made of zirconia, of different diameters were used. Ball milling was carried out for 12 hrs at 400 rpm with ball to powder ratio of 20:1 for preparing TiO_2 nanoparticles.

3. CHARACTERIZATION

3.1. X-Ray Diffraction

The compounds were characterized for Phase identification and Particle size distribution by using X-Ray diffraction. The XRD patterns of the powdered samples were recorded using a Pan-alytical X'pert pro, using Cu K$\dot{\alpha}$ radiation (=0.15406nm) as X-ray source, operated at 10kVA and 80kVA. The particle size was further verified with the help of SEM results. The crystallite dimensions of ZnO were calculated using Scherrer's equation:

$$D=0.9\lambda/B\cos\theta \qquad (1)$$

Where λ is the wavelength of the X-ray (0.15418nm), B is the full width at half maximum (FWHM, radian), and θ is the Bragg angle (degree). The value of FWHM was obtained by performing profile fitting using an XRD pattern processing software.

3.2. UV-Vis Spectroscopy

UV absorbance of the zinc oxide and titania nanoparticles was determined using UV-visible spectrophotometer (Spectrumlab, 22pc) in the range of 340-800nm. Zinc oxide and Titanium dioxide nanoparticles reveal a strong change of their optical absorption when their size is reduced.

3.3. Scanning Electron Microscopy

The structure and morphology of nanoparticles were characterized using SEM (FEI-Quanta 200). The maximum magnification obtained can be upto 1,500,000 X.

4. COATING ON SUBSTRATE

4.1. Materials

Specimens of partal wood of size 0.05 m x 0.01 m x 0.03 cm (length x height x width) were prepared from defect free wood. Isopropanol (Sigma Aldrich) and zinc oxide nanoparticles and titania nanoparticles (<100 nm) were used in the study. [2]

4.2. Treatment of Wood Surfaces with ZnO Nanoparticles Blended Isopropanol

0.5 g of ZnO nanoparticles were added to 100 ml of isopropanol and subjected to sonication in a Sonicator (Heischer ultrasound technology UP 400S) for 10 min to remove agglomeration. Similarly 0.5 g of titania (TiO_2) were mixed in 100 ml of isoprpopanol and the same procedure was followed. [2]

Then the Wood surfaces were treated with sonicated solution of ZnO and TiO_2 using sprayer and dried at room temperature [2]. Nine pieces of wood (of above mentioned dimensions) were taken. Three of them were treated with zinc oxide solution, three with titania solution and three of them were not treated with any solution and kept in as received condition. Three sets of wood pieces were made, each of which comprised of one ZnO treated, one TiO_2 treated and one untreated wood piece.

4.3. Photostability of Coated Wood Surfaces

Out of the three sets, one was exposed to UV light. The photostability of coated wood surfaces were assessed by exposing them to UV light and kept open in the atmosphere to analyse the effects of weather. The samples were removed from exposure after an interval of 15 days, and analysed for colour changes and degradation.

4.4. Degradation Due To Soil

One set of woods was kept under the soil for 15 days and the soil was watered daily. Then the samples were removed after 15 days and analysed for colour changes and degradation.

4.5. Degradation Due To Water

The last set of woods was kept in 158 ml of tap water with a pH of 6.5. The samples were removed after 15 days and analysed for colour changes and degradation.

4.6. Colour Measurements and Degradation Effect

Changes in colour of wood surfaces and degradation due to exposure to UV light, water and soil were analysed visually.

5. RESULTS AND DISCUSSION

5.1. X-Ray Diffraction

ZnO

The diffraction pattern of synthesized zinc oxide nanoparticles was recorded on Philips X'Pert PRO rotary target diffractometer using CuKα radiation having wavelength (λ=.0.154).Hexagonal wurtzite structure of ZnO was confirmed through the study of diffraction pattern.

.ZnO nanoparticles were synthesized by precipitation method and calcined at different temperature to study the effect of various temperature on nanoparticles. At different temperature rate, size and morphology of crystallite were different which affected the photocatalytic activity. It is noted that by increasing the calcination temperature, the size of the crystallite increased. Large grains are formed at high temperature by the movement of grain boundaries and combination of smaller grains. ZnO nanoparticle was prepared through precipitation method was calcined at two different temperatures .One of the sample of ZnO was calcined at 250°C and other was calcined at 350°C.The average size of the particle was calculated by using Debye-Scherrer's equation.

$$D = 0.9\lambda / B \cos\theta \qquad (2)$$

Where D represents size of the crystal, λ represents wavelength, β is full width half maximum and θ is Bragg angle. Estimated size of synthesized ZnO which was calcined at 250°C is found to be 21nm and the size of ZnO which was calcined at 350°C is found to be 42nm. The most intense peak is at 2(θ)=36.259030. Highly pure zinc oxide is confirmed from the diffraction peaks which indicates that there were no diffraction peaks for impurities.

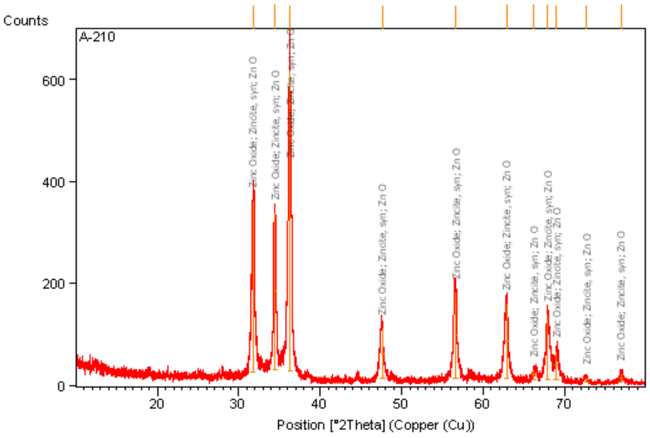

Figure 1. XRD pattern of ZnO calcined at 250˚C temperature

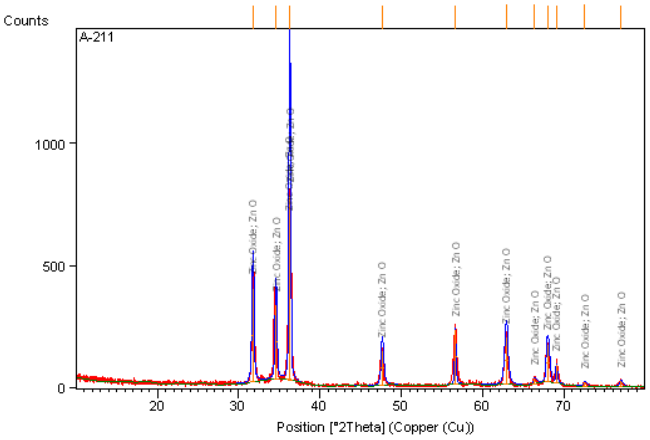

Figure 2. XRD pattern of ZnO calcined at 350˚C temperature

TiO_2

The synthesized TiO2 can be characterized by XRD,SEM and UV-VIS Spectroscopy.the particle size of TiO2 was determined by using Philips X'Pert PRO rotary target diffractometer using CuKα radiation having wavelength (λ=.0.154).Anatase or rutile structure was confirmed through the study of diffraction pattern. The sample with a porosity and rough surface showed a characteristics of high surface area and high adsorptive capacity. Also, the increased surface area of TiO_2 should be helpful to enhance the surface reaction of TiO2.

By using bottom up approach, TiO_2 nano was prepared by ball milling of titania powder in the presence of ethanol. The average size of nano TiO2 was calculated by using Debye-Scherrer's equation.

$$D = 0.9\lambda / B\cos\theta \qquad (3)$$

where D represents size of the crystal, λ represents wavelength, β is full width half maximum and θ is Bragg angle. The size of synthesized TiO2 was found to be 80nm. The most intense peak is at 2(θ)=36.259030.

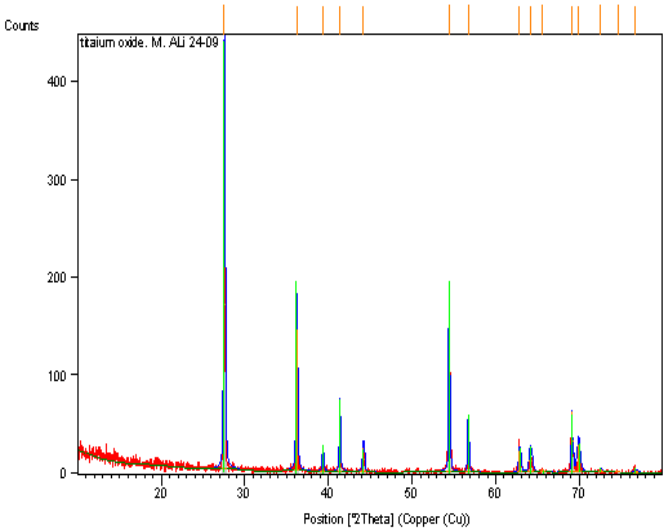

Figure 3. XRD pattern of TiO2

5.2. Scanning Electron Microscope

ZnO

The size and morphology of ZnO was analyzed by Scanning Electron Microscope quanta 200. The ZnO which is prepared through precipitation method was calcined at different temperature. The morphology and structure are greatly affected by different temperature conditions. To study the morphology and its effects SEM has been done. From the study of sem images of ZnO, it was evaluated that by varying temperature, size of the particles changed. Two experiments were carried out by varying calcination temperatures at 250˚C and 350˚C and observing the effect on particle size. It is also explained that by the variation of calcination temperature particle size changed but nano ZnO had same crystal structure. ZnO particles were agglomerated at higher calcinations temperature and hence gradually increased the particle size.

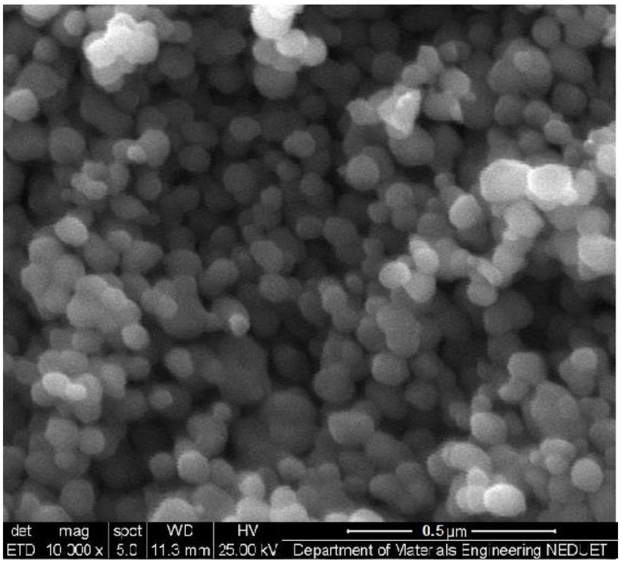

(a)

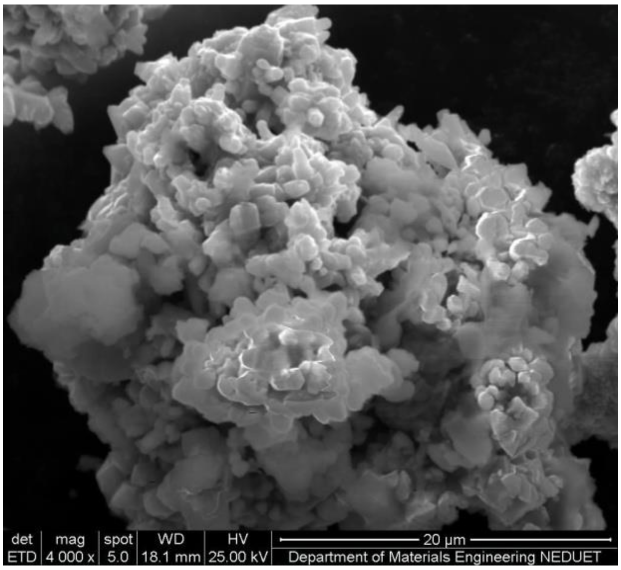

(b)

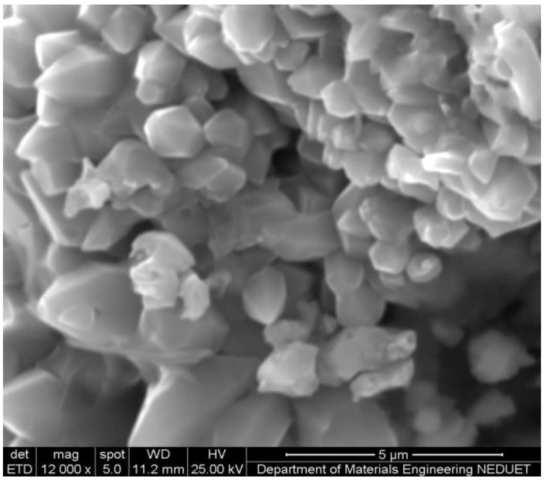

(c)

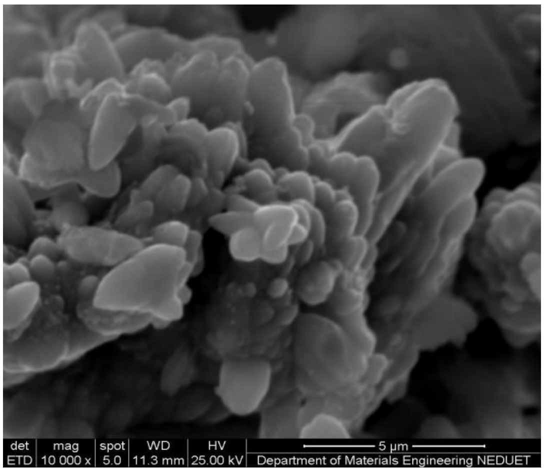

(d)

Figure 4. SEM images of ZnO

TiO₂

SEM images of titania was recorded on FEI quanta 200 model. Nano TiO2 was synthesized by ball milling of titania nano particles in the ethanol .the morphology of nano TiO2 was determined through the SEM ,which was found to be anatase and rutile phase.

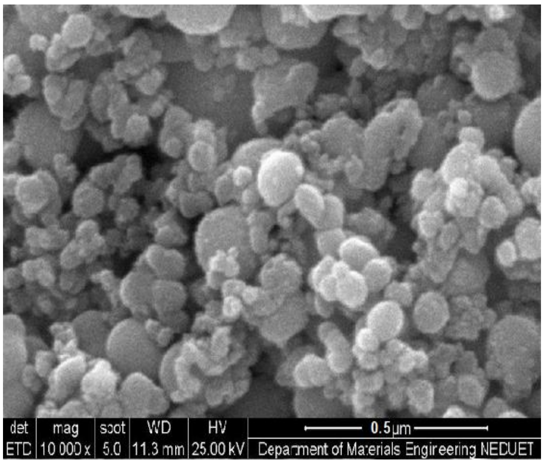

(a)

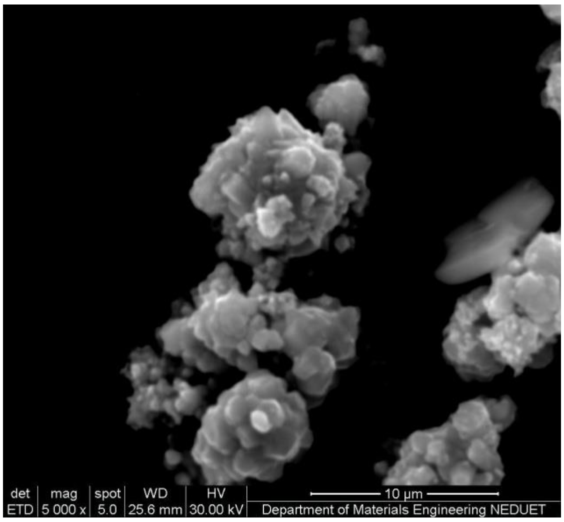

(b)

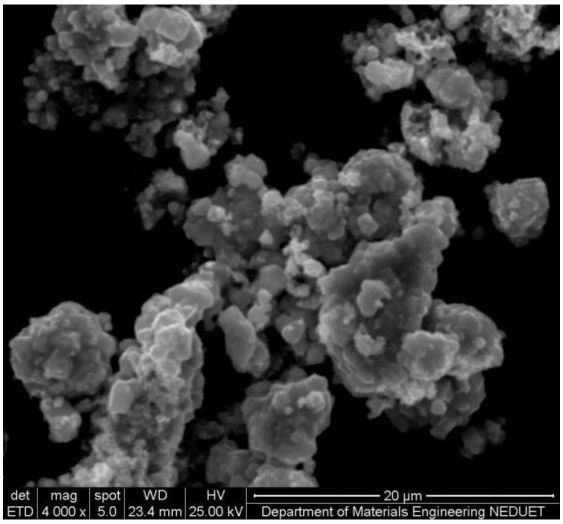

(c)

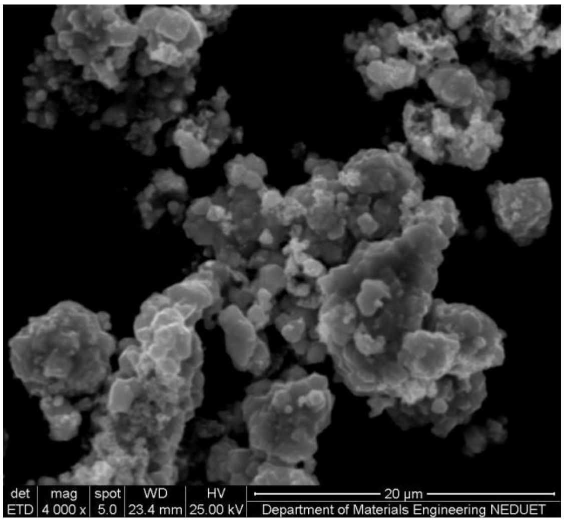

(d)

Figure 5. SEM images of TiO2

5.3. UV-Vis Spectroscopy :

ZnO :

The optical band gap *Eg* was estimated from ultraviolet diffuse reflectance spectroscopic studies (UV-DRS; Cintra UV–vis spectrophotometer) in a wavelength range from 200 nm to 800 nm.

UV-vis spectroscopy was carried out for zinc oxide nanoparticles calcined at 250˚C. The UV-visible absorption spectra of the sample is shown in Figure 6. below.

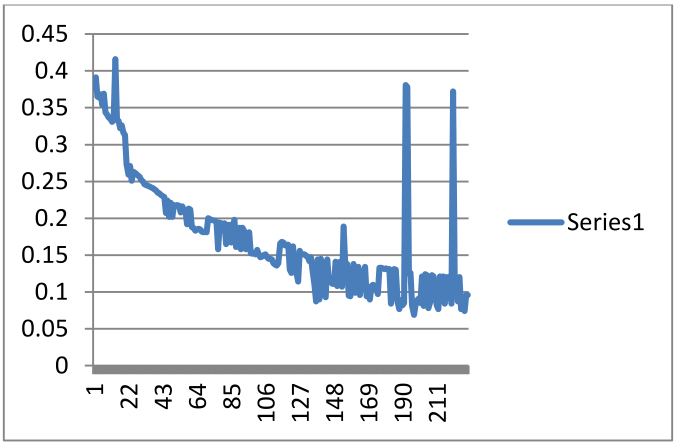

Figure 6. UV–vis absorption spectra of ZnO calcined at 250˚C temperature

The above figure shows the plot of wavelenth (x-axis-) vs. absorbance (y-axis). The samples showed a strong absorption maximum below 400 nm.

With an increase in calcination temperature, size of the particle increased but the band gap of ZnO decreased. The effect of temperature on the particle size and on the band gap of ZnO can be observed from the figure 6.

UV-vis spectroscopy was carried out for zinc oxide nanoparticles calcined at 350˚C. UV-visible absorption spectra of the sample is shown in Figure 6. below.

This shows that the particle size increases with increasing temperature. As temperature increases, the peak absorbance wavelength become red shifted due to decreasing quantum confinement with increasing particle size.

TiO2:

UV-vis spectroscopy was carried out for titania nanoparticle. UV-visible absorption spectra of the sample is shown in Figure 7. below.

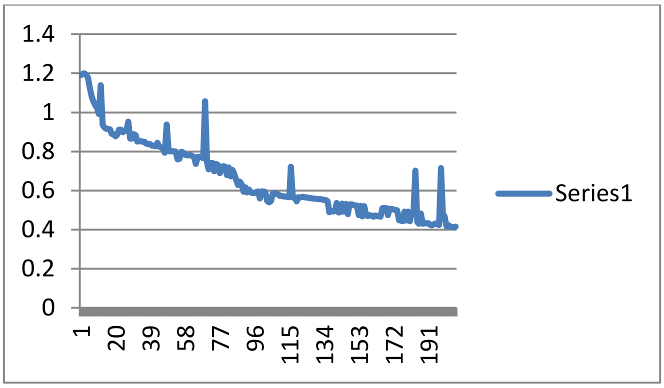

Figure 7. UV–vis absorption spectra of TiO_2

UV–vis directly provides some insight into the interactions of the photocatalytic materials (e.g. TiO_2) with photon energies The band gap energy of the titania samples was calculated by using this UV–vis DRS spectra with the equation, E (eV) = hc/λ = 1239.95/λ , where E is the band gap energy (eV), h is Planck's constant, c is the velocity of light (m/s) and λ is the wavelength in nm. It has also been reported that the increased band gap energy could be attributed to the effect of quantum size .

5.4. Visual Examination of Wood Pieces:

Effect of UV Light, Soil and Water:

Each of the sets was examined carefully. The three wood pieces of every set were examined visually to analyse the effect of UV exposure, soil and water. The pieces coated with ZnO and TiO_2 nanoparticles showed very little or no degradation and less color changes as compared to the untreated wood.

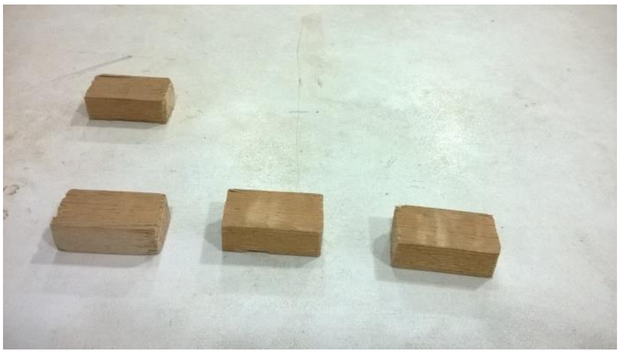

Figure 8. Coated wood specimens after exposure

Zinc oxide and titania coated wood pieces showed similar results.

6. CONCLUSIONS:

Precipitation method was successfully applied to synthesize ZnO nanoparticles with different sizes by varying the calcination temperature. The XRD and SEM analyses clearly indicate that highly pure ZnO (wurtzite) is formed by the above method. SEM images of ZnO showed that the morphology and particle size of nanoparticles was changed with calcination temperature.

The physical synthesis of TiO_2 through ball milling gave uniform shape and size and has proven to be an economical and robust process. The XRD pattern clearly identifies that only tetragonal (anatase) TiO_2 phase is present. SEM identified the morphology of titania nanoparticles. Thus, this study demonstrates the possibility of utilizing TiO_2 nanomaterial prepared by ball milling for coating purpose.

The performance of wood can be enhanced by incorporation of nanoparticles in the coatings. Untreated and isopropanol treated partal wood exhibited significant degradation of wood polymers due to UV light, soil and water which resulted in colour changes on wood surfaces. Dispersion of ZnO nanoparticles in isopropanol restricted the colour changes and photodegradation of wood polymers. This indicates potential of nanoparticle based wood coatings in future for providing protection from harmful UV radiation and environmental and weather changes in the outdoor environment.

REFERENCES :

[1] Surabhi Siva Kumar1*, Putcha Venkateswarlu2, Vanka Ranga Rao3 and Gollapalli Nagewsara Rao4., *"Synthesis, characterization and optical properties of zinc oxide nanoparticles"*, Kumar et al. International Nano Letters 2013, 3:30

[2] Jayashree Salla, Krishna K. Pandey*, Kavyashree Srinivas., *"Improvement of UV resistance of wood surfaces by using ZnO nanoparticles"*, Polymer Degradation and Stability 97 (2012) 592-596.

[3] B.C. Yadav1,2*, Tripti Shukla1, Satyendra Singh1 and T.P. Yadav3., "*Titania Prepared by Ball Milling: Its Characterization and Application as Liquefied Petroleum Gas Sensor"*

[4] Babita Baruwati, D. Kishore Kumar,Sunkara V. Manorama;"*Hydrothermal synthesis of highly crystalline ZnO nanoparticles:A competitive sensor for LPG and EtOH;*"Sensors and Actuators B 119, (2006) ,pg 676–682

[5] Khizar Hayata, M.A. Gondalb, , Mazen M. Khaleda, Shakeel Ahmedc, Ahsan M. Shemsid;"*Nano ZnO synthesis by modified sol gel method and its application in heterogeneous photocatalytic removal of phenol from water"*;Applied Catalysis A:General**,**Volume 393, 15 February 2011, Pages 122–129

[6] Zareen Abbasa, , Jenny Perez Holmberga , Anna Karin Hellstromb, Magnus Hagstromc, Johan Bergenholtza, Martin Hassellova, Elisabet Ahlberg;"*Synthesis, Characterization And Particle Size Distribution Of Tio2 Colloidal Nanoparticles*"; Colloids and Surfaces A: Physicochemical Eng. Aspects 384 (2011), pg 254– 261

[7] Hameed Ullah∗, Kabeer Ahmad Khan, Wasid Ullah Khan Department of Chemistry, Hazara University, Mansehra, KPK, Pakistan., "*ZnO/TiO2 Nanocomposite Synthesized by Sol Gel from Highly Soluble Single Source Molecular Precursor.*, Chinese Journal Of Chemical Physics Volume 27, Number 5 October 27, 2014

[8] Zafar Hussain Ibupoto *, Syed Muhammad Usman Ali Shah , Kimleang Khun and Magnus Willander., *"Electrochemical l-Lactic Acid Sensor Based on Immobilized ZnO Nanorods with Lactate Oxidase"* Sensors 2012, 12(3), 2456-2466; doi:10.3390/s120302456

[9] Gelareh Momen∗, Masoud Farzaneh., "*A ZnO-based nanocomposite coating with ultra water repellent properties,"* Applied Surface Science 258 (2012) 5723– 5728

[10] Abdulaziz Bagabas1*, Ahmad Alshammari1, Mohamed FA Aboud2 and Hendrik Kosslick3., *"Room-temperature synthesis of zinc oxide nanoparticles in different media and their application in cyanide photodegradation".*, Bagabas et al. Nanoscale Research Letters 2013, 8:516

[11] Bruna Martinello Savi, Larissa Rodrigues, Adriano Michael Bernardin., *" Synthesis Of Zno Nanoparticles By Solgel Processing".,*

[12] Ruoyu Honga,b,∗, Tingting Pana, Jianzhong Qiana, Hongzhong Lib., *" Synthesis and surface modification of ZnO nanoparticles".*, Chemical Engineering Journal 119 (2006) 71–81

[13] R.P.S. Chakradhara,∗, V. Dinesh Kumara, J.L. Raob, Bharathibai J. Basua., " *Fabrication of superhydrophobic surfaces based on ZnO–PDMS nanocompositecoatings and study of its wetting behaviour*"., Applied Surface Science 257 (2011) 8569– 8575.

MANUFACTURE AND CHARACTERISATION OF HONEYCOMB SANDWICHED CARBON FIBER REINFORCED POLYMER COMPOSITE

Taha Zafar[1*], M. Afnan Shakeel[1], Farrukh Fahim[1] and Danish Majeed[1]
1 Materials Engineering Department, NED University of Engineering & Technology,
Karachi, Pakistan

*Corresponding author. Tel.: +92 3223350338
E-mail address: *taha.zafar12@gmail.com*

ABSTRACT

A sandwiched composite is a unique type of composite materials that is manufactured by two stiff & thin sheets over thick and lightweight core. The material of the core is usually of low strength, but its greater thickness, results in a structural composite having high bending stiffness but overall low density. In this research, four layered thin sheet samples were manufactured from vacuum assisted resin transfer molding process (infusion), sample is composed of carbon fiber (200GSM/3 satin weave cloth) reinforced with epoxy (Araldite LY564/ Hardener XB3458). The infusion process was continued for eight hours and the samples were left to cure overnight with the vacuum pumps closed but the setup still sealed after the initial eight hours, they were removed the other day after a period of twenty four hours. The core material is a Nomex honeycomb (of thickness 8mm), both materials were sandwiched using epoxy resin. The manufactured final product was subjected to a variety of tests to determine their feasibility of operation in environments requiring exceptional strength and relatively harsh conditions while maintaining weight considerations. The SEM images of cloth fibers were obtained, micro hardness taken and routine mechanical tests (tensile, compressive, three point flexure tests) were conducted. The samples were further inspected for electrical and magnetic behavior by a variety of tests and the mode of failure for various samples was inspected under stereo microscope. From the tests, it was found that the final composite had a compressive strength of 99.2 MPa (modulus 156 MPa), flexural strength of 118 MPa (modulus 23.6 GPa), shore durometer hardness of 49-54 (d-scale) and tensile strength of 544 Mpa (elongation at break 1.71%). Furthermore, the sample was found to be moderately electrically conductive and offering little resistance to magnetic flux. In addition to the above, a thermal barrier coating was also developed consisting of alumina particles (5 micrometers) embedded in generic phenolic resin, two samples were coated by manual placement of the mixture on the sample's surface and provision of thermal energy for curing by placement inside muffle furnace. The samples were then exposed to temperatures ~400 for three minutes and afterwards subjected to compressive tests and found to be within limits of uncoated composite sample without heat exposure, which is around 98 Mpa, suggesting enhanced protection from heat.

Keywords: Sandwich panel, Honeycomb, Composite, Carbon fiber, Infusion, Alumina, Thermal Barrier Coating

1. INTRODUCTION:

Honeycomb sandwiched composites have remained popular within fields requiring materials with exceptional stiffness and compressive strength without adding unnecessary weight. Such structures are usually made from face sheets (glass fiber, carbon fiber, Kevlar para aramids) with the discontinuous bonding surface made from polymeric resins/foams and wood cores (mainly birch, balsa) forming the central part. In addition of being lightweight and stable, they are also low cost because of the optimal shape of honeycomb requiring lower material for optimized mechanical properties. Their properties are highly dependent upon the cell size, thickness and bonding between face sheets/sandwich materials. The other advantages of such structures are optimal weight to load bearing capacity, anti-shock properties, high rigidity combined with higher strength to weight ratio, increased fatigue life, better stability, thermal and acoustic insulation and better aesthetics.

The project includes manufacturing and subsequent testing of multi-purpose composite consisting of carbon fiber reinforced epoxy sandwiched by a DuPont's Nomex honeycomb structure, the carbon fiber part has four layers each 0/90 (bonded by epoxy resin) on top and bottom of Nomex. The final composite product is expected to have high stiffness to weight ratio, high strength to weight ratio, low density, high toughness, and high sound/vibration dampening properties, high EMI shielding, good thermal resistance and excellent environmental/chemical resistance. The composite will be manufactured by vacuum assisted resin transfer molding process (VARTM). The argument for using a honeycomb structure is because of their highly optimized design which provides the most strength for the least amount of material, hence the final product will have significant cost reduction when compared to the extensive layers of carbon fibers which would have been required if the whole composite was made of laminates, for the same level of properties.

Furthermore, the project envisages research and development of thermal barrier coating which can allow the composite to operate at temperatures above 500 C because even though carbon fiber have high temperature limits above 2000 C, most epoxy resins in which they are embedded will start to permanently degrade at significantly low temperatures of 200-250C range making the composite unable to be used in applications where high temperatures are a necessity. The prime candidate for such coating is alumina (aluminum oxide) embedded in phenolic resin.

2. MATERIALS AND METHOD

2.1. Core materials

The materials used for the project were procured from Space and Upper atmosphere research commission (SUPARCO) and Pakistan International Airlines (P.I.A.). The carbon cloth was three satin weave and rated at 200 deniers, the epoxy used was Araldite LY 564 with Hardener XB 3458. The Nomex honeycomb was acquired from PIA's reserve stock, of 8mm thickness and cell size 2 square meter (m2). The phenolic resin utilized for coating the sample was purchased locally and of generic nature. The alumina particles which were resin embedded for the coating, were acquired from Materials Engineering Department, N.E.D. University which purchased it from Benetec Limited, the approximate particle size was 5 micrometers.

2.2. Methods

The manufacturing process was completed at SUPARCO's composite manufacturing DTE, Karachi. The infusion (vacuum assisted resin transfer molding) process was successfully carried out within parameters earlier described in methodology chapter. The fiber cloth was manually cut with scissors, layers stacked over each other with flow media, perspirator and peel ply layers. The whole setup was isolated by means of vacuum bag with sealant tapes and left to cure for 24 hours. The finished product was then removed and dimensional measurements made. The final product had excellent surface finish (characteristic of infusion process) and coherent thickness.

A coating of the sample was prepared using alumina particles mixed with phenolic resin (at ratio 0.25/1) and placed manually on the sample, excess resin was drained off. Further it was cured inside an oven.

2.2.1. Scanning Electron Microscopy Images

The scanning electron microscope images of fibers (pulled from cloth) and machined dust was obtained at magnifications of 50x/200x/300x/400x/1200x and 50x/100x/110x at 1-2kV for both respectively on FEI Quanta 200 SEM microscope, MMD SEM Laboratory.

2.2.2. Shore Durometer

The sample was tested for hardness with shore durometer at D scale (Shore D) for a total of three values on each sides.

2.2.3. Compression and Flexural Testing

Both compressive and flexural testing were performed on Tinius Olsen 300KN, at the strain rate of 0.50 mm/min. A total of four tests were performed on samples of dimension 25x25 mm (width/thickness). The first two tests were performed on samples at normal conditions, the other one was performed after dipping the sample in Liquid Nitrogen (LN) for two minutes, normalized to room temperature by passive air circulation. The final test was a thermal test, designed to simulate the exposure of the composite to high temperature, the sample was coated with thermal barrier coating. First, the sample was placed inside a muffle furnace and heated to temperatures of 450C for three minutes. A single flexural three point bend test was performed on a sample with dimension 45x15 mm (width/thickness).

2.2.4. Determination of volume fraction and void content

A small piece of sample of dimension 25x25x10 mm was removed by hacksaw, weighed on digital balance and then burned in a muffle furnace at temperatures ~ 500C for 5 minutes, which resulted in ignition loss of the epoxy resin and honeycomb part, afterwards the remaining reinforcements were weighed again. The honeycomb sample (identical to the one used in the composite sample) was also weighed independently and its volume determined by Archimedes method. The weight percentages were calculated and volume fractions determined.

The void content was calculated by the formula:

Density = Mass / Volume

Volume fraction = Volume of individual components / Total composite volume

2.2.5. Determination of Magnetic properties

The magnetic characterization of the sample was performed on Lake Shore 480 Flux meter and Lake Shore 475 DSP Gauss meter, a small box made up of different small samples open on one end was utilized and readings were taken after placing a magnet (neodymium grade 40 with ceramic coating) inside the box. The three positions for the flux meter readings used were with slightly exposed magnet on the outside, middle placed magnet and with it completely touching the opposite end of the box. The two gauss meter readings were taken on slightly exposed and middle placed magnet.

2.2.6. Impact strength

The impact strength test was performed on the charpy tester under standard parameters and of dimensions 55x10 x10 mm. The test was performed on uncoated sample and under normal conditions.

3. RESULTS AND DISCUSSIONS

3.1. Volume fraction, void content

The mass of the sample (25x25x10 mm) was found to be 5.98g. After ignition loss (removal of resin and honeycomb) by placing the sample in a muffle furnace at temperatures ~ 500 C for 5 minutes, the remaining reinforcement (carbon fiber) was weighed again and its mass measured at 2.43g. The independently cut honeycomb piece was measured at 0.19g of dimensions 25x25x5 cm (similar to the one present in the sample). Its volume was determined to be 1 cm3 by Archimedes method, two measurements were made and their mean was taken. The weight percentage was calculated after dividing the mass of the fiber, resin and honeycomb with the total mass:

Weight percentage (fiber) = 2.43g/5.98g x 100
= 40.625%

Weight percentage (Nomex honeycomb)
= 0.2g/5.98g x 100
= 3.344%

Volume (composite) = 25 x 25 x 10 mm
= 6.25 cm^3

Volume (fiber) = Mass/Density
= 2.43g/1.6 = 1.518 cm^3

Volume (Nomex honeycomb)
= Mass/Density
= 0.19g/ 1.085 = 0.175 cm^3

Volume (resin + void) = Total volume – (volume of fiber and Nomex honeycomb)
= 6.25 cm^3 – (1.518+ 0.175) cm^3
= 6.25 cm^3 – 1.693 cm^3
= 4.557 cm^3

Mass (resin) = Total composite mass – Mass of (fibers + Nomex)
= 5.98g – (2.43 + 0.19) g
= 5.98g – 2.62g
= 3.36g

Volume (resin) = Mass/Density
= 3.36g/ 1.2 = 2.8 cm^3

Volume (voids) = 4.557 cm^3 – 2.8 cm^3
= 1.757 cm^3

Void content = 1.757 cm^3 / 6.25 cm^3 x 100
= 28.112%

Volume fraction of fiber
= 1.51 cm^3 / 6.25 cm^3 x 100
= 24.16%

Volume fraction of resin
= 2.8 cm^3 / 6.25 cm^3 x 100
= 44.8%

Volume fraction of Nomex honeycomb
= 0.175 cm^3 / 6.25 cm^3 x 100
= 2.8 %

3.2. Ultimate tensile strength

Since there was no tester available which could accurately measure the tensile strength of the composite, it was approximately determined from the volume fraction calculations multiplied by the manufacturer supplied/standard values of tensile strength for the individual constituents, as provided by the "rule of mixtures" method.

Ultimate tensile strength of composite sample

$= \sigma m \times Vm + \sigma f \times Vf + \sigma h \times Vh$

$$\begin{aligned} \text{UTS} &= 45(0.448) + 1600(0.241) + 85(0.028) \\ &= 20.16 + 385.6 + 2.38 \\ &= 408.14 \text{ Mpa} \end{aligned}$$

The ultimate tensile strength is comparable to Aluminum 6061-T6 alloys (310 Mpa range) [1] High strength steels – low carbon compositions strengthened with manganese (386-412 Mpa range) [2], 1018 Mild steel (439.8 Mpa range) [3] and Titanium alloy 3Al-2.5V-0.05Pd (510-620 Mpa range) [4] which is unusually high for a cored structure. However, this is important to mention that such materials aren't employed for design structures with a focus on tensile strengths.

3.3. Compressive strength tests

The compressive strength tests ran on Tinius Olsen 300 KN universal tester (on strain rate 0.50mm/min) on 25x25 (width x thickness) sample returned a value of 94 Mpa (103 Mpa modulus) and 99.2 Mpa (156 Mpa modulus), the low temperature compressive strength test (ran after dipping the sample of same dimension in a bath of Liquid nitrogen for 1.5 minutes and being allowed to return to room temperature) returned a value of 113.8 Mpa (150.7 Mpa) suggesting that extremely low temperatures (LN cryogenic fluid has a boiling point of -196C under standard conditions) had no detrimental effects on the compressive strength and actually slightly enhance it.

The fourth tests which was actually designed as a thermal test, was carried out after coating the sample with aluminum oxide embedded in phenolic resin and being exposed to temperatures ~ 450C for three minutes. The dimensions and test parameters remaining the same, the test returned a value of 98 Mpa (100.6 Mpa modulus) suggesting protection from heat as epoxy generally permanently degrades at temperatures above 220-250 C range. It is established that the coating allows the composite to continue working at much higher temperatures than epoxy/carbon fiber combination alone can permit.

The compressive values returned from all these tests are significantly higher to Concrete (17-28 Mpa range), High performance concrete (70-80 Mpa range) [5], Boron nitride (23.5 Mpa range) and comparable to Sandstone (10-120 Mpa range), Graphite (96 Mpa range), Marble (80-150 Mpa range) [6] and Granite (100-300 Mpa range) [7] with significantly less mass allowing for its usage in applications where weight is a concern. Furthermore, this material is suitable for applications at both low and high (after coating) temperatures unlike many materials which this material shows comparable compressive properties profile to.

3.4. Flexural strength tests

The flexural strength tests ran on Tinius Olsen 300 KN universal tester under standard parameters returned a value of 118 MPa (modulus 162 Mpa), a lower than expected value however this can be attributed to the force limitations of the universal tester.

The value is comparable to Graphite (50 Mpa range), [8] Steel AISI 1040 carbon steel (90 Mpa range) [9], Boron nitride (105 Mpa range) [10], Glass fiber reinforced epoxy (81-110 Mpa range) [11] and significantly higher than Concrete (4 Mpa range), Polypropylene (40 Mpa range) ABS Acrylonitrile butadiene styrene (70 Mpa range) [12].

3.5. Shore Durometer hardness test

The shore durometer hardness test performed on "d scale" on a small uncoated composite sample returned a value of 49-54 Shore D (the scale used for "harder plastics) demonstrating that the plastic based composite has a moderate hardness value. Its hardness is comparable to Polyurethanes (40-50 D range), metal forming die-pads (40-45 D range), Golf balls (50 D range), and Solid truck tires (50 D range) [13] and significantly lower than Polypropylene (68-70 D range), Polystyrene (75 D range), Nylon (80 D range), Polyamide (40-100 D range) and Polycarbonate (over 100 D range). [14]

3.6. SEM images of Carbon fiber

The SEM images were obtained from fibers pulled out of carbon fiber cloth on FEI Quanta 200 on different magnifications. The images show extremely thin strands of graphitic carbon held together as a single fiber around 5-10 micrometer in diameter in a highly aligned manner in microscopic crystal alignment, a large number of which can then be woven into a cloth, a reason for the carbon fiber's immense strength as the number of defects are lower.

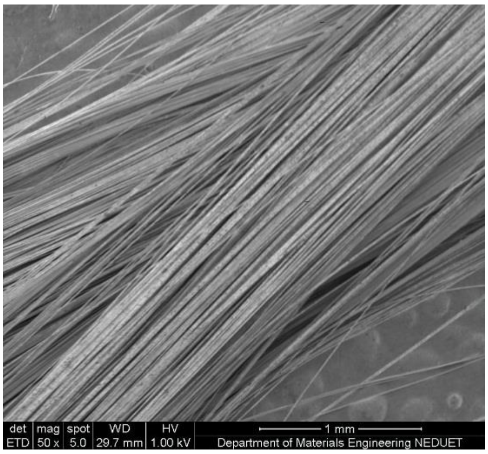

Fig 3.1 Mag 50x and HV 1.00 kV

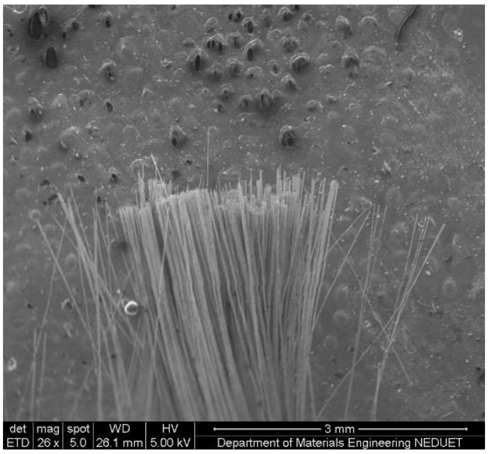

Fig 3.2 Mag 26x and HV 5.00 kV

3.7. Magnetic properties

The magnetic properties of the composite sample were determined on the Lake Shore 480 Flux meter and Lake Shore 475 DSP Gauss meter from a small box made from uncoated samples which was open at one end. The readings on the neodymium grade 40 magnet (ceramic coated on one end for easy handling) were measured 380 milliteslas (mT) for the uncoated side and 88.7 milliteslas (mT) for the coated side.

The readings taken for the fluxmeter for slightly exposed magnet with the other half lying inside the box were -18.34 milliteslas (mT) – first position, for the magnet placed at the center for the box were -17.37 milliteslas (mT) – second position and for the magnet placed at the other end of the box touching its other side were -15.47 milliteslas (mT) – third position. The readings demonstrated a percent change (decrease) of -104.82% between a magnet placed outside and first position, 5.28% (increase) between first position and second position, 10.93% (increase) between second position and third position.

The gauss meter readings for the magnet only was 3800 gauss (Gs) and for the first and second positions were -174.09 Gauss (Gs) and -176.31 Gauss (Gs). The percent change between the outside placed magnet and the first position readings were -104.58% decrease and -1.27% decrease between first and second position.

3.8. Impact testing

The charpy impact test on standard parameters on the composite sample (uncoated) was 67J for a sample of dimension 55 x 10 x 10 mm. The results of the tests are comparable to Steel NST-37-2 annealed (64.10J) [15], Titanium 4Al-3Mo-1V alloy (67.79J) [16] and Maraging Steel grade 250 (69.14J) [17] while being significantly higher than 2024 Al (14.914J) [18], Aluminum alloy Mg enhanced AC2A (12J) [19] and standalone carbon fiber composite (2.36J) [20]. The impact testing results are significantly higher but they are to be expected considering the cored structures which is excellent at absorbing energy and dissipating it inside the hollow center, also the Nomex honeycomb sandwiched CFRP shows a dramatic improvement over the energy absorbance of the standalone carbon fiber composite.

4. CONCLUSION

The Nomex honeycomb sandwiched carbon fiber reinforce polymer composites shows an interesting array of properties, which even not being significant are still higher than the average in most cases, while being low in weight, environmentally/chemically resistant, relatively low cost (than other composites of same dimensions) and tolerant to a wide range of working temperatures. The compressive strengths remained around the range of around ~100 Mpa for all tests conducted under normal conditions, low and high temperatures (after being coated) showing weight to loadbearing capability. Its hardness is moderate in range and doesn’t increase by a wide margin after coating the sample. The flexural and impact strength were significantly high owing to the cored center and benefited most from the cored structure with lower thickness than compared materials. The tensile strength is also comparable with high end aluminum and titanium alloys. The sample doesn’t allow the magnetic flux to penetrate through by a significant margin allowing for its use where shielding from magnetism is a requirement. Also, it does it all while maintaining the specific strength, high rigidity, thermal stability and aesthetic. The developed coating furthermore allowed the sample to successfully raise the working temperature to 450 C for long periods of time, an essential enhancement from the limitations of the epoxy matrix.

ACKNOWLEDGMENT:

The author would like to thank Space and Upper atmosphere research commission (SUPARCO) and the Materials Engineering department for manufacturing and testing facilities.

REFERENCES

[1] Tensile strength, American machine tools (http://www.americanmachinetools.com/tensile_strength.htm)

[2] High Strength Steels, ArcelorMittal (http://automotive.arcelormittal.com/repository2/Automotive_Product%20offer/HighStrengthSteels.pdf)

[3] AISI 1018 Mild/Low Carbon Steel, AZO materials (http://www.azom.com/article.aspx?ArticleID=6115)

[4] Titanium alloy guide, RTI metals (http://www.rtiintl.com/Titanium/RTI-Titanium-Alloy-Guide.pdf)

[5] Testing compressive strength of concrete, NRMCA (http://www.nrmca.org/aboutconcrete/cips/35p.pdf)

[6] Material Properties Charts, Ceramic industry (https://www.ceramicindustry.com/ext/resources/pdfs/2013-CCD-Material-Charts.pdf)

[7] Compression and Tension Strength of some common materials, The engineering toolbox (http://www.engineeringtoolbox.com/compression-tension-strength-d_1352.html)

[8] Properties and Characteristics of Graphite, Entegris (https://www.entegris.com/resources/assets/6205-7329-0513.pdf)

[9] Flexural and Peel Properties of High Performance Magnesium/Carbon/Fiber/PEEK Laminated Composites, M.C. Kuo et all, Key Engineering Materials Vols. 274-276 (2004), pp.1153-1159 (http://www2.nsysu.edu.tw/MSE/papers/Paper%20in%20PDF/87%20Key%2025769%20%282004%29.pdf)

[10] Investigation of the Physical and Mechanical Properties of Hot-Pressed Boron Nitride/Oxide Ceramic Composites, Rodney W truce et all, Journal of the American Ceramic Society 09/1999, 82(9):2563-2565 (http://deepblue.lib.umich.edu/bitstream/handle/2027.42/66372/j.1151-2916.1999.tb02123.x.pdf?sequence=1)

[11] Tensile and flexural strength of glass fiber epoxy composites, S. Pichi Reddy et all, International Conference on Advanced Materials and manufacturing Technologies (AMMT). December 18-20, 2014, JNTUH College of Engineering Hyderabad (http://jntuhceh.org/web/tutorials/faculty/479_ic21-2014.pdf)

[12] Material Datasheets - Flexural Strength, Rutland Plastics (http://www.rutlandplastics.co.uk/advice/materials_datasheets_flex.html)

[13] Hardness of Rubber: Durometer, RubberMill (www.rubbermill.com/PDFs/tech/durometer.pdf)

[14] What is Durometer?, Freelin wade (4tsi.com/wp-content/uploads/2012/10/What-is-Durometer.pdf)

[15] Effect of Heat Treatment on Mechanical Properties and Microstructure of NST 37-2 Steel, D.A Fadare et all, Journal of Minerals

& Materials Characterization & Engineering, Vol. 10, No.3, pp.299-308, 2011 (www.scirp.org/journal/PaperDownload.aspx?paperID=20854)

[16] Mechanical properties of titanium and aluminum alloys at cryogenic temperatures, Charles F Hickey Jr, Watertown Arsenal Laboratories, March 1962 (http://www.dtic.mil/dtic/tr/fulltext/u2/a951335.pdf)

[17] Tensile and impact properties of some Maraging steel compositions, J.E. Sprawley et all, U.S. Naval research laboratory, April 23 1963 (http://www.dtic.mil/dtic/tr/fulltext/u2/404495.pdf)

[18] Notched Bar Impact Testing of Materials, California State university (http://www.csun.edu/~bavarian/Courses/MSE%20227/Labs/2-Charpy_Impact-modified%202013.pdf)

[19] Effect of Mg enhancement in the microstructure and mechanical properties of AC2A Aluminum alloy, Niyas Salim et all, International Journal of Research in ISSN(E): 2321-8843; ISSN(P): 2347-4599 Vol. 2, Issue 2, Feb 2014, 139-148 (http://www.impactjournals.us/download.php?fname=2-77-1392522052-16.%20Eng-Effect%20of%20Mg%20Enhancement%20in%20the%20Microstructure-Niyas%20Salim.pdf)

[20] Impact strength and toughness of fiber composite materials, Lawrence J Broutman et all, Airforce office of scientific research, November 1972 (http://www.dtic.mil/dtic/tr/fulltext/u2/753101.pdf)

GREEN SYNTHESIS AND CHARACTERISATION OF ZINC OXIDE NANOPARTICLES USING ALOE VERA

Huba Kamal[1*], Yusra Mohi Khan[1], Mehwish Naeem[1] and Danish Majeed[1]
[1]Materials Engineering Department, NED University of Engineering & Technology, Karachi, Pakistan

[*]Corresponding author. Tel.: +92345-8890099;
E-mail address: mishyushubs@gmail.com

ABSTRACT

Green nanotechnology offers the chance to take off unfriendly impacts before they happen. Green synthesis of nanoparticles is a bottom-up approach of synthesis and usually involves pollutant free chemicals and embraces the use of eco-friendly solvents such as water, natural extracts. The present study reports the synthesis of Zinc Oxide nanoparticles by an eco-friendly, simple route Nanoparticles of size range 94-132 nm have been synthesized using Zinc Nitrate {Zn $(NO_3)_2.6H_2O$} and aloe vera as a benign (harmless ,not malignant or disease-causing) reducing agent. X-Ray Diffraction and UV-Vis Spectroscopy have been utilized for characterization while particle size was calculated using Debye Scherrer formula. Images from Scanning Electron Microscopy showed granular like structure of nanoparticles that were clustered and an absorption of 368 nm was exhibited by the UV-Visible Spectrum.

Keywords: Zinc Oxide; Nanoparticles; Aloe vera; Green Synthesis; Characterisation

1 INTRODUCTION

Nanoscience in the past few years has gained a great deal of attention globally for its extensive applications and versatile properties in various fields. Although many routes (physical, chemical and mechanical) have been devised for the synthesis of nanoparticles; a recent shift of attention has been diverted towards the natural or the green route. Being highly versatile in matters of acquiring morphology, Zinc oxide is a semi-conductor by nature having a band gap of approximately 3.37 eV [1]. It shows adequate thermal and optical properties. A wide variety of fields make use of this nanomaterial for applications like electronics, cosmetics, drug transfer, chemical biological sensors and many more. In medicine ZnO nanoparticles exhibits a high degree of cancer cell selectivity with the ability surpass the therapeutic indices of some commonly used chemotherapeutic agents. They are used in paints, cosmetics like sunscreens, plastic and also in rubber manufacturing, in electronics equipment including Solar cells, gas sensors, light emitting devices, photo-catalysts and pharmaceuticals products. In industrial sectors such as synthetic textiles, food packaging, medical care, as well as for construction purpose.

Not only that nano ZnO particles have a vast range of applications, their ability to acquire various shapes also allows them this versatility. Different shapes like tubes, pillars, spirals, flowers, cups, donut and more are highly interesting and fascinating [2].

Green nanotechnology can proactively impact the nanomaterials design and by-products by getting rid of or minimizing contamination generated during the synthesis of nanomaterials, taking into account the life cycle approach to nano-products, to gauge and mitigate where ecological effects may happen in the product chain, designing toxicity out of nanomaterials and utilizing nanomaterials to treat or remediate existing ecological problems. Green nanotechnology does not emerge de novo; rather, it expands on the standards of green science and engineering and centres them through another lens on the novel and frequently counterintuitive impacts that happen in nano-scaled materials [3].

This process has proven to be more effective than the usual chemical and physical methods, for these methods are costly and in chemical synthesis various toxic products get adsorbed on the particle surface which prove to be hazardous when considered for medical fields.
Synthesizing nanoparticles via green method basically involves three steps:

(a) Selection of a suitable solvent medium.
(b) A reducing medium that is eco-friendly.
(c) Components that have minimum or least toxic content for nanoparticles synthesis [4].

Green synthesis of ZnO is an environment friendly, biocompatible, inexpensive, less time consuming process that produces nontoxic by-products. ZnO nanoparticles can be synthesized by many plants like aloe vera [5], olives [6], green tea [7] and many more.

2 MATERIALS AND METHODS

Zinc Nitrate Hexahydrate {$Zn(NO_3)_2.6H_2O$} was purchased from Daejung chemical & metal Co.,Ltd, Korea while fresh aloe vera leaves were obtained from a local nursery. Beakers and equipment were provided by Materials Engineering Department. Glassware was properly washed with distilled water and dried before use. Synthesis procedure was derived from works of Phyu Phyu Win [8]

2.1 Preparation OF Extract

Leaves collected from the aloe vera plant were washed several times with distilled water to remove the dust particles. Extract was prepared by boiling finely cut slices of aloe vera leaves in 100 ml distilled water and then filtered. The filtrate was used as aloe vera extract.

2.2 Synthesis of Nanoparticles

Nanoparticles were synthesized by dissolving 3g of Zinc Nitrate Hexahydrate in 30 ml of the aloe vera extract. The solution was than stirred for 20 minutes on a magnetic stirrer. The temperature was maintained at 65°C. After 20 minutes the solution was placed in furnace at 500°C for one hour. The resultant mass was grounded and stored in air tight container for further characterisation.

Table 1. Amount of Reactants for synthesis

Materials	Quantity
Zinc Nitrate	3 g
Distilled water	100 ml
Aloe vera leaves	35 g
Extract for experiment	30 ml

2.3 Characterisation

Phillips PANalytica was used to obtain the diffraction pattern of the synthesized yellow powder of ZnO nanoparticles. Morphology images of the end product were observed in Quanta 200 FEI Scanning Electron Microscope.

3 RESULTS AND DISCUSSIONS

Experimentation was done several times in small and bulk quantities to recheck the synthesis of the granular nanoparticles and its confirmation was obtained using the afore mentioned characterisation techniques.

3.1 X-Ray Diffraction

The diffraction pattern (Fig 1) of as received powder shows peaks at 2θ values of 31.782210°, 34.429230°, 36.272940°, 47.585380°, 62.914430°, 67.942200° and 72.641750° which is in agreement with JCPDS File no.5-0566.

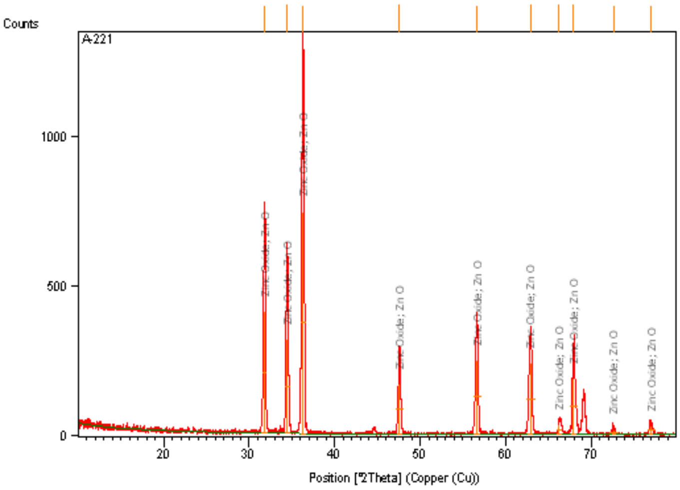

Fig 1 – XRD Pattern of Zinc Oxide

This confirmed the successful synthesis of ZnO compound.

Particle size

Nanoparticles of size range 94-132 nm were synthesized and it was determined using the Debye-Scherrer equation [9].

$$D = \frac{k\lambda}{\beta \cos\theta}$$

Where, 'λ' is wave length of X-Ray (Cu K-Alpha1 [Å]: 0.1541 nm), 'β' is FWHM (full width at half maximum), 'θ' is the diffraction angle and 'D' is particle diameter size.

3.2 Scanning Electron Microscopy

The Scanning electron microscopy images of the yellow powder revealed incomplete rod like structures as shown in {Fig 2(a), (b), (c)}. This morphology was found to be granular-like [10] and agglomeration was also observed.

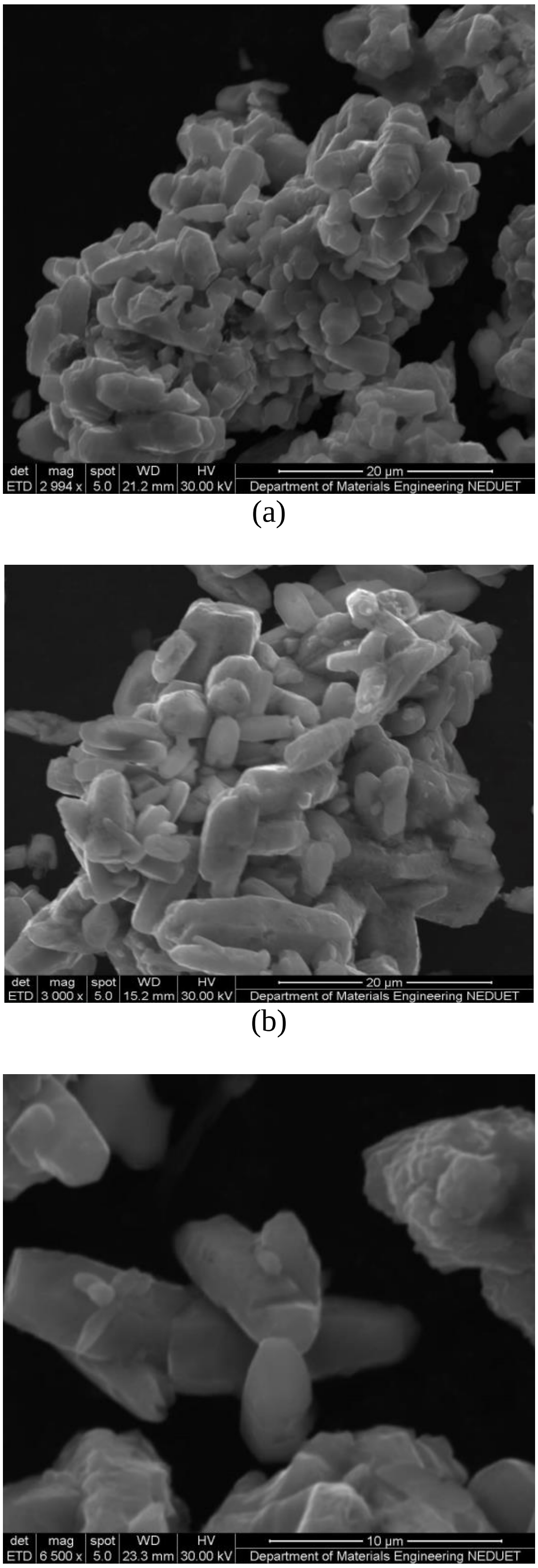

(a)

(b)

(c)

Fig 2 – (a), (b) & (c) Granular morphology of ZnO nanoparticles

3.3 UV-Vis Spectroscopy

UV-Vis of the synthesized powder confirms the formation of Zinc Oxide. The maximum absorption exhibited by the sample was 368 nm (Fig 3) which falls in the range of absorption exhibited by nano ZnO i.e. 358-375 nm [11].

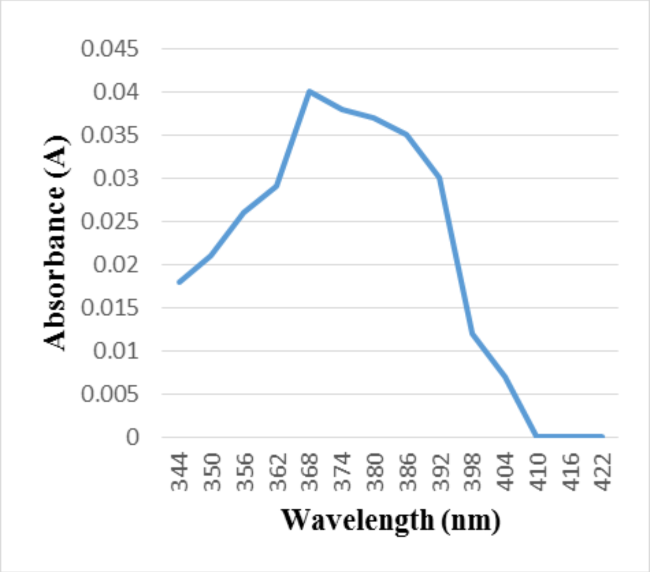

Fig 3 – UV-Vis Spectra of ZnO nanoparticles showing maximum absorption at 368 nm.

4 CONCLUSION

The synthesis of Zinc Oxide nanoparticles was a success using aloe vera as a reducing agent. XRD data confirmed the compound formation with an average particle size of 110.32 nm. The UV-Visible absorption spectra indicated maximum absorption at 368 nm which is characteristic of Zinc Oxide nanoparticles. The particles exhibited a granular like morphology that was imaged using Scanning Electron Microscopy.

ACKNOWLEDGEMENTS

All praises and glories to Almighty ALLAH who bestowed mankind with knowledge and wisdom. We would like to show our deepest gratitude to the Chairman of Department of Materials Engineering for allowing us to carry out this study. Our sincerest thanks to our supervisors and department staff for their contribution in stimulating suggestions that helped us to co-ordinate this project.

REFERENCES

[1] Siavash Iravani and Zolfaghari; *“Green Synthesis of Silver Nanoparticles Using Pinus eldarica Bark Extract”*; Hindawi Publishing Corporation BioMed Research International Volume (2013).

[2] G .C. Yi, C. Wang, W. Park*; "Znonanorods: synthesis, characterization and applications"*; Semiconductor Science and Technology (2005); 22-34.

[3] Schmidt F. Karen; *"Green Nanotechnology: It's Easier Than You Think"*; Project on Emerging Nanotechnologies, PEN (2007); **8**; 11-15.

[4] Vadlapudi Varahalarao, Behara Mohan, Devamma NagalakshmiM.; *"Green Synthesis and Biocompatibility of Nanoparticles*"; Rasayan J. Chem (2014); **7**; 219-223.

[5] Jeeva Lakshmi V*, Sharath R, Chandraprabha MN, Neelufar E, Abhishikta Hazra, Malyasree Patra; *"Synthesis, characterization and evaluation of antimicrobial activity of zinc oxide nanoparticle";* J Biochem Tech (2012); **3(5);** 151-154.

[6] Akl. M Awwad[1]*, Borhan Albiss[2], Ahmad L. Ahmad[1]; *"Green synthesis, characterization and optical properties of zinc oxide nanosheets using Olea europea leaf extract"*; Advance Materials Letters (2014).

[7] S.R. Senthilkumar, T. Sivakumar*; "Green Tea (Camellia Sinensis) Mediated Synthesis of ZinC Oxide (ZnO) Nanoparticles and studies on their Antimicrobial Activities"*; International Journal of Pharmacy and Pharmaceutical Sciences (2014); **6(6);** 461-465.

[8] Phyu Phyu Win*, MyintSanda Win; "*Synthesis of Zinc oxide nanoparticles by Precipitation Method and Simple Heating Method"*

[9] T. Theivasanthi, M. Alagar*;" X-Ray Diffraction Studies of Copper Nanopowder"*; Department of Physics, PACR Polytechnic College.

[10] Chih-Wei Tang; *"Study of Photocatalytic Degradation of Methyl Orange on Different Morphologies of ZnO Catalysts"*; Modern Research in Catalysis (2013); **2(2);** 19-24

[11] Guanalan Sangeetha, Sivaraj Rajeshwari, Rajendran Venckatesh; " *Green synthesis of Zinc Oxide Nanoparticles by aloe barbadensis miller leaf extract; Structure and Optical Properties";* Materials Research Bulletin (2011); **46**;2560-2566.

SIMULATION, OPTIMIZATION AND ECONOMIC ANALYSIS OF PLATFORMER PLANT

Muhammad Humayun[1], Syed Aijaz Rasool[1], Muhammad Obaidullah Hashmi[1], Areeb Akmaal[1], Rizwan Ahmed Qamar[1*], Engr. Shaikh Abubakr[2].
[1]Chemical Engineering Department, NED University of Engineering & Technology, Karachi, Pakistan

[*]Corresponding author. Tel.: 0331-3966739, +923422621167
E-mail address: rizwanaq@neduet.edu.pk

ABSTRACT

This work is basically related to plat-former unit of an oil refinery. The refinery is using a semi-regenerative catalytic reformer, for the reforming of low octane heavy naphtha into a finished product of octane number up to 95. The existing facility includes a plate and frame heat exchanger (PACKINOX) for the preheating of feed stream. In this work an optimized shell and tube heat exchanger network design is proposed against packinox, as a pre heating facility for the plant.

The basic goal of this work was to simulate the whole plant with rating and optimizing the heat exchanger network which is specifically used to pre-heat the incoming feed mixture, containing heavy naphtha and recycled hydrogen by using reactor effluent stream as a hot stream. For this initially a complete separate simulation is made of plat-former plant using Aspen Hysys simulation software and then Aspen EDR (exchanger design and rating) software is used for optimum design of heat exchangers train. A random search optimization technique is used in suggesting the specifications of heat exchangers. For maximum heat recovery and minimum external heating and cooling load requirements, pinch analysis and process integration is done on all the hot and cold streams. The cost comparison between designs using exchangers of different sizes and of same size is also done. After the selection of exchangers ,a cross check of the software calculation, i.e. pressure drop and vapour fractions in tubes and shell sides, is also done by designing only two exchangers using Microsoft excel with EDR specifications. A pre heating network of total 13 shell and tube heat exchangers with shell diameter 35 inches (10 exchangers) and 38 inches (3 exchangers) are selected as optimum design with total cost of $2614775 and minimum heating load requirement is of 12530KW. A payback analysis technique is also used to find the economical feasability of this project.

Keywords: Simulation; Optimization; Pinch; Exchanger design and rating; cost; payback

1. INTRODUCTION

Catalytic reforming is a chemical process used to convert petroleum refinery naphthas, typically having low octane ratings, into high-octane liquid products called reformates which are components of high-octane gasoline (also known as petrol). Basically, the process rearranges or restructures the hydrocarbon molecules in the naphtha feedstocks as well as breaking some of the molecules into smaller molecules. The overall effect is that the product reformate contains hydrocarbons with more complex molecular shapes having higher octane values than the hydrocarbons in the naphtha feedstock. In so doing, the process separates hydrogen atoms from the hydrocarbon molecules and produces very significant amounts of by-product hydrogen gas for use in a number of the other processes involved in a modern petroleum refinery. Other by-products are small amounts of methane, ethane, propane and butanes. This process is quite different from and not to be confused with the catalytic steam reforming process used industrially to produce various products such as hydrogen, ammonia and methanol from natural gas, naphtha or other petroleum-derived feedstocks. Nor is this process to be confused with various other catalytic reforming processes that use methanol or biomass-derived feedstocks to produce hydrogen for fuel cells or other uses.

This process includes preheating of heavy naphtha feed mixed with recycled hydrogen gas to reactor inlet temperature i.e. 1000°F by exchanging heat mostly from reactor effluent and remaining load is achieved from furnace.

2. SIMULATION

Aspen Hysys is used for the simulation of complete plant. A template of refinary reformer is already included in Hysys package but it is not used as it only gives final product specifications by taking feed specifications but as the composition of third reactor effluent is require(for further calculations), we are building our own simulation diagram.

As all the reactors in simulation sheet can only deal in pure components so feed is used in this form instead of pseudo components. The feed composition is illustrated in table 1

Table 1 Feed Composition

COMPONENTS	Vol%
Total iso parafins	35.34
Total n parafins	32.11
Total naphthenes	16.71
Total aromatics	15.84

Feed temperature and pressure is 243°F and 440 psia with volumetricc flow of 31550barrels/day which then mixed with Hydrogen gas, which is collected from the top of stabalizer. Initially H2/HC ratio is set at ‘3 lbmol/lbmol’ then in the end it automatically adjusted to 1.3 by recycle logic operation.

The existing plant consists of tree reactors in which a number of different rections are occuring. All these reactions cannot be solved by any one type of hysys reactor so each reactor is splitted into two reactors i.e. a conversion and an equilibrium reactor. All the hydrogenation reactions (mostly cracking reactions) are included in conversion reactor and equilibrium reactions in equilibrium reactor. The feed is first entered in conversion reactor and all the cracking is assumbed to occur in the starting as hydrogen pressure at inlet is very high and it decreases as hydrogen consumed along the reactors. Temperature of each reactor is set to 1000F by preheating feed stream by third reactor effluent and then by passing the feed stream through fire heater. Third reactor oultlet stream is then cooled to 100F and flashed to separate hydrogen gas which is then recycled and mixed with feed stream. The bottom product of flsah separator is then distilled to give product of RON 102. (Standard ‘RON’ in simulation ranged from 102-107)

3. OPTIMIZATION

Process optimization is the discipline of adjusting a process so as to optimize some specified set of parameters without violating some constraint. The most common goals are minimizing cost, maximizing profit, and/or efficiency. This is one of the major quantitative tools in industrial decision making.Here ‘Pinch analysis and process integration’ is used for the optimization of exchanger network and for external heating and cooling loads.

4. PINCH ANALYSES AND PROCESS INTEGRATION:

Pinch analysis is a methodology for minimising energy consumption of chemical processes by calculating thermodynamically feasible energy targets (or minimum energy consumption) and achieving them by optimising heat recovery systems, such as heat exchangers, energy supply methods and process operating conditions. It is also known as process integration, heat integration, energy integration or pinch technology. In other words pinch is something which describes deficiency, here in heat pinch analysis the pinch suggests the minimum or zero temperature difference in heat exchanger arrangements. [1]

Calculation of pinch temperature

Stream splitting

For the pinch calculations, the value of specific heat of any particular stream should be constant, but in our simulation the values of specific heat are the function of temperature and the streams are being condensed and vaporized as well. So the solution for this is to split one single stream into several streams. This is the most complicated and most sensitive part of pinch analysis. It is clear that data errors are most significant at the pinch. The idea of stream splitting is taken from chapter no. 09 of pinch analysis and process integration by Ian C. Kemp.

Table 2 Stream Tempratures

Stream ID in simulation sheet	Description of stream	Initial temperature (degree C)	Target temperature (degree C)
Stream-mf	Mixed feed	105	537.8
Stream-27	Reactor-3 effluent	527.4	37.78
Stream-36	De-pentanizer inlet	38.48	130
Stream-42	Bottom product of depentanizer	203.1	124.7
Stream-03	Bottom product to storage	124.7	37.78

Choosing ΔT_{min}

This is a fact that higher values of ΔT_{min} gives the higher values of heating and cooling loads and it therefore seems that we want a ΔT_{min} as low as possible, to give maximum energy efficiency. However, there is a drawback; lower ΔT_{min} values give larger and more costly heat exchangers. In a heat transfer device, the surface area A required for heat exchanger is given by equ (1):

$$A = \frac{Q}{U \Delta Tlm} \qquad (1)$$

A is in m^2, Q is the heat transferred in the exchanger (kW), U is the overall heat transfer coefficient (kW/m^2K) and ΔT_{LM} is the log mean temperature difference (K). As the heat exchanger area is usually inversely proportional to the temperature difference. Hence, low values of ΔT_{min} can lead to very large and costly exchangers, as capital cost is closely related to area.

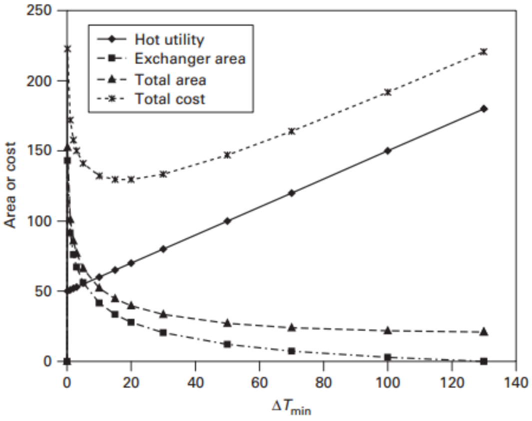

Figure 1 ΔT_{min} vs Area and Cost

Figure 1 shows the relation of ΔT_{min} with area and cost. (This is just a rough relation) [1]. Often a value of 10°C to 20°C of ΔT_{min} is best but in some industries a very low or very high value is appropriate

Here we are using ΔT_{min}=15°C.

Pinch analysis problem data

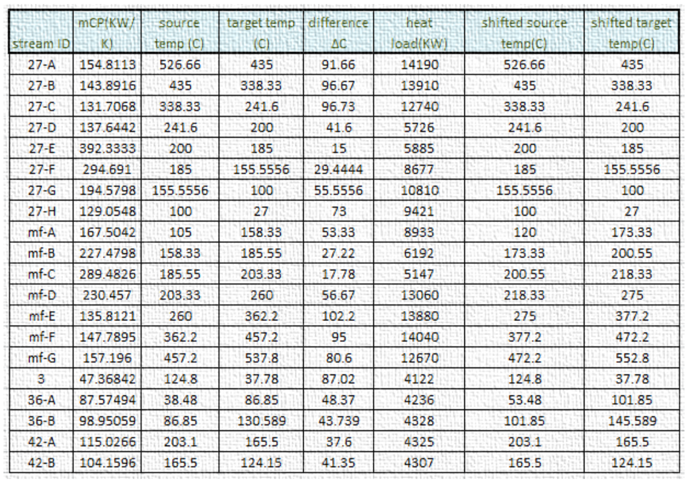

stream ID	mCP(KW/K)	source temp (C)	target temp (C)	difference ΔC	heat load(KW)	shifted source temp(C)	shifted target temp(C)
27-A	154.8113	526.66	435	91.66	14190	526.66	435
27-B	143.8916	435	338.33	96.67	13910	435	338.33
27-C	131.7068	338.33	241.6	96.73	12740	338.33	241.6
27-D	137.6442	241.6	200	41.6	5726	241.6	200
27-E	392.3333	200	185	15	5885	200	185
27-F	294.691	185	155.5556	29.4444	8677	185	155.5556
27-G	194.5798	155.5556	100	55.5556	10810	155.5556	100
27-H	129.0548	100	27	73	9421	100	27
mf-A	167.5042	105	158.33	53.33	8933	120	173.33
mf-B	227.4798	158.33	185.55	27.22	6192	173.33	200.55
mf-C	289.4826	185.55	203.33	17.78	5147	200.55	218.33
mf-D	230.457	203.33	260	56.67	13060	218.33	275
mf-E	135.8121	260	362.2	102.2	13880	275	377.2
mf-F	147.7895	362.2	457.2	95	14040	377.2	472.2
mf-G	157.196	457.2	537.8	80.6	12670	472.2	552.8
3	47.36842	124.8	37.78	87.02	4122	124.8	37.78
36-A	87.57494	38.48	86.85	48.37	4236	53.48	101.85
36-B	98.95059	86.85	130.589	43.739	4328	101.85	145.589
42-A	115.0266	203.1	165.5	37.6	4325	203.1	165.5
42-B	104.1596	165.5	124.15	41.35	4307	165.5	124.15

Figure 2 Streams' Specific Heats

Grand composite curve

A graph of net heat flow (utility requirement) against shifted temperature can then easily be plotted. This is known as the grand composite curve (hereafter abbreviated to GCC). It represents the difference between the heat available from the hot streams and the heat required by the cold streams, relative to the pinch, at a given shifted temperature. GCC for problem data is shown in Figure 3

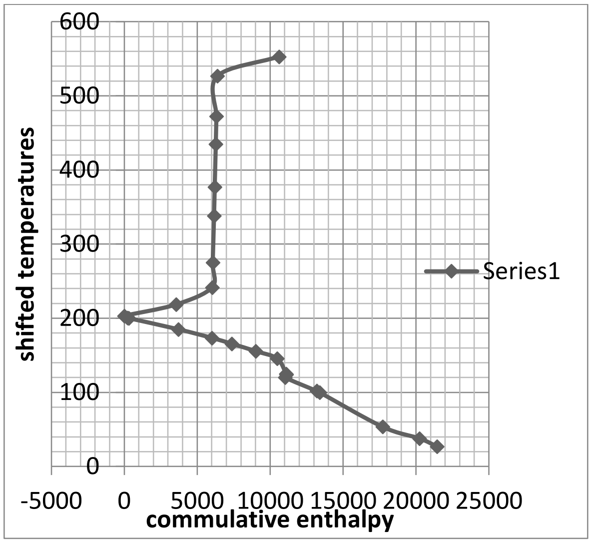

Figure 3 Grand Composite Curve

The pinch temperature is found to be 203.1C i.e 397.58F with minimum heating and cooling loads of 10610KW and 21445 KW.

Stream matching

For maximum heat recovery, three golden rules of pinch analysis must not be tolerated

- Don't transfer heat across the pinch
- Don't use cold utility above the pinch
- Don't use hot utility below the pinch

By avoiding these violations, streams are matched and heater and coolers are added where required.

The grid diagram of all the streams is shown in Figure 4

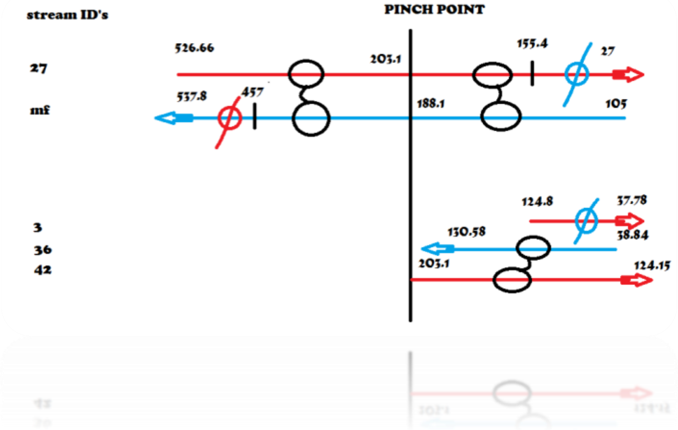

Figure 4 Stream Matching

The exchangers of streams '27' and 'mf' are optimized by using EDR (exchanger design and rating software).

5. EDR EXCHANGER DESIGN AND RATING)

Calculation mode is set to design mode with allowable pressure drop for one exchanger is of 2 psi. for vapour stream, 10 psi for liquid stream and 5-7 psi for dual phase streams depending upon how much vapour fraction is present.

The fixed specifications are; type of exchanger i.e. AES TEMA type, length of tubes i.e. 20ft, number of passes i.e. 2 passes, baffle type single segmented, baffle cut orientation vertical and exchanger material i.e. carbon steel.

The placement of hot and cold fluid is a big issue in industries because it depends upon many factors like viscosity, flow rates, density, vapour fraction etc. In our problem, we are splitting hot and cold streams at pinch point in two case and taking hot fluid in shells of exchangers which are below pinch point because too much condensation will occur which shall create vacuum and siphon and help in easy flow on the other hand if it is taken in tubes, the rapid phase change cause rupture of tubes. Also in exchangers, which are above pinch point, hot fluid is taken in shell side. By taking cold fluid in tubes we are providing ease to it to change its phase easily into vapour.

All the optimization is done by EDR and different designs are evaluated on altering the tube outside diameter and pattern of tubes in tube bundle by using random search method

The tubes outside diameter used are: 1.5in, 1in, 1.25in, and 0.75 in.

The tube patterns are: 60^o Rotated triangle, 30^o Triangular, 90^o square and 45^oRotataed square.

23 iterations are done above pinch and 8 iterations are done below pinch in suggesting the right specs.

The optimized designs are shown in figure 5

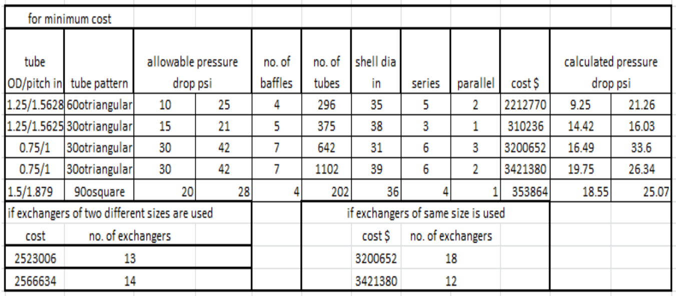

for minimum cost											
tube OD/pitch in	tube pattern	allowable pressure drop psi		no. of baffles	no. of tubes	shell dia in	series	parallel	cost $	calculated pressure drop psi	
1.25/1.5628	60otriangular	10	25	4	296	35	5	2	2212770	9.25	21.26
1.25/1.5625	30otriangular	15	21	5	375	38	3	1	310236	14.42	16.03
0.75/1	30otriangular	30	42	7	642	31	6	3	3200652	16.49	33.6
0.75/1	30otriangular	30	42	7	1102	39	6	2	3421380	19.75	26.34
1.5/1.879	90osquare	20	28	4	202	36	4	1	353864	18.55	25.07
if exchangers of two different sizes are used					if exchangers of same size is used						
cost	no. of exchangers					cost $	no. of exchangers				
2523006	13					3200652	18				
2566634	14					3421380	12				

Figure 5 Excel Sheet of Optimized Designs

The selected numbers of exchangers are 13 with shell diameters 35 and 38 inches with tube outside diameter of 1.25 inch. The total optimized cost is \$2523006(using EDR of 2012) =\$2614775.05(in 2015) using cumulative inflation rate of 3.6%.

Design of selected exchangers is attached with this report with complete specifications.

6 ECONOMIC ANALYSIS

The designed network is then compared with the existing network of BYCO petroleum Pakistan. For the comparison, the design capacity of both must be same. Hence total cost of designed network is scaled down to existing capacity by using ‘six tenth rule’ shown in equation (2).

$$cost\ of\ equipmaent\ a = (cost\ of\ equipment\ b)X^{0.6} \qquad (2)$$

Here X is the ratio of both capacities, 31550BPD and 24000BPD. The new cost is found to be \$2.2 million.

The payback analysis concluded that this network can be preferred upon buying or repairing packinox exchanger with payback period of 8 months.

ACKNOWLEDGEMENTS

We want to thank Mr Rizwan Ahmed Qamar, Sheikh Abubakar and Zeeshan Zaki who insight and expertise which greatly assisted the research.

REFRENCES

[1] Pinch analysis and process integration by Ian C. Kemp.

SYNTHESIS AND CHARACTERIZATION OF MAGNETORHEOLOGICAL FLUIDS

Syed Shan Ahmed[1], Sarah Humayun[1], Arsalan Shahid[1] and Muhammad Faizan[1]
[1]Materials Engineering Department, NED University Of Engineering & Technology, Karachi, Pakistan

Corresponding Author, TEL: +92-345-2873734
Email Address: Syedshanahmed@gmail.com

ABSTRACT

Magnetorheological Fluids from the family of smart materials have gained interest of scientists while exploring the world of smart materials which shows changes in their viscosity when external magnetic field is applied onto them. These fluids contain dispersions particles that require surface modification which are magnetically soft as well, a carrier fluid completes it, which encapsulates the particles and thus makes Magnetorheological fluids. It acts as a free flowing liquid when the magnetic field is absent but exhibits solid like characteristics under strong magnetic field. Particle size, its shape, density, particle size distribution, saturation magnetization and coercive field are the most important characteristics of the magnetically active dispersed phases. Besides magnetic particles, the base fluids, surfactants and anticorrosion additives are the most important factors that affect the rheological properties, stability and re-dispersibility of the MR fluid. The major property of these magnetic particles is their magnetization which makes it appropriate in using it multi-dimensionally from industrial to biomedical field magnetic resonance imaging (MRI), hyperthermia, drug delivery, and many more.

In this research, Magnetorheological fluids were prepared by inducing strontium based nanoparticles and surface modified carbonyl iron powder, to achieve increased viscosity in presence of strong magnetic field. The surfactant used in this method is oleic acid which controls particle size. Surface modification of carbonyl iron powder was performed to reduce oxidation and agglomeration issues. The preparation of strontium based nanoparticles was carried out by co-precipitation method using 1 molar solution of aqueous sodium hydroxide as precipitant. The reaction was carried out at controlled elevated temperature in order to study the temperature effects followed by calcinations of the product in muffle furnace and further mixing with KCl and NaCl in milling machine to lower the calcination temperature. Particle size and structural composition of the particles were characterized using SEM and X-ray powder diffraction. The results revealed the formation of strontium-ferrite phase after calcination at 800 degrees. Individually prepared $SrFe_{12}O_{19}$nano particles and modified carbonyl iron powder were mixed in the carrier fluid and the magnetic properties were investigated using Flux meter and Gauss meter.

Keywords: MR Fluid, Magnet, Nanomaterial, Magnetorheology, co-precipitation.

1 INTRODUCTION:

Today, state-of-the-art MR fluids are gaining high importance due to their applications concerning active control of vibrations or torque transfer. Shock absorbers, vibration dampers, seismic vibration dampers, clutches and seals are the most exciting applications of MR fluid.

Magnetorheological Fluids from the family of smart materials have gained interest of scientists while exploring the world of smart materials which acts as a free flowing liquid in the absence of magnetic field but under strong magnetic field, its viscosity changes drastically within few milliseconds and exhibits solid like characteristics. Many different ceramic metals and alloys can be used to prepare MR fluids as long as the particles are magnetically multi-domain and exhibit low levels of magnetic coercivity. In addition to magnetic interactions between two particles, the formation of the particles contribute to a certain level to the increase in the apparent viscosity. Particles held together by magnetic field and the chains of the particles resist to a certain level of shear stress without breaking which make them behave like a solid. When this shear stress exceeds a critical value, the structure breaks and the material starts to flow.

Stability against sedimentation and low viscosity in the absence of magnetic field are one of the many critical factors of MR fluids. These factors must be endowed for the escalation of properties in order to enhance applicability. Magnetic particles dispersed in carrier fluid pose sedimentation and agglomeration problems in the applications of MR fluids. There have been made various theoretical and experimental approaches to analyze the potential and characteristics of MR fluids. Recent advancements in the field of nanoparticles have helped in overcoming the infirmities of magnetic nanoparticles as these are believed to have reduced the tendency of settling down of the particles which was earlier witnessed when using micro sized particles. High temperature stability, durability, surface chemistry are some of the major factors that need to be monitored in order to synthesize stable MR fluids. Various processes have been adopted to design MR fluids of specific properties to suit different applications.

This research aims towards the synthesis of Magnetorheological Fluids with the help of co-precipitation method and also to characterize it by advance techniques which include XRD, SEM etc.

2 EXPERIMENTAL WORK

Materials

Ferric Chloride Hexahydrate ($FeCl_{3}.6H_2O$), Strontium Chloride Hexahydrate ($SrCl_2.6H_2O$), Sodium Hydroxide (NaOH) as an alkaline medium, Potassium chloride (KCl), Ethanol, Sodium Chloride (NaCl),Oleic acid which is used as Surfactant, Carbonyl Iron powder, Heat Transfer Oil imported from Pakistan State Oil (PSO) . Deionized Water was used several times during the experiment.

Experiment

The methodology opted for the preparation of magnetorheological fluid involved three steps.

Preparation of $SrFe_{12}O_{19}$ nanoparticles:

A particular precursor was required in order to synthesize of $SrFe_{12}O_{19}$ nanoparticles which was prepared by co-precipitation method[1]. The primary chemicals used were $FeCl_3.6H_2O$ and $SrCl_2.6H_2O$ taking the molar ratio of 9.23:1 [2]. Their salts were dissolved in deionized water and salt solution was prepared of each of these salts. A 3 molar solution of NaOH was prepared and heated up to 80 degrees in a beaker on a magnetic stirrer. The prepared salt solutions were added to NaOH solution under vigorous magnetic stirring at a rate of 1000 rpm, which resulted in brownish precipitate formation. The reaction was continued for 0.5 hour, maintaining the temperature of the experiment at 80 degrees.

The mixture was cooled naturally at room temperature and was filtered to precipitate out the precursor. The deionized water and ethanol were used several times to wash those precipitates and the precipitates were left to dry at 100 degrees overnight.

The as-dried precursor was then ground with NaCl and KCl having mass ratios 1:1. The precipitates were calcined in a muffle furnace at 850 degrees for 2 h.

To remove the impurity ($SrCO_3$) dilute HCl was used to wash calcined precipitates and again washed thoroughly with deionized water and ethanol. The powdered product was dried at 60 degrees for 12 h and then ground to obtain $SrFe_{12}O_{19}$ nanoparticles.

Surface modification of carbonyl iron powder:

Carbonyl iron powder possess high tendency to aggregate and easily gets oxidized therefore, modification of these microparticles is performed using surfactants.

The surfactant used to modify the surface of carbonyl iron powder was oleic acid. The oleic acid was taken as 10% wt of the carbonyl iron powder and was dissolved in a volume of absolute ethanol in a beaker under constant

Mechanical stirring. The temperature supplied to the flask was kept constant at 50 degrees.

Under vigorous stirring, carbonyl iron powder was introduced in the suspension and the stirring was carried out for 1 h. The suspension was then allowed to cool naturally at room temperature and was filtered out. The precipitates were washed three times with ethanol and were dried at 50 degrees for 12 h.

Introducing the particles in carrier fluid

Heat Transfer Oil was used as carrier fluid in this step in order to prepare MRF. Both of the particles were mixed in adequate proportions into the heat transfer oil by means of mechanical agitation. The mixture was ground on a three roll grinder that resulted in the formation of MRF based on heat transfer oil.

3 CHARACTERIZATION

The nanoparticles were subjected to characterizations before being mixed to the fluid. The characterizations employed at this stage were: SEM- To analyze particle size and shape, XRD analysis- To study the composition of the particles, Fluxmeter- To study the magnetic properties of $SrFe_{12}O_{19}$ particles. After mixing, certain characterizations were performed that revealed the rheological characteristics of the magnetorheological fluid. These were, Capillary rheometer and Viscometer

SEM Analysis of Nanoparticles

Scanning electron microscope (SEM) analysis of the nanoparticles was performed to analyze the morphology of particles using FEI Quanta

200 SEM microscope at 10-20 KV. The observation of SEM images was performed at different magnifications using secondary X-rays detector.

XRD Analysis of Nanoparticles

To characterize the crystal structure of $SrFe_{12}O_{19}$ nanoparticles, X-ray powder diffraction was employed using Phillips PANalytical X'Pert Pro diffractometer with with Cu Ka radiation (= 1.5406˚A). The particle size of the powdered samples were calculated using the debye scherrer.

4 RESULTS AND DISCUSSIONS

X-Ray Diffraction Analysis of Strontium Hexaferrite Nanoparticles

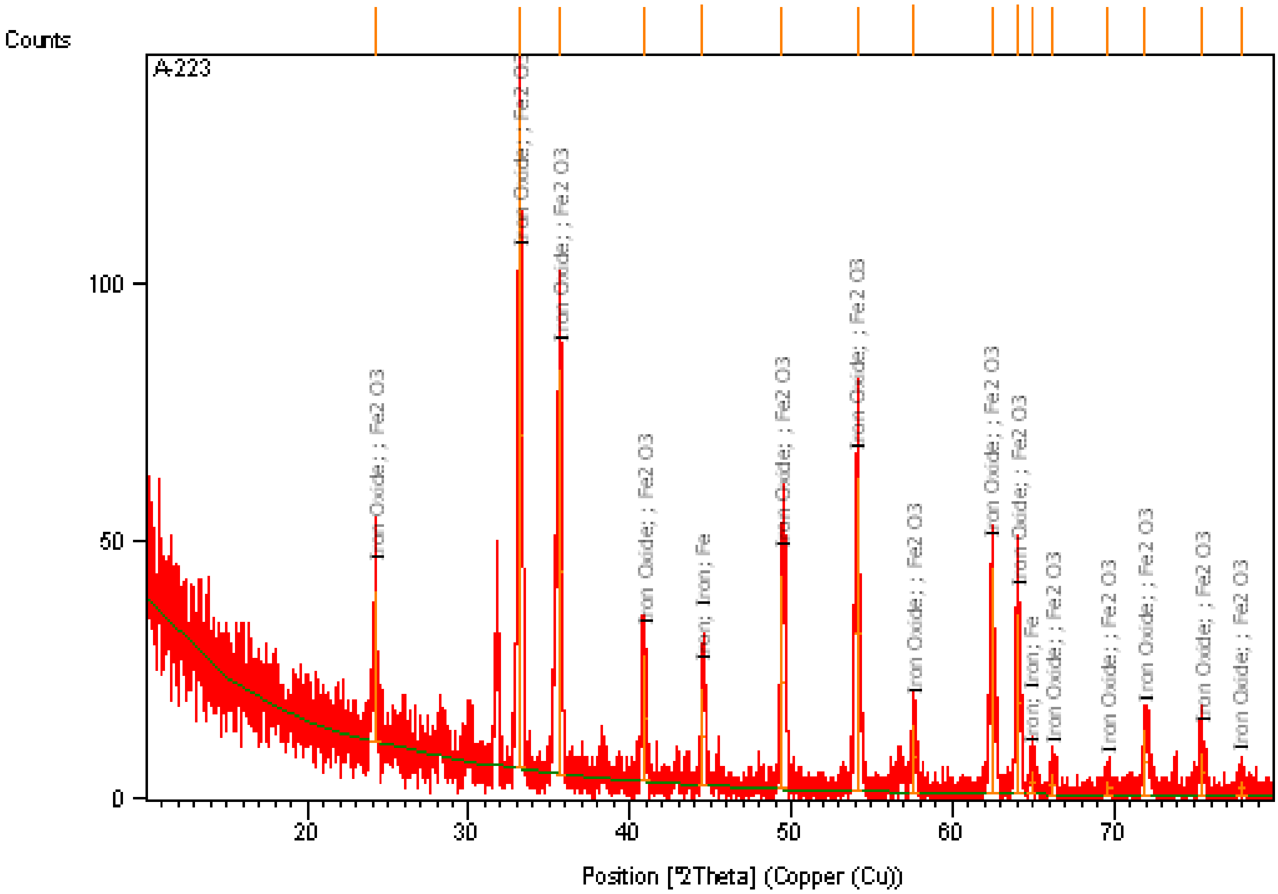

Fig. 1) XRD patterns of $SrFe_{12}O_{19}$ nanoparticles obtained at 850°C for 2 h.

Table 1) Observation Table of XRD

Pos. [°2Th.]	**Height [cts]**	**FWHMLeft [°2Th.]**	**d-spacing [Å]**	**Rel. Int. [%]**	**Particle Size [L]**
24.192610	29.600180	0.196800	3.67892	22.93	413.25 nm
33.169450	129.098500	0.275520	2.70094	100.00	300.78 nm
35.680160	78.712290	0.275520	2.51643	60.97	302.83 nm
40.886120	24.726610	0.314880	2.20724	19.15	269.42 nm
44.494740	18.953210	0.275520	2.03625	14.68	311.45 nm
49.418330	41.505620	0.275520	1.84429	32.15	317.32 nm
54.117960	61.031180	0.393600	1.69471	47.27	226.52 nm
57.639980	13.266550	0.314880	1.59926	10.28	288.14 nm
62.492990	44.144590	0.196800	1.48623	34.19	472.64 nm
64.072550	34.769330	0.354240	1.45335	26.93	264.56 nm
64.907200	4.485272	0.393600	1.43666	3.47	239.12 nm
66.197110	4.039789	0.393600	1.41176	3.13	240.85 nm
69.654330	2.578798	0.472320	1.34991	2.00	204.83 nm
71.960290	12.680330	0.275520	1.31222	9.82	356.23 nm
75.445820	8.537684	0.472320	1.26002	6.61	212.57 nm
77.936520	3.092629	0.472320	1.22587	2.40	217.33 nm

XRD is a very important experimental technique that has been used to address all issues relevant to the crystal structure of solids, including lattice constants and geometry, identification of unknown materials, orientation of single crystals, preferred orientation of polycrystals, defects, stresses, etc. In XRD, a collimated beam of X-rays with a wavelength typically ranging from 0.7 λ to 2 λ is incident on a specimen and is diffracted by the crystalline phases in the specimen according to Bragg's law.

$n\lambda = 2\,d\sin\theta$ Eq. 6.1

Where d is the spacing between atomic planes in the crystalline phase and λ is the X-ray wavelength. The intensity of the diffracted X-rays is measured as a function of the diffraction angle and the sample's orientation. This diffraction pattern is used to identify the sample's crystalline phases and to measure its structural properties. XRD is nondestructive and does not require extensive sample preparation, which very well explains the wide usage of XRD method in materials characterization.

SrFe12O19 nanoparticles were characterized by X-ray Diffraction; above table illustrates the results of XRD analysis of SrFe12O19 sample. Diffraction pattern of the sample was taken on an advance diffractometer using CuKα (1.5406 Å) radiation at room temperature in the range of 10 to 80° in the 2θ scale, with a scanning speed of 0.02°/s and a step time of 1.5 seconds. The largest size measured was 472.64 nm and the smallest size measured was 212.57 nm.

SEM Analysis of Strontium Hexaferrite Nanoparticles

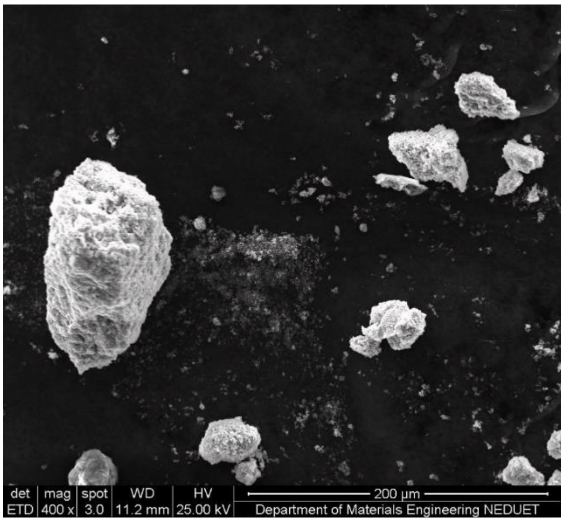

Fig 2) SEM image of agglomerated SrFe12O19 nanoparticles

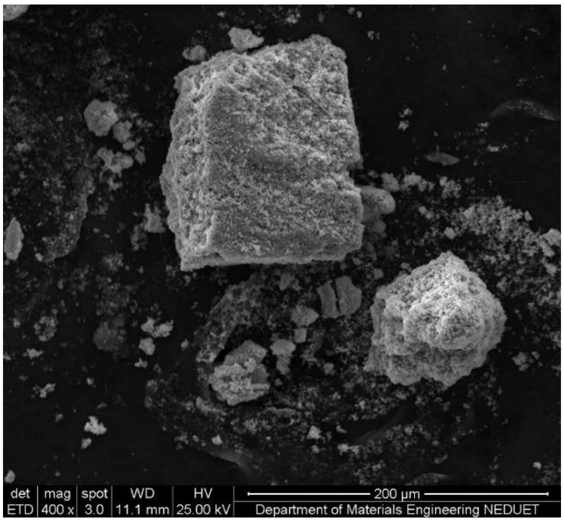

Fig 3) SEM image of agglomerated SrFe12O19 nanoparticles

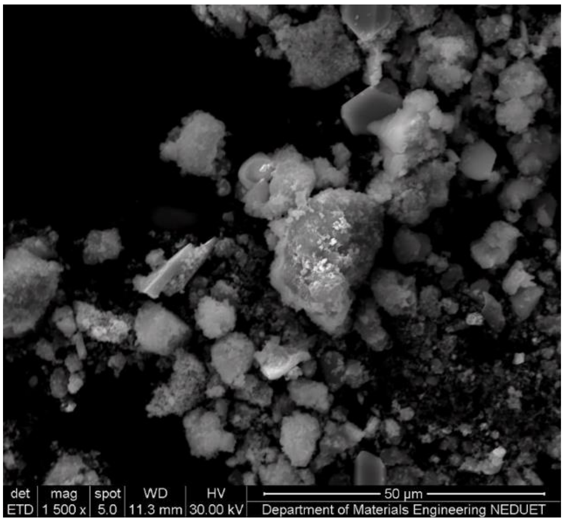

Fig 4) SEM image of agglomerated SrFe12O19 nanoparticles

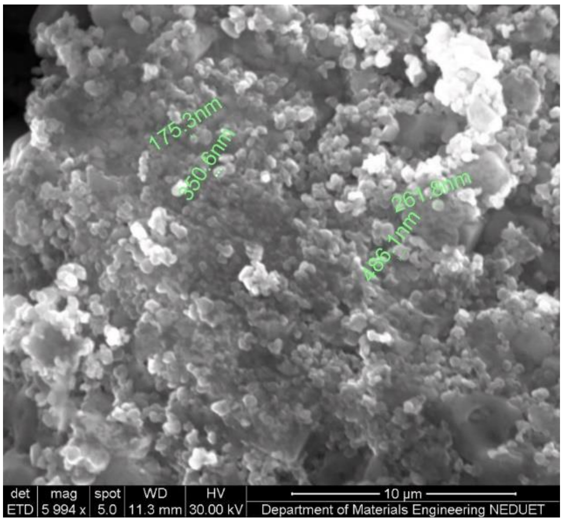

Fig 5) SEM image of smallest SrFe12O19 nanoparticles

SEM analysis was done to check the morphology of Strontium Hexaferrite Nanoparticles. In Fig. 2 and Fig. 3 the agglomerated particles were seen which was due to the increase amount of time.

The smallest particle size observed from SEM was found to be 294.8nm as marked in the figure.

5 FUTURE WORK

The MR fluid was prepared by mixing nanosized magnetite particles with micro sized iron particles in a polymer matrix. The nanoparticles were prepared by coprecipitation technique and characterized by XRD and TEM. Rheological properties of MR fluids were studied in the presence of varying magnetic field. It is observed that, varying the magnetic field has a significant effect on the viscosity of MR fluid, due to the induced particle alignment.

The results to date are being used to design MR fluids of specific properties to suit different applications. Another research showed that MR fluids were synthesized using different grades of iron powder (GRADE A, GRADE B), PDMS, and SURFACTANT A. Glycol ether based MR fluids were also synthesized. PDMS, SURFACTANT A, GRADE B based MR fluids and NPC-ST, SURFACTANT B and GRADE A based MR fluids exhibited the most stable and redispersible behavior. The pre-shearing of MR fluids had a significant effect on the rheological properties of MR fluids. The longer the pre-shearing at 110 Pa showed a yielding in the sample at shorter times at 35 Pa.

In addition to this, a number of areas need to be worked upon in order to strengthen and establish the magnetorheological fluids as a revolutionary shock absorbing tool in upcoming era. Below mentioned are the objectives that we aim to achieve in the future.

- To investigate the influence of interparticle forces on stability and dispersibility of MR fluids. Investigation of the influence of remnant Magnetization of soft magnetic particulates on the dispersibility of MR fluids is investigated.
- To investigate the on state rheological properties of MR fluids. The investigation of dependence of yield stress on the average particle size and magnetic properties of particles.
- To investigate the off state, when no magnetic field is applied, rheological properties of MR fluids. There is not much research reported on the off state viscosity of MR fluids.
- The apparent viscosity of MR fluids can be investigated. The yielding properties of MR fluids to be investigated by creep-recovery experiments.
- In an effort to address durability of MR fluids, the effect of high temperature exposures for 24 hours on the “on” and “off” state rheological properties of MR fluids was investigated.
- The study of MR fluids under heat treatment to check if it shows any significant changes in the on state yield stress which could be attributed to the protective oxide layer which lies on the surface of nanoparticles.
- The relationship between the shear stress and shear rate under higher magnetic field will be carried out in future.

6 CONCLUSION

The observations obtained from XRD and SEM studies are concluded as follows:

i. Strontium Hexaferrite Nanoparticles were synthesized by chemical co-precipitation method. Analytical grade $FeCl_3\cdot6H_2O$ and $SrCl_2\cdot6H_2O$ were used as precursors and NaOH as a precipitant. $FeCl_3\cdot6H_2O$ and $SrCl_2\cdot6H_2O$ were dissolved with a molar ratio of 9.23:1 and then calcined in a furnace at 850◦C for 2 h.
ii. Increasing the pH for the precipitated precursors strongly affects the formation of Strontium Hexaferrite Nanoparticles.
iii. The synthesis conditions were strongly influenced on the microstructure of the produced Sr-M ferrite powders.
iv. Heat Transfer oil was used instead of Natural Oil for better magnetic behavior.
v. The end product of this experiment had good magnetic saturations and intrinsic coercivities.

REFERENCES

[1] Pullar, R. C. *Hexagonal ferrites: A review of the synthesis, properties and applications of hexaferrite ceramics. Progress in Materials Science*, 57,1191–1334,2012.

[2] Claracq, J., Sarrazin, J., & Montfort, J. P. *Viscoelastic properties of magne-torheological fluids. Rheologica Acta*, 43, 38–49,2004.

[3] Odenbach, S. *Magnetic fluids-suspensions of magnetic dipoles and theirmagnetic control. Journal of Physics: Condensed Matter*, 15, S1497–S1508,2003.

[4] Wereley, N. M., Chaudhuri, A., Yoo, J. H., John, S., Kotha, S., Suggs, A., et al. *Bidisperse magnetorheological fluids using Fe particles at nanometerand micro scale. Journal of Intelligent Material Systems and Structure*, 17,393–401,2006.

[5] Lu, H. F.,Hong, R. Y., & Li, H. Z. *Influence of surfactants on co-precipitation synthesis of strontium ferrite. Journal of Alloys and Compounds*, 509, 10127–10131,2011.

[6] Hessien, M. M., Rashad, M. M., & El-Barawy, K. *Controlling the composition and magnetic properties of strontium hexaferrite synthesized byco-precipitation method. Journal of Magnetism and Magnetic Material*, 320, 336–343,2008.

[7] Jianrong Liu, Xianjun Wang, Xia Tang, Ruoyu Hong,, Yaqiong Wang, Wenguo Feng; *Preparation and characterization of carbonyl iron/strontium hexaferrite magnetorheological fluids*, Particuology ,2014.

SYNTHESIS AND CHARACTERIZATION OF BARIUM TITANATE POWDER BY SOLID-STATE AND HYDROTHERMAL ROUTES

***Muhammad Ali Siddiqui*, Waqar Ahmed, Alishah Virani, Ali Asgher Vapra and Muhammad Fahad Farooq**
Metallurgical Engineering Department, NED University of Engineering & Technology, Karachi, Pakistan

*Corresponding Author. Tel: +92(334)8848194; Fax: +92(21)99261261;
E-mail: m.siddiqui@neduet.edu.pk

ABSTRACT

Barium Titanate is one of the best know raw materials used for designing of piezoelectric devices. Material properties are related to their chemical purity and impurity content. This research based on the study the two different routes for the synthesis of Barium Titanate BaTiO3 piezoelectric powder via Solid-State and Hydrothermal Methods. In both methods $BaCO_3$ and TiO_2 were used as starting material. The XRD of the samples produced via solid state synthesis, calcined at five different temperatures i.e. 930°C, 960°C, 1000°C, 1030°C and 1060°C for 4 hours revealed the presence of $BaTiO_3$ as a major phase. The optimum calcination temperature was found to be 960°C which has relative highest amount of $BaTiO_3$ (95.15%) phase. Crystallization nature of the material was found to be tetragonal based upon the crystallographic analysis of XRD pattern as a result of which perovskite structure was obtain. The Hydrothermal method involves similar starting materials, a solution of mole ratio 1:1 was stirred and evaporated at 70°C till a clear, viscous resin was obtained which is then dried at 110°C for 20 hours. The sintering was performed at 900°C for 2 hours after drying the powder to form $BaTiO_3$ nanopowder. The XRD of the samples revealed only the presence of $BaTiO_3$ as a major phase while the crystalline nature of the material was found to be tetragonal based upon the crystallographic analysis. Poling has been performed as described in the US Pattern and the poled tablet will be checked by connecting a LED light with it.

Keywords: Barium Titanate; piezoelectric devices; XRD patterns; nanopowder; poling.

1 INTRODUCTION

Piezoelectric materials belong to a wider class of materials called ferroelectrics. The output power obtained from piezoelectric generators depends on various factors like which piezoelectric sensor has been used, it's packing density, type of strain applied to it, electronic circuitry to process the pulse generated, storage device, and load connected to it [1]. Barium titanate (BT) has been one of the best known and widely used materials for electric ceramics due to its excellent dielectric, piezoelectric, and ferroelectric properties. Barium titanate ($BaTiO_3$) is one of the widely used ceramic that can be synthesized by variety of different routes, which ultimately gives ABO_3 type pervoskite structure. Barium titanate is usually used for electric ceramics due to its excellent dielectric, piezoelectric, and ferroelectric properties [1]. It is widely used in multilayer ceramic capacitors (MLCCs), dynamic random access ferroelectric memories (DRAMs) [2]. Large piezoelectric values in this type of material make them more attractive for electronics devices and a variety of electro-optics devices such as multilayer ceramics capacitor (MLCCs), piezoelectric transducer, piezoelectric sensors, and printed circuit board [3]. It is also used in positive temperature coefficient resister (PTCR) called as thermistor etc.

The high dielectric constant of barium titanate ($BaTiO_3$) type ceramic is because of the crystal structure and its crystallographic dimension. It has four isomorphs namely Rhombohedral, Orthorhombic, Tetragonal and Cubic. The two most important crystalline phases of $BaTiO_3$ are used in microelectronics industries. The tetragonal phase of $BatiO_3$ is the most important phase in order to be used in electronic devices due to their ferroelectric properties, while the cubic phase although not ferroelectric but due to its high dielectric constant makes it suitable to be use as capacitors. The Ti^{4+} ion in the $BaTiO_3$ is slightly displaced from the center of the "cube" so that there is a separation between the centers of the positive (+ve) and the negative (-ve) charge in the unit cell leading to an electric dipole moment. The formation of electrical dipole is called polarization [4].

We followed two routes for the synthesis of $BaTiO_3$ i.e. Mechanochemical and Hydrothermal. Mechanomechanical route was a failure while from Hydrothermal route we obtained our desired results. Both the routes will be elaborately discussed in this report.

2 OBJECTIVES

The following are the objectives of the work:

- To synthesize and characterize the Piezoelectric Material via various routes. (Solid State and Hydrothermal method).
- To study the effect of Sintering Parameters on the Piezoelectric Properties.
- To study the Phase Transitional behaviour of Piezoelectric Material.
- Effect of dopant (poling) on Piezoelectric Properties.
- To publish our research paper in an international or local journal/conference.

3 EXPERIMENTAL WORK, RESULTS AND DISCUSSIONS

Two methods were used as told earlier, these process methodology are described below.

3.1.1. Solid State Method:

Ingredients were ($BaCO_3$ and TiO_2), which were mixed in equal mole ratio, grinding and dried. Calcination was performed at various temperatures and phase and crystallographic analysis was done through XRD test. The milling was performed, followed by compaction, binder burnout and finally sintering process was carried out. Macro surface analysis was done by using Stereo Microscope, Micro Surface analysis was done with the help of SEM and bulk density analysis was carried out by Archimedes Method.

Mixing:

Barium Carbonate ($BaCO_3$) and Titanium Dioxide (TiO_2) were mixed with equal molar ratio according to the following formula;

1) Wt% of $BaCO_3$;

(mol% of $BaCO_3$) (MW of $BaCO_3$) /
(mol% of $BaCO_3$) (MW of $BaCO_3$) +
(mol% of TiO_2) (MW of TiO_2)

2) Wt% of TiO_2;

(mol% of TiO_2) (MW of TiO_2) /
(mol% of $BaCO_3$) (MW of $BaCO_3$) +
(mol% of TiO_2) (MW of TiO_2)

Figure 1 shows a picture of a mixer, which was used in the experiment.

Figure 1: Mixer, used for powder mixing

Grinding and Drying

Grinding was done for 2 hours using ethanol and dried in an oven at 90°C until the mixture was completely dried.

Figures 2 and 3 are showing drying oven apparatus and ball mill apparatus respectively.

Figure 2: Drying Oven

Figure 3: Ball mill apparatus

Calcination

Calcination was performed at various temperatures as shown in Figure 4. Following reaction took place.

$$BaCO_3 + TiO_2 \Longrightarrow BaTiO_3 + CO_2$$

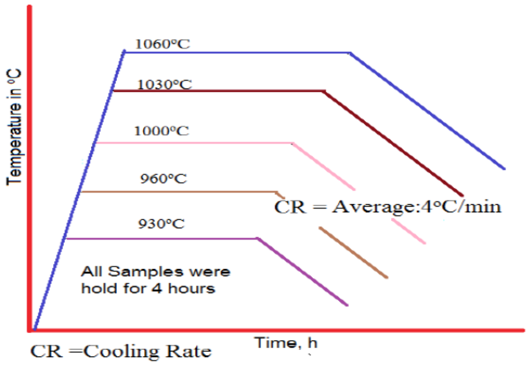

Figure 4: Different calcination cycles

Milling and Compaction

Calcined powder was again milled with PAV (Polyvinyl Alcohol) as a binder. Pellets of 25mm diameter and 2mm thickness compacted at pressure of 25MPa. Figure 5 is showing a descriptive diagram about compaction pressing machine.

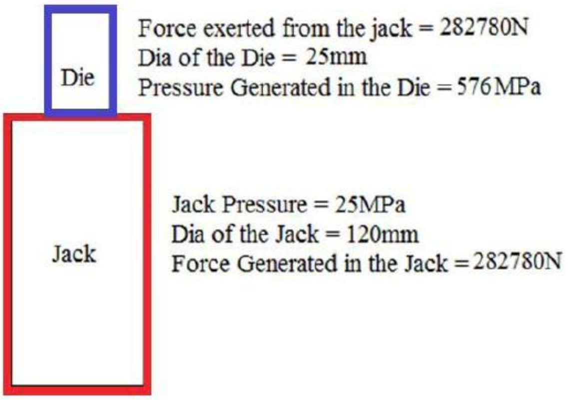

Figure 5: Compaction press

Binder Burnout and Sintering Cycle

Figures 6 and 7 are showing binder burnout and sintering cycles respectively.

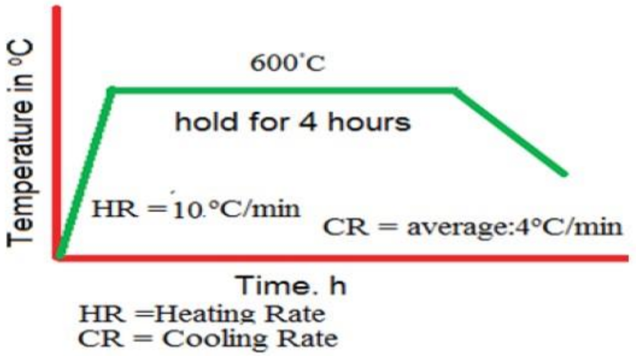

Figure 6: Binder Burnout Cycle

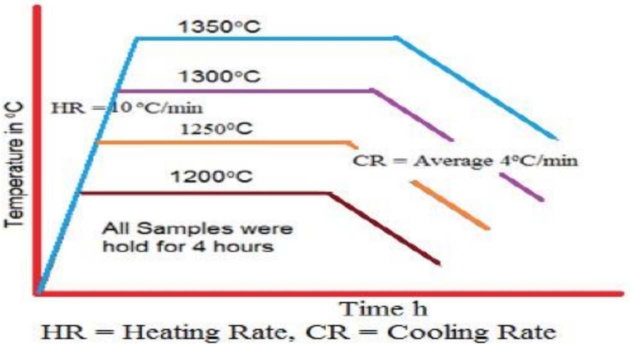

Figure 7: Sintering Cycles

3.1.1. Results

XRD Results

Figure 8, showing XRD pattern of Sample Calcined at 930˚C. Crystallization nature of the material was found to be tetragonal.

Content of $BaTiO_3$, Perovskite phase 84.86%.

$$BaCO_3 + TiO_2 \Longrightarrow BaTiO_3 + BaCO_3 + TiO_2 + CO_2$$

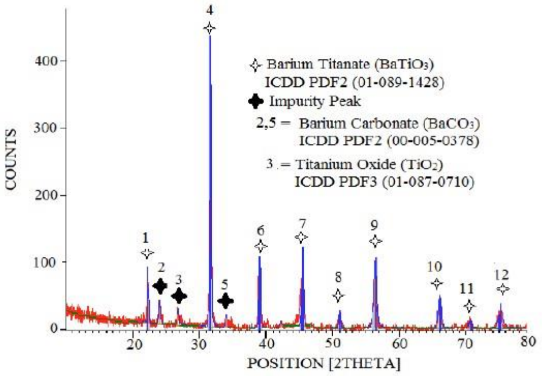

Figure 8: XRD Pattern of Calcined sample at 930˚C

Figure 9, showing XRD pattern of Sample Calcined at 960˚C. Crystallization nature of the material was found to be tetragonal.

Content of $BaTiO_3$, Perovskite phase 95.16%.

$$BaCO_3 + TiO_2 \Rightarrow BaTiO_3 + BaCO_3 + CO_2$$

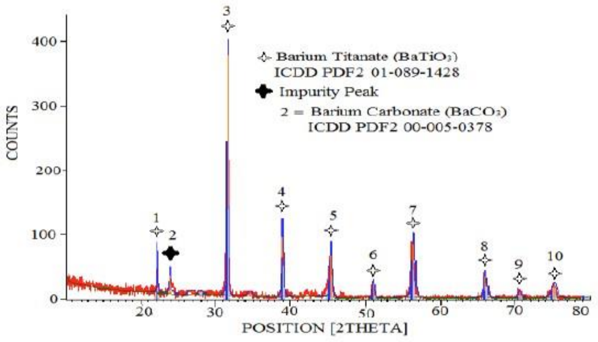

Figure 9: XRD Pattern of Calcined sample at 960˚C

Figure 10, showing XRD pattern of Sample Calcined at 1000˚C. Crystallization nature of the material was found to be tetragonal.

Content of $BaTiO_3$, Perovskite phase 94.56%.

$$BaCO_3 + TiO_2 \Rightarrow BaTiO_3 + BaCO_3 + CO_2$$

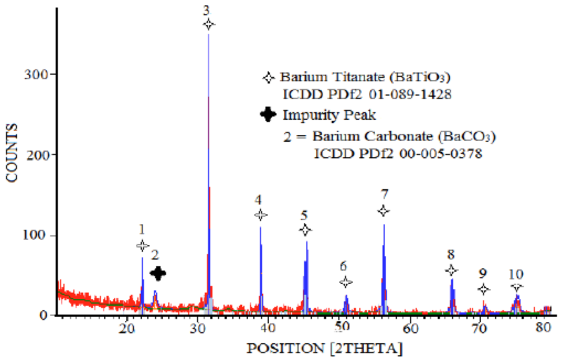

Figure 10: XRD Pattern of Calcined sample at 1000˚C

Figure 11, showing XRD pattern of Sample Calcined at 1030˚C. Crystallization nature of the material was found to be tetragonal.

Content of $BaTiO_3$, Perovskite phase 94.46%.

$$BaCO_3 + TiO_2 \Rightarrow BaTiO_3 + TiO_2 + CO_2$$

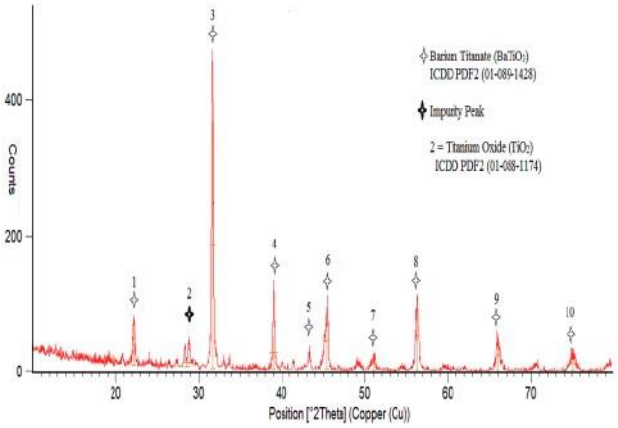

Figure 11: XRD Pattern of Calcined sample at 1030˚C

Figure 12, showing XRD pattern of Sample Calcined at 1060˚C. Crystallization nature of the material was found to be tetragonal.

Content of $BaTiO_3$, Perovskite phase 88.57%.

$$BaCO_3 + TiO_2 \Rightarrow BaTiO_3 + \text{Unknown Phase} + CO_2$$

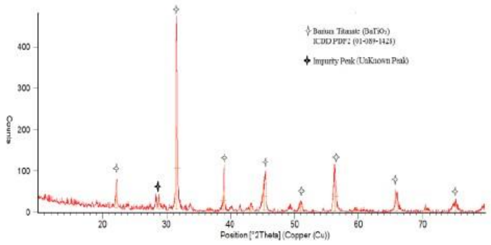

Figure 12: XRD Pattern of Calcined sample at 1060˚C

Conclusion of XRD results, optimal calcination temperature was found to be 960˚C.

Macro Surface Analysis

Macro Surface Analysis was done by Stereo Microscope. Figures 13, 14, 15, and 16 are the images of pellets at different sintering temperatures.

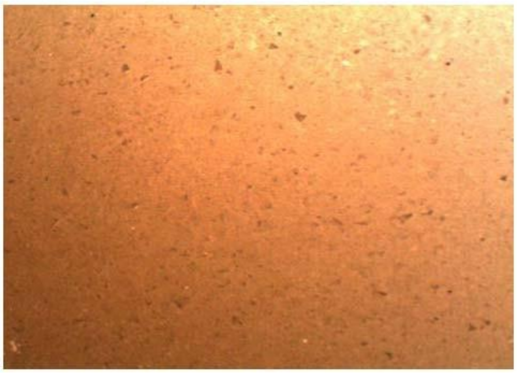

Figure 13: Stereograph of $BaTiO_3$ Pellet, Sintered at 1200°C, 7X Magnification

Figure 14: Stereograph of $BaTiO_3$ Pellet, Sintered at 1250°C, 7X Magnification

Figure 15: Stereograph of $BaTiO_3$ Pellet, Sintered at 1300°C, 7X Magnification

Figure 16: Stereograph of $BaTiO_3$ Pellet, Sintered at1350°C, 7X Magnification

Micro Surface Analysis

Figures 17 and 18 are micrographs of $BaTiO_3$ pellet sintered at 1200˚C and 1350˚C respectively.

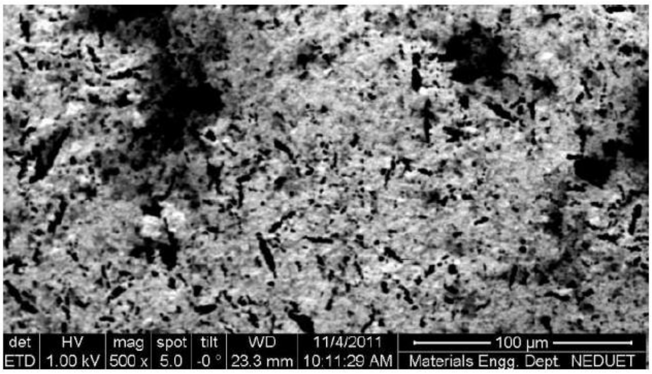

Figure 17: Micrograph of $BaTiO_3$ pellet sintered at 1200˚C

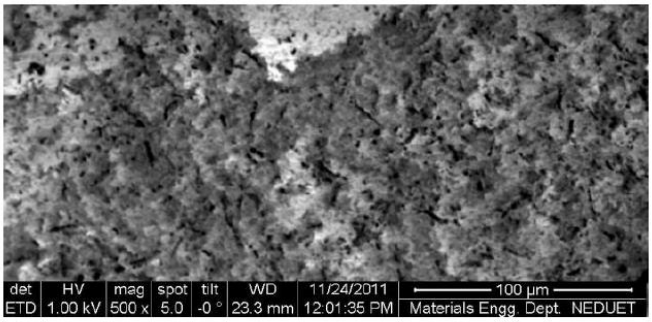

Figure 18: Micrograph of $BaTiO_3$ pellet sintered at 1350˚C

Physical Properties

Physical properties were examined by Archimedes Method ASTM-C373-88 Figure **19** is showing variation of bulk density of Barium Titanate with rise in sintering temperature.

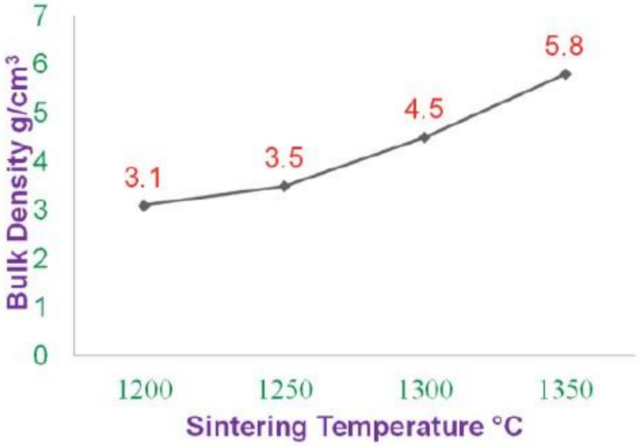

Figure 19: Variation of bulk density of $BaTiO_3$ ceramic with sintering temperature

Figure 20 is showing variation of true porosity of Barium Titanate with rise in sintering temperature.

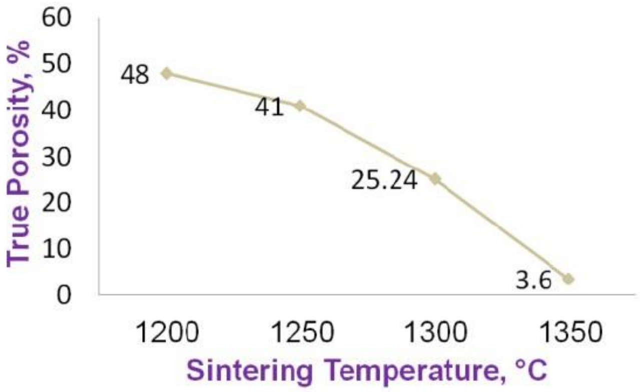

Figure 20: Variation of true porosity of $BaTiO_3$ ceramic with sintering temperature

Figure 21, is showing variation of apparent porosity of Barium Titanate with rise in sintering temperature.

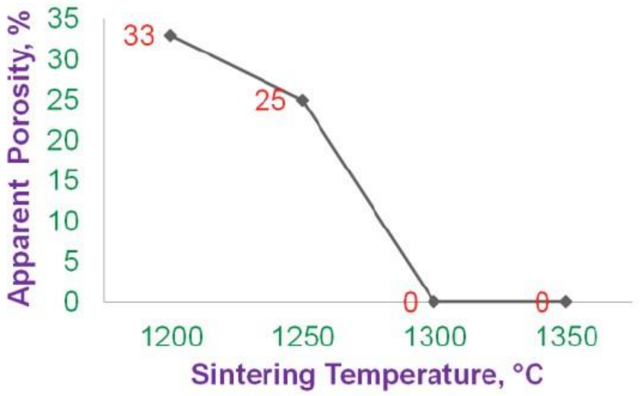

Figure 21: Variation of Apparent Porosity of $BaTiO_3$ ceramic with sintering temperature

From above results we found that optimal sintering temperature was 1350˚C.

3.1.2. Conclusion

- $BaTiO_3$ (perovskite phase) was synthesized by solid state reaction.
- The "Optimum Calcination Temperature" was found to be 960°C.
- $BaTiO_3$ has 95.15% relative amount of $BaTiO_3$ phase.
- Crystallization nature of the material was found to be "Tetragonal".
- The "Optimum Sintering Temperature" was found to be 1350°C which has a bulk density of about 5.8g/cm^3 and a true porosity of about 3.6%.

3.2. Hydrothermal Method

$BaTiO_3$ nanopowders were synthesized using organic acid precursor method. The starting materials used were barium carbonate ($BaCO_3$) and Titanium dioxide (TiO_2) powder. A solution of mole ratio 1: 1 was stirred and evaporated at 70˚C till a clear, viscous resin was obtained, then dried at 110˚C for 20 hours. The precursor formed was heated at 900˚C for 2 hours to form $BaTiO_3$ nanopowder.

Mixing

The starting materials used were barium carbonate ($BaCO_3$) and Titanium dioxide (TiO_2) powder. A solution of mole ratio 1: 1 was obtained by the following formula;

1) Wt% of $BaCO_3$;

(mol% of $BaCO_3$) (MW of $BaCO_3$) /
(mol% of $BaCO_3$) (MW of $BaCO_3$) +
(mol% of TiO_2) (MW of TiO_2)

2) Wt% of TiO_2;

(mol% of TiO_2) (MW of TiO_2) /
(mol% of $BaCO_3$) (MW of $BaCO_3$) +
(mol% of TiO_2) (MW of TiO_2)

Both the powders are mixed thoroughly using a common blender.

Viscous Resin

The mixed powder was stirred and evaporated at 70˚C till a clear, viscous resin was obtained in a hot plate magnetic stirrer as shown in Figure 22.

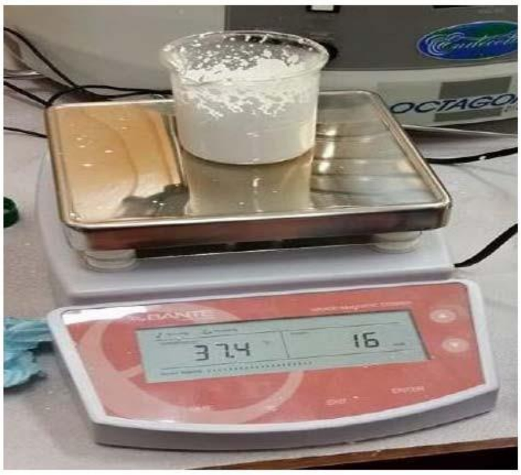

Figure 22: Hot plate magnetic stirrer.

Drying

The viscous resin was dried at 110˚C for 20 hours.

Reducing Particle Size

In order to reduce particle size the dried powder was operated in a small planetary ball mill, so that the next steps would be performed conveniently.

Compaction

Then the powder was compacted into tablets as performed in solid state method.

Sintering

Compacted tablets were sintered at 900˚C for 2 hours to form $BaTiO_3$. Figure 23 is showing the sintering cycle.

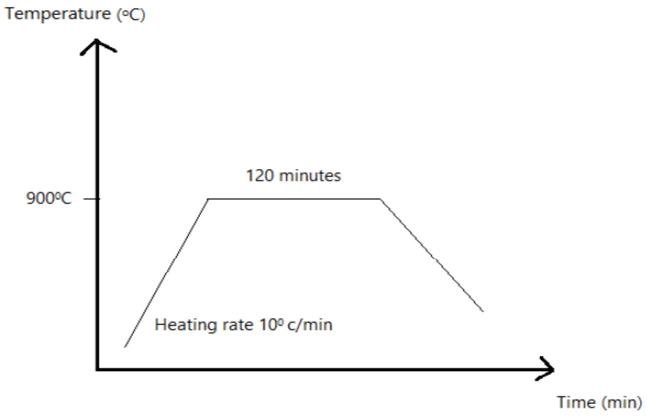

Figure 23: Heat treatment Cycle for Hydrothermal Method.

Poling

The sintered disks were polished and pasted with silver paste. Poling was done in silicone oil bath at 120˚C for 20 min under an electric field of around (10 to 30) KV, according to the US pattern. The poling apparatus and poling cycle are shown in Figures 24 and 25 respectively.

Referring to Figure 24, an apparatus for poling a piezoelectric ceramic of this invention includes a poling tank 1 in which an insulated medium 10, such as silicone oil, is contained. The insulated medium 10, if desired, may be replaced by air. However, the use of silicone oil is preferable. A first and a second electrode 11, 12 are respectively connected to the positive and negative electrodes of a DC power supply 13 and dipped in the insulated medium 10. The first electrode 11 is located right above the second electrode 12 at a certain distance. The first electrode 11 is preferably a copper plate and the electrode 12 is a metal plate. In this way, a piezoelectric ceramic disc 2 can be poled in a poling field created between said electrodes 11, 12 when said piezoelectric ceramic disc 2 is placed on the second electrode 12. The upper surface of the disc 2 is spaced from the first electrode 11 by a distance (d).

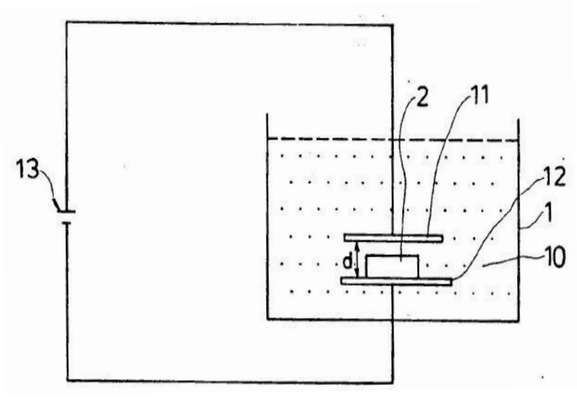

Figure 24: Poling apparatus.

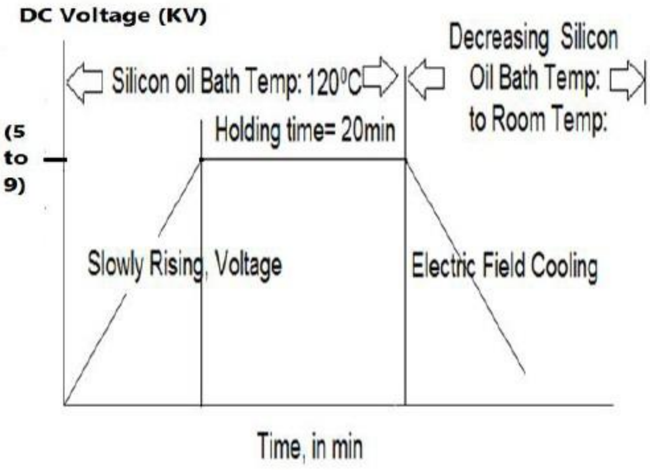

Figure 25: Poling Cycle

Figure 25, is a graphical representation of the poling cycle. By slowly rising the DC voltage and holding at the desired level for 20 minutes followed by electric field cooling to room temperature enables to pole piezoceramic successfully, Figure 26, is showing the poling apparatus glass tank in which poling was performed, and Figure 27, is showing DC power supply and Silicone oil.

Figure 26: Glass Tank Apparatus for poling

Figure 27: DC power Supply and silicone Oil

3.2.1. Results

Macro Surface Analysis

Figure 28 is showing the stereo image for examination for cracks.

Figure 28: Stereo microscopic image for examination for cracks, at 7X

XRD Result

Figure 29, is showing the XRD result obtained via hydrothermal method.

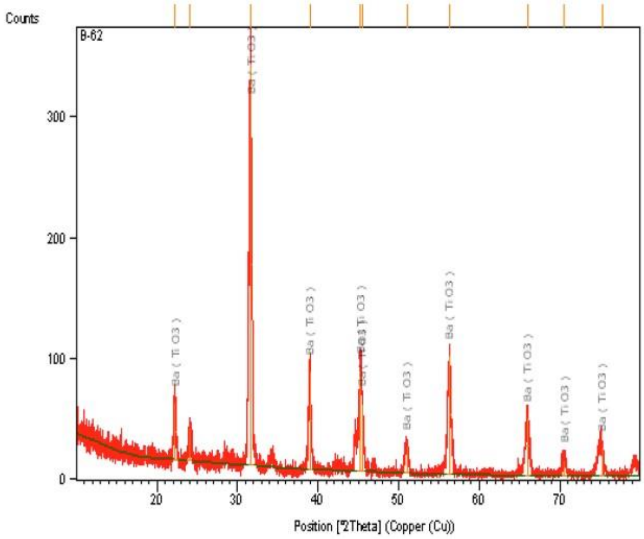

Figure 29: XRD data chart obtained by Hydrothermal Method

3.2.2. Conclusion

The second method was also a success and barium titanate was formed with tetragonal phase having pervoskite structure.

Poling was performed on the tablets, which was a great achievement and tablets will be checked soon by connecting a small LED with it.

4 REFERENCES

[1] Sengodan S, Chandar Shekar B, Sathish S, and Sathyamoorthy R, synthesis and characterization of tetragonal $BaTiO_3$ nano particles by hydrothermal method, 2012.

[2] Wongduan Maison, Reinhard Kleeberg, Robert B. Heimann, Sukon Phanichphant, Phase content, Tetragonality and Crystallite size of nanoscaled Barium Titanate synthesized by the catecholate process; Effect of Calcination temperature, Journal of the European Ceramics Society 23, 2003.

[3] Nuchnapa Tangboriboon, Synthesis of Barium Titanate as an Electroceramic Raw Materials.

[4] San Jose State University, Structure and Dielectric Properties of Pervoskite Barium Titanate ($BaTiO_3$).

SYNTHESIS AND CHARACTERIZATION OF BAMBOO FIBER REINFORCED POLMER COMPOSITE

Sana Shaikh[1*], Rimsha Javed[1], and Muhammad Faizan[1]
[1] Materials Engineering Department, NED University of Engineering & Technology, Karachi, Pakistan

*Corresponding author. Tel.: +923322334664
E-mail address: shanzae_princezz@hotmail.com

ABSTRACT

Composites are composed of two or more different constituents. The incorporation of the best qualities of each of the constituent material used is the goal of the composite manufacturing. The polymer composite using natural fibers as a reinforcement are becoming popular nowadays. The objective of the research was to make a natural fiber reinforced polymer composite using bamboo fibers as a reinforcement material and polyester resin as a matrix material. It was desired to modify the strength of fabricated composite using different fiber surface treatment methods and incorporation of fibers with different alignment. The fibers were extracted by the adoption of combined chemical and mechanical extraction techniques involving alkaline treatment and rolling mill technology (RMT). The composite was fabricated by using hand lay-up and vacuum assisted resin transfer moulding method. The fibers surface was also modified using mercerization treatment to improve the fiber matrix interaction. Two types of fiber surface treatment were done using 2M and 3.8M NaOH solution. Modified composites were made using mercerized fibers and incorporating randomly oriented and chopped bamboo fibers via vacuum assisted resin transfer moulding method (VaRTM). The characterization of the composite was carried out by using tensile testing, stereo microscopy and scanning electron microscopy. By comparing the treated and untreated fibers and their composites, it was found that the treated fiber composite of 2M NaOH solution fabricated via VaRTM has increased tensile strength than the treated fiber composite of 3.8M NaOH and the untreated fiber composite because of the increased fiber matrix interaction by alkaline treatment of fibers.

Keywords: Bamboo, Fiber, VARTM, Alkaline Treatment, Resin

1 INTRODUCTION

Scientists and researchers are moving towards “green composites” to solve the issues like high prices of conventional fibers and risk towards environment [7].Green composites or Natural Fiber reinforced polymers composite made the substitution for the traditional materials. The gaining attractiveness and efficacious utilization of NFRP is because of the ecological and economic reasons. They have high specific strength and compressive strength in addition to controllable electrical conductivity and good wear resistance and unique thermal properties [1, 4]

The key advantage of using bamboo fibers as natural fibers is their “strength to weight ratio”. They are also acknowledged because of their high specific strength, abundance, low cost, viability, eco-friendliness, low specific gravity, and stiffness. The variety of the properties of bamboo fibers is comparable to glass-fibers. Additionally bamboo fibers have some advantages over conventional glass-fibers, making it as a good supplant to glass-fibers in polymer composites. That’s why, bamboo fibers are also known as ‘the natural glass-fiber’ due to its similar properties to that of the glass-fibers. [2]

Extraction of bamboo fibers from its Culm is difficult because of the presence of high lignin content in the bamboo Culm. This makes it more brittle hence causing problem during extraction. Researchers have worked on this issue and have given several processes which are utilized for the extraction of bamboo fibers to use it as reinforcement. These extraction processes include chemical extraction, mechanical extraction and combination of both extraction techniques. [5]

However, the other difficulties faced in these composites is the poor interfacial bonding with the matrix and high water absorption ability .To resolve this problem, various chemical treatments are done.

[3] Chemical treatments increase hydrophobicity of fibers resulting in better properties due to the removal of lignin. [7]

Mercerization is the physical modification of the surface of bamboo fibers by using sodium hydroxide which improves the surface of the bamboo fibers resulting in less water absorption by the treated bamboo fibers as compared to the untreated one. Alkali is used for enhancing the properties by reducing the lignin content and removing the impurities. The factors which influence the treatments are time, concentration and temperature. [4,7].

The Bamboo reinforced polymer composites have taken the market towards the new technology. Their use has been greatly increased due to diverse applications. They are being potentially used not only in commercial, construction but are also widely used in automotive industry. [11]

2 EXPERIMENTAL WORK

2.1 Extraction of fibers

First of all, extraction which is considered to be the most critical step is carried out. We have adopted the combination method i.e. chemical and mechanical. In the chemical technique, bamboo strips were dipped in alkali solution of 0.1N NaOH for 72hrs, washed and then dried for 24hrs at room temperature. After that, mechanical treatment is done by Roller mill technique in which strips are passed from rollers until the thickness is reduced to 1mm. The aspect-ratio of fibers is determined through stereomicroscopy to check that extracted fibers fall in the category of the fiber.

2.2 Mercerization

Modification of fibers is essential for improvement in surface morphology of fibers, increase in fiber-matrix bonding. Mercerization is an alkaline treatment of modifying natural fibers. We prepared solutions of two different concentrations i.e. 2mol. and 3.8 mol. The alkaline solution was made by dissolving NaOH in distilled water; fibers were kept in the solution for 4hrs and then the bamboo fibers were washed and dried in a drying oven for 72 hours to remove any moisture contained.

2.3 Fabrication of Composite:

The composite manufacturing is done by Vacuum assisted Resin Transfer Moulding VaRTM).Inside the vacuum bag, a layer of randomly oriented bamboo fibers were placed upon the wax coated glass slab and under a high vacuum, polyester resin mixed with hardener and accelerator was injected via one of the tube. After the injection of resin, the composite was allowed to cure inside the bag for about 24 hours. Three different composites (untreated, 2 mol. 3.8 mol.) were prepared to have a comparative study.

Figure 1 Vacuum assisted Resin Transfer Molding Setup

2.4 Characterization

The fibers (treated and untreated) and composite is characterized by the tensile testing to determine the fibers strength and effect on fibers strength due to mercerization treatment; and also on composite's theoritical and actual strength. Scanning Electron Microscopy (SEM) analysis of untreated, 2mol. and 3.8 mol. fibers is carried out to check the effect of mercerization on fiber surface.

3 RESULTS AND DISCUSSION

3.1 Tensile strength of bamboo fibers

The figure shows the comparison between the tensile strength of untreated bamboo fibers, treated bamboo fibers with 3.8mol NaOH and 2mol NaOH solution.

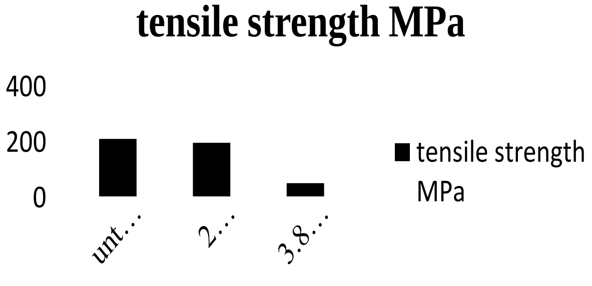

Figure 2. Bar graph of tensile strength of fibers

The untreated bamboo fibers have the highest strength among all the three. Whereas the 2mol NaOH treated fibers have strength slightly reduced than the untreated fibers because the treatment removes the lignin content at the fiber surface resulting in slight reduction of strength among the fibrils. However the fibers treated with 3.8mol NaOH solution have the lowest strength. The strength reduces because the higher concentration of alkaline solution not only remove the lignin from the fiber surface but also removes lignin between the fibril resulting n weakening of the fiber itself. Moreover the higher concentration of alkaline solution also degrades the bamboo fiber surface.

3.2 SEM Analysis of fiber surface

The surface of untreated and mercerized (2 mol and 3.8 mol NaOH) bamboo fibers were analyzed under SEM.

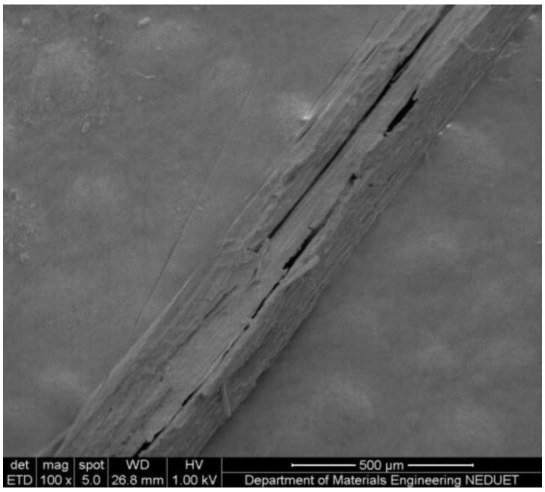

Figure 3. SEM photograph of untreated

The figure shows the surface of untreated bamboo fiber. In the above figure, it can be clearly seen that a large amount of lignin is present on the fiber surface. As this lignin is hydrophobic in nature and the polyester resin is hydrophilic so due to the presence of lignin on the fiber surface the interaction between the hydrophilic matrix and the hydrophobic fiber reduces.

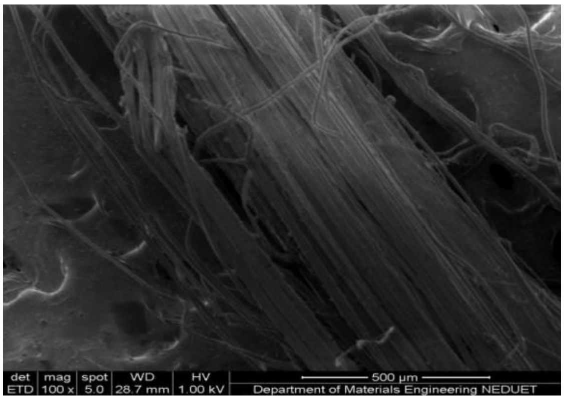

Figure 4. SEM photograph of mercerized 2mol NaOH fiber

The above figure shows the surface of mercerized fiber with 2mol NaOH solution. In the figure, it can be clearly seen that after the mercerization treatment of fibers with 2M concentration of NaOH solution, the lignin present at the fibers surface removes. But still there is some lignin content between the fibrils due to which the strength of the fibers itself remain same.

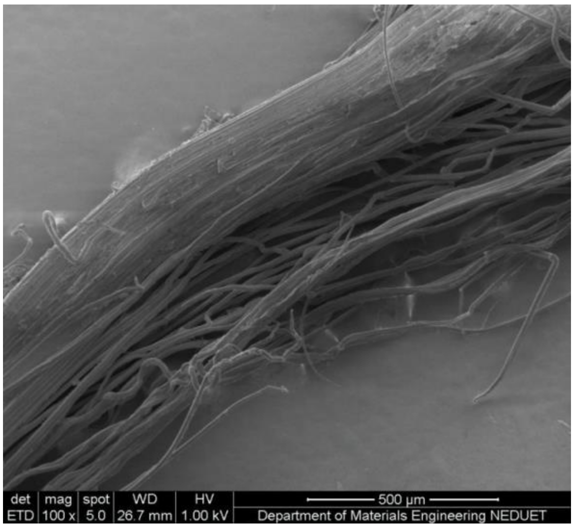

Figure 5.SEM of mercerized 3.8 mol. NaOH fiber

The above figure shows the surface of mercerized fiber with 3.8 molNaOH solution. It can be seen that due to the treatment with higher concentration of alkaline solution, the lignin content removes not only from the fibers surface but also between the fibrils, due to which the fibrils separated from each other resulting in the decrease in the fiber strength. The high concentration of NaOH solution degrades the fibers surface also.

3.3 Tensile strength of bamboo fiber reinforced polymer composite

3.3.1 Untreated composite:

The figure shows the tensile stress-strain curve of untreated BFRPC.

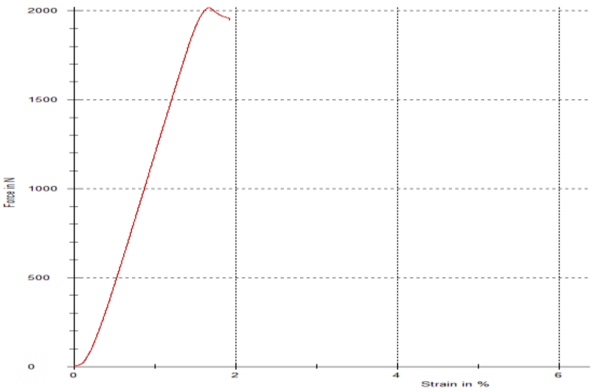

Figure 6. Tensile strength of untreated composite

From the graph, the maximum force beard by composite is found out to be 2010 N. By dividing this force with cross-sectional area of the composite, the tensile strength of composite is found out to be 20.01 MPa.

3.3.2 Treated (2 mol. NaOH) composite:

The figure shows the tensile stress strain curve of modified BFRPC with mercerized (2 mol. NaOH) fibers.

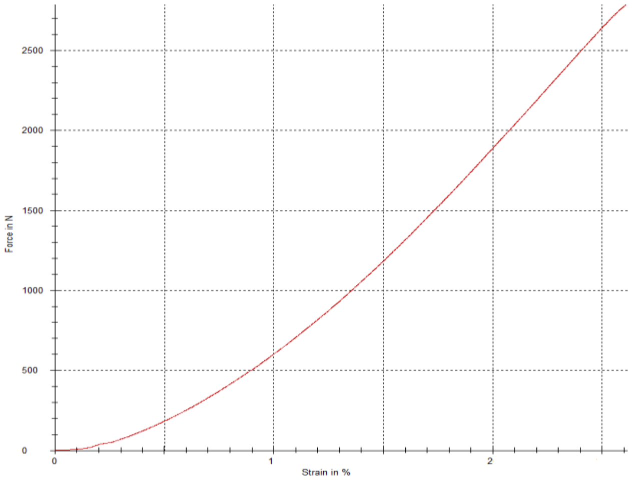

Figure 7. Tensile strength of treated (2 mol. NaOH) composite

By observing the graph, the maximum force experienced by the composite is found out to be 2798 N. By dividing the force with the cross-sectional area of composite, the tensile strength is found out to be 27.98 MPa.

3.3.3 Treated (3.8 mol. NaOH) composite:

The figure shows the tensile stress strain curve of modified BFRPC with mercerized (3.8 mol. NaOH) fibers.

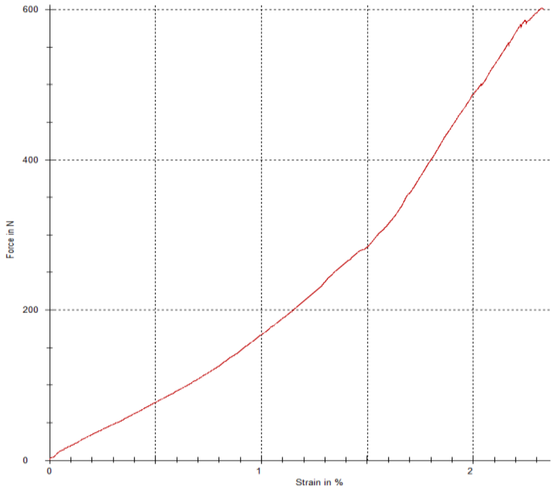

Figure 8. Tensile strength of treated (3.8 mol. NaOH) composite

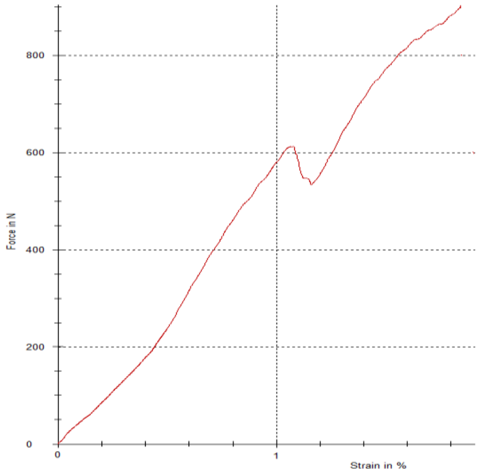

Figure 9. Tensile strength of treated (3.8 mol. NaOH) composite

By observing the figure 8 , the maximum force experienced by the composite is found out to be 601 N. By dividing the force with the cross-sectional area of composite, the tensile strength is found out to be 10.016 MPa.

By observing the above figure 9 , the maximum force experienced by the composite is found out to be 902 N. By dividing the force with the cross-sectional area of composite, the tensile strength is found out to be 15.03 MPa. From the graph, it can be observed that few fibers break at 610 N due to which a peak observed. While some fibers were still attached. And then the final fracture of the composite occurs at 902 N.

3.4 Comparative study of the tensile strength of composites:

The figure shows the comparison between the tensile strengths of untreated BFRPC, treated (2 molNaOH) BFRPC, treated (3.8 molNaOH) BFRPC and theoretical strength of composite.

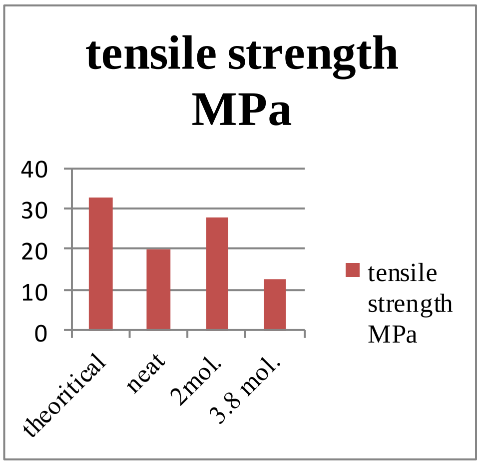

Figure 10. Bar graph of tensile strength of composite

The theoretical strength of the composite is 32.889 MPa whereas The strength of neat composite is 20.01MPa. The difference between the theoretical strength and neat composite strength is due to the poor interfacial bonding between the fibers and matrix because of the presence of large amount of lignin and impurities at the fiber surface. By modifying the fibers surface with 2M NaOH solution, the strength of composite increases to 28MPa. The increase in strength is because the modification treatment removes the lignin and other impurities from the fiber surface leading to better interfacial bonding between the polyester matrix and the bamboo fibers. Another fiber surface modification treatment was done by changing the NaOH concentration to 3.8M. The increase in the concentration of NaOH results in the surface degradation of the fiber resulting in poor strength of fiber itself. due to which the strength of composite further decreases to 12.524MPa.

3.5 Comparative study of the theoritcial and actual strength of composites

The figure shows the comparison between the theoretical and actual strength of the untreated BFRPC, treated (2 molNaOH) BFRPC and treated (3.8 molNaOH) BFRPC. All the three composites consist of 8% to 9% bamboo fibers.

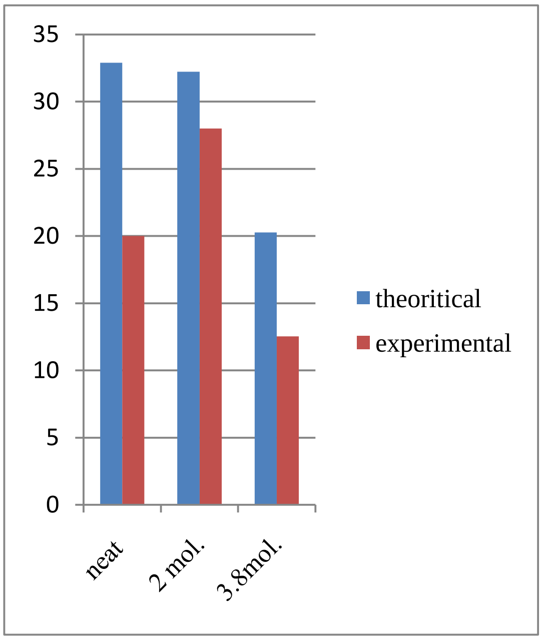

Figure11. Bar graph of theoretical and experimental strength of composites

In the figure, it can be clearly seen that there is a large difference between the theoretical and experimental strength in case of neat composite because of the poor interfacial bonding between the fibers and matrix . However in case of treated 2M NaOH composite, the difference is very small because the modification treatment improves the interfacial bonding between the fibers and the matrix. While in case of treated 3.8M NaOH composite, the difference is small as compared to neat composite. But there is difference because the fibers surface is degraded by the increase in concentration of NaOH solution which results in lowering the strength of overall composite.

4 CONCLUSION

Bamboo fibers were successfully extracted from the bamboo culm by using combined chemical and mechanical extraction techniques. The bamboo fibers were modified by the alkaline surface modification treatment, which increases the interfacial bonding between fibers and matrix by dissolving the lignin at fiber surface. The modified composite with 2mol NaOH has the highest strength among all the three composites. The modified composite with 3.8mol NaOH has the lowest strength because of the degradation of fibers surface by high concentration of NaOH. However the strength of composite achieved experimentally is lower than the theoretical strength because of the incomplete adhesion between the fibers and matrix. But the modified composite with 2mol NaOH experimental strength is nearer to the theoretical strength because of the increased interfacial bonding between fibers and matrix.

ACKNOWLEDGEMENTS

By the grace of Almighty Allah, we are able to complete our project and research work. A very special thanks to our parents whose support and encouragement motivated us to overcome all the hardships and difficulties successfully. We are thankful to our Engr. Muhammad Faizan and Engr. Danish Majeed and Engr. Humair Ahmed Siddiqui who gave their valuable time in guiding and helping us in the accomplishment of the project.

REFERENCES

[1] Extraction and preparation of bamboo fiber-reinforced composites Parnia Zakikhani , R. Zahari , M.T.H. Sultan, D.L. Majid

[2] Development of bamboo-based polymer composites and their mechanical properties Kazuya Okubo, Toru Fujii, Yuzo Yamamoto

[3] Bamboo fiber and its reinforced composites: structure and properties Dagang Liu • Jianwei Song • Debbie P. Anderson •Peter R. Chang • Yan Hua

[4] Bamboo fibre reinforced biocomposites: A review H.P.S. Abdul Khalil ,I.U.H.Bhat ,M. Jawaid ,A. Zaidon ,D. Hermawan ,Y.S. Hadi

[5] Thermal conductivity characterization of Bamboo Fiber Reinforced Polyester Composite M.Mounikal, K. Ramaniah, A.V. Ratna Prasad, K. Mohana Rao, K. Hema Chandra Reddy

[6] Extraction of Bamboo Fibers and Their use as Reinforcement in Polymeric Composites ABHIJIT P. DESHPANDE, M. BHASKAR RAO, C. LAKSHMANA RAO

[7] Synthetic Polymer Composites Reinforced by Bamboo Fibers Jean-Marc Saiter, Antonella Esposito, Larisa Dobircau, Joseph A Turner, Rameshwar Adhikari

[8] Effect of Different Parameters on Mechanical and Erosion Wear Behavior of Bamboo Fiber Reinforced Epoxy Composites Anu Gupta, Ajit Kumar, Amar Patnaik, and Sandhyarani Biswas

[9] Flexural modulus of the unidirectional and random composites made from biodegradable resin and bamboo and kenaf fibers Shinichi Shibata a,*, Yong Cao b, Isao Fukumoto a

[10] Materials science and engineering-an introduction-8th edition William D.Callister, Jr.David G Rethwisch

DESIGN AND FABRICATION OF SMALL SCALE PORTABLE FLOATING DOME BIODIGESTER

Waqar Ahmed, Danish Lakhani, Zahoor UlHussain Awan*, Saud Hashmi*, AhmedUllah
Department of Chemical Engineering, NED University of Engineering and Technology
Karachi, Pakistan

E-mail address:engr_waqar93@yahoo.com, danishlakhani33@gmail.com

ABSTRACT

Throughout the world awareness has been created on the disadvantages of relying on fossil fuels such as fluctuation in prices oil based fuels and their hazardous impact on the environment, due to these reasons people are diverting their attention from non-renewable resources towards renewable resources in order to fulfill their energy demands in a more sustainable and reliable way. Pakistan is an agricultural country and livestock is a major sub-sector and a major contributor to the national GDP of Pakistan. This industry produces huge waste and this waste can be utilized in production of bio-gas which will help to reduce energy crisis in Pakistan. Karachi being a densely populated city and people who are living in its outskirts suffered from problems such as shortage of gas and poor waste management. The anaerobic digestion of cow dung will not only serve as cheap source of fuel but will also help in waste management. The objective of this study is to design a low cost portable bio-digester to produce biogas, an efficient energy solution for remote areas of Karachi and other rural areas of Pakistan. For this purpose, designing and fabrication of 417L capacity floating dome type bio-digester is carried out. Several changes were incorporated in the digester design such as paddle mixer was introduced horizontally in the middle of the digester to prevent froth accumulation and for efficient mixing; drain was introduced at the bottom of the bio-reactor for easy cleaning and removal of exhaust slurry. In this study biogas production was investigated in which potential of cow dung (CD) and its blend with sludge water (SW) in the ratio of 1:1 was charged with a small quantity of food waste and pH varied between 6.8 and 7 throughout the retention time. Anaerobic digestion was carried out in a mesophilic temperature conditions ($28^{O}C$-$37^{O}C$) with 30 days hydraulic retention time (HRT). This study shows that a blend of cow dung and sludge water with small quantity of food waste confirms a sufficient and sustained quantity of gas under the digestion period. Composition analysis showed average methane content was found to be 65%.

Keywords---Biogas, anaerobic digestion, cow dung, Floating Dome, Bio digester

1. INTRODUCTION

After industrial revolution in 1760, the demand for fossil fuels rose, this resulted in depletion of conventional fuel reserves at a faster rate. Hence, prices of these convectional fuels rose from $19 per barrel of oil in 1998 to $48 per barrel in 2015. These convectional fuels are not only non-renewable but the pollution caused by these fuels has adverse effect on the environment, these fuels are the major cause for global warming.

Pakistan, being a nuclear power and is possessed with almost all type of minerals inside its earth crust is still facing energy crises; this is effecting its growth and development in various areas of advancement. Saleh et al reports that the imports of these convectional energy sources accounted for 40% total imports of Pakistan. It is expected that it will increase three times by 2050 [1].

Large amount of organic waste is produced by industry, particularly food, agriculture, municipal waste and cattle slurries. Decomposition of these wastes in an open environment can cause large scale contamination of land, water and air. There is a need for treatment and safe disposal for biodegradable wastes to reduce emission of greenhouse gases. These wastes can be treated using anaerobic digestion as an alternative. It is an efficient way to reduce waste volume and recovery of valuable waste products. It is neutral in pH and odorless with the possibility of nutrient recycling if applied to land as fertilizer [2].

Renewable sources of energy offer the most potential energy conservation and development option for future [3]. Being a source of renewable natural gas, Biogas has been adopted as one of the best alternatives for fossil fuels **after 1970's world energy crisi**s.

In 2022, the energy requirement of Pakistan will be 50,000MW, from power generation of 14,000MW in 2008/7. Pakistan is heavily dependent on import of hydrocarbons, the import bill in 2007/8 was USD 12 billion and it is estimated that it will be USD 41 billion in 2022, based on crude oil price of USD 70 per barrel. The government of Pakistan plans to increase renewable share to 12% in 2022 [4].

Biogas in Pakistan is not a new idea. The Government of Pakistan started a comprehensive biogas scheme in 1974[5]. In 1976 Appropriate Technology Development Organization (ATDO) installed 21 Chinese-type fixed dome plants, but was reportedly not successful due to persistent leakage, seepage and pressure problem. After that Indian design was adopted. In 1986 DGNERER (Directorate General of New and Renewable Energy Resources) installed 4000 biogas plant under PSDP project but due to lack of technical knowledge and poor field experience this project was not implemented properly. In 1993 fifty biogas plants were installed in outskirts of Islamabad/ Rawalpindi in collaboration with NGO. In 2007 Pakistan Council of Renewable Energy Technologies were assigned a task to install 2500 plants by 2008 [5, 6]. Biogas energy corridor can work as a good substitute for nearly 70% of country's population residing in rural areas of Pakistan. Installation of plants to bottle the biogas is an additional opportunity for creating jobs. The need of a national policy is imperative to bring this technology at farmer's doorstep [7].According to International Renewable Agency (IRENA) estimates that renewable energy employed 7.7 million people, directly or indirectly, around the world in 2014 in which 381,000 associated with only biogas [8].

Pakistan is an agriculture country and agriculture sector contributes 21.0 percent to country GDP (Gross Domestic Product) [9]. Livestock is the major sub-sector that accounts for 51.8 percent in agriculture sector and about 11.3 percent of national GDP [10]. According to livestock census 2006, there are 59 million animal heads (buffaloes and cows) in Pakistan owned by small and big farmers. These animals are producing 590 million kilograms of dung per day. Assuming 50 per cent collectability, the waste will produce 9 million cubic meters of gas per day [11].

Only Karachi, the biggest city of Pakistan has five big cattle colonies.

1. Bhains Colony, Landhi
2. Al-Momin Cattle Colony, Gadap
3. Nagori Cattle colony, Super Highway
4. Surjani Cattle Colony
5. Bilal Cattle Colony, Korangi Industrial Area

Karachi has a cattle population of 1 million from which 40 percent cattle heads are present in Landhi Cattle colony. It is estimated that 8000 tons of manure is produced daily from this colony [12]. This plentiful amount of waste could be transform into useful form of energy for remote areas of Karachi.

Biogas production will help to create employment opportunities for the potential producer and marketer apart from sanitizing the environment of indiscriminately dumped agro-industrial by products, refuse and animal dung [13].

The anaerobic digestion of organic wastes generates biogas with a composition that is approximately 60% methane (CH_4) along with 38% carbon dioxide (CO_2). The remaining 2% is water vapors, ammonia (NH_3) and hydrogen sulfide (H_2S) [2]. Production of bio-gas is a complex process; it involves decomposition of biomass in the absence of oxygen. Micro-biological process includes hydrolysis, acedogenesis, acetogenesis and methanogenesis [14].

$$C_6H_{10}O_4 + 2H_2O \rightarrow C_6H_{12}O_6 + 2H_2$$

$$C_6H_{12}O_6 \rightarrow 2CH_3CH_2OH + 2CO_2$$

$$C_6H_{12}O_6 \rightarrow 3CH_3COOH$$

$$CH_3COOH \rightarrow CH_4 + CO_2$$

Ravita D. Parsad et al studied the anaerobic digestion of cow dung and composition of methane was found to be 64.1% [15].

2. FLOATING DOME BIO-DIGESTER

Material of Construction

The digester was made of mild steel which is commonly available in local market. It was chosen because of ease of fabrication and its low cost as compared to other materials and then it was coated with corrosion resistant paint. Specification of mild steel is shown in table 1.

Design Characteristics

A portable, prototype modified design of Floating Dome Bio digester of 417L capacity was designed, fabricated and experimentally tested for the production of biogas. The design consisted of a movable inverted metal drum (9 in figure 1) placed on a cylindrical-shaped digester to ensure anaerobic digestion of organic waste to generate biogas. This inverted steel drum also acts as a gas storage tank for biogas. This design has number of advantages over other designs such as gas is available at constant pressure and volume of the gas produced is directly visible and proportional to the rise in height of gas holder.

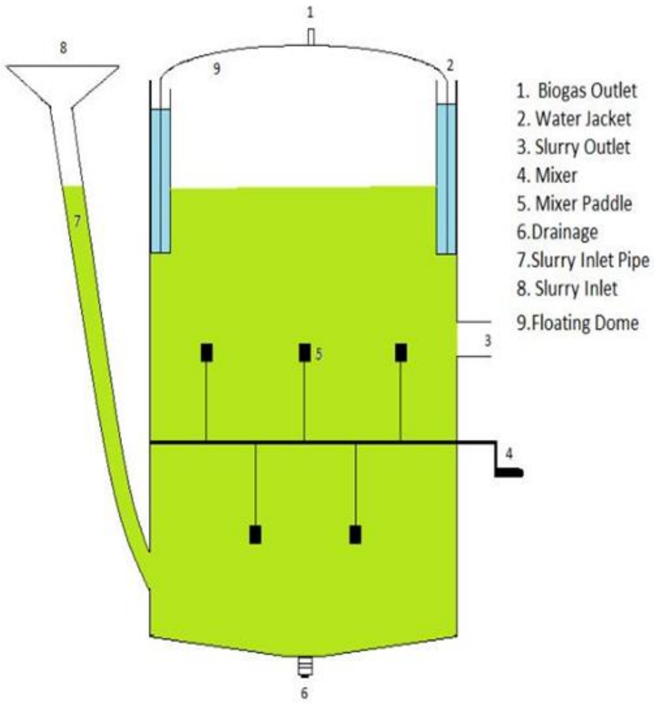

Figure.1. Schematic Diagram of Bio-Digester

Figure.2. Biogas Digester

Table.1. Sizing of Bio-Digester

1	Height of Bio digester	3'	7	Drainage Socket	2"
2	Diameter of Bio digester	2.5'	8	Length of Inlet Pipe	2.9'
3	Height to Diameter Ratio	1.2	9	Length of Outlet Pipe	6"
4	Diameter of Slurry Inlet Pipe	4"	10	Empty Space	0.5'
5	Diameter of Slurry Outlet Pipe	4"	11	Clearance of Water Jacket Collar	1"
6	Angle of Slurry Inlet Pipe	30°	12	Height of Water Jacket	1'

2.3. Designing of Bio-Digester

A biogas digester is essentially a chemical reactor which is connected to inflow and outflow channel. Biogas yield, not only depends on the biodegradability of material or micro-organisms growth it also depends on dispersion of organic solids within the digester. For biogas production following parameter must be considered [16]:

1. Retention time.
2. Specific gas production per day.
3. Amount of fermented slurry.

Design of bio digester can be varied according availability of feedstock, geological location and weather conditions.

Volume of Biodigester

V_{Bd} = Volume of Bio-**digester =** $\boldsymbol{\pi/4\ (D)^2}H$

H = 0.9144m D = 0.762m

V_{Bd} = $\boldsymbol{\pi/4(0.762)^2}(0.9144)$

V_{Bd} = 0.417 m^3 (417 Liters)

Volume of Gas Holder

V_{Gh} **= Volume of Gas Holder =** $\boldsymbol{\pi / 4(D)^2}$ H

H = 0.3048m (1 ft) D = 0.736m

V_{Gh} = $\boldsymbol{\pi/4(0.736)^2}(0.3048)$

V_{Gh} = 0.130 m^3 (130 Liters)

15% left for Disengagement of Gas = 0.0625m^3
= (62.5 Liters)

Total Slurry Volume in Digester = 0.3545m^3
= (354.5 Liters)

V_{Bd} = Retention Time x Amount of Fermented Slurry

Retention Time = 30 Days

Amount of Fermented Slurry = V_{Bd} /Retention Time
= 0.3545/30
= 0.01181m^3/day
= (11.81 Liters/day)

Mixing Ratio of Feed = 1:1

Mass = Density x Volume

Density of Slurry = 1100 Kg/m^3

Mass of Slurry = (1100 x 0.01181) = 13 Kg/day

1 Kg of Cow Dung Yields 0.030 m^3 of Biogas
Specific Gas Production = (30 Liters/kg)
Amount of Feed Material = 13/2
= 6.5 Kg/day
Daily Gas Production = Amount of feed material x Specific gas production
= 6.5 x 0.030
= 0.195 m^3/day
= (195 Liters/day)

3. MATERIALS

In this study, co digestion of cow dung (CD) and sludge water (SW) was chosen as the feedstock because cow dung and sludge water were easily available.

Cow dung was taken from a local dairy farm and stored in a drum at a room temperature. Unwanted coarse particles and breeding straws were removed manually from cow dung. Sludge water was collected from the sewerage line of chemical engineering department.

4. METHODS

4.1. Analytical Method

Samples of feed material were taken to determine volatile, fixed, total solid and moisture content by standard method (1684) provided by US environmental protection agency [17].Tests were performed on two samples to analyze the composition of feed. Moisture content and total content was calculated by initially weighing and heating the samples in evaporating dish in an oven at 103°C to 105°C for an hour (Figure.3). After an hour samples were cooled in a glass jar containing silica gel to and then it was reweighed to calculate the moisture and solid content. Dried samples were then transferred into petri dish which were labeled and weighed before it was kept in muffle furnace for 1.5 hours at 550°C (Figure.4). After this process it was reweighed to calculate the volatile solids and fixed solids in the sample. Before feeding the reactor, pH of sludge water and feed slurry was measured using digital pH meter. Gas samples were collected in rubber balloon and then composition was analyzed using flue gas analyzer in automotive department of NED University.

Figure.3. Testing of Moisture Content

Figure.4. Muffle Furnace

The pH of sludge water was 7.35 and when mixed with cow dung pH was 7.18. The results of total solid, volatile solids and moisture content was calculated from standard methods using the following formulas:

$$\%\text{Total Solid} = \frac{\text{W(total)} - \text{W(dish)}}{\text{W(sample)} - \text{W(dish)}} \times 100$$

$$\%\text{Fixed Solid} = \frac{\text{W(volatile)} - \text{W(dish)}}{\text{W(total)} - \text{W(dish)}} \times 100$$

$$\%\text{Fixed Solid} = \frac{\text{W(total)} - \text{W(volatile)}}{\text{W(total)} - \text{W(dish)}} \times 100$$

Design of Experiment

The anaerobic digestion was carried out in the floating dome biodigester. A homogenous mixture was prepared by mixing sludge water and buffalo/cow dung in equal proportion. The experiment was performed for retention period of 30 days in a mesophilic temperature range of 28^{O}C-37^{O}C. The pH and temperature were measured periodically during the digestion period.

Initially, digester was charged with 20kg of cow dung and 20 Liters of sludge water to prepare inoculum. After 5 days interval flammability test was performed by opening gas outlet valve (6 in figure1) to identify when the composition of methane in gas reached to flammability level. The gas didn't burned, but the flame of the match stick vanished immediately, indicating the presence of carbon dioxide. We assumed that at this stage, the reactor is in hydrolysis/acedogenesis stage. The contents of reactor were mixed slowly and manually on daily basis by means of paddle mixer as vigorous mixing would led to increase in death rate of microorganisms. Again after 10 days, flammability test was performed. The gas volume was sufficient to produce flame and burned with light blue discontinuous flame. On 15th day, when the methanogenic conditions were reached and maintained, then 120kg of dung and 120 liters of sludge water mixture were added. It was observed that as the feed was added dome began to rise to accommodate the entrapped gas in the reactor, showing sufficient gas production; on 25th day the position of the dome with respect to height was measured. It observed that the dome rose to 6 inches above its rest position showing collection of gas in that region of the dome. Pressure gauge showed that pressure inside the reactor is of 1.14 bar.

5. RESULT & DISCUSSION

Table.3 shows composition of feed material (cow dung) including TS, VS, FS and moisture contents of two samples.

Table 3.Result of VS, TS, FS and moisture

Feed	Sample 1	Sample 2	Average
% Moisture	31.1	26.8	28.9
% Total	68.9	73.2	71.1
% Volatile Solids	76.7	63.9	70.3
% Fixed Solids	23.3	36.1	29.7

Average of the two samples was taken so that the variation is minimized. The volatile solids in the mixture of cow dung and water produced enough gas that can be used for domestic purpose.

Table 4.Biogas Composition

Testing	Results
Composition	65% CH_4 , 35% CO_2
Flammability	Gas burned with light blue flame
pH	6.8-7.3
Gas Flow rate	3.2 L/min

When the biogas composition was tested its composition was 65% methane gas having net calorific value between 22-23 MJ/m^3. The gas burned with a continuous light blue flame due to the presence of CO_2. The pH of digested slurry varied between 6.8 and 7.3 throughout the digestion period. Gas flow rate was measured to be 3.2L/min, which depends on the weight of dome.

6. CONCLUSION

This reactor is easy to operate and supplies gas at a constant rate as constant pressure is provided by the weight and the movement of the dome, stirrer is introduced horizontally to increase the contact area between substrate and micro-organisms. It can be cleaned easily as exhaust slurry disposal is due to gravity from the bottom of the tank. It is painted black so it absorbs maximum heat from the surroundings.

Bio-digesters represent a boon for farmers and people (living in suburbs areas) to meet their energy requirements. This design requires low space as compared to traditional digesters and is easy to operate. From the results, it can be concluded that Cow Dung which is available in abundance in Pakistan especially in Karachi is a very good source of waste for Biogas production. Micro-economic benefits through energy and fertilizer substitution, additional income sources and increasing yields of animal husbandry and agriculture are other benefits. So Biogas is a good alternative source of energy and has potential to create huge number of jobs in Pakistan. The study also shows that blend of cow dung and sludge water will give sustained flammability throughout the digestion period.

Aman foundation has partnered with K-Electric and has plans to produce 11 megawatts of electricity from 2,400 tons of waste per day. The residual content will be processed into 250 tons per day high quality fertilizer

7. REFERENCE

[1] Absar Saleh," *Biogas Potential in Pakistan*" **Department of Chemical** Engineering Comsats, 2012.

[2] Zuhaib **Siddique, "***Optimisation of Hydrogen and Methane Production from Co-digested Food Waste and Biosolids using Phase Separated Anaerobic Digestion***"** School of Civil Engineering Leeds, 2010

[3] Akuzuo U, Nwankwo, Joseph I, Ibeto, Cynthia N Ofoefule, *"Biogas Production from Paper waste and its blend with Cow dung,"* Pelagia Research Library, Advances in Applied Science Research, 2010.

[4] Energy Expert Group, "Integrated Energy Plan 2009-2022," Islamabad, 2009.

[5] Prakash C. Ghimire, *Technical Study of Biogas Plants Installed in Pakistan*, Asia/Africa Biogas Programme Netherlands Development Organization (SNV) (2007).

[6] *Biogas Technology,* Appropriate Technology Development Organization, Islamabad

[7] Syed S. Amjid' , Muhammad Q. Bilal, Muhammad S. Nazir, Altaf Hussain*, Biogas, renewable energy resource for Pakistan***,** Department of Livestock Management, University of Agriculture, Faisalabad, Pakistan (2011).

[8] Renewable Energy and jobs annual review," in International renewable energy agency, 2015

[9] Finance Division, Government of Pakistan, Islamabad Economic **Adviser's Wing,** *"Highlights of Pakistan Economic survey 2013-2014,"* Government of Pakistan, Islamabad, 2013-2014.

[10] Munir Ahmad and Ikram Saeed Umar Farooq, *"Livestock Productivity in the Desert Ecologies of Pakistan:Setting the Development Priorities,"*.

[11] Muhammad Yasin, Irfan Ali Abdul Wahab Siyal, *"Performance Evaluation of Fixed dome and Floating type Biogas digesters for Tubewell operation with dual Fuel Approach in Pakistan,"*International Journal of Innovation and Applied Studies ISSN 2028-9324 Vol. 10, pp. 1225-1232, 2015.

[12] The news*, "Biogas plant commissioned in Landhi Cattle Colony*," Karachi, 2008.

[13] I.A.Adesokan, K.D Afolabi and A.H Ekeochal O.I Adeyosoye, *"Estimitation of proximate composition and biogas production from in vitro gas fermentation of sweet potato (Ipomea batatas) and wild cocoyam (Colocasia esculenta) peels.,"*African journal of environmental science, 2010.

[15] **Ayşe Hilal Yilmaz,** "*Modeling of the Anaerobic Decomposition of Solid wastes*," Energy sources, 2003. Ravita D.Parsad, "*Emperical study on factors affecting biogas production*," in ISRN Renewable energy, 2012.

[16] B.T.Nijaguna,*Biogas Technology*. Banglore, India: New Age International, 2006

[17] U.S. Environmental Protection Agency, *"Method 1684 Total, Fixed and Volatile Solids in Water, Solids and Biosolids,"* 2001.

SYNTHESIS OF HYDROGEL MEMBRANE AND ITS CHARACTERIZATION

Asif Jan*, Raza Wasim, Ahmer Saeed and Muhammad Faizan
Materials Engineering Department, NED University of Engineering & Technology, Karachi, Pakistan

Corresponding author. Tel.: +92-335-3305029; fax: +###-########
E-mail address: asifjan! 992@gmail.com (Asif Jan)

ABSTRACT

Hydrogel consists of long polymeric chains which are cross linked to each other. The three dimensional porous structure of hydrogel has the ability to absorb water up to five hundred times of its weight which is caused by its hydrophilic nature. This coruscating property of hydrogel makes it competent in variety of industrial and environmental applications. A new hydrogel synthesis technique was devised and put in to practice which utilizes a natural polymer (corn starch) and a cross linking agent (formaldehyde). The cardinal cause of using cheap and natural constituents was reduction in total synthesis cost while preserving the marvellous water absorbing property of hydrogel. The hydrogel membrane obtained was characterized using x-ray diffraction, Fourier transform infrared radiation spectroscopy, swelling behaviour test, swelling rate, evaporation rate, pH test and stereo microscopy. The characterization techniques employed proved that the hydrogel is pH sensitive and completely capable of absorbing water in its structure.

Keywords: Hydrogel, membrane, water absorption, absorption, polymer

1 INTRODUCTION

A hydrogel is a network of polymer chains that are hydrophilic, sometimes found as a colloidal gel in which water is the dispersion medium. Hydrogels are highly absorbent (they can contain over 500 to 600% water) natural or synthetic polymeric networks. A hydrogel is an example of smart material that can alter their structure in response to pH, temperature and pressure.

There are three methods for the cross linking of PVA hydro gels; physical bonding, chemical bonding and through radiations. When the cross linking was done by physical mean then the mechanical properties were found to be good as compare with other two methods but the process of freezing and thawing was a lengthy one and required repetitive cycles for the improvement of mechanical properties of PVA hydro gels.

Cross linking of PVA hydro gels through radiations was an easiest process but there was a hazard of exposure of dangerous and harmful radiations to the human body which can cause of cancer in future.

Another problem was the availability of such equipment which can produce gamma radiations is restricted. This method was also expensive or costly as compare with other two methods.

The third method of cross linking of PVA hydro gels was chemical cross linking. This method produced hydro gels with low mechanical properties but this method consume less time. To improve its mechanical properties, various experiments were conducted with different chemicals. Polysaccharides are, in general, non-toxic, biocompatible, biodegradable, and abundant. However if the polysaccharide dissolves in water it cannot form stable hydro gel. One effective method to avoid these limitations is to combine them into a synthesized polymer blend hydro gels, which is becoming a subject of academic as well as of industrial interest. Starch is one of the most abundant and cheap polysaccharides. PVA and corn starch blend was prepared by chemical cross linking technique to achieve good mechanical properties at low cost and for biomedical applications.

Hydrogel has very vast applications ranging from medical uses to agricultural uses. It provides moisture to the wounded area and since it is transparent so the healing activity can be clearly seen without removing the dressing. Hydrogels are used storehouses for various drugs. Since Hydrogels are biocompatible and their drug release rate can be controlled by their reaction with the bio-molecular stimuli. Contact lenses are made of water loving hydrogel. Hydrogels absorb water to keep lenses soft and flexible. Since hydrogel can store water up to 500 to 600% of its weight so during dry season's hydrogel will hold soil moisture and it will provide water and nutrients to root system of the plant which is vital for its growth.

2 EXPERIMENT

2.1 Materials

Polyvinyl alcohol (PVA) powder, cornstarch powder and HCl 37% concentrated solution were obtained or provided from the Materials Engineering Department. Ethanol 95% pure, formaldehyde and distilled water were purchased from local market of Karachi.

2.2 Method for Hydrogel Preparation

Prepare a solution of PVA of 10% (w/v) in distilled water. Then prepare a dispersion of cornstarch of 5% (w/v) in distilled water at 100˚C. Then prepare a reagent of formaldehyde, ethanol and HCl of 11.15% (v/v). This reagent contains 2.22% of formaldehyde, 8.89% of ethanol and 0.04% of HCl, which is the total of 11.15%. After preparation of PVA solution and cornstarch dispersion, the cornstarch dispersion is added into the PVA solution with continuous stirring to achieve a homogeneous mixture. In this mixture, add the formaldehyde (11.15%) reagent which was prepared, with constant stirring to avoid from any air bubbles entrapment. Finally cast the solution by conventional solution casting method on a non sticky surface, or use wax on the glass plate, for the easy removal of casted hydrogel membrane.

3 CHARACTERIZATION

Characterization is a very important stage to ensure that the product has all the desired properties. After the synthesis of Hydrogel membrane its characterization was carried out using XRD, FTIR, Stereo microscopy, Swelling behaviour test, PH test, Evaporation rate, Swelling rate and Absorbance comparison test.

3.1 Swelling behaviour

To analyze the swelling behavior of the hydrogel, the hydrogel was immersed in water of known pH (i.e. 8.2). Hydrogel was weighted before and after it was immersed in water and the difference in the weight was calculated to determine the water stored in the structure by the following formula;

% Swelling = (Wh- Wd)/Wd X 100

Where, Wh is the weight of the product after hydration while Wd is the weight of the dried product.

3.2 Swelling rate

To analyze the swelling rate of the hydrogel it was immersed in a solution of know pH (i.e. 8.2) for a time of 10 min. and weight the sample and repeat it for 8 to 9 times. This gave us idea about the rate at which the hydrogel swells given it is immersed in a solution.

3.3 pH test

To show that the absorbance of Hydrogel is pH dependent it was immersed in different solutions of known pH (i.e. 1.5, 5.4, 7.2 and 9.7) for one day.

3.4 Evaporation rate

Evaporation rate test was also performed to find the rate at which hydrogel evaporates the water stored in its structure. Evaporate the stored water with the help of oven at 100^{o}C and weight the sample after one minute intervals.

3.5 Stereo microscopy

Stereo microscopy was also performed to observe thickness of the membrane, transparency and surface topology.

4 RESULTS AND DISCUSSIONS

4.1 Swelling behaviour

The dry sample weight was noted (i.e. Wd = 0.32 gm) and then immersed in tap water whose pH was noted 8.2. After one day, the hydrated sample weight was noted (i.e. Wh = 2.11 gm). Then the swelling of the sample was found in terms of percentage with the help of given formula (i.e. %Swelling = (Wh-Wd /Wd) x 100). The % swelling was found about 559.375 % of the dry sample weight, which was remarkably high. From this characterization technique, the most important property of hydrogel i.e. water absorption capability was confirmed.

4.2 Swelling rate

A graph shown in Figure 1 indicate that the swelling rate of hydrogel membrane was rapid initially but after some time it decreases and then achieved to equilibrium swelling point at which the membrane stopped absorbing more water. This behavior may be due to the presence of larger voids in network initially and also due to size increase of voids as the entrapped corn starch dissolve in solution. After some time this rate decreases as the space in voids also decrease by the time and finally results in completely filled hydrogel network.

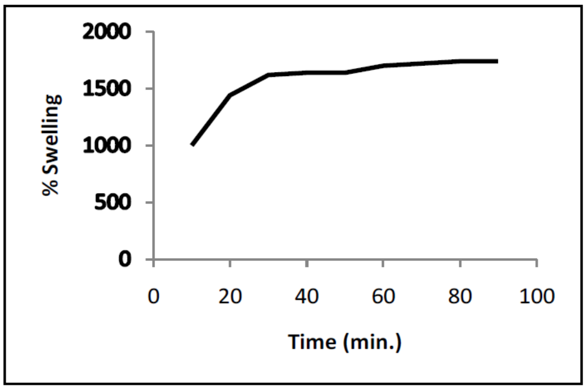

Figure 1. Graph showing swelling rate of hydrogel membrane

4.3 pH test

In Figure 2 it is clearly shown that the absorbing capability of hydrogel is comparatively lower in solution with acidic pH then the solutions which have or close to basic pH. This behavior may be due to the fact that in basic or alkaline medium corn starch become soluble and uncross linked starch entrapped in cross linked network, start dissolving and increase the size of voids present in the network. On the other hand in acidic medium free hydroxyl group converted into oxonium salts which increase its size and decrease the voids size in the network and results in low absorption capacity.

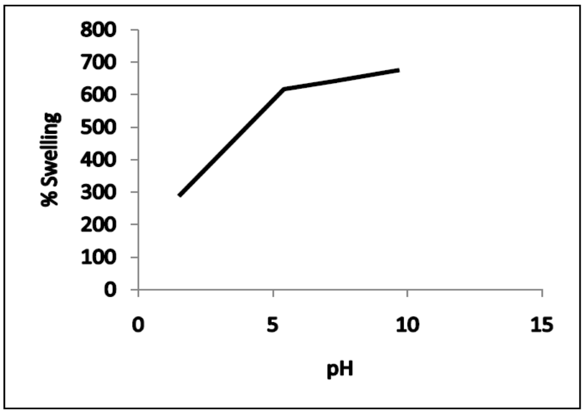

Figure 2. Graph showing pH sensitive behaviour of hydrogel membrane

4.4 Evaporation rate

In Figure 3, higher rate of evaporation is clearly shown, initially. It may be the fact that the water entrapped in voids of network evaporates rapidly. Then this rate become slower may because of the water attached with hydrophilic ends of network which require higher energy to detached and evaporate. Second time increase in rate may be due to the separation of attached water is rapid and also start to evaporates rapidly. Finally the water completely separated from the hydrogel network and evaporates at constant rate

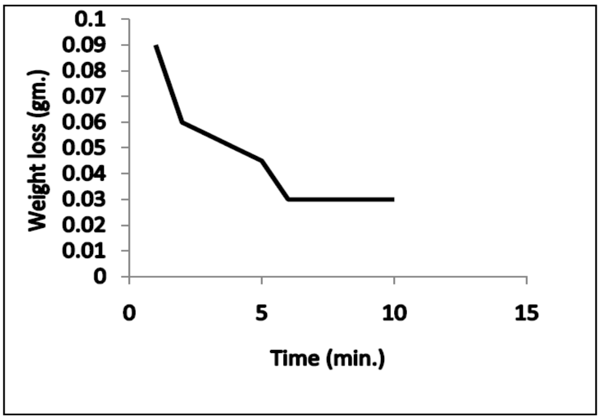

Figure 3. Graph showing evaporation rate of hydrogel membrane

4.5 Stereo microscopy

With the help of stereo microscope thickness of membrane was noted which is shown in Figures 4 and 5. Average thickness was noted about 353.45 |im. In Figure 6 transparency of membrane is shown in which the membrane is translucent. The membrane is translucent because some PVA and Corn starch was not dissolve during the synthesis of membrane and also results in non-homogeneous surface which is shown in Figure 7.

Figures 4 and 5. Showing thickness of membrane

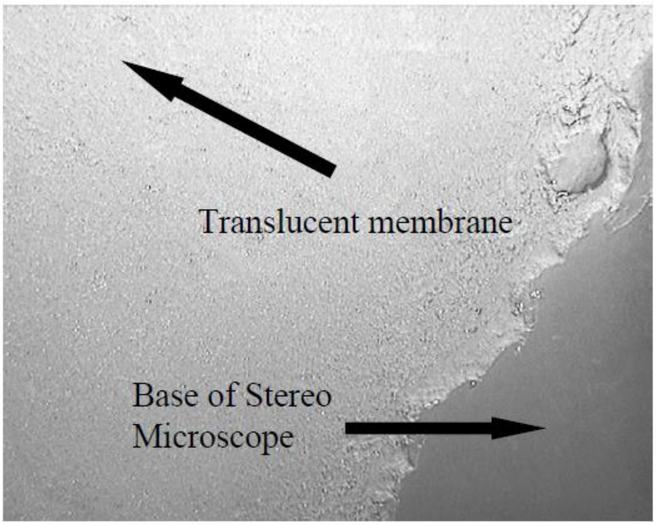

Figure 6. Showing transparency

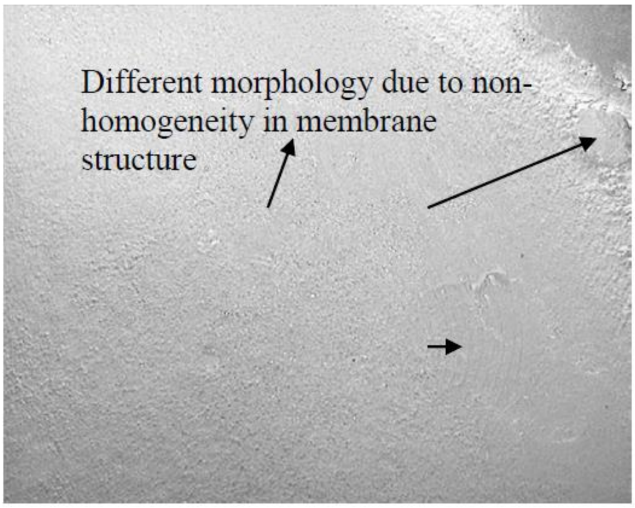

Figure 7. Non-homogeneous surface morphology is shown

CONCLUSION

The materials used for the synthesis of hydrogel membrane in this experiment are available at low cost. Although the materials used are cheaper but produced an extraordinary product of hydrogel with fantastic water absorption capability which is about 500 to 600%. Beside this coruscating property another astonishing behaviour was observed in obtained translucent hydrogel membrane that is its pH sensitivity. The product is highly pH sensitive and this give up to 50% change in its water absorption property. Some other properties were also evaluated of membrane that is its high swelling rate and low evaporation rate of absorbed water in the hydrogel structure. These marvellous properties make this material a superior choice for several different applications such as, in medical for wound dressings and during healing of wound its monitoring. It can also be used in advanced drug delivery systems. Hydrogel also used in contact lenses. It can be used in fertilizers for watering the plants and can be used in other several potential applications

ACKNOWLEDGEMENTS

The authors are thankful to materials engineering department for providing raw materials for the experiment and also allowing using their laboratories without any interference.

REFERENCES

[1] Kunal Pal, A.K.Banthia, D.K.Majumdar; "*Preparation of Transparent Starch Based Hydrogel Membrane with Potential Application as Wound Dressing*."; Trends Biomater. Artif. 0rgans.(2006); Vol. 20(1); pp 5967

[2] Elbadawy A. Kamoun, Xin Chen, Mohamed S. Mohy Eldin, El-Refaie S. Kenawy; "*Crosslinked poly (vinyl alcohol) hydrogels for wound dressing applications: A review of remarkably blended polymers*."; Arabian Journal of Chemistry (2015);vol. 8,pp 1-14

[3] Jaleh Varshosaz,Niloufar Koopaie; *"Cross-linked Poly (vinyl alcohol) Hydrogel : Study of Swelling and Drug Release Behaviour";* Iranian Polymer Journal (2002); Volume 11 Number 2;pp 123-131

Contact

Department of Chemical Engineering and
Department of Polymer & Petrochemical Engineering
NED University of Engineering & Technology,
Karachi Pakistan
Phone: (+92-21)99261261 ext 2577,2286, 2404
Fax: (+92-21)99261255
Email: ampe@neduet.edu.pk
www.nedampe.com